Optimization of Signal versus Background in Liquid Xe Detectors Used for Dark Matter Direct Detection Experiments

by

Luiz de Viveiros

Submitted in partial fulfillment of the requirements

for the degree of Doctor of Philosophy

in the Program in Physics at Brown University

Providence, Rhode Island

May 2010

This dissertation by Luiz de Viveiros is accepted in its present form

by the Physics Department as satisfying the dissertation requirement

for the degree of Doctor of Philosophy.

Date: _____   _____

Richard Gaitskell, Advisor

Recommended to the Graduate Council

Date: _____   _____

Ian Dell'Antonio, Reader

Date: _____   _____

Greg Landsberg, Reader

Approved by the Graduate Council

Date: _____   _____

Sheila Bonde, Dean of the Graduate School

Curriculum Vitae

1979	Born in São Luís, Brazil.
2001	B.A., Clark University, Worcester (USA).

Appointments and Teaching

2003-	Research Assistant. Brown University, Physics Department, Providence (USA)
2008-2009	Teaching Certificate I. Brown University, Sheridan Center for Teaching and Learning, Providence (USA).
2002-2003	Teaching Assistant. Brown University, Physics Department, Providence (USA)
2001-2002	Research Assistant. Clark University, Physics Department, Providence (USA)
1999-2001	Undergraduate Teaching Assistant. Clark University, Physics Department, Providence (USA)
1998-2001	Summer Undergraduate Research Assistant. Clark University, Physics Department, Providence (USA)

Refereed Publications

- P. Sorensen et al., *The scintillation and ionization yield of liquid xenon for nuclear recoils*, Nucl. Instrum. Meth., 2009, A601, 339-346.

- J. Angle et al., *Limits on spin-dependent WIMP-nucleon cross-sections from the XENON10 experiment*, Phys. Rev. Lett., 2008, 101, 091301.

- J. Angle et al., *First Results from the XENON10 Dark Matter Experiment at the Gran Sasso National Laboratory*, Phys. Rev. Lett., 2008, 100, 021303.

- E. Aprile et al., *Simultaneous Measurement of Ionization and Scintillation from Nuclear Recoils in Liquid Xenon as Target for a Dark Matter Experiment*, Phys. Rev. Lett., 2006, 97, 081302.

- Z. Bayindir, C. Martin, I. Minut, L. DeViveiros, T. Coffey, C.C. Agosta and M. Tokumoto, *Radio frequency measurements of the superconducting transition in $\kappa - (ET)_2 Cu(NCS)_2$ using a tunnel diode oscillator in pulsed magnetic fields*, Synthetic Metals, 2001, 120, 723 - 724.

Honors and Awards

2001 B.A. summa com laude, First Honors. Clark University, Worcester (USA).

2001 Saltman Award for Excellence in Philosophy. Clark University, Worcester (USA).

2000-2001 Erickson Scholarship. Clark University, Worcester (USA).

1998-2001 Scholarship. Clark University, Worcester (USA).

2000 Erickson Summer Research Award. Clark University, Worcester (USA).

ACKNOWLEDGMENTS

I want to thank my friends, who made life a little bigger than just grad school. Thank you to Ines, who made life a lot bigger than just grad school, and an adventure, too. To my family, which is so far away, and yet always with me. And finally, to my mother - you have always been my hero. Thank you for all the love and support through everything. All that I have achieved, I owe it to you.

CONTENTS

LIST OF TABLES

List of Figures

CHAPTER 1

DARK MATTER

1.1 Evidence for Dark Matter

1.1.1 Introduction

The existence of dark matter has been postulated to resolve the problem of "missing mass" in the universe - a wealth of evidence points to the existence of more mass than we have been able to account for from the visible component of the universe. Dark matter doesn't emit, absorb, or scatter light, but its effects are felt through the gravitational influence on other visible matter. The mounting evidence includes, but is not limited to, the rotational speeds of galaxies, orbital velocities of galaxies in clusters, the anisotropies in the Cosmic Microwave Background (CMB), the large scale distribution of matter in the universe, and the gravitational lensing of background objects by galaxy clusters (such as the famous "Bullet Cluster" [1]). Dark matter also plays a significant role in resolving a number of problems in cosmology, such as the distribution of anisotropies in the CMB, the formation of the large-scale structure of the universe, and the evolution of galaxies. The nature of dark matter remains one of the big problems in fundamental physics today.

Dark matter was first proposed in 1933, when F. Zwicky observed a very large discrepancy between the mass that was visually observable and the mass calculated by measuring the velocities of galaxies in the Coma galactic cluster [2, 3] (see Fig. 1.1 for a more recent set
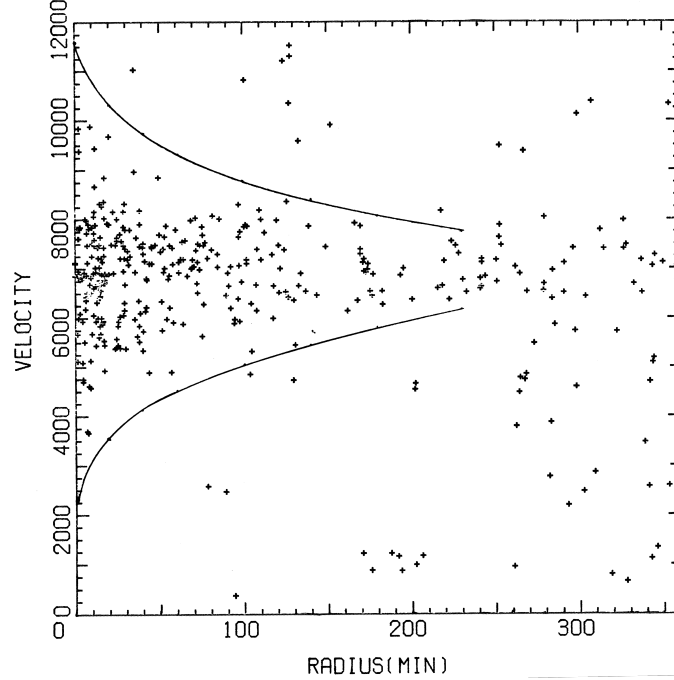
Figure 1.1: Distribution of radial velocities for galaxies in the Coma Cluster, as a function of distance from the cluster center. The plot shows the clustering of velocities in the galaxies closest to the cluster center, demonstrating that it is a gravitationally bound system. The distribution of radial velocities of 8 of the galaxies in the cluster was used by Zwicky in 1933 [2, 3] to determine that the cluster mass was $170\times$ larger than the mass estimated from the galaxies luminosity alone. Figure taken from [4].

of measurements of the Coma cluster). The virial theorem relates the kinetic and potential energies in a bound system:

$$\langle KE \rangle = -\frac{1}{2}\langle PE \rangle \tag{1.1}$$

(assumes that the system is in equilibrium, and is neither expanding nor contracting). Zwicky used measurements of the redshifts of galaxies in the Coma cluster to estimate the velocity dispersion of the cluster in the radial direction. Assuming that the velocity dispersion was isotropic (the same in all 3 dimensions), and that the mass of the galaxies is uniformly distributed in the spherical cluster, he calculated a mass for the cluster $170\times$ larger than the mass estimated from the luminosity of the galaxies alone. He then suggested that the discrepancy can be explained by the presence of a large amount of some "dark matter" in the cluster.

The second evidence for dark matter came from the rotation curve of spiral galaxies. Measurements published by Rubin and Ford in 1970 showed that the stars in disk of spiral galaxies had approximately the same orbital velocity at all radii, which is inconsistent with mass distribution deduced from the visible star distribution [5]. In a spiral galaxy, the distribution of light in the disk is approximately a falling exponential, $I/I_0 = e^{-r/r_0}$, where I is the surface brightness, and r_0 is $\sim 4\,\mathrm{kpc}$ for the Milk Way and $\sim 6\,\mathrm{kpc}$ for the M31 galaxy [6], and the light is essentially concentrated in the bulge. If all or most or the mass is due to the stars, then at large radii (e.g. $r > 3 \cdot r_0$) the orbital velocity of the starts would fall as:

$$v \propto \frac{1}{\sqrt{r}}\,. \tag{1.2}$$

However, the measurement of the rotation curve of the M31 galaxy by Rubin and Ford showed that the orbital velocity was constant outside the bulge, implying that the mass, rather than falling exponentially, increased proportionally to the radius,

$$M\left(r\right) \propto r\,, \tag{1.3}$$

where $M\left(r\right)$ is the mass inside a volume with radius r (see Fig. 1.2). Further measurements of spiral galaxies have shown similar behavior [7]. This implies the existence of a dark matter "halo" in which the visible component of the galaxy is embedded, and that it reaches well beyond the visible size of the galaxy. Estimates for the M31 galaxy indicate that the dark halo is $1 - 2$ orders of magnitude more massive than the stellar component at a radius of tens of kpc.

Further evidence indicates that most of the dark matter mass is non-baryonic and non-relativistic. Cosmological evidence such as the CMB anisotropies, measurements of the large scale structure of the universe, and Big Bang nucleosynthesis point to the existence of a non-baryonic component to the matter density of the universe. The latest measurements at the time of publication indicate that the total matter density is $27.4\% \pm 1.5\%$ of the total energy density of the universe, while the baryonic density adds up to only $4.6\% \pm 0.2\%$ (the remaining 72.6% correspond to the vacuum energy, also known as "dark energy") [9].

ROTATION CURVE AND GEOMETRY OF M31
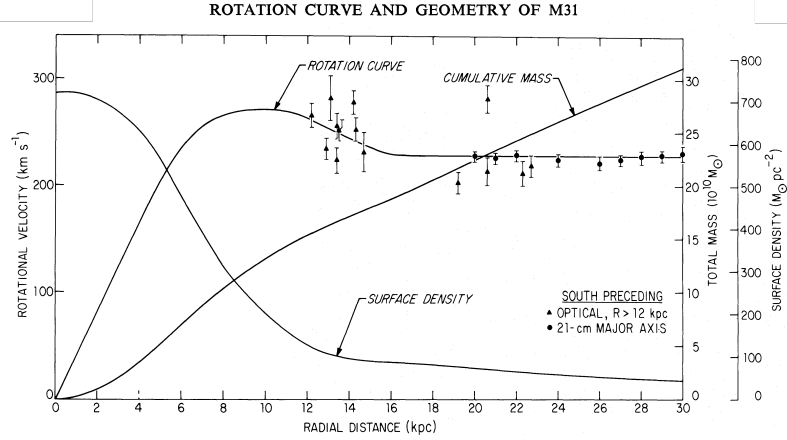
Figure 1.2: Rotation curve and mass distribution for the M31 galaxy. The plot shows the rotational velocity of the stars in the cluster vs. radial distance from the galactic center ("rotation curve"). It also shows the "surface density", the surface mass density calculated from the observed luminosity; and the "cumulative mass", the mass distribution corresponding to the observed rotation curve. Figure taken from [8].

This state of affairs is called the ΛCDM model, in which Λ stands for the cosmological constant or dark energy, and CDM for Cold Dark Matter. The model uses the cosmological constant and non-baryonic, non-relativistic dark matter to describe the universe since the inflationary period, and to explain a number of modern cosmological observations, such as the CMB and the structure of the universe.

In this section we will review some of the cosmological evidence for non-baryonic dark matter. First, we will review some preliminaries definitions and the framework for quantifying the density of the universe and its components (i.e. the Friedmann equations). We will then review some of the experiments that put constraints on the energy density of the various components of the universe, and try to determine the contribution from all matter and from baryonic matter, with the intention of making clear the discrepancy between them.

One of the most compelling pieces of evidence for the existence of dark matter in modern cosmology are the measurements of the CMB anisotropies, which have additionally shown that dark matter is non-baryonic in nature, and interacts only weakly with baryonic matter. The numerical values for the many cosmological quantities mentioned throughout this chapter (such as the energy density percentages quoted above) are taken from the combined analysis of the latest results of the CMB, Supernova Type Ia, and SDSS data, which are

listed in the WMAP 5-years results paper [9], unless otherwise stated.

1.1.2 The Friedmann Equations

The Friedmann Equations are a set of 2 equations, derived by A. Friedmann in 1922, that describe the expansion (or contraction) of the universe by relating the scale factor $a(t)$ and the curvature of the universe to the energy density $\varepsilon(t)$ and the pressure $P(t)$ summed for all the components of the universe, and assuming a homogeneous, isotropic universe. The Friedman equations can be written as:

$$\left(\frac{\dot{a}}{a}\right)^2 = \frac{8\pi G}{3c^2}\varepsilon - \frac{\kappa c^2}{R_0^2 a^2} + \frac{\Lambda}{3} \tag{1.4}$$

and

$$\frac{\ddot{a}}{a} = -\frac{4\pi G}{3c^2}(\varepsilon + 3P) + \frac{\Lambda}{3}, \tag{1.5}$$

where R_0 is the radius of curvature of the universe today $(t = t_0)$, κ is the curvature parameter, and Λ is the cosmological constant.

The cosmic scale factor, $a(t)$, is a dimensionless parameter used to specifically to describe the rate of expansion (or contraction) of the universe with time, and is normalized to $a = 1$ at $t = t_0$. Hubble's Law relates the distance of objects in space to the observed redshift, and thus to their (radial) velocity relative the observer position.

$$H(t) = z \cdot \frac{c}{r} = \frac{v_r}{r}. \tag{1.6}$$

Hubble's Law thus describes the rate of expansion of the universe as a function of time, and can be rewritten using the cosmic scale factor $a(t)$:

$$H(t) = \frac{\dot{a}(t)}{a(t)}. \tag{1.7}$$

The Hubble constant, which quantifies the rate of expansion of the universe today, is given by:

$$H_0 = \left(\frac{\dot{a}}{a}\right)_{t=t_0} = \dot{a}(t_0) = 70.5 \pm 1.3\,\mathrm{km\ s^{-1}Mpc^{-1}}. \tag{1.8}$$

The curvature parameter κ is a dimensionless constant that can take the values of 0, 1 and -1, which describe the universe as either spatially flat, a closed sphere with positive curvature, or a hyperbolic space with negative curvature, respectively. The cosmological constant was first introduced by Albert Einstein in 1915 to explain what he believed at the time to be a static universe, and it was arbitrarily set to $\Lambda = 4\pi G \cdot \varepsilon/c^2$ so that the acceleration of the expansion (or contraction) of the universe would be zero ($\ddot{a} = 0$). Today, the cosmological constant is used to describe the accelerating expansion of the universe, and is generally understood as the vacuum energy density, and is known as "Dark Energy". For now, it suffices to say that the cosmological constant can be re-expressed as as a energy density so that

$$\varepsilon_\Lambda = \frac{c^2}{8\pi G}\Lambda. \tag{1.9}$$

In the limit of $\varepsilon + \varepsilon_\Lambda \to \varepsilon$, the first Friedman equation can be written as:

$$H(t)^2 = \frac{8\pi G}{3c^2}\varepsilon - \frac{\kappa c^2}{R_0^2 a^2}.$$

In the special case of a flat universe, the curvature parameter $\kappa = 0$ further simplifies the first Friedman equation so that we have

$$H(t)^2 = \frac{8\pi G}{3c^2}\varepsilon. \tag{1.10}$$

Using this simplified form of the first Friedmann equation, we define the critical energy density ε_c as the energy density corresponding to a flat universe ($\kappa = 0$):

$$\varepsilon_c(t) = \frac{3c^2}{8\pi G}H(t)^2. \tag{1.11}$$

It is convenient to define a dimensionless *density parameter* $\Omega(t)$, defined as

$$\Omega\left(t\right) \equiv \frac{\varepsilon\left(t\right)}{\varepsilon_c\left(t\right)}. \tag{1.12}$$

Note that the density parameter can also be expressed in terms of the mass density $\rho\left(t\right)$, $\rho = \varepsilon/c^2 \Rightarrow \Omega\left(t\right) = \rho\left(t\right)/\rho_c\left(t\right)$. The density parameter can be used to characterize the curvature of the universe. A universe in which $\Omega = 1$ is spatially flat; $\Omega < 1$ results in a hyperbolic ("open") universe with negative curvature; and $\Omega > 1$ results in a close universe with positive curvature. The density parameter is often quoted as Ωh^2, where h is the dimensionless Hubble parameter:

$$h = H_0/\left(100\,\mathrm{km\ s^{-1}Mpc^{-1}}\right). \tag{1.13}$$

The notation of density parameters can also be used to quantify the density of the individual components that make up the total energy of the universe. In order to do so, we can re-write the first Friedmann equations using the Ω notation:

$$\frac{H^2}{H_0^2} = \frac{1}{H_0^2}\left(\frac{\dot{a}}{a}\right)^2 = \frac{\Omega_r}{a^4} + \frac{\Omega_m}{a^3} + \frac{\Omega_k}{a^2} + \Omega_\Lambda \tag{1.14}$$

where Ω_r and Ω_m are the energy densities of radiation and matter at the present, and Ω_Λ and Ω_κ are the energy density terms related to the cosmological constant and to curvature of the universe, relative to the critical density ε_c. At $t = t_0$ (today), $a = 1$ and these terms add up to one: $\Omega_r + \Omega_m + \Omega_k + \Omega_\Lambda = 1$.

The radiation and matter components obey different equations of state, and have a different time evolution:

$$\varepsilon_m\left(t\right) = \varepsilon_m/a\left(t\right)^3 \tag{1.15}$$

and

$$\varepsilon_r\left(t\right) = \varepsilon_r/a\left(t\right)^4, \tag{1.16}$$

where ε_r and ε_m are the energy densities of radiation and matter at the time $t = t_0$. Today we live in a matter dominated universe, in which $\varepsilon_m/\varepsilon_r \approx 3300$, and we can just drop the

Ω_r term from the first Friedmann equation. Finally, if we indeed live in a flat universe, the curvature term drops to zero, $\Omega_\kappa = 0$, so that the other terms would add up to exactly 1: $\Omega_m + \Omega_\Lambda = 1$.

We can also write the second equation as:

$$\frac{1}{H_0^2}\frac{\ddot{a}}{a} = -\frac{1}{2}\frac{\Omega_m}{a^3} + \Omega_\Lambda \,, \qquad (1.17)$$

which allows us to relate Ω_m and Ω_Λ by measuring the acceleration of the rate of expansion of the universe.

1.1.3   Type Ia Supernovae

Measurements of the rate of expansion of the universe can be done by measuring the redshift as a function of distance only when the distances are well known. In order to do this, it is necessary to make use of "standard candles", objects with known luminosity for which the distance can be determined from the apparent luminosity.

Type Ia Supernovae is a category of supernovae resulting from the explosion of a white dwarf star. A white dwarf is a small star, the remnant of a fairly massive and old star after it blows off its H envelope, leaving only the nucleus. It is typically composed by oxygen and carbon, in which fusion is no longer active. The weight of a white dwarf is supported only by electron degeneracy pressure, which can support a mass of up to $M \sim 1.38\,M_\odot$, the Chandrasekhar limit (for non-rotating stars). However, the white dwarf can accrete mass from a binary companion, and eventually exceed the Chandrasekhar limit. At this point, the electron degeneracy pressure can no longer balance the gravitational force and the star collapses, re-igniting nuclear fusion in a substantial fraction of the star in a matter of seconds, thus causing an explosion that releases $\sim 10^{62}\,$keV (99% released as neutrinos)[10] and have an average peak luminosity of $L \sim 4 \times 10^9\,L_\odot$ [11, 6]. This type of supernovae has a characteristic light curve in which the initial spectrum is dominated by intermediate weight elements, e.g. O, and the spectrum of the peak in magnitude is dominated by the heavy elements created during core collapse, e.g. Ni [12]. The shape of the light curve is also correlated with the peak luminosity, thus helping to determine the exact peak luminosity

of an observed supernova. Since the type Ia supernovae have similar, well-defined peak luminosity magnitudes and light curves, they become ideal standard candles candidates to measure the rate of expansion of the universe.

The luminosity of a light source is typically measured as the luminosity distance $d_L = \sqrt{L/4\pi f}$, where L is the object luminosity and f is the measured flux. At small redshift of $z \ll 1$, the luminosity distance scales linearly with redshift, so that

$$d_L \approx \frac{c}{H_0} z \,(\text{for } z \ll 1). \tag{1.18}$$

which allows the determination of the Hubble constant $H_0 = 70 \pm 10 \,\text{kms}^{-1}\text{Mpc}^{-1}$ [13].

The large redshift data ($z > 0.2$) can be used to place constraints in the allowed values of Ω_m and Ω_Λ. The density of matter and energy of the universe determine the deviation of d_L from linearity at large z. The luminosity distance d_L can also be expressed as the distance modulus $\mu = m - M$, where m is the apparent magnitude and M is the absolute magnitude, which is then plotted versus $\log_{10} z$. The procedure to find the constraints on the values of Ω_m and Ω_Λ is described in Perlmutter 2003 [13], and it basically involves picking a pair of values, computing the expected relation between the redshift z and either the apparent magnitude m or the distance modulus μ, and then comparing it to the observed data, as shown in Fig. 1.3.

The result of this procedure is a region in the Ω_m and Ω_Λ space that give the best fit to the supernova data - see Fig. 1.4 for a plot illustrating the parameter constraints obtained from this procedure, using the 2003 results from the Supernova Cosmology Project (SCP). The latest analysis of Type Ia Supernovae redshifts by the SCP in 2008 [15] has resulted in the following density parameters, when assuming a flat universe ($\Omega_{total} = \Omega_m + \Omega_\Lambda = 1$):

$$\Omega_m = 0.287^{+0.029}_{-0.027} \text{ (statistical) } ^{+0.039}_{-0.036} \text{ (systematics)} \tag{1.19}$$

and

$$\Omega_\Lambda = 0.713^{+0.027}_{-0.029} \text{ (statistical) } ^{+0.036}_{-0.039} \text{ (systematics)}, \tag{1.20}$$

so that $\sim 71\%$ of the universe energy is due to the dark energy component, and $\sim 28\%$ is
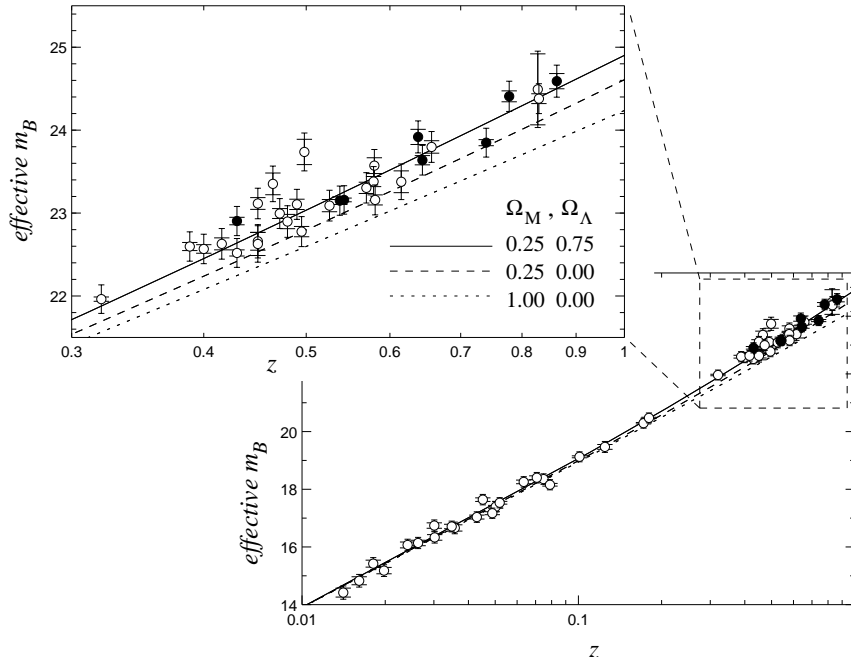
Figure 1.3: Supernova Type Ia data: effective (apparent) luminosity $m = m_B$ vs. redshift z, compared to different cosmological models (Ω_m,Ω_Λ). The circles indicate data measured by the Supernova Cosmology Project (SCP) group and published in 2003. The solid black line corresponds to the best fit to the data. Figure taken from [14].

due to matter. These constraints obtained from the supernovae data alone can be combined with the results from other cosmological measurements (i.e. the CMB) to provide better constraints on the density parameters of the universe, as shown later in Fig. 1.12.

1.1.4 CMB

The Cosmic Microwave Background (CMB) is a low energy radiation that permeates the entire universe, discovered in 1964 by Penzias and Wilson. The early universe was a hot plasma of photons, electrons and baryons, which cooled adiabatically as it expanded. At that stage, the photons were energetic enough ($T \geq 3,000\,\mathrm{K}$) to keep hydrogen ionized, and were coupled to the baryons via Thompson scattering in the plasma. Note that if there is another component to the matter density that doesn't interact directly with the photons (e.g. interacts only gravitationally), then it is not part of this "photon-baryon fluid". At $\sim 380,000$ years the temperature drops below $3,000\,\mathrm{K}$, the electrons can be captured by the ions ("recombination"), and the photons decouple from the baryons - this is known as "the
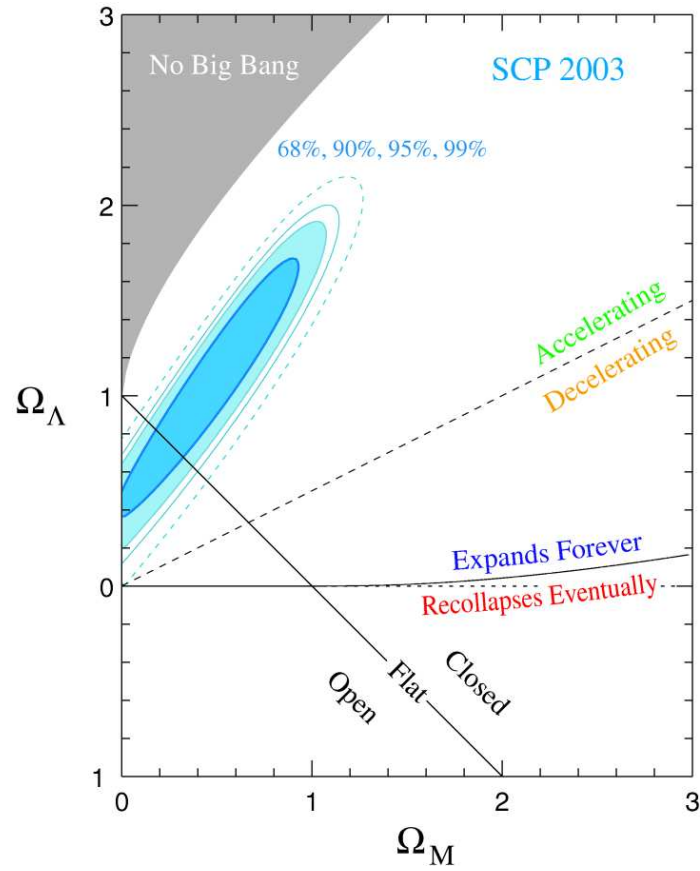
Figure 1.4: Supernova Type Ia constraints on Ω_m and Ω_Λ . Plots of the 68%, 90%, 95%, and 99% confidence regions (in light blue) derived from the Supernova Cosmology Project (SCP) measurements from 2003[14].

time of last scattering", and it occurred at a redshift 1090.88 ± 0.72 [9]. The universe is no longer opaque to the photons, which are now free to travel, creating a snapshot of the state of the universe at the time. These photons are observed today as a nearly isotropic radiation background, and have a blackbody spectrum with temperature $T = 2.725\,\text{K}$, peaking at microwave frequency - thus, the cosmic microwave background.

Before the time of last scattering, fluctuations in matter density create higher density regions that act as a potential well and compresses the photon-baryon fluid, thus attracting more mass and seeding the formation of structure in the early universe. The gravitational pull is countered by the radiation pressure, which increases as the photon-baryon fluid is compressed and causes it to expand, and consequently acoustic oscillations are generated in the photon-baryon fluid as it contracts and expands around high-density regions. At the time of last scattering, the oscillations in compression/expansion of the baryon-photon fluid is imprinted into the photon background. Regions undergoing compression have increased temperature, and thus the photons originating inside them have higher energy; expanding regions have lower temperature, and photons coming from these regions have lower energy.

The anisotropies in the background are characterized as temperature deviations from the mean $(\Delta T / T)$, which can be described as a sum of spherical harmonics

$$\frac{\Delta T\left(\hat{\mathbf{n}}\right)}{T} = \sum_{l=0}^{\infty} \sum_{m=-l}^{m=+l} a_{lm} Y_{lm}\left(\theta, \phi\right) , \tag{1.21}$$

where $\Delta T\left(\hat{\mathbf{n}}\right)/T$ is the temperature fluctuation from the mean in the direction of $\hat{\mathbf{n}}$. The CMB can be statistically characterized by the correlation function $C\left(\Theta\right)$, which is the average covariance of the temperature fluctuations for all points separated by an angle Θ:

$$C\left(\Theta\right) = \left\langle \frac{\Delta T\left(\hat{\mathbf{n}}_1\right)}{T} \frac{\Delta T\left(\hat{\mathbf{n}}_2\right)}{T} \right\rangle , \tag{1.22}$$

where $\cos\Theta = \hat{\mathbf{n}}_1 \cdot \hat{\mathbf{n}}_2$. Using the spherical harmonics expansion of $\Delta T/T$, the correlation function can be expressed in terms of Legendre polynomials P_l and the coefficients C_l:

$$C\left(\Theta\right) = \frac{1}{4\pi} \sum_{l=2}^{\infty} \left(2l + 1\right) C_l P_l\left(\cos\Theta\right) , \tag{1.23}$$

so that the correlation function can be broken down into its multipole moments C_l [16]. The correlation function is typically presented as a power spectrum of the temperature fluctuations, given by

$$\Delta_T^2 \equiv \left(\frac{l\,(l+1)}{2\pi} C_l \right) \langle T \rangle^2 \; , \tag{1.24}$$

and usually plotted as a function of either l or Θ, as seen in Fig. 1.6. The first $2\,l$ terms of the sum correspond to the monopole component ($l = 0$), which vanishes for measurements of the anisotropies, and to the dipole component ($l = 1$), which results from the Doppler shift due to our motion relative to the CMB frame of reference, and is subtracted to show the underlying anisotropies.

The anisotropies of the CMB were first measured by the Differential Microwave Radiometer (DMR) in the COsmic Background Explorer (COBE) satellite, launched in 1989. The COBE DMR used a pair of horn antennas to measure the difference in power received by each directional antenna, separated by $60°$. Measurements are recorded as the differences between points (pixels) in the sky, and after sufficient measuring time ($\sim 1\,\text{year}$) a highly redundant set of differences allows for the reconstruction of the temperature for each pixel [17]. After a series of similar measurements performed by balloon-borne detectors in the late 90's (QMAP, BOOMERanG and MAXIMA), the COBE experiment was followed up by the Wilkinson Microwave Anisotropy Probe (WMAP) satellite in 2001. It used similar measurement techniques as the COBE DMR, using 10 pairs of receivers, each pair pointing in opposite directions. While the COBE DMR experiment was only able to resolve temperature fluctuations larger than $\Theta > 7°$, WMAP has been able to make precise map the temperature fluctuations over the entire sky with an angular resolution of $\Theta \approx 0.2°$, which is shown in Fig. 1.5.

The power spectrum for the 5-year run of WMAP is shown in Fig. 1.6. There are several features to the power spectrum, and these can be used to calculate a number of cosmological parameters. The peaks in the spectrum are created by the acoustic oscillations of the density of the baryon-photon fluid being "frozen" at an extremum of compression or expansion at the time of last scattering, as already described above. The location of the first peak at $\Theta \approx 1°$ (or $l \approx 200$) corresponds to the angular size, as seen from Earth, of the Hubble
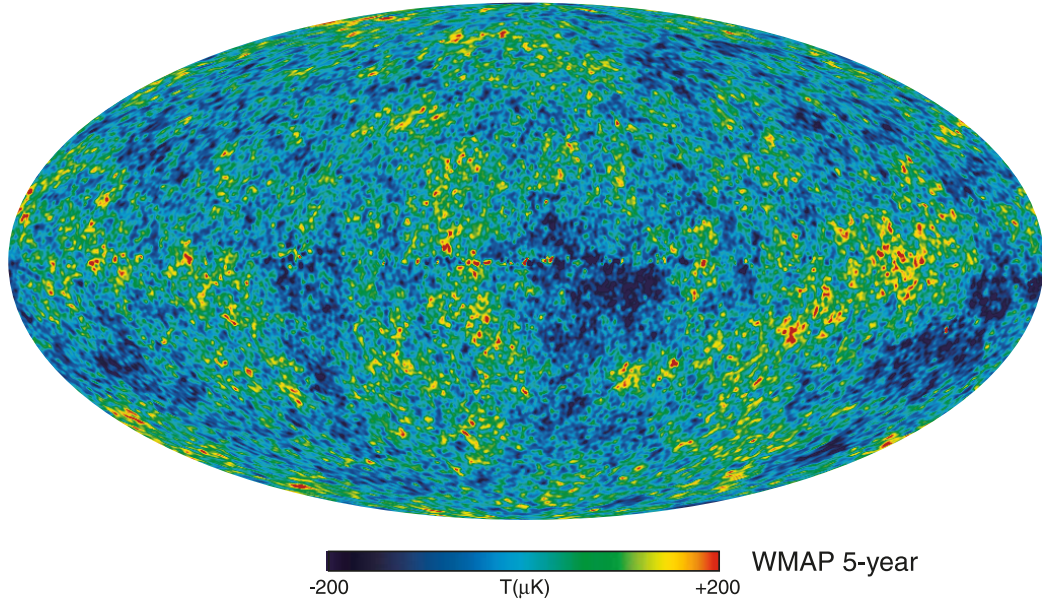
Figure 1.5: Sky map of the CMB temperature fluctuation from 5-year WMAP observations (dipole component and galaxy foreground removed) [9].

distance at the time of last scattering (the Hubble distance is the distance that a photon can travel in a period equal to the age of the universe). The exact angle where the first peak occurs depends on the curvature of the universe - the angular size of an object is smaller for a negatively curved universe than in a positively universe. The observed position of the peak is consistent with a flat universe, or $\Omega_{total} = 1$.

The amplitude of the peaks is a measure of the amount of gravitational compression of the baryon-photon fluid, which is dependent on the frequency of the oscillations, which in turn is dependent on the baryonic contribution to the fluid mass. The relative size of the first and second peak yields the baryonic matter density parameter, Ω_b. Incidentally, the baryon-to-photon ratio also sets the speed of sound in the photon-baryon fluid, which in turn sets the characteristic length of the acoustic oscillations called the "sound horizon". The sound horizon r_s is the distance that a sound wave can travel in a period equal to the age of the universe. From the WMAP 5-year data alone, the sound horizon is calculated at $146.8 \pm 1.8 \, \text{Mpc}$.

The density of the total mass component of the universe can also be inferred from the power spectrum. As CMB photons travel in and out of the gravitational potential wells
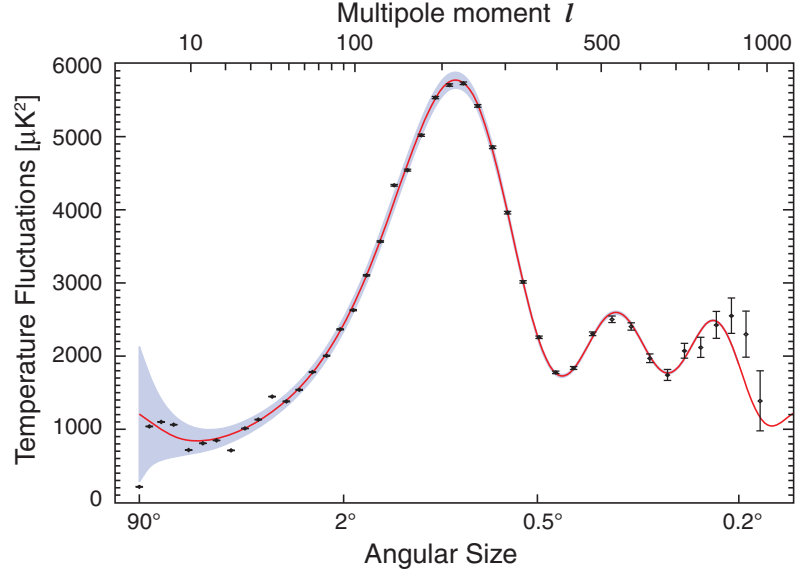
Figure 1.6: CMB angular power spectrum from 5-year WMAP Observations (figure taken from the WMAP website [18]; data reproduced from [19]). The plot shows the temperature fluctuations Δ_T^2, described in Eq. 1.24.

after the time of last scattering, they are blueshifted and redshifted proportionally to the well depth. As time passes, the potentials change and the amount of blueshift experienced when entering a well is not the same as the redshift experienced when leaving, and the total shift is depends on the variation in time of the potential wells. The creation of temperature fluctuations due to the change in the gravitational potentials is called the Integrated Sachs-Wolfe (ISW) effect, and is divided into an "early" and a "late" stage, corresponding to the transition from a radiation- to matter-dominated universe (early) and to the transition from matter- to Λ-dominated (late). The ISW effect is determined by the fluctuations at large angular scales ($\Theta > 1°$), and the early ISW can be used to determine the total matter density parameter Ω_m. Likewise, the late ISW can be used to determine the density parameter associated with the vacuum energy Ω_Λ [20].

The power spectrum is sensitive to all density parameters, Ω_m, Ω_b, Ω_Λ, and Ω_{total}, and accurate measurements of the power spectrum yield accurate measurements of these parameters. The WMAP 5-year data, combined with the Supernova data and the Baryonic Acoustic Oscillations data (described in Section 1.1.5) yields the cosmological parameters listed in Table 1.1 on page 22. Note that the density of matter and the density of baryons

is not necessarily the same, and that they are determined independently from the CMB power spectrum. In fact, the CMB results show that the matter density of the universe is $\Omega_m = 0.274 \pm 0.015$, while the baryonic matter density is $\Omega_b = 0.0456 \pm 0.0015$, which implies that the total matter of the universe is $\times 6$ larger than the baryonic mass. The non-baryonic component is thought to be non-baryonic dark matter, and its density parameter is labeled as Ω_d. The matter density parameter is then given by $\Omega_m = \Omega_b + \Omega_d$.

1.1.5 Large Scale Structure and Baryonic Acoustic Oscillations

In the same way that the potential wells created by fluctuations in the matter density of the early universe left an imprint in the CMB, they have also seeded the formation of the structure of the universe that we observe today, such as galaxy clusters and superclusters. The acoustic oscillations from the photon-baryon fluid (described in the previous section) are also imprinted on the power spectrum of baryonic matter distribution [21]. The acoustic oscillations in the fluid excite sound waves in the photon-baryon fluid, and at the time of decoupling, the baryon mass distribution is at a peak at the maxima of the sound waves. A survey of the distribution of baryonic matter in the universe today (properly scaled to a comoving frame of reference) should exhibit a peak at the length of the sound horizon r_s, which is distance that a sound wave can travel in the photon-baryon fluid in a period equal to the age of the universe at the time of the decoupling.

The Sloan Digital Sky Survey (SDSS) is a massive survey of the sky, acquiring images and spectra of more than a quarter of the sky. Through spectroscopic redshift analysis, the SDSS provides a 3-dimensional map of the local universe. The SDSS team analyzed the power spectrum of a sample of $47,000$ luminous red galaxies (LRGs), with redshifts of up to $z = 0.47$ (see sample of the galaxy survey on Fig. 1.7). The power spectrum plots the correlation function $\xi(r)$, which is a measure of the probability of finding one galaxy within a given distance r of another galaxy. We expect a large peak at small distances (due to gravitational clustering), and another peak at the sound horizon scale. The SDSS power spectrum does indeed show a small peak at $r_s = 100h^{-1}\,\mathrm{Mpc} \approx 142\,\mathrm{Mpc}$ (see Fig. 1.8), which is consistent with the value obtained from the CMB observations by WMAP.
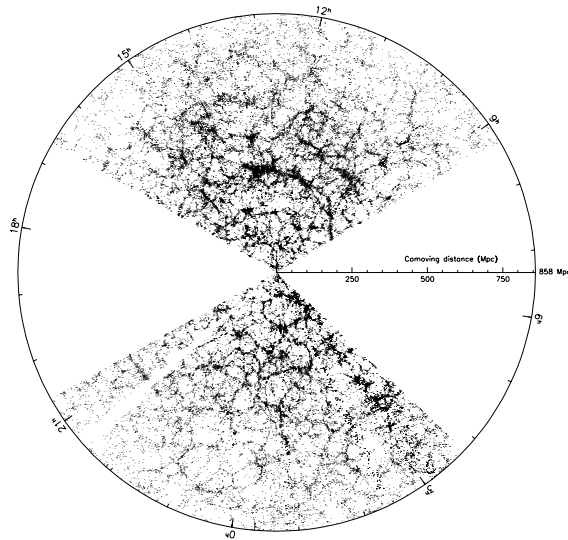
Figure 1.7: Galaxy map from the Sloan Digital Sky Survey (SDSS), taken from Gott 2005 [22].

The measurement of the Baryonic Acoustic Oscillation peak sets constraints on the ratio of baryonic to total matter density (Ω_b/Ω_m) - the observed BAO is not compatible with a large baryonic fraction of the total matter density, thus requiring a significant fraction of the matter to be non-baryonic (see Fig. 1.9). Combined with values from different experiments, the overall shape of the power spectrum can set better constraints on the total mass density Ω_m and on the vacuum energy density Ω_Λ. Table 1.1 on page 22 lists the cosmological parameters from the combined analysis of the CMB, Type Ia Supernova data, and the Baryonic Acoustic Oscillation data [9].

1.1.6 Big Bang Nucleosynthesis

Big Bang Nucleosynthesis (BBN) is the synthesis of light elements, such as D, ^{3}He, ^{4}He, ^{6}Li and ^{7}Li, in the early universe. While heavier elements are created in star cores and supernovae, the lightest elements were created in significant numbers only in the first few minutes after the Big Bang. The nucleosynthesis started when the universe was cool enough to allow formation of nuclei ($T \sim 80\,\text{keV}$, at $t \approx 180\,\text{s}$), and stopped when the expansion
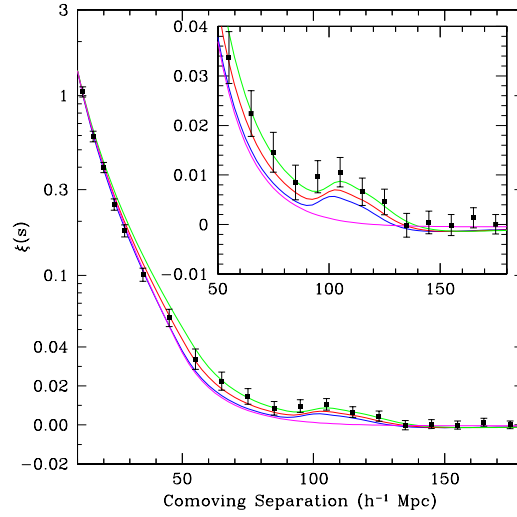
Figure 1.8: Correlation function versus galaxy separation distance; spectrum from the SDSS 5-year survey. The lines corresponds to models with different mass density parameters $\Omega_m h^2 = 0.12, 0.13, 0.14$ (green, red and blue, respectively) and baryonic density $\Omega_b h^2 = 0.024$. The line without the acoustic peak (magenta) correspond to a pure CDM model (that is, no baryons) with $\Omega_m h^2 = 0.105$. The figure is obtained from [21].
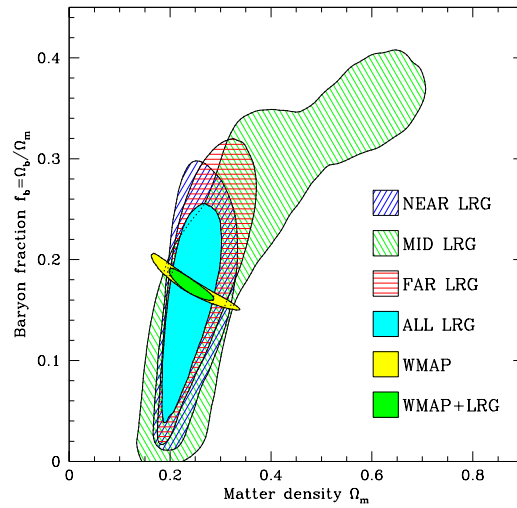
Figure 1.9: Constraints (2σ) on the total matter density and on the ratio of baryonic to total matter density (Ω_b/Ω_m) from the SDSS measurement of the BAO in the luminous red galaxies (LRG) data. The LRG data is divided into 3 datasets, one for each distance range ("near", "mid" and "far"). The light blue shape shows the constraints from the combined LRG data.. The figure also shows the constraints obtained from the WMAP CMB measurements, and from combining the WMAP and LRG constraints. Figure taken from [23].

of the universe (the Hubble parameter) was larger than the nuclear production rate, at which point the nuclei abundances were fixed [24, 6]. Although the abundances for some of these elements can change during the evolution of the universe through both creation and destruction processes, the abundance of these elements today still gives us a valuable window into the physics of the early universe.

A single parameter determines the rates of the nuclear production reactions: the ratio of densities of baryons to photons, $\eta = n_b/n_\gamma$, and the primordial abundance for all light elements can be determined from this parameter. Astronomical observations of the abundance of each of the light elements D, ^{4}He, and ^{7}Li (usually measured a ratio to the H abundance) determine their abundance in the early universe , and from each of them the value for η is determined. The measurements of the D abundance (from absorption lines in high redshift quasars) [25] result in baryonic density parameters in very good agreement to the values obtained from the CMB and SDSS [26, 27]:

$$\Omega_b h^2 \;\; = \;\; 0.0226 \pm 0.0017$$

$$\Rightarrow \Omega_b \;\; \approx \;\; 0.045 \,.$$

The measurements of ^{4}He abundance are in line with the calculated baryonic density [27]. The ^{7}Li measurements, however, indicate a photon-baryon ratio η at least 2.4× smaller than the value obtained from D and ^{4}He [28]. The significance of the ^{7}Li discrepancy is at present unknown, and it could indicate systematic measurement errors or new physics. However, all primordial abundance measurements indicate that the baryonic content of the universe is not sufficient to account for most of the observed matter density of $\Omega_m \approx 0.274$, thus adding further support to the theory of non-baryonic dark matter.

1.1.7 Gravitational Lensing

Gravitational lensing is the deflection of light from distant sources by massive objects, such as a galaxy cluster, causing a visible distortion or amplification in the object image. The effect is a result of the curvature of space-time around massive objects, and is predicted

Figure 1.10: Strong lensing in the image of the cluster Abell 2218, taken by the Hubble Space Telescope. The figure shows strongly distorted galaxy images, tangentially aligned with the cluster center, which is located close to the brightest galaxy on the upper right region. Figure taken from [31].

by general relativity. The lensing effect can be used to measure the mass of the objects between the source and observer, and is particularly interesting in cosmology as the effect is independent of the composition of the lens [29].

There are three types of gravitational lensing: strong, weak and microlensing. Strong lensing produces easily visible distortions, such as multiple images of the source, or arcs, which are strongly distorted and elongated images of the background source (see Fig. 1.10 for an example). Strong lensing can be used to place constraint of the lens (e.g. the cluster), but it requires special alignment between the lens and the background source. Weak lensing is the coherent distortion of the images of several background source objects, and the effect in an individual source is small, with a typical elongation of 1% [30]. Although the signal for an individual source (i.e. a galaxy) is small, statistical measurements of a large number of sources over a region in the sky can be used to reconstruct the coherence of the distortion (called *shear*), and thus the mass distribution of the lens. Microlensing is the amplification of the source luminosity, without any visible distortion, by a small lens object. When the lens and source are aligned, the lens causes the light from the source to be focused and thus increase the apparent luminosity of the image. Microlensing experiments typically search for the change in luminosity of background objects with time, with peaks in luminosity indicating the passage of a massive object in the foreground.

Strong and weak lensing observations have been used to map the distribution of mass

(a) Optical   (b) X-ray
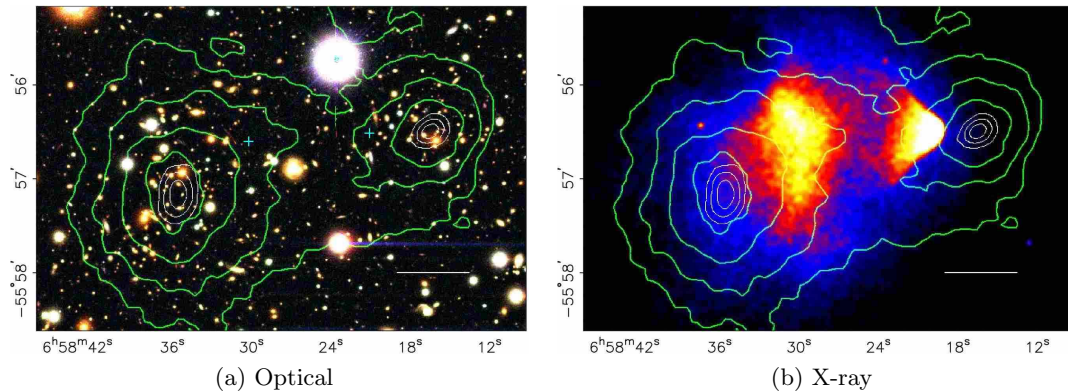
Figure 1.11: Bullet cluster (1E0667-558 Cluster Merger Object) - Shock front of collision between 2 galaxy clusters ($\sim$ 150 million years ago), showing the separation between gas component and dark matter. Left: Optical image obtained with the Magellan telescope. Right: X-ray obtained by the Chandra X-ray Observatory. The green contours indicate the mass distribution of the object (the lens) reconstructed through weak lensing, and the white contours show the peak of the mass density (at 1σ, 2σ and 3σ). The object is at redshift $z = 0.3$. The white bar indicates the scale at the distance of the object, $200\,\mathrm{kpc}$. Figure obtained from [1].

in galaxies and galaxy clusters, and show the presence of a dark component to the total mass [31]. In a famous case, the weak lensing observation of the "Bullet Cluster", which shows the collision of two galaxy clusters, leads to the reconstruction of the dark matter distribution in the cluster (see Fig. 1.11) [1]. The collision decouples the hot gas component from the galaxies, which behave as collisionless particles. The gas is the largest baryonic mass component in the clusters. The weak lensing mass distribution shows that the matter distribution peaks are offset from the X-ray signal from the hot gas, and agrees with the distribution of galaxies. If there was no dark matter, the mass distribution calculated from weak lensing would follow the X-ray gas. The figure suggests the existence of a very large mass component composed of collisionless and non-luminous matter.

1.1.8   Constraints

Bringing together the results from all the cosmological observations described in this chapter, a compelling picture starts to emerge. The constraints on the cosmological density parameters imposed by each experiment converges nicely around a narrow region in the parameter space, as shown in Fig. 1.12. Table 1.1 lists the most likely values for a set

$$\begin{array}{ll} \Omega_{total} & 1.0050^{+0.0060}_{-0.0061} \\ \Omega_\Lambda & 0.726 \pm 0.015 \\ \Omega_m & 0.274 \pm 0.015 \\ \Omega_b & 0.0456 \pm 0.0015 \\ \Omega_d & 0.228 \pm 0.013 \\ \Omega_\nu & < 0.014 \\ H_0 & 70.5 \pm 1.3\,\mathrm{km\ s^{-1}Mpc^{-1}} \end{array}$$

Table 1.1: Cosmological parameters calculated from the combined constraints obtained from the CMB (WMAP 5-years data), Type Ia Supernovae, and BAO (SDSS) data [9].

of cosmological parameters obtained from these constraints. The evidence overwhelmingly points towards a universe dominated by dark energy, with a significant fraction of matter (27.4%), of which only a small portion (4.6%) is made up of "ordinary" matter. This picture leaves one wondering about the nature of this dark energy, and about the nature of this dark matter that we have been unable to see thus far. In the next sections, we will review the currently most favored theory that explains the nature of dark matter, and explore methods to finally detect it.

1.2 WIMPs

1.2.1 Weakly Interacting Massive Particles

As seen in Section 1.1, a strong case is presented for the existence of non-baryonic dark matter. However, most evidence pertaining to the nature of the dark matter answer questions of what isn't dark matter, rather than what is dark matter. A few necessary traits for dark matter candidates become apparent, though. They must not interact via electromagnetic force (hence, they are dark); have high enough density (all dark matter components must add up to $\sim 85\%$ of the matter density of the universe); and be stable on the time scale of the age of the universe [32].

In the quest to discover the identity of dark matter, several candidates have emerged. New elementary particles have become the favored candidates, including some whose existence has been proposed in unrelated fields of physics. Most of the favored candidates have already been ruled out by previous searches and by unrelated cosmological observations.
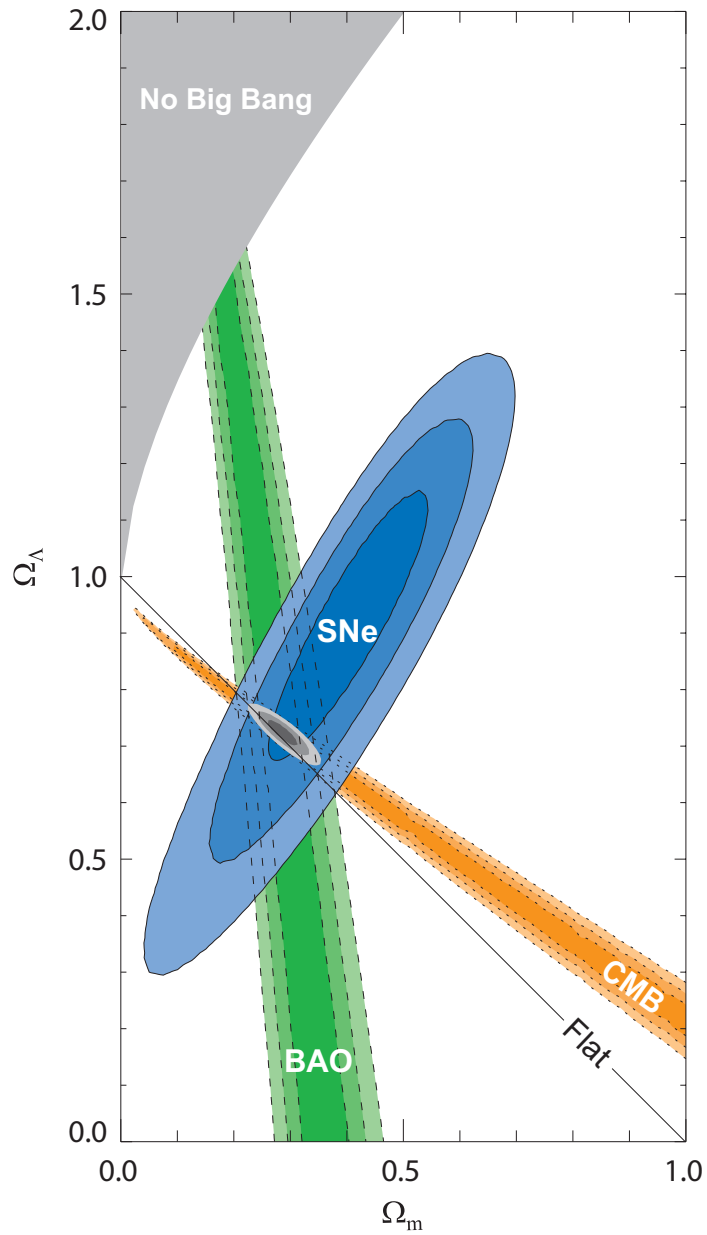
Figure 1.12: Constraints on Ω_Λ and Ω_m from the CMB (WMAP 5 years data), Type Ia Supernovae (from the Supernova Cosmology Project, 2008), and BAO (SDSS) data. Figure taken from [15].

We already know of at least one non-baryonic particle that seems to have a non-zero contribution to the matter density to the universe: neutrinos. Just like the photons in the CMB, there is also a relic neutrino background in the Universe, left over from the Big Bang. Observation of neutrino oscillations establish that neutrinos have non-zero mass, with mass of at least $m_\nu \geq 0.04\,\text{eV}$ [26]. The neutrinos are still very light, and since they were in thermal equilibrium during the early universe, they travel at relativistic speeds. A neutrino component to dark matter is thus called "hot" dark matter, to distinguish it from "cold" dark matter, made up of particles that travel at non-relativistic speeds. An excess of hot dark matter during the period of galaxy formation would cause the matter density distribution to be smeared out during the early universe, and the large structure of the universe would be different from what we have today. Measurements from the CMB and SDSS place an upper limit on the neutrino density at:

$$\Omega_\nu < 0.014\,, \tag{1.25}$$

so that a neutrino component to dark matter is possible, but makes up only a small portion.

Another candidate are axions, an elementary particle postulated in 1977 to resolve the strong-CP violation problem in quantum chromodynamics (QCD) [33]. Although the axions are also very light ($m_{axion} \gtrsim 10^{-5}\,\text{eV}$), it is thought that a non-thermal population of axions that don't travel at relativistic speeds was produced in the early universe, and thus could account for the dark matter. Several detection experiments are underway, but so far it has not been detected; only recently have the experiments started to probe the mass range where axions become good dark matter candidates, in the order of $\sim 1\,\mu\text{eV}$ [34].

The most favored dark matter candidates today are WIMPs, Weakly Interacting Massive Particles, with masses between $10\,\text{GeV}$ and a few TeV, and very small interaction cross section (in the weak force scale), produced at the time of the Big Bang. Such massive particles would have negligible abundance today if they had remained in thermal equilibrium with the rest of the universe, as the abundance is Boltzmann suppressed and it drops exponentially with temperature [35]. For a WIMP particle χ with mass m_χ, the number density at high temperature is $n_\chi \propto T^3$, but as the temperature drops below the particle

mass, it becomes

$$n_\chi \propto (m_\chi T)^{3/2} \cdot e^{-m_\chi/T} \,. \tag{1.26}$$

In the early universe, when it was very dense, hot, and the temperatures exceeded the mass $T \gg m_\chi$, thermal equilibrium of the WIMPs was maintained by the continuous annihilation with its own antiparticle $\bar\chi$ into other particles X, i.e. $\chi\bar\chi \to X\bar X$, and creation in similar manner, $X\bar X \to \chi\bar\chi$. As the universe expands and temperatures drop below the particle mass $(T < m_\chi)$, the creation process is suppressed, and the equilibrium abundance drops exponentially (Eq. 1.26) due to annihilation. The annihilation rate Γ_A per particle is

$$\Gamma_A = n_\chi \langle \sigma_A v \rangle \,, \tag{1.27}$$

where σ_A is the annihilation cross section of χ, and v is the relative velocity of two particles. As the abundance decreases, so does the annihilation rate. When the annihilation rate drops below the expansion rate of the universe $(\Gamma_A < H)$, the creation and annihilation processes "freeze out", and can no longer maintain thermal equilibrium. The abundance of χ particles remain locked in the "freeze out" density - see Fig. 1.13 for a diagram of the process. If the particle is stable, then their density today is a "relic" of the earlier time when the particles were in thermal equilibrium with the universe. If the annihilation rate was too high, or if the universe had expanded slowly enough for the χ particle to maintain thermal equilibrium, there would be no WIMPs today.

Given the freeze out conditions outlined above, and assuming typical annihilation rates in the weak scale, the freeze out temperature can be calculated as $T_f \approx m_\chi/20$. From these conditions, it follows that the energy density parameter can be calculated to be

$$\Omega_\chi h^2 = \frac{n_\chi m_\chi}{\rho_c} h^2 \approx \frac{10^{-27}\,\mathrm{cm^3 s^{-1}}}{\langle \sigma_A v \rangle} \,, \tag{1.28}$$

which is independent of the actual mass of the particles (except for logarithm corrections, not shown here) [35].

For a particle with interaction cross section in the weak scale, we obtain $\langle \sigma_A v \rangle \sim$
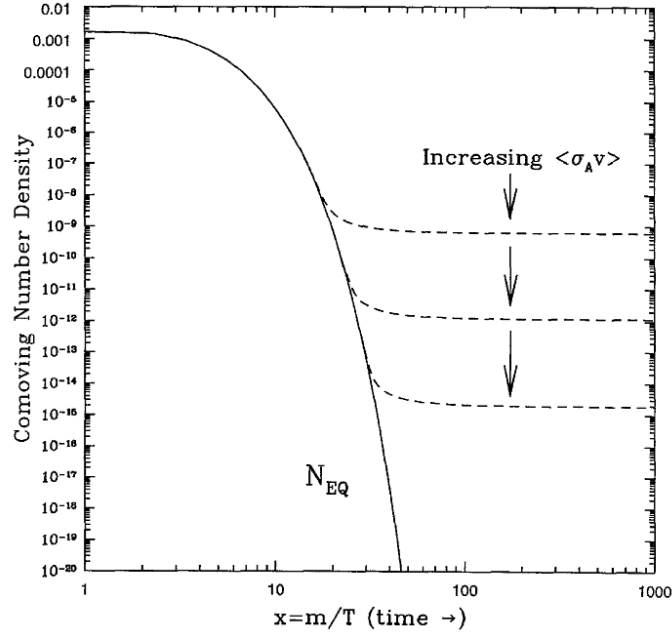
Figure 1.13: Diagram of the WIMP freeze out process, showing the density of particles in thermal equilibrium (solid line) and frozen out (dashed lines) after they fall out of equilibrium. The plot shows the behavior of the density for various annihilation cross sections, illustrating that the WIMP relic density depends primarily on the cross section scale, and not on the WIMP mass. Figure taken from [35].

$10^{-36}\,\mathrm{cm}^3\mathrm{s}^{-1}$, resulting in a relic density of $\Omega_\chi h^2 \approx 0.1$, which is remarkably close to the non-baryonic dark matter density ($\Omega_d h^2 = 0.113$) necessary to fit the cosmological observations. This match supports the case that if there is such a particle as a WIMP, it would solve the dark matter problem.

1.2.2   If it walks like a duck, quacks like a duck ...

As it turns out, a particle that fits the profile of a WIMP exists within the framework of supersymmetry (SUSY). Supersymmetry is an extension of the standard model that predicts the existence of a host of new particles: for every particle in the standard model, there is a supersymmetric counterpart, so that for every fermion we get a new supersymmetric boson, and vice-versa. For example, the electron is partnered with a s-electron, the photon with the photino, and so on. These new particles are the result of a new symmetry breaking, and all have masses greater than those in the standard model.

The parameter space for supersymmetry is very large, and there is a wide variety of

theoretical models. We will focus on the discussion of Minimal Supersymmetric Standard Model (MSSM) theories, which add one supersymmetric partner for every standard model particle, a pair of Higgs bosons, and nothing else. Most of these models offer candidate particles suitable for WIMPs, but the best motivated and most studied of the candidates is the lightest supersymmetric particle (LSP). MSSM theories introduce R-parity to explain the stability of the proton. All standard model particles have R value of 1, while all supersymmetric particles have R value of -1. If R-parity is imposed, the LSP cannot decay, as there is no lighter particle with R $= -1$, and thus it is a stable, long lived particle. The exact identity of the LSP is uncertain, but in most models it is the neutralino, a linear combination of photinos, zinos and higgsinos (the supersymmetrical partners of the photon, Z^0 and the Higgs bosons). The mass of the LSP in most models which are consistent with existing experimental constraints is in the range of $50\,\mathrm{GeV} - 1000\,\mathrm{GeV}$, and its interaction cross section with baryonic matter is at the weak scale.

Regardless of the specific combination of the LSP, a large portion of the parameter space results in particles with the characteristic necessary for the WIMPs. Other WIMP candidates will also result in density parameters of the order of Ω_χ, and will be similarly suitable to resolve the dark matter problem.

1.3 Signals

1.3.1 Indirect detection

WIMPs interact only via gravity and weak force, and the interaction probability is very small, making detection a challenge. However, if WIMPs are in fact the dark matter in the galactic halo, a significant number should scatter as they pass through a large mass such as the Sun, thus causing them to lose energy and become trapped in the Sun's gravity well. As more WIMPs accumulate and thermalize within the Sun, they begin to annihilate. A number of models predict the formation of a flux of high-energy neutrinos and/or gammas, detectable on Earth. Similar trapping would also occur in other gravity wells, such as the galactic center and even the Earth [35]. A number of experiments is actively pursuing

method of different methods of detecting this signal [36, 37, 38]. Such indirect detection experiments can add support to the WIMP dark matter model, and can be useful in setting constraints on the WIMP properties. However, the indirect detection signal is very model-dependent, and the signals we do receive on Earth could be open to interpretation. The most satisfying way to settle the WIMP dark matter question would be to directly detect them on Earth.

1.3.2   Direct Detection

WIMPs can be detected via their scattering on ordinary matter here on Earth. Although the interaction cross section of WIMPs on ordinary matter is very low, a number of MSSM theories predict the a WIMP-nucleus elastic scattering cross section of up to $10^{-41}\,\mathrm{cm}^2$ [39], making detection possible in detectors with large enough mass. One can build an experiment with the objective of detecting the energy deposited by such rare interactions of WIMPs and ordinary matter. In this section, we will calculate the rate of such interactions in a WIMP detector, and their energy spectrum, with the objective of determining what signals a detector must be looking for. We will follow the calculations detailed by Lewin and Smith [40] in order to calculate the total and differential event rate of WIMP-nucleus elastic scattering

When calculating the differential event rate, it is important to establish which kind of recoil is being observed, as electron and nuclear recoils have different signal sizes for the same amount of energy deposited, leading to different energy scales when calibrating the detector (this is statement is further discussed in Section 2.1.5). For nuclear recoil events, we quote the deposited energy as $\mathrm{keV_r}$, or "keV nuclear recoil equivalent".

The event rates are typically expressed in "differential rate unit" or dru, which is defined as $1\,\mathrm{dru} = 1\,\mathrm{event/keV/kg/day}$. The differential rate unit may be qualified with the energy scale used to measure the rate - this point is explained in Section 2.1.5. The total event rate, integrated over the entire recoil energy spectrum, is given in "total event units" or tru, which is defined as $1\,\mathrm{tru} = 1\,\mathrm{event/kg/day}$. It is also useful to quote event rates inside some range of energies, in which case we will use "integrated rate unit" or iru, which is defined

similarly to tru as $1\,\text{iru} = 1\,\text{event/kg/day}$.

1.3.2.1 The halo model

If the dark matter halo in our galaxy consists of WIMPs, then $10^4 - 10^6$ of WIMPs per cm^2 are passing through the Earth surface every second. The actual flux is depends on the characteristics of the galactic halo model, such as the density and velocity distribution of particles. The simplest model assumes that the galactic disk is embedded into a isotropic and spherically symmetric dark matter halo. The dark matter halo is not rotating like the galaxy - if it was, it would also be flat like the galactic disk. While the disk moves in circular motion and is supported against gravity by its angular momentum, the WIMPs move freely in random directions, like an ideal gas.

The average velocity of the WIMPs is approximately the same average velocity of all matter in the galaxy. Drukier et al. argue that the velocity dispersion of WIMPs is related to the circular velocity v_r of the galaxy as

$$\left\langle v_0^2 \right\rangle = 3 \cdot \frac{\left\langle v_r^2 \right\rangle}{2} \, . \tag{1.29}$$

The galactic rotation velocity has reported mean values of $222\,\text{km} \cdot \text{s}^{-1} \leq v_r \leq 243\,\text{km} \cdot \text{s}^{-1}$ [41]. For the calculation in this section, we will use the common approximation of $v_0 \approx v_r \approx 230\,\text{km} \cdot \text{s}^{-1}$[40]. The WIMPs are assumed to have a Maxwellian velocity distribution, so that the velocity distribution of WIMPs impinging on Earth is given by

$$f\left(\vec{v}, \vec{v}_E\right) = e^{-(\vec{v} + \vec{v}_E)^2 / v_0^2} \, , \tag{1.30}$$

where $\vec{v}$ is the WIMP velocity, with most likely speed of v_0; and $\vec{v}_E$ is the Earth velocity relative to the dark matter halo, given by $\vec{v}_E = \vec{u}_r + \vec{v}_S + \vec{u}_E$, where $\vec{u}_r$ is the galactic rotation, $\vec{u}_S$ is the rotation of the Sun relative to the nearby stars, and $\vec{u}_E$ is the rotation of the Earth relative to the Sun. The Earth velocity is approximately the galactic rotation

velocity, but it varies as the Earth orbits the sun, so that we have

$$v_E = 244 + 15\sin\left(2\pi y\right) \text{ km}\cdot\text{s}^{-1}, \tag{1.31}$$

where y is the date relative to March 2nd, in years. This variation in the speed of the Earth in the galactic halo translates in an annual modulation in the nuclear recoil signal, and experiments have been running to detect such modulation [42]. Particles with velocity greater than the galactic escape velocity v_{esc} (the speed necessary for an object to escape the gravitational field it is in) will leave the galaxy, and thus the velocity distribution of WIMPs have a sharp cut off at v_{esc}. The escape velocity is estimated at $v_{esc} \approx 625 \text{ km}\cdot\text{s}^{-1}$ [41].

The density of galactic dark matter halo is estimated at $0.3\,\text{GeVc}^{-2}\text{cm}^{-3} \leq \rho_d \leq 0.7\,\text{GeVc}^{-2}\,\text{cm}^{-3}$ [43]. For the calculations in this work, we will follow the value chosen in Lewin 1996 [40], $\rho_d = 0.4\,\text{GeVc}^{-2}\text{cm}^{-3}$, to set conservative limits on the WIMP event rate. As an example, if the WIMP particles have a mass of $m_\chi = 100\,\text{GeVc}^{-2}$, then the galactic halo would have about $n_\chi = 4\,\text{WIMPs/liter}$.

1.3.2.2 Elastic scattering cross section

Form Factor. The "form factor" is a modifier to the scattering cross section of a particle onto a nucleus in order to account for the internal structure of the nucleus.

In a scattering event, the momentum transfer from the WIMP to the nucleus is

$$q = \sqrt{2\cdot m_t \cdot E_r}\,. \tag{1.32}$$

If the size of the nucleus is small compared to the de Broglie wavelength associated to the momentum transfer $\lambda = h/q$ (where $h = 2\pi\hbar$), it is possible to approximate the nucleus as a point particle when calculating the cross section. In general, the cross section of the nucleus can be expressed as:

$$\sigma\left(q\right) = \sigma_0 F^2\left(q\right), \tag{1.33}$$

where σ_0 is the cross section for small q $(q \to 0)$, and F is the form factor. Incidentally, the

form factor notation also applies to the differential cross section, so that we have:

$$\frac{d\sigma\left(q\right)}{d\Omega} = F^2\left(q\right)\frac{d\sigma_0}{d\Omega}\,. \tag{1.34}$$

For low energy recoils, the form factor is unity, so that the cross section has no corrections based on the recoil energy and can be treated as a constant. At some energy, however, the form factor "kicks in" and the effective cross section begins to fall with recoil energy [44].

The WIMP-nucleus scattering can be one of two types: it is either a spin-independent or a spin-dependent interaction. There are currently experiments searching for WIMPs using both types of interaction. For spin-independent interactions, the incoming particle can scatter off any of the nucleons; for spin-dependent interactions, the particle can only scatter off an unpaired nucleon (thus, we only have spin-dependent scatterings in nuclei with an odd-number of protons or neutrons).

For a nucleus of finite size, the form factor is the Fourier transform of the spatial density distribution $\rho_N\left(r\right)$ of nucleons in the nucleus, so that:

$$F\left(q\right) = \int \rho_N\left(r\right)e^{-i\vec{q}\cdot\vec{r}}d^3r\,. \tag{1.35}$$

We can further simplify the calculation of the form factor by approximating the nucleus with a spherically symmetric nucleon distribution:

$$F\left(q\right) = \frac{4\pi}{q}\int_0^\infty r\cdot\sin\left(q\cdot r\right)\cdot\rho_N\left(r\right)dr\,. \tag{1.36}$$

The nucleus can be be crudely approximated by a *thin shell* for spin-dependent interactions, so that the shell represents the unpaired nucleon in the outer shell. The form factor is given by the spherical Bessel function $j_0\left(q\cdot r_N\right)$, so that we have:

$$F\left(q,r_N\right) = \frac{\sin\left(q\cdot r_N\right)}{q\cdot r_N}\text{ (thin shell)}, \tag{1.37}$$

where r_N is the effective nuclear radius. A more detailed calculation of the spin dependent form factor can be found in Engel [45].

For spin-independent interactions, the nucleus can be crudely approximated by a *solid sphere*, and the resulting form factor is

$$F(q, r_N) = \frac{3 \cdot j_1(q \cdot r_N)}{q \cdot r_N} = \frac{3}{(q \cdot r_N)^3} \left[\sin(q \cdot r_N) - q \cdot r_N \cdot \cos(q \cdot r_N) \right] \text{ (solid sphere)}.$$

$$(1.38)$$

The actual distribution of nucleons for spin-independent scatters can be determined experimentally by scattering neutrons off the nucleus. In the case of lack of data from neutron scattering, it is possible to approximate the distribution of nucleons using the nucleus charge distribution obtained from electron and muon scattering experiments . The charge density is typically approximated by either a Fermi or Gaussian distribution, given by

$$\rho(r) = \frac{\rho_0}{1 + \exp\left[(r - R_u)/a\right]} \text{ (Fermi model)}, \qquad (1.39)$$

$$\rho(r) = \rho_0 \left(1 + \frac{\omega r^2}{a^2} \right) \cdot e^{-r^2/a^2} \text{ (Gaussian model)}, \qquad (1.40)$$

where a is the surface diffuseness parameter, R_u is the characteristic radius parameter, and ω is the angular frequency of the oscillator in a potential well described by the function [44]. Using a truncated Gaussian distribution proposed by Helm [46], the form factor for elastic spin-independent interactions becomes:

$$F(q, r_N) = \frac{3 \cdot j_1(q \cdot r_N)}{q \cdot r_N} \cdot e^{-(q \cdot s)^2/2}, \qquad (1.41)$$

where s is a surface thickness of the nucleus, which is defined as the distance in which the density drops from 90% to 10% of its maximum. Experimental data suggests that the surface thickness is approximately constant at $s \approx 0.9 \, \text{fm}$ [40]. The effective nuclear radius r_N can also be determined experimentally, and it is found that

$$r_N = 1.14 \cdot A^{1/3} \, \text{fm} \qquad (1.42)$$

fits the available data very well for a range of A values, up to an energy transfer of $E_r \approx 400 \, \text{keV}_r$ for Iodine (it is expected to work just for Xe as well).

Coherence Factor. For spin-independent interactions, coherence effects scale the cross section approximately as the square of the mass of the nucleus A^2, thus favoring experiments with target materials with higher mass nuclei, like Ge or Xe.

The WIMP-nucleus elastic cross section for zero momentum transfer ($q = 0$) can be written as:

$$\sigma_0 = 4 \cdot G_F^2 \cdot \mu_N^2 \cdot I_N \,, \tag{1.43}$$

where μ_N is the reduced nucleus mass $\mu_N = (m_N \cdot m_\chi) / (m_N + m_\chi)$, G_F is the Fermi coupling constant $(G_F / (\hbar c)^3 = 1.166 \, \text{GeV}^{-2})$, and I_N is the interaction factor, which contains all the physics of the interaction [35]. The WIMP elastic cross section is typically normalized to *cross section per nucleon*, in order to allow the comparison of performance of detectors with different target materials. The WIMP-nucleon cross section is thus given by:

$$\sigma_{\chi,n} = \sigma_0 \cdot \frac{\mu_n^2}{\mu_N^2} \cdot \frac{I_n}{I_N} \,, \tag{1.44}$$

where μ_n and I_n are the reduced mass and interaction factor for individual nucleons. For Majorana particles, the coupling to neutrons and protons is approximately the same, so that Eq. 1.44 is the same for neutrons and protons. Conversely, the total cross section is given by

$$\sigma_0 = \sigma_{\chi,n} \cdot \frac{\mu_N^2}{\mu_n^2} \cdot \frac{I_N}{I_n} \,. \tag{1.45}$$

For Majorana particles, spin-independent interactions will have A scattering amplitudes, so that the interaction factor is $I_N/I_n = A^2$, and the cross section becomes:

$$\sigma_0 = \sigma_{\chi,n} \cdot A^2 \cdot \frac{\mu_N^2}{\mu_n^2} \,. \tag{1.46}$$

Bringing together the form factor (Eq. 1.33) and the coherence factor above (Eq. 1.46), we get a spin-independent elastic cross section of

$$\sigma_{si,el}(q) = \sigma_{\chi,n} \cdot A^2 \cdot \frac{\mu_N^2}{\mu_n^2} \cdot F^2(q) \,. \tag{1.47}$$

The factor I_N is different for spin-dependent interactions. In the spin-dependent in-

teractions, the amplitudes from each nucleon are still summed, but the contribution from paired nucleons cancels out, and only the contribution of an unpaired nucleon remains. Only nuclei with odd number of protons or neutrons (such as ^{129}Xe and ^{131}Xe) can detect spin-dependent WIMPs interactions.

The interaction factor $I_N = I_S$ for the spin-dependent interactions is

$$I_S = \frac{8}{\pi}\lambda^2 \cdot J\left(J + 1\right) , \tag{1.48}$$

where λ is the spin coupling term, and J is the total nuclear spin.

1.3.2.3   Total event rate

Given the halo model discussed in Section 1.3.2.1 above, it is possible to estimate the number of interactions of WIMPs with ordinary matter as a function of the interaction cross section $\sigma = \sigma_{si,el}$. We will focus only on the spin-independent interaction, but the spin-dependent event rate can be calculated in a similar manner by using the appropriate cross section, according to the calculations detailed in Section 1.3.2.2.

As mentioned in Section 1.3.2.1 above, the average WIMP number density n_χ is given by

$$n_\chi = \frac{\rho_\chi}{m_\chi} . \tag{1.49}$$

The WIMP number density distribution as a function of velocity can be expressed as

$$dn = \frac{n_\chi}{k} f\left(\vec{v}, \vec{v}_E\right) d^3v , \tag{1.50}$$

where $f\left(\vec{v}, \vec{v}_E\right)$ is the WIMP velocity distribution given in Eq. 1.30, and k is a normalization constant so that we can obtain

$$\int_0^{v_{esc}} dn \equiv n_\chi. \tag{1.51}$$

We can rewrite k explicitly as:

$$n_\chi \;=\; \int_0^{v_{esc}} dn = \int_0^{v_{esc}} \frac{n_\chi}{k} f\left(\vec{v}, \vec{v}_E\right) d^3 v$$

$$\Rightarrow \quad k \;=\; \int_0^{v_{esc}} f\left(\vec{v}, \vec{v}_E\right) d^3 v$$

$$k \;=\; \int_0^{2\pi} \int_{-1}^{+1} \int_0^{v_{esc}} f\left(\vec{v}, \vec{v}_E\right) v^2 dv \, d\phi \, d\left(\cos\theta\right).$$

When calculating the total event rate, we can use the approximation $v_E = 0$, since the Earth velocity will not change the number of incoming particles. In the limit $v_{esc} \to \infty$, we calculate the value of k for $v_E = 0$:

$$
\begin{aligned}
k_0 &\;=\; k\left(v_E = 0\right) \\
&\;=\; 4\pi \int_0^\infty e^{-v^2/v_0^2} v^2 dv \\
&\;=\; \left(\pi v_0^2\right)^{3/2}
\end{aligned}
$$

where $v_0 \approx 230\,\mathrm{km}\cdot\mathrm{s}^{-1}$ is the most likely WIMP velocity.

For any given particle flux, the number of interactions per second N_{tot} on a target such as a detector is given by:

$$N_{tot} = F \cdot n \cdot \sigma_{si,el} \cdot V\,, \tag{1.52}$$

where F is the particle flux, n is the number density of targets, $\sigma_{si,el}$ is the elastic interaction cross section for the whole nucleus, and V is the target volume. The rate of interaction per unit mass can be written as a function of the density function for WIMPs:

$$dR = \frac{N_0}{A} \cdot \sigma_{si,el} \cdot v \cdot dn\,, \tag{1.53}$$

where N_0 is Avogadro number per unit mass ($N_0 = N_A \cdot M_u = 6.022 \times 10^{26}\,\mathrm{kg}^{-1}$), and A is the atomic number of the nucleus of the target material. We can then calculate the

interaction rate per volume R using

$$R = \int_0^{v_{esc}} dR = \frac{N_0}{A} \cdot \sigma_{si,el} \int_0^{v_{esc}} v \cdot dn = \frac{N_0 \cdot \sigma_{si,el} \cdot n_\chi}{A \cdot k} \int_0^{v_{esc}} v \cdot f\left(\vec{v}, \vec{v}_E\right) dv \quad (1.54)$$

Thus, for $v_E = 0$, and $v_{esc} \to \infty$, the total event rate R_0 is given by

$$\begin{aligned} R_0 &= \frac{N_0 \cdot \sigma_{si,el} \cdot \rho_\chi}{A \cdot m_\chi \cdot k_0} \int_0^\infty e^{-v^2/v_0^2} v \, dv \\ &= \frac{2 \cdot N_0 \cdot \rho_\chi}{\sqrt{\pi} \cdot A \cdot m_\chi} \cdot v_0 \cdot \sigma_{si,el} \end{aligned} \quad (1.55)$$

Using Eq. 1.55 above, we can calculate the total event rate expected in a WIMP detector on Earth. For example, for a detector that uses liquid Xe as the target material ($A = 131$), we calculate that the event rate for a WIMP with $m_\chi = 100 \, \mathrm{GeVc}^{-2}$ and elastic cross section of $\sigma_{\chi,n} = 9 \times 10^{-44} \, \mathrm{cm}^2$, we expect a total event rate of $\sim 1 \, \mathrm{event/kg/15 \, days}$.

1.3.2.4 Differential event rate

Direct detection experiments are built to detect the energy deposited by the WIMPs in the detector target material by an elastic collision. These collisions have a specific energy spectrum, which becomes an important signature of the WIMP signal.

The recoil energy of the target nucleus of mass $m_t = m_N$ after being hit by a WIMP of kinetic energy E_χ is given by

$$E_r = E_\chi \cdot \varrho \cdot \frac{(1 - \cos\theta)}{2}, \quad (1.56)$$

where θ is the scattering angle and ϱ is the scattering ratio:

$$\varrho = \frac{4 \cdot m_t \cdot m_\chi}{(m_t + m_\chi)^2} \quad (1.57)$$

(in the center-of-mass frame). The maximum nuclear recoil energy is $E_{r,max} = E_\chi \varrho$. As-

suming isotropic scattering, we have a flat probability distribution across $\cos\theta$ and therefore across E_r. The differential event rate can be found by integrating

$$\frac{dR}{dE_r} = \int\limits_{E_{\chi,min}}^{E_{\chi,max}} \frac{1}{E_\chi \cdot \varrho} dR(E_\chi), \tag{1.58}$$

where $E_{\chi,min} = E_r/\varrho$ is the minimum kinetic energy required to generate a nuclear recoil with energy E_r. Using Eq. 1.54 and $E_i = m_\chi \cdot v_i^2/2$ (so that $E_0 = m_\chi \cdot v_0^2/2$ is the most likely WIMP energy), we can rewrite Eq. 1.58 as

$$\frac{dR}{dE_r} = \frac{R_0 \cdot k_0}{2\pi \cdot E_0 \cdot k \cdot \varrho \cdot v_0^2} \int\limits_{v_{min}}^{v_{max}} \frac{1}{v} f\left(\vec{v}, \vec{v}_E\right) d^3v. \tag{1.59}$$

For $v_E = 0$ and $v_{esc} \to \infty$, the differential event rate $dR(v_E, v_{esc})/dE_r$ becomes simply

$$\frac{dR}{dE_r} = \frac{R_0}{E_0\varrho} e^{-E_r/E_0\varrho}. \tag{1.60}$$

We still haven't factored in the actual v_E and v_{esc}, nor the nuclear form factor in the cross section (we have assumed a constant σ_{tot}), but Eq. 1.60 shows that the nuclear recoil rate is simply a exponential function of the recoil energy. Also, dR/dE_r is at a maximum when $\varrho = 1 \Rightarrow m_t = m_\chi$. This indicates that it is desirable to choose a target material in which the nucleus has a mass similar to the expected WIMP mass.

For non-zero v_E and finite v_{esc}, the differential event rate for isotropic scattering becomes

$$\frac{dR}{dE_r} = \frac{R_0}{E_0\varrho} \frac{\sqrt{\pi}v_0}{4v_E} \left[\mathrm{erf}\left(\frac{v_{min} + v_E}{v_0}\right) - \mathrm{erf}\left(\frac{v_{min} - v_E}{v_0}\right) \right]. \tag{1.61}$$

We can solve Eq. 1.58 while applying the total cross section calculated in Section 1.3.2.2, including the coherence and form factors, and find the spin-independent WIMP event rate as a function of nuclear recoil energy, which is shown for a $100\,\mathrm{GeV/c^2}$ WIMP in Fig. 1.14. For this WIMP mass and $E_r < 60\,\mathrm{keV_r}$, the WIMP recoil spectrum on Xe is a featureless falling exponential, and Xe yields the largest integral event rate for low energy threshold $E_{thresh} < 18\,\mathrm{keV_r}$.
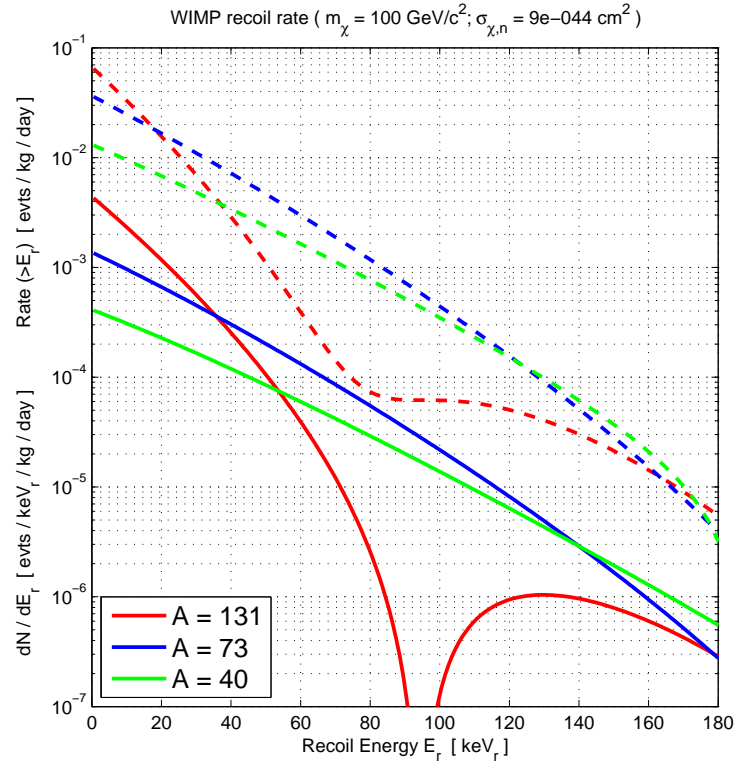
Figure 1.14: Differential WIMP event rates as a function of recoil energy, for three commonly used elements as detector targets (Xe, Ge and Ar), for a WIMP mass of $m_\chi = 100\,\mathrm{GeV/c^2}$ and a WIMP-nucleon elastic cross section of $\sigma_{\chi,n} = 9 \times 10^{-44}\,\mathrm{cm^2}$. The solid lines are the differential event rates, and the dashed lines are the integrated event rates for all recoil energies $E \geq E_r$.

CHAPTER 2

LIQUID XE DETECTORS

2.1   Liquid Xe and XENON10

XENON10 is a dark matter direct detection experiment deployed at the Laboratori Nazion-
ali Gran Sasso (LNGS) in 2006-2007. XENON10 is a dual-phase Time Projection Chamber
(TPC) with a total $\sim 23\,\mathrm{kg}$ of liquid Xe, of which $\sim 14\,\mathrm{kg}$ are used as the active target
material, defined by a Teflon cylinder and a pair of grids used to apply an electric field.
The active Xe volume is $15\,\mathrm{cm}$ in height and $20.3\,\mathrm{cm}$ in diameter. The liquid Xe chamber is
mounted inside a double cryostat system, with vacuum between the inner and outer vessels.
The cryostat is made of stainless steel, with masses of $33\,\mathrm{kg}$ (inner) and $110\,\mathrm{kg}$ (outer). The
active Xe volume is monitored by 2 arrays of Hamamatsu R8520 Photomultiplier Tubes
(PMTs), totaling 89 PMTs and allowing for both energy and 3D position reconstruction
of individual scatters in the target volume. The detector measures both primary scintilla-
tion light (S1) and ionization proportional scintillation (S2) for interactions in the liquid
Xe. A CAD rendering of the XENON10 detector is shown in Fig. 2.1. A diagram of the
detector internals and subsystems is shown in Fig. 2.2. The detector is mounted inside a
polyethylene-Pb shield to reduce backgrounds. The XENON10 shield and backgrounds are
discussed in Chapter 6. The full electronics chain, including the PMTs and data acquisition
system, is discussed in Chapter 3. In this chapter, we review the physics of a liquid Xe
detector, and the XENON10 detector setup.
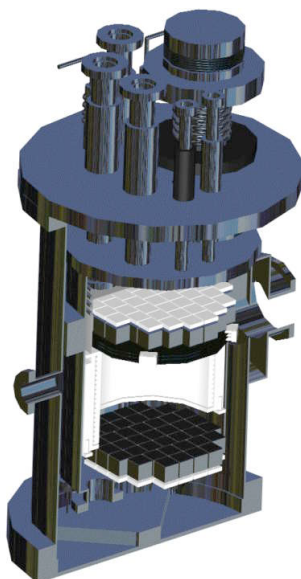
Figure 2.1: XENON10 detector CAD drawing, provided by J. Angle of the XENON10 Collaboration.
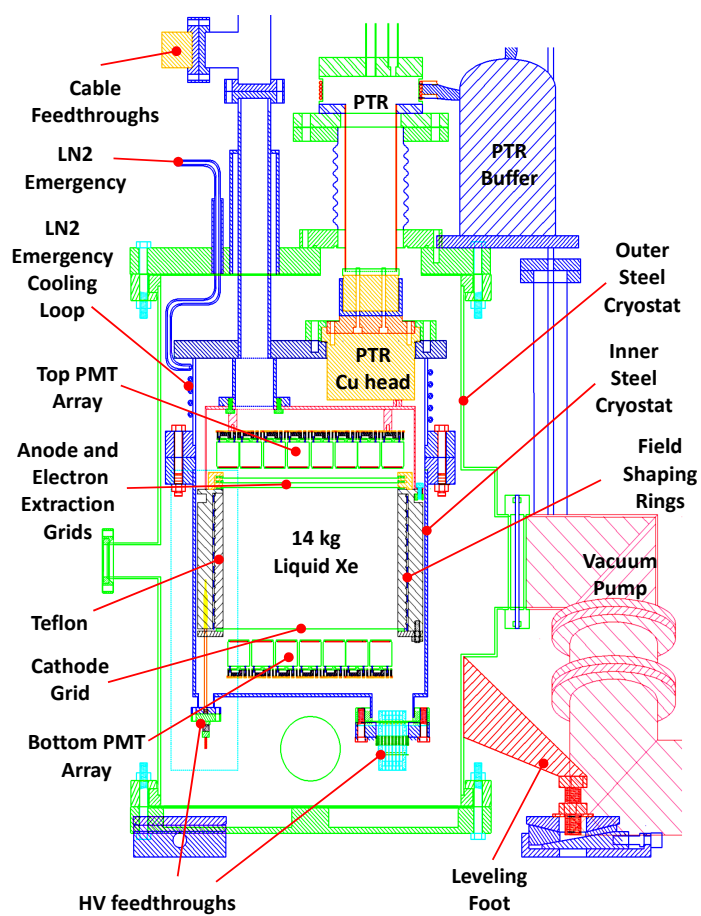
Figure 2.2: Diagram of detector with internals and subsystems.

2.1.1 Using Liquid Xe as the detector medium

Liquid Xe presents itself as an ideal medium for direct detection of WIMPs. Among the features that makes it attractive as a target material is the availability of both scintillation and ionization signals, with distinct light/charge ratio for nuclear and electron recoil scatters, which allows for efficient background discrimination on a event-by-event basis. Liquid Xe has a high density of $\sim 2.94\,\mathrm{g\ cm^{-3}}$, useful in constructing compact but massive detectors. Its high density and high Z are also useful in providing background suppression via self-shielding (see Section 2.1.6). A liquid Xe detector requires only modest cryogenics, operating at $T \sim 177\,\mathrm{K}$, a temperature easily maintained by a pulse tube refrigerator (PTR) in XENON10, a thermosyphon system in LUX, or even simply an ethanol and liquid nitrogen ($\mathrm{LN_2}$) bath, as is commonly done in small prototypes. A selection of relevant Xe physical properties are listed in Table 2.1.

Xe has a naturally high abundance of isotopes with an odd number of neutrons, necessary for probing some WIMP models using spin-dependent (SD) interactions, and its heavy nuclei ($\langle A \rangle = 131$) allows it to take advantage of the coherence factor in spin-independent (SI) interactions, as discussed in Section 1.3.2 (see Table 2.2 for a list of Xe isotopes). A liquid Xe detector can thus be used for WIMP searches for both SD and SI models. Xe also has the advantage of having no long lived radioactive isotopes, whose existence can become a troublesome background source. Neutron activation of ^{126}Xe, which has a natural abundance of 0.09%, produces ^{127}Xe, the radioactive isotope with the longest half life ($\tau = 36\,\mathrm{days}$). It β decays with $Q_\beta = 662\,\mathrm{keV}$, and the decay is accompanied by a γ, with energy $E_\gamma > 145\,\mathrm{keV}$. Neutron activation also produce $^{129\mathrm{m}}$Xe and $^{131\mathrm{m}}$Xe, with half-lives of 8.88 and 11.84 days, respectively. These activated states emit γ's with energies of 39.5 keV and 196.5 keV ($^{129\mathrm{m}}$Xe) and 164 keV ($^{131\mathrm{m}}$Xe). For comparison, the largest source of background in argon detectors is ^{39}Ar, produced by cosmogenic interactions. ^{39}Ar has a half-life of 296 years, and β decay with $Q_\beta = 565\,\mathrm{keV}$.

Interactions in the liquid Xe produce both scintillation light and free electrons. The scintillation signal (S1) is immediately observed by PMTs. A fraction of the charges are drifted up by an applied electric field, extracted into the gas phase, and drifted through

Property	Value
Atomic Number (Z)	54 [47]
Atomic Weight (A)	131.29 [47]
Boiling Point at 1 atm (T_b)	165.0 K [48]
Melting Point at 1 atm (T_m)	161.4 K [47]
Liquid Density at Boiling Point (ρ_L)	$2.94\,\mathrm{g}\cdot\mathrm{cm}^{-3}$
Refractive Index n	1.56 [49], 1.69 [50]
Liquid Dielectric Constant (ϵ)	2.85 [51]
Liquid Relative Permittivity ($\epsilon_{r,liq}$)	1.88 (at triple point)[52], 1.96 [53]
Dielectric Strength	$40\,\mathrm{kV/mm}$ [54]
Scintillation Wavelength (λ_s)	178 nm [55]
Energy / scintillation photon (W_{ph})	21.6 eV [56]
Energy / ionization electron (W)	15.6 eV[56]
$\mathrm{Xe}_2^\star$ singlet lifetime (τ)	2.2 ns [57]
$\mathrm{Xe}_2^\star$ triplet lifetime (τ)	27 ns[57]
XENON10 Temperature	177 K
XENON10 Pressure	2.11 atm
XENON10 Drift Field $\mathcal{E}_d$	$0.73\,\mathrm{kV}\cdot\mathrm{cm}^{-1}$
XENON10 Extraction Field $\mathcal{E}_d$	$\sim 12\,\mathrm{kV}\cdot\mathrm{cm}^{-1}$
XENON10 Total Xe mass	$\sim 23\,\mathrm{kg}$
XENON10 Active Xe mass	$\sim 15\,\mathrm{kg}$
XENON10 Fiducial Xe mass	$\sim 5.4\,\mathrm{kg}$
XENON10 Active Xe volume dimensions	$h = 15\,cm,\ d = 20.3\,cm$
XENON10 Fiducial Xe volume dimensions	$h = 9.4\,cm,\ d = 16\,cm$

Table 2.1: Table of select Xe physical properties.
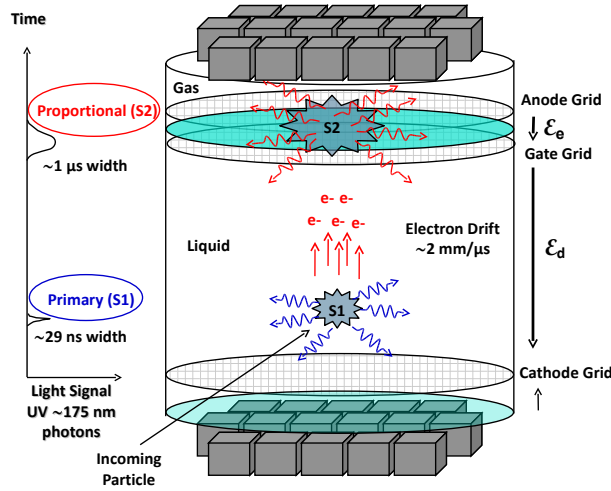
Figure 2.3: Diagram of an interaction and its associated signals in XENON10. An incoming particle scatters off a Xe atom (either electron or nucleus), producing primary scintillation light (S1) and ionizing Xe atoms. The electrons are drifted up by the electric field $\mathcal{E}_d$ until they reach the gas-liquid interface. The electrons are then extracted and accelerated through the gas phase by the field $\mathcal{E}_e$, producing proportional secondary scintillation light (S2).

the gas where they produce additional light, called the proportional scintillation (S2). The second light signal is delayed by the time that it takes for the electrons to drift up in the liquid, so that time between S1 and S2 is proportional to the depth where the interaction occurred. A detector that translates the time information into spatial coordinates is referred to as a Time Projection Chamber (TPC). The process is summarized in Fig. 2.3.

The scintillation light of Xe is in the VUV range, with peak wavelength of 178 nm [55]. Like other noble liquids, Xe is basically transparent to its own scintillation light, since the energy of the scintillation photons ($E_\gamma = 7\,\text{eV}$) is smaller than the first ionization potential (the energy required to ionize 1 electron, $12.1\,\text{eV}$); these photons can travel far enough inside the medium to allow detection. The attenuation length of photons in the liquid Xe depends on the absorption length and the Raleigh scattering length, and is given by:

$$I\left(r\right) = I_0 \cdot e^{-r/\lambda_{att}} , \tag{2.1}$$

where I is the photon beam intensity, and the attenuation length λ_{att} is

Isotope	Natural Abundance [%]
^{124}Xe	0.09
^{126}Xe	0.09
^{128}Xe	1.92
^{129}Xe	26.44
^{130}Xe	4.08
^{131}Xe	21.18
^{132}Xe	26.89
^{134}Xe	10.44
^{136}Xe	8.87

Table 2.2: Xe isotopes natural abundances.

$$\frac{1}{\lambda_{att}} = \frac{1}{\lambda_{abs}} + \frac{1}{\lambda_R} \; . \tag{2.2}$$

The absorption length has been measured at $\lambda_{abs} > 100$ cm [58]. However, the measurement was limited by the detector size (50 cm), and the data is consistent with $\lambda_{abs} \to \infty$. The Raleigh scattering length has been calculated to be 30 cm [51], and measured at 29 cm [59]. Since the Raleigh scattering is elastic, the photons generated in an event can be efficiently collected through the use of a good reflecting surface around the liquid Xe, to ensure that all photons are reflected back in and eventually reach the PMTs. A Teflon cylinder is used in defining the active Xe volume for this purpose. The refractive index of Xe to VUV photons has been measured at 1.56 at $T = 161$ K[49], and 1.69 at $T = 170$ K[50]. Due to the large refractive index, the internal reflection at the gas-liquid interface makes necessary the use of PMTs inside the liquid (the bottom PMT array in XENON10) in order to optimize light collection.

2.1.2 Scintillation Signal (S1)

Particle interactions in the liquid Xe transfer energy from the particle to the Xe atoms, which releases this energy either through electrons (ionization) or photons (scintillation), in the mechanism summarized in Fig. 2.4. Whether the interaction is a collision between the incident particle and the atomic nucleus (generating a nuclear recoil) or one of the atomic electrons (generating an electron recoil), the scintillation mechanism is the same.

The recoiling nucleus or electron deposits its energy in the liquid Xe, leaving Xe atoms in excited or ionized states. The excited atoms rapidly combine with non-excited ones in $10^{-11} - 10^{-12}$ s [60], creating excited dimers:

$$Xe^\star + Xe \rightarrow Xe_2^\star. \tag{2.3}$$

These decay with the release of VUV photons,

$$Xe_2^\star \rightarrow 2Xe + h\nu \,, \tag{2.4}$$

which have a wavelength distribution peaked at 178 nm and with FWHM = 14 nm [55]. Ionized atoms can also combine with neutral atoms, also in the same time scale of picoseconds, to form ionized dimers:

$$Xe^+ + Xe \rightarrow Xe_2^+ \,. \tag{2.5}$$

The ionized molecules can absorb electrons, leaving them on an excited state:

$$
\begin{aligned}
Xe_2^+ + e &\rightarrow Xe^{\star\star} + Xe \\
Xe^{\star\star} &\rightarrow Xe^\star + heat \,.
\end{aligned} \tag{2.6}
$$
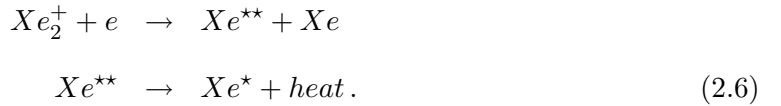
The recombination process has a characteristic time of $\tau_R = 45$ ns [57]. The resulting excited atoms can then combine and decay releasing photons, as described in Eq. 2.3 and Eq. 2.4. These photons travel through the liquid Xe and are collected by photo-multiplier tubes (PMTs). The PMTs generate a current proportional to the number of incident photons, and with amplitude dependent on the efficiency of the given PMT (more details in Section 3.1.2). This signal is called the S1 signal, and is commonly measured in units of the number of electrons generated by the photons incident on the PMTs, referred to as "photoelectrons" (phe). The dimers form in either a singlet or a triplet state, which decay with time constants $\tau = 2.2$ ns and $\tau = 27$ ns, respectively [61]. Both states still decay by releasing 178 nm photons; the only difference is in the decay time.

In the presence of an electric field $\mathcal{E}_d$, the recombination process described in Eq. 2.6 is
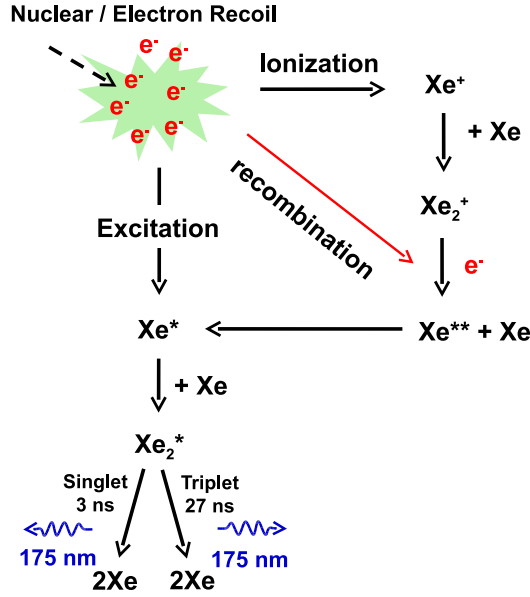
Figure 2.4: Xe scintillation process.

suppressed, and less photons are produced for the scintillation signal S1. The free electrons produced by ionization can be described as a "cloud" around the interaction site. When the electric field $\mathcal{E}_d$ is applied, some of these electrons are extracted from the cloud and drift up, lowering the number of electrons available for recombination. The higher the electric field, the more electrons escape, thus producing more charge but less light. This effect is referred to as "quenching".

The scintillation yield is commonly quoted as the number of photons emitted at field $\mathcal{E}_d$ relative to the number of photons emitted at zero field (which is the maximum number of photons emitted). The *relative scintillation yield* is given by $S = S(\mathcal{E}_d)/S(0)$. The number of scintillation photons at zero field is given by $S(0) = E/W_{ph}$, where $W_{ph} = 21.6\,\mathrm{eV}$ [62]. Fig. 2.5 shows the size of the S1 signal as a function of electric field, relative to the S1 size at zero-field. Different types of interactions (i.e. electron or nuclear recoils) have different recombination efficiencies, so that the size of S1 also varies with the type of interaction (see Section 2.1.4). In XENON10, an electric field of $\mathcal{E}_d = 0.73\,\mathrm{kV} \cdot \mathrm{cm}^{-1}$ is applied, and the relative scintillation yield is $S_e = 0.54$ for electron recoils (measured with $122\,\mathrm{keV}$ γ's) and $S_n = 0.95$ for nuclear recoils. The relative scintillation yield is obtained by measuring the number of photoelectrons in interactions of known energy (e.g. $122\,\mathrm{keV}$ γ peak from the
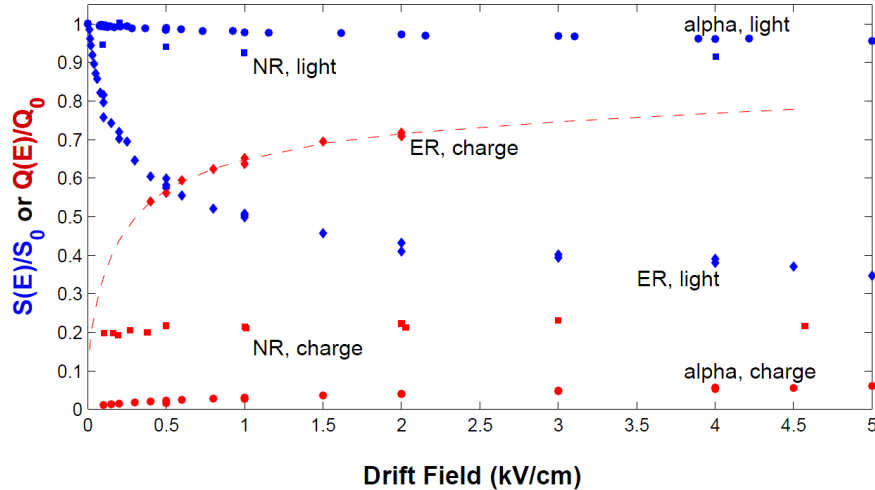
Figure 2.5: Scintillation yield $(S(\mathcal{E}_d)/S(0)$, in blue) and ionization yield $(Q(\mathcal{E}_d)/Q(\mathcal{E}_d \to \infty)$, in red) in liquid Xe versus applied electric field $(\mathcal{E}_d)$ for different types of interactions: electron recoils ($122\,\text{keV}$ γ's, diamonds), nuclear recoils ($56\,\text{keV}_\text{r}$, squares) and α particles ($5.3\,\text{MeV}$, circles). Figure obtained from [63].

^{57}Co calibration source) at zero field and at the given field $\mathcal{E}_d$.

The shape of the S1 signal is also determined by the presence of an electric field. At zero-field, the light generated by recombination dominates the time-structure of the signal, and thus the S1 has a decay time of $\sim 45\,\text{ns}$. At non-zero field $\mathcal{E}_d$, the recombination is suppressed and the S1 has a decay constant corresponding to the triplet state decay time. In XENON10, the S1 decay time has been measured at $29\,\text{ns}$, consistent with the triplet decay time - see Fig. 2.6.

2.1.3 Ionization Signal (S2)

As explained in the previous section, the application of an electric field across the liquid Xe (the drift field $\mathcal{E}_d$) suppresses the S1 signal by preventing electron recombination, thus making these electrons available in the form an ionization signal. The electric field drifts the electrons up the liquid volume until they reach the liquid-gas interface. A second electric field, called the extraction field $\mathcal{E}_e$, is applied across the interface between the liquid and the gas phase, which extracts the electrons from the liquid and accelerates them through the Xe gas, creating further scintillation light, proportional to the electric field - the proportional
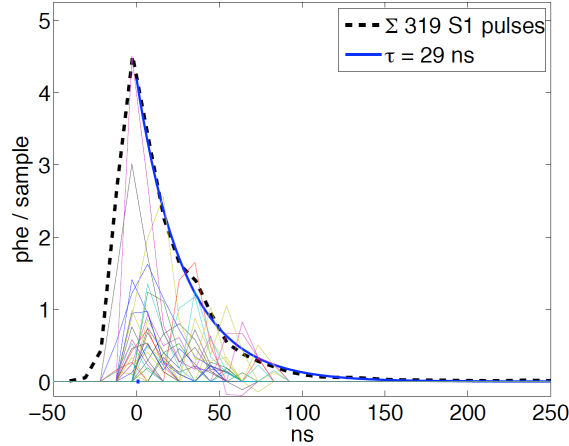
Figure 2.6: S1 signals in XENON10, showing the S1 decay time of 29 ns. The plot shows 319 individual S1 pulses of 80 phe each (thin color lines), and their sum (dashed black line) scaled down to match the tallest peak. The thick blue line indicates the best-fit exponential decay with $\tau = 29$ ns. Figure obtained from [64].

or secondary light signal S2. Like the S1 signal, the S2 signal is measured in photoelectrons.

In XENON10, the drift field is applied between a pair of grids, one of them 1.2 cm above the bottom PMTs (the Cathode grid) and another just below the gas-liquid interface (the Gate grid), with 15 cm of separation; the extraction field is applied between the Gate grid and another grid just below the top PMTs (the Anode grid), separated by 5 mm. Fig. 2.20 shows a diagram of the grids and applied fields. The volume over which the drift field is applied is called the *active volume*, as we only have both S1 and S2 signals for scatters in this region. Other liquid Xe volumes inside the detector are referred to as *non-active volumes*; since no field is applied in these areas, scatters in this region will generate scintillation signals (S1's), but not charge signals (S2's).

The drift velocity (v_d) of the electrons is a function of the drift field $\mathcal{E}_d$, and Fig. 2.7 shows a plot of the drift velocity vs. electric field measured by [65]. The time separation between the S1 and S2 signals for a scatter (called the *drift time*) depends on the electron drift velocity and the z-position of the scatter, relative to the gas-liquid interface. In XENON10, an electric field of $\mathcal{E}_d = 0.73\,\text{kV} \cdot \text{cm}^{-1}$ was applied, and it was found that the maximum time separation between S1 and S2 signals was $79.3 \pm 0.2\,\mu\text{s}$. The maximum distance an electron can be drifted is the height of the active Xe volume of 15 cm, thus yielding a drift velocity of $1.89 \pm 0.01\,\text{mm}\,\mu\text{s}^{-1}$.
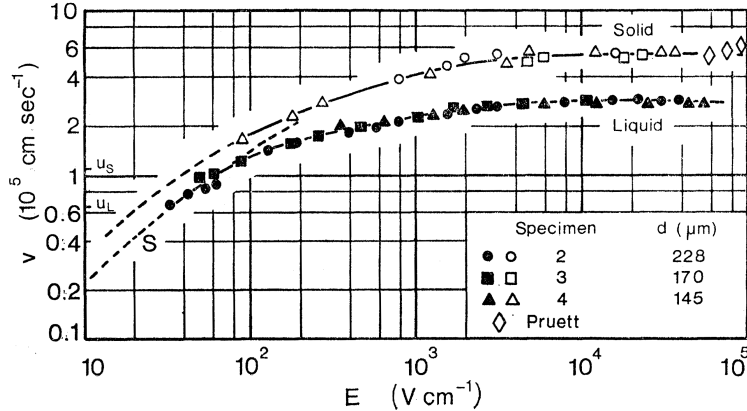
Figure 2.7: Electron drift velocity v_d vs. electric field $\mathcal{E}_d$ for liquid Xe at 163 K, taken from [65]. The value of d (μm) denotes the drift distance used in the measurement

The charge signal is only observed if the electrons are drifted all the way to the gas-liquid interface, extracted into gas, and accelerated in the gas to produce secondary scintillation light. The number of electrons extracted from the interaction site is a function of the electric field, and is expressed as the number of electrons extracted relative to the number of electrons extracted at an infinite field, $\mathcal{E}_d \to \infty$ (which is the maximum possible number of electrons extracted) The *relative ionization yield* is given by $Q\left(\mathcal{E}_d\right)/Q\left(\mathcal{E}_d \to \infty\right)$. The maximum number of extracted electrons is given by $Q\left(\mathcal{E}_d \to \infty\right) = E/W$, where E is the energy deposited by the interaction, and W is the work function ($W = 15.6$ eV for liquid Xe). For XENON10, with an applied drift field $\mathcal{E}_d = 0.73$ kV $\cdot$ cm^{-1}, the relative charge extraction is $Q\left(\mathcal{E}_d\right)/Q\left(\mathcal{E}_d \to \infty\right) = 0.61$ for electron recoils (measured with 122 keV γ's), and $Q\left(\mathcal{E}_d\right)/Q\left(\mathcal{E}_d \to \infty\right) = 0.21$ for nuclear recoils. The behavior of the relative ionization yield vs. applied field is shown in Fig. 2.5.

There is a trade-off between the number of photons and electrons available in an interaction. The relation between scintillation and ionization yield can be expressed as [56]

$$\frac{S\left(\mathcal{E}_d\right)}{S\left(0\right)} = a \cdot \left(1 - \frac{Q\left(\mathcal{E}_d\right)}{Q\left(\mathcal{E}_d \to \infty\right)}\right) + b\,, \tag{2.7}$$

where a and b are factors relating the numbers of excited and ionized states. The relation between scintillation and ionization yields is referred to as the "macroscopic" anti-correlation. The "microscopic" anti-correlation, on the other hand, refers to the fluctuation of the relative

scintillation and ionization yields on an event by event basis, and is due to the fluctuations in the electron recombination process at the interaction site. This effect is easily visible in the anti-correlation of the S1 and S2 signals for events of a fixed energy, as shown in Fig. 4.4. The anti-correlation of the S1 and S2 signals can be used to our advantage in improving the energy resolution of the detector, as explained in Section 2.1.5.

After the electrons are extracted from the interaction site, they drift up to the gas-liquid interface, and are extracted into the gas. In XENON10, the extraction field of $\mathcal{E}_e = 12\,\mathrm{kV\cdot cm^{-1}}$ ensures transmission efficiency through the gas-liquid interface of $\sim 100\%$ [60, pp. 64]. The field then accelerates the electrons through the gas phase, which produce electroluminescence. The number of photons produced per electron traveling in a gas gap of length x in a field $\mathcal{E}_e$ is given by [66]:

$$N_{ph} = 70 \cdot \left(\frac{\mathcal{E}_e}{p} - 1 \right) \cdot x \cdot p \,, \tag{2.8}$$

where p is the Xe gas pressure, measured in atm. As an example, the standard operating pressure of the XENON10 detector is 2.1 atm; for a gas gap of 2.5 mm, when the liquid level is exactly between the Gate and Anode grids, we obtain $N_{ph} = 173$ scintillation photons per extracted electron in the S2 signal. The efficiency of light collection by the PMTs reduce the S2 signal by a factor of $\sim 1/10$ (see Section 2.1.8), and the Quantum Efficiency (the efficiency that an incident photon will generate an electron in the photocathode) further reduces the signal by a factor of $\sim 1/4$. In XENON10, an S2 scintillation efficiency of $n_{ph} = 24 \pm 7\,\mathrm{phe}$ per electron was observed. The S2 signal observed by the PMTs corresponds to the combined scintillation light of all electrons extracted from the original interaction site and accelerated through the gas. The S2 signal is very large relative to the S1 signal, making the detection (and triggering) of events with small energy depositions much easier. During the WIMP search runs, the XENON10 DAQ triggers only on S2 pulses (see Section 3.1.7).

The width of the S2 signal is primarily determined from the length x of the gas gap. The electrons also move in the gas phase with velocity v_d; for a gas gap of $x = 2.5\,\mathrm{mm}$, the expected width of the S2 signal is $750\,\mu\mathrm{s}$. The S2 pulses observed in XENON10 have a Gaussian-like shape, with an average FWHM $\approx 600\,\mathrm{ns}$. The width of the S2 signal is also

affected by the z-position of the original interaction; as the electrons extracted from the interaction site drift up in the liquid, the electron cloud is diffused, causing the widening of the S2 signal for events at greater depths. The mean S2 width varies from FWHM ≈ 450 ns at $z = 0$ cm to FWHM ≈ 700 ns at $z = -15$ cm.

2.1.4 Discrimination

A particle interaction in the liquid Xe causes the target particle - either an electron or the nucleus from a Xe atom - to recoil. While gammas and charged particles are more likely to interact with the atomic electrons than with the nucleus, the reverse is true for uncharged particles; neutrons, like WIMPs, are much more likely (> 2 orders of magnitude) to interact with the nucleus than with the electrons. Events in the liquid Xe can be classified into 2 categories: electron recoil (ER) events, which include interactions by incident gammas and electrons on the atomic electrons; and nuclear recoil (NR) events, which include interactions by incident neutrons or WIMPs on the atomic nucleus. The majority of background events in a liquid Xe detector are gammas, usually by 3-4 orders of magnitude. The ability to distinguish the electron recoils from nuclear recoils provides a large reduction in background, and is crucial to the success of a dark matter experiment.

A liquid Xe detector that is sensitive to both scintillation and ionization signals can use them to distinguish between recoil types. For recoil energies above 2 keV, nuclear recoils have a larger electronic stopping power than electron recoils of the same energy. This leads to denser ionization tracks for nuclear recoils compared to electron recoils, and more efficient recombination. This causes the scintillation signal to be boosted, and the ionization signal suppressed. The net effect is that the ratio of ionization to scintillation signals ($S2/S1$) is smaller for nuclear recoils than for electron recoils:

$$\left(\frac{S2}{S1}\right)_{NR} < \left(\frac{S2}{S1}\right)_{ER}. \tag{2.9}$$

The signal ratios are usually plotted as $\log_{10}(S2/S1)$, which can be fitted by Gaussian distributions (see Fig. 2.9). For the XENON10 configuration, the average $S2/S1$ ratio for nuclear recoils is approximately $1/2$ the ratio for electron recoils in the energy range used

for the WIMP search.

Plotting the signal ratio versus energy shows the formation of two distinct bands. Fig. 2.8 plots $\log_{10}(S2/S1)$ vs. energy for data acquired in XENON10, showing the nuclear recoil and electron recoil bands, obtained from neutron and ^{137}Cs gamma calibration data, respectively. The band widths are defined at $\pm 3\sigma$ from the band centroid (μ). There is some overlap between the bands - the electron recoil band extends down to the centroid of the nuclear recoil band. However, the overlap leaves the lower half of the nuclear recoil band mostly free, and we can define a WIMP search box between the nuclear recoil band centroid μ and the $\mu - 3\sigma$ line - we search for WIMPs only among the events in which the $S2/S1$ ratio fall within the box, in the energy range of interest of $2 - 12\,\mathrm{keV_{ee}}$ (to be explained in Section 2.1.5). This WIMP search box results in an average acceptance efficiency of 45% for nuclear recoils, and an average electron recoil rejection efficiency of 99.6% for events in the energy range of interest. This means that only 0.4% of the events in the electron recoil Gaussian distribution fall within the WIMP search box, thus greatly reducing the gamma background.

The width of the electron recoil band is dominated by recombination fluctuations, and the band width is almost constant at all energies. On the other hand, the recombination fluctuations are subdominant for nuclear recoils, in which Poisson fluctuations dominate, leading to a nuclear recoil band that becomes wider at low energies. However, the separation between the centroids for the electron and nuclear recoil bands increases as recoil energy decreases ($E < 10\,\mathrm{keV_{ee}}$) [67]. This is fortunate, as it leads to improved discrimination at the lowest energy bins, which is where we expect most of the WIMP recoil signal. Fig. 2.10 shows the discrimination efficiency versus energy for XENON10, obtained from the gamma and neutron calibration data (see Section 4.1.2 for more details on the calibration data).

Discrimination is also possible in S1-only systems by looking at the ratio between singlet and triplet states. Measurements have shown that the ratio of singlet to triplet states is $I_s/I_t = 0.05$ for electron recoils and $I_s/I_t = 1.6$ for nuclear recoils [69]. Although the XENON10 digitization rate of $105\,\mathrm{MHz}$ is just enough to observe the effect of the singlet and triplet decay times ($\tau = 2.2\,\mathrm{ns}$ and $\tau = 27\,\mathrm{ns}$) on the S1 pulse shape, its resolution is

(a) Gammas
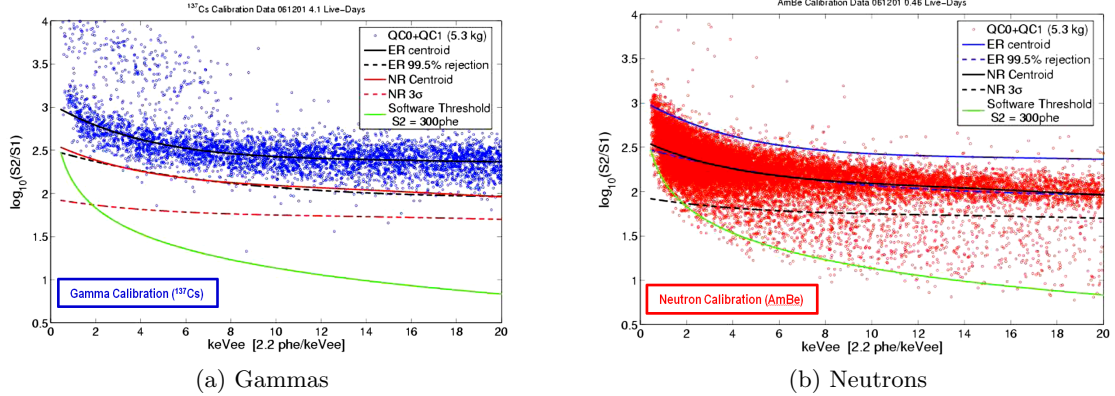
(b) Neutrons

Figure 2.8: Plot of $\log_{10}(S2/S1)$ vs Energy (S1 energy scale, $2.2\,\mathrm{phe/keV_{ee}}$) of the gamma and neutron calibration data in the XENON10 fiducial volume ($5.4\,\mathrm{kg}$), showing the electron recoil and nuclear recoil bands. The plots show the ER band centroid μ (solid blue line), and the WIMP search window defined between the NR band centroid (solid red line) and the -3σ line (dashed red line). The solid green line indicates the analysis software threshold of $S2 > 300\,\mathrm{phe}$.
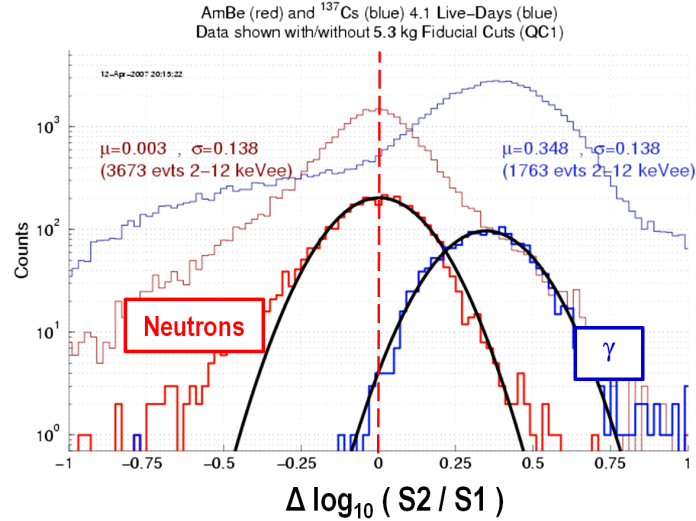
Figure 2.9: Recoil type discrimination in XENON10: $\Delta\log_{10}(S2/S1)$ histograms of electron recoil (blue) and nuclear recoil (red) calibration data show the Gaussian distribution of the discrimination parameter (the black lines are Gaussian fits). The x-axis is $\Delta\log_{10}(S2/S1) = \log_{10}(S2/S1) - \mu$, where μ is the NR band centroid (indicated by the dashed red line). Only events in the energy region of interest ($2-12\,\mathrm{keV_{ee}}$, $L_y = 2.2\,\mathrm{phe/keV_{ee}}$ - see Section 2.1.5) are shown. The plot shows events in the entire active Xe volume (thin blue and red lines) and in the fiducial volume of $5.4\,\mathrm{kg}$ (thick blue and red lines). The neutron calibration data was used for the nuclear recoils, and the ^{137}Cs calibration data was used for the electron recoils.
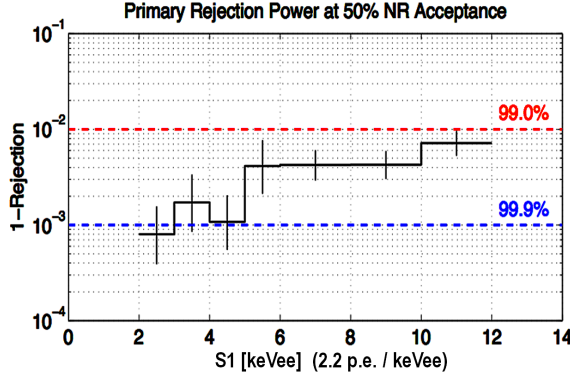
Figure 2.10: Discrimination power of the XENON10 detector - plot of electron recoil rejection efficiency for 50% nuclear recoil acceptance, using the data shown in Fig. 2.8. The average rejection in the energy range of interest ($2 - 12\,\mathrm{keV_{ee}}$, $L_y = 2.2\,\mathrm{phe/keV_{ee}}$ - see Section 2.1.5) in XENON10 is 99.6% [68].

not enough to make reliable use of this discrimination method [70].

2.1.5   Energy scales

As discussed in the previous sections, a nuclear recoil (NR) event is less efficient in generating primary scintillation light (S1) than an electric recoil (ER) event that deposits the same amount of energy. For example, in XENON10, a gamma ER event that deposits $10\,\mathrm{keV}$ in the liquid Xe will generate an S1 signal of $\sim 40\,\mathrm{phe}$, while a neutron NR event of $10\,\mathrm{keV}$ will give an S1 of $10\,\mathrm{phe}$.

Historically, energy calibrations have used only the scintillation signal S1, as many detectors (such as the XMASS experiment) do not measure the ionization signal S2. The use of an S1-only energy scale in which the number of photoelectrons generated per energy deposited (phe/keV) is calibrated by using gamma sources would lead to an underestimation of the energy of NR events. The issue is resolved through the use of 2 distinct energy scales, in which events are measured either in electron-recoil equivalent energy ($\mathrm{keV_{ee}}$), or in nuclear-recoil equivalent energy ($\mathrm{keV_r}$).

The electron-recoil equivalent energy scale is typically determined from the γ calibration data, and defined to a single calibration point. For example, calibrations of the XENON10 detector with an applied field of $\mathcal{E}_d = 0.73\,\mathrm{kV \cdot cm^{-1}}$ using the $^{137}\mathrm{Cs}$ line at $662\,\mathrm{keV}$ result in an ER scintillation light yield of $L_y = 2.2\,\mathrm{phe/keV_{ee}}$ (after taking into account the field
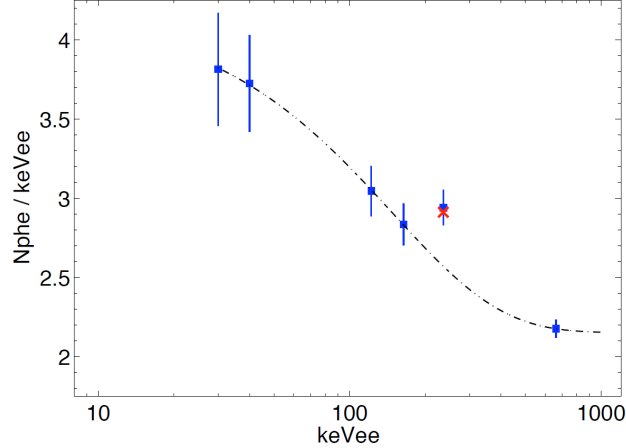
Figure 2.11: Scintillation light yield (L_y) for S1 signals in XENON10, measured in phe/keV$_{ee}$. The data is taken with applied field of $\mathcal{E}_d = 0.73\,\text{kV} \cdot \text{cm}^{-1}$, and are normalized to the average value at the center of the active volume. The measurements are made using the following lines: 30 keV K-shell x-rays; 40 keV from $^{129\text{m}}$Xe; 122 keV from ^{57}Co; 164 keV from $^{131\text{m}}$Xe; 236 keV from $^{129\text{m}}$Xe; and 662 keV from ^{137}Cs. The dashed line is a fit to the data, excluding the 236 keV point. The 236 keV line is actually due to a 2-step decay of 196 keV and 40 keV, both having larger L_y; the expected combined L_y is indicated by the red cross. Figure taken from [64].

quenching, light collection and PMT efficiencies). The energy of an event is then

$$E_{ee} = \frac{S1}{L_y}\,, \tag{2.10}$$

where $S1$ is the scintillation signal measured in phe. Using the scale $L_y = 2.2\,\text{phe/keV}_{ee}$, an event with a signal of 10 phe is equivalent to an energy deposition of 4.5 keV$_{ee}$, whether it is a nuclear recoil or electron recoil event. However, the scintillation yield is not flat nor linear with energy, though, which complicates the energy calibration. A plot of the scintillation light yield in phe/keV$_{ee}$ vs. energy in XENON10 is shown in Fig. 2.11. Because of the non-linearity, data plots that show event energy using the keV$_{ee}$ scale must always indicate what scintillation yield is being used. Results are shown using either the scale calibrated to the ^{137}Cs peak at 662 keV with $L_y = 2.2\,\text{phe/keV}_{ee}$, or calibrated to the ^{57}Co peak at 122 keV, with $L_y = 3.0\,\text{phe/keV}_{ee}$.

The nuclear-recoil equivalent energy scale is usually defined relative to a particular linear ER scale, through the use of the *relative scintillation efficiency for nuclear recoils*, $\mathcal{L}_{eff}$.

The $\mathcal{L}_{eff}$ is defined as the scintillation yield of nuclear recoil relative to scintillation yield of electron recoils *at a specific standard energy*, and at zero field $\mathcal{E}_d = 0$, in order to isolate field quenching effects. The standard energy used to calibrate the $\mathcal{L}_{eff}$ is the ^{57}Co peak at 122 keV. The $\mathcal{L}_{eff}$ can be used to convert S1 signals from the ER to the NR energy scale (given in keV$_\mathrm{r}$):

$$E_r = \frac{E_{ee}}{\mathcal{L}_{eff}} \cdot \frac{S_e}{S_n} \,, \tag{2.11}$$

where E_r is the energy in keV$_\mathrm{r}$, and E_{ee} is the energy measured in keV$_\mathrm{ee}$, given by Eq. 2.10 using the light yield for 122 keV γ's, $L_y = 3.0$ phe/keV$_\mathrm{ee}$; $S_e = 0.54$ and $S_n = 0.93$ are the field quenching factors for scintillation yield of ER events (measured with 122 keV γ's) and NR events, respectively (see Fig. 2.5). $\mathcal{L}_{eff}$ as a function of recoil energy, and thus the nuclear recoil energy scale, is determined through neutron-beam experiments. The precise value and shape of $\mathcal{L}_{eff}$ is a contended debate, and the most recent measurements have yielded contradictory results [71, 72, 73]. The XENON10 experiment has also been able to measure the value of $\mathcal{L}_{eff}$ as a function of energy, using the neutron calibration data. The determination of $\mathcal{L}_{eff}$ in XENON10 is discussed in Section 4.4. The results for $\mathcal{L}_{eff}$ measurements prior to the XENON10 result can be fitted by a constant $\mathcal{L}_{eff} = 0.19$ [74], and are shown in Fig. 2.12. Unless otherwise specified, all results in this work will assume a flat $\mathcal{L}_{eff} = 0.19$. This choice of $\mathcal{L}_{eff}$ corresponds a light yield of 0.98 phe/keV$_\mathrm{r}$.

A third energy scale combines information from both the S1 and S2 signals, and is appropriately referred to as the Combined Energy Scale (CES). The combined energy scale relates the energy of electron recoils to the number of photons and electrons emitted by an interaction:

$$E_{ces} = (n_\gamma + n_{e^-}) \cdot W \,, \tag{2.12}$$

where W is the average energy required to create either a scintillation photon or an ionization electron. it can also be expressed as:

$$E_{ces} = \left(\frac{S1}{\alpha} + \frac{S2}{\beta} \right) \cdot W \,, \tag{2.13}$$
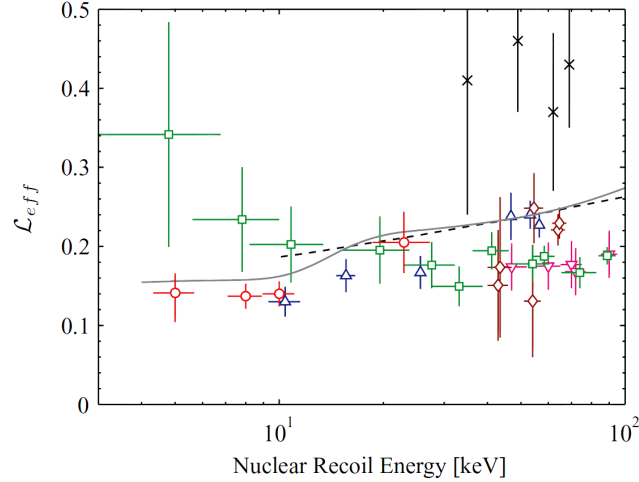
Figure 2.12: Relative scintillation yield for nuclear recoils $\mathcal{L}_{eff}$ vs. NR energy (keV$_\text{r}$) in liquid Xe. The plot shows neutron beam experiment data, taken by ($\Diamond$) Akimov 2002 [75]; ($\triangledown$) Arneodo 2000 [76]; ($\triangle$) Aprile 2005 [77]; ($\bigcirc$) Aprile 2009 [78]; ($\times$) Bernabei [79]; ($\square$) Chepel 2006 [74]. The solid line is the $\mathcal{L}_{eff}$ measured by the XENON10 experiment by fitting the neutron calibration data to MC [71]. The dashed line is the theoretical prediction by Hitachi [80]. The $\mathcal{L}_{eff}$ is measured relative to the scintillation yield of 122 keV γ's at zero field. Figure obtained from [78].

where α and β are experimentally determined parameters in units of phe/γ and phe/e$^-$, respectively. The W-value has been measured by Shutt et al. [81] at $W = 13.46 \pm 0.29$ eV. In XENON10 (operating with $\mathcal{E}_d = 0.73$ kV $\cdot$ cm^{-1} and $\mathcal{E}_e = 12$ kV $\cdot$ cm^{-1}), $\beta = 23.7$ phe/e$^-$ is measured using the single e$^-$ peak in the S2 spectrum, and $\alpha = 0.0858$ phe/γ is measured using the S1 peak at 122 keV from the ^{57}Co gamma calibration data. The combined energy scale does away with recombination fluctuations that make the scintillation non-linear with energy; it is, therefore, linear and single-valued, thus correcting any distortions in the ER energy scale that might arise from calibrating the data using only high energy gamma lines [67]. It also takes advantage of the S1-S2 anti-correlation to improve the energy resolution of the detector, as shown in Fig. 2.13. For further discussion of the details of the combined energy scale, please consult [81] and [67].

As mentioned in Section 1.3.2, differential event rates are typically measured in units called "differential rate units", or dru, which is defined as 1 dru $= 1$ event/keV/kg/day. However, the differential rate unit needs to be qualified to indicate what energy scale is used to measure the event rate - i.e. whether it is a dru with respect to the ER-equivalent
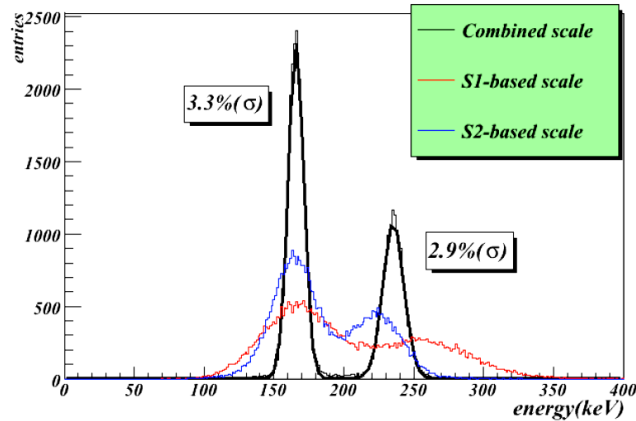
Figure 2.13: Comparison of the energy spectra using the S1-based ER energy scale with $L_y = 2.2 \, \mathrm{phe/keV_{ee}}$ (red line), an S2-based energy scale (blue line), and the Combined Energy Scale, which is described in Section 2.1.5 (black line). The plot shows data taken using activated Xe, and shows the peaks from metastable Xe decay (164 keV and 236 keV). Figure taken from [82].

energy scale or with respect to the NR-equivalent energy scale. Thus, the unit must be expressed as either $1 \, \mathrm{dru_{ee}} = 1 \, \mathrm{event/keV_{ee}/kg/day}$ or $1 \, \mathrm{dru_r} = 1 \, \mathrm{event/keV_r/kg/day}$. It is important to note that differential rate spectra using the ER equivalent energy scale calibrated for a high energy gamma will lead to the underestimation of the event rate at low energies, as the energy bin sizes are "compressed".

It is possible to plot the differential rate spectrum using the Combined Energy Scale, but this is usually only done when comparing the data to Monte Carlo simulations. The CES is ideal for comparisons with simulations because it doesn't distort the width of energy bins. In the simulations performed for this work, the energy deposition is always measured directly by the software, and not through the scintillation signal, so that scintillation yield factors do not come into play, and the simulation measures the "absolute" energy deposited. When comparing the simulation results to experimental data plots, it is necessary to match the energy scale of the data to the type of recoil being simulated; one must compare simulated gamma events with data using the the CES or the ER-equivalent energy scale, and simulated neutron events with data using the NR-equivalent energy scale.

The XENON10 experiment searches for WIMPs only inside an "energy range of interest", which was defined before the analysis of the WIMP search data at $2 - 12 \, \mathrm{keV_{ee}}$, using the $L_y = 2.2 \, \mathrm{phe/keV_{ee}}$ scale. This range corresponds to $1.5 - 8.8 \, \mathrm{keV_{ee}}$ using the $L_y =$

$3.0\,\mathrm{phe/keV_{ee}}$ scale set by the $122\,\mathrm{keV}$ calibrations, or $4.5 - 26.9\,\mathrm{keV_r}$ in the NR energy scale. The lower bound in the range is determined by the trigger efficiency, and is set to ensure $\geq 99\%$ trigger efficiency (see Section 3.1.7). The upper bound is set to ensure that the background does not overwhelm the WIMP signal. For a signal threshold of $4.5\,\mathrm{keV_r}$, $\sim 80\%$ of events occur with $E_r < 26.9\,\mathrm{keV_r}$, as seen see Fig. 1.14.

2.1.6   Self-shielding

The reduction of backgrounds is essential for the success of any rare-event search experiment. Gammas and neutrons present in the detector environment or emitted by the detector components flood the experiment. Because of its relatively large density $(2.94\,\mathrm{g} \cdot \mathrm{cm^{-3}})$ and high Z, liquid Xe provides additional self-shielding against both types of backgrounds, which can be exploited through a number of techniques.

WIMPs are expected to have small cross-sections with nucleons, and therefore are not expected to scatter more than once in the detector. On the other hand, neutrons and gammas can scatter more than once, especially as we scale up the liquid Xe volume in larger detectors. By creating an event selection cut that keeps only single scatters, we can greatly reduce background rates.

The liquid Xe provides very efficient shielding against low energy gammas ($E_\gamma <$ $500\,\mathrm{keV}$), which have relatively short attenuation length, as shown in Fig. 2.14. The low energy gammas are thus confined to the outer layers of the liquid Xe detector. Moreover, the incident particles only become a problem when they produce signals that might be identified as a WIMP, i.e. they must be single scatters and have energy depositions that fall within the energy range of interest. For a gamma to mimic a WIMP signal, it must deposit only a few $\mathrm{keV_{ee}}$ of energy, which means that it must either be a low energy gamma, or a high energy gamma that Compton scatters at a small angle, and then exits the detector without scattering again - events that scatter more than once deposit more energy, so that the energy range cut is already a very efficient single scatter cut. Because of the energy range requirement, the gamma background event rate is suppressed by $e^{-L/\lambda}$, where L is the total transit distance across the detector and λ is the gamma scattering length in Xe.
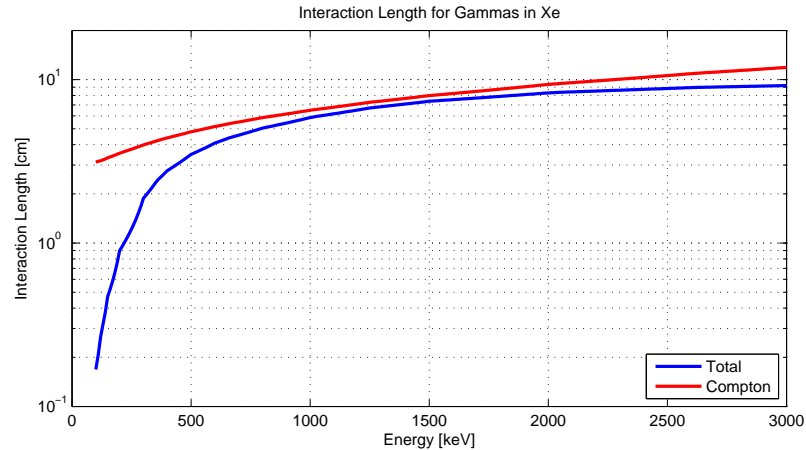
Figure 2.14: Attenuation length versus energy, for gammas in liquid Xe. The attenuation lengths displayed are calculated from the total cross section (blue line) and from the Compton scattering cross section (red line).

We can further reduce the background by selecting as WIMP candidates only events in the center region of the detector, which maximizes L and therefore maximizes the background suppression, as illustrated in Fig. 2.15. This effect contributes to the creation of a low background region in the center of the detector. The selection of the a region in the bulk of the detector to search for WIMP events is called the *fiducial volume cut*.

Neutron events deposit a lot less energy per scatter, so that we can actually have events with multiple scatters that still fall within the energy range of interest. While the energy cut imposes strong constraints in the topology of the gamma events (the gamma must be traveling straight through the bulk of the detector and generate a single scatter in the fiducial volume), it has weak constraints on the neutron event topology. Therefore, the combined fiducial volume and energy range cuts are a lot less efficient for neutrons than for gammas, as will be seen in the later chapters. Conversely, the single scatter cut is very inefficient for low energy gamma events compared to neutrons, but only because the events that would be removed as multiple scatters have already been removed from the WIMP search energy range by depositing too much energy.

The XENON10 detector is capable of reconstructing the XYZ position of every scatter in the active Xe volume (see Section 3.1.1 for more details), which allows the implementation of both the multiple scatter cut and the fiducial volume cut. The fiducial volume used by
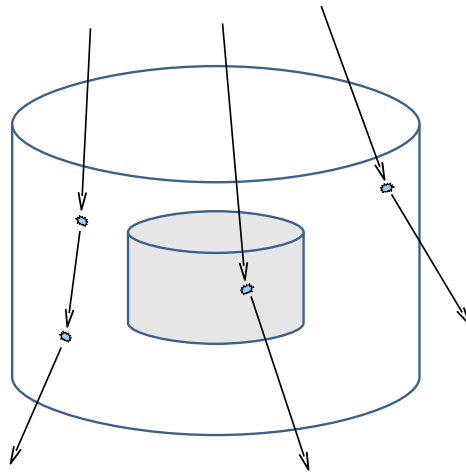
Figure 2.15: Self-Shielding and Fiducial Volume in liquid Xe detectors. The figure illustrates the use of fiducial volume to take advantage of the self-shielding properties of Xe. The liquid Xe high density $(2.94\,\mathrm{g\cdot cm^{-3}})$ and high Z (54) results in short penetration lengths for most radiation. The low energy window for WIMP events search means that gammas must enter the detector, deposit only a small amount of energy, then leave without scattering again, since multiple scatters deposit more energy than a single scatter. The background is suppressed by a $e^{-L/\lambda}$ term, where L is the length of Xe transversed by the particle, and λ is the attenuation length in liquid Xe. The low energy window also means that gammas can only scatter at small angles. Scatters in the periphery of the active Xe volume can scatter and exit the detector while transversing only a relatively small amount of Xe. By only accepting WIMP-candidate events in a *fiducial volume* (the gray cylinder), we only accept gammas that travel most of the detector length, thus greatly suppressing the background.

the XENON10 detector during the calibrations and WIMP search runs selects events with $r < 8\,\text{cm}$ and $-12.2\,\text{cm} < z < -2.8\,\text{cm}$ ($15\,\mu\text{s} < \text{drift time} < 65\,\mu\text{s}$), corresponding to a total Xe mass of 5.4 kg. Because of the importance of the fiducial volume for the WIMP search, key parameters are usually quoted relative to the center or the bulk of the detector, i.e. light collection *in the bulk* or background event rate *in the fiducial volume.*

Both the single scatter cuts and fiducial volume cuts become more efficient as we increase the detector size, and a greater fraction of the detector becomes available for the fiducial volume. The efficiency of the cuts for the XENON10 detector is discussed in more detail in Chapter 6. The increase in efficiency of the self-shielding as we increase detector size is discussed in detail in Chapter 8, and illustrated in Fig. 8.3. This figure makes very clear the significance of the Xe self-shielding for gamma background suppression.

2.1.7 Purity

The strength of the S2 signal is affected by the purity of the liquid Xe, as impurities can capture electrons as they are drifted up towards the gas interface and thus suppress the S2 signal. Scatters at greater depths will suffer greater suppression, as they have to travel a longer path. The S2 signals decrease exponentially with depth, i.e. $S2(z) = S2_0 \cdot e^{-|z|/(l_\text{e})}$, and Xe purity is usually described by the *characteristic electron drift length* l_e, or by the *electron lifetime* $\tau_\text{e} = l_\text{e}/v_\text{e}$, where $v_\text{e} = 1.89 \pm 0.01\,\text{mm} \cdot \mu\text{s}^{-1}$ is the electron drift velocity at $\mathcal{E}_d = 0.73\,\text{kV} \cdot \text{cm}^{-1}$. The purity in XENON10 is measured by fitting the S2 signal size of $122\,\text{keV}$ γ's (from a ^{57}Co source) as a function of depth (see Section 4.1.2).

The first step in ensuring Xe purity is detector cleanliness - all detector internal components are assembled in a clean room, and once assembled the detector is "baked" to force outgassing of any impurities trapped in porous surfaces. Most of the surfaces that the Xe comes into contact are either electro-polished stainless steel or Teflon. The liquid Xe used by the XENON10 detector for most its data runs (including the WIMP search run) was obtained from Spectra Gases Inc, and is rated at 99.9998% purity. The electron lifetime after filling was only $\sim 20\,\mu\text{s}$, corresponding to $\sim 1\,\text{cm}$.

After the detector is filled up with Xe, continuous circulation of the Xe through a high
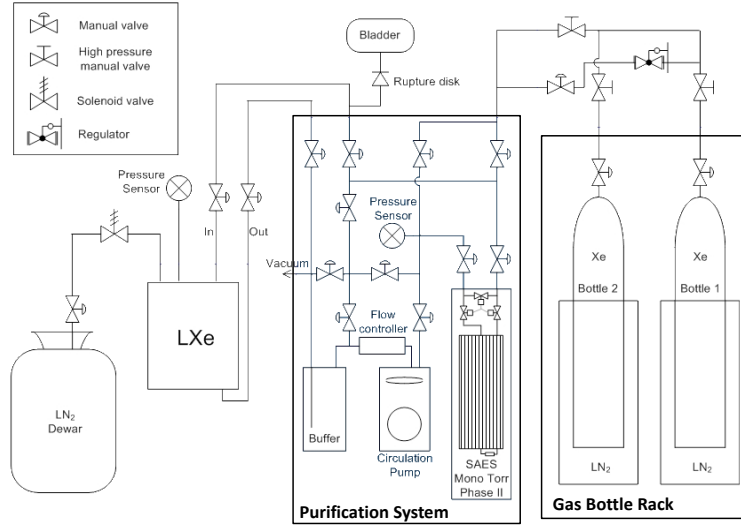
Figure 2.16: Schematic of the Xe purification system.

temperature gas purifier in a closed loop with the detector is started. The liquid Xe flows

from the detector into a buffer volume where it is vaporized and pumped out by a diaphragm

pump (KNF model N143.12E), passes through the SAES MonoTorr gas getter (model PS4-

MT3-R), and is condensed back into the detector. During XENON10 operation, a gas flow

of 2.6 slpm was maintained. Although the pump+getter system allows a maximum flow rate

of 15 slpm, the flow was limited to 2.6 slpm by the detector cooling power, so that stable

temperature and pressure was maintained. After a month of circulation at this rate, the

characteristic electron lifetime reached $\sim 2\,\mathrm{ms}$, which corresponds to $\sim 4\,\mathrm{m}$ drift length,

plenty to ensure that the S2 signal in XENON10 is uniform in size across the entire height

of the detector (15 cm). A diagram of the Xe gas purification system is shown in Fig. 2.16.

2.1.8 Light Collection

The S1 signal size is affected by the light collection efficiency, also referred to as the *geo-metrical light collection*, which is defined as the ratio of the number of photons reaching

the PMTs and the number of photons emitted. Monte Carlo simulations were performed

to characterize the light collection efficiency as a function of event position (r and z), and

are discussed in detail in [83]. The simulations follow scintillation photons emitted at every

position in the Xe volume as they travel through the Xe, are reflected (or absorbed) by

the Teflon walls, and finally reach the PMT photocathodes. The simulation results depend mainly on the reflectivity of the Teflon and the photon attenuation length in the Xe (given by Eq. 2.2). The Teflon reflectivity is estimated between 82% [84] and 95% [85]. The simulation uses a reflectivity value of $R = 95\%$, absorption length in liquid Xe $\lambda_{abs} = 100\,\text{cm}$, Raleigh scattering length $\lambda_R = 30\,\text{cm}$, and refractive index 1.61. Among the remaining parameters assumed are the 50% reflectivity for steel, and 90% optical transparency for the grids.

The simulation reproduces the ratio of the S1 signals collected by the top and bottom PMTs, which averages to $\mathcal{R} = S1_{top}/S1_{bottom} \approx 20\%/80\%$ in the fiducial volume. The ratio as a function of depth $\mathcal{R}(z)$ is compared to the data to verify the parameters used in the simulation. It is found that there is a degeneracy in the solution between the Teflon reflectivity and the absorption length. For instance, similar results can be obtained if we assume 88% Teflon reflectivity and $\lambda_{abs} \rightarrow \infty$ [83].

The light collection simulation predicts an average geometrical light collection in the bulk of the liquid Xe of $40\% \pm 15\%$. It is also useful to determine the *total light collection*, which combines the geometrical light collection with the effective quantum efficiency of the PMTs (explained in Section 3.1.2) and gives the percentage of emitted photons that actually generate an S1 signal. For an estimated effective quantum efficiency of 20% for the R8520 PMTs, we obtain the total light collection of $8\% \pm 3\%$. The measured total light collection in XENON10 can also be estimated from the S1 signal size of high energy gammas, and is calculated at $11\% \pm 3\%$, consistent with the predicted value.

As can be seen in Fig. 2.17, the geometrical light collection efficiency is not uniform for the entire active Xe volume. It is necessary to apply position dependent correction to the size of the S1 signal in order to measure it correctly for every scatter. For precise corrections to the S1 signal, they must be based on the XENON10 data, rather than simulations; ideally a map of the light response to gammas of a fixed energy should be used. The standard ^{57}Co gamma calibration data cannot be used for this purpose, as the $122\,\text{keV}$ γ's do not penetrate uniformly through the entire active volume. At the end of the WIMP search runs of the XENON10 detector, a calibration run using activated Xe was performed, using Xe exposed
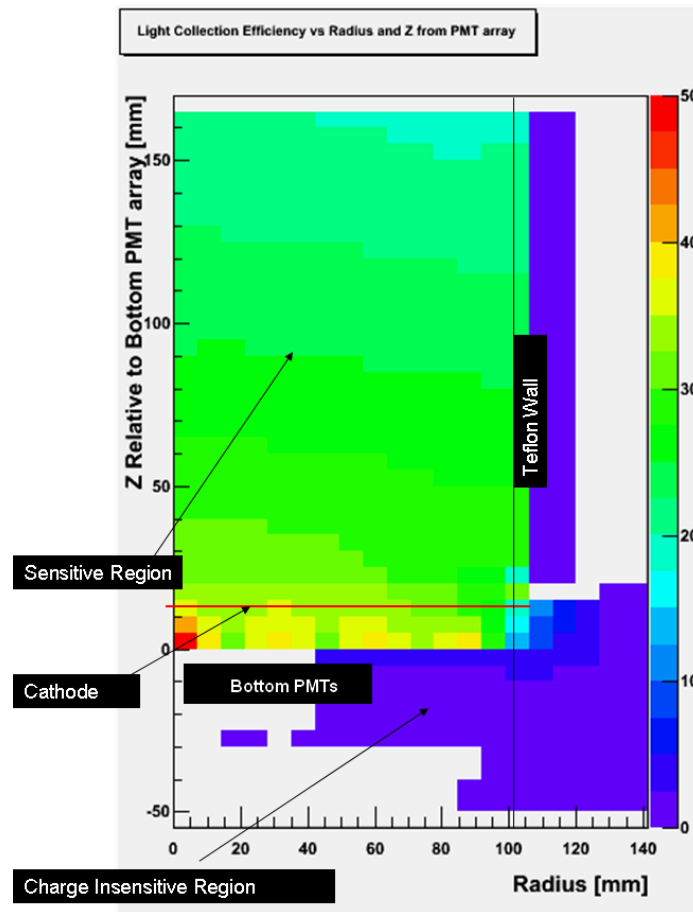
Figure 2.17: S1 light collection from simulation, obtained from R. Gomez [83].

to a neutron source. The activated Xe contains the metastate ^{131m}Xe, which decays with the emission of a 164 keV γ. The position dependence of the S1 signal was mapped out, and is shown in Fig. 2.18. The map is then used to adjust the size of the S1 signal to match the size a similar event would have at the center of the detector.

2.1.9   Subsystems

2.1.9.1   Cryogenics

The detector temperature affects both scintillation (S1) and ionization (S2) signals, as the PMT gains vary with temperature, and the proportional light yield is strongly dependent on pressure (Eq. 2.8), which changes with temperature. Stable operating conditions for the detector are important to ensure that all signals are properly calibrated. During the WIMP
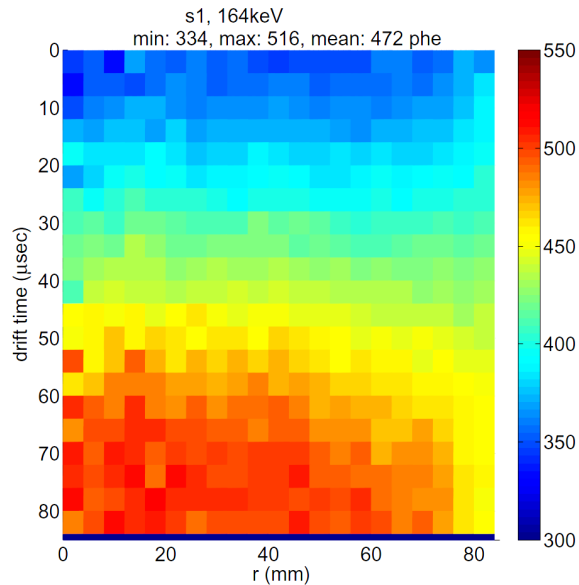
Figure 2.18: Map of the total S1 signal for $164\,keV$ gammas from the activated Xe run, collected at both top and bottom PMT arrays (color scale = average S1 size in phe). The plot illustrates the S1 light collection in the XENON10 detector. Figure courtesy of J. Kwong [70].

search run, the XENON10 detector was maintained at a temperature of $T = 177\,K$, which correspond to a Xe vapor pressure of $2.11 \pm 0.01\,atm$. A limiting factor on the temperature and pressure is the PMT technology. The R8520 PMTs are rated for use in up to $5\,atm$. It was decided that the pressure should be kept below $2.5\,atm$ to allow for a comfortable margin in the case of an emergency (i.e. cryogenics malfunction).

Thermal insulation with the environment is achieved through the use of a double cryostat system, with vacuum ($10^{-3}\,Torr$) between the inner and outer cryostats. The temperature in the liquid Xe was maintained by a pulse tube refrigerator (PTR), connected to the Xe chamber via a copper cold finger. The PTR is manufactured by Iwatani Corp, and was developed by KEK and Nihon University specifically for liquid Xe operation. The PTR is designed to deliver $\sim 100\,W$ of cooling power, sufficient to cool down and liquefy the entire Xe mass, and hold the temperature at the desired value. The PTR head is kept at a temperature of $171\,K$ using a Lakeshore Temperature Controller (model 304), and its stable temperature is achieved by using $50\,\Omega$ heaters in an active feed-back control. The XENON10 detector showed excellent stability in the 6 month period of the WIMP search
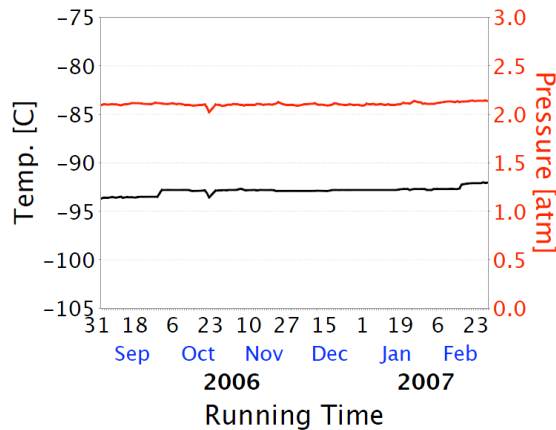
Figure 2.19: Stability of the temperature and pressure in XENON10 during the WIMP search and calibration runs, from August 2006 to February 2007.

and calibration runs, with pressure variation of < 0.06 atm and temperature variation of < 0.05 K [82]. The pressure and temperature is continuously monitored at various locations in the detector by a Slow Control System (SCS), which records crucial operating variables necessary in data analysis, and notifies the XENON10 staff in case of anomalies. Fig. 2.19 plots the temperature and pressure readings by the SCS during the WIMP search run, demonstrating the system stability.

In case of failure of the cryogenic system, the rise in pressure as the liquid Xe evaporates would crush the PMTs, and impair the experiment. However, thermal inertia of the large Xe mass (~ 24 kg) makes the rise in temperature slow enough to stop the run in a controlled way, and recuperate the Xe gas back into storage bottles. Additionally, a battery operated LN$_2$ cooling system is automatically activated by high Xe chamber pressures, keeping the cryostat cold until someone can respond to the emergency situation. A rupture disk provides a final safety measure, venting the Xe into the room in case of extremely high pressure (> 4 atm).

2.1.9.2 Grids and Electric Field

The active Xe volume is defined by grids used to apply the drift field $\mathcal{E}_d$ and the extraction field $\mathcal{E}_e$. There are a total of 4 stainless steel grids in the TPC, 2 in the liquid and 2 in the gas. The grids are electro-formed and electro-polished to ensure smooth edges and avoid
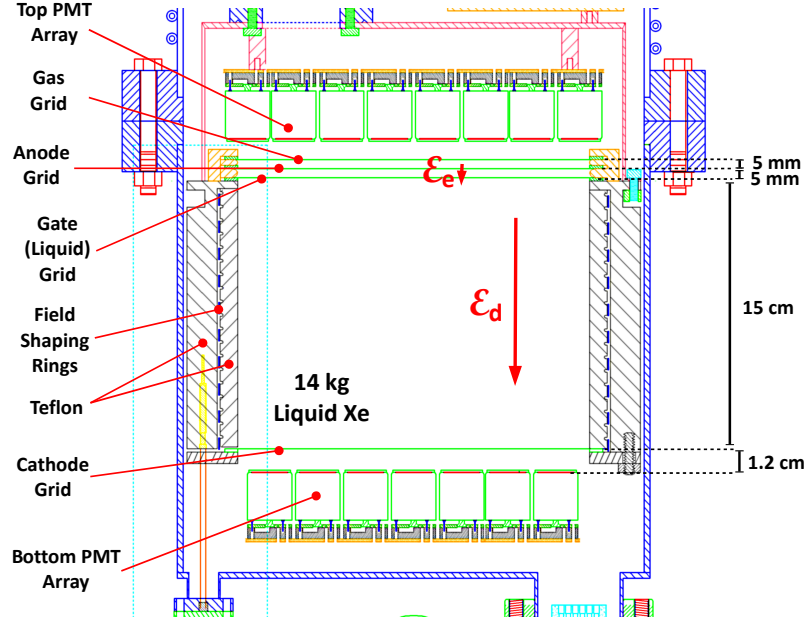
Figure 2.20: Diagram of grids and applied electric fields in XENON10.

discharges. The grids are 0.203 mm thick, and each wire is 0.182 mm wide. The spacing between wires in the grid is 2×2 mm, giving them 90% optical transparency.

As described in Section 2.1.3, the drift field $\mathcal{E}_d$ is defined by the 2 grids in the liquid, the cathode grid at -12 kV and the gate (or "liquid") grid at -1.15 kV, separated by 15 cm. A series of 19 copper shaping rings located just outside the Teflon walls and spaced uniformly are used to "straighten out" the electric field lines at the edges, ensuring the drift field in the active Xe volume is uniform. Simulations were performed with the software packages Maxwell and Garfield to optimize the field configuration [83]. The extraction field $\mathcal{E}_e$ is defined by the gate grid and the anode grid at $+3.15$ kV, in the gas, spaced at 5 mm. Given the Xe relative electric permittivity in the gas ($\epsilon_{r,gas} = 1.0$) and in the liquid ($\epsilon_{r,liq} \approx 2$), we can calculate that the extraction field in the gas is $\mathcal{E}_e = 12$ kV for a liquid level of 2.5 mm, relative to the gate grid. A fourth grid, called the "gas grid", is placed 5 mm above the anode grid and set at -1.15 kV to protect the PMTs from high electric fields. Fig. 2.20 shows a diagram of the grids and applied fields.

2.1.9.3 High Voltage

The high voltage for the shaping rings, the anode, the gate and gas grids was provided by a CAEN power supply system [86], using a CAEN 1733 board for the anode (capable of $+4\,\mathrm{kV}$) and a CAEN 1833 board for the rest (12 channel unit, capable of $-3\,\mathrm{kV}$ per channel). The HV was connected to the grids using bare feedthroughs (steel rods) inside the detector. Bare feedthroughs were used to prevent outgassing from the insulation material and improve Xe purity. Insulation was not necessary as Xe is a good insulator, with a dielectric strength of $40\,\mathrm{kV/mm}$ [54]. A voltage divider made of 19 resistors ($1\,\mathrm{G\Omega}$) mounted on the shaping rings was used to set their voltages at the appropriate levels.

The high voltage for the cathode was provided by a Heizenger PNC power supply, capable of $-100\,\mathrm{kV}$. The cathode HV was brought into the detector by a custom-made feedthrough, consisting of a steel rod wrapped in $5\,\mathrm{mm}$ of Teflon. The Teflon was necessary to prevent sparking (dielectric barrier breakdown). The feedthrough was tested to hold $> 20\,\mathrm{kV}$ in air. The manufacture of feedthroughs capable of holding large voltages is very important for liquid Xe dark matter detectors. As the detectors grow in size, larger voltages need to be applied at the cathode to sustain sufficiently high drift fields, so that enough charge is extracted and drifted from the interaction sites, and the discrimination power of the detector is maintained. Although alternative experiments have proposed the use of a "flatter" aspect ratio for the detector, allowing for greater drift fields [72], any gains in discrimination are quickly offset by the increase in background as the flatter detector cannot take full advantage of the self-shielding properties of the liquid Xe - this point is discussed in detail in Section 8.3.

The high voltage for the PMTs was also supplied by CAEN A1833 boards. The average bias voltage of the PMTs was $\sim 750\,\mathrm{V}$, with a maximum of $900\,\mathrm{V}$. A custom RC filter was used in each channel to reject frequencies $> 10\,\mathrm{Hz}$. The HV for the PMTs was brought into the detector via Kyocera [87] feedthroughs with Burndy-style connectors. Inside the detector, the HV was connected to the PMTs using Kapton insulated wires - Kapton has a dielectric strength of $80\,\mathrm{kV/mm}$ and very low outgassing. The signal gain on individual PMTs is determined by the applied bias voltage, but each PMT has a slightly different

response, so that the PMT gains needs to be calibrated to ensure uniform response to signals in the detector. The CAEN power supply system is computer controlled, which allows the quick adjustment of PMT bias voltages, thus making the gain equalization of all PMTs much easier.

2.1.9.4 Liquid Level

The liquid level between the anode and gate grids determines the extraction field ($\mathcal{E}_e$) strength. Electron extraction into the gas requires that the liquid level is between the gate and anode grids. It is also necessary to ensure that the level is parallel to the grids so that the fields are uniform across the entire gas-liquid interface.

The top of the active volume chamber (including the top PMT array) is assembled in a "diving bell" structure that keeps the liquid level constant. The liquid level is monitored by a cylindrical capacitor, made of 2 concentric stainless steel tubes 20 cm long and separated by 0.5 mm. A tilt meter is also used, consisting of four parallel plate capacitors, separated by 5 mm. The plates in each capacitor are aligned with the anode grid (on the top) and the gate grid (on the bottom). One of the parallel-plate capacitors is filled with Teflon and serves as a reference point. The detector inclination can be set by using leveling feet, accessible even when the detector is closed and inside the shield.

2.2   LUX

The Large Underground Xenon (LUX) experiment is the next step in Dark Matter experiments. It leverages the dual-phase Xe detector technology proven in the XENON10 detector, while adding improvements in key areas, such as shielding and cryogenics, to support the increase in mass and improve backgrounds. A diagram of the LUX detector is shown in Fig. 2.21.

The LUX detector is a dual-phase TPC, with a total liquid Xe mass of 350 kg. The active volume is $\sim$ 49 cm in diameter and $\sim$ 59 cm height, with and active Xe mass of $\sim$ 300 kg, defined by a Teflon Can made of 11 flat reflector panels. The active volume is vertically defined by a pair of grids, which provide the drift field $\mathcal{E}_d$. The bottom grid (the
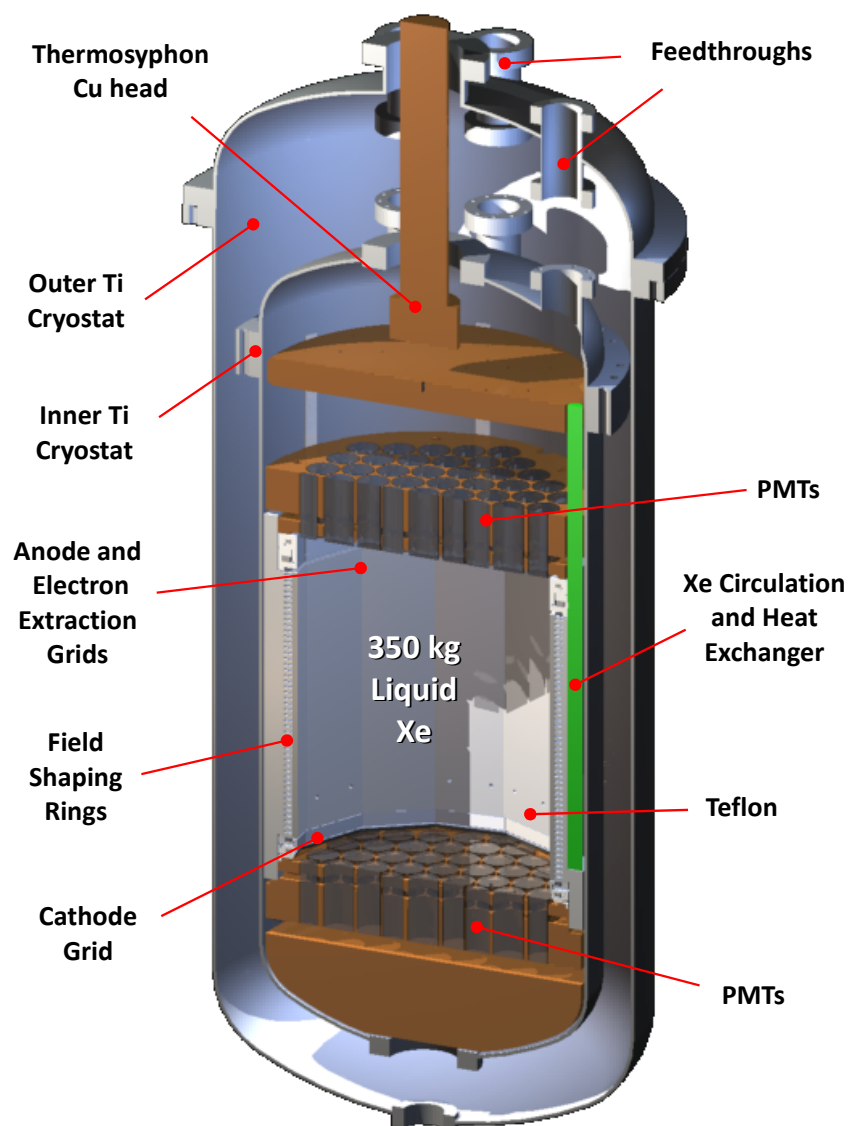
Figure 2.21: Diagram of the LUX detector, courtesy of J. White of the LUX Collaboration.

cathode) has its power supplied by a HV feedthrough capable of supplying $150\,\mathrm{kV}$ and thus generating a field of up to $\mathcal{E}_d < 2.5\,\mathrm{kV\cdot cm^{-1}}$. The LUX detector is planned to operate with a drift field of $0.2 - 1.0\,\mathrm{kV\cdot cm^{-1}}$.

The liquid Xe chamber is built inside a double cryostat, made of low background Ti and with vacuum between the inner and outer vessels. The inner cryostat is covered on the outside with a layer of high-purity copper acting as a radiation shield.

The detector will be operational in 2010 in the Davis cavern of the Sanford underground laboratory, a dedicated facility in the $4850\,\mathrm{ft}$ of the Homestake mine, the site of the Deep Underground Science and Engineering Laboratory (DUSEL). It will be deployed inside a water shield, instrumented with PMTs to serve as a muon veto. The water shield is a 300 tonnes water tank with $8\,\mathrm{m}$ diameter and $6\,\mathrm{m}$ height, illustrated in Fig. 7.15 on page 273. The water shield achieves much lower gamma and neutron background, compared to the standard polyethylene and Pb shields, such as the one used by XENON10. The water shield is especially effective against the high-energy neutron backgrounds generated by muons. The water shield is also very cost-effective, and can be readily used to house additional detectors, or the larger next-generation dark matter detectors, with minimal modifications. The water shield is further discussed in Chapter 7.

The detector uses 122 Hamamatsu R8778 PMTs, divided into 2 arrays (top and bottom) with 61 PMTs each. The PMTs are cylindrical and much larger than the R8520 PMTs used in XENON10 PMTs, with a diameter of $5\,\mathrm{cm}$, compared to the square R8520 with $2.5\,\mathrm{cm}$ side. The larger surface area means that we can reduce the number of PMTs that would be necessary to monitor the much larger detector. The R8778 PMTs that will be used in LUX have been screened for radioactive contamination, and show contamination levels per cm^2 $10\times$ larger than the R8520's. However, the increase in radioactivity from the PMTs is more than offset by the careful selection of the cryostat material, greatly reducing its contribution to the background, and the improved self-shielding derived from the larger detector mass and taller aspect ratio (which adds more Xe between the PMTs and fiducial volume). The LUX background model, including the shield, is discussed in detail in Chapter 7. The properties of the R8778 PMTs relevant to data acquisition such as quantum efficiency, as

well as upgrades to the full LUX electronics chain and data acquisition system, are discussed in Chapter 3.

Although the larger volume and taller aspect ratio reduce the light collection efficiency, Monte Carlo simulations predict that the LUX detector will have a similar scintillation light yield as XENON10, $L_y = 3\,\text{phe/keV}_{\text{ee}}$ for $122\,\text{keV}$ γ's when a $\mathcal{E}_d = 0.73\,\text{kV} \cdot \text{cm}^{-1}$ field is applied. This is due to the higher quantum efficiency of the LUX PMTs compared to the XENON10 PMTs, combined with a couple of steps taken to improve the geometric light collection: (1) the space between PMTs is covered by Teflon reflectors, and (2) the grids used to apply the electric field are designed with 95% optical transparency (compared to 90% in XENON10).

The gas purification system in LUX is similar to the one used in XENON10, also using a commercial high-temperature getter SAES MonoTorr. The limiting factor in the circulation and purification rate is the cooling power necessary, as circulation requires continuous evaporation and condensation of Xe. The baseline design calls for a Xe flow rate of $30\,\text{slpm}$, requiring $\sim 200\,\text{W}$ of cooling power. The cooling in the LUX detector is provided by a thermosyphon system, mounted above the water surface and extending down to the detector. The thermosyphon consists of a tube filled with gas and liquid nitrogen, transferring the heat in a closed loop from the evaporator section (on the bottom) to the condenser section (on the top) [88] - see Fig. 2.22 for a diagram of the process. The LUX experiment uses 3 thermosyphons. The main thermosyphon is called the "Power Thermosyphon", provides $\sim 1\,\text{kW}$ of cooling power, enough to keep up with a circulation and purification rate of $1,000\,\text{kg/day}$. The other 2 thermosyphons are called "Assisting Thermosyphons", and provide $\sim 200\,\text{W}$ of cooling power. The main function of the power thermosyphon is to drive the cooling and liquification of the Xe in the detector, while the assisting thermosyphons regulate the cooling rate and provide temperature stability.

A preliminary version of the LUX detector has been deployed at Case Western Reserve University in 2008 under the name of LUX0.1, and has been used to test all detector subsystems. The LUX0.1 detector has a full LUX-sized stainless steel cryostat, and is filled with $60\,\text{kg}$ of liquid Xe and a $270\,\text{kg}$ Al displacer block, which houses a small active Xe cell
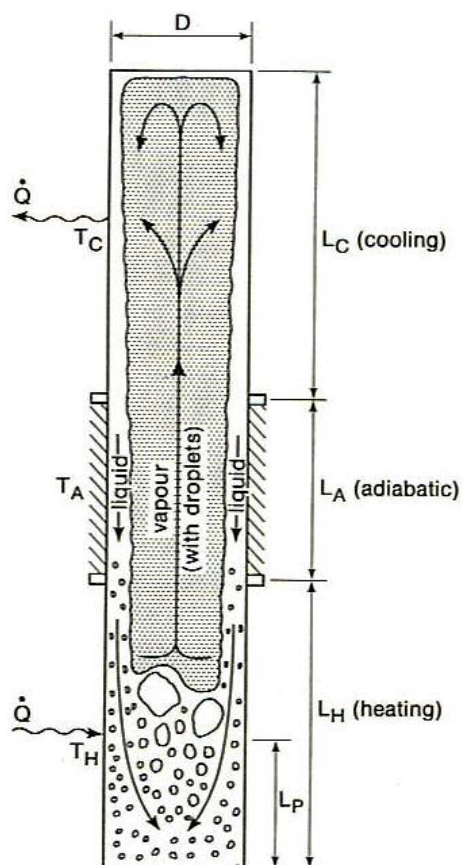
(a) Thermosyphon principle of operation. The bottom is attached to the detector via a Cu "head", and the top is immersed in a liquid N bath. Inside the thermosyphon, the nitrogen evaporates at the bottom, rises to the top where it condenses and flows back down. The closed loop system transfers heat from the bottom to the top, assisted by gravity.

(b) Picture of the LUX power thermosyphon, showing the Cu head at the bottom, which connects the detector to the thermosyphons and delivers $> 1\,\mathrm{kW}$ cooling power.

Figure 2.22: Diagram and picture of the LUX thermosyphon system, obtained from [88].

(a) Al displacer block (250 kg) being installed inside the LUX0.1 detector

(b) LUX0.1 (in the back, on the left) deployment at Case

Figure 2.23: Deployment of the LUX0.1 detector at Case Western Reserve University.

of 5 cm in height, monitored by 4 PMTs. LUX0.1 has successfully tested a number of the LUX subsystems, including the high flow purification and thermosyphon systems. The detector demonstrated fast cooling and stable temperature operation with the thermosyphon, and was able to achieve 250 kg/day purification and > 1 m drift length in < 3 days of purification. It has also been very useful in the characterization of the LUX PMTs, and in the development and testing of the trigger, data acquisition, and data analysis systems. Pictures of the deployment of the LUX0.1 detector at Case are shown in Fig. 2.23.

CHAPTER 3

DATA ACQUISITION SYSTEMS

3.1 XENON10 DAQ

The data acquisition (DAQ) system for XENON10 was designed to maximize the information from the structure and shape of the primary and secondary scintillation pulses (S1 and S2, respectively) available for analysis. The signals from all PMTs are individually digitized by an array of ADCs, with sampling rate of 105 MHz. A single electronics chain is used for all pulses, each channel consisting of a Hamamatsu 8520 PMT, a $\times 10$ Phillips amplifier, and a Struck SIS3301 105 MHz digitizer. The dynamic range of the analog chain and digitizer are optimized to allow single photoelectron resolution and digitization of events with $> 100\,$keV energy without saturation on the S1 and S2 pulses. The data acquisition is triggered by a separate trigger system, which uses the sum of the signal output from the amplifiers. Two types of trigger systems were considered and tested - an S1 trigger, and a S2 trigger. Ultimately, the XENON10 WIMP search data was taken with an S2 trigger. The data is then read from the ADCs into a computer, compressed, and then stored for later analysis. All events are saved, and no processing (i.e. DSP, pulse identification) is performed prior to the data being stored. A summary of the full DAQ chain is shown in Fig. 3.1.
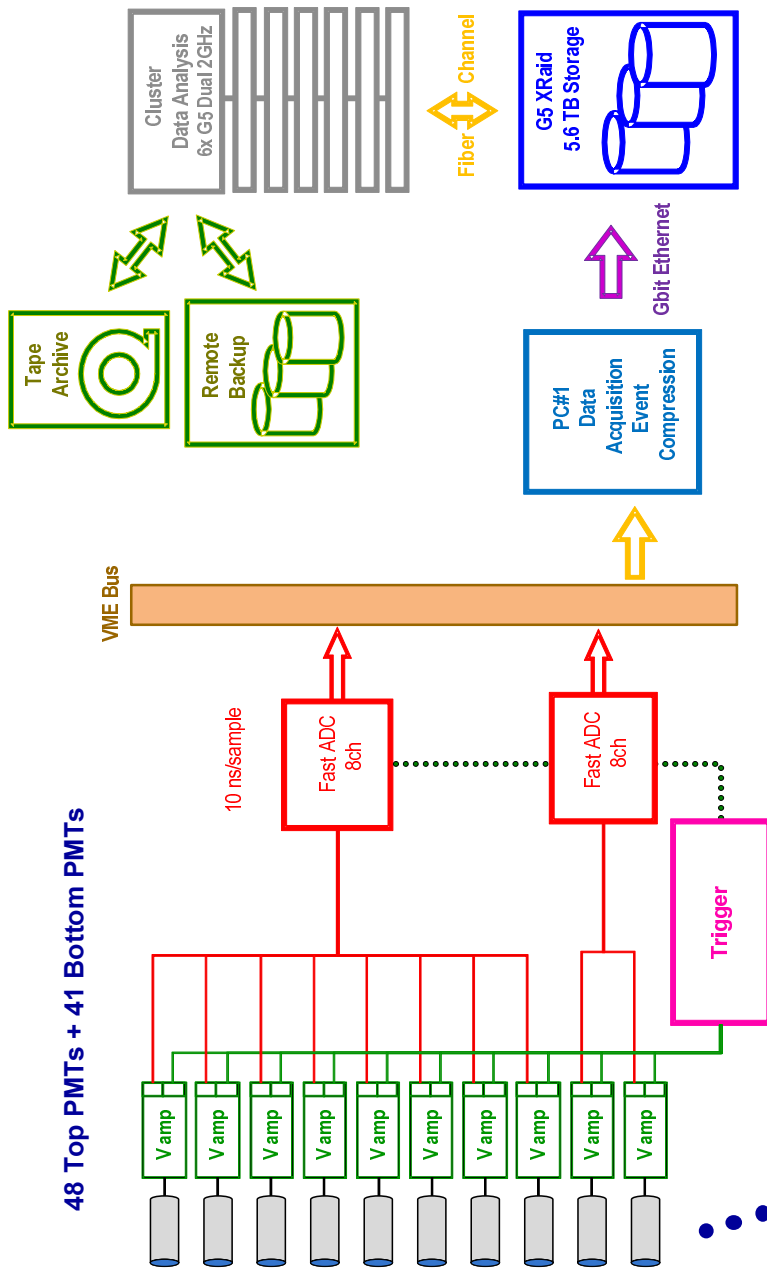
Figure 3.1: XENON10 DAQ System. Diagram of the full electronics plus data chain, from the point of generation of signals (PMTs), through amplification, acquisition and triggering, to storage and processing of data.

3.1.1   Signals

The signal for each particle interaction in the detector is characterized by two types of pulses: (1) the primary scintillation light S1, and (2) the secondary ionization S2 (see Fig. 3.2 for an example). Each pulse is a collection of photoelectron pulses distributed over many PMTs. The S1 pulses decay exponentially with a time constant of 29 ns, and are typically < 200 ns wide (see Fig. 2.6). Each S1 pulse is relatively small, and a typical event of 2 keV$_{ee}$ will have only 5 photoelectrons spread over a handful of PMTs that are not necessarily adjacent. The S1 light is approximately evenly spread for events in the bulk of the liquid Xe, and provide little information about the position of these events. The S2 pulses are much longer, with an average width of FWHM $\approx$ 600 ns. When the S2 pulse is summed over all channels, its time trace is roughly Gaussian-shaped. An S2 pulse on one channel is essentially a series of many single photoelectron pulses in a row. The S2 pulse is evenly distributed over the bottom PMTs, due to the diffuse reflection of light on the Teflon walls of the active volume. However, in the top PMTs, the S2 pulse is focused on those PMTs directly above the interaction site. The X-Y position of the interaction can be obtained from the PMT hit pattern (see Fig. 3.3). The position reconstruction algorithms are discussed in Section 4.2.1.

The time between S1 and any S2 pulses in the event trace from a single interaction is determined by the electron drift time from the interaction site to the liquid surface, which is directly proportional to the Z-position of the interaction. Given the electron drift velocity in XENON10 of $\sim$ 2 mm/μs, the maximum drift time is $\sim$ 80 μs for the active volume height of 15 cm. The Z-position of the interaction can be determined from the time separation between S1 and S2. We define Z=0 at the gas-liquid interface, so that the Z-position is typically quoted as a negative number, as positive Z points upwards.

Events with multiple scatters in the active Xe volume will have a single S1 pulse, and more than one S2 pulse. In the time trace of an event, the separation between S1 pulses is determined by the time difference for the light from each interaction site to reach the PMTs. The maximum separation for a multiple-scatter gamma event is < 1 ns, smaller than the S1 characteristic decay time ($\tau = 29$ ns), and thus all interactions from a single event will
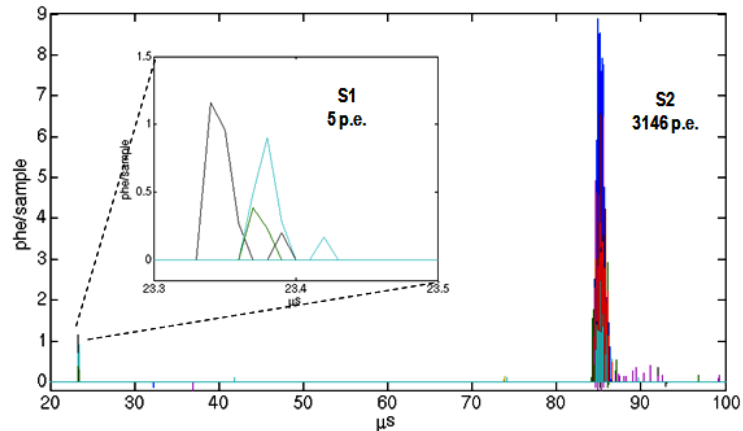
Figure 3.2: Sample Event from XENON10. The figure shows the signal versus time for each PMT overlaid (different colors for different PMTs), sampled at 105 MHz. The plot shows the major features in an event - the S1 and S2 pulse. Each of these pulses is a collection of photoelectron pulses spread over many channels. The S1 pulse, also shown in the inset, spread over about < 100 ns. The S2 pulse is typically spread over $\sim 2\,\mu$s and across more channels than an S1 pulse.

result in a single S1 pulse. The time separation between S2 pulses in the event trace is determined from their Z-separation, and proportional to the electron drift velocity - it is easy to distinguish multiple scatters with separation $\Delta Z > 1$ mm. Interactions separated in X-Y will show separate focal points on the PMT hit pattern.

The S1 and S2 pulses are separated by as much as 80 μs, and the S2 pulses in a multiple scatter event also have a maximum separation of 80 μs. To guarantee that the S1 pulse and all S2 pulses associated with an event are digitized, a full waveform of 160 μs is recorded for each event, with $\sim 80\,\mu$s pre-trigger and $\sim 80\,\mu$s post-trigger.

3.1.2 PMTs

The light from the S1 and S2 pulses is collected by 2 arrays of Hamamatsu R8620-06-AL PMTs, on the top and bottom of the detector. The XENON10 detector used 89 PMTs, divided into 48 PMTs on top, placed 2.0 cm above the liquid surface, and 41 PMTs on the bottom, immersed in the liquid and placed 1.35 cm under the cathode grid. The arrangement of PMTs into the top and bottom arrays is pictured in Fig. 3.4.

The R8520 PMTs have a compact shape with 2.5 cm $\times$ 2.5 cm $\times$ 3.5 cm dimensions - pictured in Fig. 3.5. The R8520 PMTs were certified by Hamamatsu to operate at
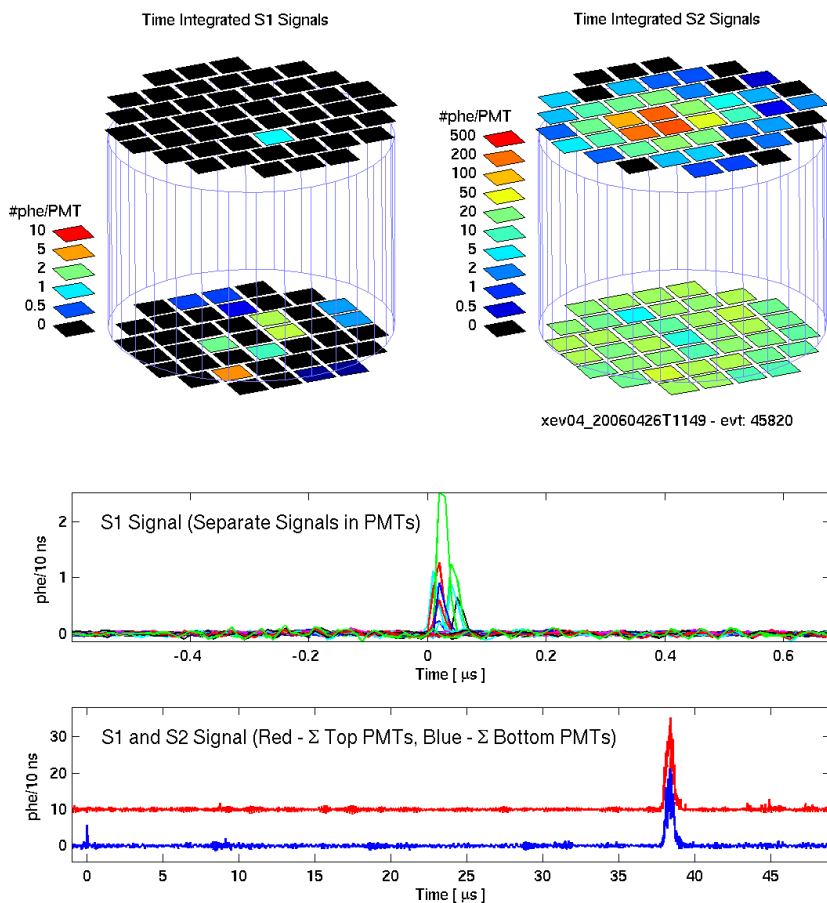
Figure 3.3: PMT Hit Pattern sample from XENON10. A sample gamma event with $5\,\mathrm{keV_{ee}}$, at approximately the center of the detector ($38\,\mu$sdrift time between S1 and S2 = 7 cm depth). The top 2 plots show the PMT hit pattern for S1 and S2 pulses, respectively. The middle plot shows the the S1 signal from individual PMTs. The last plot shows the sum event signal (S1 and S2), summed across the top PMTs (red) and bottom PMTs (blue). The Z position of the event can be reconstructed from the distance between S1 and S2, which is proportional to the electron drift velocity in liquid Xe, and the X-Y position can be reconstructed from the S2 hit pattern.

(a) Top Array   (b) Bottom Array
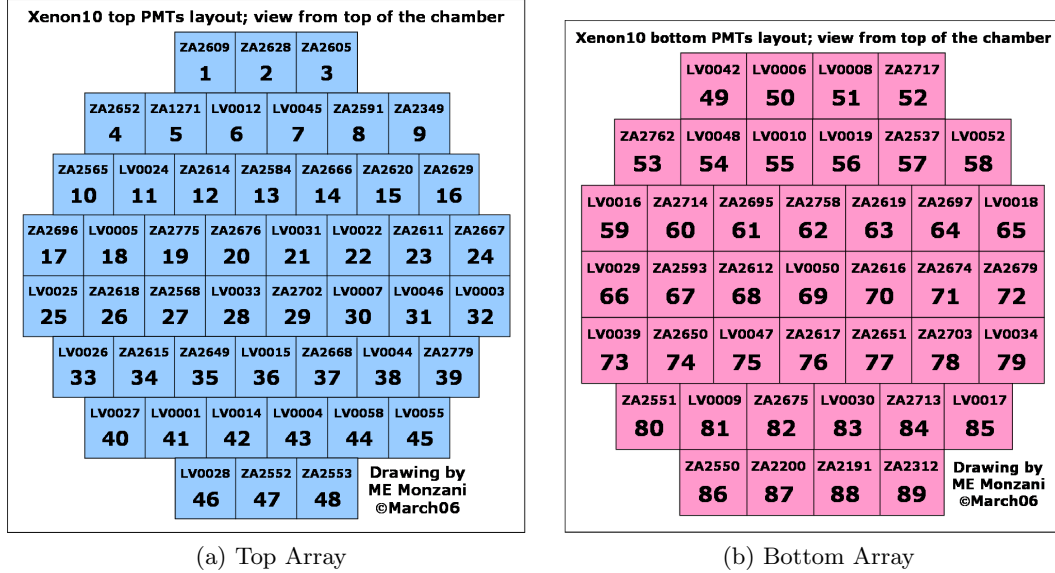
Figure 3.4: XENON10 PMT Map: Diagram of the PMT arrangement used in XENON10. For each PMT, the top number indicates the serial number, and the bottom number indicates the DAQ channel. PMT #48 was deactivated during the XENON10 data runs.

standard liquid Xe conditions of 177K and up to 5 atm. Built with a bi-alkali (Rb-Cs-Sb) UV-sensitive photocathode, and a 1" square quartz window, the R8520 PMTs have quantum efficiency in the range $20\% - 25\%$ at 300 K for 178 nm wavelength, the peak emission from Xe scintillation. The PMTs can resolve a single photoelectron ejected from the photocathode due to incident scintillation light.

The PMT signal due to incident photons is determined, among other factors, by the Quantum Efficiency (QE), the number of photoelectrons emitted by the photocathode per incident photon. The average quantum efficiency of the PMTs used in XENON10 is 0.237 ± 0.019 photoelectrons/photon for 178 nm. The QE is measured at room temperature. Increase in QE at low temperature (177 K) for commonly used PMTs has been reported: 18% increase for bi-alkali ETL 9828Q PMTs [89]; and 12% for all-metal Hamamatsu R8778 PMTs [90]. Assuming a conservative estimated increase of 12%, the average QE for 178 nm at 177 K is 26.5%.

The PMT signal is also affected by the "first-strike" probability, or Collection Efficiency (CE): the percentage of photoelectrons emitted by the photocathode that are collected in the 1st dynode. The R8520 have a CE of $(75 \pm 5)\%$. The combination of the QE and CE

(a) R8520 PMT
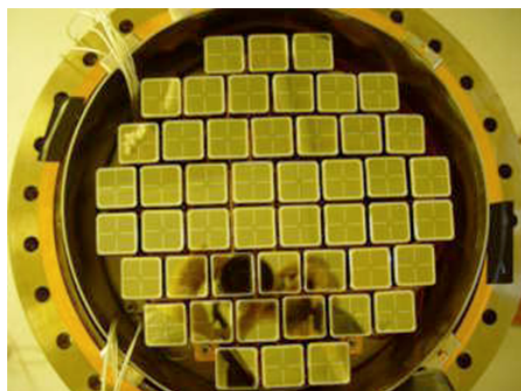
(b) XENON10 Top PMT Array

(c) XENON10 Bottom PMT Array

Figure 3.5: Pictures of the R8520 PMTs used in the XENON10 detector. The R8520 PMTs have a square shape, with 2.5 cm width. The pictures shows one PMT by itself, the top PMT array, and the bottom PMT array.

is called the Detective Efficiency (DE):

$$DE = QE \times CE.$$ (3.1)

Using the estimated quantum efficiency at 177 K we have a DE of 20%. In some works, the detective efficiency is also called the "effective quantum efficiency".

The photoelectron signal is then amplified through the dynode chain. The R8520 PMTs have a 10-stage metal-channel dynode chain, with a total amplification of $> 10^6$. The voltage for each stage is provided by a voltage divider resistor chain. During all XENON10 runs, the PMTs were operated with a total bias voltage of $\sim 780\,V$, yielding a gain of $\sim 2 \times 10^6$ (see Section 3.1.4 for details on the gain calibration).

The high voltage for the PMT bases is provided by CAEN A1733 power supply modules [86]. Each module has 12 channels, and a maximum output of $200\,\mu A$ at $4\,kV$. A low-pass filter of $f < 10\,Hz$ is used to remove noise from the PMT HV lines. The units are computer controlled, facilitating the optimization of the bias voltage and consequently the gain. The PMTs were connected to the HV units via Kyocera (Al_2O_3) feedthroughs, using Burndy-type connectors. The connections outside the detector were done using insulated 5-strand HV cables and Redel-type connectors. The connections inside the detector were done with KAP1 wire - single-strand, Au-plated Cu conductor, Kapton insulated, made by MDC. The Kapton insulation has very low out-gassing, necessary to ensure a clean environment inside the detector. The Kapton insulation is rated with a dielectric strength of $80\,kV/mm$.

The PMTs are mounted on bases built on a Cirlex substrate, which contains the voltage divider chain on a custom-made printed circuit and surface mount resistors and capacitors. The resistor chain is configured according to Hamamatsu specifications [91]. The total chain resistance is $12.6\,M\Omega$, resulting in a typical current of $62\,\mu A$ for 780 V bias voltage. The resistance between the photocathode and the 1st dynode, as well as between the 1st and 2nd dynodes, is $2\,M\Omega$. The resistance between the last dynode and the anode is $0.5\,M\Omega$. The resistance between all other dynodes in the chain is $1\,M\Omega$. The load resistance - that is, the output resistance to ground - is $R_{PMT} = 0.1\,M\Omega$.

The output signal from each PMT is amplified using off-the-shelf $\times 10$ amplifiers, Phillips

model number PS776. Each amplifier channel has 2 outputs, one used to connect to the ADC, and one for the trigger.

3.1.3 ADCs

The signals from each PMT are digitized by Struck Fast ADC modules, model number SIS3301 [92]. The Struck digitizers were chosen because of their relatively high resolution for the price, featuring a maximum sampling frequency of 105 MHz, with 14-bit sample resolution. The dynamic range on the input for these units is usually ± 1 V, but it has been customized for XENON10 with $+0.1$ V to -1.9 V. The Struck ADCs have 8 channels (see Fig. 3.6), and 11 Struck modules were used to digitize 88 of the 89 PMTs. The 89th PMT (actually, PMT #48 in the top array) was malfunctioning and it was not digitized. The Struck ADCs have been fitted with an anti-aliasing single-pole RC filter of 30 MHz at the input for every channel. The ADCs have internal memory banks of 2×128 ksamples per channel. The memory banks are run in dual bank mode, so that the memory for each channel is split in two, and acquisition can run on one bank while the other is being downloaded, decreasing dead-time. The memory banks can be used in single- or multi-event modes. In multi-event mode, the memory is divided into a N=8, 16. ..., 1024 events, and sequences of N events can be acquired without software intervention. Data is read from the digitizers at the end of a sequence, and the ADCs are re-armed after readout. There is virtually no dead time between events within a single sequence of events. For XENON10 operation, both the multi-event mode and the dual memory bank functionality were used to reduce dead time.

An event is defined as a signal that causes a trigger (1 acquisition = 1 event), and it might contain ≥ 1 S1 pulses and/or ≥ 1 S2 pulses. Events are triggered by an external trigger signal, and all channels acquire synchronously. The trigger system communicates with the DAQ with a single NIM pulse, going from the trigger to the digitizer front panel input. Timestamps are recorded for every event.

The Struck modules are 6U VME cards, and are mounted in a single VME crate. The digitizer modules communicate to a dedicated computer through the VME-PCI interface using a fiber-optic communication board (Struck model SIS1100), connecting the crate to

the computer's PCI interface. The VME interface is designed to allow for fast readout of data. Data readout by a computer is limited by the PCI transfer rate of 133 MB/s. In practice, the readout speed is limited by the VME backplane maximum transfer rate. The VME backplane allows for several transfer modes, the most efficient being block transfer mode that download the entire memory bank at once, and have speeds of 33 MB/s, 64 MB/s and 80 MB/s, for BLT32, MBLT64 and 2eVME protocols. The XENON10 acquisition used the 2eVME protocol for data readout.

The modules can run with either an internal or external clock source, with a maximum sampling rate of 105 MHz, corresponding to ~ 10 ns sampling time. In XENON10, the first module in the VME crate is configured to run using its own the internal clock, whose signal can be read on a front panel LEMO plug. The clock signal is then fanned-out across all other modules, which are configured to run with an external clock source.

The sampling time of ~ 10 ns determines the event size. In order to record an event length of $160\,\mu$s, approximately 1600 samples are needed. For 8 events per sequence, we have a maximum of 16384 samples per event. For XENON10, 16350 samples per event were acquired, corresponding to $\sim 156\,\mu$s when running at 105 MHz sampling rate. When armed, the ADCs continuously digitize the signal into a rolling buffer, allowing us to save the data acquired prior to the trigger. In order to record any S1 pulses that might occur prior to an S2 trigger, the data was taken with 8350 samples of pre-trigger ($79.5\,\mu$s), leaving 8000 samples ($76.2\,\mu$s) for post-trigger data.

3.1.4 PMT Calibration

The PMTs need to be calibrated in order to calculate the area of the photoelectron signal, to equalize their gains and to track any changes with time. The calibration is performed using a LED system at weekly intervals. One LED mounted close to the top array is used to calibrate the bottom PMTs, and one LED mounted close to the bottom array is used to calibrate the top PMTs. The LEDs emit blue light (~ 430 nm), and are covered by a Teflon cap to diffuse the light and ensure uniform illumination of the targeted array.

The calibration of the gain follows the single photoelectron method outlined in [93], and

Figure 3.6: Picture of the Struck SIS3301 Fast ADC module used in the XENON10 data acquisition system. The modules feature 105 MHz digitization rate, and 14-bit resolution with a 2V dynamic range.

the procedure used in XENON10 is described in detail in [82]. The LEDs are driven with by a pulse generator, running a series of different pulse heights to ensure low intensity light for each PMT, so that each PMT is calibrated in the single photoelectron regime. The LED light level is adjusted so that $> 80\%$ of the light pulses elicit no response from the PMT, thus ensuring that $> 90\%$ of the signals that are recorded by each PMT are single rather than multiple photoelectrons, due to Poisson statistics. The resulting pulse area spectrum, shown in Fig. 3.7, is fitted to a function corresponding to the sum of a Gaussian noise peak, a Gaussian single photoelectron peak, and a small Gaussian for to the multi-photoelectron contribution, typically $< 2\%$. The area of the single photoelectron peak is measured, and the PMT bias voltage is adjusted to equalize the photoelectron response from all PMTs. However, differences of up to $\times 3$ are allowed to remain, and the typical variation in the gain of the 89 PMTs are within $\times 2$ of the average. The variation of the PMT gain with time is $\sim 10\%$, over a 7 month period [82]. The actual single photoelectron area for each PMT is recorded and used to calculate the number of photoelectrons in a given pulse during the data analysis.

The average Gaussian distribution mean for single photoelectron peak of all 89 R8520 PMTs is $16\,\mathrm{mVns}$, referred at the PMT output. The measurement is made across a total load of

$$
\begin{aligned}
R_L &= \frac{R_{PMT} \cdot R_{in}}{R_{PMT} + R_{in}} \\
&= 50\,\Omega
\end{aligned}
$$

where $R_{in} = 50\,\Omega$ is the input resistance of the cable and electronics, and $R_{PMT} = 0.1\,\mathrm{M\Omega}$ is the resistance across the PMT output. From the single photoelectron peak area, the gain is calculated as:
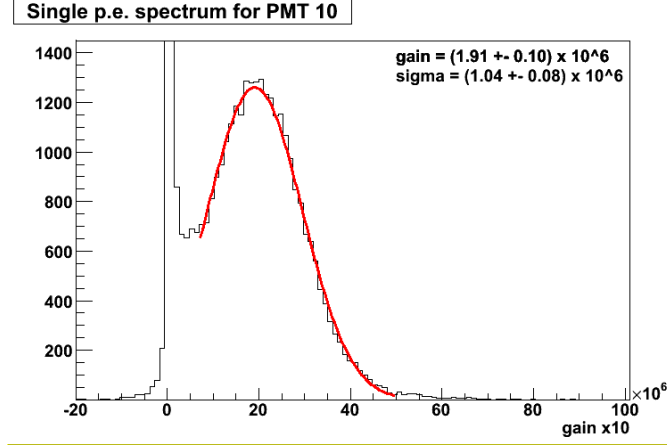
Figure 3.7: Typical single photoelectron spectrum for a R8520 PMT, measured through LED calibration in XENON10. The single photoelectron spectrum has a mean corresponding to 1.91×10^6 gain, and a relative standard deviation of $\sigma_r = 0.54$. Figure courtesy of A. Manzur of the XENON10 Collaboration.

$$
\begin{aligned}
gain &= \frac{Q_{out}}{Q_e} \\
&= \frac{V \cdot \Delta t}{R_L} \cdot \frac{1}{Q_e} \\
&= \frac{16 \cdot 10^{-3} \text{mV} \cdot 10^{-9} \text{s}}{50\,\Omega} \cdot \frac{1}{1.6022 \times 10^{-19} \text{C}} \\
&= 2 \times 10^6.
\end{aligned}
$$

The resolution on the single photoelectron peak measurement is given by the relative standard deviation, which averaged $\sigma_r = \sigma/\mu = 0.58 \pm 0.8$ for all PMTs (see example in Fig. 3.7). The fluctuation in the PMT gain are dominated by fluctuations in the yield of the 1st dynode - see [64, pp. 88] for a complete discussion.

The PMTs are also calibrated for their Detection Efficiency (DE). The relative DE is determined from the size (in photoelectrons) of the $40\,\text{keV}_{\text{ee}}$ peak from activated Xe (see Section 4.1.4), which are uniformly distributed in the liquid Xe. For each PMT, a Relative Sensitivity (RS) factor is calculated, combining the gain, quantum efficiency and collection efficiency, relative to their mean values. The RS is then applied to the signals of the individual PMTs during data analysis, so that the signals of all PMTs are normalized
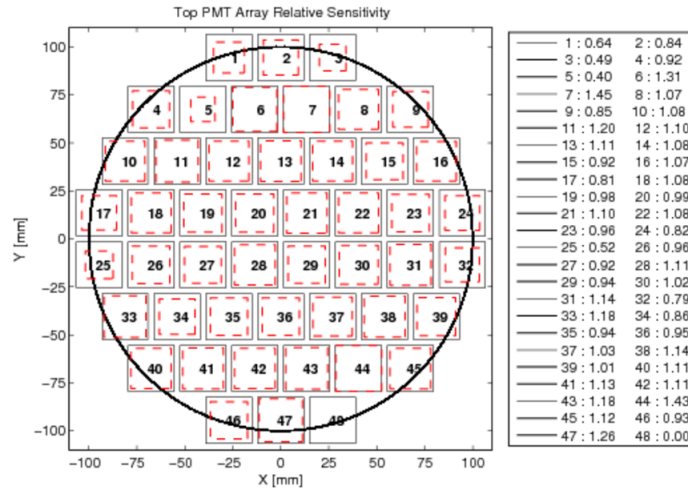
Figure 3.8: Relative Sensitivity (RS) of the XENON10 Top PMTs. The RS measures the combined gain, quantum efficiency and collection efficiency of each PMT, relative to the average values. The area of the red square in each PMT is proportional to the relative sensitivity. Figure courtesy of P. Sorensen of the XENON10 Collaboration.

to the average gain and DE. The RS map for the XENON10 top PMTs is illustrated in Fig. 3.8.

3.1.5 Software and Data Management

The XENON10 data acquisition system is controlled by in-house developed software. The purpose of the software is: (1) to configure the DAQ system (Struck ADCs + trigger) before each run; (2) to manage data acquisition, minimizing dead time due to data transfer between DAQ and computer; and (3) to write the data to disk in a format useful for analysis. The DAQ software is written in C, runs on a Linux computer, and relies on the drivers provided by the manufacturer (Struck) to communicate to the DAQ system.

All of the run settings are specified in a XML file that is read by the acquisition software at the beginning of the run. This information is used to configure the ADCs and determine how long the run will last, what to acquire and how the data will be written to disk. A copy of the XML file used in a run is saved with the data so that the information is easily available for analysis.

The data is written to disk in binary format, and it is basically a dump of data from the memory bank with added headers to indicate file contents. The data coming out of

the digitizers is saved with as little modification as possible. The data is arranged in the sequence [Samples][Channels][Events] - the file writer loops first over samples, then over channels, and finally over events. The trigger times are recorded into separate files, in order to improve speed on the calculation of trigger rate and livetime.

A baseline-flattening algorithm is applied to improve data compression and relax space requirements. The baseline-flattening algorithm runs in-line with the acquisition, and sets small fluctuations in the baseline ($\leq \pm 8$ digitizer bins) to zero, allowing for very efficient lossless data compression by a factor of $\times 20$ using open source software (gzip). The baseline compression procedure does not destroy any useful information, as the single phe (the smallest signal from the detector) has a typical height of ~ 100 digitizer bins.

After the data is written to disk, an additional baseline flattening algorithm samples the data from all channels, and sets individual threshold for baseline flattening for each channel. The flattening thresholds are in the range ± 11 to ± 24, and are still well below the typical single phe height. This additional flattening is performed after acquisition has finished (and before data analysis is performed), so that the threshold can be set according to the observed baseline fluctuations in each channels, ensuring that no important data is lost and that we achieve the best possible data compression. The data is no longer modified, and is left untouched even after analysis, which creates its own output files.

3.1.6 S1 Trigger

Two configurations of trigger systems were tried for the XENON10 data acquisition system: a S1 trigger, and a S2 trigger. The two configurations were attuned to trigger exclusively on S1 or S2 pulses, respectively. Ultimately, the S2 trigger demonstrated superior performance and was chosen as the trigger system for the XENON10 WIMP search runs and calibration. The S2 trigger is discussed in Section 3.1.7.

The S1 trigger system was based on a bank of CAEN fast discriminators, model number v814, and Fig. 3.9 shows a diagram of the S1-trigger configuration. The S1-trigger system has trigger conditions of $n \geq 6$ coincidence in a 80 ns window. Given the S1 shape ($\tau \approx$ 29 ns), 94% of the photons in a S1 pulse will fall in this window. Due to total internal

reflection on the gas-liquid interface, the S1 trigger signal is expected to be stronger on the bottom PMTs by a factor of $\times 4$ and evenly spread, so that the S1-trigger is set-up to monitor only the 41 bottom PMTs.

The trigger threshold in each channel is set to to have an acceptance rate of 80% of the single phe signal distribution, which is obtained from the method described above (Section 3.1.4). The S1-trigger efficiency for $n \geq 6$ on the bottom PMTs is $\sim 50\%$ at $9\,$phe and $> 99\%$ at $18\,$phe, and is well modeled in Monte Carlo simulations, as is shown in Fig. 3.10.

The level of noise in each channel is measured through *trigger threshold sweeps*. A sweep consists of measuring the trigger rate in each PMT at several trigger thresholds. In each iteration of a sweep, the threshold on an individual PMT is stepped by $1\,$mV, the smallest step in the discriminator unit. The process is automated, and all PMTs are measured for each step. Fig. 3.11 shows a sweep for a sample bottom PMT channel to illustrate the process. The sweep returns a large peak corresponding to the baseline and noise, plus a continuum distribution of the actual events in the detector. The procedure can also be used to identify pick-up noise, and the single phe peak for each PMT. While most noise (i.e. pickup) appears on both sides of the baseline peak, the single phe peak appears as an extra edge on the signal side only, as illustrated in the diagrams in Fig. 3.12. The signal from the sweep can be converted to the more familiar form typically used for PMT calibrations - taking the derivative of the trigger threshold sweep, one obtains the Gaussian distribution of the single phe peak, as seen in Fig. 3.11b.

The trigger threshold sweep method was routinely used to monitor the noise level on every PMT (and not only on the ones being used for S1 trigger), as a way to check for the PMT health. This method flagged two faulty PMTs previous to the WIMP search run, as they started showing anomalously elevated baseline noise levels.

3.1.7 S2 Trigger

The main advantage of the S1-trigger system is the ease of finding S2 pulses in software after an S1 pulse has been found by a hardware trigger system. However, the S1-trigger system has two big disadvantages: the low efficiency for low-energy events (only 50% at
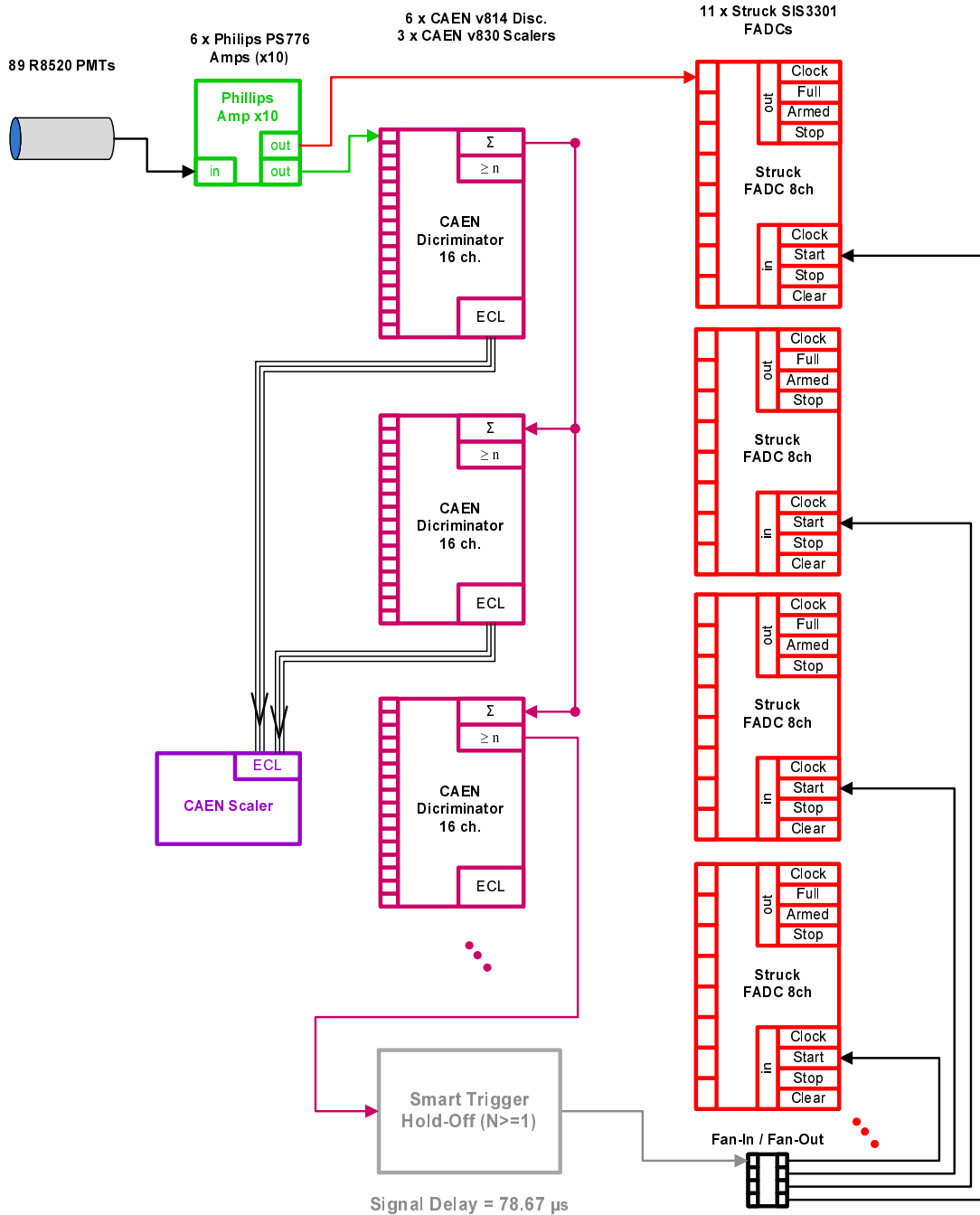
Figure 3.9: XENON10 S1 trigger diagram. The S1 trigger system used a bank of CAEN v814 discriminators to generate the trigger signal for the XENON10 DAQ. The S1 trigger system typically requires a coincidence of $n \geq 6$ on the bottom PMTs. The system also featured a CAEN v830 scaler, used to monitor the trigger rate in individual PMTs, and a "Smart Trigger Hold-Off", which requires a period of $200\,\mu s$ with no signals before allowing a trigger through, thus ensuring a clean baseline (See Fig. 3.17). The small black rectangle with 4 inputs and outputs represents a single channel from a quad-channel Fan-In/Fan-Out (Phillips 740).
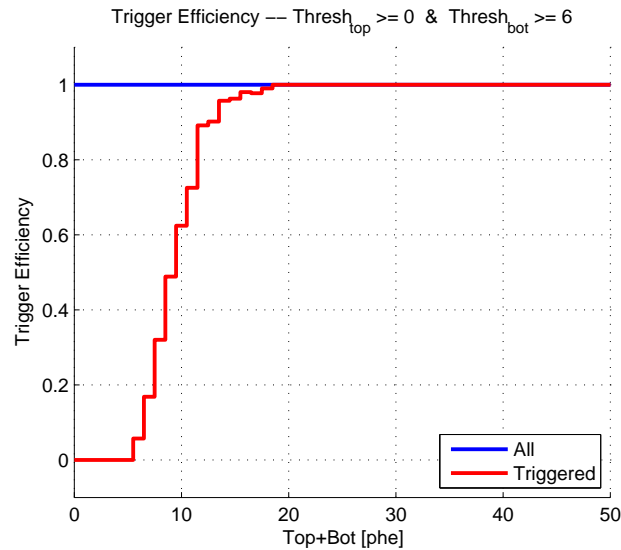
Figure 3.10: S1 Trigger Efficiency Monte Carlo - Efficiency of the S1 trigger vs. total signal size, for a coincidence requirement of $n \geq 6$ on the 41 bottoms PMTs.
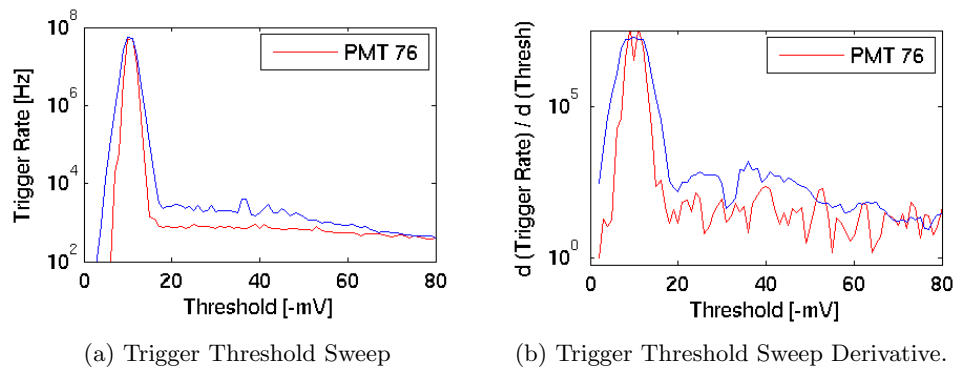
(a) Trigger Threshold Sweep

(b) Trigger Threshold Sweep Derivative.

Figure 3.11: Trigger Threshold Sweep of PMT #76. The trigger threshold sweep is primarily used to monitor the noise level around the baseline peak (centered at $10\,\mathrm{mV}$ due to a manual offset), but can also measure the single phe peak on an LED calibration run. The red line shows a background sweep, and the blue line shows the sweep of the LED signal. The single phe peak shows up as an extra edge on the trigger rate distribution (left), and as a Gaussian peak of the derivative, centered at $\sim 35\,\mathrm{mV}$ (right).

(a) Background   (b) Pick-up noise   (c) LED calibration
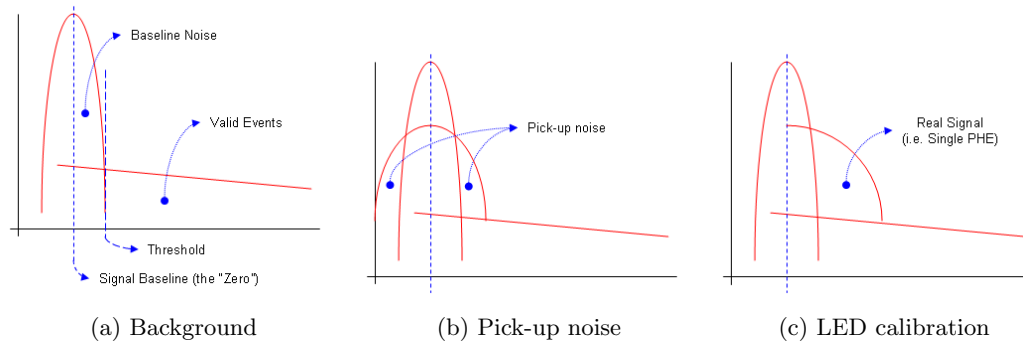
Figure 3.12: Trigger Threshold Sweep diagrams. The x-axis is the trigger threshold voltage (mV), and the y-axis is the event rate for the given trigger threshold (Hz). These diagrams illustrates a few possible rate distribution scenarios for the trigger threshold sweep of a single PMT. The large peak corresponds to the baseline and noise. Additional pick-up noise shows up a two-sided distribution also centered on the baseline. The single phe peak obtained from a LED calibration run shows up as an extra edge on the same side as the signal.

9 phe); and the high number of S1-only events, due to interaction on the non-active Xe volumes (see Section 6.4.1). The adoption of an S2-trigger resolves these two problems. The S2 trigger provides a lower threshold than is possible with an S1-based trigger, as is evident from looking at a typical event - see Fig. 3.3 - and ensures that every event has an S2 pulse, thus eliminating events that scatter only on the non-active Xe volume.

The S2-trigger monitors the sum of the 34 center PMTs of the top array (see Fig. 3.14). The summed signal is amplified by a CAEN N568B with integration time constant $1\,\mu$s and $\times 10$ gain. The shaped signal is then passed to a CAEN N845 voltage discriminator, which sets to trigger at a threshold. The S2-trigger system is sensitive to events with S2 signals as small as 24 phe, corresponding to $1\,e^-$ extracted from the liquid. For the WIMP search data runs, the trigger threshold was set at ~ 100 phe (see Fig. 3.13); this in turn corresponds to about 4 ionization electrons extracted from the liquid, which is the expected charge from an event with less than $1\,\mathrm{keV_r}$ nuclear recoil equivalent energy. At $4.5\,\mathrm{keV_r}$ (corresponding to $\sim 40\,e^-$), the trigger efficiency is $\gg 99\%$.

The trigger signal is distributed from the discriminator to all ADC modules simultaneously using a Fan-Out chain. A trigger hold-off is used to prevent the system from triggering on after-pulsing, an effect observed following large S2 pulses. The hold-off requires that no S2 trigger candidates occur for the previous $200\,\mu$s before allowing a trigger
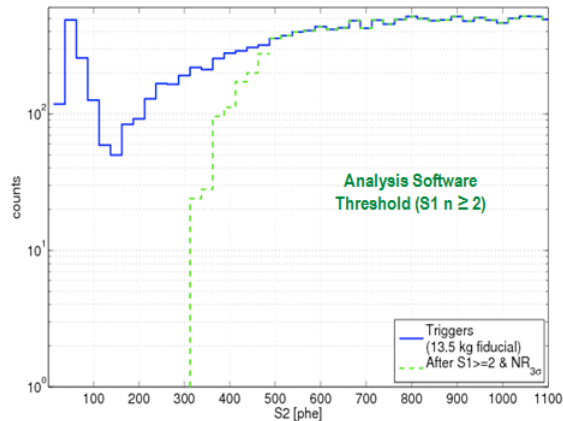
Figure 3.13: S2 histogram for AmBe events in XENON10, illustrating the S2 trigger efficiency. The blue line is the S2 histogram for all events taken during the neutron calibration run (using a AmBe source). The green dashed line shows the S2 histogram of events with an S1 identified by the Analysis Software, which has an S1 threshold of $n \geq 2$.

to start acquisition. The hold-off time is included in computing the acquisition dead time. For gamma calibration data runs, a high energy S1 veto is added to reduce the trigger rate. The veto is based on the sum of the 9 center bottom PMTs and eliminates events with an S1 $> 150 \, \mathrm{keV_{ee}}$. The high-energy veto was not used for most of the WIMP search run, and the high energy data was used to monitor the stability of the detector, as the WIMP search was running in blind mode and no one was allowed to look at the data in or close to the energy range of interest. Using the S2-trigger and no high energy veto, the acquisition rate during WIMP search mode is $\sim 2.5 \, \mathrm{Hz}$, leading to a dead time of 7%.
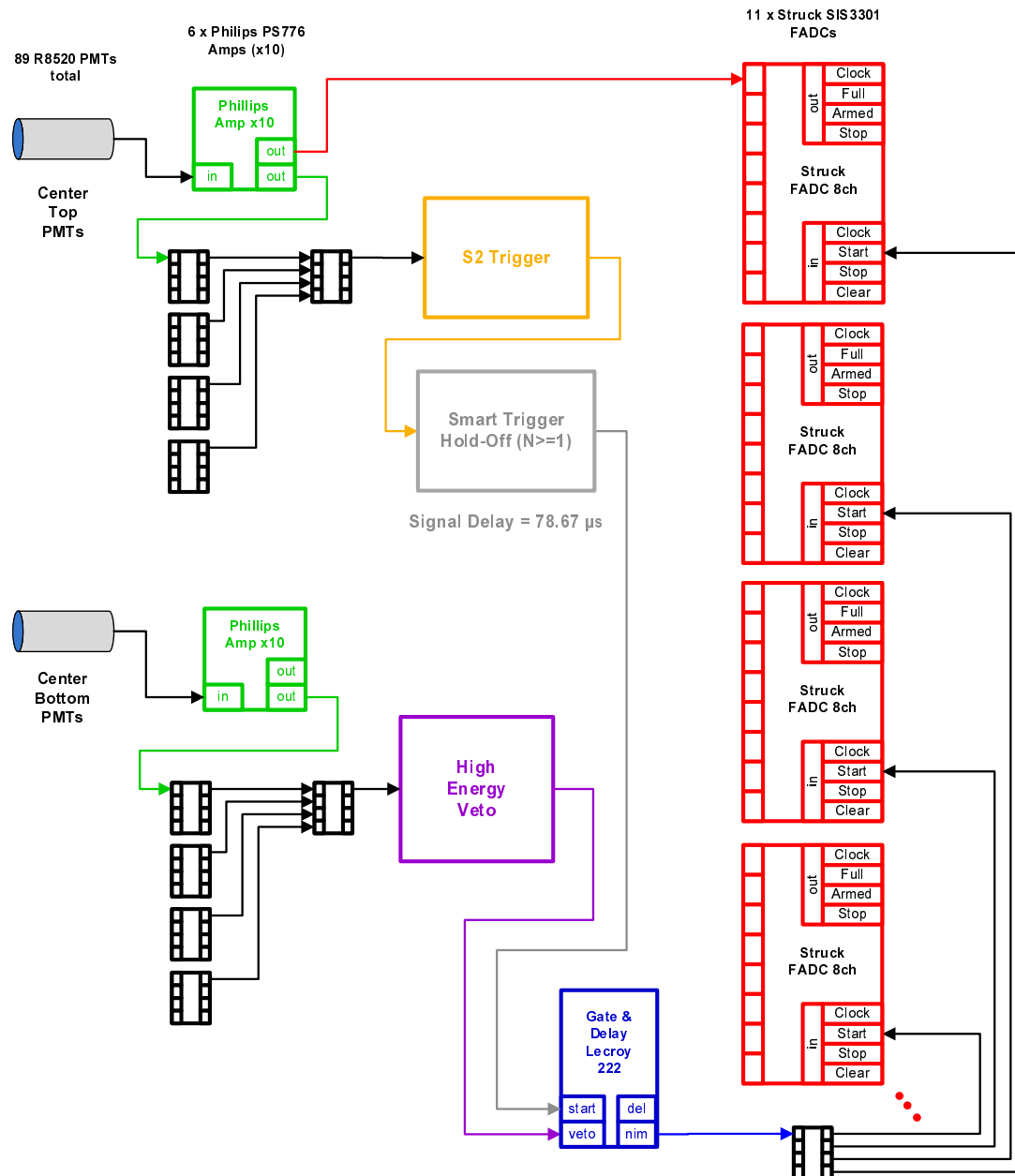
Figure 3.14: XENON10 S2 trigger diagram. The S2 Trigger uses a spectroscopy amplifier to shape and trigger on the summed signal from the central 30 top PMTs (yellow box - details shown in Fig. 3.15). The S2 trigger system features a high energy veto, applied to the summed signal from 9 center PMTs from the bottom array, thus vetoing on large S1 signals (magenta box - details shown in Fig. 3.16). The S2 trigger system also uses the "Smart Trigger Hold-Off" (silver box - details shown in Fig. 3.17) to require a period of $200\,\mu$s with no signals before allowing a trigger through. The small black rectangle with 4 inputs and outputs represents a single channel from a quad-channel Fan-In/Fan-Out (Phillips 740).
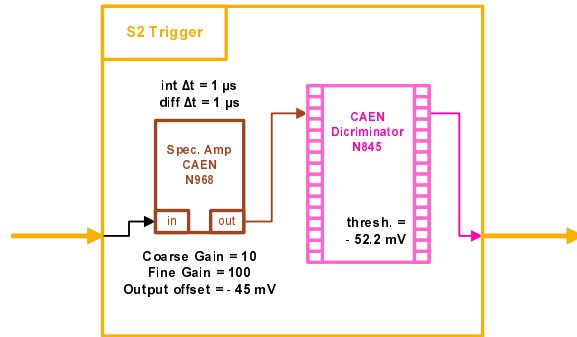
Figure 3.15: XENON10 S2 Trigger - S2 Trigger receives the summed signal from 30 center PMTs in the top array. Due to the focusing of S2 light in the top array, looking at the center of the top array optimizes the trigger for S2 pulses in the fiducial region. The S2 Trigger uses a CAEN N968 spectroscopy amplifier to shape the summed signal with a integration time of $1\,\mu$s, thus summing S2 pulses and flattening out S1 pulses. The shaped signal is then piped to a discriminator. The discriminator threshold is set manually using a gamma source to trigger on small S2's. The S2 Trigger efficiency is shown in Fig. 3.13.
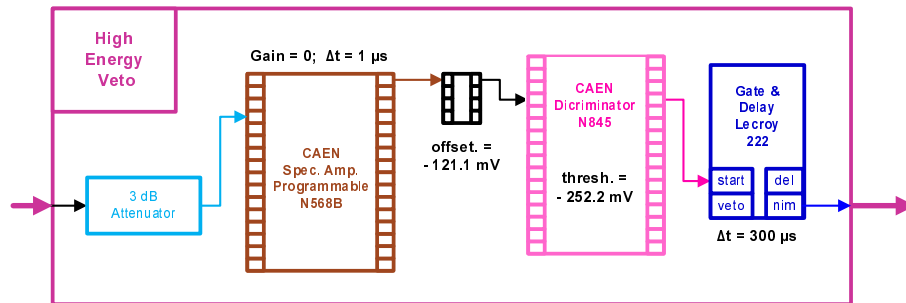
Figure 3.16: XENON10 High-Energy Veto - The high energy veto receives the summed signal from the 9 center PMTs in the bottom array. The light signal (both S1 and S2) for a high energy events ($> 100\,\mathrm{keV_{ee}}$) is uniformly distributed on the bottom PMTs. The signal is attenuated using a 3dB attenuator, shaped by a CAEN N568B spectroscopic amplifier with a time constant of $\Delta t = 1\,\mu$s (optimized for S2 detection). The signal is then piped to a CAEN N845 discrimination. The discriminator threshold is set manually to achieve the desired energy veto ($100\,\mathrm{keV_{ee}}$). A LeCroy 222 Gate & Delay is used to extend the veto signal for $300\,\mu$s, and ensure that tails of large S2 signals do not cause spurious trigger signals. The small black rectangle with 4 inputs and outputs represents a single channel from a quad-channel Fan-In/Fan-Out (Phillips 740).

Figure 3.17: XENON10 Smart Trigger Hold-Off - This circuit is used in both the S1 Trigger and S2 Trigger configurations. It is designed so that a period of $200\,\mu s$ with no trigger signals must occur before allowing a trigger through. When a signal above threshold is first detected, a trigger is generated, and a gate (labeled Δt_3) is turned on for a period of $200\,\mu s$. Any signals that occur while the gate is on are vetoed and do not generate a trigger. Any signals that occurs while the gate is on extends the veto gate for $200\,\mu s$ after the signal. Only after $200\,\mu s$ have passed with no signals above threshold that the gate is turned off, and signals can generate another trigger. This ensures that the baseline before an event is fairly "quiet" (that is, with no spurious S1 pulses), and that the signals being triggered on are not tails of larger signals detected previously. The typical hold-off gate lasts $< 400\,\mu s$. The smart trigger hold-off is assembled using a quad channel NIM logic unit (Phillips 756), and a quad channel Gate & Delay NIM unit (Phillips 794). The small black rectangle with 4 inputs and outputs represents a single channel from a quad-channel Fan-In/Fan-Out (Phillips 740). The time constants shown in the circuit diagram above are $\Delta t_1 = 20\,\mu s$, $\Delta t_2 < 1\,\mu s$, $\Delta t_3 = 200\,\mu s$ and $\Delta t_4 = 20\,\mu s$. The Smart Trigger Hold-Off also prevents the trigger system from generating a trigger signal while the digitizers are not armed - it verifies whether a sample of 3 out of the 11 Struck digitizer modules (units #0, #5 and #10, in order to cover the entire bank) are armed in order to let a trigger signal through - it was deemed unnecessary to monitor all 11 digitizer modules.

3.2 LUX DAQ

The data acquisition strategy for the LUX experiment is similar to the one used in the XENON10 experiment, with a few key upgrades in 4 main areas: (1) PMTs, (2) amplifiers, (3) trigger, and (4) digitizers. The upgrades are done with the objective of allowing the data acquisition to handle the signals from such a large detector, while keeping costs down. Fig. 3.18 shows a diagram of the LUX electronics chain and data acquisition system.

The LUX detector will use two arrays of 61 Hamamatsu R8778 PMTs to monitor the S1 and S2 light in the active Xe volume. The R8778 PMT has been selected among other

Figure 3.18: Diagram of the LUX electronics chain, data acquisition system and analysis chain.

Figure 3.19: Picture of the R8778 PMT used by the LUX experiment. The PMTs are cylindrical, with 5 cm diameter. Photo courtesy of C. Hernandez Faham.

candidates, including the R8520, in part because of its larger size of ~ 5 cm diameter, which allows for full coverage of the LUX top and bottom surfaces with a smaller number of PMTs. A picture of the R8778 PMT is shown in Fig. 3.19. The R8778 also demonstrates higher Quantum Efficiency (QE) and Collection Efficiency (CE) than the R8520s. Measurements by Hamamatsu have yielded average QE of $\sim 33\%$ and CE of 88%, resulting in an detective efficiency of 29%, or $1.5\times$ larger than the R8520s. The R8778 will be operating with a gain of 2×10^6, resulting in a single phe area of 8 mVns.

The LUX experiment uses custom-made amplifiers, developed by the LUX collaborators at the University of California (Davis) and Harvard, to amplify, shape and split the signals from the PMTs. The first challenge for the electronics chain is to accommodate a large dynamic range, as we are interested both in the small signals for low threshold, and in the larger signals to be able to characterize the backgrounds and calibrate the detector with gamma sources. The use of a "double chain", in which each channel is duplicated in a low gain and high gain chain was discarded because of the additional cost. Instead, a 2-stage system with switchable gains was chosen. The first stage is a preamplifier mounted on the detector itself, in which each channel is amplified by $\times 5$. The second stage (the shaping amp) is mounted in the data acquisition system rack, and is comprised of a shaping amplifier with 3 specific-purpose outputs per channel, and with selectable gains. The 3 outputs of the second stage amplifier are: (1) the "shaped output" for the digitizers, with $\times 1.5$ gain in area and $\times 1.0$ gain in height, with a single phe FWHM of 12 ns; (2) the "shaped trigger output", for the primary trigger system, with $\times 2.8$ gain in area and $\times 0.9$ gain in height,

with a single phe FWHM of 19 ns; (3) the "fast output", with ×18 gain in height, and single phe rise-time (10% − 90%) of 5 ns, also used for triggering and PMT health monitoring (discussed below). The first stage (preamp) has a switchable attenuator of ×1 or ×1/10, and the the second stage (shaping amp) has a switchable overall gain of ×1 or ×0.5.

It is desirable to have a large component of the amplification in the first stage, close to the detector, so that the signals are amplified prior to any pick-up on the long cables running from the detector to the data acquisition rack, thus maximizing the signal-to-noise ratio. During WIMP search mode, the electronic chain can run with full gain to maximize the single phe sensitivity and minimize the threshold. When running calibrations, specially for high energy gamma sources, the gain can be tuned by so that the important features in the spectrum (such as gamma lines) are within the dynamic range of the digitizer and trigger.

The LUX trigger system is based on the DDC-8LUX digital signal processor modules being developed by the LUX collaborators at University of Rochester. The modules have 8 channels each, and each channel receives the 2nd output (the shaped trigger output) from a sum of 8 PMTs. The DDC modules use Field Programmable Gate Arrays (FPGAs) to perform real time searches of S1 and S2 signals. The trigger system can operate in S1-trigger mode, S2-trigger mode, and S1+S2 mode. The DDC trigger system can also allow and veto triggers based not only on minimum and maximum thresholds, but also on multiplicity of signals (thus eliminating multiple scatter events) and on pattern recognition, giving it the ability of triggering only in events in the center of the detector.

The LUX trigger system also incorporates the S1-trigger system developed for XENON10 and described above in Section 3.1.6, using the same CAEN v814 discriminator modules (with additional units purchased to cover all PMTs). The CAEN discriminators monitor the output #3 from the second stage amplifiers, the "fast output", which has ×18 gain and allows for very low threshold. The S1-trigger systems allows the LUX trigger system to make decisions on the coincidence of S1 pulses across the 122 PMTs; this is necessary since the DDC trigger only looks at groups of 8 PMTs, and thus cannot distinguish a large S1 pulse in a single PMT from a smaller S1 pulses distributed in a few PMTs in the same

group. The use of the CAEN discriminators also allows us to perform trigger threshold sweeps, useful in characterizing the noise in the PMTs, setting individual PMT thresholds, and monitoring their health.

The digitization of signals in LUX is handled by the same Struck 105 MHz digitizers (model SIS3301) used in XENON10, with additional units purchased to cover the increased channel count. The modules have been upgraded to implement baseline suppression in order to improve event download rates (thus improving acquisition rate) and decrease the storage requirements. The baseline suppression mode is implemented in a firmware upgrade to the digitizer FPGAs developed by Struck and the Brown University group, and is called Pulse-Only Digitization (POD). The POD mode works by acquiring only data above a very low threshold, thus eliminating the small fluctuations around the baselines (< 3 samples). The threshold is set so low that it only eliminates the baseline and small baseline fluctuations; all pulses, including noise, are still digitized. The baseline information prior to a pulse is saved as a single entry in the data-stream. It has been demonstrated in the analysis of XENON10 data and initial runs with the LUX0.1 detector that the baseline suppression can be performed without loss of important information. Fig. 3.20 shows a sample event acquired using POD mode in the LUX0.1 detector.

The increased height of the LUX detector requires a suitably larger event window to capture all S1 and S2 signals associated with a single event. The LUX detector is $\times 4$ taller than XENON10, resulting in a maximum electron drift time of $> 300 \, \mu$s and a event windows of $\sim 700 \, \mu$s. For a digitization rate of 105 MHz, the non-POD mode would return 17 MB per event (2 bytes per sample, summed across all channels). For a maximum transfer rate of 80 MB/s from the digitizer boards to the acquisition computer across the VME bus, the maximum event rate is only ~ 4.7 Hz. We can estimate the maximum event rate for POD mode by taking into consideration a benchmark event topology of 2 S1 pulses and 2 S2 pulses per event; in this case, the POD mode acquires only 59 kB per event (summed across all channels). However, the POD mode also digitizes spurious pulses and noise in the line. If we consider an average background PMT pulse rate of ~ 500 Hz, as observed through the trigger threshold sweep of PMTs shown in Fig. 3.11, and that the spurious pulses and
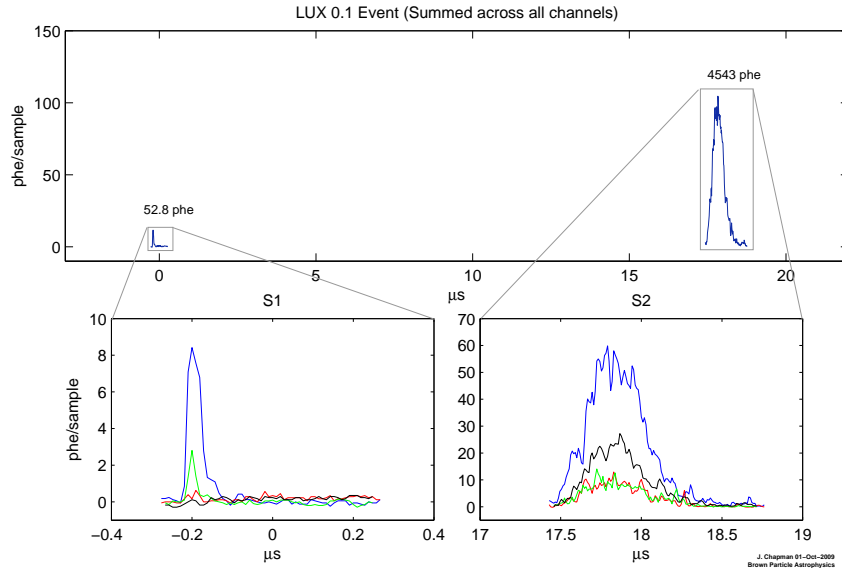
Figure 3.20: Sample event from the LUX0.1 detector, acquired using the Pulse-Only Digitization (POD) mode. The plot shows that only the pulses above some small threshold (plus a small region before and after the pulse) are acquired, thus suppressing the acquisition of baseline. *On the top*: acquired event trace, summed across the four channels. *On the bottom*: S1 pulse (left) and S2 pulse (right), showing the signals in the individual channels. Figure provided by J. Chapman of the LUX collaboration.

noise have widths similar to S1 pulses, we acquire 7.5 MB of noise data per second. For the maximum bus transfer speed of 80 MB/s, this corresponds to a maximum acquisition rate of 1.2 kHz with the LUX data acquisition system, orders of magnitude faster than what is obtainable by using "classic" (non-POD) acquisition strategies. The POD system is being developed and implemented in LUX by J. Chapman, who will report on further details [94].

CHAPTER 4

XENON10 DATA ANALYSIS

4.1 XENON10 at LNGS

The XENON10 detector operated at LNGS from the summer of 2006 to the summer of 2007. Initial operation included the purification of liquid Xe, calibration of the detector with gamma sources and LED, and the optimization of the data acquisition and trigger system. The schedule of the data acquisition and the amount of data acquired is summarized in Fig. 4.1, which plots the cumulative livetime of the WIMP search runs and calibration runs vs. real-time. The following sections offer a brief description of each of the WIMP search and calibration runs. The results obtained from the WIMP search run will be discussed in detail in Section 4.3.

4.1.1 WIMP Search Runs

The WIMP search runs are extended data-acquisition periods, each comprised of multiple datasets, in which no calibration sources are applied. The main source of events (and data) during the WIMP search runs is the background, which is discussed extensively in Chapter 6. In between the datasets that comprise a single WIMP search run, short calibration runs using the LED and gamma sources are performed to monitor the PMT gains and electron lifetime.

A total of 4 WIMP search runs were performed from the Summer of 2006 to the Summer
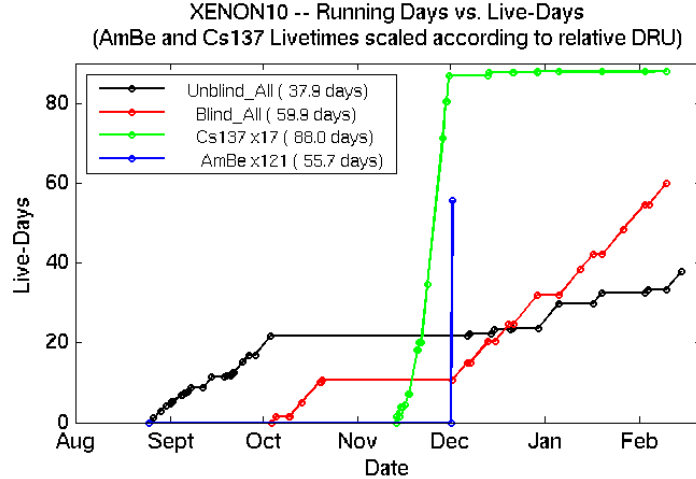
Figure 4.1: XENON10 data-taking summary. Cumulative livetime of calibration and WIMP search runs, scaled to the match the event rate (in the energy region of interest $2-12\,\mathrm{keV_{ee}}$ at $L_y = 2.2\,\mathrm{phe/keV_{ee}}$) to that of the WIMP search runs, and plotted vs. real-time. A small fraction (1.3 live-days) of the blind datasets was open for testing the analysis parameters, leaving a total of 58.6 live-days for the final blind analysis.

of 2007. The first run, WS1, was taken with an S1 trigger, and was discarded because of the relatively high threshold compared to what could be achieved with an S2 trigger (see Sections 3.1.6 and 3.1.7 for a discussion of trigger strategies). The S2 trigger was implemented for the second WIMP search run, WS2, which was taken during the month of September 2006 and was subsequently used to optimize the analysis code.

The third run, WS3, was taken in October 2006. Its data was not immediately analyzed, and was reserved to be used in the blind analysis of the WIMP search data. The final run, WS4, started in December 2006 and lasted until February of 2007. Part of the WS4 run was kept untouched for the blind analysis, and part was open for monitoring and optimization of the analysis algorithms. At the end of the run, we had acquired 59.9 live-days of blind data, and 37.9 live-days of unblinded data. After the testing and optimization of the analysis algorithms and cuts on the unblinded data, a small fraction (1.3 live-days) of the blind datasets was open for testing the analysis, leaving a total of 58.6 live-days. The combined blind WIMP search datasets are labeled either "WS3+4" or "WS34". The analysis was then locked into its final form, and blind WIMP search data was analyzed. The analysis and its results are discussed in Section 4.3.

4.1.2 LED and Gamma Calibration Runs

LED and Gamma calibration runs were routinely performed before and during the WIMP search periods, in order to calibrate and monitor the detector response to ER events. The 3 main types of calibrations are determined by the type of source used: (1) LED calibrations, (2) ^{57}Co calibrations, and (3) ^{137}Cs calibrations. The LED calibrations runs were performed on a weekly basis to calibrate and monitor the PMT gains, and are described in Section 3.1.4.

The ^{57}Co runs were used for 2 main purposes: to monitor the electron lifetime during the Xe purification phase, and to calibrate the energy scale. The ^{57}Co source emits gammas at 122 keV with 86% branching ratio and at 136 keV with 11% branching ratio. The 136 keV peak is not resolved separately from the 122 keV, and it shows as a tail to the 122 keV peak. Only the 122 keV peak is used for calibrations. The ^{57}Co gammas interact with the Xe mostly via photoelectric absorption, and thus the full energy of the gamma is deposited and a clear peak is observed both in the S1 and S2 distributions. The electron lifetime can be measured by plotting the size of the S2 signal vs. drift time, and the exponential slope of the distribution corresponds to the electron lifetime (see Fig. 4.2). Using the histogram of the S1 signal, one can measure the light yield L_y at $122\,\mathrm{keV_{ee}}$, measured in $\mathrm{phe/keV_{ee}}$, which determines the electron recoil energy scale with $L_y = 3\,\mathrm{phe/keV_{ee}}$. From the S1 histogram, one can also determine the energy resolution of the detector.

The ^{137}Cs source emits gammas at 662 keV (with 85% branching ratio), which interacts with the Xe primarily through Compton scattering. This makes the ^{137}Cs the best candidate to study the behavior of low energy depositions in the liquid Xe. Long calibration runs using ^{137}Cs were performed during November 2006, between the WS3 and WS4 runs. The objective of the ^{137}Cs run is to acquire enough low-energy data in order to define the electron recoil band, and thus determine the discrimination power of the detector at low energies, as discussed in Section 2.1.4. The calibration of the S1 signal using the ^{137}Cs peak results in a scintillation yield of $L_y = 2.2\,\mathrm{phe/keV_{ee}}$. In the energy range of interest $(2 - 12\,\mathrm{keV_{ee}}$ for $L_y = 2.2\,\mathrm{phe/keV_{ee}})$, the number of ^{137}Cs events acquired was 50% larger than the number of blind WIMP search events acquired (see Fig. 4.1).
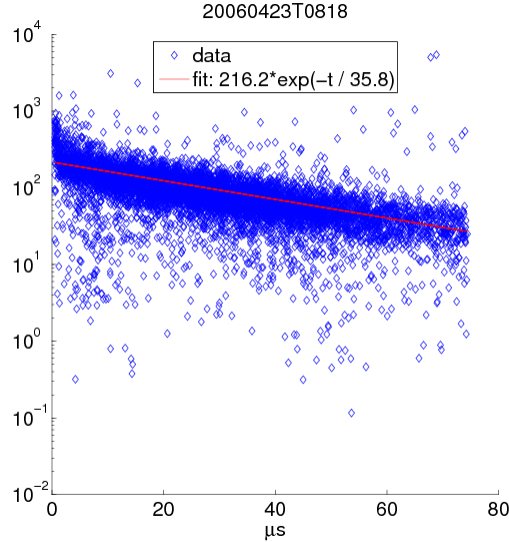
Figure 4.2: Electron lifetime measurement in XENON10 at the beginning of the purification process, showing a electron lifetime of $35.8\,\mu s$ (= $6.7\,cm$). The figure plots the size of the S2 signal in phe (y-axis) vs. the drift time, which measures the depth of the event. An exponential fit to the decay in signal size returns the characteristic drift length, or electron lifetime.

4.1.3   Neutron Calibration Run

The nuclear recoil (NR) band is defined by the events acquired in a neutron calibration run, that took place in December 2006, immediately before the WS4 run. The neutron calibration was performed using a $3.7 \pm 15\%\,\text{MBq}$ ^{241}AmBe source, placed inside the shield and next to the detector. The source emits $220\,\text{n/s}$, with average energy of $4.3\,\text{MeV}$ and maximum of $11\,\text{MeV}$. The neutron source energy spectrum is shown in Fig. 4.3. The ^{241}AmBe source also emits $4.43\,\text{MeV}$ gammas. During the calibration run, the source is placed between two $5\,\text{cm}$ Pb bricks (with one of them between the source and cryostat) to shield the detector from the gammas.

Although the ^{241}AmBe source energy spectrum is known with an accuracy of $\pm 3\%$ per bin $(0.1\,\text{MeV})$, small variations in the spectrum make little difference to the nuclear recoil spectrum in the detector. The shielding due to the Pb brick between the source and cryostat and self-shielding of the liquid Xe "washes out" the main features in the incoming neutron spectrum. The spectrum of neutrons incident on the XENON10 fiducial volume of $5.4\,\text{kg}$, after propagating through the Pb brick, detector walls and the layer of Xe between the
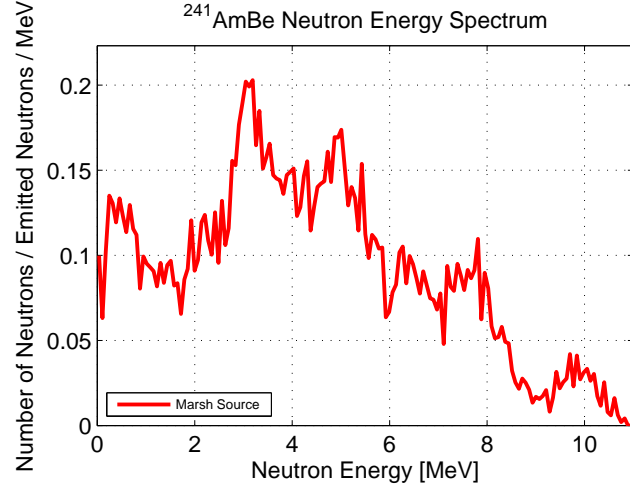
Figure 4.3: ^{241}AmBe source neutron energy spectrum measured by Marsh 1995 [95], with accuracy of $\pm 3\%$ per bin (0.1 MeV).

source and the fiducial volume, is a double exponential decay, falling 1 decade in 3 MeV for $E_n < 2$ MeV and 1 decade in 7 MeV for $E_n > 2$ MeV (see Fig. 4.4).

The detector was exposed to the neutron source for a single run of 12 live-hours, acquiring at a rate of 6.5 Hz. The use of neutron sources at LNGS is strictly controlled, due to the presence of several low background experiments, thus limiting the neutron exposure in XENON10. A high energy veto at $E < 100$ keV$_{ee}$ is used to suppress high energy γ events. The neutron calibration data is used to define the nuclear recoil band, described in Section 2.1.4, and also to determine the efficiency of the analysis algorithms and cuts on NR events, the trigger and software thresholds on NR events, and the detector response to NR events, specifically the light yield of nuclear recoils. The latter is further discussed in Section 4.4.

The acquired neutron calibration data shows the main population of elastic scatters falling exponentially with energy, plus two peaks due to inelastic scatterings at 40 keV and 80 keV (see Fig. 4.5). The elastic scattering population of neutron events is used to define the nuclear recoil band. The distribution of the discrimination factor $\log_{10}(S2/S1)$ for single elastic scatters is Gaussian in each energy bin (see Fig. 2.9). The nuclear recoil band is defined by the $\pm 3\sigma$ contours of the $\log_{10}(S2/S1)$ distribution for neutron elastic scatters.
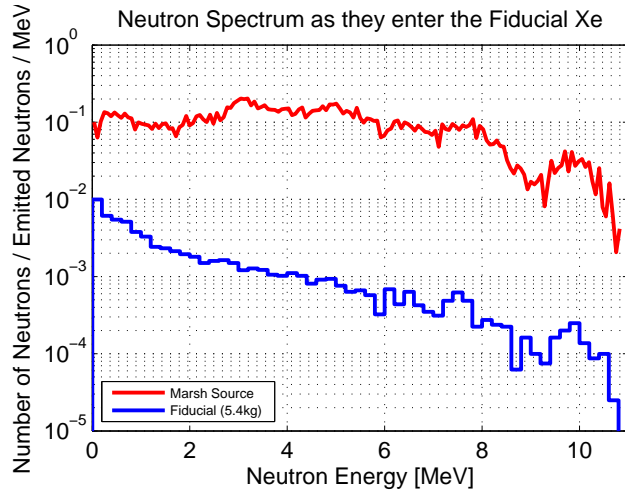
Figure 4.4: Neutron spectrum incident on the XENON10 fiducial volume (blue line) generated using the AmBe neutron spectrum from Marsh 1995 [95] (red line) and full transport of neutrons through Pb shield, detector and liquid Xe layer outside the fiducial volume (2 cm thick).
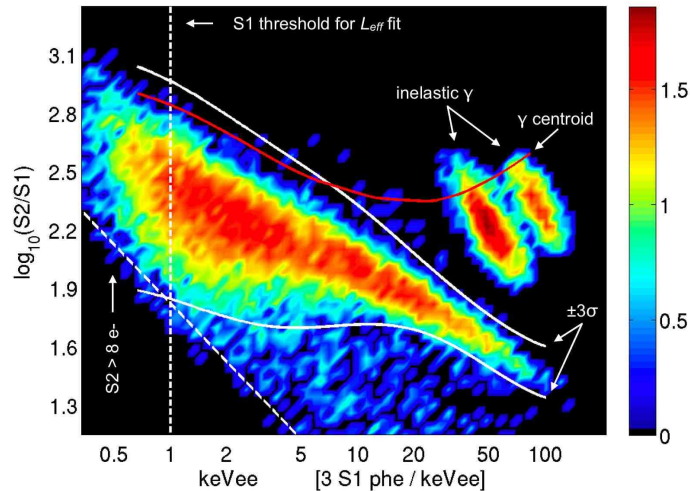
Figure 4.5: Nuclear recoils in Xe from the neutron calibration data, plotted as $\log_{10}(S2/S1)$ vs. energy (using the S1 energy scale $L_y = 3.0\,\mathrm{phe/keV_{ee}}$). Basic quality cuts (QC0) and the fiducial volume (5.4 kg) cut are applied. The color scale indicates $\log_{10}$ (counts). The plot shows the elastic scatter population (the largest population, on the left), plus two peaks due to inelastic scatterings at 40 keV and 80 keV. A high energy veto at $E < 100\,\mathrm{keV_{ee}}$ suppresses the 80 keV peak and all high energy γ events. The solid white lines indicate the $\pm 3\sigma$ lines of the NR band, and the solid red line indicates the centroid of the ER band. The dashed lines indicate the software thresholds used for the $\mathcal{L}_{eff}$ analysis, described in Section 4.4.

4.1.4 Activated Xe Run

After the WIMP search run WS4 was completed, a run with neutron-activated Xe was performed to calibrate the position dependence of signals in the detector. The Xe was activated at Yale University, by exposing $1\,\mathrm{kg}$ of Xe to a high intensity ^{252}Cf neutron source. Measurements indicated an activity of $100\,\mathrm{Bq/kg}$ immediately after the activation. Half of the activated Xe was shipped to LNGS, and half was kept at Yale for monitoring. The activated Xe was introduced in the XENON10 detector 2 weeks after activation.

The neutron activation produces the $^{129\mathrm{m}}$Xe and $^{131\mathrm{m}}$Xe metastates, which decay producing $236\,\mathrm{keV}$ and $164\,\mathrm{keV}$ gamma lines, and have half-lives of 8.9 and 11.8 days, respectively. The $164\,\mathrm{keV}$ gamma line is particularly interesting for calibration purposes. Relatively low energy gammas, such as the $122\,\mathrm{keV}$ produced by ^{57}Co sources, only penetrates a few mm into the liquid Xe because of self-shielding, and thus cannot provide uniform calibration for the entire volume. The use of high energy gamma sources such as ^{137}Cs are disfavored for calibrations of the low energy detector response because of systematic uncertainties due to the non-linearity of the PMT response and of the Xe scintillation yield. The activated Xe provides a solution, as it can produce relatively low energy gammas ($164\,\mathrm{keV}$) that are uniformly distributed in the detector volume, by mixing the activated Xe into the rest of the liquid Xe. Using the activated Xe data, one can calibrate how the S1 and S2 signals vary with depth (drift time) and X-Y position. The adjustments to the signal based on the activated Xe data are discussed in Section 4.2.3.

4.2 Analysis Framework

After the signals from the PMTs are digitized by the data acquisition system, they are downloaded into a computer, and then transferred to a computing and storage cluster, where they will be analyzed. The process is carried out by two independent analysis chains, one based in Matlab, and one based in ROOT. The main reason for the analysis to be performed into two chains was to promote comparison and cross-checking - results arrived at by independent analysis have a stronger claim to being correct. The two analysis chains

are parallel, have similar functions and duplicate the entire framework. In this section, we describe the analysis chain and algorithms developed using Matlab, unless otherwise stated. Note that the ROOT analysis chain will have very similar structure, similar algorithms and similar cuts. Both analyses were frozen before the opening of the blind WIMP Search data. However, prior to the unblinding, the collaboration agreed on publishing only the results from the ROOT analysis. The ROOT analysis was chosen for publication over the Matlab analysis because of its simpler Advanced Quality cuts (see QC2 in Section 4.2.2.3 below), and is thus referred to as the *primary analysis*, while the Matlab analysis is referred to as the *secondary analysis*. The results described in this chapter are derived from the ROOT analysis results, unless otherwise stated.

4.2.1 Analysis algorithms

The analysis of the XENON10 data is done in two main stages, the first pass and second pass analysis. The first pass analysis search for pulses in the digitized data, measuring some basic properties such as height, width, area and rise-time, while remaining indifferent as to whether the pulses are S1, S2 or noise. The second pass analysis is the decision-making stage of the analysis. At this stage, the pulses identified in the first pass are tagged as either S1 or S2 pulses, and a number of data quality cuts are applied to remove glitches and noise.

In the first pass analysis, pulses are identified in an event by looking at the summed trace of all PMTs. An event is defined as a time trace of $\pm 80\,\mu$s around a trigger, and it may contain one or more S1 and S2 pulses. The pulse identification algorithms use double *sliding box* filters, which integrate candidate pulses with time constants of $200\,$ns and $2\,\mu$s, corresponding to the maximum width of S1 and S2 pulses, respectively. The filters are necessary because small S2 pulses (from only one or a few e$^-$) are basically a few phe ($1\,$e$^-$ has only $\sim 24\,$phe) spread over 89 PMTs in $\sim 1\,\mu$s. It is a very sparse signal and it looks like a small collection of individual single phe pulses. By applying the $2\,\mu$s filter, the pulses are collected together into a single feature in the trace.

The pulse identification process is done in two steps. In the first step, the analysis software applies the $2\,\mu$s filter to the summed trace, searches for pulses, and measures the

pulse parameters. In the second step, the analysis software applies the 200 ns filter, searches for additional pulses in the region before the largest pulse identified thus far (we don't expect S1 pulses after an S2), and measures their parameters. The first pass analysis only saves a predefined number of pulses with each filter, up to $N_{(2\,\mu S)} = 3$ and and $N_{(200\,ns)} = 2$. Note that the identification of a pulse as either S1 or S2 will only occur later, in the second pass analysis. The first pass analysis software sorts the pulses in each event by area, from largest to smallest. A series of parameters, called Reduced Quantities (RQs), are extracted for every pulse. These include: area, maximum height, 10% rise and fall time, 50% rise and fall time, 10% width, 50% width, position (in the trace) of 10% pulse height, 50% height, and pulse maximum. Each of these parameters are calculated both for the summed trace, and for the summed trace with the $2\,\mu$s filter applied. The pulse areas are recorded for each individual PMT. The pulse areas are recorded in number of phe, using the conversion factors found through LED calibration, as detailed in Section 3.1.4. At this point, no decision has been made whether this pulse is an S1 or an S2 - a pulse found through the 200 ns filter might still be tagged as an S2, or as a glitch, on the next stage of the analysis. Because of this "egalitarian" approach to pulses, the 1st pass analysis is known as REEFrunner, in which REEF is an acronym for "REally Equal Footing".

The second pass analysis uses the pulse shape RQs calculated in the first pass to tag individual pulses as either S1 and S2 pulses, based on width and pulse shape. The parameters for the decision-making are tested and tuned with the gamma and neutron calibration datasets before being applied to the WIMP search data. The second pass also calculates a number of additional RQs, such as multiplicity (number of S2 pulses), drift time (time between the S1 and S2 pulses, which determines the Z position of each scatter), and X-Y position.

The position reconstruction uses the PMT hit pattern of an S2 pulse to calculate the X-Y position of a scatter in the active Xe volume. Because of the small electron diffusion coefficient, the electrons remain horizontally concentrated as they are drifted up by the electric field from the interaction site. The extraction and acceleration of the electrons in the gas phase produces a focused S2 signal on the top PMT array (it is very diffuse on the

bottom array). For events with multiple S2 pulses, the X-Y position for each pulse can be fully reconstructed, as long as the pulses are fully separated in the event time trace (i.e. $\Delta t > 1\,\mu\mathrm{s}$).

The XENON10 analysis considered four techniques for position reconstruction: (1) center of gravity; (2) minimum χ^2; (3) maximum likelihood; and (4) neural networks. The center of gravity method is the simplest method, and it calculates the scatter X-Y position from a weighted sum of the PMTs X-Y positions. Both the minimum χ^2 and maximum likelihood methods compare the hit pattern to photon distribution maps generated through Monte Carlo simulations. The simulations are performed in Geant4, and are similar to the light collection simulation described in Section 2.1.8. In this simulation, a large number of photons ($\sim 10^5$) are emitted at each point on the gas volume, with $1\,\mathrm{mm} \times 1\,\mathrm{mm}$ horizontal resolution. In the minimum χ^2 method, the event position is determined by comparing the data hit pattern to each simulated hit map, and minimizing the χ^2 given by:

$$\chi^2\left(x,y\right) = \sum_{i=1}^{47} \frac{\left[S2_i - S2_{MC,i}\left(x,y\right)\right]^2}{\sigma_i^2}\,, \tag{4.1}$$

where $S2_i$ is the S2 signal detected by the ith PMT, $S2_{MC,i}\left(x,y\right)$ is the S2 signal in the ith PMT for in the Monte Carlo simulation of photons emitted at (x,y), and σ_i^2 is the total variance in the signal, including the standard deviation of the gain as calculated from the single phe spectrum (described in Section 3.1.4) and statistical fluctuations of the phe emission from the photocathode of the PMT. For large signals ($S2 > 2000\,\mathrm{phe}$), the variance is well-determined and the minimum χ^2 method works well. The maximum likelihood method is similar, but more precise, especially for small S2 pulses. It works by maximizing the likelihood function given by

$$L\left(S2_{MC,i}\right) = \prod f\left(S2_i, S2_{MC,i}\left(x,y\right)\right)\,, \tag{4.2}$$

where $f\left(S2_i, S2_{MC,i}\left(x,y\right)\right)$ is the probability that $S2_i$ matches the expectation value given by the simulated hit maps, $S2_{MC,i}\left(x,y\right)$. Ultimately, the neural network method was used for the results reported in publications [68, 96]. A detailed description of the neural network

method is given in [97].

After the pulses have been identified and measured, a series of adjustments are applied, to correct the area of the S1 and S2 pulses based on their positions. The adjustments are based on the data obtained in the gamma, neutron and activated Xe runs, and are explained in Section 4.2.3 below. A series of simple quality cuts (collectively called QC0) are applied to the data to remove obvious glitches and events that do not pertain to the WIMP search, such as multiple scatters. After the QC0 cuts are applied, the data is stored in separate data files, to be used by the final user. The final step in the data processing consists in the application of analysis-specific cuts, such as energy cut, fiducial volume cut, and advanced quality cuts. The latter cuts depend on the specific analysis being performed, i.e. WIMP search or calibration. All cuts are explained in Section 4.2.2. Finally, the data is ready to be plotted in the usual forms: energy histograms, event position distributions, and energy vs. discrimination parameter. The latter is commonly used for identification of WIMP candidate events in the data, and plots $\log_{10}\left(S2/S1\right)$ vs. $S1$. The plots and results of the WIMP search data are discussed in Section 4.3.

4.2.2 Cuts

The cuts are a method of selecting events for the final analysis. They are grouped into 3 categories: the level 0 or basic quality cuts (QC0), which remove glitches and non-interesting events for the WIMP search, such as multiple scatters; the level 1 quality cuts (QC1), which are the fiducial volume cut and the WIMP window cuts; and the level 2 or advanced cuts (QC2), which target special classes of events. The cuts thresholds and efficiencies are determined by the gamma and neutron calibration datasets, and on a small portion of the (non-blind) background data, and are frozen before being applied to the blind WIMP search data.

The efficiency of each cut is assessed on the neutron calibration data, to determine the acceptance of nuclear recoil events. The combined cut acceptance efficiency averaged over the energy range of interest is 86% (percentage of NR events kept); the combined cut efficiency for each energy bin is listed in Table 4.1.

4.2.2.1 QC0 (basic quality cuts)

The basic quality cuts remove glitches, noisy events, events with no S2 pulses, and multiple scatter events, since these are not valid WIMP candidates. The combined cuts efficiency is $\sim 99\%$ for legitimate single scatter events.

Saturation. Removes events in which the signal saturates a digitizer channel. For gamma calibrations, this requirement can be waived, as the PMT directly above the scatter saturates at $\sim 200\,\mathrm{keV_{ee}}$.

S2 Size. Requires $S2 > 300\,\mathrm{phe}$. For events with smaller S2 signals, the S1 signal might be too small to detect.

S1 Coincidence. The S1 signal must be detected in at least 2 PMTs, with a threshold on the S1 signal on an individual PMT of $S1_i > 0.35\,\mathrm{phe}$.

Single S1. Allows only events with a single S1 pulse before the S2 pulse. Additional S1 pulses are due to time coincidence between events or between an event and a glitch. Especially problematic is the presence of scatters in the non-active Xe volume, which generate S1 light but no S2. These occur at a high rate and thus increase the probability of overlap.

Single S2. Allows only events with a single S2 pulse, indicating a single scatter event. Multiple scatter events are eliminated since they are not WIMP candidates. If more than one S2 pulse is found, the event is only rejected if a secondary S2 pulse is at least 5% of the total S2 area and at least $40\,\mathrm{phe}$. This cut also eliminates events without S2 pulses, when the hardware S2-trigger threshold is below the the software threshold.

S1 Width. Selects events with S1 FWHM $< 300\,\mathrm{ns}$. This cut ensures that the S1 is not a misidentified S2.

S1 Rise (Decay) Time. This cut selects events based on the S1 pulse shape. It is uses different criteria for the Matlab and ROOT analysis chains. The Matlab analysis looks at

the risetime (rt) and requires $rt_{S1} < 50\,\mathrm{ns}$. The ROOT analysis looks at the decay time and requires $\tau_{S1} < 57\,\mathrm{ns}$.

S2 Width. Selects only events with S2 width in the defined range. The cut looks at both the unfiltered S2, and at the S2 after the application of the $2\,\mu\mathrm{s}$ filter. The cuts require the filtered pulse width in the range $1.6 - 2.4\,\mu\mathrm{s}$, and the unfiltered pulse width in the range $0.45 - 2.25\,\mu\mathrm{s}$.

S2 Top/Bottom Ratio. The cut removes events in which the S2 signal is disproportionally large in the bottom array. From the light collection simulations, we expect a $60\%/40\%$ ratio in the S2 light in the top and bottom PMT arrays, respectively. The cut requires $S2_{top}/S2_{bottom} > 0.54$.

χ^2 **(Position Reconstruction).** This cut removes events in which the χ^2 of the position reconstruction, given by Eq. 4.1, is too high, indicating that the position of the event was not properly reconstructed.

S2 Fraction. It is expected that the majority of the event area is concentrated in the S2 pulses. This cut measures the ratio between the S2 area and the total trace area, and requires $S2\_area/event\_area > 0.5$. Events that fail this cut might indicate a wandering trace baseline, or an electric discharge.

Pulse Area/Height Ratio (Matlab Only). Eliminates events in which the S2 height is too high for the measured S2 area, indicating the possible misidentification of an S1 as an S2.

Good Baselines (Matlab Only). For each channel, checks whether any of the first 50 samples in the trace exceeds a pre-specified threshold. If the test fails, the trace is deemed too noisy to determine the correct trace baseline, necessary to calculate the S1 and S2 pulse height and area.

Drift Time Range. It requires: (1) the S1 to happen after the first 500 ns of the signal trace, so that it does not affect baseline measurements; (2) the S2 to happen before the last 2 μs of the signal trace, to avoid S2 pulses being cut-off. It also requires the separation between S1 and S2 to be $\Delta t > 10$ ns (1 sample), to prevent overlap and misidentification of S1 pulses as S2 pulses.

4.2.2.2 QC1 (fiducial volume and WIMP window cut)

The QC1 cuts define the acceptance and sensitivity of the XENON10 detector to WIMP candidate signals.

Energy Cut. It requires $2 \leq E \leq 12\mathrm{keV_{ee}}$ (with $L_y = 2.2\,\mathrm{phe/keV_{ee}}$), or $4.5 \leq E \leq 26.9\,\mathrm{keV_r}$. The energy range is defined on the lower end by the pulse detection threshold ($> 99\%$ at $2\,\mathrm{keV_{ee}}$) and on the higher end is set to ensure that the expected WIMP signal is not overwhelmed by background. For a signal threshold of $2\,\mathrm{keV_{ee}}$, $\sim 80\%$ of events occur with $E < 12\,\mathrm{keV_{ee}}$.

WIMP Discrimination Window Cut. It requires $\log_{10}(S2/S1) \in [-3\sigma_{NR}, \mu_{NR}]$, where μ_{NR} is the nuclear recoil band centroid and σ_{NR} is the width of the nuclear recoil band. This cut is designed to take advantage of the discrimination power of the liquid Xe detector, as described in Section 2.1.4. The electron recoil and nuclear recoil events form 2 distinct bands, with a partial overlap of the bottom half of the ER band and the top half of the NR band. The band centroids and widths are defined using the gamma calibration data (^{137}Cs) and the neutron calibration data. The $-3\sigma_{ER}$ edge of the ER band lies very close to the nuclear band centroid. We select an acceptance window in the range $[-3\sigma_{NR}, \mu_{NR}]$, that is, we only accept WIMP candidate events that fall into this window. This acceptance window has an acceptance efficiency of 50%, and a leakage rate of 0.4%. The leakage rate indicates the percentage of ER event Gaussian distribution that fall within the acceptance window.

Fiducial Volume Cut. This cut requires $R < 8\,\text{cm}$ and $15 \leq dt \leq 65\,\mu\text{s}$, where dt is the drift time and it corresponds to the Z position of the event. The fiducial volume cut takes advantage of the self-shielding properties of Xe to reduce backgrounds. This is the fiducial volume used in the WIMP search blind analysis, and is determined by looking at the gamma calibration data (^{137}Cs) and the unblinded background data (WS2 and $16\,\text{live-days}$ from WS3+WS4). The fiducial volume is defined as the volume in which no leakage events in the NR acceptance box occur, after all other cuts (including the WIMP discrimination window and energy cuts) are applied to the data.

4.2.2.3 QC2 (advanced cuts)

The QC2 cuts are sub-divided into 2 categories: the advanced quality cuts, designed to remove the noise or glitch events not removed by the QC0 basic cuts; and cuts designed to remove non-Gaussian leakage events, that is, gamma events that are tagged as nuclear recoils due to the partial loss of the charge signal. These events are collectively known as the Gamma-X events. The Gamma-X cuts are discussed in Section 4.3.2, and the nature of these events are discussed in more detail in Section 6.4. Note that the cuts labeled as "Matlab Only" are not applied to the data analysis in the WIMP search results presented in this chapter and in publications. The combined efficiency for NR events of the QC2 cuts applied in the WIMP Search primary analysis is 86% in the fiducial volume ($5.4\,\text{kg}$) and in the energy range of interest ($2-12\,\text{keV}_\text{ee}$). The efficiency is calculated for using the neutron calibration run, and applies only to the WIMP signal box (with 50% NR band acceptance).

Pulse Area Fraction Cut (Matlab Only). This cut measures the amount of noise in an event. A well-formed event (such as the one shown in Fig. 3.3) has most of its area in the S1 and S2 pulses. Events in which a large fraction ($\gtrsim 8$) of the event trace area is outside the pulses is cut out.

S1 10% Width Cut (Matlab Only). The QC0 cuts already include a S1 width cut, but it looks at the 50% height width (the FWHM). This cut is design to remove events in which the S1 has unusually long tails.

S1 Asymmetry (ROOT Only). This cut removes events in large amount of light in the top PMT array. Because of internal reflection on the gas-liquid interface, we expect most of the S1 light to be in the bottom array ($\sim 80\%$ at high energies, i.e. $E > 15 \, \mathrm{keV_{ee}}$). The cut is energy dependent, as Poisson fluctuations dominate the photon distribution for low energy depositions.

Gamma-X cuts. A series of cuts were developed and applied to the WIMP search data to remove non-Gaussian leakage events, gamma events that are identified as nuclear recoils due to the partial loss of the charge signal S2, and thus have a $\log_{10}\left(S2/S1\right)$ that falls within the NR band. These cuts are discussed in Section 4.3.2, and the nature of the Gamma-X events are discussed in more detail in Section 6.4.

4.2.3   Adjustments

A series of correction factors are applied to the S1 and S2 signals to adjust the signal size based on the event position. These adjustments are applied after the reconstruction of the event position, and are applied to the WIMP Search data used in the blind analysis described in Section 4.3.

PMT Relative Sensitivity (RS) Factor. The RS factor combines the PMT gain, quantum efficiency and collection efficiency, relative to their mean values (see Section 3.1.4). The RS is applied to the signals of the individual PMTs during data analysis, so that the signals of all PMTs are normalized to the average gain and detective efficiency (DE). The RS factor is illustrated Fig. 3.8, which maps the RS for the top PMTs in XENON10.

S1 Z Correction. The light collection efficiency for S1 signals depends on the Z position of the event, as discussed in Section 2.1.8. The size of the S1 signal in each PMT is adjusted as a function of the position of the event. The adjustment factor is calibrated on the $164 \, \mathrm{keV}$ line from the Activated Xe run. The Z dependence of the S1 signal size is shown in Fig. 2.18. The X-Y position dependence is not significant in the fiducial volume and immediately around it.
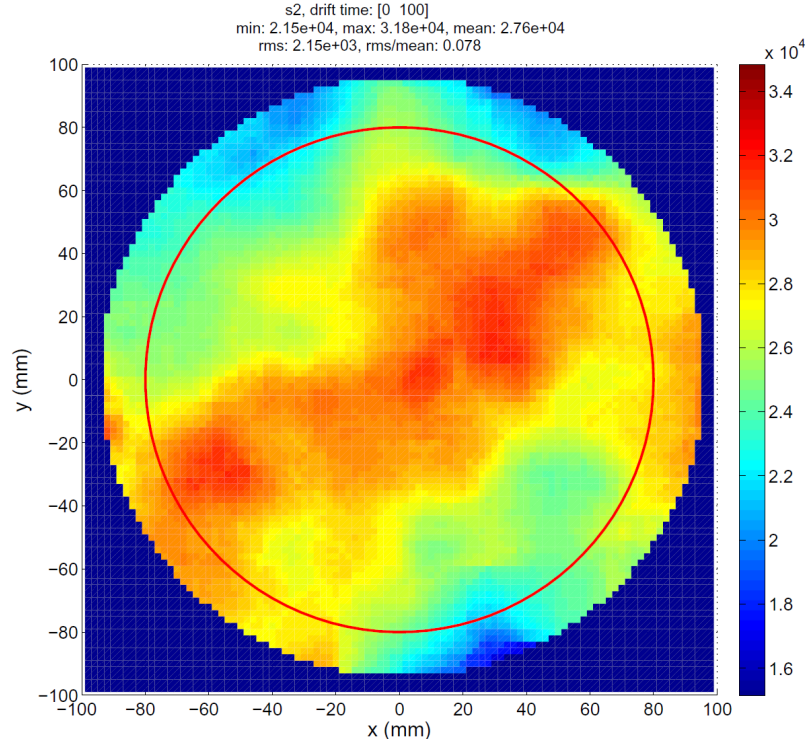
Figure 4.6: X-Y dependence of the S2 signal amplitude, calibrated using the 164 keV line from the Activated Xe run in XENON10.

S2 Z Correction (electron lifetime). Charge loss as the electrons are drifted from the scatter region to the liquid-gas interface affects the amplitude of the S2 signal (this effect is illustrated in Fig. 4.2). The characteristic length for electron loss, measured in drift time, is called the electron lifetime. The electron lifetime depends on the Xe purity, and improves as circulate the Xe through the purification system. The electron livetime in XENON10 reaches a maximum $\sim 2\,\text{ms}$, corresponding to $\sim 4\,\text{m}$ drift length. The size of the S2 in each channel is adjusted to account for this charge loss.

S2 X-Y Correction. The amplitude of the S2 signal depends on the strength of the extraction field $\mathcal{E}_e$, applied by the Gate and Anode grids. Changes on the field due to grid imperfections or bending affect the size of the S2 signal in the X-Y region of the anomaly. The S2 dependence on the X-Y position of the event is mapped out using the 164 keV line from the Activated Xe run, and is shown in Fig. 4.6. The S2 signal in each PMT is scaled to match the mean of the S2 X-Y dependence.

E bin [keV$_\mathrm{r}$]	ϵ_{cuts}	$1 - R_{ER} \times 10^{-3}$	N_{evt}	N_{leak}
$4.5 - 6.7$	0.94	$0.8^{+0.7}_{-0.4}$	213	$0.2^{+0.2}_{-0.1}$
$6.7 - 9.0$	0.90	$1.7^{+1.6}_{-0.9}$	195	$0.3^{+0.3}_{-0.2}$
$9.0 - 11.2$	0.89	$1.1^{+0.9}_{-0.5}$	183	$0.2^{+0.2}_{-0.1}$
$11.2 - 13.4$	0.85	$4.1^{+3.6}_{-2.0}$	190	$0.8^{+0.7}_{-0.4}$
$13.4 - 17.9$	0.83	$4.2^{+1.8}_{-1.3}$	332	$1.4^{+0.6}_{-0.4}$
$17.9 - 22.4$	0.80	$4.3^{+1.7}_{-1.2}$	328	$1.4^{+0.5}_{-0.4}$
$22.4 - 26.9$	0.77	$7.2^{+2.4}_{-1.9}$	374	$2.7^{+0.9}_{-0.7}$
Total			1815	$7.0^{+1.4}_{-1.0}$

Table 4.1: Energy bins in the XENON10 WIMP Search data analysis. The table lists the software cut acceptance efficiency (ϵ_{cuts}) for nuclear recoils; the electron recoil (ER) rejection efficiency R_{ER} (also called the discrimination), which averages to 99.6% over the entire energy range; the number of ER events N_{evt} detected in each energy bin; and the expected number of Gaussian leakage events N_{leak} for the given ER rejection and ER events. The errors are due to the statistical uncertainty on the Gaussian fit of the ER band using the ^{137}Cs calibration data, and of the NR band using the neutron calibration data.

4.3 WIMP Search

The WIMP search data is analyzed using the algorithms and cuts discussed in Section 4.2. A blind analysis is performed, to prevent biasing of the results. The blind analysis procedure involves keeping a portion of the acquired data (58.6 live-days) untouched and unseen until the final analysis. All algorithms, cuts and signal adjustments are tested and optimized on calibration and unblinded data. Once the parameters and thresholds are agreed upon by the entire collaboration, the analysis code is locked down, and the blind data is opened for analysis.

The blind analysis looks for signals particularly within the WIMP signal box, defined by the energy range of interest ($2 - 12\,\mathrm{keV_{ee}}$, for light yield $L_y = 2.2\,\mathrm{phe/keV_{ee}}$, or $4.5 - 26.9\,\mathrm{keV_r}$ for $\mathcal{L}_{eff} = 0.19$) and the discrimination parameter $y = \log_{10}(S2/S1)$. The WIMP signal box is bounded by the nuclear recoil band centroid μ, and the -3σ line of the band. The band's μ and σ as a function of energy are determined from the neutron calibration run. The WIMP signal box was set by fitting the discrimination parameter y distribution of the neutron data to a Gaussian for each energy bin. The energy bins are listed in Table 4.1.

The WIMP search data from the 58.6 live-days is shown in Fig. 4.7. The plot shows

only the data selected after all cuts are applied, and in the fiducial volume of 5.4 kg. The data is plotted as $y' = \Delta \log_{10}(S2/S1)$ versus S1, measured in keV$_{\text{ee}}$ normalized to the light yield of $L_y = 2.2\,\text{phe/keV}_{\text{ee}}$, obtained from the ^{137}Cs calibration. The y' parameter is defined as $y' = y - \mu_{ER}$, where μ_{ER} is the electron recoil band centroid, defined by the ^{137}Cs calibration data. The coordinate transformation makes it visually simpler to identify events falling out of the ER band and into the NR band. Moreover, the use of the transformed coordinates result in an expectation value of $y' = 0$ for electron recoil background events.

The unblinding of the WIMP search data (WS34) revealed 1815 events in the ER band, and 10 events in the WIMP signal box, after all cuts (QC0, QC1 and QC2). The 10 WIMP candidate events are marked by circles in Fig. 4.7. The ER distribution is Gaussian shaped, and thus reaches down into the WIMP signal box. For the number of events in the ER band, we expect $7^{+1.4}_{-1.0}$ events in the WIMP box (see Table 4.1). Of the events in the WIMP search box, 5 are consistent with being ER band events falling into the WIMP signal box, and are marked by blue labels (events 3, 4, 5, 7, 9). These are called the "Gaussian leakage" (the events of the ER band "leak" into the NR band). One of the remaining WIMP candidate events (event 1) turned out to have been removed by the Basic Quality cuts (QC0) in the secondary Matlab analysis. The event was removed by the "S1 coincidence" cut. Inspection of the event trace confirmed that the event was in fact a glitch due to coherent noise pickup in 2 PMTs.

The remaining 4 WIMP candidate events (2, 5, 8, 10) are not consistent with WIMP events, and are rather likely to be Gamma-X events. The 4 events are clustered at the high end of the energy range, while we expect the WIMP signal to favor low energies - as discussed in Section 1.3.2, the WIMP recoil energy spectrum is expected to be an exponential decay (see Fig. 1.14 on page 38). A plot of the spatial distribution of the WIMP search events (Fig. 4.11) shows that the 4 candidate events are clustered at the bottom and outer edge of the detector. While the WIMP signal is expected to be uniformly distributed throughout the detector, the Gamma-X events are expected to be clustered on the outer bottom corner of the detector, as shown by Monte Carlo simulations in Fig. 6.35. Finally, 3 of the 4 events are removed by the Gamma-X cuts of the secondary Matlab analysis. Only 1 of the events
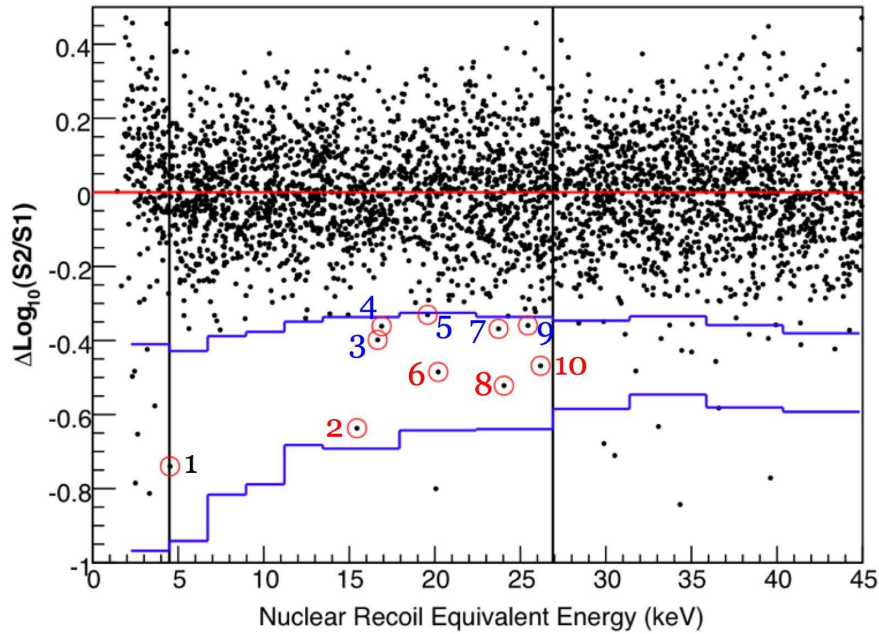
Figure 4.7: WIMP Search data for the blinded run of 58.6 live-days, in the fiducial volume of 5.4 kg. The data is plotted as $y' = \Delta \log_{10} (S2/S1)$ vs. S1 (given in keV$_\mathrm{r}$, and converted using $\mathcal{L}_{eff} = 0.19$), where The $\Delta \log_{10} (S2/S1)$ is the value of $\log_{10} (S2/S1)$ relative to the ER band centroid, defined by the ^{137}Cs calibration data. The blue lines indicate the WIMP signal box boundaries, the NR band centroid μ and the -3σ line, with 50% acceptance. The black lines indicate the energy region of interest: $2 - 12 \, \mathrm{keV_{ee}}$ (for $L_y = 2.2 \, \mathrm{phe/keV_{ee}}$) or $4.5 - 26.9 \, \mathrm{keV_r}$ (for $\mathcal{L}_{eff} = 0.19$). The red line indicates the ER band centroid. Plot reproduced from [68].

remains in the WIMP signal box after both the ROOT analysis and Matlab analysis cuts are applied. However, this event is not likely to be a WIMP signal, as it is not a low energy event ($E > 15 \, \mathrm{keV_r}$), and it occurs far from the NR band centroid: $S2/S1 = 2\sigma$ from the band centroid. Finally, a small change in the Gamma-X cut threshold, resulting in a 1% decrease in the cut acceptance, removes the event. The Gamma-X cuts and the treatment of the WIMP candidate events is discussed in Section 4.3.2.

4.3.1   WIMP Cross-Section Limits

Using the distribution of events observed in the WIMP search analysis, we can set limits on the WIMP-nucleon cross-section. Although the events in the WIMP signal box are ultimately inconsistent with WIMP signals, all 10 of the WIMP candidate events are considered

when calculating the cross-section limits. Because this is a blind analysis, we must treat all events that fall within the WIMP signal box as valid WIMP events when calculating the limits, and thus we apply no background subtraction. Events are not removed even if they belong to well-understood backgrounds, such as the ER band Gaussian leakage into the NR band. The inclusion of all events results in a conservative upper limit on the cross-section.

The cross-section calculations use the standard assumptions for the galactic halo and form factors discussed in Section 1.3. The limits are set by using the "maximum gap" method proposed by Yellin [98]. The method is designed to find the lowest possible upper limit of a signal in cases in which the background (or at least one of its components) is poorly understood, or in which it cannot be subtracted. It therefore makes no assumption as to whether the Gamma-X background is well understood or not.

The maximum gap method is a way of comparing the observed distribution of events to the expected distribution for a given signal. It looks at the largest gap in the event distribution in some parameter in which the distribution from the background and from the signal is different. In this case, we use the maximum gap method to look at the event energy distribution, since we know that the signal distribution (WIMP events) favors low energies while the background distribution (gammas) is flat with energy (see Chapter 6 for the gamma background model). The maximum gap is the largest energy separation between 2 events in the WIMP signal box. In the XENON10 WIMP Search data, the largest gap is between the first 2 events, at $2.01\,\mathrm{keV_{ee}}$ and $6.9\,\mathrm{keV_{ee}}$ (see Fig. 4.7).

In order to compare the observed distribution and the expected signal from WIMPs, we must convert all spectra to the same energy scale. We convert the WIMP Search data event energies from $\mathrm{keV_{ee}}$ to $\mathrm{keV_r}$ using $\mathcal{L}_{eff} = 0.19$, as described in Section 2.1.5. The events in the WIMP signal box are ordered according to their energies. The gap between events i and $i+1$, with energies E_i and E_{i+1}, is measured as the expected number of events x_i in the gap:

$$x_i = \int\limits_{E_i}^{E_{i+1}} \frac{dN}{dE} dE \,, \tag{4.3}$$

where dN/dE is the differential event rate of the WIMP signal for a WIMP-nucleon cross-

section σ_χ and WIMP mass m_χ, plus any known backgrounds, such as the ER band leakage. The number of expected events increases as σ_χ increases. If σ_χ is too large, so is the number of expected events. The definition of "too large" is dependent of the desired confidence limit for the limit. For example, if we want to calculate the 90% C.L. upper limit on the cross-section σ_χ for a WIMP mass m_χ, then we want to find the value of σ_χ for which 90% of random experiments would have $\leq x_i$ events in the largest gap.

Using the maximum gap method, one calculates a 90% C.L. upper limit for the Spin-Independent WIMP-nucleon cross-section of $\sigma_\chi = 8.8 \times 10^{-44}\,\text{cm}^2$, for a WIMP mass of $m_\chi = 100\,\text{GeV/c}^2$. The cross-section upper limit as a function of WIMP mass is plotted in Fig. 4.8, and it shows the lowest upper limit of $4.5 \times 10^{-44}\,\text{cm}^2$ for $m_\chi = 30\,\text{GeV/c}^2$. The XENON10 detector set the lowest limits on the WIMP cross-section at the time of publication [68], but it has since been surpassed by the latest limits set by CDMS-II for masses $m_\chi \geq 40\,\text{GeV/c}^2$ [99], and by ZEPLIN-III for masses $m_\chi \geq 90\,\text{GeV/c}^2$ [72]. The XENON10 detector also sets upper limits on the Spin-Dependent WIMP-nucleon cross-section. The calculation of the SD cross-section limits and the results are discussed in [96].

4.3.2   Gamma-X

The Gamma-X events are gamma events that are tagged as nuclear recoils due to the partial loss of the S2 charge signal. Charge loss can happen in the case of multiple scatter events in which one vertex is in the fiducial volume, and another is in a non-active region of the detector, such as the space below the cathode grid, called the Reverse Field Region (RFR). Because of the electric field configuration, no charge is collected from scatters in this region. Such events have an S1 pulse corresponding to the 2 scatters, but an S2 signal from only one of the scatters. Its S2/S1 ratio is reduced and the event might fall into the NR band, thus being identified as a WIMP candidate event. Such fake nuclear recoils events are called "Gamma-X" events, because of their unknown ("X") component in the non-active Xe regions.

The multiple scatter events with a vertex in the RFR can be identified in the data by
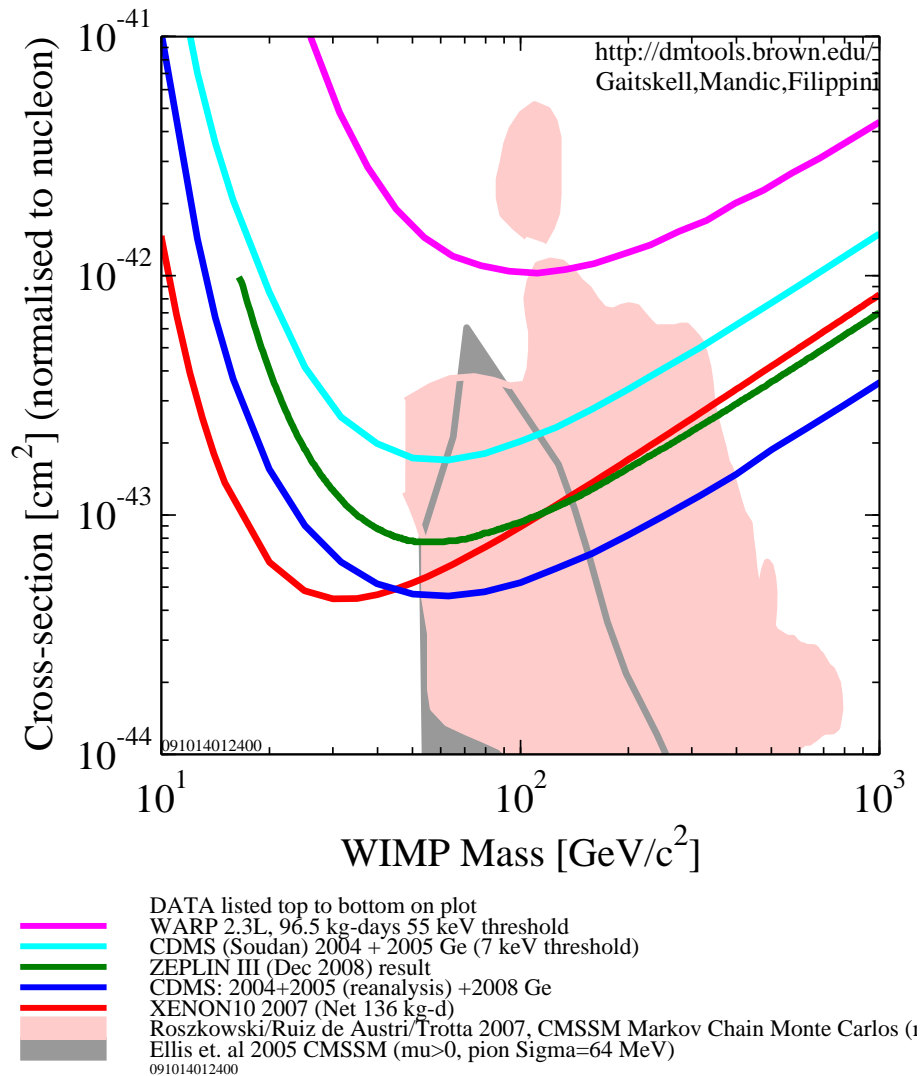
Figure 4.8: Upper limits (90% C.L.) on the Spin-Independent WIMP-nucleon cross-section versus WIMP mass, set by XENON10 detector (red line) [68]. The shaded area are for the WIMP parameter space calculated from Constrained Minimal Supersymmetric Models (CMSSM), and are included in the to illustrate WIMP cross-sections obtained from theory. Plot generated using DMTools [100].

(a) Gamma event, $\Delta t = 43\,\mu$s   (b) Gamma event, $\Delta t = 68\,\mu$s   (c) Gamma-X event, $\Delta t = 40\,\mu$s
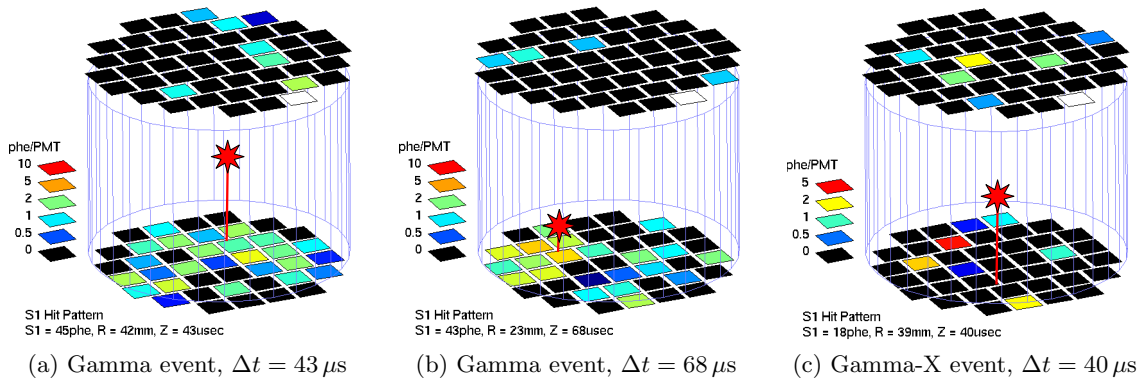
Figure 4.9: Using S1 hit-patterns to identify Gamma-X events. The red stars indicate the location of the event reconstructed from the S2 signal hit pattern and drift time, and the red line indicates the X-Y position. S1 signals are typically evenly distributed across the bottom PMT array (a). Events close to the bottom of the detector produce focused S1 signals, close to the scatter location (b). However, in some events we see a highly localized S1 signal, away from the location reconstructed from the S2 signal (c). Such events indicate a multiple scatter event, with one vertex where the S2 signal is located (the red star) and another vertex in the RFR volume, just above the bottom PMT with the most hits.

using the S1 light hit pattern on the bottom PMT array. S1 signals are typically evenly distributed across the bottom PMT array. Events close to the bottom of the detector produce focused S1 signals, though, and the S1 signal from events just above the bottom PMT windows might be absorbed by just 1 or 2 PMTs. Thus, an over-concentration of S1 signal on a single PMT or a couple of PMTs might indicate the occurrence of a scatter in the RFR volume. This effect is illustrated in Fig. 4.9.

The RFR Gamma-X events are just one of the categories of Gamma-X events. The complete characterization of the Gamma-X events, and the conditions in which they occur, is given in Section 6.4. In this section, we offer a brief description of the cuts developed by the two analysis chains to identify and eliminate Gamma-X events.

4.3.2.1 Primary Analysis Gamma-X cut

The primary ROOT analysis, used in the published XENON10 results, uses a single cut to remove Gamma-X events, the RMS cut, specialized in the removal of multiple scatter events with a vertex in the RFR volume.

RMS Cut. The cut is designed to remove multiple scatters with a vertex in the RFR region (close to the bottom PMTs), or with one vertex in the Xe gas region (close to the top PMTs). It is looks for events with the S1 light overly focused on a single PMT in the bottom (or top) PMT array, which identifies scatters close to the PMT surface. The cut removes events with a large S1 signal RMS, defined for either the top or bottom PMT array as

$$RMS = \sqrt{\frac{1}{n} \sum (S1_i - \langle S1 \rangle)^2}, \tag{4.4}$$

where n is the number of PMTs summed over, and $\langle S1 \rangle$ is the mean S1 signal in either the top or bottom PMT array. The S1 signals are ordered by size, so that only the n largest S1 signals are summed. For the WIMP Search analysis, $n = 5$ for the top PMTs and $n = 10$ for the bottom PMTs. A detailed discussion of the thresholds used in the analysis is given in [82].

4.3.2.2 Secondary Analysis Gamma-X cuts

The secondary Matlab analysis has developed a number of additional cuts, aimed at Gamma-X event with several topologies. A very detailed description of the cuts and their thresholds is given in [64]. These cuts were developed independently from the main analysis (in ROOT).

S1 Reverse Field Region (RFR) Cut. This is the main Gamma-X cut, and it measures anomalous concentration of the S1 signal in one PMT in the bottom array. The cut looks at the quantity $G_i = S1_i/S1_{bot} \cdot \sqrt{S1_{bot} + S1_{top}}$, where $S1_{bot}$ and $S1_{top}$ are the total S1 signal in the bottom and top array, respectively, and $S1_i$ is the S1 signal deposit on the ith PMT, ordered by S1 signal size. The cut looks at $i = 1 - 4$, and its threshold is tuned on the ^{137}Cs calibration data to remove all non-Gaussian leakage events.

S1 Edge-to-All Ratio (E2A) Cut. This cut is designed to remove leakage events due to charge loss on the edge of the detector, as the charge generated by scatters close to the surface between the Xe and Teflon can is lost (either totally or partially) as it drifts up the detector (see Section 6.4.1 for a discussion of the effect). The cut works similarly to

the S1 RFR Cut, but looks only at outer edge PMTs. It cuts on the quantity $E_{frac} = S1_{edge}/S1_{total}$, where $S1_{edge}$ is the S1 signal deposited in all PMTs on the outer edge of the bottom PMT array. The thresholds are set to remove all non-Gaussian leakage events in the ^{137}Cs calibration data not removed by the S1 RFR Cut.

S1 Top Fraction (S1TF) Cut. This cut is designed to remove multiple scatters with a vertex in the gas region. Note that scatters in the gas region are very rare compared to the number of scatter in the liquid, due to the mass difference ($\rho_{liq} = 2.94\,\mathrm{g} \cdot \mathrm{cm}^{-3}$ and $\rho_{gas} = 0.02\,\mathrm{g}\cdot\mathrm{cm}^{-3}$). The cut looks at the quantity $T_{frac} = S1_{top}/S1_{total}$. It did not remove any of the events in the WIMP signal box for either the WIMP Search data or the ^{137}Cs calibration data. The cut has a very high acceptance efficiency ($eff = 99\%$), so it is kept by the secondary analysis.

Partial Gamma-X (PGX) Cut. According to the electric field simulations of the XENON10 detector reported in [83], the region for which no charge is extracted (the RFR) extends up to 1 mm above the cathode grid. Scatters in the edge of the RFR region might have a small amount of S2 charge signal. The Partial Gamma-X Cut is designed to remove RFR events which have one scatter in the fiducial volume and one scatter at the edge of the RFR region. The cut looks for small amounts of charge released at the depth of 15 cm (drift time $\approx 80\,\mu\mathrm{s}$).

4.3.2.3 Gamma-X events

The XENON10 primary analysis identifies 23 events in the WIMP signal box after the application of the basic quality cuts (QC0) and WIMP signal box cuts (QC1), but before the application of advanced cuts (QC2). The 23 events are shown in Fig. 4.10, and their spatial distribution is shown in Fig. 4.11. The box is defined by the parameter space containing WIMP candidate events; however, as we have seen previously, all events in the box can be explained by gamma backgrounds (and one by noise). The lowest energy event (labeled event 1) is due to coherent noise pick-up and is not a legitimate event. Of the 22 legitimate events, some are consistent with being the tail end of the ER band Gaussian
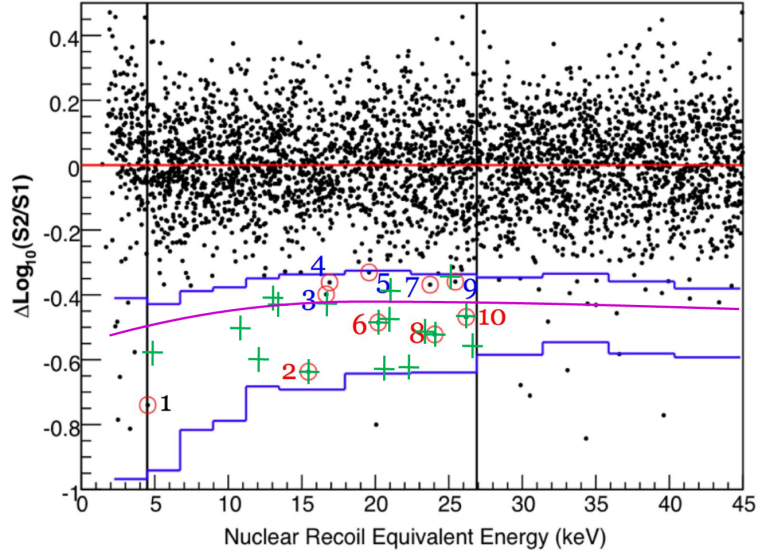
Figure 4.10: Gamma-X events identified in the WIMP Search data for the blinded run of 58.6 live-days, in the fiducial volume of 5.4 kg. The green crosses ($+$) indicate events flagged as Gamma-X events by the Gamma-X cuts in the primary and secondary analysis. The data is plotted as $\Delta \log_{10}(S2/S1)$ vs. S1 (given in keV$_r$, and converted using $\mathcal{L}_{eff} = 0.19$), where The $\Delta \log_{10}(S2/S1)$ is the value of $\log_{10}(S2/S1)$ relative to the ER band centroid, defined by the ^{137}Cs calibration data. The blue lines indicate the WIMP signal box boundaries, the NR band centroid μ and the -3σ line, with 50% acceptance. The black lines indicate the energy region of interest: $2 - 12$ keV$_{ee}$ (for $L_y = 2.2$ phe/keV$_{ee}$) or $4.5 - 26.9$ keV$_r$ (for $\mathcal{L}_{eff} = 0.19$). The purple line indicates the 99.9% line of the ER band. The red line indicates the ER band centroid..

distribution, leaking into the WIMP signal box, and the remaining events are consistent with Gamma-X backgrounds.

Given the discrimination power observed in XENON10, we expect $7^{+1.4}_{-1.0}$ events from the ER band Gaussian distribution to fall into the WIMP signal box (as we have seen in Table 4.1). These events should happen on the top end of the WIMP signal box, closer to the ER band. For a total of 1815 events in the ER band ($\pm 3\sigma_{ER}$), we expect ~ 2 events below the 99.9% line, and thus we should expect ~ 5 events between the NR band centroid and the ER band 99.9% line. Visual inspection of the event distribution in WIMP signal box (Fig. 4.10) shows 9 events fall above the 99.9% line of the ER band distribution. Of these 9 events, 4 are tagged by the primary analysis Gamma-X cuts, indicating that only the other 5 of the events are actually part of the Gaussian ER distribution, matching the expected number of events.

Of the 22 legitimate events in the WIMP signal box, 13 events fall below the 99.9% line of the ER band distribution. For a total of 1815 events in the ER band, we expect only ~ 2 events below the 99.9% line, indicating that ~ 11 events are not consistent with the ER Gaussian distribution. Gamma-X cuts in the primary blind analysis identify 9 of the 13 events below the 99.9% line as Gamma-X events. As discussed earlier in Section 4.3.2, 3 of the remaining 4 events are identified by the cuts developed by the secondary blind analysis as Gamma-X events, and the last event is also consistent with Gamma-X backgrounds - a small decrease (1%) in the cut efficiency for the cuts results in tagging of the event as Gamma-X.

By adding up all events tagged as Gamma-X in the primary and secondary analysis, we find that 17 events are identified as Gamma-X. Monte Carlo simulations are performed in Geant4 to model the behavior of Gamma-X events in the XENON10 detector, and are discussed in Chapter 6. The models incorporates the detector geometry, and mimic the analysis techniques used in the XENON10 data analysis to characterize events. The simulations indicate that the Gamma-X backgrounds result in 14.4 ± 5.3 events. The Gamma-X background model is in good agreement with XENON10 data analysis, and explains all events found in the WIMP signal box. This adds support to the conclusion that no WIMP events were observed by the XENON10 detector.

4.4 Nuclear Recoils Light Yield ($\mathcal{L}_{eff}$)

4.4.1 Neutron Calibration: Simulation vs. Data

The XENON10 sensitivity to the WIMP-nucleon interactions depend on the detector energy threshold, as the WIMP signal increases exponentially as the threshold is lowered (see Fig. 1.14 on page 38). The energy threshold is determined by the trigger and software thresholds, and by the scintillation yield for nuclear recoils produced by elastic scattering - the larger the yield, the larger the signal (number of phe) for a given event energy (keV_r). Thus, measuring the nuclear recoil scintillation yield not only establishes the nuclear recoil energy scale, it also determines the detector sensitivity to WIMP events. The nuclear recoil
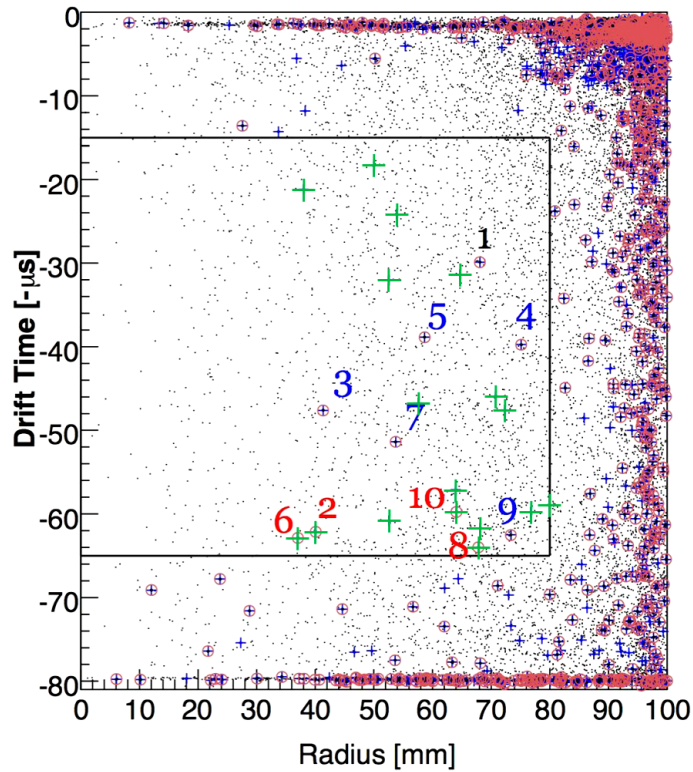
Figure 4.11: Spatial distribution of events in the WIMP Search data for the blinded run of 58.6 live-days, in the fiducial volume of 5.4 kg. The blue crosses (+) indicate events in the WIMP signal box before QC2 cuts; the red circles (∘) indicate the remaining events in the WIMP signal box after the application of the primary analysis QC2 cuts; the green crosses (+) indicate all events flagged as Gamma-X events by the Gamma-X cuts in the primary and secondary analysis in the fiducial volume only. Only events in the energy region of interest are shown: $2 - 12\,\mathrm{keV_{ee}}$ (for $L_y = 2.2\,\mathrm{phe/keV_{ee}}$) or $4.5 - 26.9\,\mathrm{keV_r}$ (for $\mathcal{L}_{eff} = 0.19$). The black line indicates the fiducial volume of 5.4 kg.

yield is usually defined relative to the electron recoil yield, and is quoted as $\mathcal{L}_{eff}$, the nuclear recoil scintillation yield relative to $122\,\mathrm{keV}$ γ's from $^{57}\mathrm{Co}$ at zero-field, which is described in Section 2.1.5.

The electron recoils scintillation yield L_y can be determined by measuring the ratio phe/keV$_\mathrm{ee}$ at various energies using gamma sources with well defined lines in the spectrum. In order to determine the nuclear recoil scintillation yield, it is necessary to determine the energy of the nuclear recoil in a manner independent of the liquid Xe response. A neutron beam experiment using a monoenergetic neutron source can be used for this purpose, since the energy deposited is a function of the elastic scattering angle θ. The nuclear recoil energy E_{NR} is given by

$$E_{NR} \approx 2E_n \frac{m_n M_N}{(m_n + M_N)^2} \left(1 - \cos\theta\right) , \qquad (4.5)$$

where E_n is the incoming neutron energy, m_n and M_N are the neutron and nucleus masses, and θ is the scattering angle. An independent neutron detector is placed at an angle θ relative to the incident beam on the liquid Xe chamber (see Fig. 4.12). The events are selected through coincidence between the liquid Xe detector and the neutron detector (accounting for the time-of-flight between them). The angle is varied in order to measure the scintillation yield at several nuclear recoil energies. Measurements performed using this method are described in [74] and [78]. The XENON10 neutron calibration data offers a new method for measuring $\mathcal{L}_{eff}$, by comparing the observed signal spectrum in the neutron data to the energy spectrum obtained from Monte Carlo simulations. In this case, there is tagging of neutron events by an independent detector, and the measurement is done for the entire energy range rather than for discrete points. The method is described in [64], and the results obtained with the XENON10 data are reported in [71]. Below is a brief summary of the method and results.

The neutron calibration data, described in Section 4.1.3, is acquired with the same conditions as the WIMP Search data, using the same trigger and analysis software. Basic quality cuts (QC0) and fiducial volume (5.4 kg) cuts are applied to data. Only single elastic scatter events are selected. Single scatters are selected via a single S2 cut in QC0, and

(a) Conventional Neutron Beam Setup   (b) XENON10 Neutron Calibration
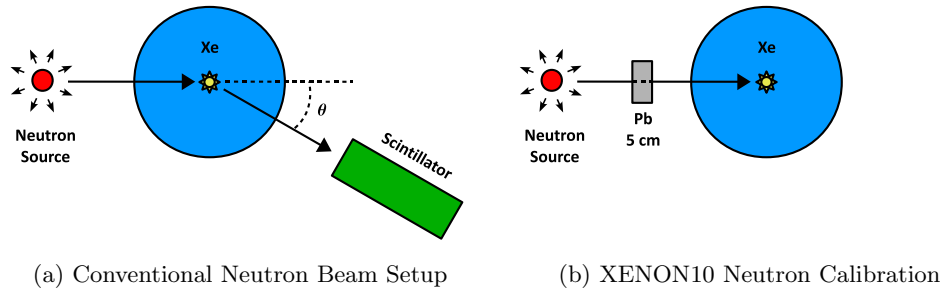
Figure 4.12: Diagram of experimental setup used for nuclear recoil scintillation yield measurements. (a) conventional neutron beam setup, using a scintillator as an independent neutron detector to tag events with a specific energy. (b) XENON10 neutron calibration setup, using a ^{241}AmBe neutron source and 5 cm of Pb to attenuate the emitted γ's with 4.43 MeV.

the elastic scatters are selected by accepting only events within the $\pm 3\sigma$ lines of the NR band, since the inelastic scatter events fall outside the band (as seen in Section 4.1.3). The resulting spectrum is plotted using the electron recoil energy scale (in units of keV$_{\text{ee}}$) calibrated at 122 keV using a ^{57}Co source, which gives $L_y = 3.0$ phe/keV$_{\text{ee}}$.

Monte Carlo simulations of the neutron calibration are performed using Geant4.8.3. The source emits neutrons with the energy spectrum shown in Fig. 4.3. The simulation reconstructs the full XENON10 geometry, and it measures the energy deposition by elastic single scatters in the fiducial volume. Geant4 uses the JEFF3.0 / ENDF/B-VI neutron elastic scattering cross-section tables for Xe. The Monte Carlo nuclear recoil energy spectrum was scaled to match the cross-section given by the newer ENDF/B-VII Xe neutron scattering tables, which are based on Optical Model Potential (OMP) calculations. The neutron cross-section and the OMP are discussed in Section 4.4.2. The nuclear recoil energy spectrum from the simulation is converted from keV$_{\text{ee}}$ to keV$_{\text{r}}$ using Eq. 2.11, and convolved with the measured S1 energy resolution. $\mathcal{L}_{eff}$ is then varied to find the maximum likelihood fit between the Monte Carlo and the data energy spectra. The Monte Carlo and best-fit spectra are shown in Fig. 4.13.

$\mathcal{L}_{eff}$ is calculated at 7 points (2, 5, 10, 15, 25, 50 and 100 keV$_{\text{r}}$), and the shape of $\mathcal{L}_{eff}$ as a function of energy is obtained from piece-wise cubic spline fit. The resulting $\mathcal{L}_{eff}$ vs. energy is shown in Fig. 4.14, along with some previous measurements using
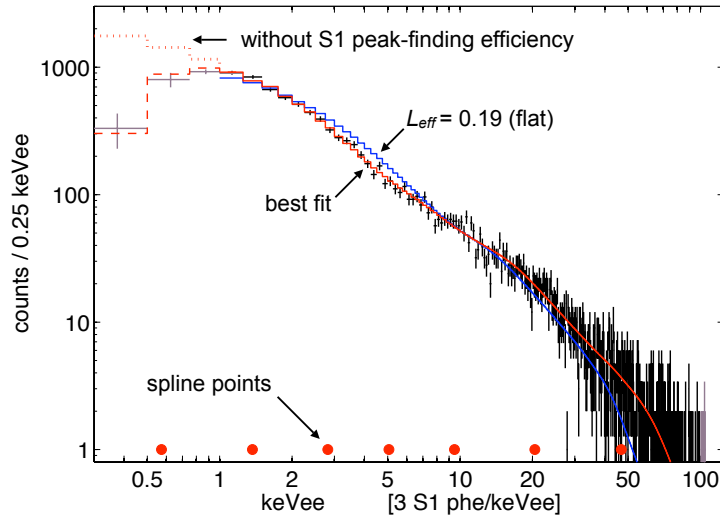
Figure 4.13: Neutron energy spectrum in XENON10: single scatter nuclear recoil data (black line, with 1σ error bars) acquired during the neutron calibration run (described in Section 4.1.3), using a ^{241}AmBe neutron source and with an applied drift field of $\mathcal{E}_d = 0.73\,\mathrm{kV\cdot cm^{-1}}$. The plot also shows the energy spectrum obtained from Monte Carlo, using the best-fit $\mathcal{L}_{eff}$ (red line), and the flat $\mathcal{L}_{eff} = 0.19$ (blue line). The best-fit $\mathcal{L}_{eff}$ is shown in Fig. 4.14. The Monte Carlo best-fit did not use the data with $E < 1\,\mathrm{keV_{ee}}$. The small red dots show the energy spectrum obtained from Monte Carlo below $1\,\mathrm{keV_{ee}}$; the dashed red line shows the energy spectrum after applying the S1 peak-finding efficiency. The energy of the spline fit points for the $\mathcal{L}_{eff}$ calculation are shown as red dots close to the x-axis. Figure obtained from [71].
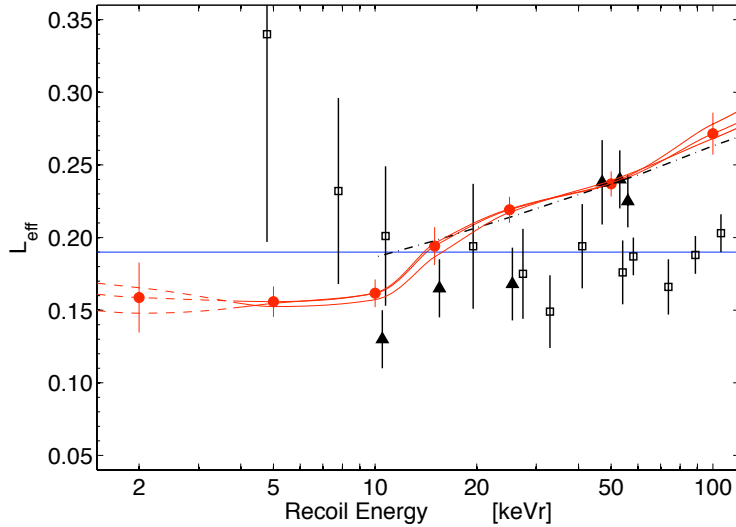
Figure 4.14: Best-fit $\mathcal{L}_{eff}$ vs. energy, obtained from matching the single scatter nuclear recoil spectrum measured in XENON10 to Monte Carlo simulation results (see Fig. 4.13). The red dots indicate the spline fit points used in the $\mathcal{L}_{eff}$ calculation. The error bars correspond to the 1σ statistical error. The additional 2 solid red lines above and below the main result correspond to variation in the neutron-Xe elastic scattering cross-section due to $\pm 3\%$ variation in the Optical Model Potential depth (see Section 4.4.2). The plot also shows the flat $\mathcal{L}_{eff} = 0.19$ (blue line); the $\mathcal{L}_{eff}$ results in Aprile 2005 [77](triangles) and Chepel 2006 [74] (squares); and the theoretical prediction by Hitachi [80] (black dashed line). Figure obtained from [71].

neutron beam experiments (already seen in Fig. 2.12). The statistical uncertainty of the $\mathcal{L}_{eff}$ measurement is estimated by running 10^4 Monte Carlo "experiments", in which the number of counts in each bin is allowed to Poisson-fluctuate. $\mathcal{L}_{eff}$ is measured again for each of these "experiments". The distribution of $\mathcal{L}_{eff}$ value at each of the spline fit points is Gaussian shaped, and the 1σ error on the $\mathcal{L}_{eff}$ is calculated and shown in Fig. 4.14. Another important systematics in the measurement is the uncertainty in the neutron elastic cross-section, which is discussed in Section 4.4.2 below. A discussion of the other systematics in the measurement is presented in [64].

The WIMP-nucleon cross-section upper limits shown in Section 4.3.1 use the flat value of $\mathcal{L}_{eff} = 0.19$, proposed in [74] as the best fit to existing measurements at the time. However, the uncertainty on the value of $\mathcal{L}_{eff} = 0.19$ is a large systematic uncertainty in cross-section limits measured by XENON10, specially at the low-energy range $E < 20\,\mathrm{keV_r}$ where the older data (Aprile 2005 [77] and Chepel 2006 [74]) shows conflicting trends.

Allowing the $\mathcal{L}_{eff}$ to vary between the older measured values of $\mathcal{L}_{eff}$ results in a variation of the cross-section limits measured by XENON10 of $\sim 18\%$ for $m_\chi = 100\,\mathrm{GeV/c^2}$ and as much as $\sim 40\%$ for $m_\chi = 30\,\mathrm{GeV/c^2}$ [78]. Using the energy-dependent $\mathcal{L}_{eff}$ shown in Fig. 4.14, the WIMP cross-section is calculated at $\sigma_\chi = 10.2 \times 10^{-44}\,\mathrm{cm^2}$ for a WIMP mass of $m_\chi = 100\,\mathrm{GeV/c^2}$, a 16% increase in the WIMP cross-section limit, which is within the variation due to the uncertainty in previous $\mathcal{L}_{eff}$ measurements.

4.4.2 Neutron Cross-Sections

The $\mathcal{L}_{eff}$ analysis presented in the previous section relies on the comparison between the XENON10 neutron calibration data and simulations performed using Geant4. The nuclear recoil spectrum obtained form the Monte Carlo simulation depends on the neutron cross-section used by the software - more specifically, on the differential Xe(n,n)Xe cross-section, for which no experimental data is available. Any errors and uncertainties in the cross-section will affect the recoil spectrum, which in turn affects both the $\mathcal{L}_{eff}$ analysis and the WIMP cross-section limits. Thus, it is necessary to determine how reliable the simulation is, and the systematics associated with the uncertainty in the neutron cross-section.

In the section, we look at the optical models used to calculate the elastic cross-section, then modify these models according to reasonable estimates of the uncertainties in the model, and calculate the resulting cross-sections using the EMPIRE software [101]. EM-PIRE reads the input parameters for the optical models from the library called RIPL-2, and allows us to change the optical model potential parameters.

Using the standard neutron differential elastic cross-section from Geant4 (the same as ENDF/B-VI and JEFF3.0), we calculate the nuclear recoil spectrum for the XENON10 fiducial region. We then calculate how the nuclear recoil spectrum changes for the cross-sections obtained for modified optical models, and thus we find the scale factors in the the nuclear recoil spectrum for each case. Finally, we apply the scale factors to the nuclear recoil spectrum found in the Geant4 MC, and repeat the $\mathcal{L}_{eff}$ analysis for the spectra obtained from the modified optical models.

4.4.2.1   The Optical Models

Upon inspection, we learned that Geant4 uses the JEFF3.0 tables for neutron elastic cross-section. The JEFF3.0 is the European library of evaluated nuclear data. The older version of the ENDF library (ENDF/B-VI) uses the same tables as JEFF3.0 for Xe. The elastic cross-section in this library is obtained from the calculations based on the optical model parameters by Wilmore-Hodgson from 1967 [102].

The Optical Model Potential is a simple approach to calculating scattering reactions of nucleons-nuclei where no data is available, by describing the reaction as the interaction of a particle and a spherical potential. The potential $U(r) = V(r) + iW(r)$ has a real component to describe elastic scatterings and an imaginary component to describe all inelastic processes. Initial attempts at the optical model used the familiar square well potential, which approximates the nucleus as a solid sphere. Latter models are based on the Saxon-Woods potential, which has the shape of a Fermi distribution (as seen in Section 1.3.2.2, Eq. 1.39):

$$V\left(r\right) = \frac{V_0}{1 + \exp\left(\frac{r - R_u}{a_u}\right)} \,, \tag{4.6}$$

where R_u is the characteristic radius parameter and a_u is the surface diffuseness parameter [44]. More recent models use even more complex forms, as well as highly specialized parameters for specific nuclei.

Research of the optical models used to calculate elastic cross-sections for neutron scattering reveal that latest version of the ENDF library (ENDF/B-VII) uses calculations based on the optical models developed by Shen Qingbiao and Zhang Zhengjun from the China Nuclear Data Center (CNDC) in 2000 specifically for the Xe nuclei [103]. Although the ENDF library does not make reference to any published papers, the Reference Input Parameter Library 2 (RIPL-2 [104]) library from the IAEA compiles parameters for theoretical calculations of nuclear reactions, and it includes entries for the Shen optical models. The RIPL-2 library contains a series of "generic" spherical optical model to fit large ranges of nucleon-nuclei cross-sections, and also customized optical models for each nucleus whenever

possible. The RIPL-2 library selects the Shen optical models for the nuclei-specific models to be used for Xe nuclei. The Xe models are labeled #532-539 for the Xe isotopes 123, 124, 129, 131, 132, 134, 135 and 136. Through private communication with M. Herman (Coordinator of the EMPIRE project, member of RIPL-2) and P. Oblozinsky (member of EMPIRE and RIPL-2), we confirmed that the best available models for Xe nuclei are the Shen optical models.

In the next section, we compare the cross-sections used in Geant4 (ENDF/B-VI) with the cross-sections obtained from calculations done with the Shen optical models (ENDF/B-VII). We also change the magnitude of the Shen optical model within the limits of the theoretical uncertainty on the OMP parameters, in order to establish what effect these uncertainties have on the cross-sections. A report was produced by the Brookhaven National Lab and published by the National Nuclear Data Center with the goal of estimating neutron cross-section covariances for a large number of nuclei, and it indicates $\pm 3\%$ as a conservative estimate on the uncertainty of the optical model potential related to elastic scatterings of neutrons on nucleons [105]. This point is discussed further in Section 4.4.2.3.

4.4.2.2 Cross-Section Calculations

Using the EMPIRE software (version 3.0beta [101]), we have calculated the cross-sections and angular distributions for the elastic neutron scattering on Xe isotopes for the Shen Optical Model Potentials (OMP) #532-539. The software includes a feature that allows us to use a "multiplicative factor" to be applied to the OMP, thus changing the depth of the potential. Using the OMP multiplicative factor , we scaled the potential well depth by $\pm 3\%$, and calculated the resulting cross-sections and angular distributions for each case.

We obtained the neutron cross-section used in Geant4 from the JEFF3.0 (ENDF/B-VI) cross-section tables and converted the ENDF files to differential cross-sections in Matlab. Figures 4.15 and 4.16 show comparisons between the Geant4/JEFF3.0 and Shen optical models (original and $\pm 3\%$ potential depth) for ^{132}Xe (OMP #536).
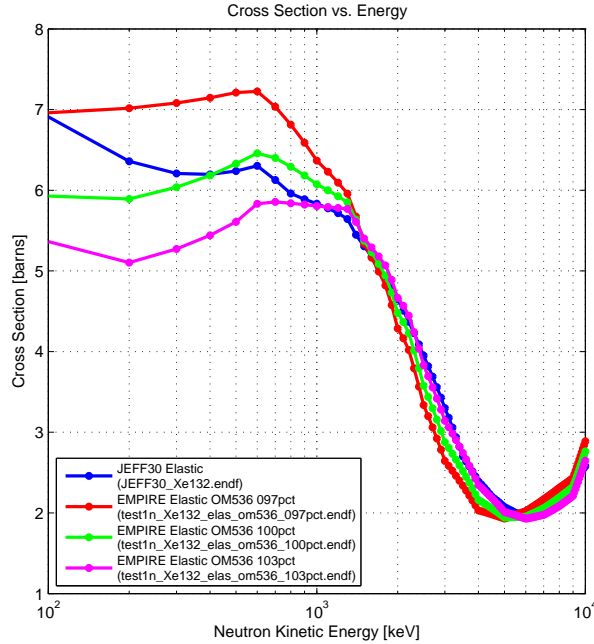
Figure 4.15: Cross-section calculations from EMPIRE: Elastic scattering cross-section of neutrons on ^{132}Xe, using the data from JEFF3.0 / ENDF/B-VI tables (blue line), from the Shen Optical Model /ENDF/B-VII (green line), and using a modified Shen Optical Model with well depth changed by -3% (red line) and $+3\%$ (magenta line).

4.4.2.3 Uncertainties

Comparing the Geant4/JEFF3.0 cross-section and the one obtained from the EMPIRE calculation using the Shen OMP, we find that they differ by an average 4.5% over the energy range $100\,\text{keV} - 10\,\text{MeV}$, with a maximum of 14% (see Fig. 4.17a).

A large scale comparison of calculated vs. measured cross-sections and angular distributions for several nuclei was performed in 2003 [106], with most of the data derived from 2 experiments performed in the Los Alamos National Labs in 1993 and 2001. From this comparison, a group from Brookhaven National Labs developed an extensive set of covariances for neutron cross-sections in order to obtain uncertainty data for neutron-nucleus reactions [105]. The BNL report indicates that $\pm3\%$ uncertainties on the optical model potential can be used as a conservative estimate for all nuclei where data is lacking, based on the average uncertainty for all nuclei studied.

We calculate the change in the neutron elastic cross-section $\sigma(E)$ for ^{132}Xe when we vary
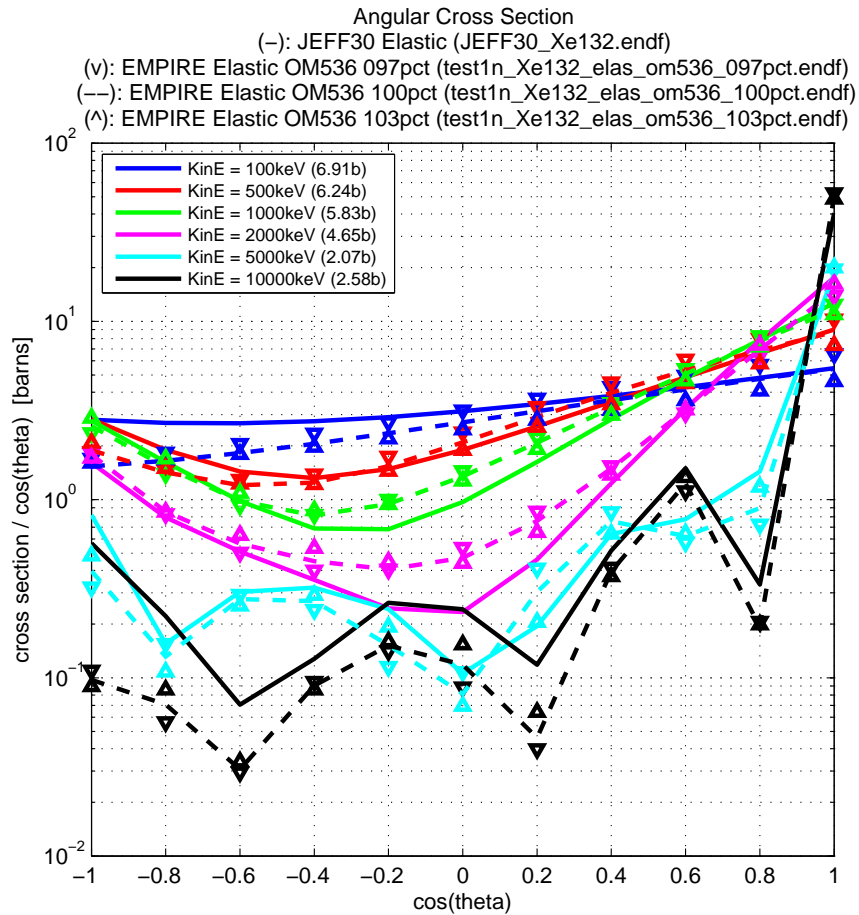
Figure 4.16: Angular Cross-section calculations from EMPIRE: Differential cross-section for elastic scattering of neutrons on ^{132}Xe. Each color represents the cross-section for a given neutron kinetic energy: 100 keV (blue), 500 keV (red), 1 MeV (green), 2 MeV (magenta), 5 MeV (cyan), and 10 MeV (black). The cross-sections are calculated using the data from JEFF3.0 / ENDF/B-VI tables (solid lines), from the Shen Optical Model /ENDF/B-VII (dashed lines), and using a modified Shen Optical Model with well depth changed by −3% (down triangle) and +3% (up triangle).
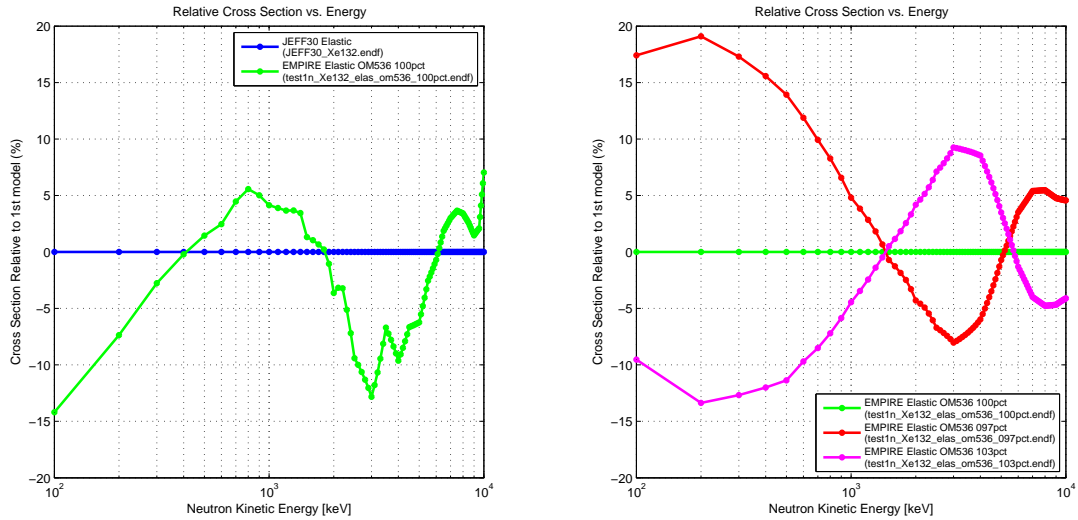
(a) Comparing Geant4 (JEFF3.0) and Shen OMP.

(b) Comparing Shen OMP ±3%

Figure 4.17: Cross-section uncertainty for ±3% variation on the optical model potential depth for ^{132}Xe (OMP #536). (a) elastic cross-section of neutrons on ^{132}Xe calculated using the Shen OMP (green line), relative to the JEFF3.0 cross-section (blue line). (b) elastic cross-section calculated using the Shen OMP with well depth modified by −3% (red line) and +3% (magenta line), relative to the standard Shen OMP (green line).

the OMP depth by ±3%, and we find an average change of $\Delta\sigma(E) \sim 5\%$ and a maximum of 19% (see Fig. 4.17b). This is the variation of the cross-section *relative to the original Shen OMP.* The change in cross-section is the best estimate of the uncertainty in the cross-section due to the uncertainty in the OMP parameters. The effect of the variation in OMP on the angular distribution is also calculated (see Fig. 4.16), as it is crucial for calculating the nuclear recoil spectrum and performing the $\mathcal{L}_{eff}$ analysis, since they are both dominated by the forward scattering component of the angular distribution.

4.4.2.4 The Nuclear Recoil Spectrum

Using as a starting point the flux of neutrons in the XENON10 fiducial volume, with the energy spectrum shown in Fig. 4.4 (blue line), we can calculate the nuclear recoil spectrum in the liquid Xe using Eq. 4.5 and the cross-sections obtained in Section 4.4.2.2 . We analytically calculate the recoil spectrum using the cross-section calculated from the standard Shen OMP, and using the ±3% variation on the Shen OMP well depth. The
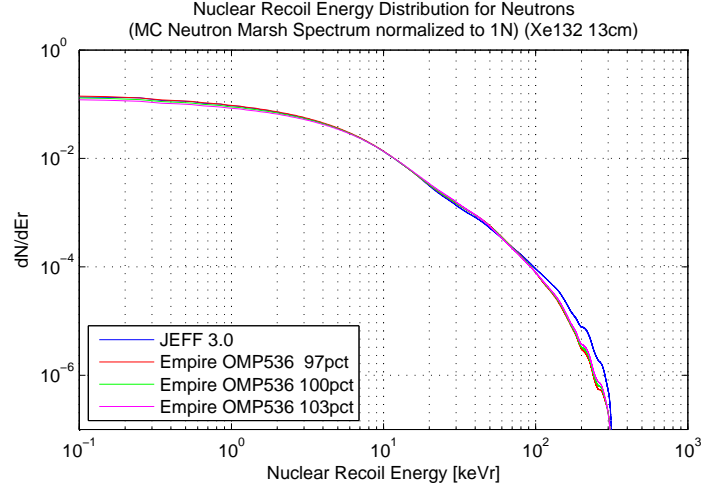
Figure 4.18: Calculated nuclear recoil spectra using the JEFF3.0 (ENDF/B-VI) elastic cross-section of neutrons on ^{132}Xe, and using the EMPIRE cross-sections calculated from the Shen OMPs (ENDF/B-VII).

nuclear recoil spectra calculated analytically is a very simplistic approximation, and cannot match exactly either the data or simulation. However, it can be used to assess the effect of changes in the scattering cross-section on the recoil spectrum.

From each of the calculated recoil spectra, we extract the scaling factor for each energy bin, relative to the recoil spectrum calculated using the JEFF3.0 cross-section. We then apply these 3 scaling factors found (Shen OMP, -3% and +3%) to the nuclear recoil spectrum obtained from a full scale neutron simulation using Geant4 and the JEFF3.0 / ENDF/B-VI cross-section, and thus obtain 3 new recoil spectra.

Figures 4.18 and 4.19a show the change in the nuclear recoil spectrum when we use the cross-sections obtained from the Shen OMPs. The mean difference between the recoil spectra from Geant4 and the one using the Shen OMP cross-section is 6% in $1\,\text{keV}_\text{r}\,-\,100\,\text{keV}_\text{r}$, with a local maximum of 11% at $35\,\text{keV}_\text{r}$.

When we vary the Shen OMP depth by $\pm 3\%$, we also see a small change in the nuclear recoil spectrum in the energy range $1\,\text{keV}_\text{r}-100\,\text{keV}_\text{r}$ relative to the original Shen OMP (see Fig. 4.19b). For a OMP change of -3%, we get a mean change of 1.5% with a maximum of 6%, and for a change of $+3\%$, we get a mean change of 2.5% with a maximum of 6% (in the energy range $1\,\text{keV}_\text{r}\,-\,100\,\text{keV}_\text{r}$).
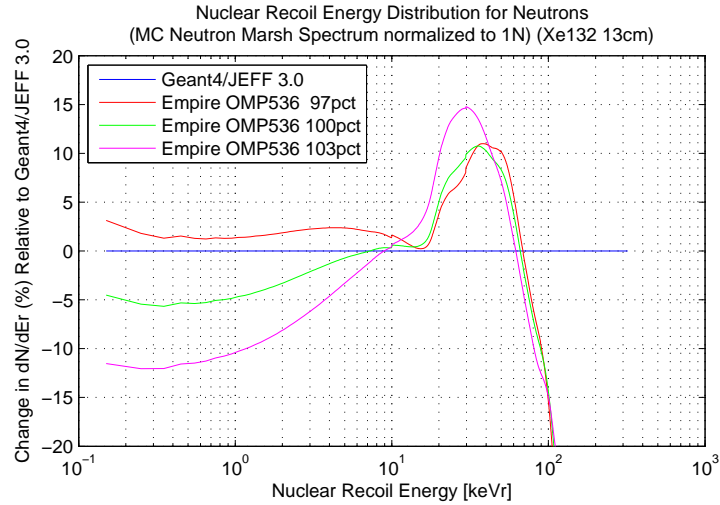
(a) Nuclear recoil spectra relative to the spectra obtained by using the JEFF3.0 (ENDF/B-VI) cross-section.
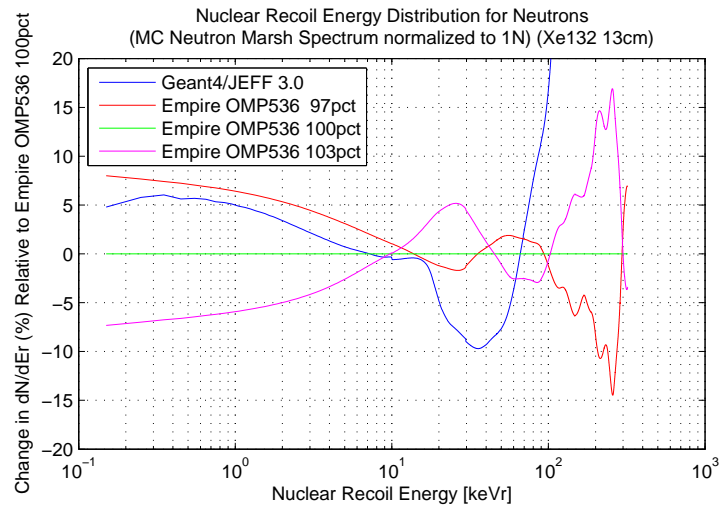
(b) Nuclear recoil spectra relative to the spectra obtained by using the standard She OMP cross-section.

Figure 4.19: Change in the nuclear recoil spectrum obtained by using different cross-sections. The plot compare the spectra obtained from using cross-sections from Geant4/JEFF3.0 (ENDF/B-VI), and the Shen OMP $\pm 3\%$ (see Figure 4.18). The plots show the changes (a) relative to the spectrum obtained by using the Geant4/JEFF3.0 cross-section; and (b) relative to the spectrum obtained by using the original Shen OMP cross-section.

4.4.2.5 Uncertainty in $\mathcal{L}_{eff}$

In Section 4.4.2.4 above, we determined how the nuclear recoil spectrum changes when we assume the cross-sections given by different optical models, and obtained the scaling factors relative to a spectrum using the standard cross-section in Geant4 (see Fig. 4.19a). We applied these scaling factor to the recoil spectrum obtained from the full-scale XENON10 neutron simulation, and repeated the $\mathcal{L}_{eff}$ analysis for each of the resulting spectra (see Fig. 4.20). When we compare the $\mathcal{L}_{eff}$ curves obtained from the original Geant4 spectrum to the $\mathcal{L}_{eff}$ obtained by using the spectrum using the Shen OMP, and we see a mean difference of 2.3%, with a maximum of 6% at the lowest energy bin in the range selected in Figure 4.20 $(3.4\,\mathrm{keV_r} - 100\,\mathrm{keV_r})$.

Changing the Shen OMP by -3% yields a $\mathcal{L}_{eff}$ 1.4% larger averaged over the energy range $3.4\,\mathrm{keV_r} - 100\,\mathrm{keV_r}$ (2.2% smaller at the lowest energy bin) than the one obtained by using the unchanged Shen OMP, and changing the it by $+3\%$ returns a $\mathcal{L}_{eff}$ 2.1% smaller averaged over the energy range $3.4\,\mathrm{keV_r} - 100\,\mathrm{keV_r}$ (4.5% larger at the lowest energy bin) than the one obtained by using the unchanged Shen OMP. This means that for an uncertainty of $\pm3\%$ in a given optical model, we end up with a possible variation of $\sim 2\%$ on the $\mathcal{L}_{eff}$ magnitude, but that the shape of the $\mathcal{L}_{eff}$ curve remains essentially unchanged.

In Fig. 4.14, the middle red line corresponds to the $\mathcal{L}_{eff}$ calculated by using the nuclear recoil spectrum with the standard Shen OMP cross-section, which is the same cross-section found in the ENDF/B-VII table. The 2 additional red lines correspond to the $\mathcal{L}_{eff}$ calculated using nuclear recoil spectra for the Shen OMP with a well depth by modified -3% and $+3\%$. The variation in $\mathcal{L}_{eff}$ due to the variation the OMP well depth is smaller than the statistical uncertainty, and both are listed in Table. 4.2.
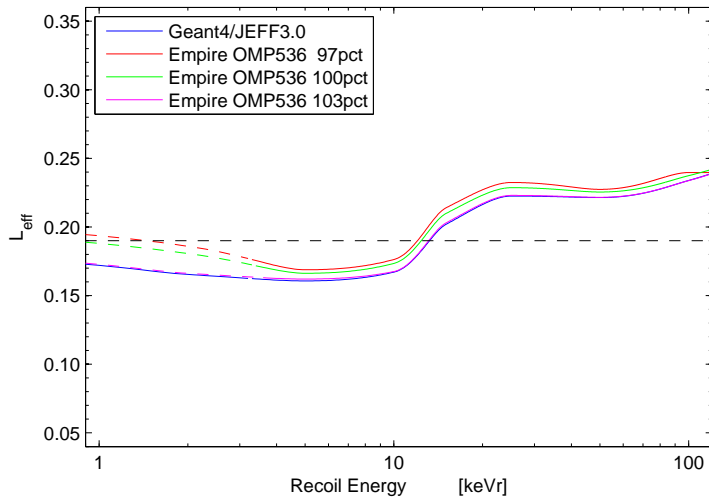
(a) $\mathcal{L}_{eff}$
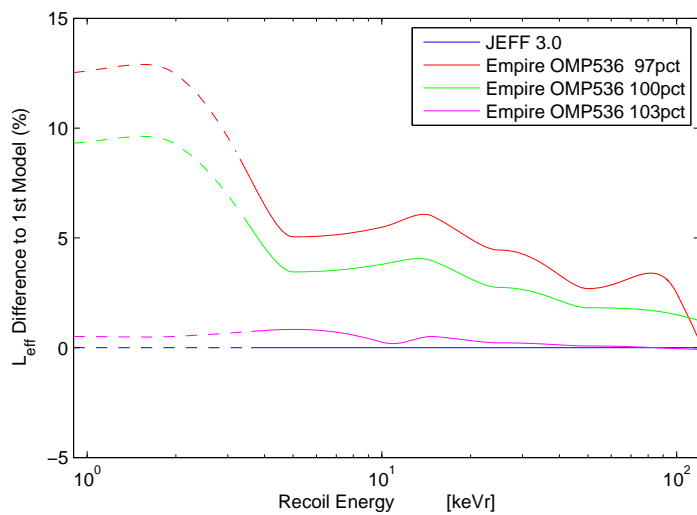
(b) $\Delta\mathcal{L}_{eff}$, relative to the Geant4 recoil spectrum, in % of $\mathcal{L}_{eff}$

Figure 4.20: $\mathcal{L}_{eff}$ calculated by comparing the XENON10 data to the original Geant4 MC recoil spectrum (blue line), and by comparing the data with the recoil spectrum obtained by scaling the original Geant4 spectrum to match different OMPs (the original Shen OMP and $\pm 3\%$). Note that plot (b) shows the change *relative to the original* - it is a percentage of the value of $\mathcal{L}_{eff}$.

Spline fit points [keV$_\mathrm{r}$]	$\mathcal{L}_{eff}$	statistical uncertainty	Variation due to $\pm 3\%$ change in OMP depth
2	0.160	± 0.014	± 0.009
5	0.156	± 0.011	± 0.001
10	0.162	± 0.012	± 0.002
15	0.194	± 0.011	± 0.005
25	0.220	± 0.012	± 0.001
50	0.237	± 0.009	± 0.001
100	0.274	± 0.010	± 0.005

Table 4.2: Uncertainties in the $\mathcal{L}_{eff}$ measurement. For each spline fit point shown in Fig. 4.14, the table shows the $\mathcal{L}_{eff}$, the statistical uncertainty, and the variation due to $\pm 3\%$ change in the OMP depth, corresponding to the uncertainty in the differential elastic cross-section.

CHAPTER 5

MATERIALS SCREENING

5.1 SOLO

5.1.1 The SOLO counting facility

A materials screening program was established within the XENON10 collaboration in order to characterize the radioactive contamination found in the material used for the XENON10 detector, with the objectives of (1) selecting low-radioactivity components for the fabrication of detector subsystems (i.e. capacitors, resistors and substrate material used for the PMT bases) and (2) characterizing the radioactivity present in the detector in order to build an accurate background model. The screening program was initially spearheaded by Brown, which used its SOudan LOw background counting facility (SOLO) since 2004 to screen a variety of materials for the XENON10 experiment [107]. Later the XENON10 collaboration commissioned the screening of several materials to the counting facility at the Laboratori Nazionali del Gran Sasso, to be done in parallel with the counting at SOLO [108, 109].

The SOLO counting facility was constructed by Brown in January 2003, with support from the Pacific Northwest National Laboratory (PNNL), the University of Minnesota and the Soudan Mine. It has been in operation at the Soudan Underground Laboratory since March 2003, and it has been used to screen materials for the Majorana, CDMS, XENON10 and LUX experiments.

The SOLO facility has housed 3 High-Purity Ge (HPGe) detectors: TWIN and Diode-M, owned and operated by Brown; and Gator, owned and operated by the University of Florida. The detectors TWIN and Diode-M have 1.05 kg and 0.6 kg Ge mass, respectively, and were both previously used by the Double Beta Decay Experiments at Homestake. The TWIN detector was decommissioned due to an electronics failure, and replaced on April 2005 by Gator, a 2 kg HPGe detector. All screening for the XENON10 experiment was performed using either Diode-M or Gator. Gator was moved out of SOLO in May, 2007, and SOLO has been operating with a single detector.

Each detector has an independent data acquisition system. The output of each detector is connected to a Spectroscopy Amplifier with $2\,\mu$s shaping time, which is then connected to a pulse height ADC, controlled by the acquisition software running on a dedicated PC. The energy scale is calibrated using a ^{57}Co source with a gamma line at 122 keV, the background ^{40}K line at 1462 keV, and the background ^{210}Pb line at 46.5 keV. The calibration results in an average energy bin width of 1.34 keV. The number of counts for each energy bin over a 4-hour period is recorded to individual files on disk, which are then made available for off-site analysis.

5.1.2 Backgrounds

Each detector consists of a HPGe cylinder encased in a Cu tube, a built-in readout system, and is connected via a Cu arm to a LN bottle for cooling. Diode-M has 7.75 cm diameter and 2.4 cm length, with a 1.5 mm thick Cu enclosure. The detectors are housed within a single Pb shield with thickness of >30 cm on all directions. The shield was initially constructed with 2 chambers, in order to house 2 detectors, but it has been rebuilt to have a single large chamber in May, 2007. The Pb shield is build with ~ 10 tonnes of Pb bricks sized $2\,\text{in} \times 4\,\text{in} \times 8\,\text{in}$, with activity of 50 Bq/kg. An 2"-thick inner liner of 200 year old Pb bricks with low ^{210}Pb activity, estimated at 50 mBq/kg, has been added to the cavity to further reduce the background. The shield structure is enclosed in airtight $50\,\mu$m thick Mylar, and the entire structure is flushed with N gas from a LN dewar boil-off at a rate of $3\,$cfh, to remove any contaminants in the air. Pictures of the detector and setup are shown

in Fig. 5.1.

The background spectrum is measured in units of *differential rate unit* (dru), where $1\,\mathrm{dru} = 1\,\mathrm{event/keV/kg/day}$. Measurements of the empty chamber for Diode-M after initial deployment in 2003 show a background spectrum with 1.7 dru at 150 keV (See Fig. 5.2). The spectrum shows a large peak of 15 dru at $\sim 50\,\mathrm{keV}$, consistent with the 46.5 keV line emitted from ^{210}Pb β^- decay. The background also show a featureless exponentially falling spectrum from 150 keV to 700 keV, where it flattens off and become dominated by fluctuations. The most prominent feature at high energies ($> 700\,\mathrm{keV}$) is the a peak with with 0.5 dru at 1461 keV, from the ^{40}K electron capture or β^+ decays.

The installation of the Gator detector in the SOLO shield led to an increase in the Diode-M background to 3.2 dru at 150 keV. The ^{210}Pb peak at 46.5 keV line was also increased, to 200 dru. The increase in background can be caused by 2 factors: (1) the reconstruction of the Pb shield has moved Pb bricks with higher concentration of ^{210}Pb within direct line of sight of the detector, and (2) contaminants present on the air and in the dust were deposited on the walls of the detector. An attempt to treat the Pb surfaces of the chamber with dilute nitric acid (May 2005) did not yield noticeable changes in the background, ruling out the deposition of contaminants in the inner surfaces of the Pb shield. In November 2005, the shield was again taken apart to fix installation problems with the Gator detector, and the opportunity was seized to acid treat the Cu encasing of Diode-M. This treatment reduced the background to 2.5 dru at 150 keV, and also the continuum between 150 keV and 700 keV by 35%. The reduction in background was likely a result of removing Rn plating the Cu enclosure. The peak at 46.5 keV remained at 200 dru, and it was not reduced until the next reconstruction of the shield, when Gator was removed in May 2007. Following the removal of the second detector, the chamber for Diode-M was expanded by a factor of $\times 2$, to 1000 cubic inches (See Fig. 5.3). Great care was taken to ensure that all high-activity Pb bricks would be well hidden behind the low-^{210}Pb bricks, specially at the corners. After the reconstruction of the chamber, the background was indeed reduced to 2 dru at 150 keV, and the 46.5 keV peak from ^{210}Pb was reduced to 3 dru.

Increases in the background are occasionally seen, following a change of sample. Sample

(a) Diode-M detector, outside of shield
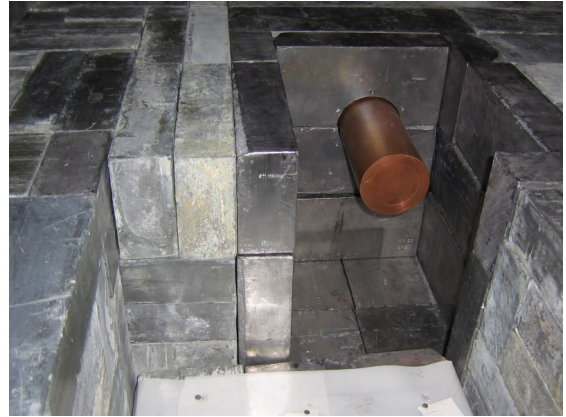
(b) Diode-M in the SOLO shield

(c) SOLO

Figure 5.1: Pictures of the Diode-M detector and the SOLO shield.
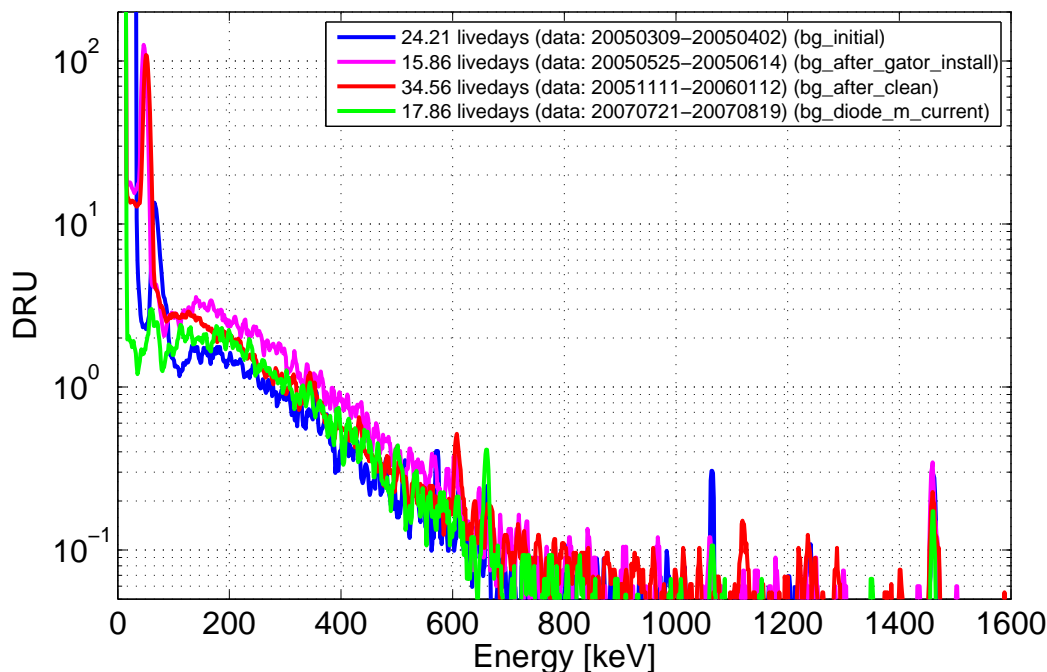
Figure 5.2: SOLO/Diode-M Background Spectrum, taken over a period of 2.5 years, during which several reconfigurations of the SOLO chamber were made.

changes require the opening of the shield cavity, and Rn lines are observed in the acquired spectrum up to ~ 3 hours after the chamber is closed again (See Fig. 5.4). Data acquired within $4 - 8$ hours of a sample change is discarded to allow the purge to reduce the Rn background to acceptable levels.

5.1.3 Analysis of results

The radioactivity contamination level in the samples counted is typically measured in Bq/sample, or Bq/kg. Contamination is identified by searching for prominent peaks in the sample spectrum and matching them to well-known gamma lines of contaminants. Typically, only 4 contaminants are considered: the ^{238}U chain, the ^{232}Th chain, ^{40}K and ^{60}Co. With the exception of ^{40}K, which has a single gamma line, only 2 peaks are checked for each contaminant, and for the ^{238}U and ^{232}Th chains , we chose only the 2 largest peaks. Table 5.2 on page 163 lists the lines typically used to identify contamination levels in the sample. For a diagram of the ^{238}U and ^{232}Th decay chains, see Fig. 6.19.
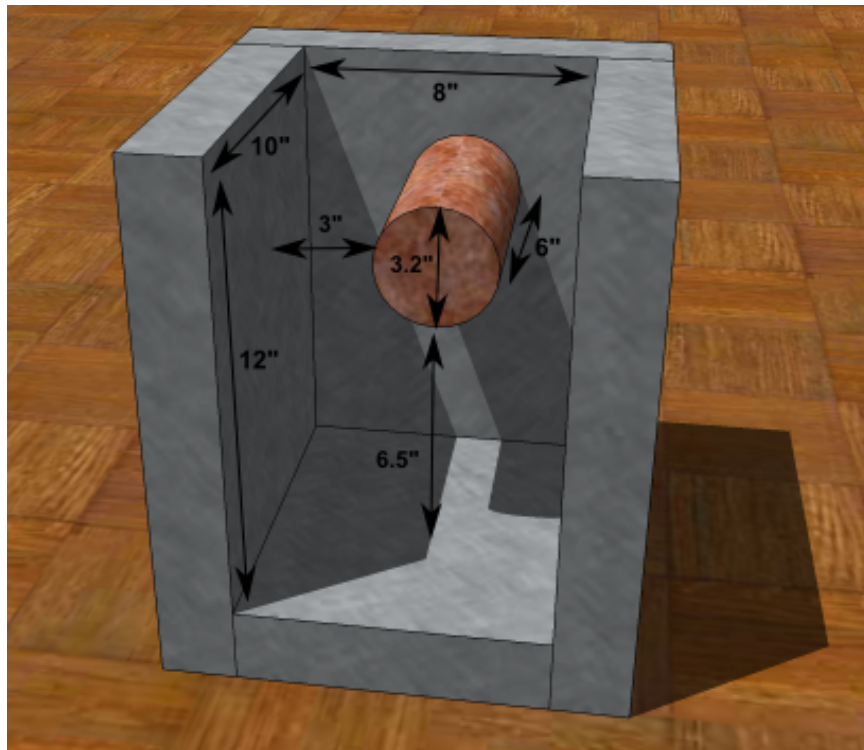
Figure 5.3: Diagram of the Diode-M detector inside the SOLO chamber after the reconstruction of the SOLO shield on May 2007. The copper cylinder is the Diode-M detector, a 0.6 kg high-purity Ge detector housed in copper. The detector is inside a Pb shield with > 30 cm Pb thickness in all directions. The chamber is flushed with N gas to remove any contaminants in the air.
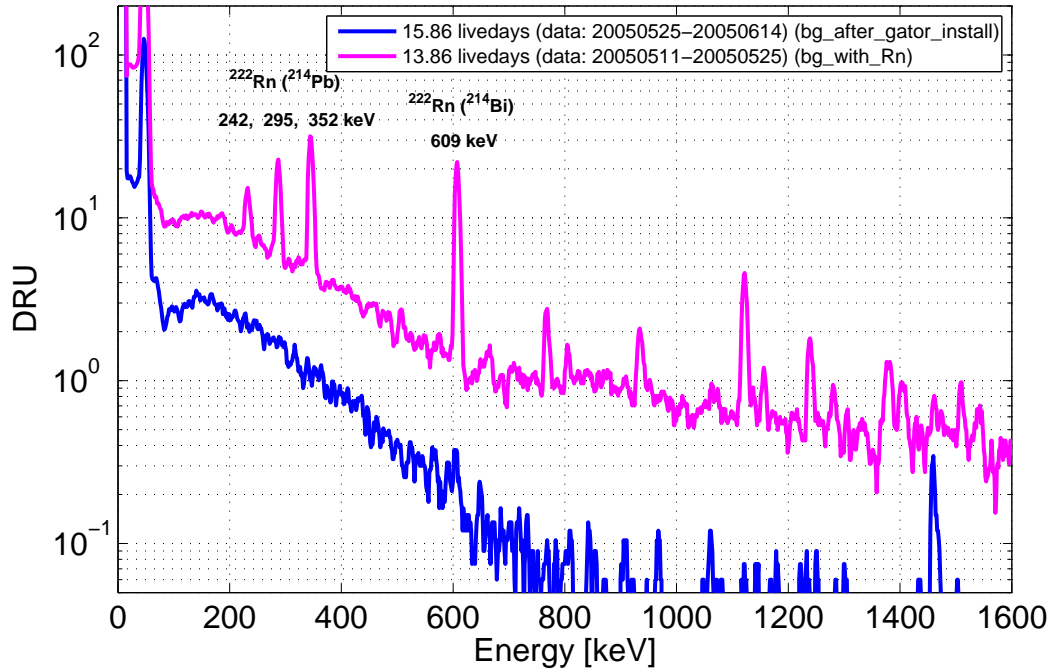
Figure 5.4: SOLO spectrum after opening and closing of chamber shows lines from Rn in air.

The contamination level is calculated by matching the peak size for each line to the results of simulations of the SOLO detector. Peaks are fitted using a Gaussian curve, and their size calculated by integrating the spectrum $\pm 2\sigma_{peak}$ from the peak center (σ_{peak} characterizes the peak width). The peak size contains both the background and the signal from the gamma line, and can be expressed as

$$N = S + B_{signal}\,, \tag{5.1}$$

where N is the total number of counts in the peak, S is the actual *signal*, and B_{signal} is the *underlying background* (as illustrated in Fig. 5.5a). The number of background counts B_{signal} must be calculated by averaging the spectrum counts before and after the peak, so that $B_{signal} = B_{left} + B_{right}$ (where the width of B_{left} and B_{right} is $2\sigma_{peak}$). For non-flat spectra, B_{signal} cannot be measured with accuracy, since features can be due to fluctuations either in the signal or in the background, and fluctuations in the spectrum around the peak we are trying to measure make an estimation of the background B_{signal} very difficult. It

Z-value	Confidence Level
1	68%
1.66	90%
2	95.5%
2.6	99%

Table 5.1: Table of confidence levels for a few select Z-values (Z_{peak} in Eq. 5.3)

is more practical to measure the background in a separate data acquisition with an empty chamber, so that:

$$\frac{N}{t_N} = \frac{S}{t_N} + \frac{B}{t_B} , \tag{5.2}$$

where t_N is the acquisition time with a sample, and t_B is the acquisition time with no sample. The background is calculated by integrating the empty chamber spectrum over the same energy range as the peak. In cases where the underlying background when a sample is present is much larger than the background for an empty chamber (see Fig. 5.5b), then B_{signal} must be used. All subsequent equations remain the same by substituting $B \rightarrow B_{signal}$.

In the limit $N \gg B$, we can safely ignore the background B when calculating the contamination levels. For most cases, the challenge lies in distinguishing the peak due to a gamma line from fluctuations in the background. It is necessary to verify that the peak size is inconsistent with simple statistical fluctuations from the background. The *Z-value* of the peak is defined below, and it gives us the *confidence level* that the peak is not a statistical fluctuation:

$$Z_{peak} = \frac{S}{\sigma_B} = \frac{N - B\left(\frac{t_N}{t_B}\right)}{\sqrt{B}} , \tag{5.3}$$

where $\sigma_B = \sqrt{B}$ is the standard deviation of the background due to Poisson fluctuations. The confidence level that the peak is not statistical fluctuation of the background is given in Table 5.1.

In the case in which N and B are obtained in different time intervals, we need to scale them down - that is, we need to find the values of N and B as if they had been taken for

(a) Sample Continuum $\simeq$ Background

(b) Sample Continuum $>$ Background
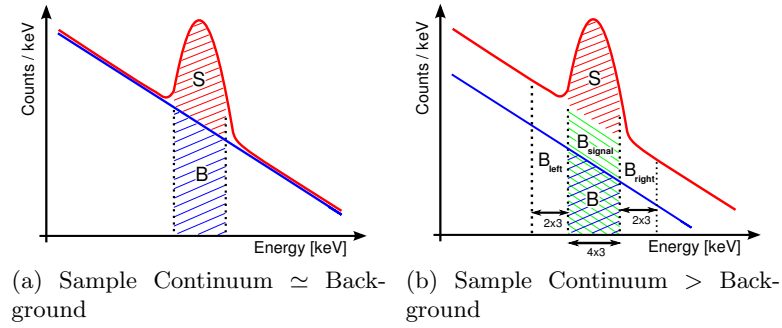
Figure 5.5: Calculating the signal and background from the number of counts in a peak (Signal = N-B). The diagrams illustrate the calculation for the case in which the signal is simply a peak above the background (a), or is a peak plus a continuum which raises the entire background (b).

a period equal to the smaller of the time intervals, either the background livetime or the sample counting time. We scale down because the acquisition with the smallest livetime also has the lowest quality, and Z_{peak} is essentially a measurement of the *peak quality*, and tells us how many σ's the signal is above the background.

The signal S is linear with the *contamination level* α, and we define $S = \varepsilon \cdot \alpha$. The efficiency ε depends on the acquisition livetime t_N and on the Peak Detection Ratio (PDR), that is, the ratio of events detected to decays in the sample. Thus, we have $\varepsilon = t_N \cdot \text{PDR}$ and the signal can be expressed as:

$$S = \varepsilon \cdot \alpha = t_N \cdot \text{PDR} \cdot \alpha \tag{5.4}$$

or

$$\frac{S}{livetime}\left[\frac{\text{cts}}{\text{s}}\right] = \text{PDR} \cdot \alpha \left[\frac{decays}{s}\right]. \tag{5.5}$$

The PDR is a function of the energy of the gamma line, and of the geometry of the sample and detector. Monte Carlo simulations are performed using Geant4 to calculate the PDR for each contaminant, assuming that the contamination is uniformly distributed in the sample mass, and using the full geometry of the SOLO detector and of the sample. The Monte Carlo simulations are necessary in order to ensure that the calculation of the PDR takes into account the the distances between the sources and the detector, and any self-

shielding effects in the source material. It is assumed that the radioisotopes in the source material are in equilibrium - that is, each isotope decays at the same rate it is produced, and all isotopes in a chain decay with the same rate. From the resulting spectra, the PDR for each gamma line is calculated as the ratio of events in the peak to the number of decays in the simulation. Table 5.4 contains examples of PDR, calculated for the screening of the Hamamatsu R8520 PMTs in SOLO.

An estimate of the PDR can be estimated analytically with a few assumptions. For $d_{source} \gg r_{source}$, where d_{source} is the distance from the source to the detector and r_{source} is the source radius (sample size), the PDR can be found using the following factors:

$$
\begin{aligned}
\# \text{ of events} \;=\; & \# \text{ of decays} \times \text{branching ratio} \\
& \times \frac{\Omega_{\text{detector}}}{2 \cdot \pi} \times \text{Prob. absorption in Ge} \,.
\end{aligned}
\tag{5.6}
$$

The number of events is calculated only for the "photopeak", that is, only for events with full energy deposition. Energy depositions for gamma rays occur through 3 processes: Compton scattering, pair production, and photoelectric absorption. The probability of interaction for each of these processes can be described by the interaction length, such that

$$
\lambda_{interaction}(E_\gamma) = \frac{1}{\sigma_{interaction}(E_\gamma) \cdot \rho} \,,
\tag{5.7}
$$

where ρ is the detector density and $\sigma_{interaction}$ is the interaction cross-section. For the cases when the gamma energy is such that the Compton interaction length is in the same order as the detector size ($\lambda_{Compton} \sim r_{det}$), and the energy is smaller than that necessary for pair production ($E_\gamma < 1022 \, \text{keV}$), then

$$
\text{Prob. absorption in Ge} = 1 - e^{-r_{det}/\lambda_{ph.el.}(E_\gamma)} \,,
\tag{5.8}
$$

where $\lambda_{ph.el.}$ is the interaction length for photoelectric absorption in Ge. As an example, we can calculate the PDR for the 609 keV line from the ^{238}U chain (from the ^{214}Bi isotope),

assuming a small source placed directly under the detector and placed 18 cm away from the center of the detector (2.5 cm above the chamber surface in the current shield configuration):

$$\text{branching ratio (609 keV)} = 46.1\% \tag{5.9}$$

$$\Omega_{\text{detector}} = 4 \cdot \arcsin \left(\frac{h_{det} \cdot r_{det}}{\sqrt{\left(4 \cdot d_{source}^2 + h_{det}^2 \right) \cdot \left(4 \cdot d_{source}^2 + r_{det}^2 \right)}} \right) = 4.5 \times 10^{-3} \tag{5.10}$$

$$\text{Prob. absorption in Ge} = 1 - e^{-7.75\,\text{cm}/85.7\,\text{cm}} = 9\% \tag{5.11}$$

$$\text{PDR} = \frac{\#\text{of events}}{\#\text{of decays}} = 1.8 \times 10^{-4}\,. \tag{5.12}$$

The estimated PDR matches well with the PDR calculated from simulation for the 609 keV line from R8520 PMTs, shown in Table 5.4. However, PDR values typically cannot be calculated from first principles, as they vary with sample mass, size, and positioning in the detector. It is always necessary to run a Monte Carlo simulation of the detector plus sample in order to calculate the PDR for a given counting process.

For large peaks where $Z_{peak} > 1$ and the underlying background remains unchanged, the contamination level can be calculated from counting data by rewriting Eq. 5.5 as:

$$\alpha \left[\frac{decays}{s} \right] = \frac{1}{PDR} \left(\frac{N}{t_N} - \frac{B}{t_B} \right)\,, \tag{5.13}$$

where t_N and t_B are the livetimes for the sample counting and for the background, respectively. The error in the contamination levels is determined by the standard deviation in the number of counts in the peak (σ_N) and in the background (σ_B). The number of events in the peak and background is determined by Poisson statistics, so the standard deviation is:

$$\sigma_N = \sqrt{N} \quad \text{and} \quad \sigma_B = \sqrt{B}\,. \tag{5.14}$$

The error in the measurement of the signal depends on fluctuations both in the peak size and in the underlying background. Thus, the total standard deviation is calculated by adding the individual standard deviations in quadrature, and the error on the contamination level measurement is given by:

$$\sigma_\alpha = \frac{1}{PDR} \left(\sqrt{\left(\frac{\sigma_N}{t_N}\right)^2 + \left(\frac{\sigma_B}{t_B}\right)^2} \right) . \tag{5.15}$$

For small peaks where $Z_{peak} < 1$, or for sample spectra in which no peak is apparent, a direct calculation of the contamination level becomes undesirable or impossible. For such cases, it is possible to calculate the upper limit on the contamination level for select gamma lines. The measured peak size N is determined by Poisson statistics:

$$p(N, \mu) = \frac{e^{-\mu} \cdot \mu^N}{N!} , \tag{5.16}$$

where μ is the *expected* peak size (including the background) for a given contamination level, and can be expressed as $\mu = \varepsilon \cdot \alpha + B$ (See Eq. 5.1 and Eq. 5.4). The confidence level that the expected size is is between 0 and an arbitrary value μ_0 is given by:

$$CL = \frac{\int_0^{\mu_0} p(N, \mu) d\mu}{\int_0^{\infty} p(N, \mu) d\mu} . \tag{5.17}$$

Through variable substitution ($\mu \to \varepsilon \cdot \alpha + B$) we get:

$$CL = \frac{\int_0^{\alpha_0} p(N, \varepsilon \cdot \alpha + B) d\alpha}{\int_0^{\infty} p(N, \varepsilon \cdot \alpha + B) d\alpha} . \tag{5.18}$$

Substituting Eq. 5.16 into Eq. 5.18, and integrating it, we can find the confidence level CL as a function of N and α_0:

$$
\begin{aligned}
CL &= \frac{\int_0^{\alpha_0} e^{-(\varepsilon \cdot \alpha + B)} \cdot (\varepsilon \cdot \alpha + B)^N / N! \, d\alpha}{\int_0^{\infty} e^{-(\varepsilon \cdot \alpha + B)} \cdot (\varepsilon \cdot \alpha + B)^N / N! \, d\alpha} \\
&= 1 - \frac{\int_{\alpha_0}^{\infty} e^{-(\varepsilon \cdot \alpha + B)} \cdot (\varepsilon \cdot \alpha + B)^N / N! \, d\alpha}{\int_0^{\infty} e^{-(\varepsilon \cdot \alpha + B)} \cdot (\varepsilon \cdot \alpha + B)^N / N! \, d\alpha}
\end{aligned}
$$

$$
\begin{aligned}
X &= \int_0^\infty e^{-(\varepsilon\cdot\alpha+B)} \cdot (\varepsilon\cdot\alpha + B)^N / N!\, d\alpha \\
&= \frac{e^{-B}}{\varepsilon} \cdot \frac{B^N}{N!} - \int_0^\infty e^{-(\varepsilon\cdot\alpha+B)} \cdot (\varepsilon\cdot\alpha + B)^{N-1} / (N-1)!\, d\alpha \\
&= \frac{e^{-B}}{\varepsilon} \cdot \sum_{n=0}^{N} B^n / n!
\end{aligned}
$$

$$
\begin{aligned}
Y &= \int_{\alpha_0}^\infty e^{-(\varepsilon\cdot\alpha+B)} \cdot (\varepsilon\cdot\alpha + B)^N / N!\, d\alpha \\
&= \frac{e^{-\varepsilon\cdot\alpha_0 - B}}{\varepsilon} \cdot (\varepsilon\cdot\alpha_0 + B)^N \\
&\quad + \int_{\alpha_0}^\infty e^{-(\varepsilon\cdot\alpha+B)} \cdot (\varepsilon\cdot\alpha + B)^{N-1} / (N-1)!\, d\alpha \\
&= \frac{e^{-B}}{\varepsilon} \cdot e^{-\varepsilon\cdot\alpha_0} \cdot \sum_{n=0}^{N} (\varepsilon\cdot\alpha_0 + B)^n / n!
\end{aligned}
$$

$$
CL = 1 - \frac{Y}{X} \tag{5.19}
$$

$$
\Rightarrow CL = 1 - e^{-\varepsilon\cdot\alpha_0} \cdot \frac{\sum_{n=0}^{N} (\varepsilon\cdot\alpha_0 + B)^n / n!}{\sum_{n=0}^{N} B^n / n!} \,. \tag{5.20}
$$

Eq. 5.20 can be solved numerically and to give the confidence level that the actual con-tamination α is between 0 and α_0, for a measurement of N counts in the peak. Conversely, the equation can be used to find the upper limit for the contamination α_{UL}, the value for which we have a confidence CL that the actual contamination α is between 0 and α_{UL}:

$$
\alpha_{UL}(CL) = \alpha_0(CL)\,. \tag{5.21}
$$

When measuring low radioactivity samples, the actual contamination level might be impossible to determine, but it is still desirable to set upper-limits on the contamination levels for well-known radioactive contaminants. The upper-limits will be limited by the

sensitivity of the the detector, and Section 5.1.4 discusses the sensitivity of the Diode-M detector.

5.1.4 Sensitivity

The *sensitivity of the detector* is defined as minimum amount of radioactive contamination that the detector is able to measure and distinguish from background. For counting results, the sensitivity α_{min} is the amount of radioactive contamination α_{min} necessary to generate a signal S that is equal or greater than fluctuations in the background:

$$S \geq Z \cdot \sigma_B(t_N) , \tag{5.22}$$

where Z is the required confidence level, and $\sigma_B(t_N)$ is the expected standard deviation of the background for an acquisition time of t_N. If $\sigma_B = \sqrt{B}$, then $\sigma_B(t_N) = \sqrt{B \cdot \frac{t_N}{t_B}}$. Using Eq. 5.4, we see that the sensitivity of the detector to radioactive contamination is determined by 3 factors: the background event rate, the counting time, and the Peak Detection Rate.

$$\alpha_{min} \cdot t_N \cdot \text{PDR} = Z \cdot \sqrt{B \cdot \frac{t_N}{t_B}} , \tag{5.23}$$

$$\alpha_{min} = Z \cdot \frac{\sqrt{B/t_B}}{PDR \cdot \sqrt{t_N}} \left[\frac{decays}{s} \right] . \tag{5.24}$$

Typically, sensitivity estimates are quoted for $Z = 1$. Table 5.2 lists the estimated the Diode-M sensitivity to well-known gamma lines, using PDRs estimated analytically in the method described above (see Eq. 5.12).

Contamination levels are usually quoted normalized to the mass of the sample, or to the number of samples, in units of Bq/kg or Bq/unit. We can rewrite Eq. 5.24 to give the contamination level in Bq/kg for a background rate given in dru$_{ee}$:

$$\alpha_{Bq/kg} = \epsilon \cdot \sqrt{\frac{B_{rate}[\text{dru}_{ee}]}{t_N[days]}} , \tag{5.25}$$

where

$$\epsilon = \frac{\sqrt{4 \cdot \sigma_{peak} \cdot m_{det}}}{m_{sample} \cdot \text{PDR}} \cdot \frac{1}{86400} = \frac{1}{\sqrt{4 \cdot \sigma_{peak} \cdot m_{det}}} \cdot \frac{mBq/kg}{DRU} \ . \tag{5.26}$$

Quoting the sensitivity of the detector in Bq/kg provides guidance to users on how much mass is necessary for measuring the contamination level per mass. The number of decays per second is directly proportional to the concentration of the isotope in the material. Thus, the contamination level can also be expressed as the concentration of contaminants in the sample, given in *parts per billion* (ppb). The conversion factor from Bq/kg to ppb is given in Table 5.3. However, it is necessary to keep in mind that when sensitivities are quoted in ppb, they refer to a specific sample configuration and mass, and that the detector will not necessarily achieve the same sensitivity for different samples.

As an example, we can calculate the sensitivity of Diode-M for the 609 keV line from the ^{238}U chain, using the analytical estimate PDR $= 1.8 \times 10^{-4}$. From the background measurements shown in Figs. 5.2 and 5.4, we have that the background rate is $B_{rate} = 0.19 \, \text{dru}_{\text{ee}}$ in the current shield configuration, and that the peak width for the 609 keV line is $\sigma_{peak} = 4.5 \, \text{keV}$. Assuming a sample of $m_{sample} = 1 \, kg$ and 15 live-days of counting, we calculate that for positive detection of a peak in the sample spectrum we need $\alpha_{Bg/kg} = 24 \, \text{mBq}/kg$, or 2 ppb.

The sensitivity of the detector can be improved by either reducing the background, increasing both the sample size and mass, and running acquisitions longer. The reconstruction of the SOLO Pb shield after the removal of the Gator detector involved for the expansion of the Diode-M chamber to 8" × 10" × 12", allowing for large sample size and mass to be inserted. In the current shield configuration, sensitivities of 0.05 ppb, 0.1 ppb and 115 ppb for ^{238}U, ^{232}Th and ^{40}K, have been achieved for the counting of large Ti samples for 15 days of counting. Studies are under way to install newly acquired low-activity Pb bricks, in an effort to further reduce the background and improve the sensitivity of the Diode-M detector.

Isotope	Peak Energy [keV]	Peak Detection Ratio (PDR×10^{-6})	Sensitivity [mBq/kg]
^{238}U chain (^{214}Pb)	351	580	14
^{238}U chain (^{214}Bi)	609	180	24
^{232}Th chain (^{208}Tl)	511	130	40
^{232}Th chain (^{208}Tl)	583	375	12
^{40}K	1461	16	210
^{60}Co	1173	109	12
^{60}Co	1332	114	8

Table 5.2: Peak Detection Ratio (PDR) and sensitivity for a 1 kg sample and 15 live-days, calculated analytically. It assumes the current SOLO background, and sources placed at the bottom of the chamber, directly below the detector.

Isotope	Concentration for 1 Bq/kg [ppb]
^{238}U	81
^{232}Th	246
^{40}K	32000

Table 5.3: Conversion table from Bq/kg → ppb

5.2 PMT counting

5.2.1 XENON10 PMTs and Bases

In order to characterize the backgrounds in the XENON10 detector, a program was established to measure the radioactive contamination levels in the Hamamatsu R8520 PMTs used for the experiment. The program was initiated at the SOLO counting facility, where 2 PMTs and components used to construct the PMT mounting bases were screened. Further counting took place at the LNGS counting facility, where 63 of the 89 PMTs used in the XENON10 detector were screened.

5.2.1.1 PMTs

The measurement of 2 Hamamatsu R8520 PMTs (model R8520-M4F) at SOLO provided the first characterization of PMT radioactivity levels within the XENON10 program. The PMTs were counted for 37.39 live-days, and the resulting spectrum was compared to a background spectrum with 15.86 live-days. Peaks were identified corresponding to the

Isotope	Peak Energy [keV]	Peak Detection Ratio (PDR×10^{-6})	Peak Confidence Level (Z_{peak})	Measured Contamination [mBq/PMT]
^{238}U chain (^{214}Bi)	609	160	1	< 17
^{232}Th chain (^{208}Tl)	511	330	1.4	< 6.2
^{232}Th chain (^{208}Tl)	583	220	0.8	< 5.9
^{40}K	1461	66	2.7	308 ± 73

Table 5.4: Peak Detection Ratio (PDR) and contamination levels for the R8520 PMTs counted at SOLO. Upper Limits quoted for 90% confidence level; error bars for 1σ. Peak Detection Ratios (PDR) obtained from Monte Carlo simulations of the PMTs in the SOLO chamber

gamma lines for ^{238}U, ^{232}Th and ^{40}Kr. The peaks for ^{238}U and ^{232}Th appeared consistent with background fluctuations upon visual inspection, and had Z_{peak} values ranging from 0.8 to 1.4 (confidence level of 58% to 84%). The peak for the ^{40}K gamma line at 1461 keV is noticeably above background and has $Z_{peak} = 2.7$ (99.3% confidence level). Simulations were run to find the Peak Detection Ratio for the identified gamma-lines. Upper limits on the contamination levels for the ^{238}U and ^{232}Th chains, and the contamination level for ^{40}K, were calculated and are listed in Table 5.4. Because of the high contamination level of ^{40}K, the particular R8520 PMTs counted at SOLO were not used by the XENON10 experiment during the WIMP search runs.

To convert the peak event rates in the detector to contamination levels in the samples (PMTs), we performed a Monte Carlo simulation of the SOLO detector using Geant4. The PMTs are very light and have negligible stopping mass. The simulation assumes that the gamma ray source is evenly distributed throughout the entire body of the PMT. We ran one simulation for each contaminant (^{238}U, ^{232}Th, ^{60}Co and ^{40}K) for the 2 PMTs combined, so that the activities of each contaminant could be matched individually. From the simulation, the Peak Detection Ratio for each gamma line is calculated and listed in Table 5.4.

Low radioactivity R8520 PMTs were procured from Hamamatsu, and sent for counting at the LNGS screening facility. The new model R8520-06-AL demonstrated lower activity levels for all isotopes. Most of the PMTs were counted only after the end of the XENON10 WIMP search runs. Of the 89 PMTs used for the WIMP search runs, 63 were counted (70% of all PMTs), and their measured radioactivity are listed in Table 5.5. The
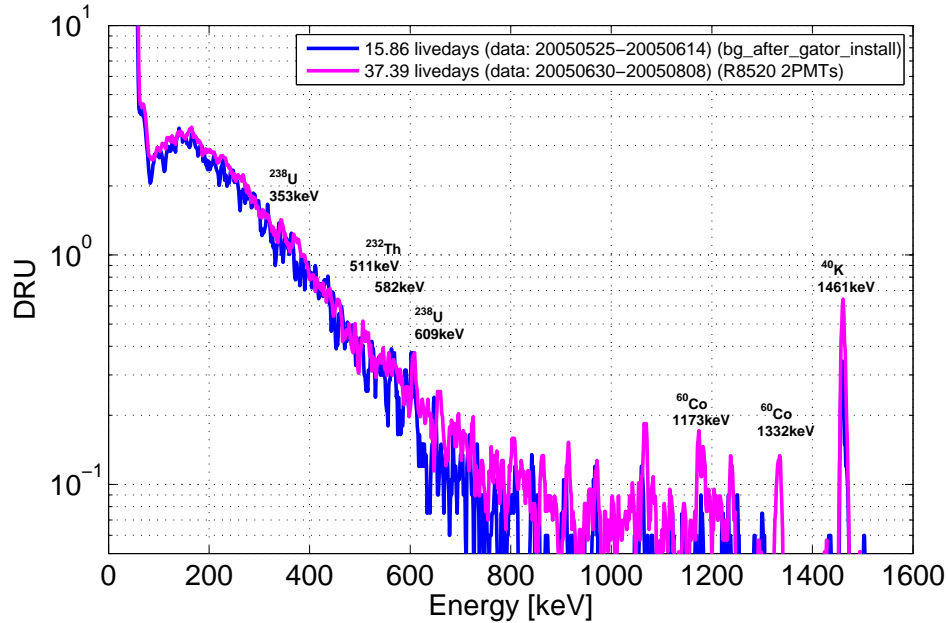
Figure 5.6: Energy Spectrum 2 Hamamatsu R8520 PMTs counted in SOLO, for 37.39 live-days, overlaid with the background spectrum (empty chamber, with N_2 gas purge) counted for 15.86 live-days. Measurements made with the High-Purity Ge detector Diode-M (0.6 kg).

contamination levels for the ^{238}U and ^{232}Th chains was sub-mBq for all PMTs, and averaged 0.15 mBq/PMT. The largest contamination measured is ^{40}K, with an average of 8.1 mBq/PMT. However, ^{40}K decays with a single gamma at 1461 keV, with a branching ratio of 11%, and thus its effect is reduced. The most concerning contamination is ^{60}Co, measured at 1.9 mBq/PMT, and which produces 2 γ's with 1173 keV and 1332 keV for every decay, generating $4\times$ as many γ/s as ^{40}K. Five of the R8520 PMTs measured at LNGS showed levels of ^{137}Cs at 17 mBq/PMT. All other measurements of R8520 PMTs indicated vanishingly small amounts of ^{137}Cs contamination in the PMTs (< 0.1 mBq/PMT), suggesting that the 5 PMTs with high ^{137}Cs contamination levels were a fluke. The ^{137}Cs averages to 1.1 mBq/PMT.

5.2.1.2 Base components

The components used to construct the PMT mounting bases were also screened for radioactivity, prior to base construction. A few choices of capacitors, resistors and material for making the base plates were screened and rejected due to their high level of radioac-

Isotope	Maximum Contamination [mBq/PMT]	Average Contamination [mBq/PMT]
^{238}U	0.39	0.16
^{232}Th	0.38	0.14
^{40}K	12	8.1
^{60}Co	2.8	1.9
^{137}Cs	17	1.1

Table 5.5: R8520 PMT radioactive contamination levels measured at the LNGS screening facility. 63 of the 89 PMTs used for the XENON10 WIMP search runs were counted at LNGS.

tivity. The final choice of components were screened at SOLO and at LNGS, and their contamination levels is listed in Table 5.7.

A sample of 135 capacitors, weighing 4.9 grams total, was sent to SOLO for counting for 22 live-days. The radioactivity contamination for ^{238}U, ^{232}Th and ^{40}K were in the hundred μBq/Capacitor level, and the contamination for ^{60}Co was too small to be measured, setting an upper limit of $10\,\mu$Bq/Capacitor. A sample containing 3 spools of resistor material, weighing a total of 303 grams, was sent to SOLO for counting for 41 live-days. A package of 603 resistors was weighted at 2.7 grams. The radioactivity contamination for ^{238}U was at the hundred μBq/Resistor level, but ^{232}Th and ^{40}K only have a few μBq/Resistor. The contamination for ^{60}Co was again too small to be properly measured, setting an upper limit of $0.6\,\mu$Bq/Resistor. The measurement of the capacitors and the resistors was compared to background measurements of 35 live-days, and were both performed after the cleaning of the Diode-M detector in Nov. 2005, allowing for good sensitivity.

A sample with 48 Cirlex PMT bases, totaling 115 grams of Cirlex, was sent to the LNGS facility, and counted for 6 live-days. The ^{238}U and ^{232}Th contamination level was on average 100 μBq/base. The contamination levels for ^{40}K and ^{60}Co was too small for direct measurement, and upper levels were set at < 160 and $< 10\,\mu$Bq/base. An upper level for ^{137}Cs was also set, at $< 15\,\mu$Bq/base.

5.2.2 LUX PMTs

The LUX experiment is designed to hold an active Xe volume of $350\,$kg, with $49\,$cmdiameter and $59\,$cm height. The LUX experiment has opted not to use the 1" square R8520 PMTs
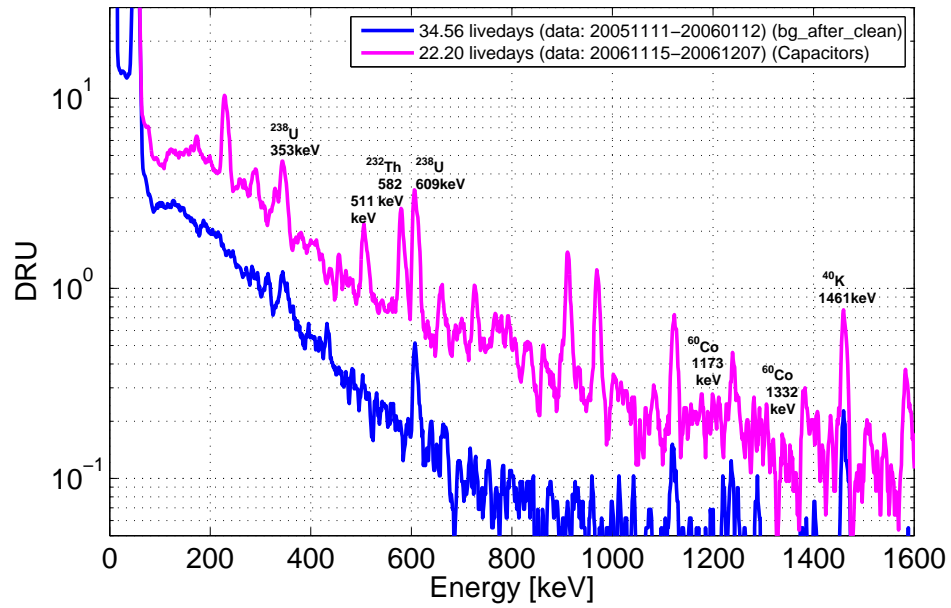
(a) Capacitors
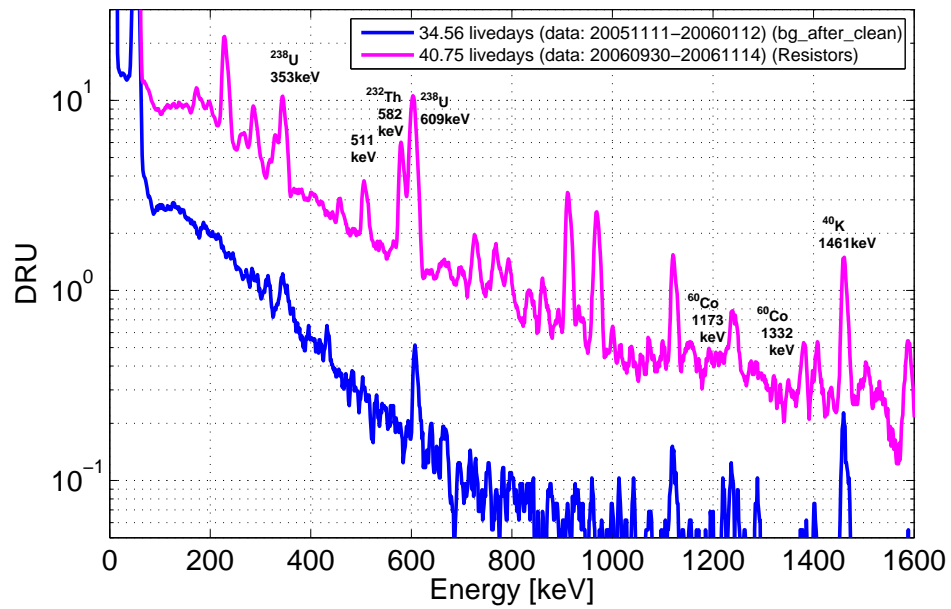
(b) Resistors

Figure 5.7: Measurement of PMT base components (Capacitors and Resistors) at SOLO. The results are shown in Fig. 5.7.

Isotope	Average Contamination [mBq/unit]		
	Cirlex Bases	Capacitors	Resistor
^{238}U	0.16 ± 0.02	0.540 ± 0.029	0.078 ± 0.02
^{232}Th	0.07 ± 0.02	0.158 ± 0.010	0.014 ± 0.001
^{40}K	< 0.16	0.033 ± 0.001	0.003 ± 0.0001
^{60}Co	< 0.01	< 0.010	< 0.0006
^{137}Cs	< 0.015	-	-

Table 5.6: Radioactive contamination levels for the components of the PMT mounting bases used in XENON10. The Cirlex bases were measured at the LNGS screening facility, while the resistors (manufactured by KOA) and capacitors (manufactured by AVX) were measured in the SOLO screening facility (see measurements in Fig. 5.7). ^{137}Cs levels for the resistors and capacitors were not measured.

used in XENON10, because of their small size compared to the size of the detector. The LUX experiment will be using the 2.2" diameter round R8778 Hamamatsu PMTs. The R8778 PMTs are expected to have contamination levels 1 order of magnitude higher than the R8520 PMTs. The expected contamination levels for each line are based on current survey work of the R8778 PMT by Hamamatsu in the period 2003-2004, which show the contamination per PMT to be in the ranges 5-18mBq for ^{238}U, 13-17mBq for ^{232}Th, 3-12mBq for ^{60}Co and 13-30mBq for ^{40}K. These ranges were used for the performance assessment of the detector for the LUX proposal in 2007. The highest level for each of these contaminants are also the latest measurement prior to SOLO, and were performed in Feb. 2004. Monte Carlo simulations using the upper limit of these ranges have shown that the resulting background would be acceptable for LUX to achieve its sensitivity goals.

Two batches of five available Hamamatsu R8778 PMTs were sent to SOLO. The shield cavity can comfortably fit five R8778 PMTs at a time. For a schematic of the PMT arrangement in the chamber, see Fig. 5.8. The 2 batches were counted separately and show similar spectra. Also, two of the five PMTs in the first batch were also counted separately, and we find that the activity is reduced accordingly. From this we conclude that the analysis of the first batch of 5 PMTs, which were counted for a longer period, is sufficient to obtain representative values of the PMT contamination level.

The first batch of five PMTs was counted for 11.2 live-days, and peaks were identified for the ^{238}U and ^{232}Th chains,^{60}Co and ^{40}K - see the energy spectrum in Figure 5.9. Monte

Carlo simulations for each isotope and for each PMT are performed to calculate the Peak Detection Ratio (PDR), and the activity is calculated for each peak. The contamination levels for each component are listed in Table 5.7. The average contamination level for the first batch of PMTs measured at SOLO is 9 mBq, 3 mBq, 2.6 mBq and 92 mBq for ^{238}U, ^{232}Th, ^{60}Co and ^{40}K, respectively. The contamination level measured for the PMTs are consistent with the observed contamination ranges for ^{238}U and ^{60}Co, and lower than expected in the ^{232}Th case. However, the measured contamination level of ^{40}K exceeds the upper limit on the range (30mBq) by a factor of x3. The second batch of 5 PMTs was counted for 4.5 days, enough to establish that it had similar contamination levels to the first batch. The average contamination level for the second batch is 13mBq, 1.6mBq, 5.6mBq and 82mBq for ^{238}U, ^{232}Th, ^{60}Co and ^{40}K, respectively. The results are consistent with the first measurement.

A mechanical sample of the PMTs fabricated for LUX was acquired from Hamamatsu and counted for 17.2 live-days in SOLO. Similar contamination levels were found, with the exception of the ^{232}Th peaks. The 511 keV and 583 keV peaks for ^{232}Th were not clearly defined, and we calculate upper limits on the contamination level consistent with the measured activity. The mechanical sample has similar activity to the the PMTs already at hand: 27 mBq, <6 mBq, 3 mBq and 100 mBq per PMT for ^{238}U, ^{232}Th, ^{60}Co and ^{40}K.

Screening of PMT fabrication materials provided by Hamamatsu ruled them out as the major source of ^{40}K radioactivity observed in the R8778 PMTs. The samples were screened at SOLO, and the measured contamination levels are listed in Table 5.8. The first sample consisted of 219 grams of crushed glass, and was counted for 6.2 live-days. The second sample was a set of 20 insulator plates weighing 100 grams total, and counted for 9.9 live-days. PMT fabrication uses 22 grams of glass for the window, and 2 insulator plates inside the PMT. Both datasets were compared to the same background run used for the PMT measurements, with 17.9 live-days. In neither set ^{60}Co peaks were observed. The contamination levels for ^{238}U combined in both components is higher than the PMT ^{238}U contamination by a factor of $\times 2$, suggesting specially "dirty" component samples. However, the ^{40}K contamination in the components is only $\times 1/10$ of the levels measured from the

Isotope	Peak Energy [keV]	Contamination Level per PMT [mBq/PMT]		
		1st batch of 5 PMTs	2nd batch of 5 PMTs	1 Mechanical Sample
^{238}U chain (^{214}Pb)	351	8.2 ± 1.5	11.5 ± 2.2	28 ± 4.4
^{238}U chain (^{214}Bi)	609	9.3 ± 1.2	14.8 ± 2.2	26 ± 3.6
^{232}Th chain (^{208}Tl)	511	2.7 ± 1.2	< 6.6	< 5.8
^{232}Th chain (^{208}Tl)	583	2.8 ± 0.6	1.6 ± 0.7	$-$
^{40}K	1461	92 ± 9	82 ± 14	100 ± 23
^{60}Co	1173	2.6 ± 0.53	5.6 ± 1	2.7 ± 1.2
^{60}Co	1332	2.6 ± 0.5	$-$	$-$

Table 5.7: Radioactive contamination levels per PMT for the 2 batches of 5 R8778 PMTs (11.2 and 4.5 live-days) and the mechanical sample (17.2 live-days). Screening of the first batch of PMTs initiated on 2007-08-21.

PMT samples.

The measurements of the R8778 PMTs at SOLO indicate an increased amount of ^{40}K in the PMTs relative to the expected values. However, the increase is not significant. The ^{40}K 1461keV gamma has a 11% branching ratio, while the ^{238}U chain emits 2.5 gammas per decay on average, and the ^{232}Th chain emits 4.5 gammas per decay. This means that per decay, ^{40}K emits $\times 30$ less gammas than the ^{238}U/^{232}Th chains combined (with a 1:2 ratio). Even though the ^{40}K contamination level is almost $\times 8$ higher than the ^{238}U/^{232}Th contamination combined, the number of ^{40}K gammas emitted is still $\times 4$ times smaller.

The full impact of the radioactive contamination levels in the PMTs will be assessed in Sections 6 and 7, which construct the background model for the XENON10 and LUX detectors. Due to their proximity to the liquid Xe volume, and the inability to shield the detector from them, the PMTs are one of the major components in the background for LXe detectors. For larger detectors in which the self-shielding properties of the LXe screen out most background components, such as LUX, the PMT radioactivity becomes the dominant component and sets the limit on the detector sensitivity. Thus, the characterization of the PMT radioactive contamination is crucial to the understanding of the detector background model and of the detector performance.
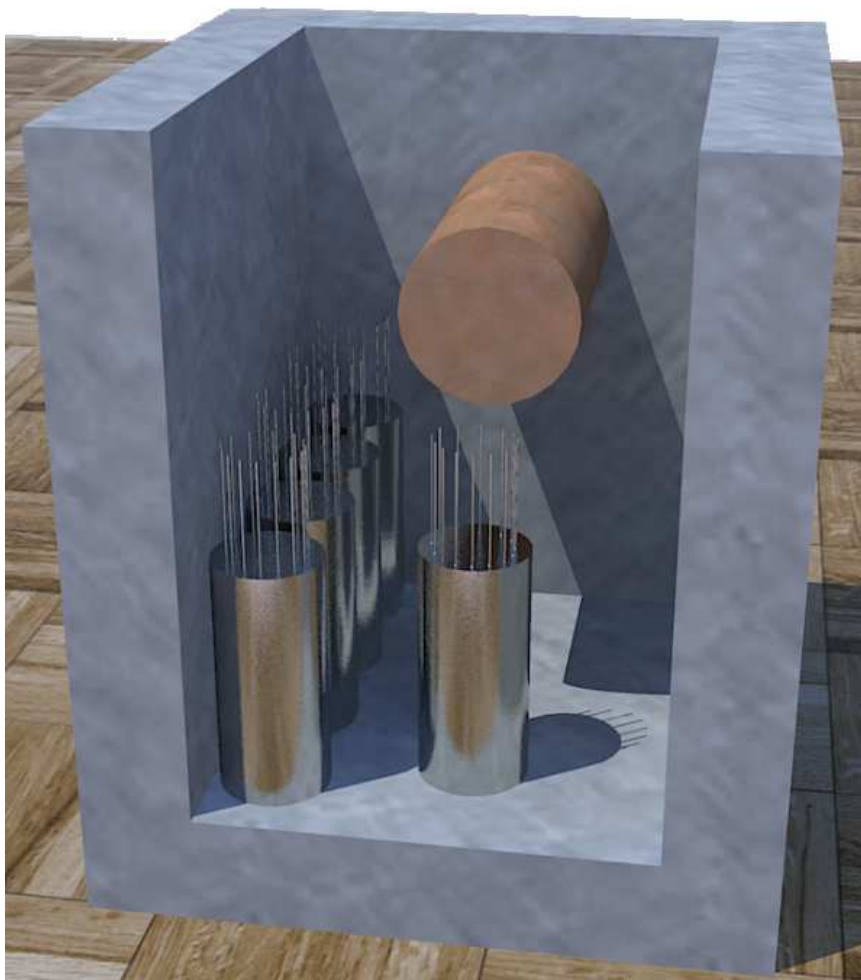
Figure 5.8: Diagram of the arrangement of PMTs inside the SOLO chamber. The copper cylinder is the Diode-M detector, a 0.6 kg high-purity Ge detector housed in copper. The detector is inside a Pb shield with > 30 cm Pb thickness in all directions. The chamber is flushed with N gas to remove any contaminants in the air. Note that the arrangement of the PMTs inside the chamber was chosen to facilitate the reproduction of the arrangement when counting other PMTs.

Isotope	Average Contamination [mBq/PMT]	
	Glass	Insulator Plates
^{238}U	6.5 ± 1.4	12.1 ± 2.4
^{232}Th	1.5 ± 0.6	< 5
^{40}K	11 ± 4.6	< 1.6

Table 5.8: Radioactive contamination levels for components of the R8778 PMTs, measured at SOLO screening facility. First Sample: 219 grams of crushed glass, counted for 6.2 live-days. Second Sample: 20 insulator plates, weighting 100 grams, counted for 9.9 live-days. Each PMT contains 22 g of glass and 2 insulator plates.
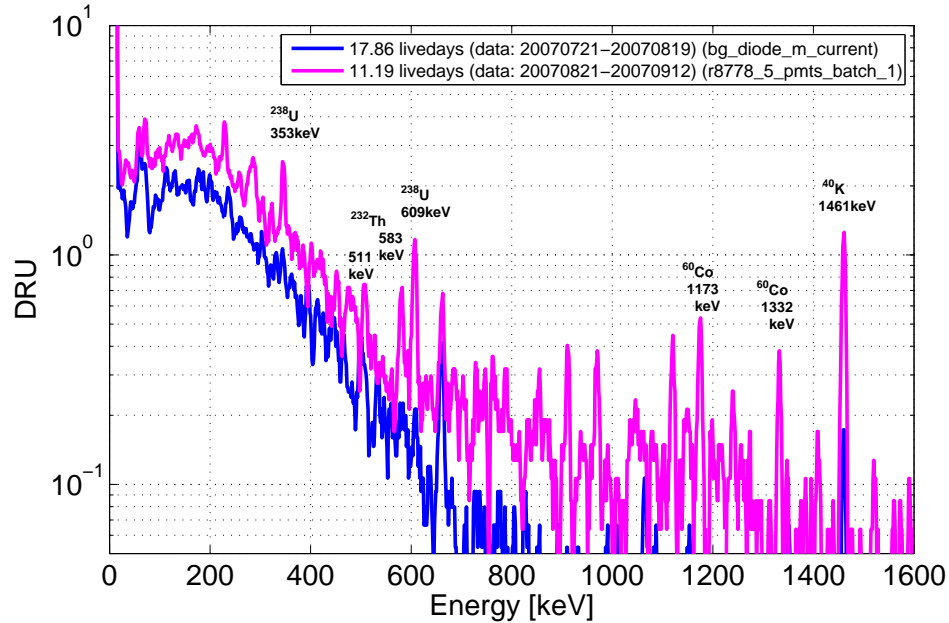
Figure 5.9: Energy Spectrum for the first batch of 5 R8778 PMTs counted in SOLO, for 11 live-days, overlaid with the background spectrum (empty chamber, with N_2 gas purge) counted for 18 live-days. Measurements made with the High-Purity Ge detector Diode-M (0.6 kg).

5.3 Other materials

5.3.1 XENON10 shield materials

The XENON10 shield consists of a 20 cm layer of high-density polyethylene (HDPE) sheets inside a 20 cm layer of Pb bricks, mounted in a cubic arrangement and supported by a steel structure. The Pb layer is made of 2 types of Pb bricks. The inner 5 cm layer uses low-background Pb purchased from the *Fonderies de Gentilly* [110], measured at the LNGS screening facility to have 17 ± 5 mBq/kg of ^{210}Pb activity. The outer 15 cm layer uses Pb bricks acquired from Poland, and have ^{210}Pb activity of 560 ± 90 mBq/kg. The remaining materials in the XENON10 shield were screened by the Diode-M and Gator detectors in the SOLO facility, and by the LNGS facility. The screening results for the main shield components are listed in Table 5.9, and the results for samples of the steel used during the shield construction are listed in Table 5.10.

Isotope	Average Contamination [mBq/kg]		
	Pb (inner)	Pb (outer)	Polyethylene
^{238}U	< 3.9	< 1.6	< 5.2
^{232}Th	< 6.8	< 5.7	< 6.6
^{40}K	< 28	14 ± 6	< 64
^{60}Co	< 0.19	< 1.1	-
^{137}Cs	< 0.85	< 2.1	< 2.6
^{210}Pb	$(17 \pm 5) \times 10^3$	$(560 \pm 90) \times 10^3$	-

Table 5.9: Radioactive contamination levels for the XENON10 shield components, measured at the LNGS counting facility

Isotope	Average Contamination [mBq/kg]				
	Steel (I-beams)	Steel $\left(\begin{smallmatrix}\text{side}\\\text{panels}\end{smallmatrix}\right)$	Steel $\left(\begin{smallmatrix}\text{ceiling}\\\text{plate}\end{smallmatrix}\right)$	Steel (Bolts)	Steel $\left(\begin{smallmatrix}\text{pre-purchase}\\\text{sample}\end{smallmatrix}\right)$
^{238}U	7.8 ± 3.2	< 3.5	< 8.3	< 13	< 7
^{232}Th	< 4.1	< 4.7	< 8.7	20 ± 10	< 7
^{40}K	< 15	< 26	< 42	< 41	< 28
^{60}Co	170 ± 3	2.4 ± 0.7	2.9 ± 1.2	< 8	11 ± 2
^{137}Cs	< 1.4	< 2.2	< 2.8	< 5	< 3

Table 5.10: Radioactive contamination levels for samples of the steel used in the XENON10 shield, measured at the LNGS counting facility

Isotope	Average Contamination Levels [mBq/kg] Ti
^{238}U	< 0.18
^{232}Th	< 0.2
^{40}K	< 0.9
^{60}Co	-
^{137}Cs	-
^{46}Sc	23

Table 5.11: Radioactive contamination levels for samples of the Ti stock used to manufacture the LUX cryostat, measured at the Oroville counting facility. Measurements provided by A. Smith of LBNL.

5.3.2 Ti for LUX Cryostat

The Ti used for the LUX cryostat walls was procured from Titanium Metal Supply Inc., and a sample was provided for screening before the purchase was finalized. The sample was screened at the Oroville Low Background Counting Facility [111], and the results are provided by A. Smith from LBNL. The screening of the Ti was done with a High-Purity Ge detector. The sample counted consisted of 20 individual Ti pieces, with a total mass of 8 kg. The measured contamination levels are listed in Table 5.11.

5.3.3 Miscellaneous materials

A variety of other materials were screened at the SOLO facility since operation commenced on 2003. The list of material includes, but is not limited to:

- Hamamatsu R9288 PMTs, used in the small LXe detector prototype XeBaby (115 g of active LXe) built at the Nevis Lab (Columbia University) and operated by the XENON10 collaboration.

- Different models of resistors and capacitors considered as candidates for building the PMT bases.

- Resistors for the HV voltage divider used on the field shaping rings, located immediately outside the Teflon can enclosing the active LXe volume.

Isotope	R9288 PMTs [mBq/PMT]	HV Shaping Ring Resistors [mBq/resitor]	Ceramic feedthroughs [mBq/kg]	Stainless Steel Sample [mBq/kg]
^{238}U	400 ± 67	0.240	125×10^3	< 61
^{232}Th	120 ± 21	0.220	13.2×10^3	< 21
^{40}K	2000 ± 160	0.520	6.3×10^3	< 12
^{60}Co	-	< 0.020	-	101 ± 8

Table 5.12: Radioactive contamination levels for miscellaneous materials used in the XENON10 experiment.

- High-Voltage feedthroughs, including samples of the raw material (ceramic pieces). None of the materials counted at SOLO was used for the feedthrough fabrication, as it was decided to make feedthroughs using steel rather than ceramic.

- Stainless steel samples believed to be representative of the steel used in the detector fabrication.

The radioactive contamination levels for some of these materials is listed in Table 5.12. Of special interest is the counting stainless steel samples. Several samples were sent to be counted both at SOLO and at the LNGS screening facility. However, *samples of the steel used to build the XENON10 cryostat were never counted.* Models of the detector background, reviewed in Section 6, would indicate that this was a mistake, as it is shown that the steel Cryostat is the dominant component in the background in XENON10.

CHAPTER 6

BACKGROUND MODEL FOR

XENON10

In order to assess its sensitivity, it is necessary to fully characterize the backgrounds in the XENON10 detector, through calculations and Monte Carlo simulations based on the radioactivity of the detector components and its environment. The XENON10 background model is built using (1) the radioactive contamination levels in the detector components learned through the XENON10 materials screening program; (2) estimates based on the available literature for contamination levels for the materials not screened by the collaboration; (3) measurements of the neutron and γ flux in the Laboratori Nazionali de Gran Sasso, where the experiment was deployed. We performed a series of Monte Carlo simulations that determine the expected background due to the radioactive contamination in the detector components (the *internal background*), and the expected background due to environmental neutron and γ flux (the *external background*), taking into account the effect of the XENON10 shield. The expected background is compared and matched to the observed event rate during the WIMP search runs, described in Chapter 4.

6.1   Shield Design

The XENON10 detector design has already been described in Chapter 2. The detector is placed inside the custom-built shield, which consists of 2 shielding elements, a 20 cm layer of high-density polyethylene (HDPE, chemical composition CH_2, with density $\rho = 0.935\,\mathrm{g \cdot cm^{-3}}$) sheets inside a 20 cm layer of Pb bricks ($\rho = 11.340\,\mathrm{g \cdot cm^{-3}}$). The total shield mass is $m_{HDPE} = 1.5\,\mathrm{tonnes}$ and $m_{Pb} = 33.2\,\mathrm{tonnes}$. The shield is mounted in a cubic arrangement and supported by a steel structure - see Fig. 6.1 for a diagram of the shield design. The HDPE sheets and the Pb bricks are secured to steel panels on the outside of the shield structure with long steel bolts, pressed together and arranged in such a fashion to leave no empty spaces between Pb bricks or HDPE sheets. The whole structure sits atop HDPE sheets totaling 15 cm thickness. The Pb layer is made of 2 types of Pb bricks. The inner 5 cm layer uses low-background Pb purchased from the *Fonderies de Gentilly* [110], measured at the LNGS screening facility to have $17 \pm 5\,\mathrm{mBq/kg}$ of ^{210}Pb activity. The outer 15 cm layer uses common Pb bricks acquired from Poland, and have ^{210}Pb activity of $560 \pm 90\,\mathrm{mBq/kg}$. The construction of the shield was contracted out to a local company, Comasud. The construction took place from May to August, 2006.

The internal cavity of the shield has dimensions $90\,\mathrm{cm} \times 90\,\mathrm{cm} \times 107.5\,\mathrm{cm}$, and the detector occupies 30% of its volume. The detector is mounted on I-beams attached to a single wall, which also works as the door to the shield. The door moves along rails to allow access to the detector. All feedthroughs are connected through the door wall, and have been arranged in a Z-shape and away from the detector center whenever possible, to minimize line-of-sight paths for external radiation. The gaps in the Pb shield around the feedthrough cables was filled with Pb shavings, and the gaps in the HDPE sheets were filled with low-radioactivity silicon gel. The cavity is flushed with N gas from a liquid N dewar boil-off, which enters the cavity from the top at a rate of 1.5 ± 0.1 standard liter/min, and exits through the bottom. Low radioactivity silicon gel is used to seal all seams, and a 10 mm rubber "lip" in a 5 mm deep trench running along the edges of the door render the cavity airtight. All shield components were cleaned with Ethanol during the construction process.

The shield is designed to reduce the external neutron and γ backgrounds well below
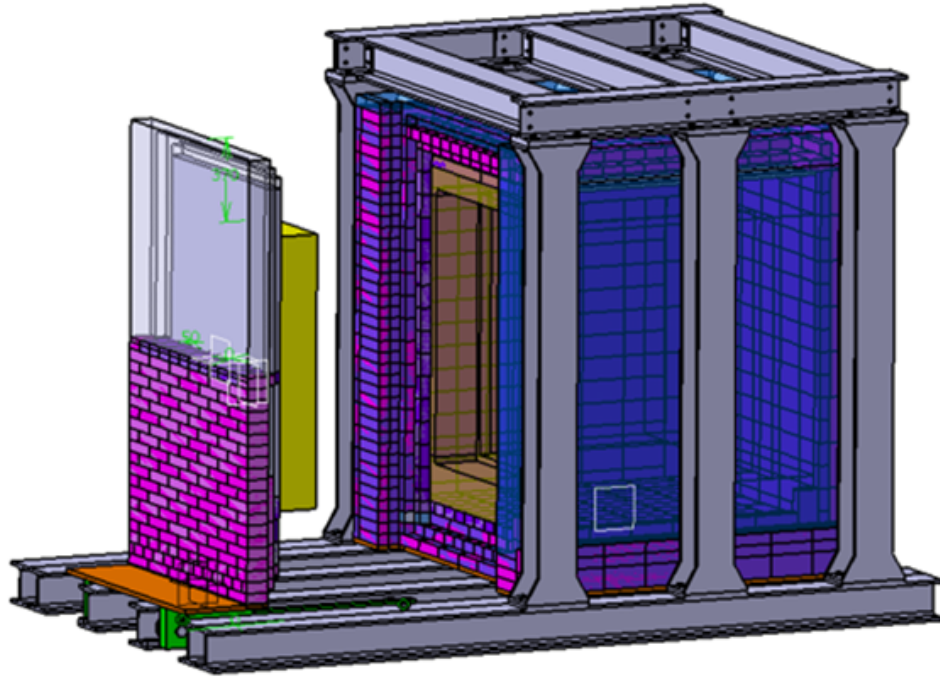
Figure 6.1: XENON10 Shield Diagram. The Pb bricks are shown in purple and dark blue, the HDPE sheets in yellow.

the backgrounds from internal detector components. The shielding material is chosen to optimize the attenuation of the main components of the external backgrounds. The layer of Pb bricks is target at attenuating the external γ background, mostly from the rock and concrete in the lab walls, floor and ceiling, and the HDPE is added to shield against the external neutron background, also originated at the rock surrounding the lab. Monte Carlo simulations of the external backgrounds were performed prior to the construction of the shield to estimate the shield performance and advise on the optimal dimensions and arrangement of the shield. The final dimensions of the shield were specified to achieve balance between the desired background activity and financial constraints.

The attenuation of γ rays is done via interactions of the γ's with electrons in the shielding material, through 3 types of process: photoelectric absorption, Compton scattering, and electron-positron pair production. All these processes work through transfer of energy from γ's to electrons, either partial (Compton scattering) or complete (photoelectric absorption and pair production). The photoelectric absorption process is dominant for low energy γ
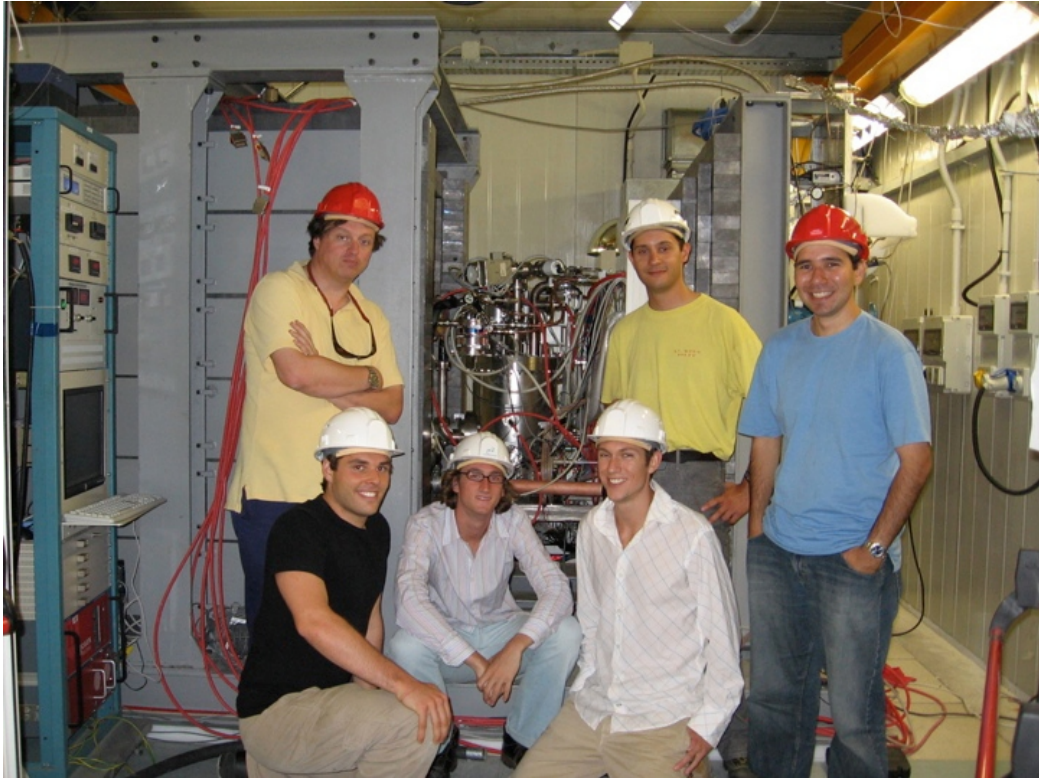
(a) Brown group, with XENON10 detector inside open shield. From left to right: R. Gaitskell, E. Baker, A. de Chaumont Quitry, P. Sorensen, S. Fiorucci, L. de Viveiros.

(b) Shield Open

(c) Shield Closed

Figure 6.2: Photos of the XENON10 Shield

rays ($E_\gamma < 100\,\text{keV}$), and its cross section at these energies can be roughly approximated as

$$\sigma_{ph.el.} \sim C \times \frac{Z^{4.5}}{E_\gamma^{3.5}} \tag{6.1}$$

where C is an arbitrary constant [112, p49]. The actual photoelectric cross section $\sigma_{ph.el.}$ is not a smooth function of energy, and it shows discontinuities at the binding energies of electron shells in the atoms of the material under consideration. Pair production requires energies greater than $2 \times m_e c^2 = 1.02\,\text{MeV}$ (where m_e is the electron mass), and is dominant for high energy γ rays ($E_\gamma > 10\,\text{MeV}$). The probability of pair production also increases for high Z materials:

$$\sigma_{pair\,prod.} \sim Z^2 \tag{6.2}$$

For intermediary energy γ rays, attenuation is dominated by Compton Scattering, in which the probability of interaction increases linearly with the number of electrons in the atoms of the shielding material:

$$\sigma_{cs} \sim Z \tag{6.3}$$

In Compton Scattering, the γ particle is not absorbed by the atom, but has its energy reduced. A γ ray particle may undergo Compton scattering several times before it is finally absorbed in the shielding material. It is clear from the behavior of the γ ray interaction cross sections that high Z materials are ideal for attenuation of the γ ray flux. The attenuation can be described using the *attenuation length*

$$\lambda = 1/N \cdot \sigma \tag{6.4}$$

where $\sigma = \sigma_{ph.el.} + \sigma_{pair\,prod.} + \sigma_{cs}$ is the total interaction cross section and N is the density of atoms, $N = N_A \cdot \rho/A$ (N_A =Avogadro's number, ρ =density of the material, and A =molecular weight). Monte Carlo simulations of a $20\,\text{cm}$ Pb shield ($Z = 82$) results in a flux attenuation of $> 10^5$ for typical γ background energy distributions. The HDPE sheets offer much smaller attenuation. HDPE is a polymer consisting of a chain of ethylene molecules C_2H_4, with density $\rho = 0.935\,\text{g} \cdot \text{cm}^{-3}$. Its density and Z distribution is similar

to water, and their attenuation length is approximately the same. Monte Carlo simulations indicate that 20 cm of water, and thus of HDPE, correspond to a $\times 3$ attenuation for a typical γ spectrum from rock radioactivity. The attenuation of the external gamma background by the XENON10 shield is further discussed in Section 6.3.

Neutrons interact with the nuclei in the shielding material, and the interaction can be of a few types: elastic scattering, inelastic scattering, neutron capture, fission, and high-energy hadron shower production. Neutron capture and fission processes are most likely for *slow* or *thermal* neutrons, which have energy comparable to room temperature energy ($E_n \simeq kT_{room} \simeq 0.025\,\mathrm{eV}$). At higher energies ($E_n \gtrsim 1\,\mathrm{MeV}$), elastic and inelastic scatters become the dominant mode of interaction. The attenuation of neutron fluxes occur through the process of *moderation*, in which the neutrons scatter (elastically or inelastically) several times in the shielding material, losing energy until they reach energies low enough to undergo capture or fission processes. The main mechanism for neutron energy loss in the energy scale $E_n \sim 1\,\mathrm{MeV}$ is elastic scatters. Conservation of energy calculation show that the energy of the scattered neutron is limited to

$$\left(\frac{A-1}{A+1}\right)^2 E_n < E'_n < E_n \tag{6.5}$$

where E_n is the initial neutron energy, E'_n is the energy of the neutron after scattering, and A is the atomic number. It follows that for materials with higher A, the maximum energy deposition per collision is only a small fraction of the initial neutron energy, and moderation becomes very inefficient. The best moderation material is then single protons or Hydrogen, where $A = 1$ and the neutron can lose all of its energy in a single collision. Hydrogen rich materials such as water (H_2O) or hydrocarbons (CH_2) become ideal for shielding against neutrons. The Pb shield also affects the external neutron flux, and two effects are observed: the increase in the number of neutrons due to fission, and the reduction in the average neutron energy, due to moderation and also to the fact that the neutrons resulting from fission each have energy smaller than the initial neutron. Because of the increase in the number of neutrons, it's recommended to add a layer of HDPE inside any Pb shield. Since the overall energy of the neutron spectrum after the Pb shield is reduced relative to the

external neutron spectrum, the HDPE shield becomes more effective at moderating these neutrons. Thus, to optimize the attenuation of the external neutron background, it is recommended to place *at least* part of the HDPE shield inside the Pb shield. The optimal dimensions and configuration for the shield are detailed in Section 6.2.

6.2 Neutron Backgrounds

The discrimination power of the XENON10 detector, as seen in Chapter 2, offers no respite from neutron backgrounds, as a nuclear recoil from a neutron event is indistinguishable from a nuclear recoil from a WIMP event. Thus, the neutron background has the potential to become the most troublesome background in the detector and limit its sensitivity to WIMP events. It becomes the goal of any experiment attempting direct detection of WIMPs to reduce their neutron backgrounds such that the neutron event rate becomes subdominant to the the expected WIMP event rate. Monte Carlo simulations using Geant4 software were performed for each major source of neutron background in order to characterize the expected nuclear recoil event rate in the XENON10 detector, and to direct the construction of a shield to be used to reduce the external neutron backgrounds.

The major sources of neutron backgrounds are environmental radioactivity and muon-induced neutrons. The environmental radioactivity neutrons are produced by radioactive processes in the rock and concrete walls of the lab where the detector is deployed. These are typically *fast neutrons* ($1\,\mathrm{keV} < E_\mathrm{n} < 10\,\mathrm{MeV}$) and can be effectively moderated by the use of a shield built with low Z materials. The neutron production rate, effectiveness of shield and event rates in the XENON10 detector are detailed in Sections 6.2.1 and 6.2.1.3. The muon-induced neutron background is primarily generated through muon collisions in the cavern rock and on the shielding material. These go to much higher energies ($E_\mathrm{n} > 10\,\mathrm{MeV}$), which cannot be effectively moderated by the shield. The muon-induced neutron background is discussed in detail in Section 6.2.2. Neutrons are also produced through radioactive processes in the detector components, and as such cannot be moderated by the use of a shield. Section 6.2.3 characterizes the internal neutron background and their event rate in the detector.

Our simulations of the neutron background demonstrate the principle of self-shielding, in which the liquid Xe in the active volume provides additional shielding against backgrounds, and relatively low backgrounds can be achieved by selecting a *fiducial volume* in the center of the detector. Results for the background simulations will generally be quoted as event rates in the fiducial volume used by the XENON10 detector during the WIMP search runs, where the fiducial volume is defined as $r < 8\,\mathrm{cm}$ and $15\,\mu\mathrm{s} < $ drift time$<65\,\mu\mathrm{s}$ ($2.8\,\mathrm{cm} < z < 12.2\,\mathrm{cm}$), with a total mass of 5.4 kg. Cuts are also applied to remove multiple scatter events, as the probability of WIMPs scattering multiple times in the detector is vanishingly small. The single scatter cut used in the XENON10 background simulation is a cut on the spread of the energy-weighted spatial distribution of scatters for each event, i.e. $\sigma_x = \left(\sum E_\mathrm{i} \cdot x_\mathrm{i}\right) / \sum E_\mathrm{i}$, with the thresholds of $\sigma_z \leq 2\,\mathrm{mm}$ and $\sigma_r \leq 5\,\mathrm{mm}$. The reason for this technique is that in Geant4 sometimes a single scatter is actually made up from several energy depositions (i.e. e^- tracks), and these small energy depositions should not be treated like individual scatters, but part of a single scatter. The single scatter cut parameters are limited by the z and r spatial resolution. The particular choices of fiducial cuts and single scatters cut parameters is determined from the simulation of the γ background and is discussed on Section 6.3.

The original XENON10 proposal stipulates the goal in sensitivity of the XENON10 detector at $\sigma_{\chi,n} = 2 \times 10^{-44}\,\mathrm{cm}^2$ for a representative WIMP mass of $m_\chi = 100\,\mathrm{GeV}/c^2$. Fig. 6.3 plots the resulting nuclear recoil spectrum, for standard assumptions of WIMP halo density and velocity distribution (as discussed in Section 1.3); the differential event rate is quoted in units of $1\,\mathrm{dru_r} = 1\,\mathrm{event/keV_r/kg/day}$, where $1\,\mathrm{keV_r} = 1$ keV nuclear recoil. The sensitivity goal corresponds to a total interaction rate of 20 events / year in the fiducial volume of 5.4 kg, and a low energy WIMP differential event rate of $\Gamma_{WIMP} = 8 \times 10^{-4}\,\mathrm{dru_r}$ for a detection threshold of $5\,\mathrm{keV_r}$. For the XENON10 WIMP search run of $\sim$ 2 months, the WIMP interaction rate corresponds to 3.3 events. For a neutron background of 0.8 events / 2 months, there is a 5% probability that the event rate will fluctuate to > 3 events in this period. Thus, for a 2σ (95%) confidence on the sensitivity limit, the nuclear recoil background must be kept at < 0.8 events / 2 months, or < 5 events / year. Thus, the
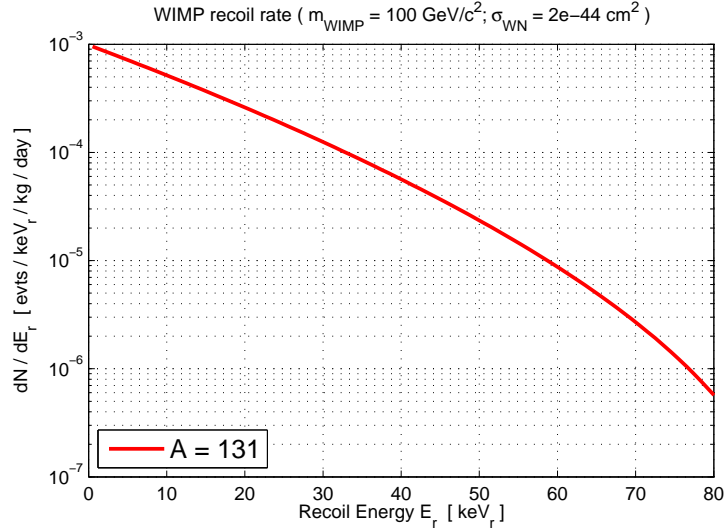
Figure 6.3: Nuclear recoil event rate for the WIMP signal $\sigma_{\chi,n} = 2 \times 10^{-44}\,\text{cm}^2$ and $m_\chi = 100\,\text{GeV}/c^2$ - the XENON10 sensitivity goal. The event rate is calculated for WIMP interactions with ^{131}Xe, following the calculation detailed in [40] and summarized in Section 1.3.2.

nuclear recoil background goal for XENON10 is < 5 events / year in the fiducial volume of $5.4\,\text{kg}$, in the energy range of interest ($2 - 12\,\text{keV}_{\text{ee}}$, $L_y = 2.2\,\text{phe/keV}_{\text{ee}}$).

In the subsequent subsections, the major components of the neutron background are described and discussed. Table 6.1 lists the major sources of neutron backgrounds, and their associated event rate in the XENON10 detector. The neutron background is assessed only for events in a energy region of interest of $5 - 25\,\text{keV}_{\text{r}}$, a similar energy range to the one chosen for the XENON10 WIMP search data analysis, and only for single scatter events in the fiducial volume of $5.4\,\text{kg}$. The main source of nuclear recoils in XENON10 are the μ-induced neutrons from the Pb shield, which contribute 1.7 events / year in the fiducial volume and in the energy of interest, due to the combination of 2 factors: the large mass of the shield, and the high multiplicity of neutrons generated by μ-induced processes in Pb. The internal neutron background produced in the detector components inside the shield (such as the cryostat and the PMTs) is potentially a major source of nuclear recoils as well. Due to the complex nature of the internal components, such as the PMTs internal composition and geometry, a precise simulation of the internal backgrounds has not been attempted. Instead, an upper limit is found based on analytical calculations performed in

Neutron Source	Differential rate (μdru$_\mathrm{r}$) at $5\,\mathrm{keV_r}$	Total rate (events/year) ($5-25\,\mathrm{keV_r}$)
(α,n) + fission neutrons Cavern Rock and Concrete Walls	15	0.2
μ-induced Pb Shield	85	1.7
μ-induced Cavern Rock and Concrete Walls	-	< 0.42
μ-induced Polyethylene Shield	-	< 0.13
(α,n) + fission PMT/Cryostat	-	< 1.8

Table 6.1: Summary of Neutron Backgrounds. Differential and total (integrated) neutron event rates quoted for single scatter events, in the standard XENON10 fiducial volume (5.4 kg). The differential recoil rate is quoted at $5\,\mathrm{keV_r}$, and the total rate is integrated in the energy range of interest $5-25\,\mathrm{keV_r}$.

[64]. It is estimated that the neutron event rate in the fiducial volume of $5.4\,\mathrm{kg}$ in the energy range of $5-25\,\mathrm{keV_r}$ due to the major internal components is < 1.8 events/year.

Adding up the contributions from the major sources of neutron background, and using the upper limits for sources where only the limits has been determined, we estimate a total of 4.25 events/year, for single scatters in the energy range of $5-25\,\mathrm{keV_r}$, in the XENON10 fiducial of 5.4 kg. This translates to 0.69 neutron events in 59 live-days, or 0.35 neutron events after the 50% nuclear recoil acceptance used for the XENON10 WIMP search "box". This gives us a 29% probability of having at least 1 neutron event during the WIMP search run of 59 live-days (see Chapter 4). Analysis of the XENON10 WIMP search run data show no events consistent with a nuclear recoil from a neutron. All single scatter events falling within the WIMP search box, which covers the lower half of the nuclear recoil (NR) band, are consistent with either electron recoil events leaking into the NR band, or Gamma-X events (see Section 4.3.2). Analysis of multiple scatter events in the fiducial volume also returned no events consistent with nuclear recoils from neutrons.

6.2.1 Environmental Fast Neutrons

6.2.1.1 Environmental Fast Neutron Flux at LNGS

The environmental *fast neutron* background ($E_n > 1\,\text{MeV}$) is dominated by neutrons generated through radioactive processes inside the materials surrounding the detector. The majority of mass around the detector is in the cavern rock and concrete of the lab (35 cm thick on the walls, 45 cm thick on the floor), and these the are primary source of neutrons external to the shield. The neutrons are mainly generated by 2 processes: spontaneous fission of ^{238}U nuclei; and ^{238}U and ^{232}Th α-decays, in which the generated α-particles collide with nuclei in the source material, i.e. rock or concrete, which in turn generate (α,n) neutrons. The environmental neutron flux is thus determined by the level of ^{238}U/^{232}Th contamination in the rock and concrete.

Spontaneous fission occurs naturally in nuclei with atomic masses > 230 a.m.u., the most well know of these being ^{235}U, ^{238}U, ^{232}Th, ^{239}Pu, ^{240}Pu, and ^{252}Cf. Of these, only ^{235}U, ^{238}U and ^{232}Th exist in nature. ^{232}Th and ^{235}U have relatively small fission branching ratios ($1.8 \times 10^{-9}\%$ and $< 7 \times 10^{-9}\%$, respectively [113]) compared to ^{238}U ($5.4 \times 10^{-5}\%$), so that we need to consider only ^{238}U when calculating the neutron production rate through fission in rock and concrete. ^{238}U has a half-life of 4.47×10^9 years, and it generates 2.07 neutrons per fission, or 13.6×10^{-3} n/s/g of ^{238}U [114, pp. 137]. The fission neutron production rate for rock and concrete then becomes 0.43 n/year/g/ppm of ^{238}U.

The energy distribution of neutrons generated through fission, either spontaneous or due to neutron capture, can be fitted using the Watt distribution[114, pp. 145], which can be expressed as

$$\chi(E_n) = a \cdot e^{-E_n/b} \cdot \sinh \sqrt{c \cdot E_n} \tag{6.6}$$

$$
\begin{aligned}
a &= \frac{e^{-c \cdot b/4}}{\sqrt{\pi \cdot c \cdot b^3/4}} \\
b &= T_w \\
c &= 4 \cdot E_w/T_w^2
\end{aligned}
$$
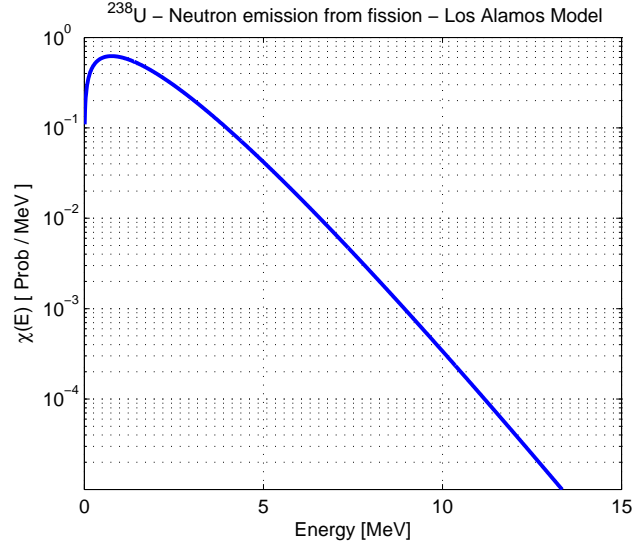
Figure 6.4: Neutron Energy Distribution for Spontaneous Fission of ^{238}U, using the Watt distribution (Eq. 6.6) with parameters $b = 0.7124\,\text{MeV}$, $c = 5.6405\,\text{MeV}^{-1}$.

where $\chi(E_\text{n})$ is the differential event rate, E_n is the produced neutron energy, and the Watt parameters $[a, b, c]$ are functions of the nucleus excitation energy (T_w) and of the fission fragment average kinetic energy E_w [115]. For nuclides in which no empirical fission data exists, the Watt parameters are calculated using the "Los Alamos model", and their values can be found in the ENDL library [116]. The Watt distributions for all elements are peaked at $\sim 0.7\,\text{MeV}$, and have an average energy of ~ 2 MeV. For ^{238}U spontaneous fission, the $b = 0.7124\,\text{MeV}$, $c = 5.6405\,\text{MeV}^{-1}$ [117], and the distribution is shown on Fig. 6.4.

^{238}U and ^{232}Th decay primarily through α-decay, with 100% branching ratios, and half-life of 4.47×10^9 and 1.405×10^{10} years, respectively. The α-particles can interact with nuclei in the rock and concrete, producing neutrons through (α,n) reactions. The (α,n) reaction cross-section is a function of the α-particle energy and of the atomic mass of the target material, and it tends to be larger for low Z materials because of the smaller Coulomb barrier. The production of neutrons on a target with a single element can be described as

$$Y_j = \int_0^R n_j \cdot \sigma_j(E)\, dx \tag{6.7}$$

where Y_j is the yield of neutrons, R is the range for some initial α-particle energy E_i, E is the α-particle energy, n_j is the number density of the target material, and σ_j is the (α,n)

cross section for the element j. It can then be rewritten as

$$
\begin{aligned}
Y_j &= \int_0^{E_i} n_j \cdot \sigma_j(E) \frac{1}{dE/dx} \, dE \\
&= \int_0^{E_i} n_i \cdot \sigma_i(E) \frac{N_A}{n_j \cdot A_j \cdot S_j(E)} \, dE \\
&= \frac{N_A}{A_j} \cdot \int_0^{E_i} \frac{\sigma_j(E)}{S_j(E)} \, dE
\end{aligned}
$$

where N_A is Avogadro's number, A_j is the atomic mass of the element j, and $S_j(E) = \frac{dE}{dx}$ is the stopping power of α-particles in the material of element j. The calculation of the neutron yield for compound materials is detailed in [118, pp. 40]. Basically, the neutron yield per α-particle for individual elements in the target material can be obtained by using Bragg's additivity law (or the "mixture rule"), which states that the stopping power of a compound may be estimated by the linear combination of the stopping powers of individual elements

$$
Y_{j,mix} = \frac{M_j \cdot S_j(E_0)}{\sum_j M_j \cdot S_j(E_0)} Y_j(E_i) \tag{6.8}
$$

where M_j is the mass fraction of the element j in the target material (i.e. rock and concrete), and E_0 is a chosen reference energy . The procedure assumes that the *ratio* of stopping powers for the elements in the compound is independent of α-particle energy. It has been shown that this approximation introduces an uncertainty of $< 5\%$ in the neutron yield for $E_\alpha > 3\,\text{MeV}$ [119, pp. 499]. A reference energy is then chosen at high energy ($E_0 = 8\,\text{MeV}$ in [118, pp. 40]), since most neutron yield comes from the high energy α-particles and the ratio of stopping particles is energy-independent at high energy. As an example, the mass stopping power of H for $8\,\text{MeV}$ α-particles is $S_H(8\,\text{MeV}) = 1.59\,\text{MeV} \cdot \text{cm}^2 \cdot \text{mg}^{-1}$. Tables of α-particle stopping powers can be found on the ASTAR database [120].

Although no measurements exist for the neutron flux in the specific area where the XENON10 detector was installed, measurements of the neutron flux in the main experimental lab areas (Halls A, B and C) at LNGS are reported in [121], [122], [123], [124],

[125], and [126] (see Table 6.2). The measurements fall within a large range, and their results are discussed on [117]. Measurements of the ^{238}U / ^{232}Th contamination levels in the cavern rock and the concrete walls in the lab halls at LNGS are also reported in [121] and [117], and are listed on Table 6.3. Using the measured contamination levels, Monte Carlo simulations using Geant4 were performed in [117] in order to provide an independent verification of the neutron flux in the LNGS experimental halls. Simulations were performed for both ^{238}U fission and (α,n) neutrons from ^{238}U / ^{232}Th α-decays using the measured contamination levels, the composition of the rock and of the concrete for the areas close to experimental halls. The only unknown quantity is the percentage of water content in the concrete, and thus simulations for 2 degrees of "wetness" were performed: "dry" concrete (8% water content) and "wet" concrete (16% water content). The resulting neutron flux for one of the experimental halls is shown on Fig. 6.5. The simulation of Hall A rock plus dry concrete yields results similar to the neutron flux measurements by [121] (assuming a Watt distribution of fission neutrons), and so we will use this flux measurement as the standard neutron flux at LNGS. The measurements of the Hall A neutron flux give a total of 3.8×10^{-6} n·cm^{-2}·s^{-1} in the $0 - 10$ MeV range, 0.75×10^{-6} n·cm^{-2}·s^{-1} in the 1 keV $- 10$ MeV range, and 0.60×10^{-6} n·cm^{-2} · s^{-1} in the 1 MeV $- 10$ MeV range.

Although the ^{238}U/^{232}Th contamination level in the Hall A rock is more than $\times 10$ higher than at Hall B and C, as shown in Table 6.3, the neutron flux in Halls A and in Hall B/C differ only by a factor of $\times 1/2$, indicating that the 35 cm thick concrete walls on the experimental labs moderate the neutron flux from the rock. The simulations predict that at $E_\mathrm{n} > 1$ MeV, the spectral shape of the neutron flux is essentially a falling exponential with a 1.4 MeV slope with residual features at high energies (> 5 MeV) due to the alpha particle energy in (α,n) processes, and that the neutron production rate is roughly the same for both fission and (α,n) processes, as shown in Table [117].

6.2.1.2   Simulation of Environmental Fast Neutrons for XENON10

Monte Carlo simulations using Geant4 are constructed to study the effect of shielding against environmental fast neutrons, and to determine the expected neutron event rate

Energy Interval (MeV)	Neutron flux (10^{-6} n·cm^{-2}·s^{-1})						
	Wulandari '04 [117]	Belli '85 [121]	Arneodo '99 [122]	Aleksan '88 [123]	Bellotti '89 [124]	Rindi '88 [125]	Cribier '95 [126]
$0 - 5\times10^{-8}$	0.53 ± 0.36	1.07 ± 0.05					
$5\times10^{-8} - 10^{-3}$	1.77 ± 0.45	1.99 ± 0.05					
$10^{-3} - 2.5$	1.22 ± 0.32	0.53 ± 0.08					
$1 - 2.5$	0.35 ± 0.12	0.38 ± 0.06	0.14 ± 0.12				
$2.5 - 5$	0.18 ± 0.05	0.18 ± 0.04	0.13 ± 0.04				
$5 - 10$	0.05 ± 0.02	0.04 ± 0.01	0.15 ± 0.04			2.56 ± 0.27	
$10 - 15$		$(7 \pm 2) \times10^{-4}$	$(4 \pm 4) \times10^{-4}$	0.78 ± 0.3	3.0 ± 0.8		0.09 ± 0.06
$15 - 25$		$(1 \pm 3) \times10^{-7}$					
Total Flux	3.75 ± 0.67	3.81 ± 0.11					
Flux $E_\mathrm{n} > 1$MeV	0.58 ± 0.13	0.60 ± 0.7					

Table 6.2: Measured and simulated neutron flux in the LNGS experimental halls, collated from a variety of sources. The first column lists the results from simulations performed by [117]. All other columns lists the measurements of neutron fluxes in the Gran Sasso experimental halls, and are obtained from [117]. The simulation performed by [117] show good agreement to the Belli measurement [121], which is used in the simulations performed for this work as the standard Gran Sasso neutron flux.

	Hall A	Hall B	Hall C	"Dry" Concrete (8% water)
U [ppm]	6.80 ± 0.67	0.42 ± 0.10	0.66 ± 0.14	1.05 ± 0.12
Th [ppm]	2.167 ± 0.074	0.062 ± 0.020	0.066 ± 0.025	0.656 ± 0.028

Table 6.3: Measured contamination levels for LNGS rock and concrete, obtained from [117].
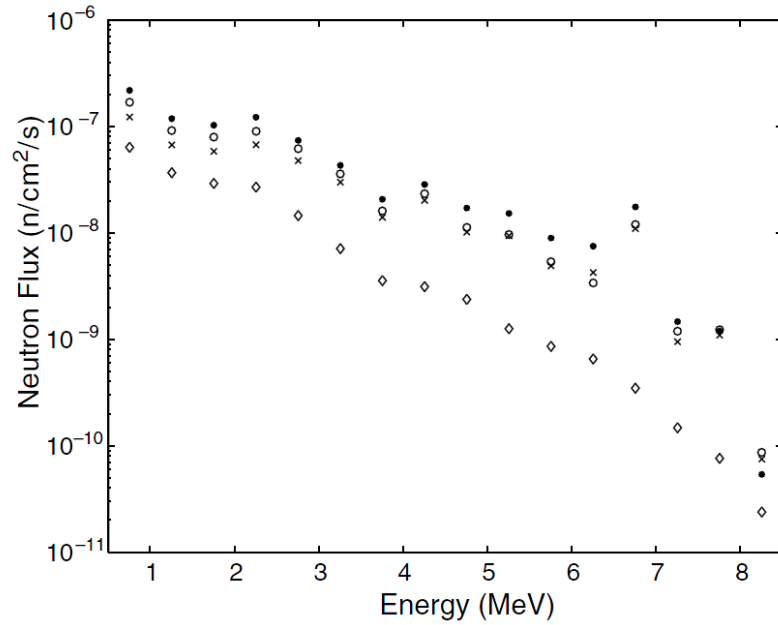
Figure 6.5: Neutron flux at LNGS obtained from Monte Carlo simulations. $\bullet$: hall A, dry concrete; $\times$: hall A, wet concrete; $\diamond$: hall A, dry concrete, fission reactions only; and $\circ$: hall C, dry concrete. Each point shows the integral flux in a 0.5MeV energy bin. Figure obtained from [117].

	Neutron production rate $[\mathrm{n} \cdot \mathrm{year}^{-1} \cdot \mathrm{g}^{-1}]$			
	Hall A rock	Hall B	Hall C	Concrete (8% water)
^{238}U fission	3.54	0.22	0.34	0.55
(α,n)	4.38	0.25	0.39	0.51

Table 6.4: Neutron production rate over all energies due to ^{238}U fission and (α,n) processes in Gran Sasso rock, obtained from Monte Carlo simulations [117]. The simulation yields a neutron production rate by fission of $0.52\,\mathrm{n} \cdot \mathrm{year}^{-1} \cdot \mathrm{g}^{-1}$ per ppm of ^{238}U contamination. The (α,n) neutron production rate is calculated from the chemical composition of the Gran Sasso rock, and results in $0.57 / 0.24\,\mathrm{n} \cdot \mathrm{year}^{-1} \cdot \mathrm{g}^{-1}$ per ppm of ^{238}U / ^{232}Th in rock. The total neutron production rate from fission for rock and concrete, and from (α,n) processes for rock is calculated by multiplying the neutron yield by the contamination levels listed in 6.3. The (α,n) neutron production rate for individual contaminants in concrete is not available; the total rate is obtained from [117].
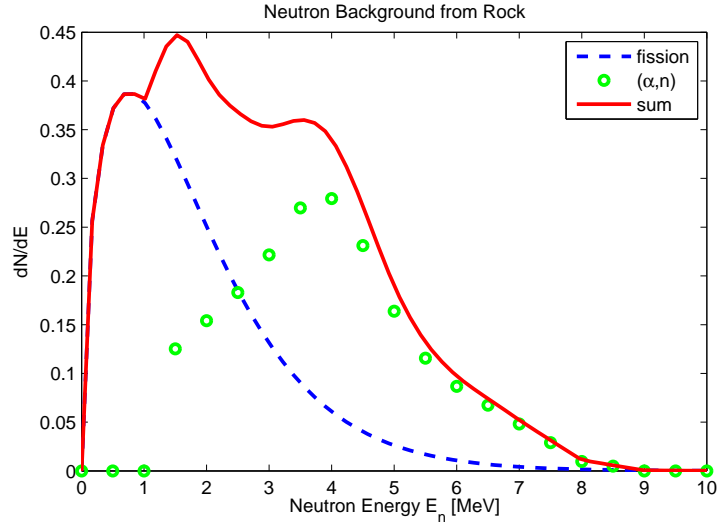
Figure 6.6: Rock neutron spectrum, combining the fission neutron spectrum [117] and (α,n) neutron spectrum [127] for Gran Sasso rock. The neutron production rates have been scaled to match the fission / (α,n) production rate ratio shown in Table 6.4. The plot shows the spectrum with arbitrary normalization on y-scale. The spectrum is normalized to match the neutron flux measured by Belli [121], shown in Table 6.2.

in the XENON10 detector. The initial neutron spectrum is created by combining the neutron spectra from ^{238}U fission and from (α,n) processes. The fission neutron spectrum is the same one detailed in the previous section, and shown in Fig. 6.4. The (α,n) neutron differential spectrum could not be obtained from the sources mentioned in the previous section. Instead, we use the (α,n) differential spectrum from a similar rock formation, from the only available source with a detailed (α,n) spectrum for an underground lab [127]. The fission and (α,n) neutron spectra are scaled to equal flux contribution, and then combined in a single spectrum shown in Fig. 6.6, using an arbitrary y-scale. The total neutron spectrum is normalized so that the flux of neutrons with energies $> 1 \, \mathrm{MeV}$ matches the measurement at Hall A of $\phi_{E_n > 1} \, \mathrm{MeV} = 0.6 \times 10^{-6} \, \mathrm{n \cdot cm}^{-2} \cdot \mathrm{s}^{-1}$, as measured by Belli [121] (see Table 6.2). The resulting spectrum is in agreement with the neutron spectrum given by [117], shown in Fig. 6.5, to $< 10\%$ at any point in the $1 \, \mathrm{MeV} - 10 \, \mathrm{MeV}$ range.

6.2.1.3 Effect of Shield on Environmental Fast Neutrons

It is necessary to moderate the neutron flux so that the nuclear recoil spectrum due to neutrons is subdominant to the expected recoil spectrum of WIMP at the XENON10 sensitivity

goal. A very rough estimate of the desired moderation can be calculated by making some approximations for the neutron event rate in the detector. The incoming neutron flux is $\phi_{E_n>1}\mathrm{MeV} = 0.6 \times 10^{-6}\,\mathrm{n \cdot cm^{-2} \cdot s^{-1}}$ with average energy of $E_\mathrm{n} \sim 3\,\mathrm{MeV}$. This corresponds to 80 n / day entering the entire XENON10 active volume. The probability that a neutron will scatter at least once for a length l of liquid Xe is:

$$Prob_{\geq 1 \text{ scatter}} = 1 - e^{-l/\lambda_{n,Xe}} \tag{6.9}$$

where $\lambda_{n,Xe}$ is the mean free path of neutrons in liquid Xe. The mean free path for fast neutrons is in the same order as the XENON10 active volume dimensions: $\lambda_{n,Xe}(1\,\mathrm{MeV}) \sim 12\,\mathrm{cm}$ and $\lambda_{n,Xe}(3\,\mathrm{MeV}) \sim 15\,\mathrm{cm}$. The probability a 3 MeV neutron traveling straight up the detector will scatter at least once is thus 63%. Averaging over all possible neutron directions, we have that the probability that a 3 MeV neutron will scatter at least once is $\sim 30\%$. For a 3 MeV neutron, the maximum recoil energy is $90\,\mathrm{keV_r}$. Thus, the average nuclear recoil rate for the initial neutron flux is $\Gamma_\mathrm{nr} \sim 0.02\,\mathrm{dru_r}$. The XENON10 sensitivity goal on its original proposal is $\sigma_{WIMP} = 2 \times 10^{-44}\,\mathrm{cm^2}$ for $m_{WIMP} = 100\,\mathrm{GeV}/c^2$, corresponding to a recoil rate of $\Gamma_{WIMP} = 8 \times 10^{-4}\,\mathrm{dru_r}$ at the threshold energy of $5\,\mathrm{keV_r}$. In order to match the neutron event rate Γ_nr to the signal rate Γ_{WIMP}, we need to reduce the neutron flux to 5% of its original value. In order to render the neutron event rate subdominant by a factor of $\times 1/10$, then we need to construct a shield that reduces the neutron flux to $\sim 0.5\%$ of its initial value.

Geant4 simulations of several configurations of Pb and polyethylene shields were performed to determine the optimal shield configuration for the XENON10 detector. They demonstrate that a 20 cm thick polyethylene shield inside a 20 cm thick Pb shield are sufficient to bring down the external neutron flux well below the requirements of the XENON10 experiment.

The simulations for assessing shield effectiveness use the initial neutron energy distribution described in the previous section and shown in Fig. 6.6, but with a lower bound of 100 keV. Lower energy neutrons cannot produce nuclear recoils with energies greater than the simulation energy threshold of $5\,\mathrm{keV_r}$ (see Section 6.2.1.4). Simulations are run

by propagating the initial neutron flux through five different shielding configurations and measuring the resulting neutron flux. The following shield configurations were considered: 20 cm Pb; 20 cm polyethylene; 30 cm polyethylene; 20 cm Pb + 20 cm polyethylene; 20 cm Pb + 30 cm polyethylene. All simulations follow the same basic setup: a single neutron point source, with isotropic angular distribution, adjacent to a Pb wall, which is followed by a HDPE wall, both with infinite width and height.

The neutron energy distribution after each shield configuration, normalized to initial neutron flux, is shown in Fig. 6.7. The simulation demonstrates that 20 cm Pb shield is not very effective by itself in reducing the neutron flux - approximately 1/4 of all neutrons travel the entire length of the Pb shield. However, the Pb shifts down the energy distribution of the neutrons, thus improving the effectiveness of any subsequent shielding material. The initial flux has 85% of neutrons with kinetic energy $E_n > 1$ MeV; after the Pb shield, less than half of the surviving neutrons have $E_n > 1$ MeV. This suggests that placing the polyethylene shield inside the Pb shield will maximize its effectiveness in moderating the external neutron flux. A 20 cm polyethylene shield by itself reduces the initial neutron flux by ×1/25, with only one third of the remaining neutrons with energy > 1 MeV. Placing the 20 cm polyethylene shield inside the 20 cm Pb shield reduces the total neutron flux to 0.6% of the initial flux, and only 0.11% of the neutrons retain an energy > 1 MeV. The 30 cm polyethylene shield by itself produces results very similar to 20 cm Pb + 20 cm of polyethylene, both in the total flux and in the energy distribution, except for a slightly larger propensity for higher energy neutrons. That is, the net effect of an additional 10 cm of polyethylene on the neutron flux on top of a 20 cm polyethylene shield is similar to the effect obtained by adding an external 20 cm Pb shield.

6.2.1.4 Event rates in XENON10 due to Environmental Fast Neutrons

The energy of nuclear recoils E_{nr} produced by an elastic neutron collision is given by

$$E_{nr} = E_n \cdot \frac{4 \cdot m_{Xe} \cdot m_n}{(m_{Xe} + m_n)^2} \cdot \left(\frac{1 - \cos(\theta)}{2} \right) \tag{6.10}$$

	$< 0.2\,\mathrm{eV}$	$0.2\,\mathrm{eV} - 100\,\mathrm{keV}$	$> 100\,\mathrm{keV}$	$> 1\,\mathrm{MeV}$	Total
Initial Flux	-	-	100%	84%	100%
20 cm Pb	0	1%	25%	12%	26%
20 cm polyethylene	1.85%	0.48%	1.43%	1.08%	3.8%
30 cm polyethylene	0.30%	0.07%	0.24%	0.18%	0.60%
20 cm Pb + 20 cm polyethylene	0.40%	0.06%	0.14%	0.11%	0.60%
20 cm Pb + 30 cm polyethylene	0.04%	0.01%	0.02%	0.02%	0.07%

Table 6.5: Moderation of the external neutron background by several shielding configuration using Pb and HDPE. Monte Carlo simulations of a neutron source for several shield configurations show the relative efficiency of each shielding material in moderating the external neutron flux. The efficiency is calculated as the percentage of neutrons of the initial flux to survive after the given shield configuration. The simulation uses an isotropic neutron source, emitted with the initial energy spectrum of $E_\mathrm{n} > 100\mathrm{keV}$ shown in Fig. 6.6. These results are also summarized in Fig. 6.7.
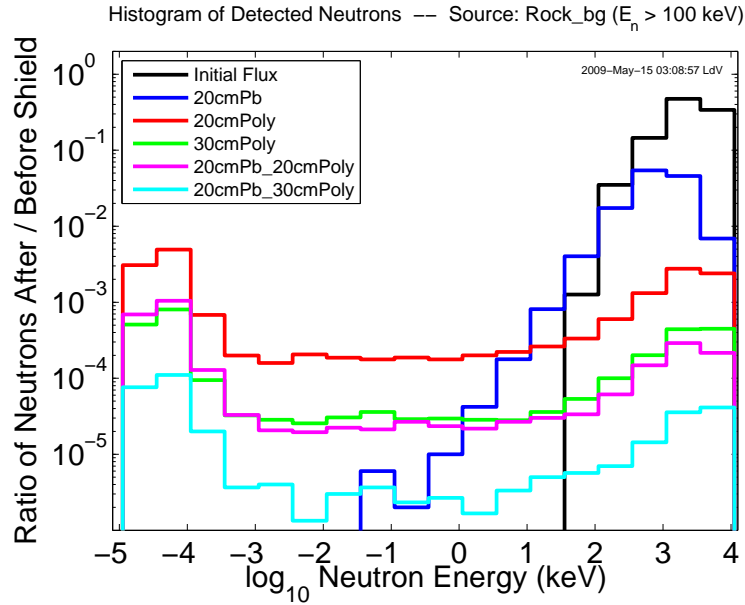
Figure 6.7: Energy histogram of neutrons after shielding - Monte Carlo simulations of a neutron source for several shield configurations show the relative efficiency of each shielding material in moderating the external neutron flux. The simulation uses an isotropic neutron source, emitted with the initial energy spectrum of $E_\mathrm{n} > 100\mathrm{keV}$ shown in Fig. 6.6. These results are also summarized in Table 6.5.
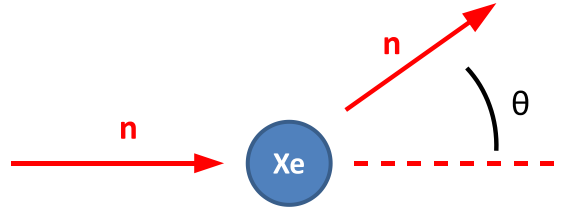
Figure 6.8: Nuclear Recoil Diagram

where E_n is the neutron kinetic energy, m_n is the neutron mass, m_{Xe} is the mass of a Xe atom, and θ is the angle of the neutron after the collision, relative to its original path (as shown in Fig. 6.8). The maximum recoil energy (maximum energy deposition) occurs for $\theta = \pi$, that is, the neutron hits the Xe atom and recoils straight backwards. For atoms with large mass relative to a neutron, as is the case with Xe, this is approximately

$$E_{\mathrm{nr},max} = E_\mathrm{n} \cdot \frac{4}{A_{Xe}} \tag{6.11}$$

where A_{Xe} is the mass number of the Xe atom. For 1 MeV neutrons and and a ^{132}Xe target, this corresponds to $E_{\mathrm{nr},max} \sim 30\,\mathrm{keV_r}$. Conversely, in order to produce nuclear recoils above the desired energy threshold of $E_{\mathrm{nr},thresh} = 5\,\mathrm{keV_r}$, a neutron needs to have kinetic energy of at least $E_\mathrm{n} = 167\,\mathrm{keV}$. The distribution of recoil energies for a monoenergetic neutron beam can be easily calculated for individual isotopes using the angular cross section (see Fig. 6.9a and 6.9b). In the example given, a 1 MeV neutron beam on a ^{132}Xe target produces a nuclear recoil spectrum with a mean $\langle E_{\mathrm{nr}} \rangle \sim 8.5\,\mathrm{keV_r}$. An analytical solution to the full nuclear recoil spectrum in XENON10 due to environmental neutrons is possible, but becomes non-trivial when we attempt to take into consideration the effect of the shield on the incoming neutron spectrum. To obtain the full nuclear recoil spectrum, a Monte Carlo simulation becomes necessary.

Geant4 simulations of the environmental fast neutron flux are used to determine the resulting nuclear recoil spectrum in the detector. The simulation uses the initial neutron flux described above (see Section 6.2.1.2), and it simulates the detector inside the 20 cm Pb + 20 cm polyethylene XENON10 shield. The environmental fast neutrons produce a nuclear recoil spectrum with $43 \times 10^{-6}\,\mathrm{dru_r}$ in the lowest energy bin, with a $8\,\mathrm{keV_r}$ slope,

(a) Cross Section

(b) Energy Distribution
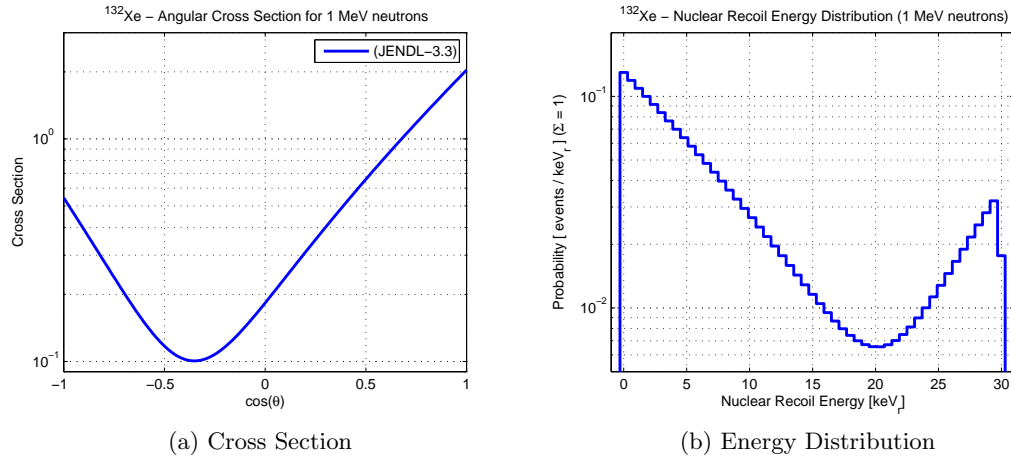
Figure 6.9: Nuclear recoil energy histogram for $1\,\mathrm{MeV}$ neutrons on $^{132}\mathrm{Xe}$

as shown in 6.10. The background event rate due to environmental fast neutrons is $\times 1/23$ smaller than the XENON10 sensitivity goal. The application of the standard XENON10 fiducial volume cut ($m_{fid} = 5.4\,\mathrm{kg}$) and a single scatters cut further reduces the background spectrum by 35% to $28 \times 10^{-6}\,\mathrm{dru_r}$ in the lowest energy bin, still with a $8\,\mathrm{keV_r}$ slope. The fiducial volume cut reduces the nuclear recoil spectrum both because the surrounding active Xe provides extra shielding, and because neutrons might scatter once in the fiducial volume and again in the surrounding active Xe. The simulation has a nuclear recoil energy threshold of $E_{\mathrm{nr}} > 0.2\,\mathrm{keV_r}$ to remove thermal neutrons. This single scatter event rate corresponds to 0.5 nuclear recoils *per year* for $E_{\mathrm{nr}} > 0.2\,\mathrm{keV_r}$, or 0.2 nuclear recoils per year in the range $5\,\mathrm{keV_r} < E_{\mathrm{nr}} < 25\,\mathrm{keV_r}$ in the XENON10 fiducial volume.

6.2.2 Muon Induced Neutrons

Cosmic ray muons contribute to the nuclear recoil background through the generation of neutrons in the shield materials and surrounding rock. Muon-induced neutrons can have energies well in excess of $E_{\mathrm{n}} > 10\,\mathrm{MeV}$ (called *high energy neutrons*), which cannot be effectively moderated by the Pb + polyethylene shield. The reduction of the muon-induced neutron background is achieved through the reduction of the muon flux by going deeper into the Earth, where the rock provides shielding against the cosmic muon flux. The choice of site becomes essential in achieving a low neutron background.
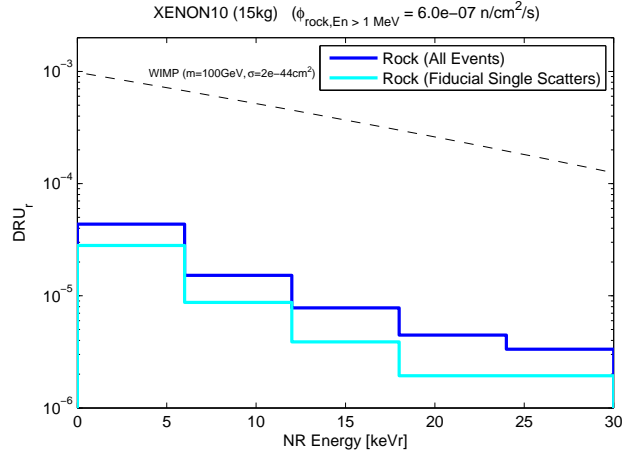
Figure 6.10: Nuclear recoil event rate due to fission and (α,n) neutrons from the cavern rock and concrete walls, using 1×10^{-6} n·cm^{-2}·s^{-1}, obtained from simulations of the XENON10 detector in the 20 cm polyethylene + 20 cm Pb shield.

6.2.2.1 Muon Flux

Cosmic rays include all stable charged particles, and it is composed primarily of protons ($\sim 90\%$), alpha particles ($\sim 9\%$) and heavier nuclei ($< 1\%$). Most of them have large kinetic energy (comparable to their rest mass), traveling at relativistic speeds, and hit the atmosphere with a flux of $1000\,\mathrm{m}^{-2}\mathrm{s}^{-1}$ [128]. Cosmic ray proton collisions with nuclei in the upper regions of the atmosphere ($\sim 15\,\mathrm{km}$) create charged mesons, which decay preferentially into muons and neutrinos (neutral mesons decay into photons and electrons). The primary channel of cosmic muon generation is pion decay

$$\pi^+ \;\rightarrow\; \mu^+ + \nu_\mu$$
$$\pi^- \;\rightarrow\; \mu^- + \nu_\mu$$

but kaons also contribute to the muon flux, with $\sim 5\%$ for $E_\mu < 100\,\mathrm{GeV}$, up to 8% of the flux at $\sim 100\,\mathrm{GeV}$, and increasing to 27% at the highest energies ($> 1\,\mathrm{TeV}$) [128]. Contribution from heavier mesons are negligible. Positively charged muon flux at sea level exceeds the negatively charged flux by $10\% - 40\%$ between $1\,\mathrm{GeV} - 10\,\mathrm{TeV}$[26]. This muon flux charge ratio is indicative of the fact that protons are more abundant than neutrons

in the primary cosmic ray showers, and that cosmic ray collisions produce an excess of positively charged mesons. Muons are generated in a cone-shaped shower within $1°$ of the path of the original cosmic ray particle. At sea level, the angular distribution at $E_\mu \sim 4\,\mathrm{GeV}$ is proportional to $\cos^2(\theta)$, becoming steeper for lower muon energies, and wider for higher energies $(E_\mu \gg 115\,\mathrm{GeV})$, approaching a $\sec(\theta)$ distribution for $\theta < 70°$ [26].

A review of the available data and results from analytical models for the muon spectrum in the atmosphere, at sea level and underground, are presented in [129]. At sea level, the mean muon energy is $\langle E_\mu \rangle \simeq 4\,\mathrm{GeV}$, and the energy spectrum below $E_\mu < 1\,\mathrm{GeV}$ is essentially flat. Above 1 GeV, the spectrum rolls off gradually until $\sim 100\,\mathrm{GeV}$, when it becomes very steep due to the lack of pions, which at energies above $E_\pi > 115\,\mathrm{GeV}$ tend to interact in the atmosphere before decaying into muons. The vertical muon flux at sea level for $E_\mu > 1\,\mathrm{GeV}$ is $\phi_{\mu,\theta=0} = 70\,\mathrm{m}^{-2}\mathrm{s}^{-1}\mathrm{sr}^{-1}$ [129], or $\phi_{\mu,\theta=0} = 1\,\mathrm{cm}^{-2}\mathrm{min}^{-1}$ for horizontal detectors.

The flux of muons underground has been extensively studied, with surveys presented by [130], [129], and [131]. The propagation models for muons in matter are detailed in [129]. The muon flux data for specific sites of interest to Dark Matter experiments, such as the Gran Sasso laboratory and the Homestake mine, is presented in [131].

The flux and energy distribution of muons at an underground site are functions of the density and composition of the rock overburden. In order to compare analytical models and measurements, results are usually normalized either to water-equivalent depth, which is the depth necessary in water to achieve the same attenuation of the muon flux (given in kilometers-water-equivalent, or km.w.e.), or to depth in "standard rock". The rock standard is defined as the overburden of the Cayuga Rock Salt Mine near Ithaca, New York [132]. It is characterized by its average density of $2.65\,\mathrm{g} \cdot \mathrm{cm}^{-3}$ and average atomic number 11, and the parameters $\langle Z^2/A \rangle = 5.5$ and $\langle Z/A \rangle = 0.5$ [133].

Muon passage through matter leads to energy loss through several processes: ionization of the propagation medium, Bremsstrahlung, e^+e^- pair production, and inelastic interactions with nuclei. Energy loss due to ionization varies little with energy, and in standard

rock it can be expressed as

$$\frac{dE_\mu}{dx} \simeq - \left[1.9 + 0.08 \cdot \ln \left(\frac{E_\mu}{\text{GeV}} \right) \right] \text{MeV} \cdot \text{cm}^2 \cdot \text{g}^{-1} \tag{6.12}$$

for $E_\mu > 10\,\text{GeV}$, with an accuracy of $\sim 5\%$ [134]. For most purposes, the mass stopping power of muons of sufficiently low energy (defined below in Eq. 6.17) can be described by the approximation for minimal-ionizing particles

$$\frac{dE_\mu}{dx} = -2\,\text{MeV} \cdot \text{cm}^2 \cdot \text{g}^{-1} \tag{6.13}$$

[128].

Although the energy loss through Bremsstrahlung, e^+e^- pair production and interactions with nuclei occur in discrete bursts along the muon path, the average energy loss is proportional to the muon energy E_μ and it can be characterized as a continuous function, such that

$$\frac{dE_\mu}{dx} = -\frac{E_\mu}{\xi_i}, \tag{6.14}$$

where ξ_i is the interaction coefficient for Bremsstrahlung (ξ_B), e^+e^- pair production(ξ_{pair}), or interactions with nuclei ($\xi_{hadronic}$). In general, the energy loss of muons is

$$\frac{dE_\mu}{dx} = -\alpha - \frac{E_\mu}{\xi}, \tag{6.15}$$

where α is the energy loss due to ionization, and $\frac{E_\mu}{\xi}$ is the energy loss by all other processes, such that

$$\xi^{-1} = \xi_B^{-1} + \xi_{pair}^{-1} + \xi_{hadronic}^{-1}. \tag{6.16}$$

For muon propagation through standard rock, $\alpha \simeq 2\,\text{MeV} \cdot \text{cm}^2 \cdot \text{g}^{-1}$ (from Eq. 6.13) and $\xi \simeq 2.5 \times 10^5\,\text{g} \cdot \text{cm}^{-2}$ [128] or $\xi \simeq 2.5\,\text{km.w.e.}$[132] for water-equivalent depth x. From Eq. 6.15, we can define a critical energy ϵ_μ below which muon energy loss is dominated by the ionization process:

$$\epsilon_\mu = \alpha \cdot \xi \simeq 500\,\text{GeV}. \tag{6.17}$$

Solving Eq. 6.15, we obtain the mean energy of muons with initial energy $E_{\mu 0}$ (at sea level) after traveling a distance x within a medium:

$$\langle E_\mu (x) \rangle = (E_{\mu 0} + \epsilon_\mu) \cdot e^{-x/\xi} - \epsilon_\mu. \tag{6.18}$$

The minimum energy for a muon to reach a depth h underground is then

$$E_{\mu,min} (h) = \epsilon_\mu \left(e^{h/\xi} - 1 \right), \tag{6.19}$$

so that low energy muons are *filtered out* as we move deeper underground. Not only is the muon flux reduced, its energy distribution is shifted to higher energies. Furthermore, the muon flux and the energy distribution underground can both be characterized by the mean muon energy at the given depth.

The muon flux at an underground site can be divided into two parts: *through-going muons*, high energy muons with enough momentum to keep traveling deeper, and *stopping muons*, a lower energy component of the flux, likely to deposit all its energy at the site depth. For large depths ($h > 1\,\mathrm{km.w.e.}$), the ratio of stopping muons to through-going muons becomes $< 0.5\%$.

The energy distribution of muons in underground sites has the same general shape, which can be fitted by

$$\frac{dN_\mu}{dE_\mu} = A \cdot e^{-(\gamma_\mu - 1) \cdot h/\xi} \cdot \left(E_\mu - \epsilon_\mu \left(1 - e^{-h/\xi} \right) \right)^{-\gamma_\mu} \tag{6.20}$$

[128, 131], where A is a normalization constant, and γ_μ is a fit parameter. For the underground sites considered in this work, the fit parameters have been calculated to be $\gamma_\mu = 3.7$, and the critical energy is $\epsilon_\mu = 693\,\mathrm{GeV}$ [132, 131]. From Eq. 6.20, the average muon energy can be calculated as

$$\langle E_\mu (h) \rangle = \frac{\epsilon_\mu \left(1 - e^{-h/\xi} \right)}{\gamma_\mu - 2} \tag{6.21}$$

(see Fig. 6.11). Table 6.6 lists the average muon energy at several underground sites,
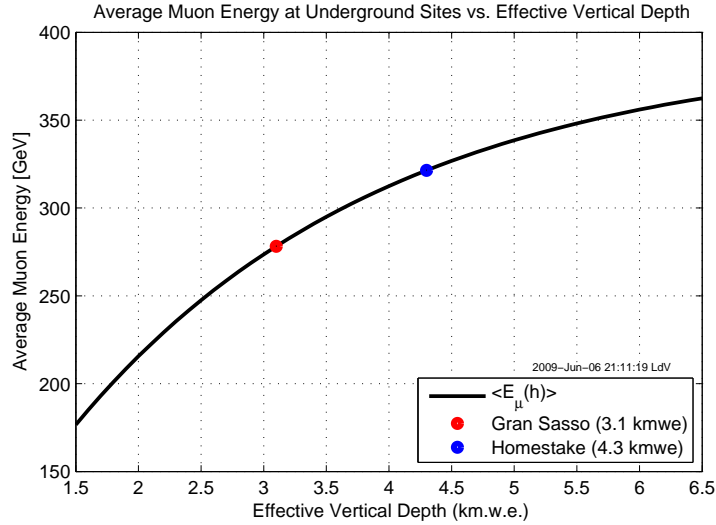
Figure 6.11: Average muon energy as a function of depth, calculated using Eq. 6.21 and the fit parameters $\epsilon_\mu = 693\,\text{GeV}$, $\xi = 2.5\,\text{km.w.e.}$, and $\gamma_\mu = 3.7$ [132]. The calculated values for Gran Sasso and Homestake mine are marked by dots.

Site	Average Muon Energy (GeV)	
	Calculated	Measured
WIPP	184	-
Soudan	212	-
Kamioka	219	-
Boulby	264	-
Gran Sasso	278	270 ± 18 [135]
Homestake	321	-
Sudbury	356	-

Table 6.6: Average muon energy at several underground sites, calculated using Eq. 6.21 and the fit parameters $\epsilon_\mu = 693\,\text{GeV}$, $\xi = 2.5\,\text{km.w.e.}$, and $\gamma_\mu = 3.7$ [132].

calculated using Eq. 6.21 and the fit parameters from [132].

The differential muon flux intensity underground can be expressed as a function of slant depth h by the empirical formula known as the Depth-Intensity-Relation (DIR):

$$I_\mu(h) = I_1 \cdot e^{-h/\lambda_1} + I_2 \cdot e^{-h/\lambda_2}, \tag{6.22}$$

valid for the range $1 - 10\,\text{km.w.e.}$ [129]. Measurements of the differential muon flux at several sites, as well as a fit to the DIR equation, are presented in [131]. For underground sites with flat-overburden, it is possible to rewrite the intensity as a function of vertical
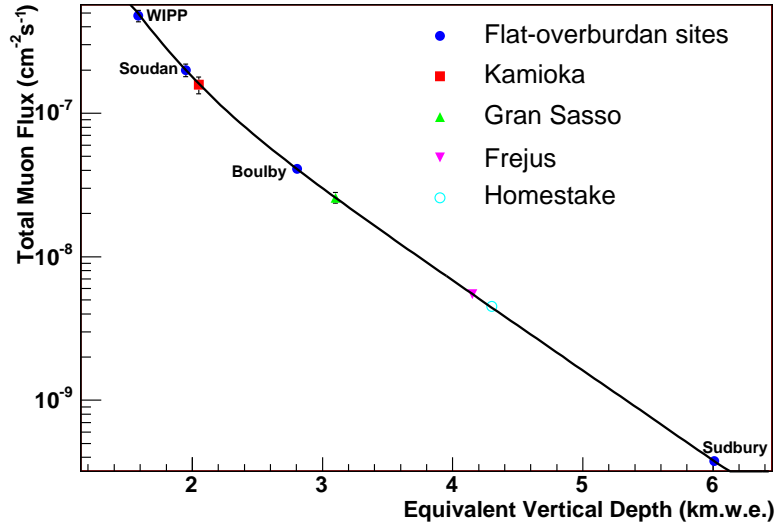
Figure 6.12: Total muon flux at several underground sites. The smooth line is a fit of the data using Eq. 6.23. Figure obtained from [131]

depth h_0 (in units of km.w.e.). Using flux measurements performed at a few sites with flat-overburden and well-known vertical depth, the DIR is rewritten as

$$I_\mu\left(h_0\right) = \left(67.97 \times 10^{-6} \cdot e^{-h_0/0.285} + 2.071 \times 10^{-6} \cdot e^{-h_0/0.698}\right) \text{ cm}^{-2}\text{s}^{-1}, \qquad (6.23)$$

[131]. The fit, as well as the total muon flux, is shown in Fig. 6.12. Fitting the total muon flux measurements for sites with non-flat overburden (i.e. mountains), one can find the effective vertical depth for each site, equivalent to a flat-overburden and measured in km.w.e.. Table 6.7 lists the total muon flux and the effective vertical depth of several sites.

In order to reduce the backgrounds due to cosmic ray muons, the XENON10 experiment was deployed at the Laboratori Nazionali del Gran Sasso, which has an effective depth of 3.1 km.w.e., and a total muon flux of $\phi_\mu = (2.58 \pm 0.3) \times 10^{-8} \text{ cm}^{-2}\text{s}^{-1}$, or $\phi_\mu \approx 1 \text{ m}^2 \text{ hr}^{-1}$, 6×10^{-5} times smaller than at the surface. The average muon energy at the laboratory, measured by the MACRO Collaboration, is $270 \pm 18 \text{ GeV}$ [135], consistent with the value calculated from Eq. 6.21 (see Table 6.7).

Site	Total Flux $\mu \cdot \text{cm}^{-2}\text{s}^{-1}$	Effective Depth km.w.e.
WIPP	$(4.77 \pm 0.9) \times 10^{-7}$[136]	1.585 ± 0.011
Soudan	$(2.0 \pm 0.2) \times 10^{-7}$[137]	1.95 ± 0.15
Kamioka	$(1.58 \pm 0.21) \times 10^{-7}$[138]	2.05 ± 0.15
Boulby	$(4.09 \pm 0.15) \times 10^{-8}$[139]	2.805 ± 0.015
Gran Sasso	$(2.58 \pm 0.3) \times 10^{-8}$[131]	3.1 ± 0.2
	$(2.78 \pm 0.2) \times 10^{-8}$[140]	3.05 ± 0.2
	$(3.22 \pm 0.2) \times 10^{-8}$[141]	2.96 ± 0.2
Homestake	$(4.4 \pm 0.1) \times 10^{-9}$[131]	4.3 ± 0.2
Sudbury	$(3.77 \pm 0.41) \times 10^{-10}$[142]	6.011 ± 0.1

Table 6.7: Total muon flux at several underground sites. Table obtained from [131]

6.2.2.2 μ-induced Neutron Flux

Muons contribute to the neutron background at underground sites through 4 possible processes:

1. Capture of negative stopping muons by nuclei. This process is subdominant to depths > 0.3 km.w.e., since the ratio of stopping to through-going muons is $< 1\%$ at these depths [131].

2. Inelastic scattering of muons on nuclei. The collision of high energy muons with a nucleus causes nuclear disintegration; this process is also called direct μ-induced spallation.

3. Inelastic scattering of hadrons from muon-induced nuclear showers. High energy collisions of muons and nuclei can produce mesons and nucleons, generating a particle shower, which in turn can collide with other nuclei. Neutrons are then produced by nucleon-induced or meson-induced spallation. Neutron production at Gran Sasso depth is dominated by secondary processes, such as π^- spallation, rather than direct muon spallation.

4. Photonuclear interaction by photons from muon-induced electromagnetic showers. This process becomes important for heavy materials (such as Pb), because the electromagnetic interaction cross section is proportional to Z^2/A.

Site	Flux (10^{-9} n·cm^{-2}·s^{-1})			
	Total	$> 1\,\mathrm{MeV}$	$> 10\,\mathrm{MeV}$	$> 100\,\mathrm{MeV}$
WIPP	34.1	10.78	7.51	1.557
Soudan	16.9	5.84	4.73	1.073
Kamioka	12.3	3.82	3.24	0.813
Boulby	4.86	1.34	1.11	0.277
Gran Sasso	2.72	0.81	0.73	0.201
Homestake *	0.54	-	0.28	0.059
Sudbury	0.054	0.020	0.018	0.005

Table 6.8: Total μ-induced neutron flux at several underground sites obtained from Monte Carlo simulations performed by [131], except for Homestake. *The Homestake total flux is calculated from Eq. 6.25; the fluxes for $E_n > 10\,\mathrm{MeV}$ and $E_n > 100\,\mathrm{MeV}$ are calculated from Eq. 6.27 (which breaks down for $E_n < 10\,\mathrm{MeV}$), assuming fit parameters similar to the ones for Gran Sasso, and using the mean muon energy for Homestake (see Table 6.7).

Muon interactions can occur in the rock and laboratory walls surrounding the detector, or in the detector components themselves, such as the shield. The total μ-induced neutron background is reduced as we move deeper underground, but not as fast as the muon flux intensity, since the number of neutrons produced increases with the muon energy. The number of neutrons produced in the surrounding rock per muon in a site at effective vertical depth h_0 is approximately [143]

$$N_{\mathrm{n}}\left(h_0\right) \propto \left\langle E_\mu\left(h_0\right)\right\rangle^{0.75}. \tag{6.24}$$

Monte Carlo simulations of the μ- induced neutron background at underground sites were performed in [144], [145] and [131], using FLUKA and Geant4. The neutron fluxes at the rock / cavern boundary for specific sites of interest, such as Gran Sasso and Homestake, are presented in[131], and reproduced on Table 6.8. The μ-induced neutron flux from rock at the several underground sites can be fitted as a function of effective vertical depth h_0, which is given by

$$\phi_{\mathrm{n}} = P_0 \cdot \left(\frac{P_1}{h_0}\right) \cdot e^{-h_0/P_1}, \tag{6.25}$$

where the empirical fit parameters are $P_0 = (4.0 \pm 1.1) \times 10^{-7}\,\mathrm{cm}^{-2}\mathrm{s}^{-1}$ and $P_1 = 0.86 \pm 0.05\,\mathrm{km.w.e.}$ [131], and is shown in Fig 6.13.
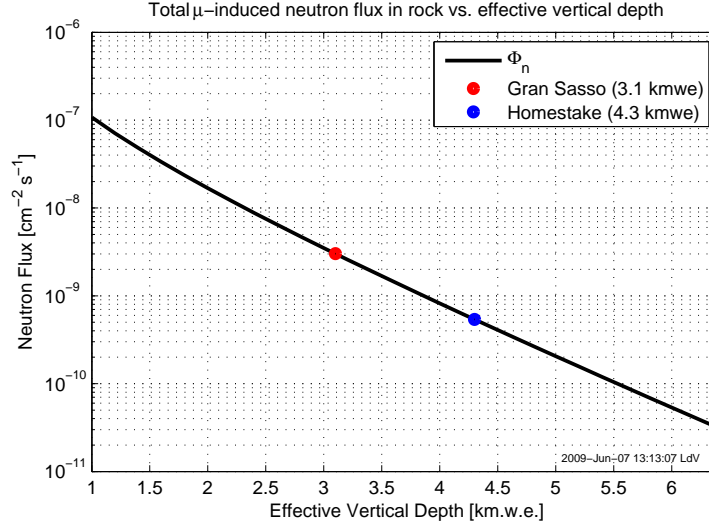
Figure 6.13: Total μ-induced neutron flux in rock vs. depth h , using Eq. 6.25. The circles indicate the values calculated for the depth of specific sites of interest: Gran Sasso and Homestake.

The energy spectrum of the μ-induced neutrons is fitted by the empirical function

$$\frac{dN}{dE_{\mathrm{n}}} = A_\mu \left(\frac{e^{-a_0 E_{\mathrm{n}}}}{E_{\mathrm{n}}} + B_\mu \left(E_\mu \right) e^{-a_0 E_{\mathrm{n}}} \right) \tag{6.26}$$

in [145], and a correction factor for high-energy neutrons is introduced by [131]:

$$\frac{dN}{dE_{\mathrm{n}}} = A_\mu \left(\frac{e^{-a_0 E_n}}{E_{\mathrm{n}}} + B_\mu \left(E_\mu \right) e^{-a_0 E_{\mathrm{n}}} \right) + a_2 E_{\mathrm{n}}^{-a_3} \tag{6.27}$$

where A_μ is a normalization constant, a_i are fit parameters, E_μ is the mean muon energy at the site, in GeV, and

$$B_\mu \left(E_\mu \right) = 0.344 - 0.641 \cdot e^{-0.014 \cdot E_\mu}, \tag{6.28}$$

valid for $E_n > 10 \, \mathrm{MeV}$. The a_i fit parameters for underground sites of interest in this work, and the resulting mean neutron energy, are given by [131] and are listed in Table 6.9. Although no fit parameters have been provided for the neutron flux at Homestake, the spectrum shape presents little variation with depth, and we calculate the Homestake μ-induced neutron spectrum by using the fit parameters for Gran Sasso. The resulting

Site	$\langle E_n \rangle$	a_0	a_1	a_2	a_3
Generic [145]	-	7	2	0	0
Soudan	76 MeV	7.333	2.105	-5.35×10^{-15}	2.893
Boulby	88 MeV	7.882	2.212	-2.342×10^{-14}	2.613
Gran Sasso	91 MeV	7.828	2.23	-7.505×10^{-15}	2.831

Table 6.9: Fit parameters for μ-induced neutron energy spectra at select underground sites, to be used in Eq. 6.27. Table obtained from [131].
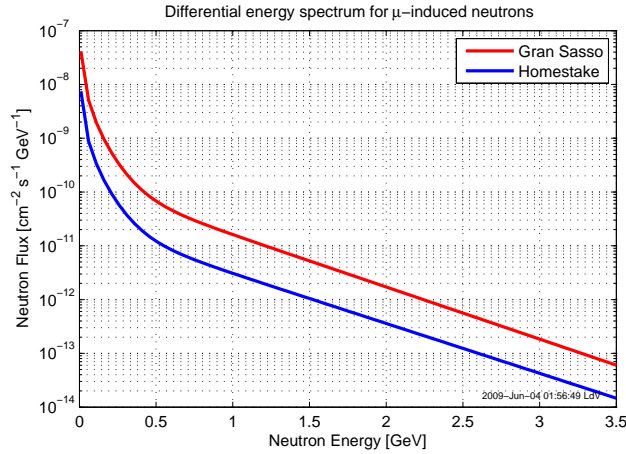
Figure 6.14: Differential energy spectrum for high energy μ-induced neutrons in rock at Gran Sasso and Homestake depths, calculated using Eq 6.27, and the fit parameters for Gran Sasso listed in Table 6.9.

spectrum is normalized using the total flux calculated from Eq. 6.25. The μ-induced neutron spectra for Gran Sasso and Homestake calculated from Eq. 6.27 are shown in Fig. 6.14.

Production of μ-induced neutrons can also occur in the detector components. Since the shield is the most massive component of the XENON10 experiment, it is the dominant source of neutrons inside the cavern. The production of neutrons in the shield is dependent on the chemical composition of the shielding material. The neutron yield per muon at the Gran Sasso depth for a few common materials is given in Fig. 6.15, along with a empirical fit, described by [131]:

$$\langle N_n \rangle = 4.54 \times 10^{-5} \cdot A^{0.81}\, \mathrm{n}/\left(\mu \cdot \mathrm{g} \cdot \mathrm{cm}^{-2}\right), \tag{6.29}$$
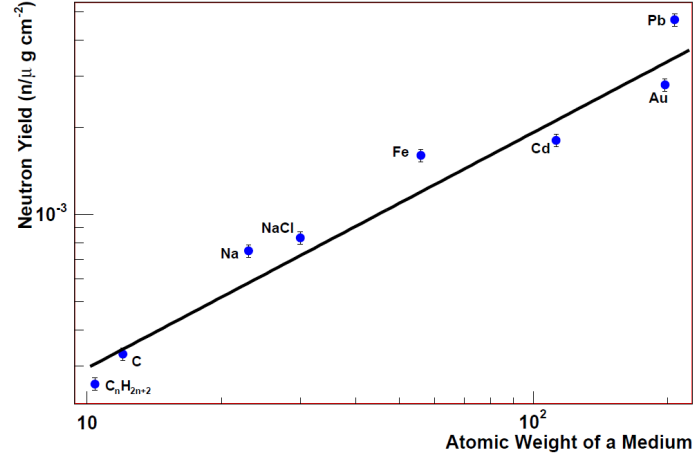
Figure 6.15: Neutron production rate vs. atomic weight of medium. Figure obtained from [131]

Material	Neutron Yield $[\text{n}/\left(\mu \cdot \text{g} \cdot \text{cm}^{-2}\right)]$
Pb	4.5×10^{-3}
Polyethylene	2.5×10^{-4}

Table 6.10: Neutron yield per muon for different shield materials at Gran Sasso depth, obtained from Monte Carlos simulations [131].

where A is the atomic weight of the medium. The neutron yield for the XENON10 shielding materials, Pb and polyethylene, are listed in Table 6.10. The total neutron production rate in detector components can be fitted using Eq. 6.25, and the fit parameters are listed in Table 6.11.

6.2.2.3 μ-induced Neutron Event Rate in XENON10

The XENON10 shield has a 20 cm polyethylene layer, inside the Pb shield, constructed with the purpose of reducing the neutron background. However, the attenuation factor for high energy neutrons $(E_n > 10\,\text{MeV})$ in the XENON10 shield is less than 1 order of magnitude.

Material	P_0	P_1
Pb	$(7.84 \pm 2.21) \times 10^{-8}$	0.86 ± 0.05
Polyethylene	$(6.89 \pm 1.95) \times 10^{-9}$	0.86 ± 0.05
Copper	$(2.97 \pm 0.838) \times 10^{-8}$	0.87 ± 0.05

Table 6.11: Fit parameters for μ-induced neutron production rate in a few common materials calculated at Gran Sasso depth, to be used in Eq. 6.25. Table obtained from [131].

E_n [MeV]	λ [cm]	Attenuation in 20 cm of polyethylene
1	4.17	$\times 1/121$
10	10	$\times 1/7.4$
100	59.5	$\times 1/1.4$

Table 6.12: Neutron attenuation length λ for polyethylene, and the attenuation factor for 20 cm polyethylene (thickness of XENON10 polyethylene shield). .

The attenuation length, as well as the attenuation factor for 20 cm of polyethylene for neutrons with different energies is listed in Table 6.12. From Table 6.8, we can see that high energy neutrons ($E_n > 10\,\mathrm{MeV}$) contribute significantly to the μ-induced neutron flux from rock at underground sites, $\sim 1/4$ of the total flux at Gran Sasso. Since the lower energy neutrons are strongly attenuated by the polyethylene shield, we need only concern ourselves with the high energy component of the μ-induced neutron flux external to the polyethylene shield, i.e. generated in the rock or in the Pb shield.

The XENON10 shield has external dimensions of $170\,\mathrm{cm} \times 170\,\mathrm{cm} \times 187.5\,\mathrm{cm}$, with a total surface area of $18.5\,\mathrm{m}^2$. The μ-induced neutron flux from the rock at Gran Sasso is $2.72 \times 10^{-9}\,\mathrm{n\cdot cm^{-2}\cdot s^{-1}}$. Assuming that its angular distribution is isotropic, this corresponds to an incident neutron rate of $5 \times 10^{-4}\,\mathrm{n \cdot s^{-1}}$ on the outer surface of the Pb shield.

μ-induced neutrons are also generated in the detector and shielding material. Because of the large mass of the shield ($m_{shield} \approx 35\,\mathrm{tonnes}$) relative to the mass of other detector components, we can safely assume that the μ-induced neutron contribution from the other components can be ignored. Using the neutron yield for the shield materials given in Table 6.10, we calculate the total neutron production rate in the shield to be $4 \times 10^{-3}\,\mathrm{n \cdot s^{-1}}$ and $1 \times 10^{-5}\,\mathrm{n \cdot s^{-1}}$ in the Pb and in the polyethylene, respectively (see Table 6.13). The μ-induced neutron production rate in the Pb is $\times 8$ larger than the integrated neutron flux incident in the Pb shield, and $\times 400$ larger than the neutron production rate in the polyethylene. Although there is additional shielding for the neutrons produced in the Pb relative to the neutrons produced in the polyethylene, the integrated neutron flux from the Pb will still be at least 1 order of magnitude larger than the integrated flux from the polyethylene. This can be seen from the attenuation expected from the polyethylene (listed in Table 6.12). If we take only the high energy component of the neutron background from

Source	Total background contribution
Rock	$5 \times 10^{-4}\,\mathrm{n \cdot s^{-1}}$
	(incident on the Pb shield outer surface)
Pb	$4 \times 10^{-3}\,\mathrm{n \cdot s^{-1}}$
	(generated in the Pb)
Polyethylene	$1 \times 10^{-5}\,\mathrm{n \cdot s^{-1}}$
	(generated in the polyethylene)

Table 6.13: μ-induced neutron background sources: cavern rock, Pb and polyethylene from XENON10 shield. The contributions from the sources is not equivalent - while the "rock" contribution is the integrated neutron flux incident on the Pb shield outer surface, the Pb and polyethylene contributions refer to the rate of neutrons generated inside the shielding material.

Pb (1/4 of the total flux), and apply an attenuation factor of $\times 1/7.5$, we are still left with a flux of $4 \times 10^{-3}\,\mathrm{n \cdot s^{-1}} \times 1/4 \times 1/7.5 = 1.3 \times 10^{-4}\,\mathrm{n \cdot s^{-1}}$, 1 order of magnitude larger than the neutron production rate in the polyethylene. Clearly, the μ-induced neutron generation in the Pb shield dominates the high energy neutron background for the XENON10 experiment, by at least 1 order of magnitude.

A simulation of the μ-induced neutrons generated in the Pb shield was performed in order to gauge the resulting detector event rate. The simulation generates neutrons in the Pb shield, with isotropic angular distribution, and assuming the initial neutron energy spectrum shown in Fig. 6.14 for Gran Sasso, with a flat distribution for $E_n < 10\,\mathrm{MeV}$. The flux is normalized to the neutron production rate shown in Table 6.13. The resulting event rate in the detector is $230\,\mu\mathrm{dru_r}$ at the lowest energy bin, reduced to $125\,\mu\mathrm{dru_r}$ after the application of the standard XENON10 fiducial volume cut ($m_{fid} = 5.4\,\mathrm{kg}$) and a single scatters cut. The spectrum is a featureless exponential decay with a slope of $13\,\mathrm{keV_r}$ (see Fig, 6.16), resulting on a total event rate in the detector of 1.7 nuclear recoils per year ($5\,\mathrm{keV_r} < E_{nr} < 25\,\mathrm{keV_r}$).

Of the neutrons that resulted in nuclear recoils in the detector with reasonable energies for detection ($E_{nr} > 5\,\mathrm{keV_r}$), 98% had initial energy $E_n > 10$ MeV and 57% had initial energy $E_n > 100$ MeV (see Table 6.14), demonstrating that the very high energy neutron background is a significant component of the neutron background in Dark Matter detectors.

Although we did not run a simulation for the μ-induced neutrons in rock and polyethy-
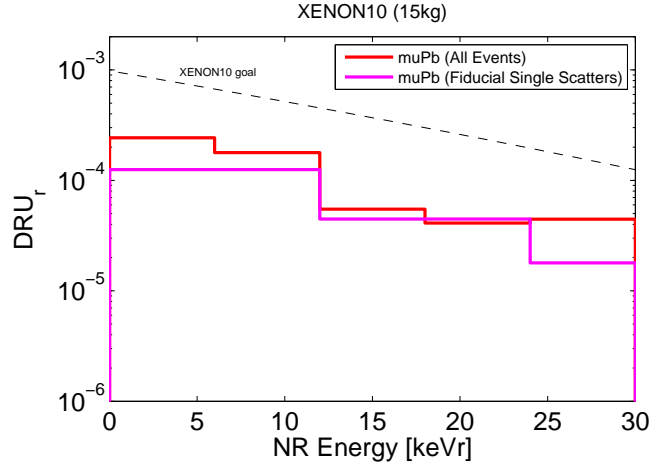
Figure 6.16: XENON10 event rate due to μ-induced neutrons generated in the Pb shield (20 cm shield thickness).

		Initial Neutron Energy		
		$E_n > 1$ MeV	$E_n > 10$ MeV	$E_n > 100$ MeV
Nuclear Recoil	$E_{nr} > 0\,\mathrm{keV_r}$	96%	80%	48%
Energy	$E_{nr} > 5\,\mathrm{keV_r}$	100%	98%	57%

Table 6.14: Initial energy distributions for μ-induced neutrons generated in the Pb shield (20 cm shield thickness) that deposited energy in the XENON10 fiducial volume (5.4 kg)

lene, we can set an upper limit on the XENON10 event rate for these background components. The integrated μ-induced neutron flux from rock incident on the Pb shield is $\times 1/8$ smaller than the neutron production rate in the Pb shield. Since we assume isotropic angular distribution of the neutrons produced in the Pb shield, we can estimate that $1/2$ will be going inwards. On the other hand, the additional Pb shielding for the neutron from rock (relative to neutrons produced inside the Pb) reduce the outside neutron flux. Thus, the μ-induced neutron flux from rock incident on the detector has to be $< 1/4$ the flux of μ-induced neutron generated in the Pb, and the event rate has to be < 0.43 nuclear recoils per year. Likewise, from the energy spectrum of the μ-induced neutrons and their attenuation length, we have seen that they cannot be attenuated by more than a factor $\times 1/4 \times 1/7.5 = \times 1/30$ by 20 cm of polyethylene shielding. Thus, the contribution from polyethylene is at most $\times 30$ greater than the contribution from Polyethylene *per emitted neutron*. Since the neutron production rate in the Pb shield is $\times 400$ larger than the rate in the polyethylene shield, the maximum event rate due to μ-induced neutrons from polyethy-

lene is $< 1/13$ the rate from Pb, or < 0.13 nuclear recoils per year.

6.2.3 Internal Neutron Sources

Neutrons are generated inside the detector shield through spontaneous fission of ^{238}U nuclei, and α-decay of ^{238}U and ^{232}Th, which generate neutrons through (α,n) reactions in the detector and PMT internal components. These are the same processes already described in Section 6.2.1. Both processes are directly dependent on the level of ^{238}U and ^{232}Th contamination in the detector components. The main components to be examined are the PMTs, the PMT bases, the cryostat, the HV feedthroughs, and the Teflon cylinder (which defines the active volume).

Using the data from the materials screening program discussed in Chapter 5, we can calculate the contamination level per PMT. Each PMT base in XENON10 contains 14 resistors, 3 capacitors, and 1 base plate, so that the average base radioactivity is $2.87 \, \text{mBq/PMT}$ and $0.74 \, \text{mBq/PMT}$ for the ^{238}U and ^{232}Th chains, respectively. The average contamination level of the XENON10 PMTs is $0.16 \, \text{mBq/PMT}$ and $0.14 \, \text{mBq/PMT}$ for the ^{238}U and ^{232}Th chains. The contamination levels for each of the PMT and base components is listed in Table 6.17, along with the combined total.

As discussed in Section 6.2.1, the neutron contribution from fission is dominated by ^{238}U, which has a branching ratio of 5.4×10^{-7}, and generates 2.07 neutrons per fission, leading to a neutron production rate of $1.1 \times 10^{-6} \, \text{n} \cdot \text{s}^{-1}/\text{Bq}$. The (α,n) neutron production rate is a function of the chemical composition of the target material for the α-particles, i.e. the components in the vicinity of the decays site. A comprehensive calculation of the neutron production rate in XENON10 detector components is presented in [64], where conservative upper limits on the neutron production rate are calculated and listed in Table 6.15. The main sources of the (α,n) neutrons are the PMTs and the cryostat, which have a yield of $< 4 \times 10^{-6} \, \text{n} \cdot \text{s}^{-1}/\text{Bq}$ and $< 4 \times 10^{-7} \, \text{n} \cdot \text{s}^{-1}/\text{Bq}$, respectively. The neutron production rate in the PMTs is $0.76 \, \text{n/PMT/year}$. The combined neutron production rate (PMTs + Cryostat) is < 28.85 neutrons per month, or < 346 neutrons per year. We can compare this rate to the μ-induced neutron production rate in the polyethylene of 315 neutrons per year

	neutron production per month		
	(α, n)		fission
Component	^{238}U	^{232}Th	^{238}U
89 PMTs^a	0.25	0.24	0.29
89 Bases^b	2.95	1.22	0.56
5 HV feed-through	2.61	0.91	2.12
143 kg stainless steel	2.94	1.75	11.72
10 kg Teflon	0.78	0.50	0.01
Total (by type)	9.53	4.62	14.70
Total: 28.85			

Table 6.15: Calculated neutron production per month in XENON10 from ^{238}U/^{232}Th activity in XENON10 components. Table obtained from [64].

(as seen in Table 6.13).

Monte Carlo simulations were performed to the event rate in the XENON10 detector due to the neutron background generated in the 2 major components: the steel cryostat and the PMTs (including bases), which are responsible for 56% and 20% of the neutron production rate, respectively. The other components should have negligible event rate in the detector due to small production rate (in the case of the Teflon) and due to placement (in the case of the HV feedthroughs). The simulations used the initial neutron spectrum depicted in Fig. 6.6, but normalized to the neutron production rate for (α,n) and fission neutrons in the cryostat and PMTs equal to the upper limits given by [64] and shown in Table 6.15. The simulation assumes isotropic angular distribution, and has an energy threshold of $0.2\,\mathrm{keV_r}$, to remove thermal neutrons.

The resulting event rate from both sources is very similar (see Fig. 6.17). The nuclear recoil spectrum for neutron emitted from the cryostat has a maximum of $130\,\mu\mathrm{dru_r}$ at the lowest energy bin and a slope of $11.3\,\mathrm{keV_r}$, reduced to $\sim 80\,\mu\mathrm{dru_r}$ at the lowest bin after the application of the standard XENON10 fiducial volume cut ($m_{fid} = 5.4\,\mathrm{kg}$) and the single scatters cut. The event rate due to PMT neutrons is $140\,\mu\mathrm{dru_r}$ at the lowest energy bin and a slope of $12\,\mathrm{keV_r}$, which is also reduced to $\sim 80\,\mu\mathrm{dru_r}$ after the application of the standard XENON10 fiducial volume cut and the single scatters cut. In each case, the slope of the energy distribution is kept after cuts. The corresponding total neutron event rate in the energy range of interest $(5-25\,\mathrm{keV_r})$ is ~ 0.8 and ~ 1 events/year for the cryostat and PMTs, respectively (see Table 6.1). This sets the upper limit on the neutron event rate in the XENON10 detector in the fiducial volume $(5.4\,\mathrm{kg})$ and in the energy range of interest
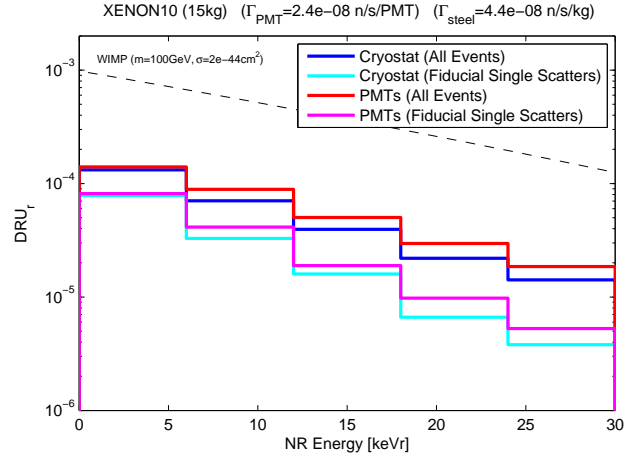
Figure 6.17: XENON10 event rate due (α,n) and fission neutrons emitted from 2 of the major components of the neutron background inside the shield: PMTs (including bases) and steel cryostat.

$(5 - 25 \, \mathrm{keV_r})$ at $< 1.8 \, \mathrm{events/year}$.

6.3 Gamma Backgrounds

The main source of background events in a liquid Xe detector are the environmental gamma radiation and the gammas emitted from the radioactive contaminants in the detector components. The gamma background generates an event rate orders of magnitude higher than the neutron background. The discrimination power of the dual-phase liquid Xe detector ameliorate the gamma background issue, as we can now immediately reject electron recoil (ER) events, as the WIMP signals we are searching for are nuclear recoil (NR) events. However, a fraction of the ER events still "leaks" into the NR signal window. From the XENON10 gamma and neutron calibration data, we estimate a leakage rate of 0.4% (see Section 2.1.4 for an description of the recoil type discrimination) - that is, 0.4% of gamma events are mis-identified as a nuclear recoil. Therefore, it is crucial to understand the gamma background.

6.3.1 The gamma background model

The first objective of the XENON10 gamma background model is to determine the event rate in the energy range of interest. The background model for the XENON10 detector
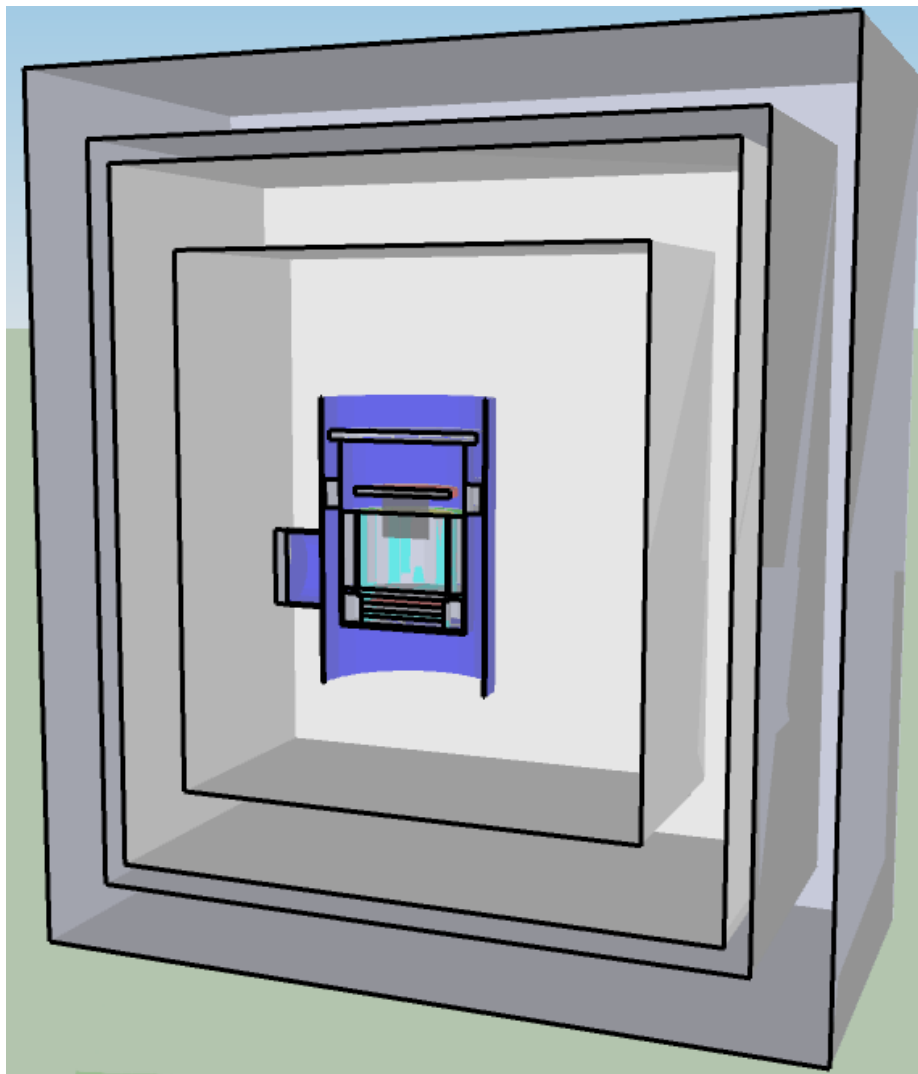
Figure 6.18: XENON10 Geant4 model: geometry used in Monte Carlo simulations of the XENON10 backgrounds.

is built in three parts: material screenings, Monte Carlo simulations, and matching the results from simulations to the observed background. The materials screening program aims to determine the contamination level of the materials used in the detector fabrication, so that the simulations use realistic sources and produce a realistic prediction for the event rate. Using the contamination levels from the screening program, we used Monte Carlo simulations run with Geant4 to model the expected gamma event rate in the XENON10 detector. A diagram of the detector and shield geometry used in Geant4 for the XENON10 background simulations is shown in Fig. 6.18.

The screening program, however, was not as comprehensive as desirable - although it did screen most of the PMTs, PMT base components, Pb bricks and samples of other material used in the detector, it did not measure the radioactive contamination levels of the stainless steel cryostat, which turned out to be a major radioactivity source. The cryostat steel radioactivity had to be deduced from the background run itself, by matching the data to the simulated event rate spectrum for the higher energy peaks - see Section 6.3.2.5 for details.

Simulations are run for several of the detector components, and for the several isotopes that make up the typical radioactive contamination in the simulated materials: ^{238}U and ^{232}Th decay chains, ^{60}Co, ^{40}K and ^{137}Cs. Simulations are run separately for each contaminant (decay chain or isotope), so that their activities can be adjusted individually. The decays of individual isotopes is not simulated; instead, the gammas from each decay are emitted individually, and normalized to match the branching ratio of each line. The gamma production rate assumes that each decay chain is in equilibrium, and it has isotropic angular distribution. For a diagram of the decay chain of ^{238}U and ^{232}Th, see Fig. 6.19. Because gammas from each line are emitted individually, it becomes difficult to apply coincident emission cuts, and these are not considered in this work. The resulting event rate in the detector is normalized to match the measured contamination levels for the given material.

Through the simulations of the various background sources, it was determined that the primary sources of gamma background for the XENON10 detector are ^{238}U and ^{232}Th decay chains and ^{40}K contamination in the R8520 PMTs and in the stainless steel cryostat. Other major contributions to the gamma background are ^{137}Cs deposited in the inner cryostat walls, Bremsstrahlung radiation due to ^{218}Pb contamination in the Pb shield, and beta decays of ^{85}Kr in the liquid Xe.

The event rate spectrum from all components is added up and compared to the gamma spectrum obtained from the WIMP search run labeled WS004, as shown in Fig. 6.20. The ultimate objective of the simulations is to provide a better understanding of the gamma background expected in the WIMP search window ($1.3 - 8\,\mathrm{keV_{ee}}$ at $L_y = 3\,\mathrm{phe/keV_{ee}}$), so we can use the full background spectrum in order to match the data to the simulation results
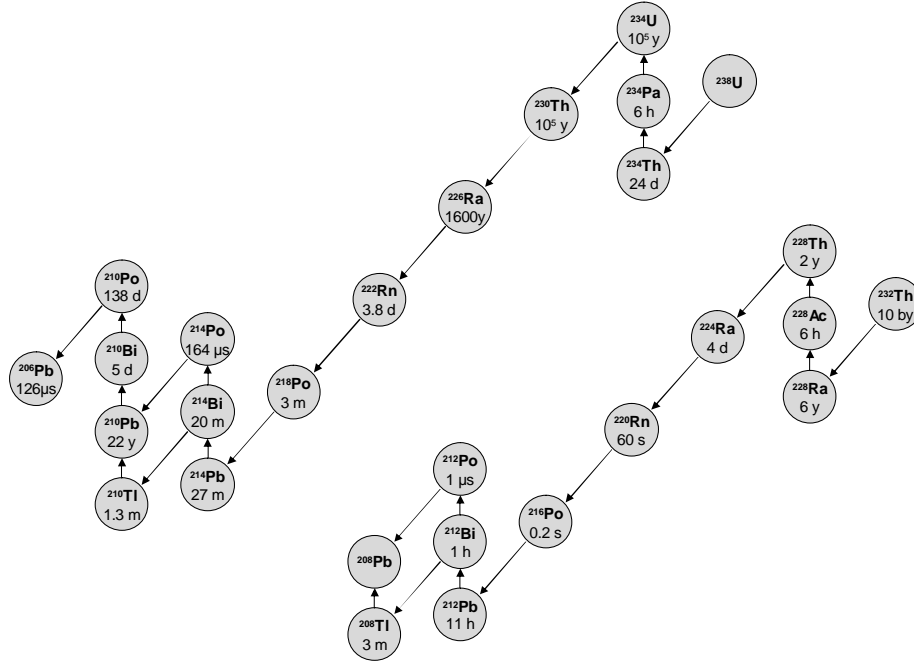
Figure 6.19: ^{238}U and ^{232}Th decay chains, indicating both the isotopes and their lifetimes.

at higher energies. The peaks in the $200 - 700 \, \mathrm{keV_{ee}}$ range are particularly interesting, as they provide features unique to different components, allowing us to match the results from a particular contaminant to the data in question.

The data spectrum used for comparison was obtained from the ROOT analysis of the run labeled WS004. Results for both the background simulations and the WIMP search data are always quoted as event rates in the fiducial volume used by the XENON10 detector during the WIMP search runs: $r < 8 \, \mathrm{cm}$ and $15 \, \mu\mathrm{s} < $ drift time$< 65 \, \mu\mathrm{s}$ ($2.8 \, \mathrm{cm} < z < 12.2 \, \mathrm{cm}$), with a total mass of 5.4 kg. The data is selected from a single quadrant from the active region, in order to reduce systematics in the energy scale calibration related to "sagging" of the grids. By choosing a single quadrant, the data is assured a more uniform field and energy scale. Basic quality cuts were also applied to the data to remove glitches and coincidentals, as discussed in Section 4.2.2.

6.3.1.1   Energy scale

From the data analysis point of view, the most important part of the background spectrum is the WIMP search window of $5 - 25 \, \mathrm{keV_r}$, corresponding to $1.3 - 8 \, \mathrm{keV_{ee}}$ for
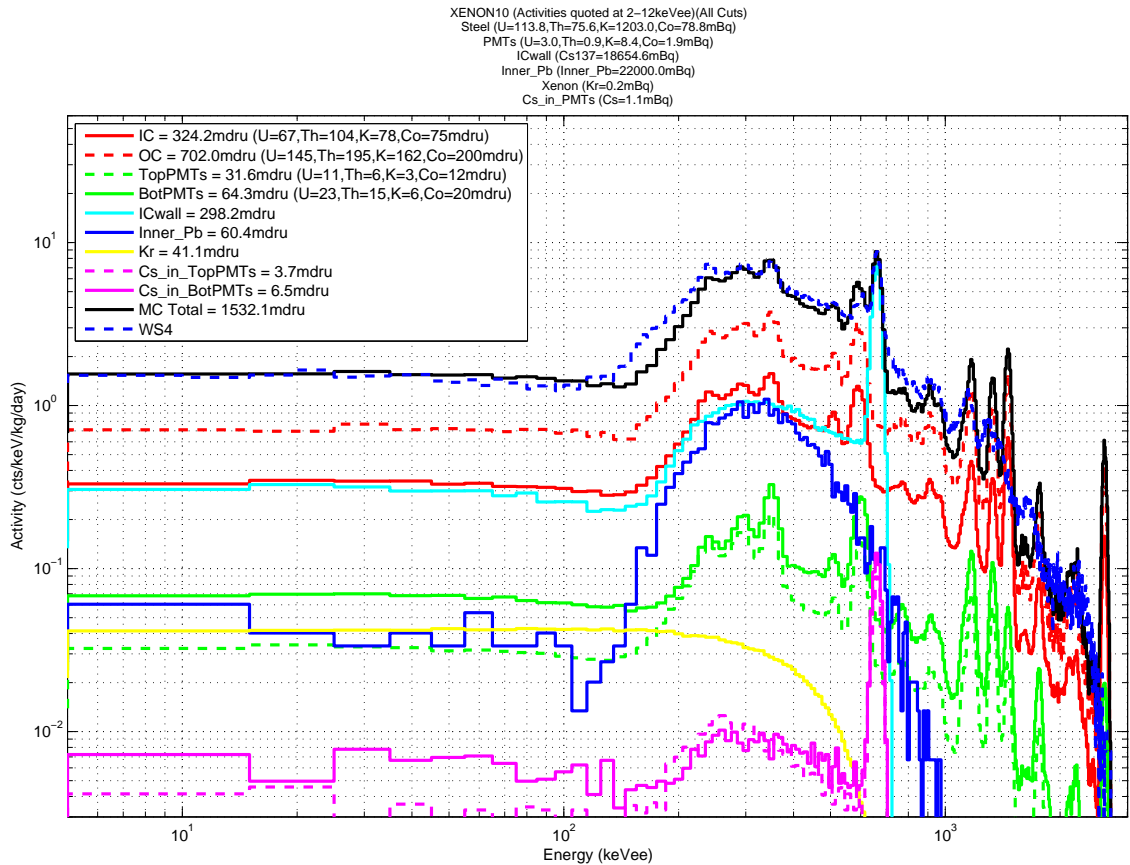
Figure 6.20: XENON10 Gamma Background: Electron recoil event rate in the XENON10 fiducial volume (5.4 kg), in the energy region $2 - 12 \, \mathrm{keV_{ee}}$, comparing the data observed during the WIMP search run (dashed blue line) and the spectra obtained from Monte Carlo simulation (solid black line, and miscellaneous color lines). The contamination levels shown are obtained through least-squares optimization routines that match the simulation spectra to the observed data. The simulations displayed in this plot use the "unconstrained" parameter set (or optimization set A) listed in Table 6.16. In the "unconstrained" optimization set (A), the Kr concentration in the liquid Xe and the levels for the steel in the cryostat were allowed to vary freely; the ^{210}Pb levels could vary within the 1σ boundaries; however, the contamination levels of the PMTs were fixed. The values for the PMTs, as well as the assumptions used for each source, are discussed in Section 6.3.2.

$L_y = 3\,\mathrm{phe/keV_{ee}}$, or $2 - 12\,\mathrm{keV_{ee}}$ for $L_y = 2.2\,\mathrm{phe/keV_{ee}}$. When comparing the data to the Monte Carlo spectrum, it is not advisable to use the S1 energy scale, as it tends to "contract" the energy bins at low energies and thus artificially increases the differential event rate. The data is plotted using the Combined Energy Scale (explained in Section 2.1.5), and it shows a differential event rate of $1.5\,\mathrm{dru_{ces}}$ at low energies $(5 - 105\,\mathrm{keV_{ces}})$. Both the data and the simulations show that gamma background spectrum is essentially flat below $150\,\mathrm{keV_{ces}}$. Event rates from the Monte Carlo simulation will be quoted in the $2 - 12\,\mathrm{keV_{ee}}$ range.

In order to compare the Monte Carlo spectrum to the data, it is necessary to apply an energy resolution to "smear out" the peaks in the Monte Carlo spectrum, and a single scatter cut that reproduces the efficiency of the cut in the data. Simulations produce very sharp peaks $(\Delta E < 1\,\mathrm{keV_{ee}})$, while the peaks in the data are Gaussian-shaped. The energy resolution of the data was determined from the ^{137}Cs 662 keV peak, the most prominent peak in the spectrum. The ^{137}Cs 662 keV peak has a resolution of $\sigma_E/E = 2.5\%$ in the data spectrum, using the Combined Energy Scale. The energy resolution in the XENON10 WIMP search run spectrum used here can be described as:

$$\frac{\sigma_E}{E} = \frac{2.02\%}{\sqrt{E/\mathrm{MeV}}}\,. \tag{6.30}$$

6.3.1.2 Single scatters cut

The single scatter cut used in the simulation is a cut on the spread of the energy-weighted spatial distribution of scatters for each event, i.e.

$$\sigma_x = \frac{\sum E_\mathrm{i} \cdot x_\mathrm{i}}{\sum E_\mathrm{i}}\,. \tag{6.31}$$

As discussed previously, the reason for this technique is that in Geant4 sometimes a single scatter is actually made up from several energy depositions (i.e. e^- tracks), and these small energy depositions should not be treated like individual scatters, but part of a single scatter. The single scatter cut parameters are limited by the z and r spatial resolution. To determine what threshold on σ_z and σ_r to apply, we compare the effect of the cut for several values of
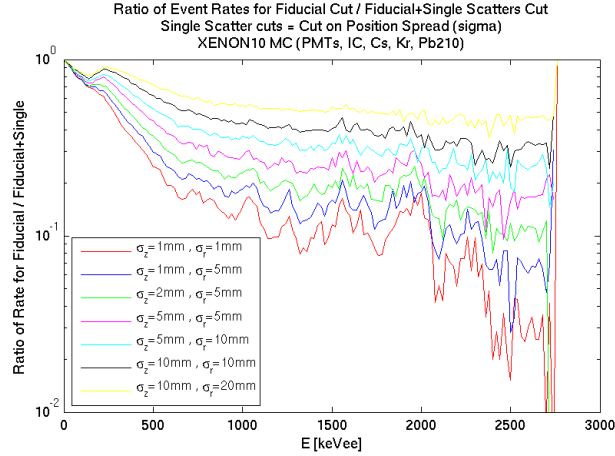
Figure 6.21: Effect of the single scatter cut on the gamma spectrum obtained from Monte Carlo simulation, plotted as the ratio of single scatters to total number of events versus energy. Each line corresponds to a different combination of thresholds on σ_r and σ_z, the energy-weighted spread of scatters for each event (as seen in Eq. 6.31). The XENON10 WIMP search data matches the ratio for $\sigma_z \leq 2\,\text{mm}$ and $\sigma_r \leq 5\,\text{mm}$.

sigma (see Fig. 6.21) and selected the thresholds that corresponded to the single scatter cut efficiency in the data for the ^{137}Cs 662 keV peak. The WIMP search data shows an efficiency of $25\% - 30\%$ for the single scatter cut on the 662 keV peak. To match this efficiency, we must use a cut with thresholds of $\sigma_z \leq 2\,\text{mm}$ and $\sigma_r \leq 5\,\text{mm}$ in the simulation, as seen in Fig. 6.21.

6.3.1.3 Saturation

The data spectrum shows a large loss of detection efficiency at high energies, due to saturation of the DAQ dynamic range. The average PMT gain for XENON10 is 2×10^6, which gives a pulse area of 16 mVns/phe before the $\times 10$ voltage amplifier, or 160 mVns/phe after the amplifier. The maximum voltage on a DAQ channel is 2 V; for a S2 pulse width of 800 ns, the maximum S2 pulse area is $2\,\text{V} \times 800\,\text{ns} = 1.6 \times 10^6\,\text{mVns}$. This means that each DAQ channel can see up to 10^4 phe. Adding all bottom PMTs, we have a maximum of 4×10^5 phe on the bottom array. The S2 light ratio for top and bottom PMTs is $\sim 60\%/40\%$, so that the maximum number of photoelectrons on both arrays is $\text{S2} = 10^6$ phe. The $\log_{10}(\text{S2/S1})$ ratio at high energy is less than 2.2, but we can make the approximation $\log_{10}(\text{S2/S1}) = 2.2$, and we get a maximum at $\text{S1} = 6000$ phe. Using the flat $\mathcal{L}_{eff} = 0.19$ and the light yield
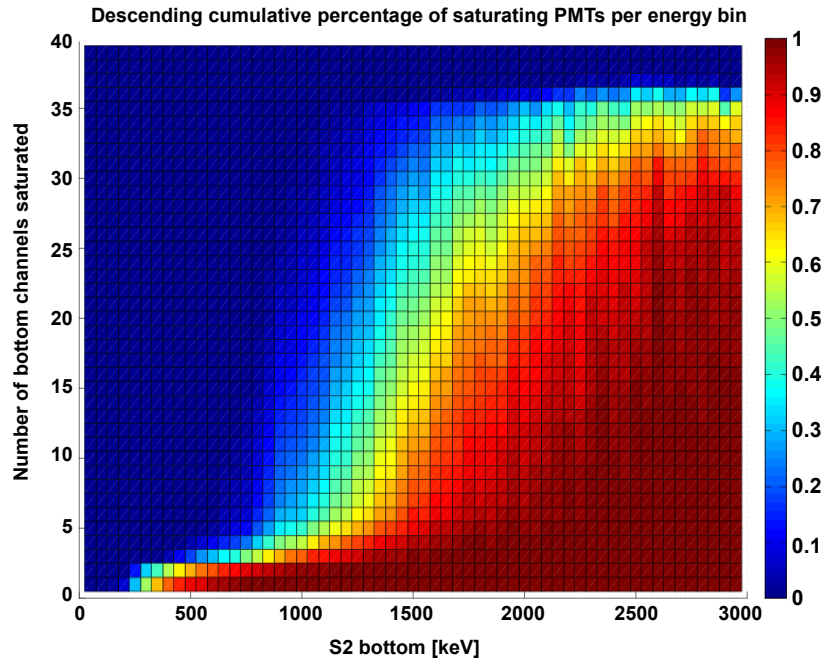
Figure 6.22: Saturation of bottom PMTs in the WIMP search run WS004. The plots shows the number of saturated PMTs vs. event energy, as estimated from the bottom S2 signal; the color indicates the fraction of events that show saturation. For example, the data for $500\,\mathrm{keV_{ee}}$ events show that 85% of events have saturation in at least 1 PMT, that 70% of events show saturation in 2 PMTs, and $< 30\%$ of events show saturation in 3 PMTs; no events in that energy range seem to show saturation in 4 or more PMTs.

of $3\,\mathrm{phe/keV_{ee}}$ to convert the maximum signal size into a maximum energy, we find that the saturation energy is $\sim 2000\,\mathrm{keV_{ee}}$, assuming that the light is evenly distributed on all PMTs. If the light distribution is not perfectly uniform, some channels will saturate before others. Fig. 6.22 shows the percentage of saturated channels for a given event energy. It shows that saturation becomes noticeable above $\sim 1500\,\mathrm{keV_{ee}}$, and it affects almost all channels at $\sim 2500\,\mathrm{keV_{ee}}$,. Therefore, we expect to lose efficiency at high energies - i.e. we start to lose events above $\sim 1500\,\mathrm{keV_{ee}}$.

6.3.1.4 Optimization

We apply the method of non-linear least squares fitting to match the simulated spectra to the data, in order to determine and verify the contamination levels for each detector component. The electron recoil spectrum for each isotope in each component is converted

to a single line, and each is normalized to a contamination level, thus resulting in 12 free parameters, listed in Table 6.16.

Some of these parameters are heavily constrained. For example, the PMT contamination levels are very well know, as they have been individually counted by the XENON10 screening program; their contamination levels are allowed to vary only by $\pm 10\%$. Others, such as the steel cryostat and the Kr contamination in the liquid Xe, have no reliable independent verification on their contamination levels, and are thus allowed to vary freely.

The best fit parameters (and the resulting χ^2) are listed in Table 6.16. Two sets of optimizations were performed: (A) the first set was more loosely constrained, i.e. the Kr could vary freely, and the ^{210}Pb levels could vary within the 1σ boundaries; (B) in the second set, both Kr and ^{210}Pb were fixed. In both optimization sets, the contamination levels of the PMTs were fixed, and the levels for the steel in the cryostat were allowed to vary freely. A weighting function was applied to force the optimization routine to give more importance to the low energy region, and less importance for the high energy region: $\times 5$ for $0 - 100\,\mathrm{keV_{ces}}$; $\times 1$ for $100 - 700\,\mathrm{keV_{ces}}$; and $\times 1/5$ for $> 700\,\mathrm{keV_{ces}}$. The parameters for each fit are listed in Table 6.16. The optimization set A produces a better fit (lower χ^2), and matches the data spectrum very well. It indicates, among other things, that the ^{210}Pb levels are higher than expected, and that the Kr contamination levels are not necessarily as high as we estimated. The optimization set B was included to illustrate the effect of fixing the value on the ^{210}Pb and, more importantly, on the Kr contamination in the Xe. A description of the major sources, the assumptions used for the simulation of each one of them, as well as the results obtained from the optimization routine, are discussed below in Section 6.3.2.

The resulting electron recoil spectrum is shown in Fig. 6.20, with individual lines for each background component and the XENON10 WIMP search data shown for comparison (dashed blue line). Note that most of the background events occur at high energies ($E > 150\,\mathrm{keV_{ces}}$), away from the energy range of interest ($1.3 - 8\,\mathrm{keV_{ee}}$). The spatial distribution of low energy events is shown in Fig. 6.23, which also illustrates the self-shielding properties of liquid Xe: the event rate in the core of the detector is $\times 1/4$ times smaller than at the

edges.

6.3.2 Major gamma background sources

6.3.2.1 PMTs

The most extensively characterized components of the gamma background are the PMTs. The radioactive contamination levels of the PMTs (and of the PMT base components) used in the XENON10 detector were assessed through the XENON10 screening program, detailed in Chapter 5.2. Out of the 89 Hamamatsu R8520 PMTs used in the XENON10 WIMP search run, 63 were counted (70% of the PMTs) at the LNGS screening facility, and their radioactivity levels are listed in Table 5.5. The remaining 26 PMTs were not counted, but all PMTs used in the XENON10 WIMP search run are manufactured in the same process, and thus their radioactivity is expected to match that of the counted PMTs. Each PMT is mounted on a Cirlex base plate, and each base contains 14 resistors and 3 capacitors. The Cirlex plates, resistors and capacitors used in the fabrication of the PMT bases were counted at the SOLO facility, and their radioactivity levels are listed in Table 5.7.

The average activity for the PMT and each of the base components, along with the total contamination level per PMT plus base, is shown in Table 6.17. The gamma background Monte Carlo simulations shown in Fig. 6.20 normalizes the event rate due to PMTs to these contamination levels. This indicates the most likely contribution of the PMT to the overall gamma background observed in the WIMP search run. The PMTs account for $110\,\mathrm{mdru_{ces}}$, or just 7.5% of the electron recoil rate in the range $2-12\,\mathrm{keV_{ces}}$. The biggest contributors to the PMT background are the ^{238}U chain and ^{60}Co, each making up 2.5% each of the total gamma event rate in the $2-12\,\mathrm{keV_{ces}}$ range.

Note, however, that not all PMTs were screened for their contamination levels. In order to estimate the possible effect of the 30% of PMTs that were not screened, we can look into the change in total radioactivity per PMT if we were to consider the remaining 30% to have contamination levels equal to the maximum levels observed. The maximum PMT contamination levels for the R8520 PMTs counted at LNGS are listed in Table 6.18, along

Source	Contaminant	Optimization set A (unconstrained Pb and Kr)		Optimization set B (constrained Pb and Kr)	
		Contamination Level [mBq/PMT or mBq/kg]	Event Rate [mdru$_{ces}$]	Contamination Levels [mBq/PMT or mBq/kg]	Event Rate [mdru$_{ces}$]
Steel Cryostat (inner and outer)	^{238}U	114	212	147	275
	^{232}Th	76	299	99	393
	^{40}K	1200	240	0.0	0
	^{60}Co	79	275	0.0	0
	^{137}Cs	18.6 Bq (integrated)	298	20.3 Bq (integrated)	324
PMTs (top and bottom)	^{238}U	3.00	34	3.0	34
	^{232}Th	0.88	21	0.88	21
	^{40}K	8.4	9	8.4	9
	^{60}Co	1.95	32	1.95	32
	^{137}Cs	1.1	10	1.1	10
Pb Shield	^{210}Pb	22×10^3	60	17×10^3	47
Liquid Xe	^{85}Kr	1 ppm	41	12 ppm	493
totals		$\chi^2 = 0.076$	1532	$\chi^2 = 0.131$	1638

Table 6.16: Radioactive contamination levels and ER event rate in the XENON10 fiducial volume (5.4 kg), in the energy region 2 – 12 keV$_{ces}$. The table shows the results from optimization routines to match the simulation spectra to the observed data during the WIMP search run (WS004). Two sets of optimizations were performed: (A) "unconstrained set", in which Kr could vary freely, and the ^{210}Pb levels could vary within the 1σ boundaries; (B) constrained set, in which both Kr and ^{210}Pb were fixed. In both optimization sets, the contamination levels of the PMTs were fixed, and the levels for the steel in the cryostat were allowed to vary freely. The fixed values for the PMTs, Kr and ^{210}Pb are discussed in Section 6.3.2. χ^2 indicates how good the fit is for the entire energy spectrum.
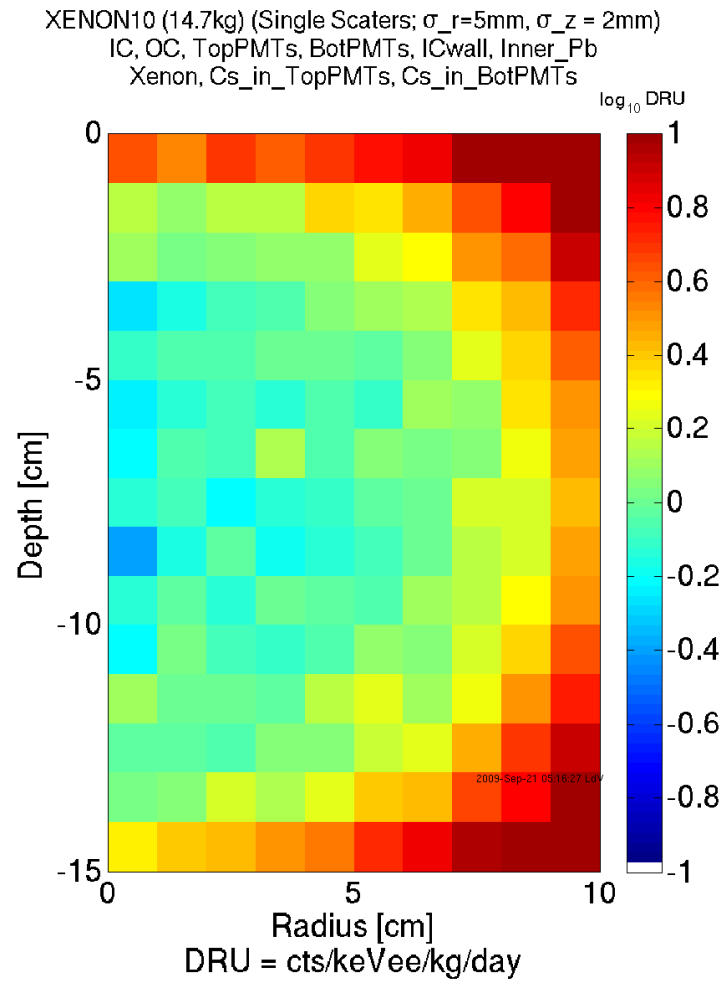
Figure 6.23: Spatial distribution of the single scatter electron recoil background events in XENON10 in the energy range $2 - 12 \, \text{keV}_{\text{ces}}$, from the simulation of the gamma background model. The event rate is given in dru ($1 \, \text{dru}_{\text{ces}} = 1 \, \text{event/kg/keV}_{\text{ces}}/\text{day}$), and is normalized to match the radioactive contamination levels listed in Table 6.16 (optimal set A).

	Average Contamination [mBq/unit]				
	^{238}U	^{232}Th	^{40}K	^{60}Co	^{137}Cs
PMTs	0.16	0.14	8.1	1.9	1.1
Cirlex bases	0.16	0.07	0.16	0.01	0.015
Resistors	0.078	0.014	0.003	0.0006	-
Capacitors	0.540	0.158	0.033	0.010	-
1 PMT + 1 Cirlex basis + 14 Resistors + 3 Capacitors	3.0	0.88	8.4	1.95	1.1

Table 6.17: PMT and base radioactive contamination levels measured by the XENON10 screening program and used in the gamma background Monte Carlo simulations. The data is collated form Tables 5.5 and 5.7.

	Maximum Contamination [mBq/unit]				
	^{238}U	^{232}Th	^{40}K	^{60}Co	^{137}Cs
PMTs	0.39	0.38	12	2.8	17
1 PMT + 1 Cirlex basis + 14 Resistors + 3 Capacitors	3.1	0.95	9.5	2.21	5.8

Table 6.18: Maximum PMT radioactive contamination levels measured by the XENON10 screening program at LNGS (see Table 5.5), and the resulting total activity per PMT plus base if we assume that the 26 PMTs not counted (out of a total of 89) had the maximum observed contamination levels. Note that this increases the total activity by $< 15\%$ for ^{238}U and ^{232}Th decay chains, ^{60}Co and ^{40}K, and a factor of $\times 5$ for the ^{137}Cs component. The base component data is the same shown in Table 6.17.

with the total activity per PMT when the maximum levels are considered. The increase in PMT radioactivity is $< 14\%$ for ^{238}U / ^{232}Th / ^{40}K / ^{60}Co, and cause a change in event rate due to PMTs to go from $110\,\mathrm{mdru_{ces}}$ to $120\,\mathrm{mdru_{ces}}$, which is $< 1\%$ increase in the total event rate. However, 5 of the R8520 PMTs measured at LNGS showed ^{137}Cs levels of $17\,\mathrm{mBq/PMT}$, a lot higher than the average of $1.1\,\mathrm{mBq/PMT}$. If we assume the 30% of PMTs that were not counted to have such high contamination levels, then we increase the average ^{137}Cs activity by $\times 5$, which in turn increases the total event rate by 3% in the energy range $2 - 12\,\mathrm{keV_{ces}}$.

6.3.2.2 ^{137}Cs contamination in detector components

The gamma background spectrum shows a peak at $662\,\mathrm{keV_{ee}}$, consistent with ^{137}Cs contamination. There are 2 models to account for the ^{137}Cs line in the spectrum: ^{137}Cs

contamination in the PMTs and ^{137}Cs on the steel in the (inner) cryostat.

^{137}Cs contamination in the PMTs

When using the average contamination levels for the PMTs, the ^{137}Cs peak at $662\,\mathrm{keV_{ee}}$ in the PMT simulation accounts for only 3% of the peak observed in the data. Even for a scenario in which the ^{137}Cs activity in the PMTs not counted is maximized and the total ^{137}Cs activity is $\times 5$ higher (see Table 6.18), the contribution from the PMT still only accounts for 14% of the $662\,\mathrm{keV}$ peak. Thus, at least 86% of the ^{137}Cs event rate must be due to ^{137}Cs contamination elsewhere in the detector.

^{137}Cs contamination in the cryostat

Another model for the contamination is that we have ^{137}Cs contamination in the cryostat steel walls. We model the ^{137}Cs as an even distribution of ^{137}Cs atoms on the inner surface of the inner steel cryostat. Fitting the peak due the ^{137}Cs in the simulation to the background data, we estimate a total ^{137}Cs activity of $\sim 20\,\mathrm{Bq}$ (integrated over the entire cryostat). If this activity is due to contamination in the steel mass of the inner cryostat only, this would correspond to a contamination level of $19\,\mathrm{Bq}/33\,\mathrm{kg} = 576\,\mathrm{mBq/kg}$. If this activity is due to contamination in the steel mass of the inner cryostat plus the outer cryostat, it corresponds to a contamination level of $19\,\mathrm{Bq}/25\,\mathrm{kg}/3 = 192\,\mathrm{mBq/kg}$ in the inner cryostat. We divide the activity by 3 because the ratio of contributions to the background spectrum coming from the inner and outer cryostat is approximately 1:2 at the energy range of the ^{137}Cs peak, as seen from the event rate of the $609\,\mathrm{keV}$ peak due to ^{214}Bi (from the ^{238}U chain) in the steel cryostat (see Fig. 6.20) - that is, the inner cryostat is responsible for 1/3 of the activity, and the outer cryostat for 2/3. Either of these contamination levels are unlikely, as we have not observed any steel samples with ^{137}Cs contamination levels in the hundreds of mBq/kg.

A final option is that the activity is due to ^{137}Cs coating the inside the inner steel cryostat - a thin layer of ^{137}Cs atoms over its inner surface. At an early stage of the XENON10 development, a CsI photocathode was installed at the bottom of the cryostat, taking the place of the bottom PMT array, which could have left a Cs deposit over the cryostat surface. The cryostat has an inner surface of $24 \times 10^3\,\mathrm{cm}^2$. In order to match

the observed activity, we must have $0.8\,\mathrm{mBq/cm^2}$, which corresponds to a surface density of $1.1 \times 10^6\,^{137}\mathrm{Cs}$ atoms/cm^2. Is this level of surface contamination realistic? We can compare it to the limits established by the US Nuclear Regulatory Commission [146] for acceptable levels of ^{137}Cs surface contamination: $830\,\mathrm{mBq/cm^2}$ and $170\,\mathrm{mBq/cm^2}$ ("fixed" and "removable", respectively). From this comparison, we can at least determine that the contamination level indicated by MC is not absurdly high. The ^{137}Cs layer on the inner surface of the cryostat is formed by ionic bonding of Cs$^+$ atoms to the oxide surface layer, typically $1\,\mu$m thick (note that "stainless" steel just means that it oxidizes less than regular steel, not that it does not oxidizes at all).

6.3.2.3 Pb Shield

The XENON10 shield (already described above in Section 6.1) consists of a 20 cm layer of HDPE ($\rho = 0.935\,\mathrm{g \cdot cm^{-3}}$) sheets inside a 20 cm layer of Pb bricks ($\rho = 11.340\,\mathrm{g \cdot cm^{-3}}$). Monte Carlo simulations of the $20\,\mathrm{cm}$ Pb shield indicate that the shield reduces the external gamma flux (with a typical γ energy spectrum from rock radioactivity) by a factor of $> 10^5$, while the HDPE sheets offer $\times 3$ attenuation. Standard rock gamma backgrounds (with the typical contamination levels listed in Table 7.12 on page 277) have a typical flux of

$$\Phi_{\gamma,\,\mathrm{standard\ rock}} \;=\; 1.7\,\gamma \cdot \mathrm{cm^{-2} \cdot s^{-1}},$$

which gets reduced in the shield cavity to $\Phi_{\gamma,\,\mathrm{cavity}} = 5.7 \times 10^{-6}\,\gamma \cdot \mathrm{cm^{-2} \cdot s^{-1}}$. The internal cavity of the shield has dimensions $90\,\mathrm{cm} \times 90\,\mathrm{cm} \times 107.5\,cm$, so that the integrated flux inside the cavity is $\int \Phi_{\gamma,\,\mathrm{cavity}} = 0.3\,\gamma \cdot \mathrm{s^{-1}}$. For comparison, the 89 R8520 PMTs generate a total of $1.5\,\gamma \cdot \mathrm{s^{-1}}$ (for a list of conversion factor from Bq to $\gamma \cdot \mathrm{s^{-1}}$, please consult Table 6.19). The contribution of the external gamma background to the electron recoil event rate is at most 1/5 of the PMT contribution. The Pb shield renders the external background subdominant, and it can clearly be ignored in the construction of the XENON10 background model.

However, we must also consider the activity due to radioactivity in the Pb bricks themselves. U and Th impurities are subdominant, but the ^{210}Pb content of the Pb bricks can

	γ/decay
^{238}U chain	2.261
^{232}Th chain	4.479
^{40}K	0.117
^{60}Co	2.0
^{137}Cs	0.851

Table 6.19: Gammas emitted per decay for the major radioactive contaminants in the materials in the XENON10 background model.

potentially be a major background source - as shown in Fig. 6.19, ^{210}Pb is part of the ^{238}U decay chain; it decays into ^{210}Bi, which is a β emitter with $Q_\beta = 1162$ keV. In order to reduce the ^{210}Pb radioactivity in a cost-effective manner, the Pb shield is divided into 2 layers - an outer layer of 15 cm with high levels of impurities, and a cleaner inner layer 5 cm thick - see Table 5.9 for the measured radioactivity levels.

Since the inner layer shields the detector from the outer layer, we need to simulate ^{210}Pb decays only in the inner layer, which has a radioactivity level of 17 ± 5 Bq/kg. For the Pb shield Monte Carlo simulations, we let Geant4 handle the decay ^{210}Pb and its daughter particles, instead of simply emitting the gamma lines individually, like we have done for all other isotopes. The simulation geometry does not include the Steel support structure. When calculating the optimal fit of the simulation to the data spectrum, we let the ^{210}Pb contamination level vary in the range $12 - 22$ Bq/kg.

6.3.2.4 Kr contamination in the liquid Xe

The effect of the Kr contamination in the XENON10 WIMP search run was determined by comparing the background event rate of the run with the event rate obtained by replacing the liquid Xe used with liquid Xe $\sim 1000\times$ cleaner. Kr contamination is a problem due to the presence of the ^{85}Kr isotope, which is a beta emitter with lifetime $\tau_{1/2} = 10.76$ years and $Q_\beta = 687$ keV. Kr is present in the atmosphere with concentration of 1.10 ± 0.01 ppm [147], with a ^{85}Kr contamination level of $N_{(^{85}Kr)} = 1.2 \times 10^{-11} N_{(Kr)}$. Commercially purified Xe has a Kr concentration level of a few ppb at best.

When simulating the effect of the Kr presence in the liquid Xe, we need to know the activity (Bq/kg) corresponding to a given concentration of Kr (ppm). For a Kr concentration

of $C = 1\,\mathrm{ppm}$, in 1 kg of Xe ($M_{Xe} = 1\,\mathrm{kg}$), the mass of Kr atoms in the liquid will be:

$$M_{Kr} = 83.8\,\mathrm{u} = 83.8 \cdot \frac{g}{N_A} = 83.8 \times 10^{-3} \cdot \frac{kg}{N_A} = 1.39 \times 10^{-25}\,\mathrm{kg}, \qquad (6.32)$$

so that we get the following number of Kr and ^{85}Kr atoms:

$$
\begin{aligned}
N_{(Kr)} &= C \cdot \frac{M_{Xe}}{M_{Kr}} = C \cdot \frac{1\,\mathrm{kg}}{1.39 \times 10^{-25}\,\mathrm{kg}} = 7.186 \times 10^{-24} \cdot C \\
N_{(^{85}Kr)} &= 1.2 \times 10^{-11} \cdot N_{(Kr)} = 1.2 \times 10^{-11} \times 7.186 \times 10^{-24} \cdot C = 8.62 \times 10^{13} \cdot C.
\end{aligned}
$$

The lifetime (τ) and decay constant (λ) of the ^{85}Kr isotope are calculated from the half-life ($\tau_{1/2}$):

$$
\begin{aligned}
\tau &= \frac{\tau_{1/2,\,^{85}Kr}}{\log 2} = 4.88 \times 10^{8}\,\mathrm{s} \\
\lambda &= \frac{1}{\tau} = 2.05 \times 10^{-9}\,\mathrm{s}^{-1}.
\end{aligned}
$$

Finally, the activity (in Bq/kg) is given by the decay rate in 1 kg of Xe:

$$
\begin{aligned}
\frac{1}{M_{Xe}} \frac{dN}{dt} \left[\frac{\mathrm{Bq}}{\mathrm{kg}} \right] &= -\lambda \cdot N_{(^{85}Kr)} \cdot \frac{1}{M_{Xe}} = \frac{2.05 \times 10^{-9}}{\mathrm{s \cdot kg}} \times 8.62 \times 10^{13} \cdot C \\
&= 0.176 \times 10^{6} \cdot \mathrm{s}^{-1} \cdot \mathrm{kg}^{-1} \cdot C \\
&= 0.176\,\mathrm{s}^{-1}\mathrm{kg}^{-1} \cdot C/\mathrm{ppm}.
\end{aligned}
$$

To calculate the event rate due to Kr, we perform a simulation of the ^{85}Kr contamination in the liquid Xe, and compare it to data with a high level of Kr, before the Xe was "cleaned" to reduce the Kr concentration. Fig. 6.24 shows such a comparison, and yields an efficiency of $40\,\mathrm{dru_{ee}/ppm}_{Kr}$ when using a flat energy scale of $2.1\,\mathrm{phe/keV_{ee}}$. Note that this energy scale is obtained from ^{137}Cs gamma calibration runs, and is only accurate at higher energies ($E > 300\,\mathrm{keV_{ee}}$). Applying a light yield more appropriate for the low energy range (i.e.~ $3\,\mathrm{phe/keV_{ee}}$), the Kr event rate becomes $60\,\mathrm{dru_{ee}/ppm}_{Kr}$.

The XENON10 purification system does not remove noble gases, so that the liquid Xe
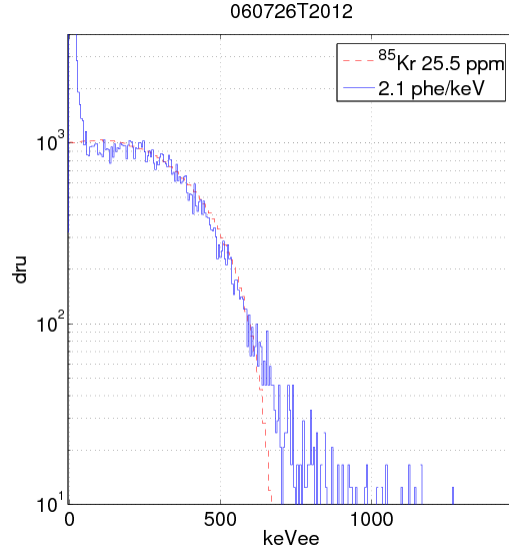
Figure 6.24: Electron recoil event rate due to ^{85}Kr contamination in the liquid Xe. The blue line indicates data acquired in XENON10 in a run prior to the WIMP search run; the red dashed line indicates the results form a Monte Carlo simulation with a Kr concentration of 25.5 ppm. The liquid Xe was subsequently changed for the WIMP search runs, with the new Xe having Kr contamination levels of ~ 1 ppm. $1 \text{ dru}_{ee} = 1 \text{ event/kg/keV}_{ee}/\text{day}$.

used in the WIMP search run was sent to the company Spectra Gas for purification and Kr removal. Spectra Gas quotes a Kr concentration after removal of ≤ 9 ppb, corresponding to an activity of 1.6 mBq/kg and an expected event rate of ≤ 540 mdru$_{ee}$. The Case Western Reserve University (CWRU) XENON10 group developed a Kr-removal system capable of achieving ppt concentration levels. After the end of the WIMP search run WS004 (April 2007), the liquid Xe from Spectra Gases was replaced by Xe purified with the CWRU method, with a concentration upper limit of < 3 ppt. Measurements of the background event rate show a reduction of $\times 2$ (see Fig. 6.25), suggesting that the Kr was responsible for $1/2$ of the total event rate observed in the WIMP search run, or 750 mdru$_{ee}$. This corresponds to a Kr concentration of 12 ppb.

However, fitting to the Kr event rate in simulations to the XENON10 WIMP search data (see Fig. 6.20) yields a much lower Kr concentration - if we allow the Kr parameter to vary freely, then the optimal fit is at 1 ppm. This suggests that other factors might have affected the event rate measured in XENON10 after the Case Xe was introduced. The only measurement available with the cleaner Xe were short runs in liquid level was below
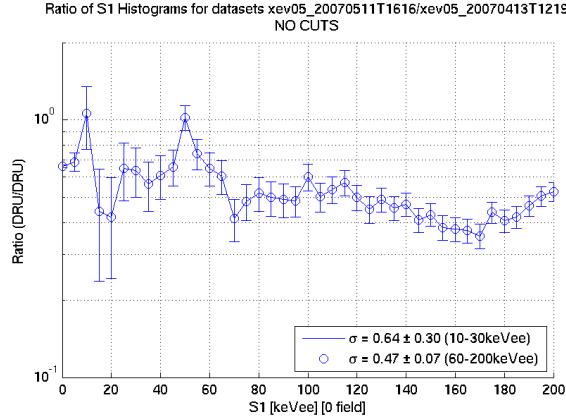
Figure 6.25: Kr reduction ratio, comparing the activity in XENON10 with the Spectra Gas Xe and the activity with Xe purified using the CWRU Kr-removal system, capable of achieving ppt concentration levels.

the grids; the fact that the active volume wasn't full and the liquid level wasn't set to its proper value could have affected either the background rate or the energy scale, introducing systematics in the measurement and in the Kr concentration estimate.

6.3.2.5   Cryostat

The cryostat could not be screened for practical reasons - since the chamber used to count materials in the screening facility was too small, counting the cryostat would be a very destructive procedure. The radioactive contamination levels of the steel cryostat are determined from a comparison of the data to the simulated spectrum for several high energy peaks. Specifically, we compared $511\,\mathrm{keV}$ and $583\,\mathrm{keV}$ peaks in the ^{232}Th chain; the triple peak of $242\,\mathrm{keV}$, $295\,\mathrm{keV}$ and $352\,\mathrm{keV}$ in the ^{238}U chain, and the $609\,\mathrm{keV}$, also from the ^{238}U chain; the $1461\,\mathrm{keV}$ peak from ^{40}K; the $1173\,\mathrm{keV}$ and the $1332\,\mathrm{keV}$ peaks from ^{60}Co; and the $662\,\mathrm{keV}$ peak from ^{137}Cs, already discussed above (Section 6.3.2.2). The contamination levels are adjusted until the peak sizes are matched to the data. In the case of the ^{40}K and ^{60}Co peaks, which are in an energy region with poor detection efficiency due to saturation, their contribution to the low energy continuum (due to Compton scatters) becomes a deciding factor in determining their radioactivity levels. In the fitting routines used to calculate the contamination levels in the steel by optimizing the match between data and simulation, all isotopes are allowed to vary freely. The simulations assume that the contamination levels

in the inner cryostat and in the outer cryostat are the same.

6.3.2.6   Rn in the Shield Cavity

The shield cavity was monitored for ^{222}Rn gas concentration. The lab where the XENON10 detector was deployed has a measured ^{222}Rn gas concentration of $\sim 130\,\mathrm{Bq/m^3}$. Monte Carlo simulations of the gamma background due to ^{222}Rn gas in the shield cavity with a contamination density of $100\,\mathrm{Bq/m^3}$ result in $300\,\mathrm{mdru_{ee}}$ in the $2-12\,\mathrm{keV_{ee}}$ energy range. A nitrogen gas purge was used to decrease the ^{222}Rn gas contamination by using the gas from boil-off from a liquid N dewar. During the main WIMP search runs (WS003 and WS004), the gas flow was kept at $1.5 \pm 0.1\,\mathrm{lpm}$. Measurements with a Durridge RAD-7 indicate that the average ^{222}Rn concentration in the shield cavity was $5.4 \pm 0.3\,\mathrm{mBq/m^3}$ (see Fig. 6.26). This concentration level leads to a differential event rate of $\sim 16\,\mathrm{mdru_{ee}}$ in the $2-12\,\mathrm{keV_{ee}}$ energy range, which is $6\times$ lower than the background due to PMTs. Note that this particular simulation was performed before the fiducial volume for XENON10 was finalized, and it has a 8.6 kg fiducial volume instead of the standard XENON10 fiducial volume of 5.4 kg. Since the final fiducial volume is even smaller, the resulting event rate will also be smaller. Since the event rate due to the ^{222}Rn gas contamination is subdominant, it is not included in the background simulation model used to compare to the data in this chapter.

6.4   Gamma-X

The electron recoil rejection (or discrimination) in XENON10 relies on the S2/S1 ratio in an event to classify it either as an electron or nuclear recoil event. In a plot of S2/S1 ratio vs. energy, the electron and nuclear recoil events neatly align themselves into 2 bands. In some cases, though, the gamma background can produce events with an S2/S1 ratio similar to that expected of nuclear recoil events. One way in which this can happen is through the natural fluctuation in the S1 and S2 sizes, which have Gaussian distributions, in such a way that the S2/S1 ratio falls within the nuclear recoil band. This effect is referred to as the "Gaussian leakage" (as in events "leaking down" from the ER to the NR band), and
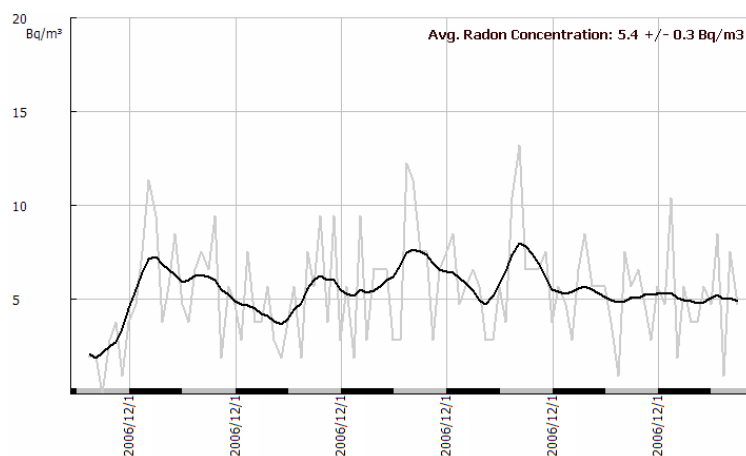
Figure 6.26: Radon concentration measurements in the XENON10 shield cavity taken shortly after the end of the WIMP search run (WS004), from 2006/12/13 to 2006/12/19. The measurements were made with a N_2 gas purge with flow rate of 1.5 lpm, the same rate used during the WIMP search runs.
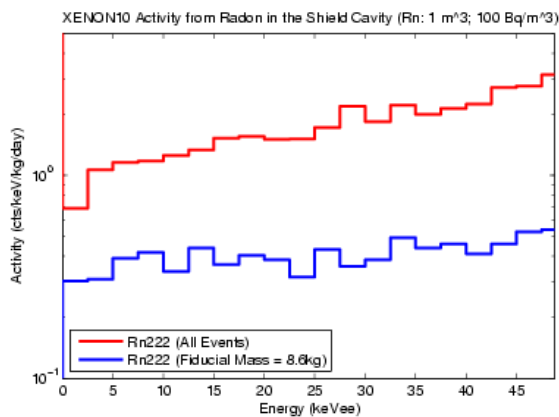
Figure 6.27: Electron recoil event rate in XENON10, obtained from Monte Carlo simulation of the ^{222}Rn contamination in the shield cavity, for a $100\,\text{mBq/m}^3$ concentration (to be used as a reference).

it has already been discussed in Section 2.1.4. Another possibility is a multiple scatter in which the S2 of one of the scatters is lost, thus causing the S2/S1 ratio of the event to also fall within the nuclear recoil band. These events might then be mis-identified as neutrons or WIMP events. Because of the danger that such misidentification brings to a rare event search, it is very important to understand how and at what rate these events happen.

In multiple scatter events in the active Xe region, S1 and S2 signals are generated for each scatter. Because of the speed of the light signals and the limitations of the digitizer resolution, S1 pulses from multiple scatters are indistinguishable; the S2 signals from each scatter, on the other hand, are readily distinguishable, specially if they are spatially separated in Z (see Fig. 6.28a). The XENON10 detector has a few regions with "non-active" Xe, in which scatters do not generate a charge signal. These regions are also called Charge Insensitive Regions. The light signal from a scatter in the non-active Xe might still reach the PMTs, in which case the scatter generates an S1 but no S2. Multiple scatter gamma events in which one (or more) scatter happens in the active region, and another scatter (or more) happens in one of the non-active Xe regions will yield a S2/S1 ratio lower than expected for a gamma event (see Fig. 6.28b), and it might be mis-identified as a nuclear recoil event. Such "fake" nuclear recoils events are called "Gamma-X" events, because of their unknown ("X") component in the non-active Xe regions.

6.4.1 Non-active Xe regions

The main regions of non-active Xe in the XENON10 detector are:

1. The Reverse Field Region (RFR), the space between the cathode grid and the bottom PMTs. In this region, the electric field is pointing in the direction opposite to the electric field in the active region, so that electrons are dragged down rather than up, and thus we do not collect charge signals from scatters in this region. The separation between the cathode and PMT windows is 1.2 cm, so that the liquid Xe mass in the RFR is 1.1 kg (compared to the active Xe mass of 14 kg). Light collection simulations of the XENON10 detector performed by R. Gomez [83, pp. 46] indicate that the light collection in the RFR is on average higher than the light collection in the active Xe

(a) Multiple Scatter event   (b) Gamma-X event
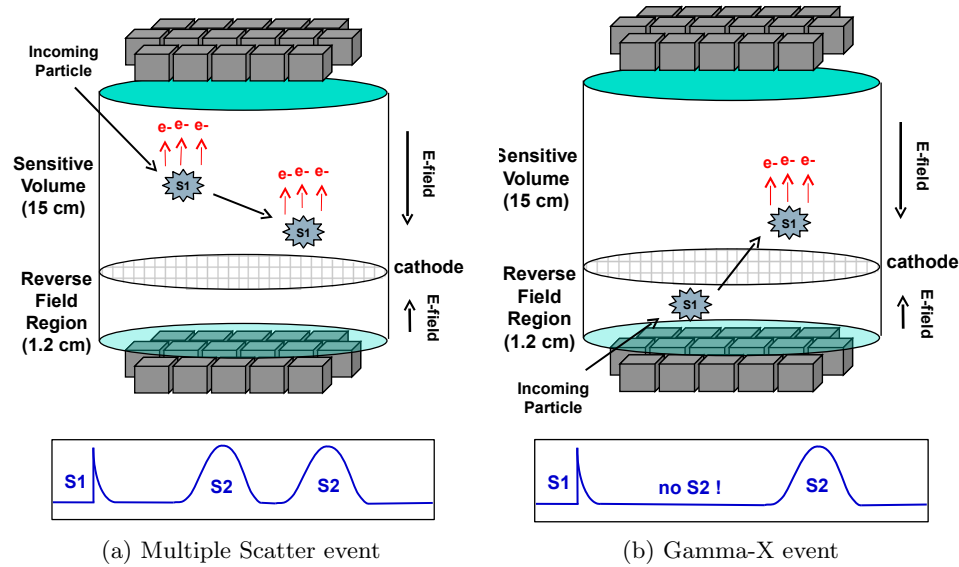
Figure 6.28: Diagrams of a typical a multiple scatter event and a "Gamma-X" event, in the Reverse Field Region (RFR). The Gamma-X event is a multiple scatter gamma event in which one (or more) scatter is in the active Xe region, and one (or more) scatter is in a non-active Xe region, so that the event produces a lower S2/S1 ratio than expected for gamma events.

region by $\sim 30\%$.

2. The region around and below the bottom PMTs. The XENON10 design left empty spaces around and below the bottom PMT array. In these regions, charge is not drifted, so that there are no S2 signals from scatters in this region. The total mass of non-active Xe around and below the bottom PMTs is $\sim 6.3\,\mathrm{kg}$ - approximately $1.3\,\mathrm{kg}$ directly below the bottom PMT array, and $5\,\mathrm{kg}$ around it (see Fig. 6.29). The region around the PMTs do not have direct line-of-sight to the PMTs, as they are located under the Teflon can wall. The region behind the PMTs also do not have direct line-of-sight to the PMT faces. Thus, the light coupling between these 2 regions and the PMTs is very weak: XENON10 light collection simulations indicate that the average light collection in this region is $< 2.5\%$. As seen in Fig. 6.20, most of the scatters in the liquid Xe are high energy interactions, with $E > 150\,\mathrm{keV_{ee}}$. Due to the poor light collection, these high energy interactions register as small energy events, thus "pushing down" these events into the energy range of interest, and effectively

increasing the rate of events with this topology in the low energy range. From the point of view of Gamma-X events, it is desirable that the light collection for scatters in this region is either high enough ($\geq 50\%$) that the events fall outside the energy range, or low enough ($\leq 1\%$) that the region around and below the PMTs is effectively decoupled from the PMTs. The behavior of the Gamma-X event rate as we vary the light collection is studied below, in Section 6.4.2.

3. The Charge Loss region, adjacent to the inner surface of the Teflon cylinder, with a skin thickness of 2 mm. The charge released in a scatter is drifted upwards in the XENON10 active volume by the field applied between the cathode and anode grids ($\mathcal{E}_d = 0.73\,\mathrm{kV} \cdot \mathrm{cm}^{-1}$). The active volume is surrounded by (and defined by) the Teflon can walls, which is a very good dielectric. Field shaping rings are built into the Teflon can walls to make the field lines in the active volume more uniform. The charge released close to the Teflon wall will lose some of its electrons as it drifts up. Moreover, the field lines next to the Teflon walls actually curve outwards, thus causing charges released by interactions very close to the wall to be completely lost. Electric field simulations using the Comsol multiphysics software show that there is $\sim 100\%$ charge loss in a $2\,\mathrm{mm}$ thick region adjacent to the Teflon walls[83, pp. 44]. Although the Charge Loss region comprises only $0.55\,\mathrm{kg}$ of the Xe mass, the outer regions of the liquid Xe are prone to a greater event rate than the rest of the active volume (see Fig. 6.23), so that the contribution of this region for the total Gamma-X rate cannot be ignored. The behavior of the Gamma-X background in this region is further detailed in Section 6.4.2.

A number of other regions have been identified during the running of the XENON10 detector, such as a small pocket of liquid Xe in a hole made in the Teflon wall for a resistor chain used by the field shaping rings. However, these other regions were deemed small and are not included in the XENON10 model, and thus are not considered for their contribution to the Gamma-X background. Fig. 6.29 depicts a diagram of the XENON10 active and non-active Xe volumes.
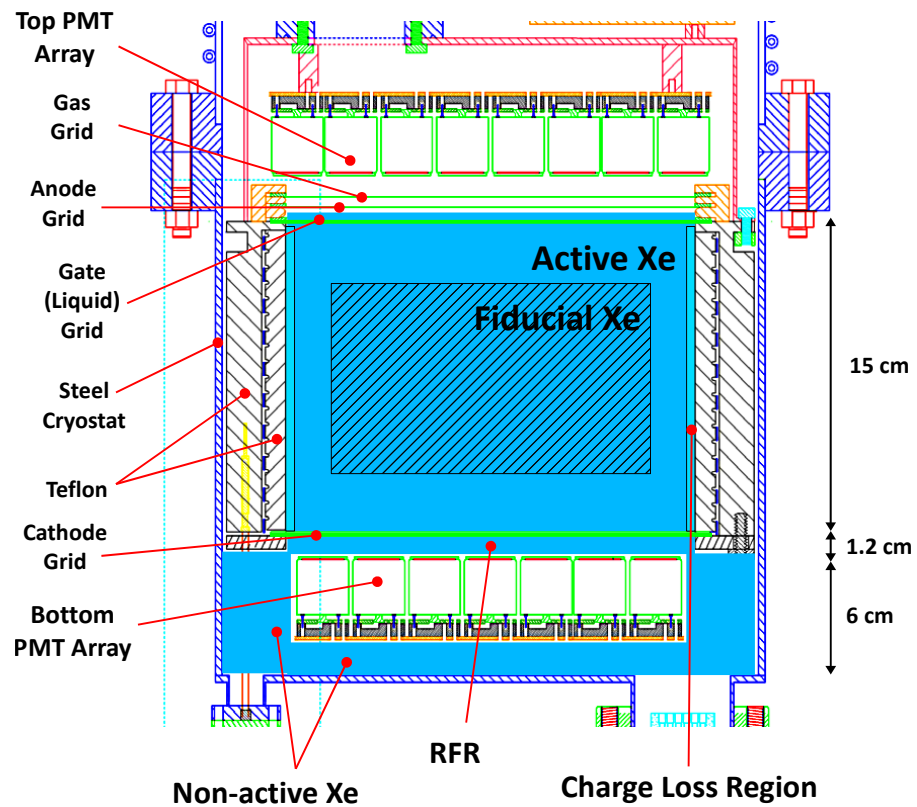
Figure 6.29: Diagram of the XENON10 active and non-active Xe volumes used for the Gamma-X background simulations in Geant4.

6.4.2 Light and charge collection parameters

Monte Carlo simulation were performed to determine the level of Gamma-X contamination in the XENON10 WIMP data. The Monte Carlo simulation of the XENON10 Gamma-X events have the same geometry used for the XENON10 gamma background depicted in Fig. 6.18. The Gamma-X background simulations were performed using only the most active sources in the detector: the steel cryostat (including the ^{137}Cs component) and the PMTs. The activities were matched to those found in best fit to the XENON10 background, listed in Table 6.16, and the sources have the same spectra shown in Fig. 6.20. The Monte Carlo simulations are designed to determine what fraction of gamma events are Gamma-X events, the plots depicting the results show the ratio of Gamma-X events to single scatter electron recoil events in each energy bin.

The criteria for identification of an event as a Gamma-X event in the simulation mimics the process in the physical detector, with the objective of identifying events that would fall within the nuclear recoil band. The simulation records quantities equivalent to the S1 and S2 from the data:

$$
\begin{aligned}
S1_{MC} &= \sum_i E_i \cdot L_{coll}(i) \\
S2_{MC} &= \sum_i E_i \cdot Q_{coll}(i) \,,
\end{aligned}
$$

which sums the energy deposited for each scatter E_i, multiplied by a light collection factor (L_{coll}) or a charge collection factor (Q_{coll}) to compute $S1_{MC}$ and $S2_{Mc}$. The nuclear recoil band center is approximately $\times 1/2$ lower in S2/S1 than the electron recoil band center in $S2/S1$ for XENON10 2.1.4. Since the WIMP search window in the S2/S1 vs. energy plot contains only the lower half of the NR band, only the Gamma-X events with a S2/S1 ratio that fall below the center of the NR band present a problem. The criterion for tagging an event as a Gamma-X event in the simulation is then:

$$
\text{Gamma-X}: \quad \frac{S2_{MC}}{S1_{MC}} < \frac{1}{2}. \tag{6.33}
$$
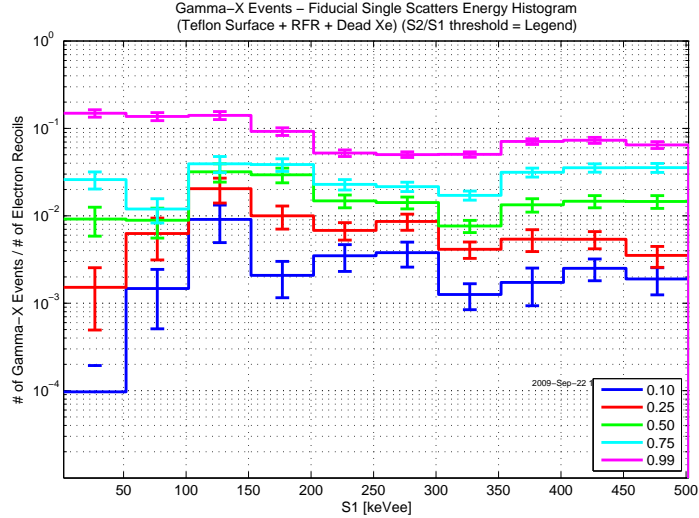
Figure 6.30: Gamma-X event rate vs. S2/S1 threshold: Ratio of Gamma-X event rate to ER event rate vs. energy, for events with scatters in the combined charge insensitive regions (depicted in Fig. 6.29), obtained from the XENON10 gamma background simulation. Each line corresponds to a value for the $S2_{MC}/S1_{MC}$ threshold for Gamma-X events. The light and charge collection factors (L_{coll}, Q_{coll}) assumed by the simulation results shown here are listed on Table 6.21. The simulation uses the gamma background emitted from the steel cryostat and PMTs, with the initial energy spectra shown in Fig. 6.20.

The behavior of the Gamma-X rate for several value of $S2_{MC}/S1_{MC}$ threshold is shown in Fig. 6.30. Increasing the threshold is equivalent to increasing the acceptance of the WIMP search box - it is not surprising that as we increase the threshold, we become more vulnerable to Gamma-X contamination in the data.

The light collection (L_{coll}) and charge collection (Q_{coll}) factors for each region in the detector are obtained from electric field simulations using Comsol and light response simulations using Geant4 [83], and are normalized so that $L_{coll} = 1$ and $Q_{coll} = 1$ averaged over the active Xe region. The resulting factors are listed in Table 6.20. While the factors for the Reverse Field Region (RFR) are well known, neither the light collection factor for the non-active Xe region below and around the PMTs nor the charge collection factor for the Charge Loss region are well-defined. A series of simulations are performed for each of the non-active Xe regions, and plot the behavior of the Gamma-X event rate as we change either L_{coll} or Q_{coll}. The results are shown in Fig. 6.31, Fig. 6.32 and Fig. 6.33.

For both the RFR and the area around and below the bottom PMTs, the charge collec-

	L_{coll}	Q_{coll}
Active Xe Region	1	1
Reverse Field Region	1.3	0
Around and below bottom PMTs	< 0.025	0
Charge Loss Region	1	< 1

Table 6.20: Light collection (L_{coll}) and charge collection (Q_{coll}) factors for XENON10 active and non-active Xe regions, normalized so that $L_{coll} = 1$ and $Q_{coll} = 1$ for the active Xe region, obtained from electric field simulations using Comsol and light response simulations using Geant4 [83].
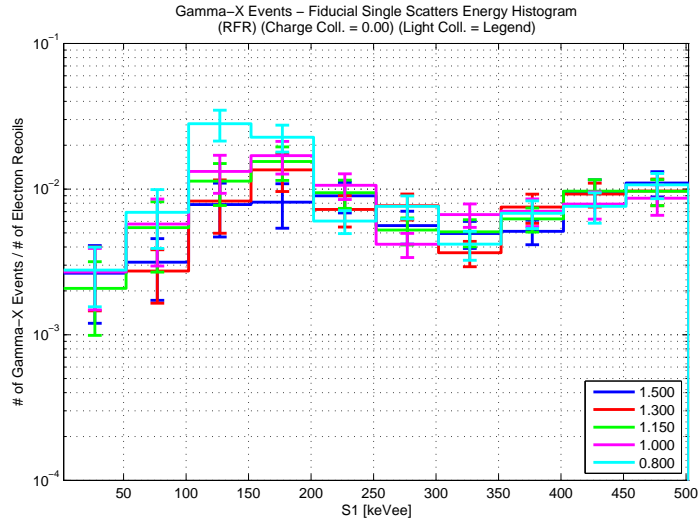
Figure 6.31: Gamma-X RFR event rate vs. Light Collection: Ratio of Gamma-X event rate to ER event rate vs. energy, for events with scatters in the Reverse Field Region (RFR), from the XENON10 gamma background simulation. Each line corresponds to a value for Light Collection (L_{coll}). The simulation assumes that the charge collection in the region is $Q_{coll} = 0$, and it uses the gamma background emitted from the steel cryostat and PMTs, with the initial energy spectra shown in Fig. 6.20.
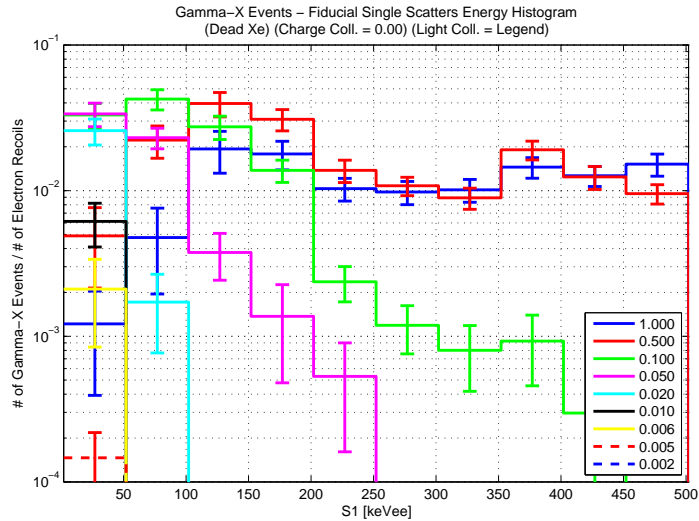
Figure 6.32: Gamma-X event rate around and below PMTs vs. Light Collection: Ratio of Gamma-X event rate to ER event rate vs energy, for events with scatters in the region around and below the Bottom PMTs (depicted in Fig. 6.29), obtained from the XENON10 gamma background simulation. Each line corresponds to a value for Light Collection (L_{coll}). The simulation assumes that the charge collection in the region is $Q_{coll} = 0$, and it uses the gamma background emitted from the steel cryostat and PMTs, with the initial energy spectra shown in Fig. 6.20.
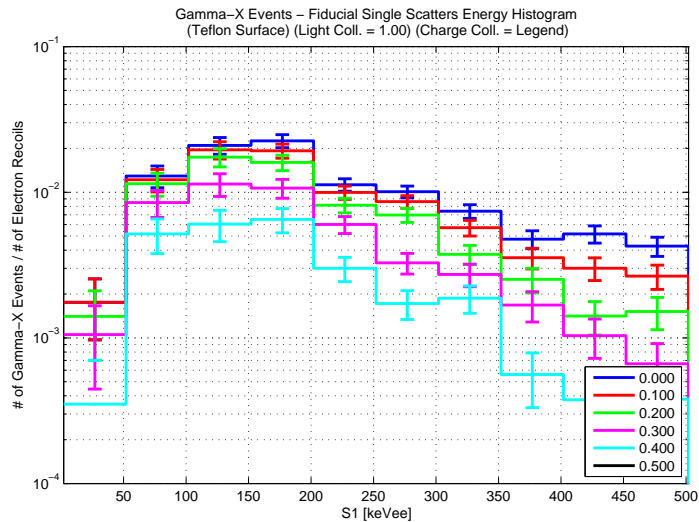
Figure 6.33: Gamma-X event rate (Charge Loss Region) vs. Charge Collection: Ratio of Gamma-X event rate to ER event rate vs energy, for events with scatters in the Charge Loss region (2 mm thick, depicted in Fig. 6.29), obtained from the XENON10 gamma background simulation. Each line corresponds to a value for Charge Collection (Q_{coll}). The simulation assumes that the light collection in the region is the same as the active region, $L_{coll} = 1$, and it uses the gamma background emitted from the steel cryostat and PMTs, with the initial energy spectra shown in Fig. 6.20.

tion factor is well defined at $Q_{coll} = 0$, and we look at how the Gamma-X rate change with L_{coll}. The ratio of the number of Gamma-X events to electron recoil events in the XENON10 fiducial region (5.4 kg) for events in the RFR with $L_{coll} = 1.3$ is $(2.7 \pm 1.3) \times 10^{-3}$ in the lowest energy bin ($E < 50\,\mathrm{keV_{ee}}$), and it varies very little as we vary the light collection factor around 1 (see Fig. 6.31). The rate of Gamma-X events due to scatters in the area around and below the bottom PMTs is strongly dependent on the L_{coll} - it goes down by 2 orders of magnitude as we change L_{coll} from 2% to 0.5% (see Fig. 6.32). Note that for light collection factors higher than 1%, the Gamma-X event rate is inconsistent with the event rate observed in the XENON10 WIMP search run (see Section 6.4.3), and thus we conclude that the light collection must be $L_{coll} \leq 1\%$. Light simulations performed for the full XENON10 geometry indicate that the light collection for the region around and below the bottom PMT array is on average 1%[83].

The light collection for the Charge Loss region is also well known, and is approximately the same as the active Xe region, $L_{coll} = 1$. Thus, to understand the behavior of the Gamma-X events due to scatters in this region, we hold the light collection factor constant, and vary the charge collection between 0 and 100%. For charge collection factors $\geq 50\%$, the Gamma-X rate drops to zero, as the S2/S1 of the events stay above the NR band center; even at 40%, the Gamma-X rate at low energies ($E < 50\,\mathrm{keV_{ee}}$) is already vanishingly small (see Fig. 6.33). The maximum Gamma-X rate for Charge Loss region is for total charge loss ($Q_{coll} = 0$), yielding a ratio of the number of Gamma-X events to ER events in the fiducial volume of $(1.2 \pm 0.8) \times 10^3$ in the energy bin $E < 50\,\mathrm{keV_{ee}}$, a little less than half the rate of events expected from the RFR region.

6.4.3 Gamma-X events in XENON10

Combining the Gamma-X event rate due to scatters in each of the identified charge insensitive regions, we obtain the total Gamma-X rate in the XENON10 detector. The spectrum for the combined Gamma-X event rate is shown in Fig. 6.34, and it uses the light and charge collection factors listed in Table 6.21. Note that while the plots in the previous section were for a single charge insensitive region, the plot shown in Fig. 6.34 combines all 3 effects, so
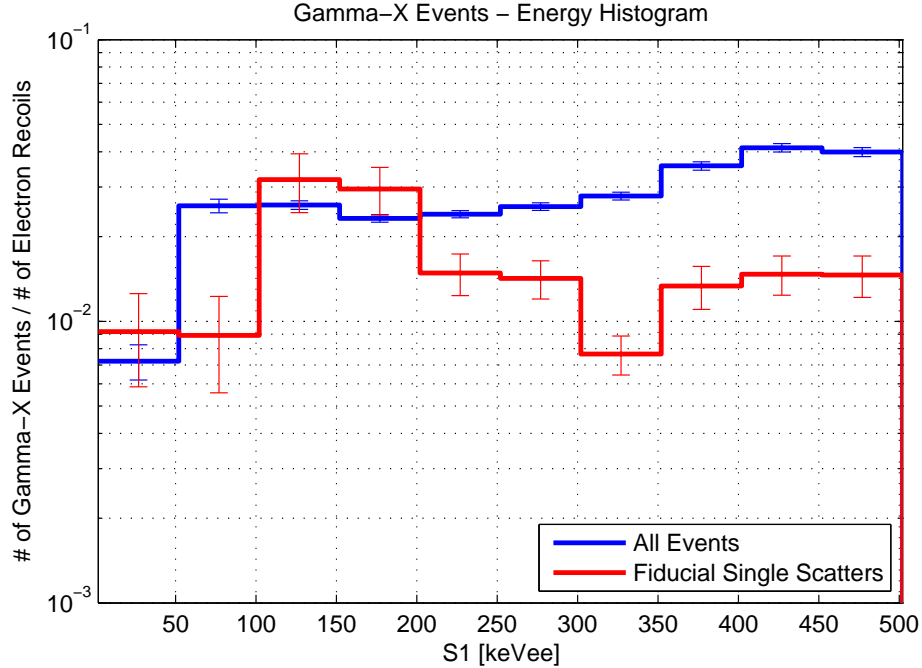
Figure 6.34: Ratio of Gamma-X event rate to ER event rate vs. energy, for events with scatters in the charge insensitive regions (depicted in Fig. 6.29), obtained from the XENON10 gamma background simulation. The light and charge collection factors (L_{coll}, Q_{coll}) assumed by the simulation are listed on Table 6.21. The simulation uses the gamma background emitted from the steel cryostat and PMTs, with the initial energy spectra shown in Fig. 6.20.

that both the total Gamma-X rate and the ER rate are affected, and the total spectrum is not simply a sum of the individual spectra shown in Fig. 6.31, Fig. 6.32 and Fig. 6.33. In this model, the Gamma-X event rate is dominated by the events in the charge insensitive region around and below the bottom PMTs.

In Section 4.3.2, we reviewed the methods for identification of Gamma-X events in the XENON10 data. The WIMP search run had a total of 1815 events in the ER band, in the energy region of interest, in the fiducial volume of 5.4 kg. Using the expected ratio of the Gamma-X rate to the ER event rate, we can estimate the expected number of Gamma-X events at 14.4 ± 5.3. Analysis of the XENON10 WIMP Search data identifies 17 events in the WIMP signal box as Gamma-X events 4.3.2.3, consistent with the number predicted by the model discussed here. This add support to the interpretation of the data that all "leakage" events (that is, events in the WIMP search box) not removed by quality cuts are

	L_{coll}	Q_{coll}	$\dfrac{\text{\#Gamma-X events}}{\text{\#ER events}}$	Gamma-X events expected in XENON10
Reverse Field Region	1.3	0	$(3.0 \pm 1.4) \times 10^{-3}$	4.7 ± 2.2
Around and below bottom PMTs	0.01	0	$(5.5 \pm 3.0) \times 10^{-3}$	8.6 ± 4.7
Charge Loss Region	1	0	$(1.4 \pm 0.8) \times 10^{-3}$	2.2 ± 1.2
Total			$(9.2 \pm 3.4) \times 10^{-3}$	14.4 ± 5.3

Table 6.21: Gamma-X events expected in the XENON10 data in the energy region of interest ($2 - 12\,\text{keV}_{\text{ee}}$), obtained from the XENON10 gamma background simulation. The number of Gamma-X events expected in XENON10 is calculated for the fiducial volume of $5.4\,\text{kg}$ and exposure of 58.6 live-days of the WS34 WIMP Search data, in which 1815 ER events are recorded. The number of Gamma-X events is calculated after accounting for the combined cuts efficiency of 86% (see Section 4.2.2). The light and charge collection factors (L_{coll}, Q_{coll}) assumed by the simulation are listed on the table. The simulation uses the gamma background emitted from the steel cryostat and PMTs, with the initial energy spectra shown in Fig. 6.20. The value in the "Total" row is less than the sum of the individual components because they are not completely orthogonal.

simply Gamma-X events, and not evidence for WIMPs.

The expected spatial distribution of the Gamma-X events in the XENON10 detector is shown in Fig. 6.35, and it shows a preference for the lower outer corner of the liquid Xe volume. Fig. 4.11 shows that the spatial distribution of the Gamma-X events identified in XENON10 is consistent with expected spatial distribution.

(a) Z

(b) R
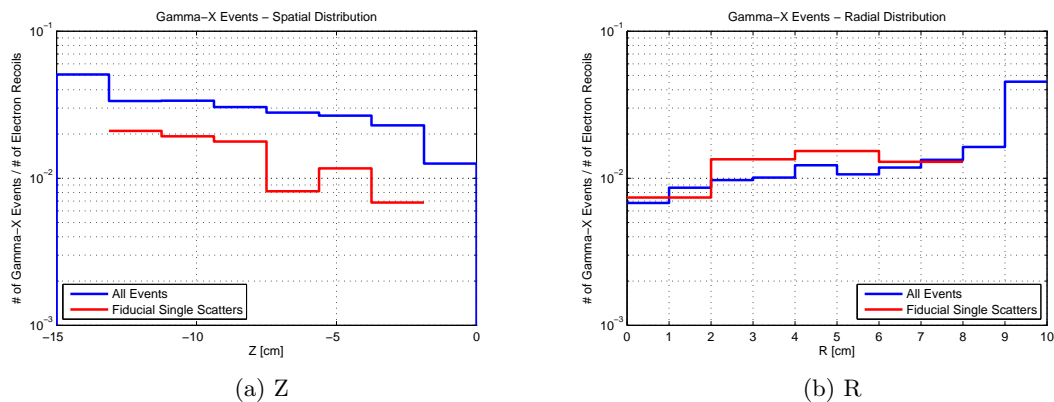
Figure 6.35: Spatial distribution of Gamma-X events - Ratio of Gamma-X event rate to ER event rate vs. depth and radius, for events with scatters in the charge insensitive regions (depicted in Fig. 6.29), obtained from the XENON10 gamma background simulation. The light and charge collection factors (L_{coll}, Q_{coll}) assumed by the simulation are listed on Table 6.21. The simulation uses the gamma background emitted from the steel cryostat and PMTs, with the initial energy spectra shown in Fig. 6.20.

CHAPTER 7

BACKGROUND MODEL FOR LUX

The current generation of detectors aims to push the WIMP sensitivity limits achieved in the XENON10 detector by a few orders of magnitude. The main limitation on the sensitivity of WIMP detectors is the background event rate, and thus the biggest challenge in the construction of the new generation detectors is the reduction of backgrounds, specifically the backgrounds with signals similar to the expected WIMP signal.

In order to estimate the sensitivity of the LUX detector, the signals are assessed using the same parameters used for XENON10, which is useful in comparing the performance of the different detectors. The LUX detector takes advantage of well-established liquid Xe techniques, and is designed to achieve an energy threshold as low as $5\,\mathrm{keV_r}$. When assessing the backgrounds, event rates are determined for a representative energy range of $5-25\,\mathrm{keV_r}$, and in the "WIMP box" defined by the electron recoil and nuclear recoil bands (see Section 2.1.4). The WIMP box defined by the ER and NR bands in XENON10 result in a discrimination power of 99.6% rejection of ER events and a nominal acceptance efficiency of 50% for NR events, averaged over the energy range $5-25\,\mathrm{keV_r}$. For a conservative assessment of the LUX background performance, we select rejection efficiencies per energy bin 1σ worse than the observed in XENON10, leading to an average of 99.4% ER rejection in the energy range of interest. Also, we select a narrower WIMP search window in the discrimination parameter, defining it between the NR band centroid μ and -2σ (compared to μ and -3σ in XENON10) in order to reduce the possible number of outlier events,

leading to a NR acceptance efficiency of 45%. These parameters for ER rejection and NR acceptance are used to assess the benchmark values of the expected LUX background.

The LUX collaboration aims to increase the limits on the sensitivity by building a detector 20 times larger in mass than XENON10, with an active Xe mass of $\sim 300\,\mathrm{kg}$, and an expected fiducial mass of 100 kg (see Section 7.1.1.1 for a discussion of the fiducial volume). The larger detector size enhances the self-shielding properties of liquid Xe for reducing the backgrounds due to detector component radioactivity. Two more factors remain crucial in the effort to push the sensitivity limits of the LUX detector, and both are aimed at reducing the backgrounds external to the detector: (1) deployment of the detector at the Davis laboratory, in the 4850 ft level of the Homestake mine, an underground site with small muon flux (e.g. ~ 7 orders of magnitude smaller than the surface flux); (2) construction of a 300 tonnes water shield, far superior than the Pb + polyethylene shield used in XENON10, for reducing the external high energy neutron and gamma backgrounds. The limiting factor for the LUX detector background will be the event rate due to PMT radioactive contamination, studied in detail in this chapter.

Sensitivity Goals. The LUX collaboration has set as their goal being able to achieve sensitivity to spin-independent WIMP-nucleon interactions with cross section $\sigma_{\chi,n} = 7 \times 10^{-46}\,\mathrm{cm^2}$ for WIMP mass $m_\chi = 100\,\mathrm{GeV}/c^2$, which corresponds to an average differential event rate of $14\,\mu\mathrm{dru_r}$, $(1\,\mathrm{dru_r} = 1\,\mathrm{events/keV_r/kg/day})$ in the energy range of $5-25\,\mathrm{keV_r}$, shown in Fig. 7.1 (the calculation of event rates for a given cross section is reviewed in Section 1.3.2). For the expected fiducial mass of 100 kg, the differential event rate results in a total event rate of 8.6 events in 300 days, or 3.9 events after the 45% NR event acceptance. This sensitivity goal sets constraints on the electron recoil and nuclear recoil background event rates; both the goal and background limits are listed in Table 7.1.

The detector sensitivity and corresponding event rates are calculated by using the expected background performance, and depend on the fiducial mass used and the length of the WIMP search run. The sensitivity corresponds to the WIMP event rate that is high enough to be positively identifiable above the background event rate, to within a given confidence limit. The probability distribution of the number of events detected for a given fiducial

WIMP signal sensitivity goal and upper limits for background event rates $(5 - 25\,\mathrm{keV_r},\ 1.3 - 8\,\mathrm{keV_{ee}})$	Event Rate limits for 300 live-days exposure in 100 kg fiducial volume
WIMPs ($m_\chi = 100\,\mathrm{GeV}/c^2$, $\sigma_\chi = 7 \times 10^{-46}\,\mathrm{cm}^2$)	8.6
WIMPs (after 45% NR band acceptance)	3.9
ER events (before ER band discrimination)	170
ER events (after 99.4% rejection)	1.0
NR neutrons	2.2
NR neutrons (after 45% NR band acceptance)	1.0

Table 7.1: WIMP signal sensitivity in the LUX detector, and upper-limits on the background event rates for the corresponding detector exposure (acquisition live-time $\times$ fiducial mass). The background event rates serve as a reference on the maximum ER and NR event rate allowed for the proposed WIMP sensitivity in order to achieve 90% C.L. limit on the WIMP cross-section. The WIMP and background event rates are calculated in the energy range of interest of $5 - 25\,\mathrm{keV_r}$, equivalent to $1.3 - 8\,\mathrm{keV_{ee}}$, and for an exposure of 300 live-days in a 100 kg fiducial mass.
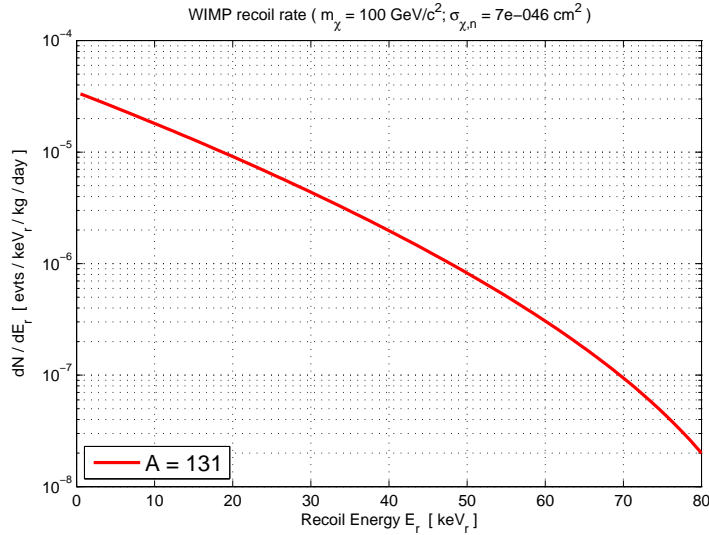
Figure 7.1: Nuclear recoil event rate for the WIMP signal $\sigma_{\chi,n} = 7 \times 10^{-46}\,\mathrm{cm}^2$ and $m_\chi = 100\,\mathrm{GeV}/c^2$ - the LUX sensitivity goal (see Table 7.1). The event rate is calculated for WIMP interactions with ^{131}Xe, following the calculation detailed in [40] and summarized in Section 1.3.2.

mass and livetime is described by using Poisson statistics:

$$Prob\,(k) = \frac{e^{-\lambda} \cdot \lambda^k}{k!}, \tag{7.1}$$

where k is the number of events measured, and λ is the expectation value (that is, the "ideal" event rate). The detector background performance is attuned to result in ≤ 1 "leakage" background events (that is, background events with signals similar to the expected WIMP signal). We can then calculate the expectation value λ so that the measured event rate will be > 1. For a 90% confidence limit, the expectation value λ of the event rate so that the measured number of events is positively larger than the background (that is, it will have 2 events or more) is given by:

$$
\begin{aligned}
\sum_{k=2:\inf} Prob\,(k) &\geq 90\% \\
\Rightarrow \sum_{k=0:1} Prob\,(k) &\leq 10\% \\
\Rightarrow e^{-\lambda}\,(1 + \lambda) &\leq 10\% \\
\Rightarrow \lambda &\geq 3.9.
\end{aligned}
$$

That is, allowing for 1 background leakage event requires a WIMP signal of 3.9 events in the WIMP search box to set a 90% C.L. limit on the WIMP-nucleon cross section. Thus, the total number of nuclear recoil events is 8.6 events (before the 45% NR acceptance).

Background assessments of the LUX detector indicate that background performance of < 1 leakage events can be attained for the estimated fiducial mass of 100 kg with a WIMP search run of 300 live-days (as seen on Table 7.2 and Table 7.10), and thus the detector total exposure is limited to 30,000 kg-days. A WIMP signal of 8.6 events corresponds to a differential event rate of 1.4×10^{-5} $\mathrm{dru_r}$ ($\mathrm{dru_r}$ = events/$\mathrm{keV_r}$/kg/day) in the $5 - 25\,\mathrm{keV_r}$ energy range, which in turn corresponds to the spin-independent WIMP cross section of $\sigma_{\chi,n} = 7 \times 10^{-46}\,\mathrm{cm^2}$ for the WIMP mass of $m_\chi = 100\,\mathrm{GeV}/c^2$.

A larger exposure, obtained either from a longer run or a larger fiducial mass, can

extend the sensitivity limit of the detector even further, as long as the background rate is still below the desired goal. For the current sensitivity goal, the background goal is set by the limit of a single event in the WIMP parameter box, for the entire exposure of 30,000 kg-days. This corresponds to 2.2 nuclear recoil events, before the 45% NR acceptance, or 180 electron recoil events before the 99.4% ER rejection (see Table 7.1). Further reduction of the backgrounds, or improvements on the ER rejection (which effectively reduces the background), allows for a larger total exposure, thus pushing down the differential event rate and the corresponding WIMP cross section sensitivity.

Background Assessment. A series of Monte Carlo simulations and analytical calculations have been performed to determine the optimal design of the detector and shield in order to achieve background rates well below the desired goals, and assess the expected background and sensitivity of the final detector design.

Although the actual discrimination power of the detector will not be determined until data is available, a benchmark value of the backgrounds is obtained by assuming ER rejection (99.4%) and NR acceptance (45%). The background assessment also uses event selection techniques commonly used in liquid Xe data analysis, specifically the application of a fiducial volume cut and of single scatter cuts, as will be described in Section 6.2. The fiducial cut uses the self-shielding properties of the liquid Xe to isolate a smaller volume at the center of the detector where the background rate per kg is much lower than at the outer surface, by as much as $\times 1/300$. The use of the fiducial volume cut effective reduces the sensitive mass of the detector, and thus reduces its sensitivity limit. A balance between the total exposure of the detector and the resulting background needs to be achieved to determine the optimal fiducial volume.

The background assessment is divided into 2 parts: internal background, corresponding to the backgrounds arising from radioactive contamination in the components of the detector itself; and external backgrounds, concerned with the backgrounds arising outside the shield, and from the shield itself. The LUX collaboration pursues an aggressive program of materials screening, and all internal backgrounds are rendered sub-dominant to the background due to the PMT arrays.

The external background is composed mainly of gammas and neutrons generated from rock radioactivity, and muon interactions in the rock. Special attention is given to the high energy neutron backgrounds arising from muon interactions in the rock, which are highly penetrating in any material and are thus particularly difficult to shield against. The best way to reduce this background is to move the detector deep underground to reduce the incident muon flux.

Detector Deployment. The LUX detector will be deployed at the 4850 ft level of the Homestake mine in 2009, and is expected to yield its first results in 2010. The laboratory is located at the effective depth of 4.3 km.w.e., with the muon flux listed in Table 6.7. The Homestake mine is currently being transformed into a national laboratory called the Deep Underground Science and Engineering Laboratory (DUSEL), which will span several levels, going as deep as the 7400 ft level. The initial laboratory construction and experiment deployment is being privately funded and carried out under the name of Sanford Underground Science and Engineering Laboratory (SUSEL). The LUX detector will be deployed in the Davis laboratory, a cavern in the 4850 ft level used for the neutrino experiment headed by Ray Davis and John Bachall, built in the 1960s [148].

The detector will be installed inside a 300 tonnes water tank. The tank size was chosen primarily to moderate the external high-energy neutron backgrounds. The LUX water shield will reduce all external gamma and neutron backgrounds well below the background goals set by the internal backgrounds.

7.1   LUX Internal Backgrounds

The LUX detector has been designed with the background reduction as one of its primary goals. The water shield, described in Section 7.2, reduces the external background far below the expected background rate due to internal components. The use of fiducial volume cuts also renders most backgrounds generated in the detector components negligible, so that only the most radioactive components, that are also closest to the active volume, will dominate the background in the detector. Due to the geometry of the LUX detector, described

	Differential Event Rate fiducial volume (100kg) $5 - 25\,\mathrm{keV}$	Total Event Rate 30,000 kg-days (fiducial) $5 - 25\,\mathrm{keV_r}$ $(1.3 - 8\,\mathrm{keV_{ee}})$	Ref.
γ's emitted by PMTs	$(384 \pm 81)\,\mu\mathrm{dru_{ee}}$	0.46 ± 0.1	Table 7.4
neutrons emitted by PMTs	$(0.52 \pm 0.02)\,\mu\mathrm{dru_r}$	0.140 ± 0.005	Table 7.7

Table 7.2: LUX internal backgrounds - event rates for the main internal backgrounds in the LUX detector, due to PMT radioactive contamination. The total event rates are calculated for the given exposure after we apply the NR band acceptance of 45%, and ER rejection of 99.4%, in the energy range of interest $5 - 25\,\mathrm{keV_r}$ $(1.3 - 8\,\mathrm{keV_{ee}}$ for $L_y = 3.0\,\mathrm{phe/keV_{ee}})$. The assumptions and methodology used to calculate the event rates are discussed in Section 7.1.

in Section 2.2, the PMTs and the cryostat are the most likely components to dominate the background rate. The PMTs are a prime candidate for high background rates in the detector, due to their mandatory placement next to the active liquid Xe volume, and due to the limited control by the LUX collaboration on their radioactivity levels (see Section 5.2.2). The cryostat, on the other hand, can be custom-built using low-radioactivity materials to fit the LUX specifications, and is in fact being constructed using low-radioactivity Ti to ensure subdominant backgrounds (see Section 5.3.2).

The main task in the assessment of the internal backgrounds is thus to determine the background event rates expected due to radioactive contamination in the PMTs. It is also necessary to determine what is the sensitivity limit of the LUX detector for the expected background, which will depend directly on the maximum size of the fiducial volume that can be obtained so that the background event rate remains below the background goals (listed in Table 7.1). The total event rates expected in the LUX detector due to the PMTs is listed in Table 7.2.

7.1.1 PMT Gamma Background

Monte Carlo simulations using Geant4 were performed to assess the background event rates in the LUX detector, using similar techniques as the ones described in Chapter 6. The simulations use a simplified detector geometry, which consists of: a cylinder of liquid Xe, 49 cm diameter and 59 cm height; the lower 5 cm of the liquid Xe are below the Cathode

grid (the Reverse Field Region, see Section 6.4.1), leaving us with an active Xe mass of 300 kg. The simulation geometry also includes space for Xe gas above the liquid, 4 cm in height; space for the PMT arrays above and below, matching the dimensions of the Hamamatsu R8778 PMTs with 11 cm height; a Teflon cylinder 3 cm thick wrapped around the liquid Xe; a cryostat, 4 cm thick, wrapped around the liquid Xe plus PMTs plus Teflon. The simulations were performed early on during the planning phase of the LUX detector, and used a very thick Cu cryostat. The structure of the cryostat is not included in the simulation, since its details had not been finalized during the planning phase, and a single hollow cylinder with thick walls is used. Since then, the collaboration has opted to use double walled cryostat, with a Ti inner and outer walls of ~ 0.65 cm thickness, separated by 10 cm of vacuum. The inner cryostat is covered on the outside with a layer of high-purity Cu acting as a radiation shield. The thickness of the cryostat walls in the Monte Carlo will have a sub-dominant effect on the event rate due to the PMT radioactive contamination. The PMTs are very light and have negligible stopping mass, and thus their structure is not included in the simulation. The simulation uses radiation sources with the shape and size of the entire PMT arrays on the top and bottom of the detector, and it assumes that the gamma ray source is evenly distributed throughout the entire body of the PMT array. Each of the PMT array consists of 61 PMTs. The remaining detector details are not included in the simulations, as their effect on the background rate should be subdominant to the major components. The entire cryostat is placed inside a water shield with 8 m diameter and 6 m height, as shown in Fig. 7.2.

Simulations are run separately for each of the major contaminants in the PMT (^{238}U and ^{232}Th decay chains, ^{60}Co, and ^{40}K), so that their activities can be adjusted individually. The decays of individual isotopes is not simulated; instead, the gammas from each decay chain are emitted individually, and normalized to match the branching ratio of each line. The gamma production rate assumes that each decay chain is in equilibrium, and it has isotropic angular distribution. The event rate in the detector is normalized to match the contamination levels in the Hamamatsu R8778 PMTs, determined through the LUX materials screening program (see Section 5.2.2), and listed on Table 7.3. The emission of individual lines makes
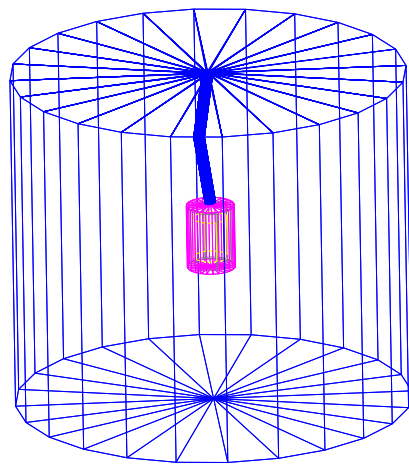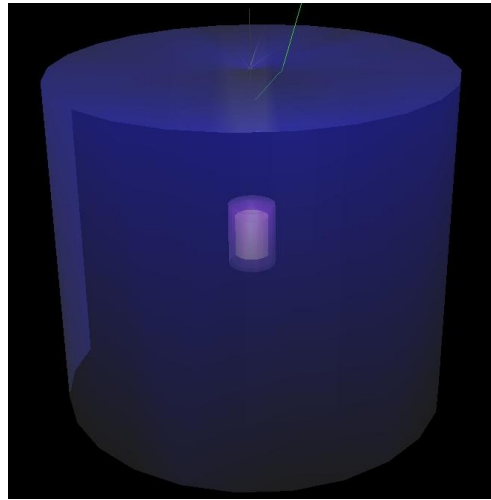
(a) Wireframe (b) VRML

Figure 7.2: Geant4 model of the LUX detector inside the water shield of 8 m diameter and 6 m height, generated using 2 different renderers. The LUX Geant4 model has the detector placed at the center of water shield; however, the LUX detector will be placed with a Z displacement of -59 cm, as determined in Section 7.2.1.3. The Geant4 model includes the active liquid Xe volume, 49 cm diameter and 59 cm height, with a total mass of 330 kg, plus space for Xe gas above the liquid, 4 cm in height; space for the PMT arrays above and below, matching the dimensions of the Hamamatsu R8778 PMTs with 11 cm height; a Teflon cylinder 3 cm thick wrapped around the liquid Xe; a Steel cryostat cylinder, 4 cm thick, wrapped around (plus above and below) the liquid Xe plus PMTs plus Teflon. The model also shows the feedthrough pipe connecting the detector to the surface of the water tank, providing an outlet for gas and cable connections.

Isotope	Estimated from Hamamatsu Data (Feb. 2004)		Measured at SOLO (Aug. 2007)	
	Contamination Level (mBq/PMT)	LUX Event Rate (μdru$_{ee}$)	Contamination Level (mBq/PMT)	LUX Event Rate (μdru$_{ee}$)
^{238}U	18	204	8.9 ± 1.5	101 ± 23
^{232}Th	17	368	2.8 ± 0.8	61 ± 20
^{40}K	30	54	92 ± 9	165 ± 18
^{60}Co	8	200	2.6 ± 0.5	65 ± 14
Total		826		391 ± 82

Table 7.3: Predicted electron recoil event rate due to PMT radioactivity based on Geant4 simulations of the LUX detector. The table lists the resulting event rate contribution for each component for a given contamination level, using both (A) the upper limit of the values quoted by Hamamatsu and (B) the average values measured at SOLO. For a discussion of the contamination levels listed here, please refer to Section 5.2.2. The event rate 1σ error includes the uncertainty of the PMT contamination level and statistical uncertainty from the Monte Carlo simulation.

it impossible to simulate the background reduction due to correlated gamma emission. In many of the decays, 2 or more gammas are emitted, making it possible to veto the event as a multiple scatter cut (provided they travel in the direction of the detector). We estimate a background reduction factor of $\times 1/3$ by vetoing correlated gammas emitted by the PMTs. This reduction is not taken into consideration for the event rates calculated throughout this chapter.

7.1.1.1 Defining the Fiducial Volume

The spatial distribution of the resulting electron recoils in the liquid Xe is shown in Fig. 7.3. As can be seen, most of the event rate is limited to the outer edges of the active volume, and the center is relatively quiet. This allows for the use of a fiducial volume cut, in which we only look at events that occur within a given volume in the center of the detector, to reduce the effective background. Fig. 7.4 shows the gamma background rate vs. fiducial volume radius, demonstrating that the event rate falls exponentially with radius with an e-folding length of 2.8 cm. Due to the concentration of events in the top and bottom of the detector (the regions closest the PMTs), it is found that the optimal fiducial volume shape is a cylinder with a Height/Diameter ratio of 0.9. We vary the fiducial volume mass
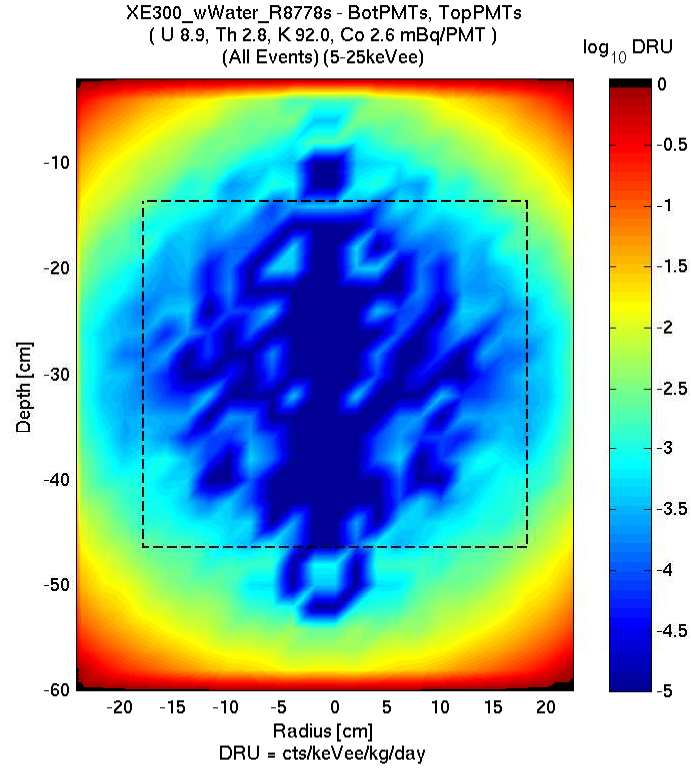
Figure 7.3: Spatial distribution of the gamma background in LUX due to PMT radioactivity, in the energy range of $5 - 25\,\mathrm{keV_{ee}}$, obtained from a Geant4 simulation of the LUX detector. The event rate is normalized to the PMT radioactive levels measured at SOLO and listed in Table 5.2.2. The black box indicates the LUX benchmark fiducial volume of 100 kg.

by decreasing the radius and height of the fiducial volume cut proportionally, and the rate of events is calculated for the resulting fiducial volume in the energy region of interest. Fig 7.5 shows the event rate as a function of the fiducial volume mass.

The fiducial volume for the LUX detector is originally designed using benchmark values for the PMT contamination values, which were subsequently updated as the screening data from SOLO became available. During the planning phase for the LUX detector, no R8778 PMTs had been screened yet, and we performed background assessments using the upper limits of the contamination levels derived from the screening data made available by Hamamatsu (see Section 5.2.2), as a way of setting conservative limits on the background event rate and estimating the size of the fiducial volume. Using the Hamamatsu contamination levels, it was determined that the maximum fiducial volume mass that would result in < 180
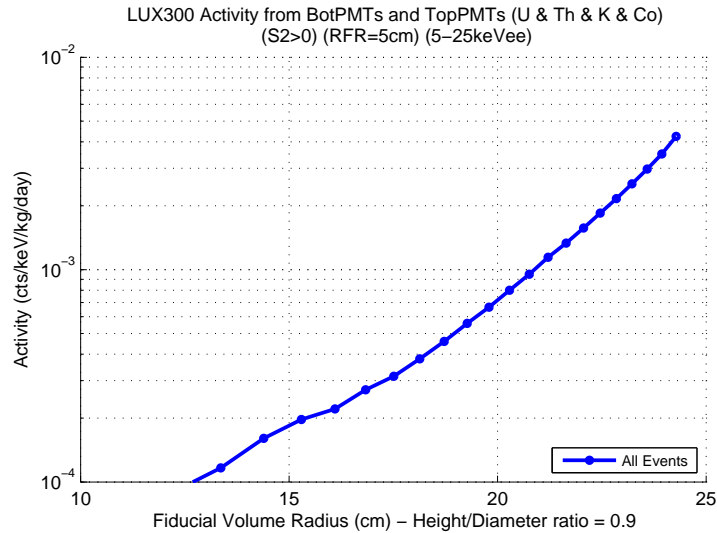
Figure 7.4: Electron recoil event rate due to PMT radioactivity vs. fiducial volume radius. The line shows the exponentially decreasing rate inside the fiducial volume of the given radius, as we reduce the size of the fiducial volume, with a e-folding length of 2.8 cm. The fiducial volume has an aspect ratio of Height/Diameter = 0.9. The rate is calculated from Monte Carlo simulations, using PMT contamination levels equal to the average values measured at SOLO (blue line) - see Table 7.3. For a discussion of the contamination levels listed here, please refer to Section 5.2.2.
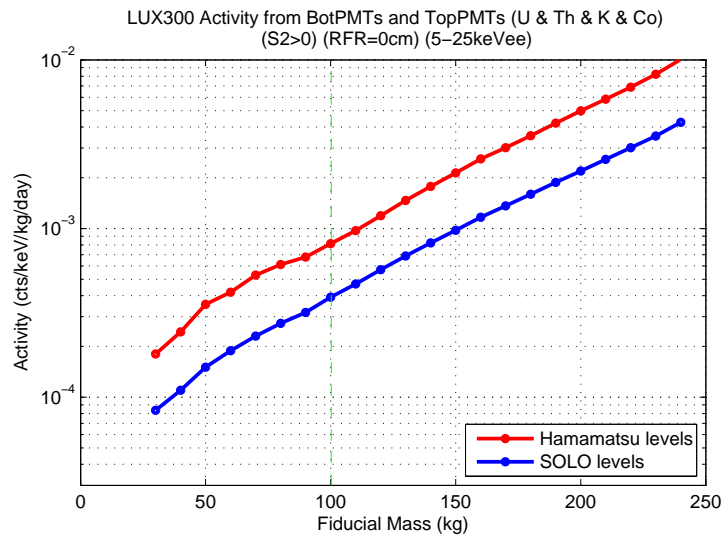
Figure 7.5: Electron recoil event rate due to PMT radioactivity vs. fiducial volume mass. The lines shows the exponentially decreasing rate as we reduce the size of the fiducial volume. The lines show the gamma event rate for PMTs with contamination levels equal to the upper limit of the values quoted by Hamamatsu (red line) and the average values measured at SOLO (blue line) - see Table 7.3. For a discussion of the contamination levels listed here, please refer to Section 5.2.2.

	Event Rate $(5 - 25\,\mathrm{keV_{ee}})$
Total (no cuts)	$(115 \pm 21)\ \mathrm{mdru_{ee}}$
Single Scatters	$(114 \pm 21)\ \mathrm{mdru_{ee}}$
Fiducial Cut (100 kg)	$(391 \pm 82)\ \mu\mathrm{dru_{ee}}$
Single Scatters + Fiducial Cut	$(384 \pm 81)\ \mu\mathrm{dru_{ee}}$

Table 7.4: Predicted electron recoil event rate due to PMT radioactivity based on Geant4 simulations of the LUX detector, using several cuts during analysis. Assumes the Hamamatsu R8778 PMT average contamination levels measured at SOLO (see Table 7.3).

electron recoil events in 300 days livetime in the energy range of $1.3 - 8\,\mathrm{keV_{ee}}$ was 103 kg, with a height of $\sim 59\,\mathrm{cm}$ and diameter of $\sim 49\,\mathrm{cm}$. Using the actual contamination levels for the R8778 measured in SOLO (Table 7.3), the maximum fiducial volume mass for < 180 electron recoil events in 300 days livetime in the energy range of $1.3 - 8\,\mathrm{keV_{ee}}$ is 130 kg. However, it was decided by the LUX collaboration to use a 100 kg fiducial volume as the benchmark fiducial volume for LUX, as it is a more practical number to calculate rates and makes comparisons between different models easier. The actual fiducial volume for LUX will only be determined during analysis from the actual spatial distribution of events in the detector.

The electron recoil event rate in the benchmark fiducial volume of $\sim 100\,\mathrm{kg}$ is $391\ \mu\mathrm{dru_{ee}}$ in the $5 - 25\,\mathrm{keV_{ee}}$ range, $\times 1/290$ smaller than the differential rate without any fiducial cuts and averaged over the entire detector (see Table 7.4), and the energy distribution of the events is essentially flat at low energies ($E_{\mathrm{er}} < 50\,\mathrm{keV_{ee}}$), as shown in Fig. 7.6. This differential event rate corresponds to 80 events in the 100 kg fiducial volume for 300 days livetime. Conversely, it is possible to run the detector for 690 days before achieving the upper limit of 180 electron recoil events, which corresponds to 1 event after the benchmark ER rejection of 99.4% (see Table 7.1). The application of a single scatters cut has negligible effect for events with low energy deposition, because events that scatter more than once tend to deposit more energy, so that a energy cut that selects only low energy events is equivalent to a single scatter cut for gammas. When using the benchmark single scatter cut with $\sigma_z \leq 1\,\mathrm{cm}$ and $\sigma_r \leq 1\,\mathrm{cm}$ we obtain only a 2% reduction in the event rate (see Table 7.4).
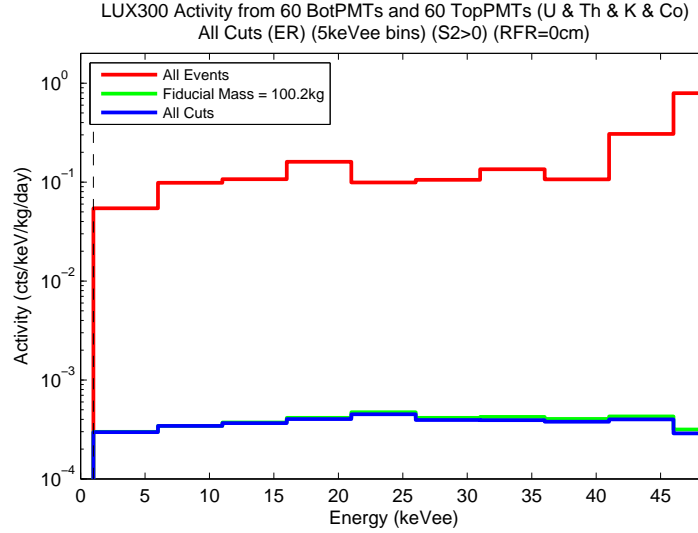
Figure 7.6: Energy histogram of the gamma electron recoil background in LUX due to PMT radioactivity, using the PMT contamination levels measured at SOLO (see Table 7.3). The average event rate in the energy range of $5 - 25\,\text{keV}_{\text{ee}}$ is $391\,\mu\text{dru}_{\text{ee}}$ in the LUX fiducial volume of 100 kg. The blue line for "All Cuts" includes the fiducial cut and a single scatter cut. Note that the single scatter cut makes little difference for energy depositions in the $5 - 25\,\text{keV}_{\text{ee}}$ range (See Table 7.4).

7.1.1.2 Dominant Gammas Lines

The penetration of gammas into the fiducial volume is determined by the attenuation length λ in liquid Xe, shown as a function of energy in Fig. 2.14. The probability that a gamma will travel a length l of liquid Xe without scattering once is given by

$$P\left(l\right) = e^{-l/\lambda}. \tag{7.2}$$

From the attenuation length plot versus energy, one can guess that only gammas with high enough energy ($E_\gamma > 500\,\text{keV}_{\text{ee}}$) will penetrate through the liquid Xe enough to reach the fiducial volume, scatter in it, and leave the fiducial volume without scattering again. Therefore, both the layer in front and behind the fiducial volume (from the point of view of the incoming particle) act as a shield.

A Monte Carlo simulation was performed to determine the energy of the gammas that do contribute to the event rate in the fiducial volume. The source consisted of a series of lines with energy multiples of $100\,\text{keV}$, up to $3000\,\text{keV}$, with the same geometry as the
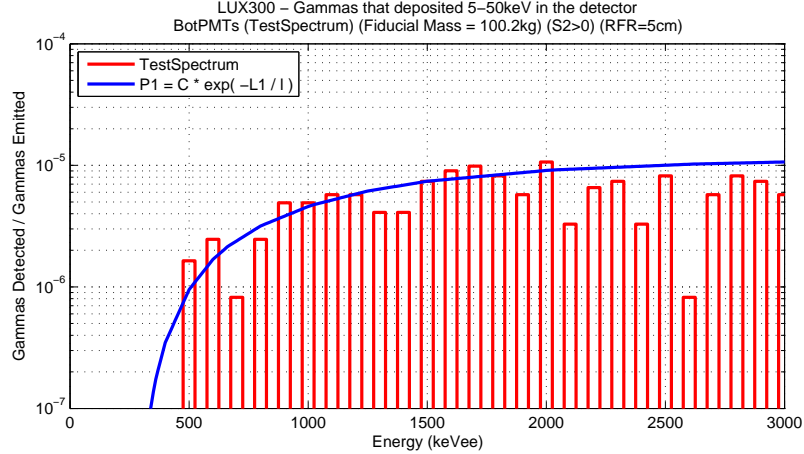
Figure 7.7: Ratio of detected gammas / emitted gammas in the LUX fiducial volume of 100 kg, obtained from Geant4 simulation of the gammas emitted by the PMTs in the bottom array. The source is a series of gamma lines with energy multiple of 100 keV, with the same geometry as the bottom PMT array. Only gammas that deposit $5 - 50 \, \mathrm{keV_{ee}}$ are counted as detected gammas. The blue line is a fit using the penetration probability for gammas traveling from the PMTs to the fiducial volume P1 $= \mathrm{C} \cdot e^{-\mathrm{L}1/l}$), where L1 is the distance between the PMTs and the top surface of the fiducial volume and l is the penetration length of gammas with energy E, and C is a normalization constant.

bottom PMT array. Fig. 7.7 shows the ratio of the number of gammas that deposited $5 - 50 \, \mathrm{keV_{ee}}$ over the number of gammas emitted for each energy line. In this plot, the energy range used is larger $(5 - 50 \, \mathrm{keV_{ee}})$ to improve statistics. The distribution can be fitted by Eq. 7.2, such that

$$\text{detection ratio}\,(E_\gamma) = C \cdot P\,(l, \lambda) = C \cdot e^{-l/\lambda(E_\gamma)}, \tag{7.3}$$

where l is the space between the bottom PMT array and the fiducial volume ($l = 7.5 \, \mathrm{cm}$ for the $m_{fid} = 100 \, \mathrm{kg}$), $\lambda\,(E_\gamma)$ is the attenuation energy for a gamma with energy E_γ, and C is a normalization constant. The energy distribution of gammas that deposit $5 - 50 \, \mathrm{keV_{ee}}$ in the fiducial volume shows that only events with energy $E_\gamma > 500 \, \mathrm{keV_{ee}}$ start contributing significantly to the background, and that the detection rate starts to flatten out above $E_\gamma > 1000 \, \mathrm{keV_{ee}}$. The detection rate is 50% of the maximum at $E_\gamma > 1000 \, \mathrm{keV_{ee}}$, 1/3 at $E_\gamma > 750 \, \mathrm{keV_{ee}}$, and 1/10 at $E_\gamma > 500 \, \mathrm{keV_{ee}}$.

Using the data from the PMT simulations and the contamination levels measured at SOLO (listed in Table 7.3), one can determine which gamma lines contribute the most to the
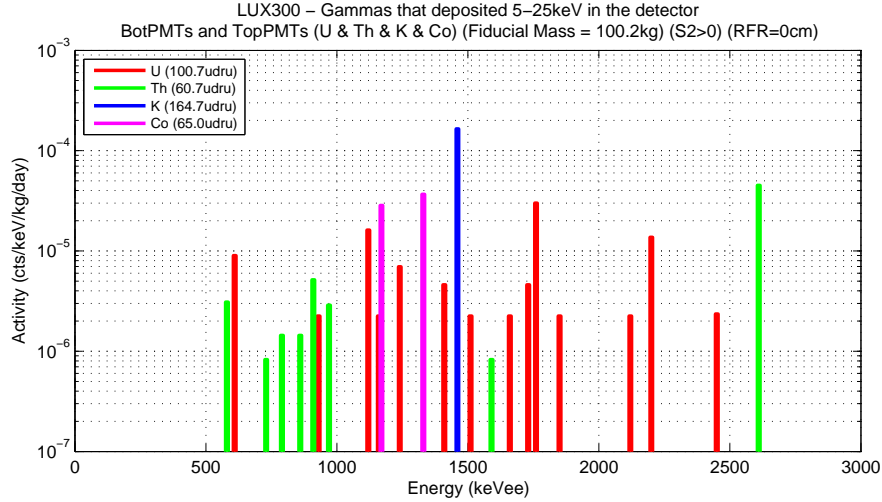
Figure 7.8: Histogram of the Initial Energy of Gammas originating in the bottom PMTs, and that deposited $5-25\,\mathrm{keV_{ee}}$ in the LUX fiducial region (100kg), obtained from a Monte Carlo simulation of the LUX detector. The simulation uses the PMT contamination levels measured at SOLO (Table 7.3). The lines are listed in Table 7.8.

background event rate in the fiducial volume. Fig. 7.8 shows a histogram of the initial energy - that is, the energy of the original gamma from the source - for all gammas that deposited $5-25\,\mathrm{keV_{ee}}$ in the LUX fiducial volume of 100 kg. The plot is normalized to give the event rate in the detector. From the plot is easy to see that the largest contribution comes from the $1461\,\mathrm{keV}$ line from ^{40}K, responsible for $165\,\mu\mathrm{dru_{ee}}$ (out of the total of $391\,\mu\mathrm{dru_{ee}}$), and the second largest comes from the $2614\,\mathrm{keV}$ line from ^{208}Tl (part of the ^{232}Th decay chain), responsible for $45\,\mu\mathrm{dru_{ee}}$ of the background event rate. The predominance of the $1461\,\mathrm{keV}$ line is due to the relatively high contamination level of ^{40}K in the PMTs, compared to ^{60}Co and the ^{238}U and ^{232}Th decay chains, and underlines the need to control the ^{40}K contamination in the PMT fabrication process.

7.1.1.3   Discussion of the PMT contamination levels

The measurement of the PMT contamination levels at SOLO indicate that the ^{40}K contamination level is $\times 3$ larger than the amount expected from the data supplied by Hamamatsu (see Table 7.3). However, this does not constitute an obstacle for LUX to achieve the desired background goal, because ^{40}K does not cause much relative "damage" - although the contamination level (mBq/PMT) is much higher, its contribution to the background event

Peak Energy [keV]	Event Rate [μdru$_{ee}$]
1760	30
1120	16
2200	14
610	9
1240	7
1410	5
1730	5
2450	2
930	2
1160	2
1510	2
1660	2
1850	2
2120	2

(a) ^{238}U-chain

Peak Energy [keV]	Event Rate [μdru$_{ee}$]
2610	45
910	5
580	3
970	3
790	1
860	1
730	1
1590	1

(b) ^{232}Th-chain

Peak Energy [keV]	Event Rate [μdru$_{ee}$]
1461	165

(c) ^{40}K

Peak Energy [keV]	Event Rate [μdru$_{ee}$]
1330	37
1170	28

(d) ^{60}Co

Table 7.5: List of emission lines that contribute the most to the ER event rate in the LUX fiducial volume (100 kg), in the energy region of $5 - 25\,\mathrm{keV_r}$ for each of the major contaminants, sorted by the event rate. These lines correspond to the lines shown in Fig. 7.8.

rate is equal to the combined contributions from the ^{238}U and ^{232}Th decay chains.

First consider that the 1461keV gamma line from ^{40}K has a 10% branching ratio, while the ^{238}U chain emits 2.5 gammas per decay on average, and the ^{232}Th chain emits 4.5 gammas per decay. This means that per decay, ^{40}K emits $\times 1/30$ less gammas than the ^{238}U/^{232}Th chains combined (with a 1:2 ratio). Even though the ^{40}K contamination level is almost $\times 8$ higher than the ^{238}U/^{232}Th contamination combined, the number of ^{40}K gammas emitted is still $\times 1/4$ smaller.

This assessment is confirmed by the PMT simulations. From Table 7.3, one can see that ^{40}K contributes $1.8\,\mu$dru$_{ee}$/mBq to the total event rate. Going from 30mBq to 92mBq increases the event rate by $\Delta = 110\,\mu$dru$_{ee}$, only 14% of the total event rate obtained when using the Hamamatsu supplied data, $826\,\mu$dru$_{ee}$. Actually, since the activity measured at SOLO for ^{232}Th and ^{60}Co are 1/6 and 1/5 of the expected, the total event rate due to PMTs is much smaller. This means 2 things: (1) that we have a greater "event rate budget" left to spend with ^{40}K; and (2) that the ^{40}K is a greater factor in the event rate than expected. The first point is that the expected total event rate due to PMTs (when using the Hamamatsu contamination levels) was $826\,\mu$dru$_{ee}$, but when we use the SOLO measured contamination levels, the total PMT event rate is reduced to $391\,\mu$dru$_{ee}$, so that a $\times 3$ increase in ^{40}K does not exceed the background goal. The second point is that when using the Hamamatsu quoted contamination levels, ^{40}K contributed 7% of the total PMT activity; when using the SOLO measured levels, ^{40}K contributes 42% of the total PMT event rate.

During the early planning phase of the LUX detector, event rate projections were calculated using the contamination levels based on the Hamamatsu data. In fact, these were the contamination levels quoted in the original LUX proposal submitted to the funding agencies in 2007. Although the measured ^{40}K level was higher than expected, the event rate when we assume the measured PMT contamination levels is actually 50% of the activity projected in the proposal.

7.1.2 PMT Neutron Background

Due to the low radioactivity of Ti cryostat (listed in Table 5.11) and miscellaneous detector components, it is expected that the neutron event rate in the LUX detector will be dominated by neutrons generated by the PMT radioactivity. Neutrons are generated mainly by 2 processes: spontaneous fission of ^{238}U nuclei, and α-decay of ^{238}U and ^{232}Th, which generate neutrons through (α,n) reactions in the detector and PMT internal components. These processes were already been described for the XENON10 PMTs in Section 6.2.3.

Monte Carlo simulations using Geant4 were performed to assess the neutron event rate in the LUX detector due the PMT radioactivity. The simulation used the same geometry as the PMT-gammas simulation described in the preceding section. The sources were also the top and bottom PMT array bodies, and emit neutrons with the same energy spectrum as the XENON10 simulation (see Fig. 6.6), but normalized to a benchmark neutron production rate of $5\,\mathrm{n/PMT/year}$.

The actual neutron production rate of the Hamamatsu R8778 PMTs used by LUX has not been measured, but we can make a reasonable estimate, given a few assumptions. Neutrons are generated in the PMT through fission and (α,n) processes. As discussed in Section 6.2.1, the neutron contribution from fission is dominated by ^{238}U , which has a branching ratio of 5.4×10^{-7}, and generates 2.07 neutrons per fission, leading to a neutron production rate of $1.1 \times 10^{-6}\,\mathrm{n \cdot s^{-1}/Bq/PMT}$ for ^{238}U. The (α,n) neutron production rate is a function of the chemical composition of the target material for the α-particles, i.e. the components in the vicinity of the decays site. The chemical composition of the R8778 PMT internal components has been made available by Hamamatsu to the LUX Collaboration [149], but is protected by a confidentiality agreement. The mass of the PMT is dominated by Fe, Ni and Co from the PMT steel body and electrodes, and by Si and O on the glass of the PMT window and stem. A list with the approximate mass for the major chemical components in the PMT body is given in Table 7.6. We can calculate the (α,n) neutron production rate for each one of the listed compounds by using the "Neutron Yield" tool [150] developed by the LUX collaborators at the University of South Dakota, which follows the techniques detailed in Mei 2008 [151]. If we assume that the radioactive

Chemical	Z	Mass [g]	Location
Fe	26	65	steel body and electrodes
Ni	28	40	steel body and electrodes, Ni wires
O	8	25	window and stem glass, ceramic insulators
Co	27	15	steel body and electrodes
Si	14	15	window and stem glass
Al	13	10	ceramic insulators
Cr	24	5	steel body and electrodes
Total Mass		175	

Table 7.6: Approximate chemical composition of the Hamamatsu R8778 PMT body and internals. The precise chemical composition of the R8778 PMT internal components has been made available by Hamamatsu to the LUX Collaboration [149], but is protected by a confidentiality agreement. The table shows only the elements that account for $\geq 1\%$ of the total PMT mass.

contamination given in Table 7.6 is evenly spread on the entire PMT mass, and use the PMT contamination levels measured at SOLO (listed in Table 7.3), we obtain a neutron production rate of $1.2 \times 10^{-6}\,\mathrm{n \cdot s^{-1}}/\mathrm{Bq}/\mathrm{PMT}$ for ^{238}U and $2.0 \times 10^{-6}\,\mathrm{n \cdot s^{-1}}/\mathrm{Bq}/\mathrm{PMT}$ for ^{232}Th. Combining the neutron rate generated by fission and by (α,n) processes we obtain a total neutron production rate of $1\,\mathrm{n}/\mathrm{PMT}/\mathrm{year}$. However, we use a more conservative benchmark neutron production rate of $5\,\mathrm{n}/\mathrm{PMT}/\mathrm{year}$ in the Monte Carlo simulations for 2 reasons: (1) the estimate neutron production rate does not take into account the exact ratios and distributions of contaminants in the PMT, nor the contamination level in the bases, so that a factor of $\times 5$ should gives a safety margin when calculating the total neutron rate; (2) it is the neutron production rate that will result in 1 background event in the 100 kg LUX fiducial volume in 1,000 days, as will be shown in this chapter.

The spatial distribution of the resulting nuclear recoils in the liquid Xe is shown in Fig. 7.9, and a plot of the nuclear recoil rate vs. the fiducial mass is shown in Fig. 7.10. It can be seen that the decrease in neutron event rate as we decrease the fiducial volume is a lot less steep than for gammas - the event rate is reduced only by a factor of $\times 1/2$ in the fiducial volume of 100 kg, compared to the $\times 1/290$ reduction for gammas in the fiducial volume. However, the single scatters cut is much more effective - while it has negligible effect on the gamma background, only 1/10 of the events that scatter in the fiducial volume are single scatters. The neutron event rates for the several cuts are listed in Table 7.7.
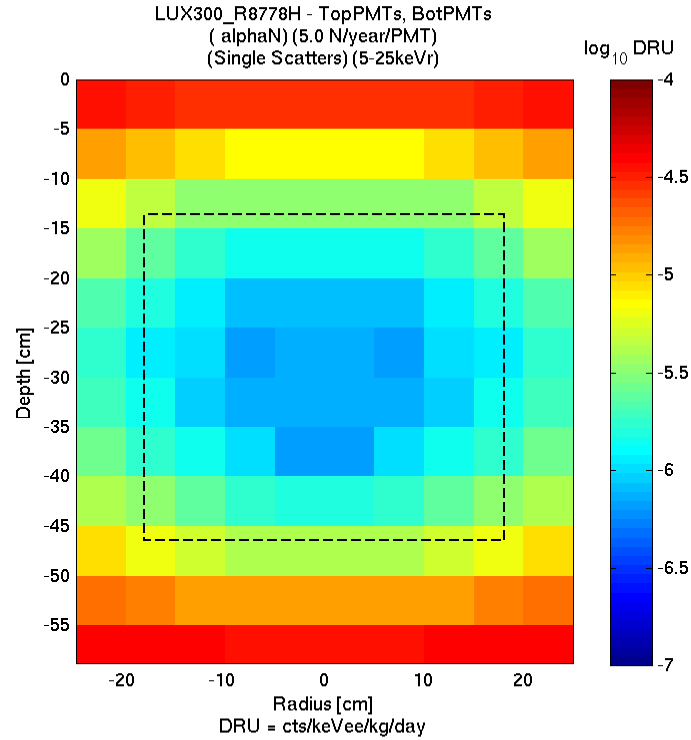
Figure 7.9: Spatial distribution of the neutron background in LUX due to PMT radioactivity, in the energy range of $5 - 25\,\mathrm{keV_{ee}}$, for single scatter events only. The black box indicates the LUX benchmark fiducial volume. The simulation uses the benchmark neutron production rate of 5 n/PMT/year, which is 5× higher than the expected PMT activity, in order to set conservative limits on the neutron background. The simulations use the same neutron emission spectrum used in the environmental fast neutrons simulation, shown in Fig. 6.6.

The energy distribution of nuclear recoil events is an exponential decay with $\sim 8.5\,\mathrm{keV_r}$ slope, and the average differential event rate in the $5 - 25\,\mathrm{keV_r}$ energy range is $1.57\,\mu\mathrm{dru_r}$ after the single scatter and fiducial volume cuts. This corresponds to a total event rate of 0.94 events in for the 100 kg fiducial, 300 live-days run, which is just below the upper limit on the background goal.

The background rate is further reduced by considering the electromagnetic component associated with each nuclear recoil event. Thus far we have only plotted the distribution of nuclear recoils; however, a portion of the events will also generate electron recoils. The electron recoils are generated mainly from 2 processes: neutron inelastic interaction in the liquid Xe; and thermal neutron capture, either in the liquid Xe or, to a lesser degree, in
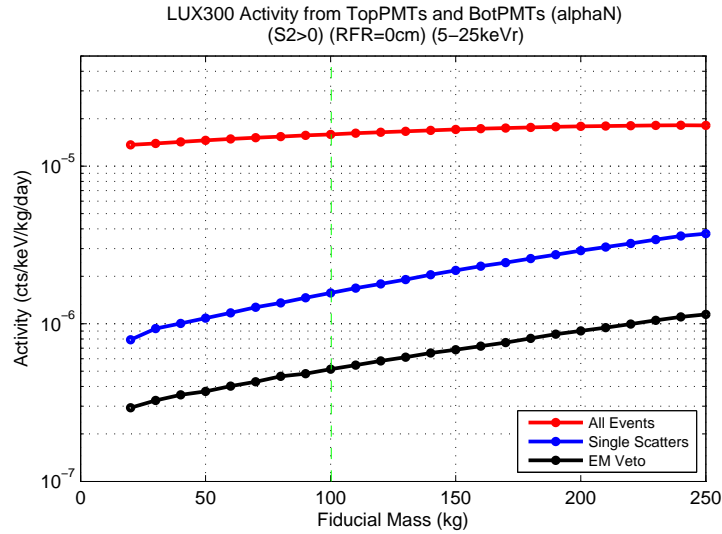
Figure 7.10: Nuclear recoil event rate due to PMT radioactivity vs. fiducial volume mass, obtained from a Monte Carlo simulation of the neutron background emitted by PMTs. The lines shows the exponentially decreasing rate as we reduce the size of the fiducial volume. The simulation uses the benchmark neutron production rate of 5 n/PMT/year, which is 5× higher than the expected PMT activity, in order to set conservative limits on the neutron background. The simulations use the same neutron emission spectrum used in the environmental fast neutrons simulation, shown in Fig. 6.6.

	Event Rate $(5 - 25\,\mathrm{keV_r})$
Total	$(29.7 \pm 0.1)\ \mu\mathrm{dru_r}$
Fiducial Cut (100 kg)	$(15.9 \pm 0.1)\ \mu\mathrm{dru_r}$
Single Scatters Cut	$(10.80 \pm 0.05)\ \mu\mathrm{dru_r}$
Single Scatters + Fiducial Cuts	$(1.57 \pm 0.03)\ \mu\mathrm{dru_r}$
Single Scatters + Fiducial Cut + EM-veto Cuts	$(0.52 \pm 0.02)\ \mu\mathrm{dru_r}$

Table 7.7: Predicted nuclear recoil event rate due to PMT radioactivity, using several cuts during analysis. The simulation uses the benchmark neutron production rate of 5 n/PMT/year, which is 5× higher than the expected PMT activity, in order to set conservative limits on the neutron background.
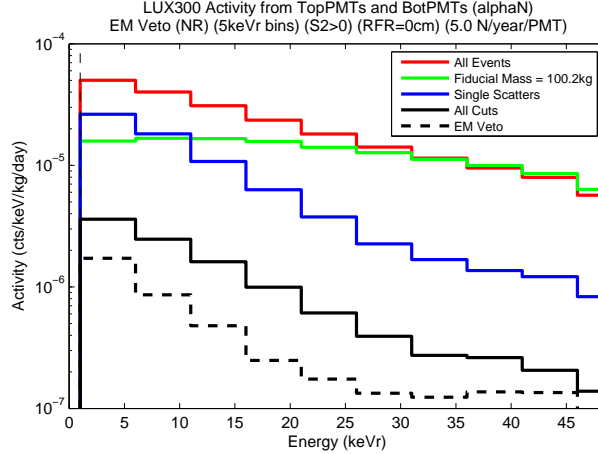
Figure 7.11: Energy Spectrum (in units of keV$_{\rm r}$) of the neutron background in LUX due to PMT radioactivity, assuming $5 \, {\rm n/PMT/year}$. The average event rate in the energy range of $5 - 25 \, {\rm keV_r}$ is $\sim 500 \, {\rm ndru_{ee}}$ (All Cuts + EM-veto). The black line for "All Cuts" includes the fiducial cut and a single scatter cut, but not the EM-veto. The EM-veto cut is applied separately on top of all other cuts (dashed black line).

the water. Both processes in Xe leave the Xe nuclei (or in the case of thermal capture in water, H nuclei) in an excited state that decay through the emission of gammas. After a neutron scatters once in the liquid Xe, it can escape into the water shield, where it will thermalize, and it can either be captured in the water itself, or in the liquid Xe. Neutron capture in water generates a $2.2 \, {\rm MeV}$ gamma, which has a $\lambda = 21.2 \, {\rm cm}$ attenuation length in water, $\lambda = 5.5 \, {\rm cm}$ in Ti, and $\lambda = 2.8 \, {\rm cm}$ in Cu. Thus, neutron captures within the first few cm around the cryostat can produce electron recoils in the liquid Xe, and improve the veto efficiency. Fig. 7.12 shows the electron recoil histogram for events with nuclear recoils that deposited $5 - 25 \, {\rm keV_r}$ in the active liquid Xe. The histogram shows lines from the inelastic nuclear recoils (i.e. $39.6 \, {\rm keV_{ee}}$ and $236 \, {\rm keV_{ee}}$ from $^{129}{\rm Xe}$; $80.2 \, {\rm keV_{ee}}$ and $164 \, {\rm keV_{ee}}$ from $^{131}{\rm Xe}$), the $2.2 \, {\rm MeV}$ from thermal neutron capture in water, and a couple of lines at $\sim 9 \, {\rm MeV_{ee}}$ from thermal neutron capture in the liquid Xe.

Approximately 2/3 of the nuclear recoil single scatters that deposit $5 - 25 \, {\rm keV_r}$ in the fiducial volume (100 kg) also have a electromagnetic component with energy $E > 20 \, {\rm keV_{ee}}$. Vetoing these events (the "EM-veto" cut) further reduces the event rate in the fiducial volume by a factor of at most $\times 1/3$. The differential nuclear recoil rate is then reduced to $0.52 \, \mu {\rm dru_r}$ (assuming the PMT contamination levels measured at SOLO and listed in Table
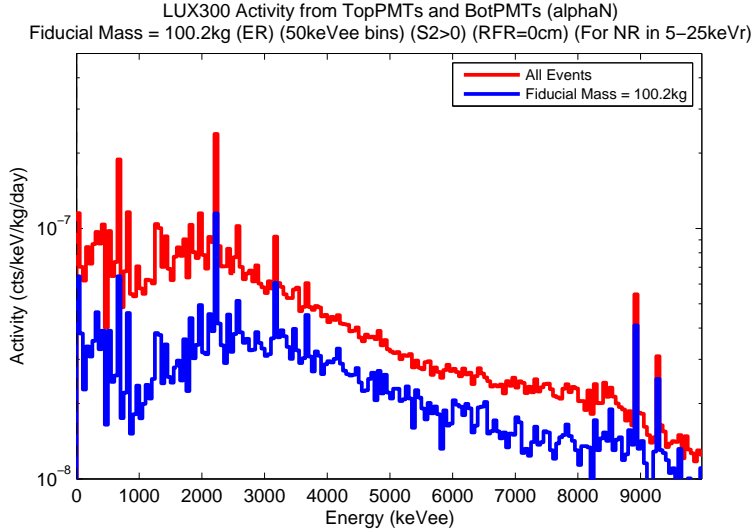
Figure 7.12: Electron recoil histogram from neutron simulation of the LUX detector in the water tank. The histogram shows only events that also deposited $5 - 25\,\mathrm{keV_r}$ in the liquid Xe through nuclear recoils. One can identify the $2.2\,\mathrm{MeV_{ee}}$ peak due to capture of thermal neutrons in water, and higher energy peaks at $\sim 9\,\mathrm{MeV_{ee}}$ from neutron capture in Xe.

7.3), which results in a total event rate of 0.3 events for the 100 kg fiducial, 300 live-days run, which is low enough relative to the nuclear recoil background goal of 2.2 events (before the 45% nuclear recoil acceptance cut).

7.1.3 "Gamma-X" Background

The gamma background due to the PMT radioactivity will also generate a Gamma-X background, multiple scatter gamma events that are misidentified as single scatter nuclear recoil events when all but one scatter occur in non-active liquid Xe. The nature and morphology of the Gamma-X events are explained in detail in Section 6.4.

Great care has been taken in the design of the LUX detector to eliminate regions of non-active liquid Xe, such as pockets of liquid around the PMTs, with the purpose of reducing the Gamma-X background. However, the use of high-voltage grids in the liquid to create a field for drifting electrons towards the gas phase will inevitably create a region of non-active Xe. The cathode grid, which defines the bottom of the active Xe region, has to be placed at some distance from the bottom PMTs distance to protect them from the high fields. The LUX design uses an additional grid (called simply the Bottom Grid) set at the same

voltage as the one applied to the PMT bias, so that no high fields are applied across the PMT body. The region below the cathode will have a field vector pointing in the opposite direction relative to the drift field - this is the Reverse Field Region (RFR). Since the field is pointing in the "wrong" direction, no electrons are drifted to the gas phase, and no S2 signals are generated for events in the RFR, thus leading to Gamma-X events.

Since these events can be mistakenly identified as nuclear recoils during analysis, it is desirable that their rate fall well below the background goal for nuclear recoil events. We can compare the ratio of Gamma-X event rate over the electron recoil event rate to the discrimination of electron recoil backgrounds - the Gamma-X ratio should be lower than 1-rejection of ER events. Monte Carlos simulations were analyzed to assess the rate of Gamma-X, and to advise the designing of the detector on the optimal placement of the cathode grid to reduce their rate.

The assessment of the Gamma-X background is done using the data from the Monte Carlo simulation for the PMT gamma background (detailed in Section 7.1.1). From the existing data, we can calculate the ratio of the number of events with 1 scatter in fiducial volume plus 1 or more scatters in the RFR volume over the total number of events with 1 scatter in the fiducial volume. The ratio is calculated for RFR volumes of different heights, and is shown in Fig. 7.13. Only events that deposit $1 - 50 \, \mathrm{keV_{ee}}$ in the fiducial volume of 100 kg or in the RFR are considered. The benchmark discrimination factor of 99.4% corresponds to a ratio of 6×10^{-3} Gamma-X events/ER events, which can be obtained with RFR height of $\leq 5 \, \mathrm{cm}$ for events in the energy range of $1 - 50 \, \mathrm{keV_{ee}}$. Based on this recommendation, the LUX detector was designed with a spacing of 5 cm between the cathode grid and the top surface of the bottom PMTs.

The ratio of Gamma-X events / ER events increase with energy, as shown in Fig. 7.14. The Gamma-X background can be reduced very efficiently by selecting events with low energy depositions, i.e. reducing the energy range from $1 - 50 \, \mathrm{keV_{ee}}$ to $1 - 25 \, \mathrm{keV_{ee}}$ reduces the ratio to $\sim 2 \times 10^{-3}$, corresponding to a discrimination of 99.8%; selecting the energy range of $1 - 10 \, \mathrm{keV_{ee}}$ reduces the Gamma-X event rate to $\sim 7 \times 10^{-4}$, corresponding to a discrimination of 99.93%. The Gamma-X event rate can be reduced even further by the
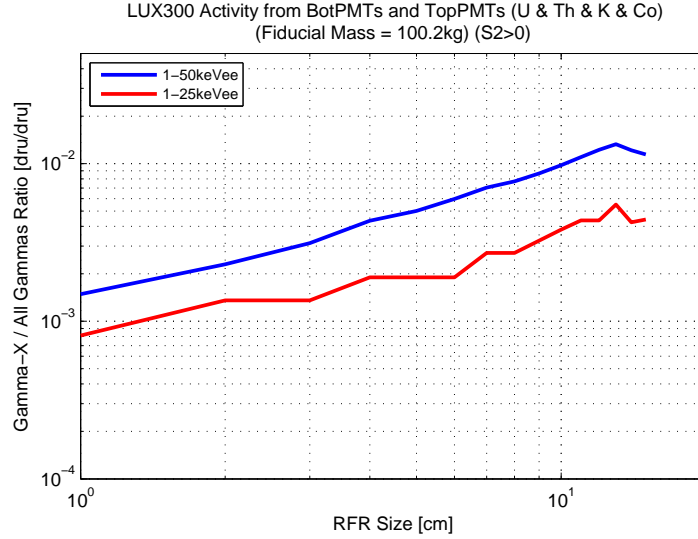
Figure 7.13: Ratio of Gamma-X event rate / electron recoil rate vs. size of the reverse field region (RFR), the space between the cathode and the bottom PMT array. The lines show the Gamma-X rate ratio for events that deposit $1 - 25\,\mathrm{keV_{ee}}$ (red) or $1 - 50\,\mathrm{keV_{ee}}$ (blue) in the LUX fiducial volume (100 kg).

application of Gamma-X cuts similar to the ones used in the XENON10 data analysis - see Section 4.3.2 for a discussion of the cuts.

7.2 LUX External Backgrounds and the Water Shield

The LUX detector is placed inside a 300 tonne water tank (see Fig. 7.15), which provides efficient shielding against the external neutron background, and reduces the external gamma background to negligible levels. Geant4 simulations of the external neutron and gamma backgrounds were performed to determine the optimal size and configuration of the water shield prior to construction.

Simulations using standard models of environmental gamma and neutron radiation in underground labs (see Table 7.8 for a list) are used to estimate the flux reduction in a water shield. Fig. 7.16 shows the flux vs. depth in water for gamma and neutron backgrounds. The flux reduction is measured as the number of particles that travel beyond a depth Z, divided by the number of emitted particles. For the neutron flux, an energy cut of $E_{\mathrm{n}} > 1\,\mathrm{keV}$ is applied to remove low energy and thermal neutrons. The fast neutrons ($1\,\mathrm{keV} < E_{\mathrm{n}} < 10\,\mathrm{MeV}$) generated by radioactive processes in the rock are moderated very efficiently
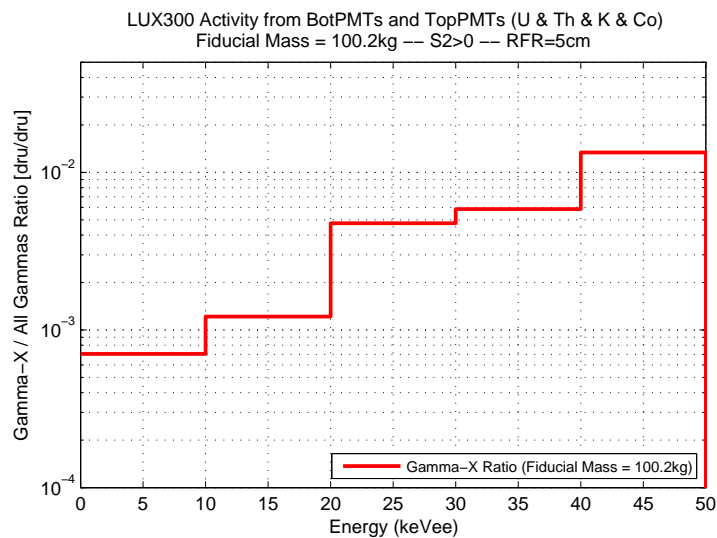
Figure 7.14: Ratio of Gamma-X rate / electron recoil rate versus energy, for events that deposit $1-50\,\mathrm{keV_{ee}}$ in the LUX fiducial volume $(100\,\mathrm{kg})$ and for a reverse field region (RFR) of 5 cm. The ratio is obtained from a Monte Carlo simulation of the gammas emitted by the LUX PMTs from the bottom and top arrays.
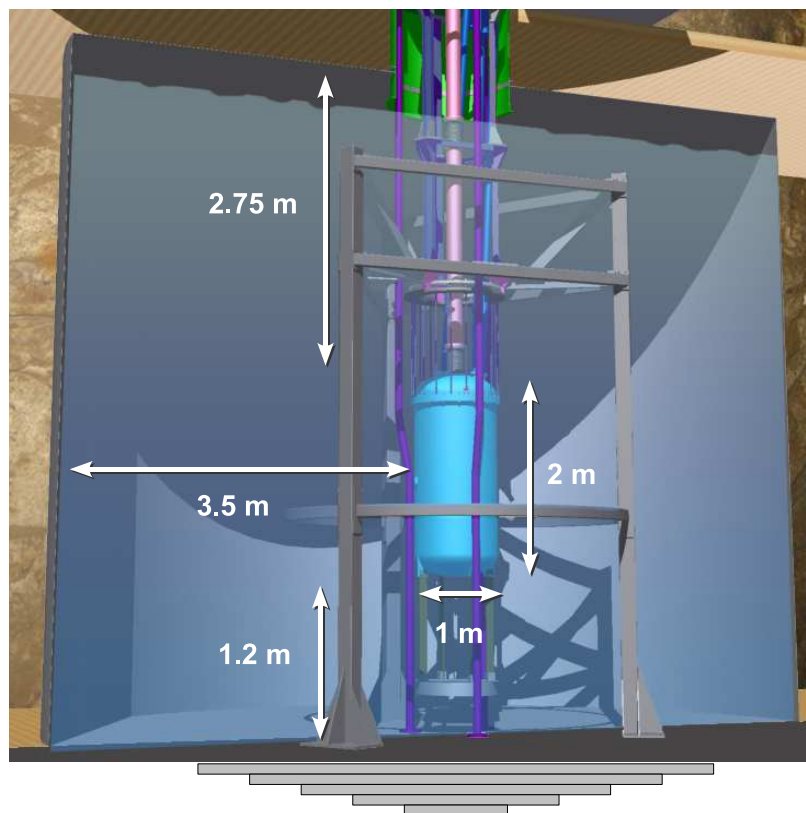
Figure 7.15: LUX detector inside the 300 tonnes water tank, with 8 m diameter and 6 m height. CAD drawing provided by John Thomson of the LUX Collaboration.

Background Type	References	Spectrum
γ's from rock	Carson, 2005 [152]	7.19 on page 281
(α,n) and fission neutrons from rock	Luzon, 2004; and Wulandari, 2004 [127, 117]	6.6 on page 192
μ-induced neutrons	Mei and Hime, 2005 [131]	6.14 on page 207

Table 7.8: LUX external background references - List of references for the background spectra used for the simulation of the LUX event rate due to external backgrounds, and the location of the spectra in this work.

by water, with a reduction of $\times 1/10$ in 11 cm of water. For the gamma background, 37 cm are necessary to achieve a $\times 1/10$ flux reduction. The most penetrating background is the μ-induced high energy neutron background ($E_n > 10\,\text{MeV}$), which requires $\sim 50\,\text{cm}$ to reduce the neutron flux by $\times 1/10$. Both neutron fluxes drop sharply in the first few centimeters, then stabilizing as exponential functions of depth, with a much gentler slope. This effect is due to the low end of the initial energy spectrum being moderated more efficiently than the rest; after the first few centimeters, the neutron flux becomes dominated by neutrons with higher initial energy. The effect is much more pronounced in the μ-induced neutrons, for which the flux drops by 1 order of magnitude in the initial 50 cm, but requires an additional 350 cm to drop 2 more orders of magnitude.

The final water shield design uses a water tank with 8 m diameter and 6 m height, plus steel plates placed under the tank to further reduce the gamma background (see Fig. 7.15). Such a large size is required to reduce the high energy neutron background well below the LUX background target, defined by the desired sensitivity limit. Although the overall shield size is driven by the high energy neutron background requirements, the assessment of the shield efficiency is done both for the gamma background and for the neutron backgrounds. The choice of shield dimensions and configuration is first detailed in Section 7.2.1, where we assess its effect on the gamma background.

7.2.1 Environmental Gamma Background and Shield Design

A series of Geant4 simulations analyze the effect of the water shield on the expected gamma background due to rock radioactivity in the Davis cavern laboratory. The gamma background goal in LUX is set by considering the event rate due to PMT gammas of 391 μdru_{ee}
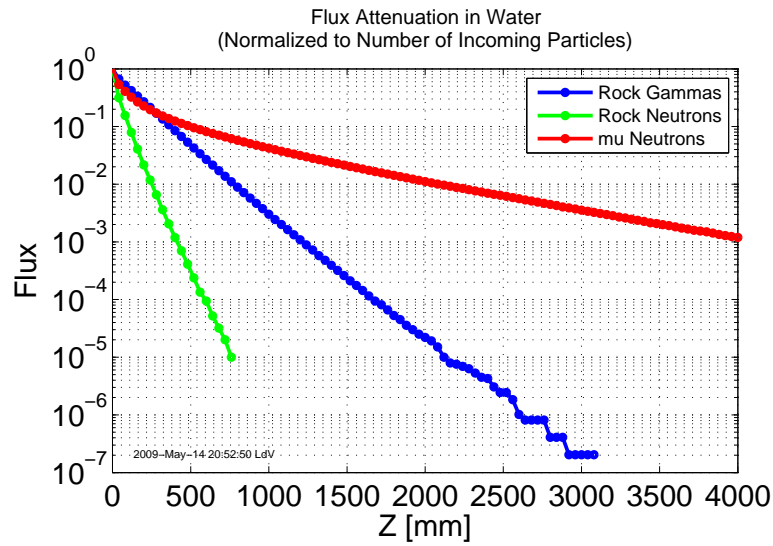
Figure 7.16: Flux reduction in water. The flux reduction is measured in a semi-infinite wall of water, and is defined as the number of particles that travel beyond a depth Z, divided by the number of emitted particles. For the neutron flux, an energy cut of $E_n > 1\,\text{keV}$ is applied to remove low energy and thermal neutrons.

| | Integrated Flux Reduction (Γ) | | |
| | (ratio of particles incident on cryostat / incident on shield) | | |
	2.5 m x 2 m shielding	3.5 m x 2 m shielding	+ steel plates
γ's from rock	1.2×10^{-7}	8×10^{-9}	2×10^{-10}
μ-induced high energy neutrons	4×10^{-4}	8×10^{-5}	-
fast neutrons from rock	3×10^{-16}	6×10^{-22}	-

Table 7.9: Integrated flux reduction for external background for several water shield configurations. The integrated flux reduction is ratio of the total number of gammas incident outer surface of the detector cryostat to the total number of gammas incident on the outer surface of the water shield. The integrated flux reduction summarizes the reduction in the number of incident particles due to the flux attenuation of the water shield, and due to geometrical effects (such as the solid angle occupied by the detector relative to the cavern cavity). The integrated flux reduction is obtained through a combination of Monte Carlo simulations and analytical calculations (see Section 7.2.1.2). The empty fields indicate that the integrated flux was not calculated.

	Differential Event Rate fiducial volume (100kg) $5 - 25\,\mathrm{keV}$	Total Event Rate 30,000 kg-days (fiducial) $5 - 25\,\mathrm{keV_r}$ $(1.3 - 8\,\mathrm{keV_{ee}})$
γ's from rock	$0.54\,\mathrm{ndru_{ee}}$ (no rhyolite) $27\,\mathrm{ndru_{ee}}$ (all rhyolite)	1×10^{-4} 6×10^{-3}
μ-induced high energy neutrons from water shield	$(121 \pm 8)\,\mathrm{ndru_r}$	$(73 \pm 5) \times 10^{-3}$
μ-induced high energy neutrons from rock	$\sim 54\,\mathrm{ndru_r}$	$\sim 33 \times 10^{-3}$

Table 7.10: LUX external backgrounds - event rates for the external background, using the full LUX shield (8 m diameter $\times$ 6 m height tank, with 20 tonnes of steel plates underneath).

in the 100 kg fiducial region, as discussed in 7.1.1. It is desired that the water shield be designed to ensure that all external gamma backgrounds are subdominant. The external gamma background is dominated by the radioactive decays in the Davis cavern rock of ^{40}K and the ^{238}U / ^{232}Th chains.

Starting with some basic assumptions about the shape of the gamma background expected at the Davis cavern (detailed in Section 7.2.1.1), the simulation estimates what event rate we should expect in the LUX detector for a given level of radioactive contamination in the surrounding rock, for several shield configurations. A two-stage simulation was created to determine the flux reduction in the water shield and the subsequent event rate in the detector separately, allowing for flexibility on shield configuration and results with high statistics. In each of these simulations, a different part of the detector serves as the sensitive volume (where events are recorded) - first, we measure just the incident flux on the *cryostat walls*, then we measure the resulting event rate in the *liquid Xe volume* (see Table 7.11). More than one tank size are considered in the simulations. Steel plates are also added under the detector to further reduce the gamma background.

7.2.1.1 Initial Gamma Background

The gamma simulation source is surface wrapped tightly around the water shield, and gammas are emitted with isotropic angular distribution and energy spectrum similar to what is found in well-documented underground environment. There is no measurement of

Sensitive Volume	Dimensions	Objective	Simulation used
Water "Wall"	100 m $\phi \times$ 100 m height	Measure flux in water	Flux attenuation in water (Fig. 7.16)
Cryostat	1 m $\phi \times$ 2 m height (actual LUX) 70 cm $\phi \times$ 93 cm height (MC)	Measure the flux incident on the cryostat	Section 7.2.1.2 Section 7.2.1.3
liquid Xe	49 cm $\phi \times$ 59 cm height	Measure event rate in the LUX detector	Section 7.2.1.4

Table 7.11: Sensitive Volumes used for the several Monte Carlo simulations. Note that the Water "Wall" is only used to calculate the flux attenuation in water (Fig. 7.16), and is not used in the remaining LUX simulations.

Site	Sample	Radioactive Contamination Levels [ppm]		
		^{238}U	^{232}Th	^{40}K
Homestake mine	HST-05A	0.080	0.250	1040
	HST-06	0.160	0.200	1540
	HST-07	0.550	0.300	21200
	HST-08	9.4	12.2	39800
	HST-09	8.3	10.1	33100
	HST-10	8.0	8.6	28000
	HST-11	8.6	12.2	16900
Boulby mine	-	0.060	0.300	1300
Granite	Standard	2.2-6.1	8-33	-

Table 7.12: Rock radioactive contamination levels, measured from several samples in the Homestake mine: rock samples from the 4850 ft level (HST-06), from the 7300 ft level (HST-05A and 07), and from rhyolite intrusions (HST-08, 09, 10 and 11) [153]. Also listed are values for the Boulby mine rock [152], and standard values for the contamination level of granite obtained from [154].

the gamma flux at the Homestake mine in the 4850 ft level, nor there is a measurement of the rock radioactive contamination levels in the Davis cavern, where the LUX detector will be deployed. Radiometric surveys on the Homestake mine analyzes several samples, and indicate that the rock of the Davis cavern is much lower ($\times 1/20$) than "standard" rock (see Table 7.12). Geological surveys of the mine suggest that most of the rock is of the same type as the sample labeled HST-06 in the radiometric analysis [153].

The water shield simulations uses the energy spectrum of the gamma flux at the rock-cavern interface used to simulate the Boulby Mine rock spectrum in [152] (see Fig. 7.17). The Boulby mine gamma spectrum was generated through Geant4 simulation of the ra-
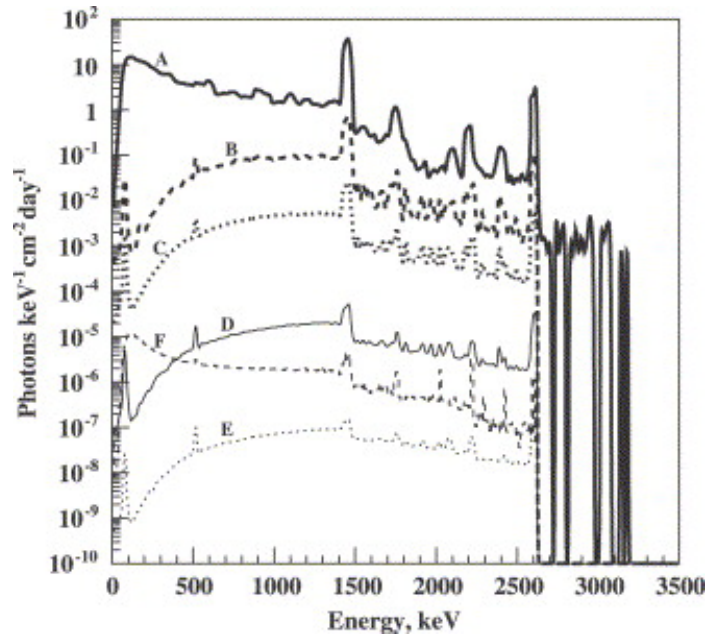
Figure 7.17: Boulby Mine rock gamma spectrum, from [152]. The lines represent the gamma flux at (A) rock-cavern interface; and the flux after several shield configurations: (B) 10 cm Pb; (C) 20 cm Pb; (D) 30 cm Pb; (E) 20 cm Pb + 40 cm of polyethylene.

dioactive isotopes in the rock, and it corresponds to the radioactive contamination levels given in Table 7.12. The choice of spectrum is based on several criteria: (1) similarity of the total radioactive contamination within a factor of $\times 2$, and in similar ratios; (2) availability of a full simulation of the Boulby mine background, from flux generation to detector event rate, allowing for comparison of techniques and results; (3) availability of full flux spectrum at the rock-cavern interface.

The Boulby mine walls are mostly salt, and thus expected to be rich in K. The total gamma flux ($E_\gamma > 0\,\mathrm{keV}$) of the Boulby Mine is

$$\Phi_{\gamma,\,\mathrm{Boulby}} = 0.09\,\gamma \cdot \mathrm{cm}^{-2} \cdot \mathrm{s}^{-1} \tag{7.4}$$

integrated over the entire energy spectrum [152]. Standard rock gamma backgrounds have a typical flux of

$$\Phi_{\gamma,\,\mathrm{standard\ rock}} = 1.7\,\gamma \cdot \mathrm{cm}^{-2} \cdot \mathrm{s}^{-1}.$$
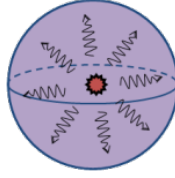
Figure 7.18: Diagram for gamma flux calculation: we can estimate the gamma flux from the rock wall by calculating the outwards gamma flux in a sphere of rock, with radius equal to the attenuation gamma length (see Eq. 7.6).

The most prominent features in the spectrum are the ^{40}K peak at 1.46 MeV and the ^{232}Th peak at 2.6 MeV. They have areas equal to 18.6% and 4.6% of the total spectrum, respectively.

This level of contamination seen in the Homestake mine HST-06 sample leads to a spectrum similar to the one used in Boulby mine simulation, with 50% less ^{232}Th, ×3 more ^{238}U, and 20% more ^{40}K. The ^{238}U and ^{232}Th decay chains yield 2.26 and 4.48 γ/decay in equilibrium, respectively, and ^{40}K emits a single gamma line with a branching ratio of 11%. based on the increase in the contamination levels, the total gamma flux in the Homestake mine relative to the flux in the Boulby mine should be larger by a factor of ×1.5.

A second method to estimate the total gamma flux ($E_\gamma > 0$ keV), is to analytically calculate the flux for a single gamma line and scale the entire flux accordingly. We apply this method by looking at the 2.6 MeV peak from the ^{232}Th chain. The flux from the cavern wall can be approximated by calculating the flux in a sphere of rock, with the radius equal to the attenuation length for 2.6 MeV gammas in rock $R = \lambda = 10$ cm (see Fig. 7.18), since we do not expect gammas further than $\lambda = 10$ cm from the rock wall surface to greatly contribute to the background. First, we convert the contamination level of ^{232}Th to radioactivity in **Bq/kg** using the conversion factors in Table 7.13, such that

$$1\,\text{ppm} \rightarrow 4.1\,\text{Bq/kg} \Rightarrow 0.200\,\text{ppm} \rightarrow 0.82\,\text{Bq/kg} \left(^{232}\text{Th}\right) \tag{7.5}$$

The flux can be expressed as:

	$1\,\mathrm{Bq/kg} \rightarrow \mathrm{ppm}$	$1\,\mathrm{ppm} \rightarrow \mathrm{Bq/kg}$
$^{238}\mathrm{U}$	0.081	12.4
$^{232}\mathrm{Th}$	0.245	4.1
$^{40}\mathrm{K}$	32	0.031

Table 7.13: Conversion factors - ppm to Bq/kg

$$
\begin{aligned}
\mathrm{flux} \quad &= \quad \frac{I\,[\gamma/\mathrm{s}]}{Area\,[\mathrm{cm}^2]} \\
&= \quad \frac{yield\,[\gamma/\mathrm{s/Bq}] \cdot activity\,[\mathrm{Bq/kg}] \cdot mass\,[\mathrm{kg}]}{Area\,[\mathrm{cm}^2]} \\
&= \quad \frac{yield \cdot activity \cdot \left(\rho \cdot \frac{4\pi}{3} \cdot R^3\right)}{4\pi \cdot R^2} \\
&= \quad yield \cdot activity \cdot \rho \cdot \frac{\lambda}{3} \quad\quad\quad (7.6)
\end{aligned}
$$

where *yield* is the number of gammas emitted per decay, and *activity* is the radioactive contamination level of the material. Using the density of rock of approximately $\rho = 3\,\mathrm{g/cm}^3$, we can calculate the flux as:

$$
\begin{aligned}
\mathrm{flux}\,(2.6\,\mathrm{MeV}) \quad &= \quad (1\,\gamma/\mathrm{s/Bq}) \cdot (0.82\,\mathrm{Bq/kg}) \cdot \left(3 \cdot 10^{-3}\,\mathrm{kg/cm}^3\right) \cdot \left(\frac{10\,\mathrm{cm}}{3}\right) \\
&= \quad 8.2 \cdot 10^{-3}\,\gamma \cdot \mathrm{cm}^{-2} \cdot \mathrm{s}^{-1}
\end{aligned}
$$

From the spectrum, one can see that the $^{232}\mathrm{Th}$ peak corresponds to 4.6% of the flux, so that the total gamma flux ($E_\gamma > 0\,\mathrm{keV}$) is $8.2 \cdot 10^{-3}\,\gamma \cdot \mathrm{cm}^{-2} \cdot \mathrm{s}^{-1}/4.6\% = 0.180\,\gamma \cdot \mathrm{cm}^{-2} \cdot \mathrm{s}^{-1}$ - ×2 larger than the Boulby mine flux:

$$
\Phi_{\gamma,\,\mathrm{Homestake\ rock}} \sim 0.180\,\gamma \cdot \mathrm{cm}^{-2} \cdot \mathrm{s}^{-1} \quad\quad\quad (7.7)
$$

Geological surveys also show rhyolite intrusions in the rock with much higher radioactivities, comparable to standard rock, with contamination levels of 8.6 / 10.8 / 29,000 ppm for $^{238}\mathrm{U}$ / $^{232}\mathrm{Th}$ / $^{40}\mathrm{K}$, averaged from the 4 rhyolite rock samples from the Homestake mine (HST-08, 09, 10 and 11 in Table 7.12). Geology experts familiar with the Homestake rock
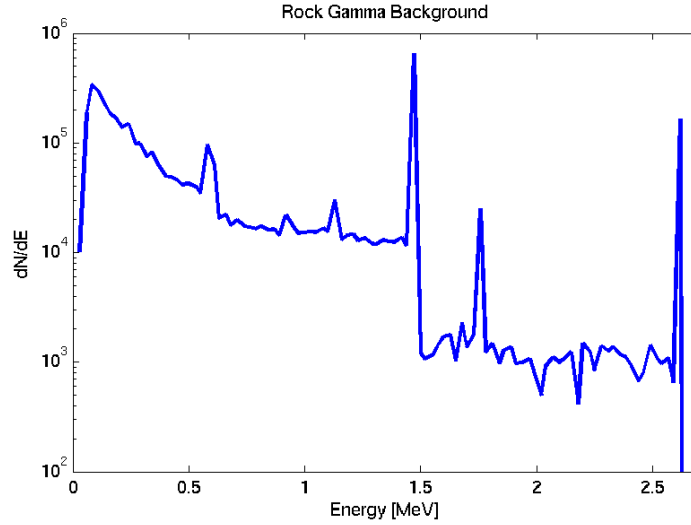
Figure 7.19: Rock gamma background: Initial spectrum used in the LUX external gamma background Monte Carlo simulations. The spectrum is equal to the Boulby Mine gamma spectrum shown in Fig. 7.17 in the range $100\,\mathrm{keV} - 2650\,\mathrm{keV}$, but normalized to match the expected gamma flux in the Davis laboratory where LUX will be deployed, shown in Eq. 7.7.

formations estimate the rhyolite intrusions to occupy a solid angle of less than 5% of the cavern[155]. Such level of rhyolite doubles the total radioactivity of the cavern. However, the actual percentage of rhyolite intrusions on the cavern surface is unknown at the time of writing. In order to set a conservative estimate of the gamma event rate in the detector, Monte Carlo simulations are normalized to the gamma flux corresponding to a cavern completely composed of rhyolite:

$$\Phi_{\gamma,\,\mathrm{rhyolite}} \sim 9\,\gamma \cdot \mathrm{cm}^{-2} \cdot \mathrm{s}^{-1}. \tag{7.8}$$

7.2.1.2 Gamma Flux Reduction by the Water Shield

The LUX water shield design was determined through a combination of Monte Carlo simulations and calculations in order to reduce computation time. The method consists of simulations of a smaller water shield, followed by analytical calculations to find the proper flux attenuation for a larger shield. In Section 7.2.1.3, a completely analytical method for calculating the flux is used, matching the results found through the combined Monte Carlo plus analytical method.

The LUX shield final design consists of a 8 m diameter, 6 m high tank with steel plates underneath, for a detector (cryostat) size of approximately 1 m diameter and 2 m height. In the actual LUX shield configuration, the detector is not placed in vertical center of the tank, but is displaced from the center by -0.59 m, since the steel plates provide extra shielding from gammas coming from the bottom. The effect of the steel plates and how they affect the shielding configuration are discussed in Section 7.2.1.3. In this section we only discuss the effect of the water shield on the external gamma background. Therefore, we will consider the effect of the water shield for a detector placed in the geometric center of the tank.

Integrated Flux Reduction. The *integrated flux* at a given surface is the total number of gammas incident on the entire surface, such that

$$\#\text{gammas incident} = \int_S \Phi \cdot \mathrm{d}A = \Phi_{\text{surface}} \cdot A_{\text{surface}} \tag{7.9}$$

where Φ_{surface} is the average gamma flux through the surface, in $\gamma \cdot \text{cm}^{-2}$.

The reduction in the gamma integrated inwards flux (Γ_γ) due to the water shield is defined as *the number of gammas incident on the cryostat surface, divided by the number of gammas incident on the entire surface of the water shield*:

$$\begin{aligned}
\Gamma_\gamma &= \frac{\#\text{gammas incident on cryostat}}{\#\text{gammas incident on water shield}} \\
&= \frac{\Phi_{\text{cryostat surface}} \cdot A_{\text{cryostat surface}}}{\Phi_{\text{shield surface}} \cdot A_{\text{shield surface}}}
\end{aligned} \tag{7.10}$$

where Φ_{surface} is the average gamma flux incident at the given surface, and A_{surface} is the total surface area. The integrated flux reduction is more useful than just the flux attenuation because it folds in both the flux attenuation due to shielding material, and effects due to the water tank geometry, making comparison between different configurations more straightforward. For the special case in which there is no material between the surfaces, the flux through the inner surface of the system ($\Phi_{\text{cryostat surface}}$) is equal to the flux through the outer surface ($\Phi_{\text{shield surface}}$), and thus the integrated flux reduction is simply $\Gamma_\gamma = A_{\text{cryostat surface}}/A_{\text{shield surface}}$.

The calculation of the integrated flux reduction is simpler for the special case of a spherical detector centered in a spherical water shield, such that the flux on the cryostat surface is a function of the flux attenuation in the shielding material:

$$\Phi_{\text{cryostat surface}} = e^{-t_{water}/\lambda_{water}} \cdot \Phi_{\text{shield surface}}, \tag{7.11}$$

where t_{water} is the thickness of the water shield. The integrated flux reduction becomes

$$\Gamma_{\gamma,\text{sphere}} = e^{-t_{water}/\lambda_{water}} \cdot \frac{r_{cryo}^2}{r_{shield}^2}, \tag{7.12}$$

where r_{cryo} and r_{shield} are the outer radii of the cryostat and water shield, respectively. For example, let's take a cryostat with 90 cm radius, and a spherical water tank with 2.5 m shield thickness. The flux attenuation for 2.5 m of water is $e^{-t_{water}/\lambda_{water}} = 2 \times 10^{-6}$ (see Fig. 7.16), and the integrated flux reduction is $\Gamma_{\gamma,\text{sphere}} = 1.4 \times 10^{-7}$. This shows good agreement with the integrated flux reduction found through simulations for a cylindrical shield with 2.5 m on the sides and 2 m on top and bottom (see Table 7.9).

The integrated flux reduction is not as easily calculated for the LUX water tank, since it has a cylindrical shape and the shield thickness is not uniform in all directions. In order to obtain the integrated flux reduction, it is necessary to either run a Monte Carlo simulation, or a detailed calculation integrating the flux attenuation at all points of the shield surface. Both methods will be used in this chapter to calculate the flux reduction in different shield configurations.

Monte Carlo simulations of water shield models and calculations of the flux attenuation in water determined the total reduction in gamma integrated flux is $\Gamma_\gamma = 8 \times 10^{-9}$ for the water shield with 2 m water shielding on the top and bottom, plus 3.5 m shielding on the sides, and with the detector placed in the geometric center. The integrated flux reduction is improved by the addition of steel plates below the tank, and the vertical displacement of the detector downwards to match the background from the top and bottom - this will be addressed in Section 7.2.1.3. This integrated flux reduction is calculated in 2 steps: (1) Monte Carlo simulation of a smaller water tank, with 2 m water shielding on the top and

Peak	Flux Contribution
2.6 MeV (Th)	76%
1.46 MeV (K)	13%
Others	11%

Table 7.14: Contribution of gamma lines in the initial gamma spectrum to the total flux in the cavity (that is, of the gammas that made it into the cavity) - most of the gammas entering the cavity are due to the high energy peaks from the Th chain (2.6 MeV) and K decays (1.46 MeV) in the incoming gamma spectrum

bottom, plus 2.5 m shielding on the sides; (2) the flux from the sides is reduced to match the attenuation for 3.5 m of water shielding.

Monte Carlo simulations. Monte Carlo simulations using Geant4 were performed for 2 water shield configurations: 2.5 m shielding on top and bottom, and 2.0 m shielding on top and bottom, both with 2.5 m shielding on the side. In both cases, the target was the volume where the cryostat will be located, represented in the Monte Carlo simulation by an empty cavity of 0.7 m diameter × 0.93 m height (see Fig. 7.20 for diagram of MC geometry). The size of the cavity used in the simulation is not the same as the actual size of the LUX cryostat, which is ∼1 m diameter × 2 m height - the simulations were performed before the design of the LUX cryostat was finished, and its size was unknown at the time. The change in size of the cryostat will not affect the estimate of the integrated flux reduction.

In both simulations, a large number of gammas ($\sim 10^{11}$) with the energy distribution discussed in Section 7.2.1.1 and shown in Fig. 7.19 are emitted isotropically (4π) from a thin shell wrapped around the water shield. The number of gammas incident on the water shield surface and incident on the cryostat cavity surface is counted, and the resulting integrated flux reduction is $\Gamma_\gamma = 5 \times 10^{-8}$ and $\Gamma_\gamma = 1.2 \times 10^{-7}$ for the water shields with 2.5 m and 2.0 m (top and bottom), respectively.

The spectrum of the gammas entering the water shield cavity is given in Fig. 7.21. Most of the gammas entering the cavity are due to the high energy peaks from the Th chain (2.6 MeV) and ^{40}K decays (1.46 MeV) in the incoming gamma spectrum (see Table 7.14). Figure 7.22 shows the energy distribution of the *initial gammas* that entered the cryostat cavity.
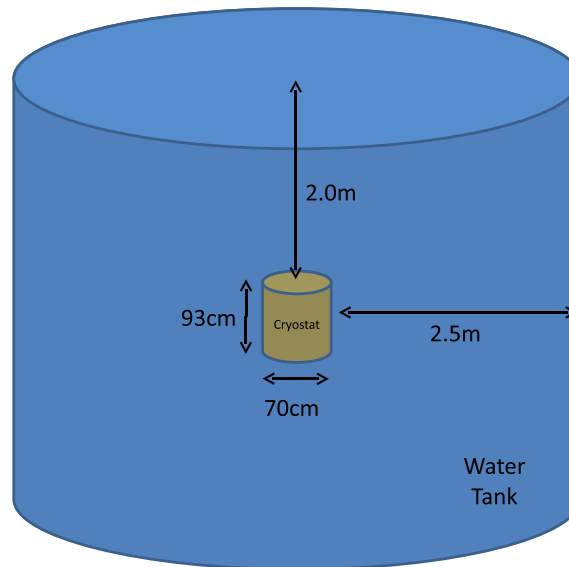
Figure 7.20: Monte Carlo geometry for preliminary water shield simulations *only* - the actual LUX shield has 3.5 m shielding on the sides, 2.75 m on top, 1.2 m on the bottom, and 20 tonnes of steel plates underneath the tank (see Fig. 7.15).
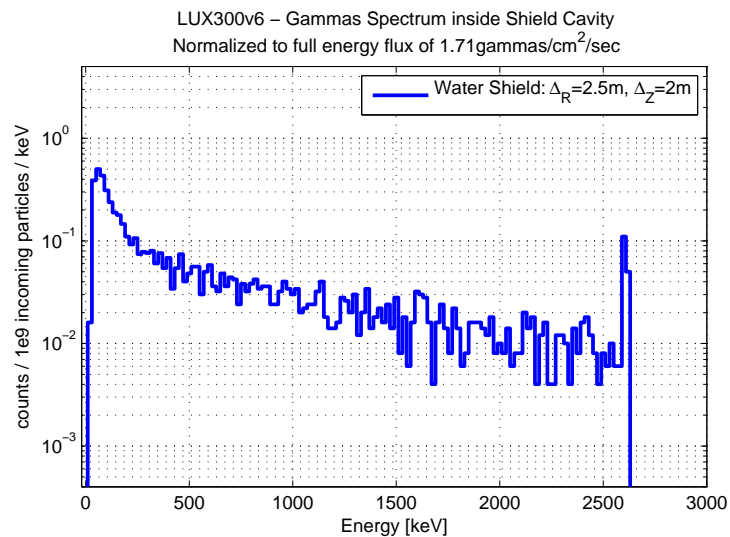
Figure 7.21: Gamma spectrum incident on the LUX cryostat. Note that the spectrum y-axis is normalized to the number of particles emitted in the MC $\times 10^{-9}$.
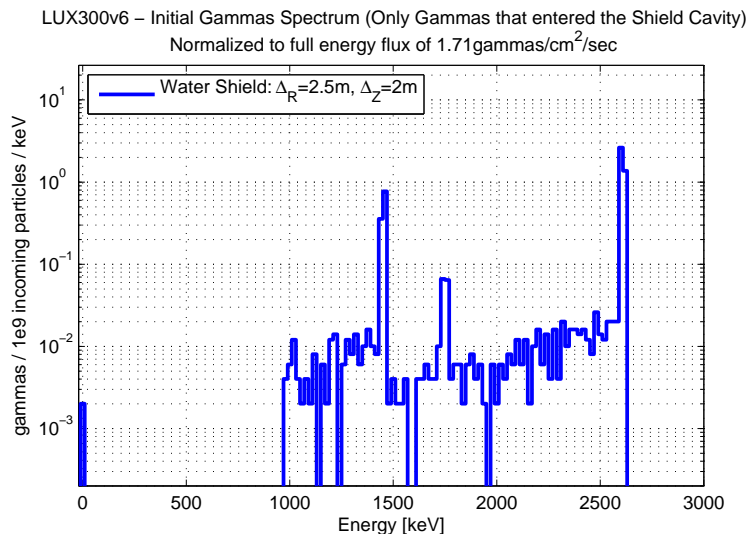
Figure 7.22: Histogram of the initial energy of gammas that transversed the water shield and reached the cryostat surface. Note that the spectrum is normalized to the number of particles emitted in the MC $\times 10^{-9}$.

The relative flux contribution by gammas coming from the sides and from the top and bottom is shown in Table 7.15. For a water tank diameter of 3.5 m shield thickness, the flux reduction of the gammas coming from the sides is 2 orders of magnitude better than a water tank diameter with 2.5 m shield thickness (see Fig. 7.16). The flux reduction is calculated for gammas incident at each point in the water shield surface, with a 10 cm resolution. The method used for such calculation is described in the next section (Section 7.2.1.3). The total integrated flux reduction for 3.5 m water shield thickness on the sides, plus 2 m shield thickness on top and bottom, is $\Gamma_\gamma = 8 \times 10^{-9}$. The gamma flux in such a shield is entirely dominated by the flux from the top and bottom (see Table 7.15).

7.2.1.3 Gamma Flux Reduction by the Water Shield plus Steel Plates

The LUX water shield is being build on top of steel plates with the intent of enhancing its shielding power, specifically by reducing the gamma flux from the top and bottom. The steel plates are arranged in an *inverted-pyramid* formation, to take advantage of the greater shielding by the corners of the water tank and thus reduce the total steel mass and its associated cost. This section details the method for calculating analytically the gamma flux

	Incident on water shield		
Incident on cryostat	All	Sides	Top+Bottom
All	100%	36%	64%
Sides	51%	31%	20%
Top+Bottom	49%	5%	44%

(a) 2.0 m × 2.5 m water shield thickness

	Incident on water shield		
Incident on cryostat	All	Sides	Top+Bottom
All	100%	0.6%	99.4%
Sides	31.5%	0.5%	31%
Top+Bottom	68.5%	0.1%	68.4%

(b) 2.0 m × 3.5 m water shield thickness

Table 7.15: Relative contributions to the gamma flux from the top+bottom and from the sides. The table lists where the gammas incident on the cryostat are coming from; e.g. for the 2.0 m × 3.5 m water shield thickness, 31% of gammas incident on the sides of the cryostat entered the water tank through the top and bottom surfaces.

reduction for the water shield and for the steel plates, and the method for optimizing the arrangement of steel plates for maximum shielding power.

The steel plate configuration for the water tank floor is a function of the total steel mass, which in turn is a function of the desired shielding to be provided by the water tank. The flux reduction obtained from adding steel is limited by the gamma flux from the top and sides of the tank, and by the radioactive contamination of the steel itself. The optimal tank configuration has a total steel mass of 20 tonnes, resulting in a ×40 reduction in the gamma rate compared to a water shield with no steel floor, going from $\Gamma_\gamma = 8 \times 10^{-9}$ to $\Gamma_\gamma = 2 \times 10^{-10}$ attenuation, when arranged in the configuration given in Figure 7.29. The optimal configuration is ∼ 31 cm thick at the center and 0 cm at 2.8 m radius (see Table 7.16), and requires the center of the detector to be displaced by $-59\,cm$ from the center of the water tank. The amount of steel used is limited by the radioactivity of the steel. For 20 tonnes of steel, the shield requires a combined contamination levels of 10 mBq/kg or lower for ^{238}U, ^{232}Th and ^{60}Co.

Calculating the Integrated Flux Reduction.   The total integrated flux reduction can be computed by calculating the total flux reduction for gammas originating from each point

(a) Without steel plates   (b) With steel plates
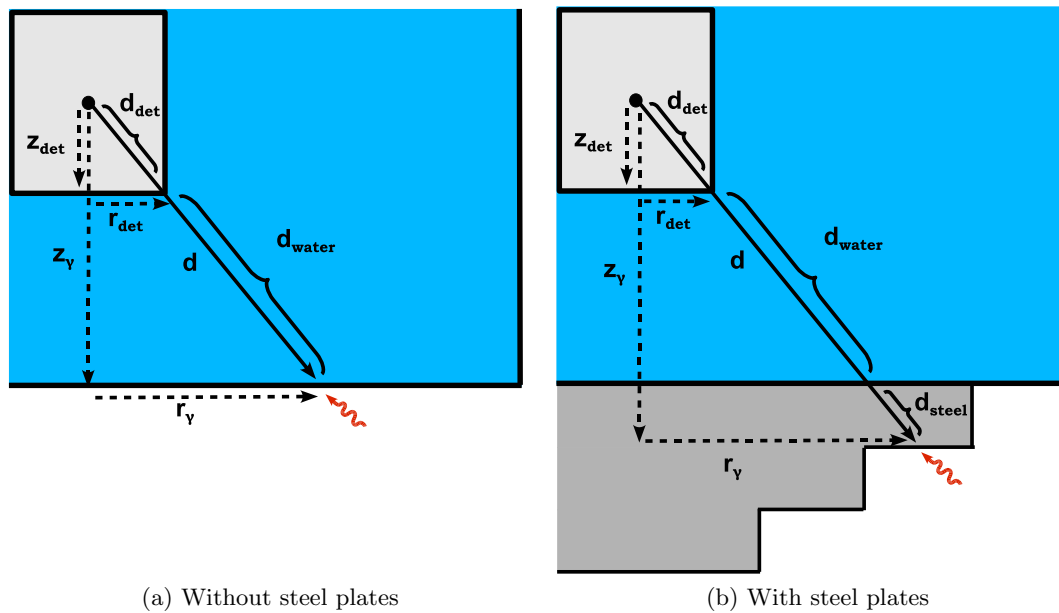
Figure 7.23: Water shield diagram for calculating flux reduction, illustrating the dimensions used in Eq. 7.14 to calculate the flux attenuation of the external background both by the water and by the steel plates placed underneath the water tank. The dimensions are exaggerated for didactic purposes.

in the tank surface. The integrated flux reduction is dominated by the attenuation of gammas in the shield material, which is a function of the distance between the point of origin of the gamma in the shield surface (r_γ, z_γ) and a point in the detector surface,

$$d = (r_{det}, z_{det}) - (r_\gamma, z_\gamma). \tag{7.13}$$

Since the detector is in a fixed position and z_γ is the same for all gammas entering the water shield from the bottom, the integrated flux reduction due to the addition of steel plates can be computed as a function of r_γ, the radius at which the gamma entered the shield.

The calculation of the integrated gamma flux reduction uses a simplified model, with just a water tank and an empty cavity, for where the detector should be. The model uses a cryostat cavity with 35 cm radius and 93 cm thickness, surrounded by a water shield 4 m in radius (3.65 cm shield thickness), 2 m shield thickness on top and 2 m of shield thickness on the bottom. The size of the cryostat cavity is the same as the simulation detailed in the previous section, so that results can be compared directly. The discrepancy between the

simulation and the actual cryostat size will not affect the estimate of the flux reduction.

We will focus the discussion of the method on the gammas emitted from the bottom of the water tank, as these are affected by the water tank and steel plates on the floor. The attenuation of gammas from the top and side is computed in the exact same manner, but with steel thickness $d_{steel} = 0$. The effect of steel shielding is computed for increments of steel plates 5 cm thick. The gammas emitted from the bottom and top of the shield are grouped in radial bins 4 cm thick. The gammas emitted from the sides are grouped in bins of 10 cm height.

The reduction in the integrated gamma flux from the bottom of the water tank is described by 3 factors:

1. The attenuation of photons in the shielding material is proportional to $e^{-d/\lambda_{material}}$:

$$attenuation = exp\left(-\frac{d_{water}}{\lambda_{water}} - \frac{d_{steel}}{\lambda_{steel}}\right) \qquad (7.14)$$

   where $\lambda_{material}$ is the *total attenuation length*. For the external gamma radiation spectrum used in the previous simulations, we have average attenuation lengths of $\lambda_{water} = 18.7\,cm$ and $\lambda_{steel} = 2.2\,cm$.

2. The effective solid angle of the detector as seen from each radial bin, $\Omega_{eff} \propto \frac{1}{d^2}$. Gammas from $r_\gamma = 0$ are more likely to reach the detector than gammas from the edge of the shield at $r_\gamma = 400\,cm$, even without the attenuation of water. Ω_{eff} is the solid angle covered by the detector (Ω_{det}) over the solid angle of the inside surface of the water shield wall (2π). For the top and bottom flux, $\Omega_{det} = \Omega_{cone}$ and

$$\Omega_{eff,top+bottom} = \frac{\Omega_{cone}}{2\cdot\pi} = \frac{2\cdot\pi\left(1 - cos\theta\right)}{2\cdot\pi} = 1 - \frac{d}{\sqrt{\left(d^2 + r_{cryo}^2\right)}} \qquad (7.15)$$

   where r_{cryo} is the cryostat radius. For the flux coming from the sides of the water tank, $\Omega_{eff} = \Omega_{pyramid}$ and

$$\Omega_{eff,sides} = \frac{\Omega_{pyramid}}{2\cdot\pi} = \frac{4\cdot\arcsin\left(\frac{h_{det}\cdot r_{det}}{\sqrt{\left(4\cdot d^2 + h_{cryo}^2\right)\cdot\left(4\cdot d^2 + r_{cryo}^2\right)}}\right)}{2\cdot\pi} \qquad (7.16)$$

where h_{cryo} is the cryostat height.

3. The number of gammas emitted in each radial bin $\propto r$:

$$N_{emitted}(r) = \Phi \cdot A_r = \Phi \cdot 2\pi \cdot r \cdot \Delta r \qquad (7.17)$$

where Φ is the gamma flux ($\gamma \cdot \mathrm{cm}^{-2} \cdot \mathrm{s}^{-1}$).

The gamma reduction for a single radial bin in the tank surface is just:

$$\Gamma_r = attenuation \cdot \Omega_{eff} \qquad (7.18)$$

and the integrated flux reduction is calculated by simply adding the reduction for each radial bin, while properly weighting the number of gammas emitted:

$$\Gamma_{total} = \frac{\sum_r \left[N_{emitted}(r) \cdot attenuation \cdot \Omega_{eff} \right]}{\sum_r N_{emitted}(r)} \qquad (7.19)$$

Using no steel plates, the method described above can be used to calculate the integrated flux reduction for a water shield with 2 m thickness on top and bottom, and 2.5 m shield thickness on the sides, yielding $\Gamma_{total} = 1 \times 10^{-7}$. We can compare this integrated flux reduction with the one found through Monte Carlo simulation in Section 7.2.1.2, $\Gamma_{MC} = 1.2 \times 10^{-7}$. For a water shield shield with 2 m thickness on top and bottom, and 3.5 m shield thickness on the sides, the integrated flux reduction is $\Gamma_{total} = 8 \times 10^{-9}$.

As we add steel below the water tank (in increments of 5 cm), the flux attenuation for each radial bin is improved accordingly. Figure 7.24 shows the effect of adding steel plates for individual radial bins. The figure clearly shows that the outer edges of the steel tank do not need a lot of steel to bring the gamma flux to a very low level; adding a uniform plate of steel under the entire bottom of the tank would be a waste of steel.

Optimizing on dΓ/dm. One criteria to selecting the best arrangement of steel is to find a steel plate distribution in which the change in gamma reduction when more steel is added depends only in the amount of steel added, and not in the specific location the steel is
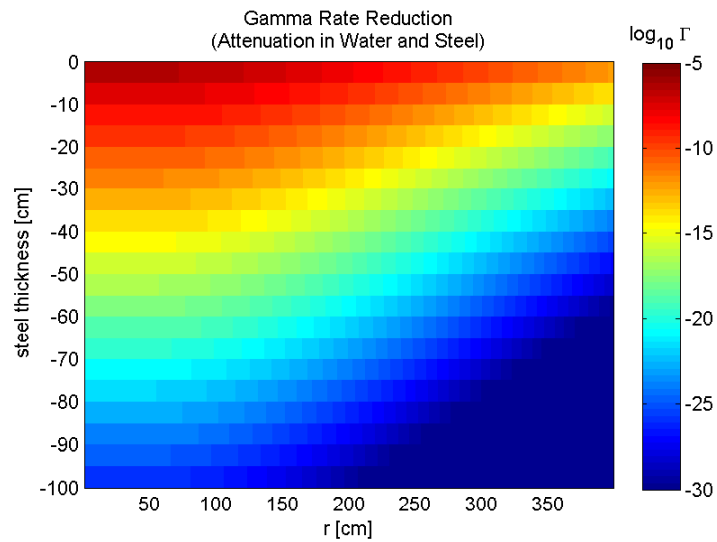
Figure 7.24: Gamma flux attenuation vs. steel thickness. The plot shows the flux attenuation (Eq. 7.14) for gammas originating in the given radial bin (x-axis) for the amount of steel added to the shield (y-axis). The flux attenuation already includes the attenuation of the water tank (2 m thickness at the bottom), for the detector at the geometric center of the tank (the effect of displacing the detector downwards will be shown later). For example, the left-top corner of the plot indicates that the flux attenuation for gammas originating in the first radial bin (0 - 4 cm), with no steel added, is 10^{-5}. Likewise, the bin at the center of the plot indicates that for gammas originating in the radial bin centered at 200 cm, and for 50 cm of steel thickness, the flux is attenuated by 10^{-18}.
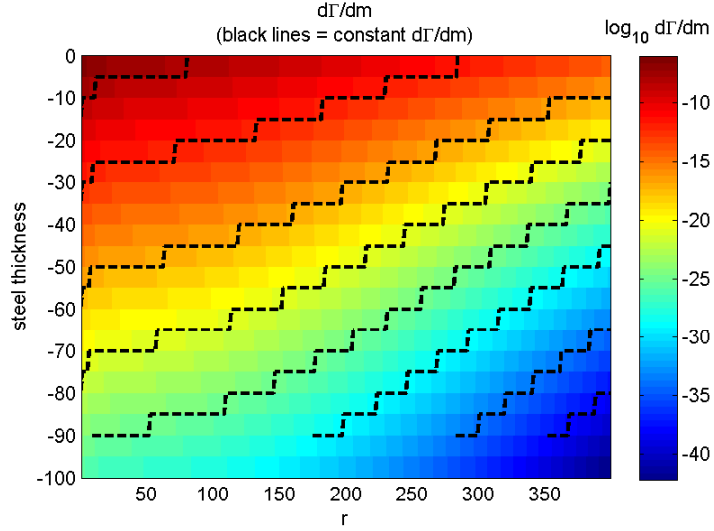
Figure 7.25: $d\Gamma/dm$. The plot shows the change in gamma flux reduction ($\frac{d\Gamma}{dm}$) as we increase the amount of steel (y-axis) for each redial bin (x-axis) (see Fig. 7.24). The dashed black lines indicate examples of contours of equal $\frac{d\Gamma}{dm}$ (the same on all radial bins). These lines are the **contours for the optimal arrangement of steel plates** *for a detector placed in the middle of the water tank.* The attenuation if only for gammas emitted from the bottom of the detector.

added. In other words, we want to find a thickness distribution such that the change in attenuation for gammas emitted from a given radial bin ($d\Gamma$) when we add steel (dm) is independent of radius - that is, $\frac{d\Gamma}{dm} = C$ across all radial bins.

In Fig. 7.25, we plot $\frac{d\Gamma}{dm} = \frac{d\Gamma}{d\,z_{steel}} / \frac{dm}{d\,z_{steel}}$, where z_{steel} is the steel thickness. Both derivatives are related to the change in thickness: $\frac{d\Gamma}{d\,z_{steel}}$ is the change in gamma flux reduction (for the bottom) in a radial bin as we add more steel, and $\frac{dm}{d\,z_{steel}}$ is the change in mass in a radial bin as we add more steel thickness. The lines of constant $\frac{d\Gamma}{dm}$ (the black lines in Fig. 7.25) are the contours of the optimal steel plate distributions *for a detector in the geometric center of the water tank.* Finally, we integrate the total gamma flux reduction (Γ_{total}) and the total steel mass for each of these contours, and obtain the attenuation vs. steel mass displayed in Figure 7.26. As we add steel, the flux from the bottom is reduced, but we remain limited by the flux from the top and sides of the tank. *We must move the detector downwards, so that the total gamma reduction from gammas above and below the detector are in equilibrium.*
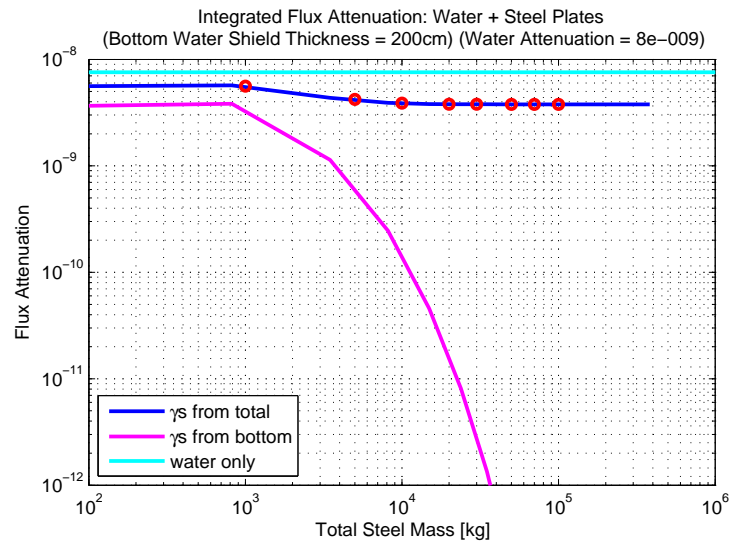
Figure 7.26: Attenuation due to Steel vs Total Steel Mass for Lines of equal dΓ/dm, *for a detector placed on the middle of water tank*. The plot illustrates that is not enough to simply add steel, as the background is dominated by the top flux - it will be necessary to move the detector downwards to match the background from the top and bottom. The detector is also shielded by 2 m water on top and bottom, and by 4 m of water on the sides. The red line shows the flux reduction for gammas emitted from all directions, and the blue line shows the flux reduction for gammas emitted from the bottom of the detector only. While the flux from the bottom is continuously reduced by the addition of more steel mass, the total effectiveness of the tank is limited by the flux from the top of the detector.

Radius (cm)	Steel Thickness (cm)
0-10	31
10-70	26
70-118	21
118-158	16
158-198	11
198-250	6
250-282	1

Table 7.16: Optimal steel plate configuration for 20 tonnes steel plates under the water tanks. Note that this configuration requires the center of the detector to be moved $-59\,cm$ from the center of the water shield.

Moving the detector down. The optimal arrangement of steel and the optimal placement of the detector is calculated so that the contribution of the gamma background from the top and bottom of the detector are equal, for a given amount of steel. Note that in order to simplify this exercise, we can ignore the gamma contribution from the sides in finding the equilibrium point. The contribution from the sides is added back again when calculating the total flux reduction for the shield.

The calculation is simply an iteration on the method described in the previous sections. We calculate optimal steel plate distribution and the resulting flux reduction for the detector at the center of the water tank; then we move the detector down a little, calculate the new steel distribution contours and masses, and obtain the steel mass necessary for the flux reduction of gammas from below and above to match. We keep doing this until we have the optimal steel mass for each detector z-position (see Figure 7.28). Then we can go back and calculate the total gamma reduction and steel distribution contours for the desired steel masses (see Figures 7.27 and 7.29).

For 20 tonnes of steel mass, the detector needs to be moved downwards by $-59\,$cm, relative to the position at the center of the water tank. The steel plate optimal configuration for 20 tonnes has, $\sim 31\,$cm thick at the center and $0\,$cm at $2.8\,$m radius, as seen on Table 7.16.

Limits on the Steel Radioactivity. Adding steel plates reduces the activity in the detector due to external radiation, but it might increase the total background if the steel
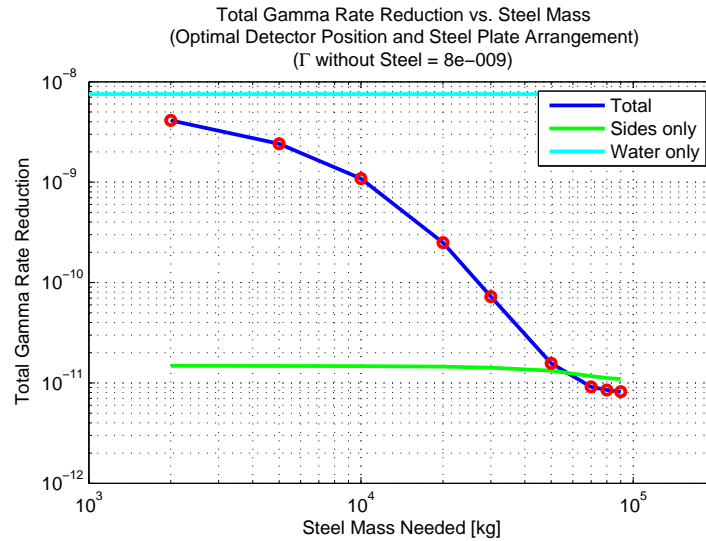
Figure 7.27: Total Attenuation vs. Total Steel Mass for Optimal Detector Position. The plot shows the total gamma flux reduction for the given amount of steel. At some point (50 tonnes), the gamma flux reduction becomes limited by the contribution from the sides.
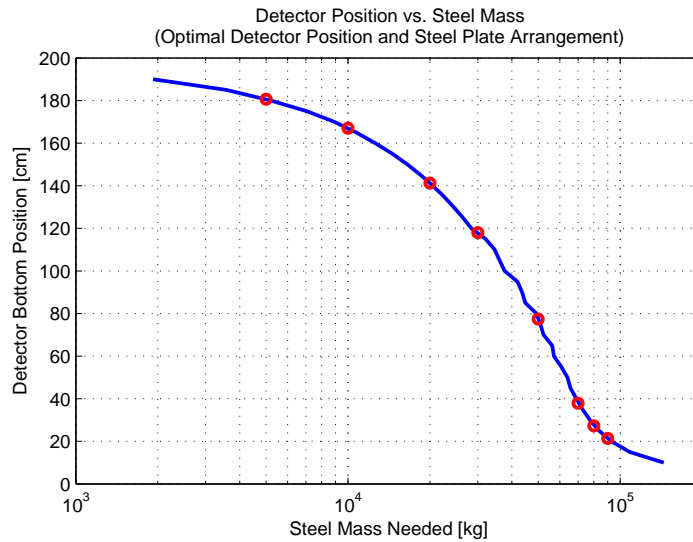
Figure 7.28: Optimal Detector Position vs. Total Steel Mass. The plot shows the z-position of the bottom of the detector so that the gamma flux reduction from above and below the water tank is the same for several steel masses.
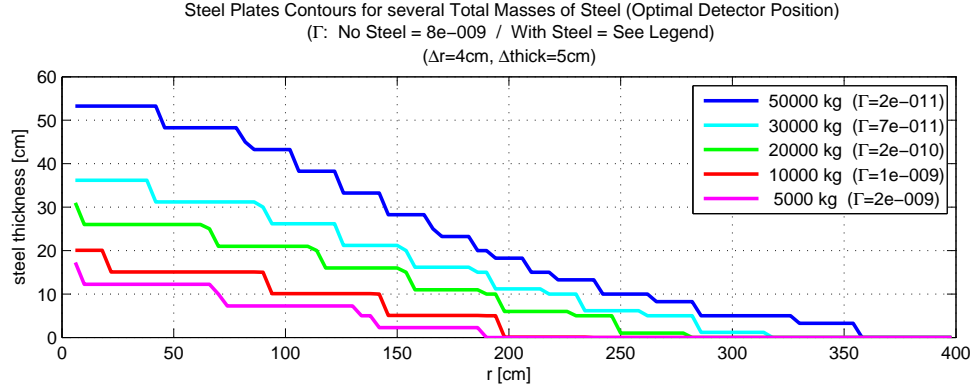
Figure 7.29: Contours of the optimal steel plate distribution for a set of steel masses. The legend indicates the total gamma flux reduction for each steel mass in the set.

plates themselves have large activity compared to the external radiation. As an example, the addition of 20 tonnes of steel plates below the water tank reduces the background by a factor of $\times 40$. To a first approximation, this would require the steel to be $\times 1/40$ cleaner than the rock surrounding the water shield. Because the detector is moved down in the water tank and the bottom of the detector is now at 140 cm (see Fig. 7.28), the water is less effective at shielding radiation from the steel by a factor of $10^{-\frac{200-140 \, \text{cm}}{43 \, \text{cm}}} = 1/25$, meaning that the steel has to be approximately $\times 1000$ less radioactive than the rock. However, the maximum tolerable contamination level in the steel is actually found by matching the flux due to some contamination in steel to the external gamma flux for a given steel plate configuration.

The flux from the steel is estimated by considering the flux from a sphere of steel with the radius equal to the attenuation length $\lambda_{steel}(E_\gamma)$, where E_γ is the energy of a gamma line emitted by the isotope. The calculation is performed for each gamma line from a given isotope, and all lines are added together to obtain the total flux per isotope. Eq. 7.22 gives us the flux as a function of contamination level. Fig. 7.30 shows the maximum contamination level for each isotope vs. the total steel mass so that the gamma flux from the steel matches a flux of $0.2 \, \gamma \cdot \text{cm}^{-2} \cdot \text{s}^{-1}$ from the rock. The plot shows that if we take the contamination levels from a sample of steel used for the XENON10 shield and measured at Gran Sasso (7 / 7 / 11 mBq/kg for ^{238}U / ^{232}Th / ^{40}K - see Table 5.10), the steel plates are limited to a total mass of 20 tonnes.
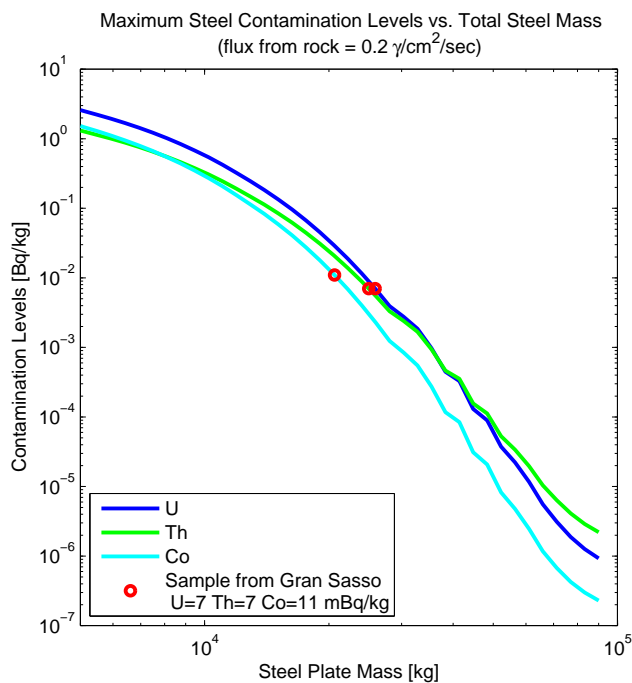
Figure 7.30: Maximum Steel Contamination vs. Steel Plate Mass. The maximum contamination levels assume that the entire gamma flux coming from the steel belongs to the given isotope. The plot shows that if we take the contamination levels from a steel sample measured at Gran Sasso for XENON10, the steel plates are limited to a total mass of 20 tonnes.

	γ's incident on cryostat		
	All	Sides	Top+Bottom
LXe	100%	81.3%	18.7%

Table 7.17: Contribution from the cavity gamma flux to the detector event rate, for uniform flux over cryostat surface.

7.2.1.4 Gamma Event Rate

The final stage in the assessment of the shield efficiency consists of calculating the resulting detector event rate due to the gamma flux. Monte Carlo simulations use the gamma flux in the shield cavity (shown in Fig. 7.21) as the source spectrum. The simulation geometry contains the LUX liquid Xe cylinder with 49 cm diameter, 59 cm height, wrapped in Teflon 4 cm thick, with a vacuum space wrapped in a single-walled steel cryostat 4 cm thick with external dimensions of 93 cm height and 70 cm diameter. The cryostat dimensions differ from the final LUX design as the simulations were run before the cryostat design was finalized and commissioned. As mentioned above, the final design uses a double walled cryostat, with a Ti inner and outer walls of ~ 0.65 cm thickness, separated by 10 cm of vacuum, and the inner cryostat is covered on the outside with a layer of high-purity Cu acting as a radiation shield. The source is a thin shell wrapped tightly around the cryostat. Gammas are emitted uniformly on the surface, with isotropic angular distribution. The flux normalization only counts gammas emitted inwards. The event rate in the detector fiducial volume of 100 kg is calculated for the energy region of interest $5 - 25\,\mathrm{keV_{ee}}$, and is normalized to the flux on the cryostat surface. Assuming that the source emits gammas uniformly spread through the surface of the cryostat, we obtain $6\,\mu\mathrm{dru_{ee}}/\left(\gamma \cdot \mathrm{s}^{-1}\right)$, or $0.166\,\mathrm{dru_{ee}}/\left(\gamma \cdot \mathrm{cm}^{-2} \cdot \mathrm{s}^{-1}\right)$ *for the flux on the cryostat surface.* The contributions from gammas from the side and from the top and bottom are listed on Table 7.17.

Combining this result with the flux reduction due to the LUX water shield (with the inverted-pyramid steel plates) calculated in the previous section, $\Gamma_\gamma = 2 \times 10^{-10}$, we have an event rate ratio of $1.26 \times 10^{-15}\mathrm{dru_{ee}}/\left(\gamma \cdot \mathrm{s}^{-1}\right)$, for γ's incident on the water tank. Normalizing the event rate to the external gamma flux, we get the event rate as a function of the external flux:

$$\frac{event\,rate}{\Phi_\gamma} = 3\,\text{ndru}_{\text{ee}}/\left(\gamma \cdot \text{cm}^{-2} \cdot \text{s}^{-1}\right) \tag{7.20}$$

in the fiducial volume of 100 kg, in the energy region of $5 - 25\,\text{keV}_{\text{ee}}$, for the LUX water tank with $3.5\,\text{m}$ shield thickness on the sides, 20 tonnes of steel plates underneath, and a detector displaced from the center by $-59\,\text{cm}$. For a conservative limit, we can estimate the event rate in the LUX fiducial volume in the case of a cavern *completely covered in rhyolite.* Using the flux due to rhyolite (Eq. 7.8), we get event rate= $27\,\text{ndru}_{\text{ee}}$, 4 orders of magnitude below the gamma background goal (see Table 7.1).

The expected event rate due to external gammas is far below the background goal - 2 orders of magnitude below goal would be sufficient to render it subdominant to the internal gamma background. However, the extra shielding provides a safety factor against any systematics in the background model, such as the uncertainty in the rock radioactivity in the Davis cavern. Moreover, the shield was designed to provide backgrounds low enough to allow the expansion of the DUSEL scientific program, either through the installation of a larger detector, or the installation of additional detector of similar size. Because of the extra shielding, the LUX detector can be safely moved laterally to make room for a second detector. Calculating the integrated flux reduction for the detector at different X-Y positions, we estimate that by moving the center of the detector by 1.5 m laterally from the center of the tank will raise the event rate to 1% of the background goal. However, the backgrounds from the sides quickly become a problem, and moving the detector by 2 m laterally from the center of the tank will raise the event rate to 20% of the goal, at which point it would become a major component of the gamma background.

7.2.1.5   Feedthroughs

The placement of the detector inside a water shield requires the use of feedthrough pipes to feed in cables and gas pipes. Such pipes form holes in the shield, and could become sources of background for the detector. Typical solutions include the addition of a "dog-leg", that is, a bend in the middle of the detector to eliminate line-of-sight paths for the external gammas. However, calculations and Monte Carlo simulations have been performed and

| Shield | Flux Attenuation | Flux Reduction due to solid angle | |
Thickness	in water	3 in pipe	6 in pipe
2 m shield	1.9×10^{-4}	1.8×10^{-4}	7.3×10^{-4}
2.59 m shield	1.5×10^{-5}	1.0×10^{-4}	4.3×10^{-4}

Table 7.18: Flux attenuation for gammas emitted above the water tank into straight feedthrough pipes in the LUX water tank, for a 2.6 MeV gamma point source placed directly above the feedthrough pipe entrance, centered with the detector. The flux reduction is calculated from the attenuation due to water shielding (see Fig. 7.16), and due to the solid angle of the pipe (using Eq. 7.21). The flux reduction is calculated both for 2 m of water (detector at center of tank), and for 2.59 cm of water (for the detector displaced by -59 cm from the center of the water tank - see Section 7.2.1.3).

indicate that the feedthrough pipes will not add significantly to the background, and no "dog-leg" is necessary.

Feedthrough pipes with 3 in and 6 in diameters are considered for use in the LUX detector. A simple calculation demonstrates that the reduction given by the solid angle of the hole at the end of the pipe is similar to the reduction given by the attenuation effect of water shield. The gamma flux incident on the cryostat is dominated by the most penetrating gamma, the ^{232}Th line at 2.6 MeV. The flux attenuation in 2 m of water for 2.6 MeVgammas is 1.9×10^{-4} (detector at center of tank), and for 2.59 cm of water the attenuation is 1.5×10^{-5} (for the detector displaced by -59 cm from the center of the water tank - see Section 7.2.1.3). The flux reduction due to the solid angle is

$$\Gamma = \frac{\Omega_{\text{hole}}}{\Omega_{\text{total}}} = \frac{\pi \cdot (\frac{d_{pipe}}{2})^2}{2 \cdot \pi \cdot (\text{shield thickness})^2} = \frac{d_{pipe}^2}{8 \cdot (\text{shield thickness})^2} \qquad (7.21)$$

for gammas emitted towards the water shield, where d_{pipe} is the pipe diameter. The flux reduction due to the solid angle of the pipe is listed in Table 7.18. The number of gammas reaching the detector through the feedthrough pipe of 3 in diameter is the same as the number that would reach the detector if there was no pipe for a 2 m water shield. The effect of adding a 3 in pipe is therefore minimal for the gamma background on the detector.

This result is confirmed by Monte Carlo simulations. Using Geant4, the water shield detector is simulated with feedthrough pipes of 3 in and 6 in diameter and 2 m water shield thickness on top and bottom, the same as the water shield simulations (see Fig. 7.2). The
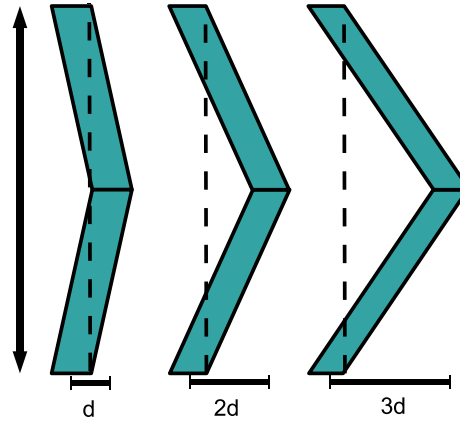
Figure 7.31: Feedthrough pipe "dog-leg": the center of the bend is displaced by N $\times$ diameter from the center of the pipe at the detector, for N = 1, 2, 3.

Bending	Flux Attenuation	
($\times$N displacement)	3 in	6 in
Straight Pipe	1.2×10^{-7}	4.1×10^{-7}
N=1		2.5×10^{-7}
N=2		1.9×10^{-7}
N=3		1.6×10^{-7}
No pipe		1.2×10^{-7}

Table 7.19: Flux attenuation for gammas emitted above the water tank into feedthrough pipes in the LUX water tank, obtained from Monte Carlo simulations for a gamma source placed directly above the feedthrough pipe entrance, centered with the detector. Gammas are emitted from a disc source, emitted with isotropic angular distribution and with energy spectrum of rock gammas (see Section 7.2.1.1). The flux reduction is calculated both for 2 m of water shielding (detector at center of tank), and for feedthrough pipe with dog-legs such that the center of the bend is displaced by N $\times$ diameter from the center of the pipe, for N = 1, 2, 3 (see Fig. 7.31). In the case "No pipe", the flux is attenuated only by the water tank. The 3 in diameter feedthrough pipe does not affect the flux.

gammas are emitted from a flat disc source directly above the feedthrough pipe, with the same diameter as the pipe and centered with the detector. The gammas are emitted with isotropic angular distribution, with the same spectrum as gammas from rock (see Section 7.2.1.1). To test the effect of dog-legging, a bend is introduced in the middle of the pipe (in Geant4, 2 pipes are merged at an angle). The angle of the bend is such that the center of the bend is displaced by N $\times$ diameter from the center of the pipe at the detector, as shown in Fig. 7.31. We simulate the feedthroughs for N = 1, 2, 3 and the results are tabulated in Table 7.19.

The simulations measured the flux through the outer surface of the cryostat, relative to the initial gamma flux, and the results are shown in Fig. 7.32. The addition of a 3 in pipe increases the gamma background directly under the pipe (diameter of 3 in) by a factor of 4, but the total background, integrated over the surface of the entire cryostat, remains consistent with having no pipe. A dog-leg is not needed for a 3 in pipe. A feedthrough pipe of 6 in diameter increases the background directly under the pipe by as much as ×20, and the overall background by a factor of ×3 (relative to no pipe). A dog-leg that displaces the center of the pipe by 1-diameter, and thus eliminates line-of-sight, reduces this factor to ×2 (relative to no pipe). Greater displacements do not reduce the background significantly and are not recommended. The vertical displacement of the detector by −59 cm from the center will further reduce the background. The LUX detector will be built using a set of 2 feedthrough pipes of 3 in diameter each; no bending will be necessary.

7.2.2 Environmental Neutron Background

The major sources of external neutron backgrounds are environmental radioactivity in the rock, and μ-induced neutrons in the rock and shielding material. The processes through which the neutron backgrounds are generated have been detailed in Section 6.2.1 and Section 6.2.2. The LUX water shield (see Fig. 7.15) has been designed to reduce the external neutron backgrounds well below the background goals (see Table 7.1), and to make it subdominant to the internal backgrounds. The most troubling of the external backgrounds is the μ-induced neutron background, with a very penetrating high-energy component ($E_\mathrm{n} > 10\,\mathrm{MeV}$), reduced only ~ 3 orders of magnitude by the water shield (see Fig. 7.16).

7.2.2.1 Environmental fast neutrons

The environmental *fast neutron* background ($E_\mathrm{n} > 1\,\mathrm{MeV}$) is dominated by neutrons generated through radioactive processes in the surrounding rock and concrete. The neutron are mainly generated by ^{238}U spontaneous fission, and α-decays in the ^{238}U and ^{232}Th chains, which generate (α,n) neutrons through the collision of α-particles with nuclei in the rock and concrete. Ultimately, the fast neutron background is not a concern for the LUX experiment

(a) 3 in diameter
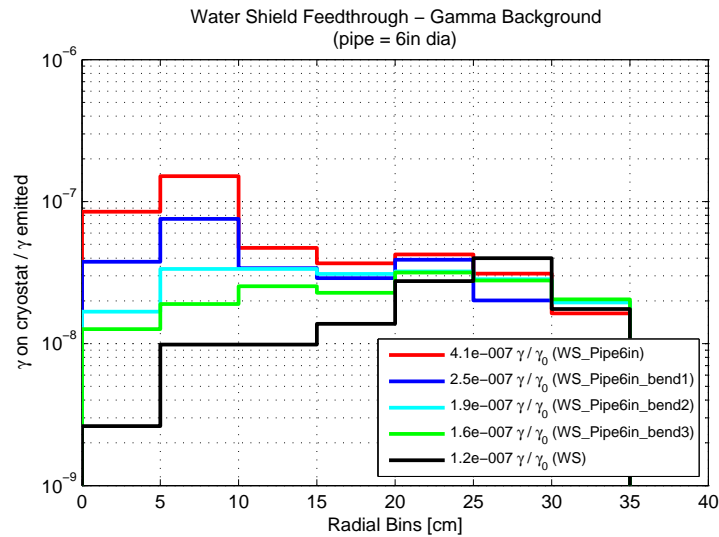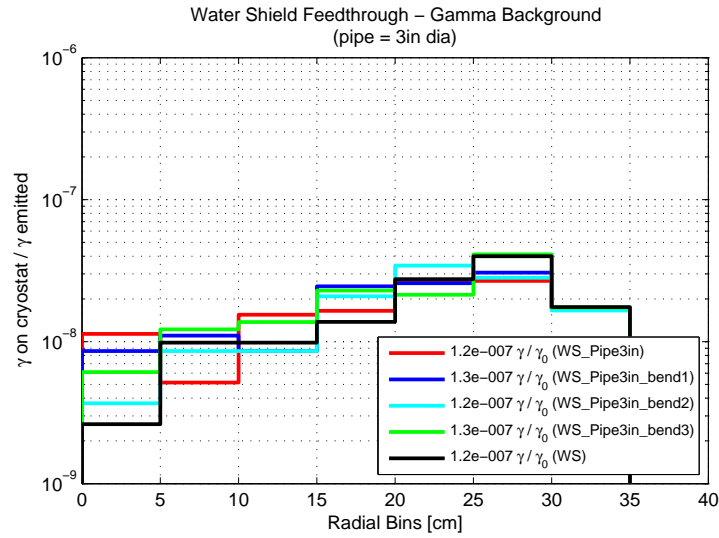

(b) 6 in diameter

Figure 7.32: Monte Carlo simulation of gamma background in the water shield feedthrough pipes. Radial distribution of gamma flux on the cryostat top surface, normalized to the number of gammas emitted directly above the pipe opening. Feedthrough pipe diameter of 3 in and 6 in.

- the water shield can efficiently reduce this background well below requirements.

Although there are no measurements of the neutron flux in the Davis laboratory, the environmental neutron background can be estimated by scaling the flux measured in the Gran Sasso laboratory (see Table 6.2) to match the contamination levels found in the Homestake rock and concrete (see Table 7.12). At the time of writing, the Davis laboratory is still being commissioned, and the concrete to be used has not been selected, and thus there is no information about its actual radioactivity. It is reasonable to expect that the concrete will be selected to match the contamination levels in the surrounding rock (without rhyolite intrusions: 0.160/0.200 ppm or 2/0.8 Bq/kg for ^{238}U / ^{232}Th), and thus not increase to the expected gamma and neutron background.

The rock contamination level at Gran Sasso is 6.80/2.17 ppm or 84/8.8 Bq/kg   for ^{238}U / ^{232}Th, and yields a neutron flux of 0.6×10^{-6} n·cm$^{-2} \cdot$ s^{-1} for $E_{\mathrm{n}} > 1$ MeV. Approximately half of the neutron background is due to ^{238}U fission, and half to the (α,n) neutrons from ^{238}U/^{232}Th decays. The neutron flux at Gran Sasso is almost entirely determined from the ^{238}U contamination level. From the ratio of contamination levels, we expected the flux at the Davis laboratory to be $\times 37$ lower than the flux at Gran Sasso, or 16.2×10^{-9} n·cm$^{-2} \cdot$ s^{-1} for $E_{\mathrm{n}} > 1$ MeV.

The fast neutron background is moderated very efficiently by the water shield. The flux is initially attenuated by a factor of $\times 1/3300$ in the first 50 cm of water, and afterwards with an attenuation length of $\lambda = 7.75$ cm. The fast neutron flux is attenuated by a factor of 2×10^{-15} by 2.5 m of water, and by a factor of 5×10^{-21} by 3.5 m of water (see Fig. 7.16). We can make a rough approximation to the integrated flux reduction by calculating the flux for a spherical water shield and using Eq. 7.12. The integrated flux is reduced by 6×10^{-22}, corresponding to only $\sim 2 \times 10^{-16}$ neutrons/year incident on the cryostat surface.

7.2.2.2 μ-induced neutrons in LUX

The μ-induced neutron background is a cause of great concern for Dark Matter experiments, since they have energies reaching well above 10 MeV, at which point they become very penetrating and very difficult to shield against. As can be seen in Fig. 7.16, the moderation

of high energy neutrons ($E_n > 10\,\text{MeV}$) is ineffective compared to the moderation of low- or medium-energy neutrons ($E_n < 10\,\text{MeV}$), as it requires as much as 4 m of water shielding to reduce the flux by 3 orders of magnitude. The μ-induced neutron background expected for LUX is generated primarily in the rock surrounding the laboratory, and in the water shield itself. The use of a muon veto can be used to reduce this background quite efficiently, specially the neutrons generated in the water shield; however, it will be seen that the neutron rates expected for LUX are low enough that a veto is not strictly necessary to achieve LUX sensitivity goal.

The processes by which cosmic ray muons generate neutrons in underground sites have been addressed in Section 6.2.2, as well as the characteristics of the muon background expected in the Homestake mine. The Davis laboratory is located in the 4850 ft level of the Homestake mine, with an effective depth of 4.3 ± 0.2 km.w.e. corresponding to a muon flux of $(4.4 \pm 0.1) \times 10^{-9}\,\mu\text{cm}^{-2}\text{s}^{-1}$ (see Table 6.7). The average energy of muons at such depths is $321\,\text{GeV}$.

There are no measurements of the μ-induced neutron flux in the Davis laboratory. However, the neutron flux from the rock has been measured at several underground sites, and the neutrons flux vs. depth can be fitted by an empirical equation [131]. Using Eq. 6.25, the neutron flux from the rock at Homestake is calculated to be $\phi_n = (0.54 \pm 0.01) \times 10^{-9}\,\text{n·cm}^{-2} \cdot \text{s}^{-1}$.

The energy distribution of μ-induced neutrons from the rock can be calculated using equation 6.27. The fit parameters for the energy distribution of a number of sites has been given in [131] and is listed in Table 6.9, but there are no parameters for Homestake. We can estimate the energy spectrum at the Davis laboratory by using the fit parameters from Gran Sasso, the closest site to Homestake 4850 ft level in depth, and the mean energy calculated for the Homestake depth. The resulting energy spectrum is shown in Fig. 6.14.

A Monte Carlo simulation of the high-energy neutrons is used to calculate the attenuation of the neutron flux in the water shield, and the results are shown in Fig 7.16. The high-energy neutron flux attenuated by a factor of $\times 1/170$ by 2.5 m of water, and by a factor of $\times 1/500$ by 3.5 m of water. The simulation uses the initial neutron energy spectrum

shown in Fig. 6.14, and propagates the neutrons through a semi-infinite water wall. The flux attenuation is calculated as the ratio of neutrons past a depth Z over the number of emitted neutrons; an energy cut of $E_\text{n} > 1\,\text{keV}$ is applied to remove low energy neutrons.

The integrated flux incident on the water shield outer surface (with 8 m diameter and 6 m height) is $1.36 \times 10^{-3}\,\text{n} \cdot \text{s}^{-1}$. Using Eq. 7.12 to estimate the integrated flux reduction, we calculate that the integrated flux of high-energy rock neutrons incident on the cryostat walls is $\Phi_\text{n} \sim 1 \times 10^{-7}\,\text{n} \cdot \text{s}^{-1}$.

The μ-induced neutron background in the water shield can be calculated from the neutron yield in water. Fig. 6.15 shows the neutron yield per muon for several materials, calculated by [131] through Monte Carlo simulations using MACRO and Geant4. The neutron yield in water should be very similar to the yield in polyethylene (CH_2) of $2.5 \times 10^{-4}\,\text{n}/\left(\mu \cdot \text{g} \cdot \text{cm}^{-2}\right)$. For a water tank of 8 m diameter and 6 m height, with a cryostat of 1 m diameter and 2 m height inside, this corresponds to a neutron production rate of $\Phi_\text{n production,shield} = 3.3 \times 10^{-4}\,\text{n} \cdot \text{s}^{-1}$ in the entire water shield. This corresponds to a production rate per mass of $\dfrac{\Phi_\text{n production,shield}}{m_\text{shield}} \sim 1.1 \times 10^{-9}\,\text{n} \cdot \text{kg}^{-1}\text{s}^{-1}$.

The moderation of neutrons in water still applies, and thus the neutrons generated at large radius will contribute much less to the flux incident on the detector. We can make a rough estimate of the flux of neutrons incident on the cryostat by using a modified version of Eq. 7.22, and calculating the flux for a sphere of radius equal to the attenuation length on high-energy neutrons in water:

$$
\begin{aligned}
\text{flux} \quad &= \quad \frac{\text{production rate}\,[\text{n} \cdot \text{s}^{-1}]}{Area\,[\text{cm}^2]} \\[2mm]
&= \quad \frac{\left(\dfrac{\Phi_\text{n production,shield}}{m_\text{shield}}\right) \cdot mass\,[\text{kg}]}{Area\,[\text{cm}^2]} \\[2mm]
&= \quad \frac{\left(\dfrac{\Phi_\text{n production,shield}}{m_\text{shield}}\right) \cdot \left(\rho \cdot \frac{4\pi}{3} \cdot R^3\right)}{4\pi \cdot R^2} \\[2mm]
&= \quad \frac{\Phi_\text{n production,shield}}{m_\text{shield}} \cdot \rho \cdot \frac{\lambda}{3}
\end{aligned}
\tag{7.22}
$$

where $\dfrac{\Phi_\text{n production,shield}}{m_\text{shield}}$ is the neutron production rate per unit mass in the water

shield, ρ is density in kg/cm^3 and λ is the attenuation length on high-energy neutrons in water. The biggest systematic in this calculation is the neutron attenuation length, since it changes rapidly over the first meter in the water. Using the initial attenuation of 1 order of magnitude in 50 cm, we get an attenuation length of $\lambda = 22$ cm, and a high-energy neutron flux of 8×10^{-12} n·cm$^{-2} \cdot$ s^{-1}. The integrated flux of high-energy neutrons generated in water and incident on the cryostat walls is $\Phi_n \sim 6.3 \times 10^{-7}$ n · s^{-1}. The flux of high-energy neutrons generated in water shield is approximately $\times 6$ higher than the flux of neutrons generated in the surrounding rock.

A Monte Carlo simulation of the μ-induced neutrons from the water shield is performed using Geant4 to determine the expected event rate in the LUX detector. The simulation emits neutrons in the water with the expected energy spectrum shown in Fig. 6.14, and follows the neutrons from the point of generation until the energy deposition in the liquid Xe. The simulation uses a geometry similar to the one used in the previous simulations, described in the beginning of Section 7.1.1 and shown in Fig. 7.2, with the detector placed in the center of the tank. However, since neutron flux is dominated by the neutrons generated close to the detector, the water shield has been reduced to a 1 m thickness on the top, bottom, and sides, in order to reduce the CPU processing time. The simulation emits neutrons uniformly distributed throughout the body of the water shield and with isotropic angular distribution. Note that since we are generating the neutrons in the body of the water shield, there is no uncertainty on the attenuation due to water nor on the flux for a given neutron production rate - the only uncertainty is in the neutron production rate in the water. The displacement of the detector downwards in the water tank has negligible effect on the obtained results.

The event rate of μ-induced neutrons in water is shown in Fig. 7.33, and the total event rate in the energy region of $5 - 25$ keV$_r$ is listed in Table 7.20. The application of the fiducial volume cut for 100 kg and of the single scatters cut reduces the event rate by a factor of $\times 3$. The event rate due to neutrons generated in the water tank is thus 121 ndru$_r$ in the energy range of $5 - 25$ keV$_r$, in the 100 kg fiducial volume, corresponding to a total event rate of 73×10^{-3} nuclear recoil events in 300 live-days, 100 kg fiducial.
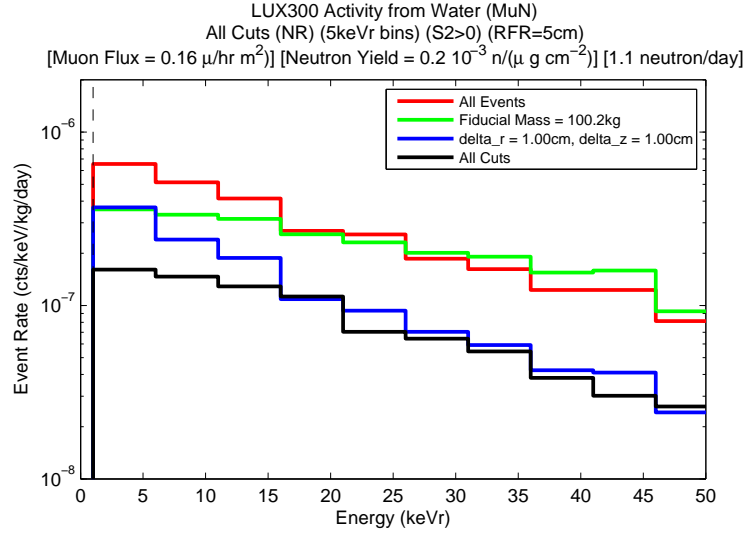
Figure 7.33: Event rate for μ-induced neutrons from the water tank, in the LUX detector, using several cuts. The nuclear recoil differential rate corresponding to the LUX sensitivity goal is shown in Fig. 7.1.

	Event Rate $(5 - 25\,\mathrm{keV_r})$
Total	(382 ± 12) ndru$_\mathrm{r}$
Fiducial Cut (100 kg)	(294 ± 14) ndru$_\mathrm{r}$
Single Scatters Cut	(170 ± 7) ndru$_\mathrm{r}$
Single Scatters + Fiducial Cuts	(121 ± 8) ndru$_\mathrm{r}$

Table 7.20: Event rate for μ-induced neutrons from the water tank, in the LUX detector, using several cuts.

Shield Configuration	Event Rate $(5 - 25\,\mathrm{keV_r})$ $[\mathrm{ndru_r}]$
20 cm polyethylene + 20 cm Pb	3770 ± 160
40 cm polyethylene + 20 cm Pb	585 ± 21
2 m water	224 ± 21
4 m water	22 ± 5

Table 7.21: Event rate in the LUX detector for μ-induced neutrons from rock, using several shield configurations.

7.2.2.3 μ-induced neutrons from rock

A series of Monte Carlo simulations were performed to assess relative effectiveness of different shield configuration on the μ-induced high-energy neutrons generated in rock. The source for the simulation is the neutron flux on the rock-cavern interface. The simulations use the expected high-energy neutron flux at Homestake depths, with the energy distribution shown in Fig. 6.14. The neutrons are emitted uniformly over a surface wrapped tightly around the shield, and with isotropic angular distribution. The simulation uses a very simple geometry, with just a liquid Xe cylinder with height equal to the radius, and mass of 63 kg. No cryostat or any other detector component was included. The shields are concentric cylinders around the detector, with the thickness of the shield on top and bottom equal to the thickness of the shield on the sides. Four shield configurations were tested: (1) 20 cm polyethylene plus 20 cm Pb (same as XENON10); (2) 40 cm polyethylene plus 20 cm Pb; (3) 2 m water; (4) 4 m water.

The resulting event rate in the liquid Xe is shown in Fig. 7.34, and the total event rate in the energy region of interest $5 - 25\,\mathrm{keV_r}$ is listed Table 7.21 for each shield configuration. The results show that a water shield is very efficient in the reduction of external high-energy neutrons - a 4 m water shield has $\times 1/27$ better background suppression than a 40 cm polyethylene + 20 cm Pb shield.

These results can be used to estimate the neutron event rate in LUX, due to μ-induced high-energy neutrons in rock. The LUX shield has 2.75 m on the top, 1.2 m on bottom and 3.5 m on the sides. The flux from 3.5 m water shielding and 4 m water shielding differ only by a factor of $\times 1/2$ - this suggests that the differential event rate should be $11\,\mathrm{ndru_r}$ for a 3.5 m water shield. The flux from 2.75 m water shielding is $\times 1/2$ of the flux from 2 m
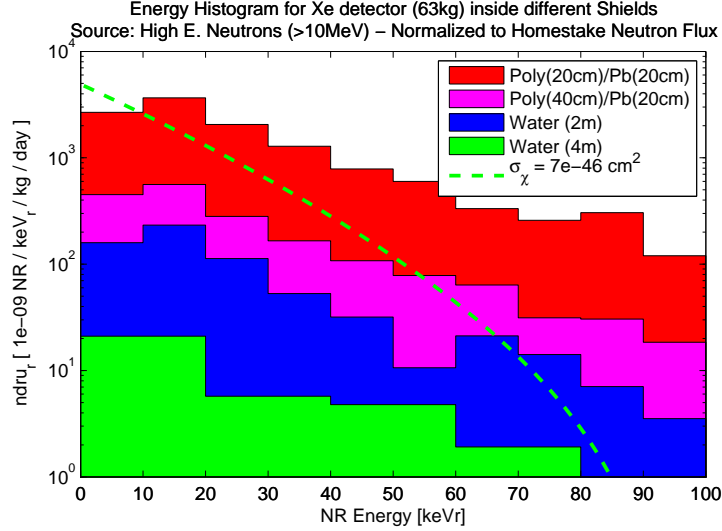
Figure 7.34: Energy spectrum of energy deposited by μ-induced neutrons from rock, for several shield configurations. Using a large liquid Xe cylinder (63 kg) as a detector, without any other detector components.

of water, so that rate for a 2.75 m water shield should be 110 ndru$_r$. The flux from 1.2 m water shielding is a factor of $\times 3$ higher than the flux from 2 m water shield, so that a water shield with just 1.2 m water thickness on all directions would have 670 ndru$_r$ event rate. Clearly the rate from the bottom dominates the neutron rate in LUX.

The bottom of the water shield accounts for 1/5 of the total shield surface area, and thus for 1/5 of the incident neutron flux (from the rock). We can make a rough estimate on the total event rate in the LUX detector by adding up the contributions from each direction:

$$\frac{1}{5} \cdot 670 \, \text{ndru}_r + \frac{1}{5} \cdot 110 \, \text{ndru}_r + \frac{3}{5} \cdot 11 \, \text{ndru}_r = 163 \, \text{ndru}_r \, (\text{no cuts}). \qquad (7.23)$$

The application of a fiducial volume cut and single scatter cut should have the same effect as seen for high-energy neutrons generated in the water shield - that is, a reduction of $\times 1/3$. Thus, the LUX single scatter differential event rate in the fiducial volume of 100 kg should be

$$163 \, \text{ndru}_r \times 1/3 = 54 \, \text{ndru}_r \, (\text{fiducial single scatters}) \qquad (7.24)$$

in the energy range of $5 - 25 \text{keV}_r$, corresponding to a total event rate of $\sim 33 \times 10^{-3}$ nuclear recoil events in 300 live-days, 100 kg fiducial.

Muon Veto. The total nuclear recoil background due to μ-induced high-energy neutrons, including the components from the cavern rock and generated in the water itself, adds up to 0.1 neutrons in the energy range of $5 - 20 \,\mathrm{keV_r}$, for a total exposure of 30,000 kg-days. The nuclear recoil rate is 1 order of magnitude below the background goal, and a muon veto is not necessary for the operation of the LUX detector. However, it is preferable that the projected background rate should be more than just 1 order of magnitude below the goal, to render it subdominant to any internal components of the background, and to allow for systematics that might increase the actual event rate. Finally a muon veto becomes necessary in a discovery experiment, to ensure that no WIMP candidate events are associated with muons. A Muon veto of at least 90% rejection efficiency should be implemented.

The LUX water shield will be instrumented with PMTs, and act as a Cherenkov-light detector to identify muon events. The muon veto will consist of an array of 20 Hamamatsu R7081 PMTs, 10 in diameter each, mounted on the outer tank walls and facing inwards. Monte Carlo simulations performed by the LUX collaboration indicate that the muon veto have rejection efficiency $> 90\%$.

CHAPTER 8

LARGER DETECTORS

Whether the LUX program proves successful in the positive detection of Dark Matter particles or not, it will be desirable to continue pushing down the detector sensitivity, leading us to next-generation detectors with lower backgrounds and larger masses. These next-generation detectors will allow us to explore further the WIMP parameter space, and in the case of positive detection in the current generation of detectors, larger detectors will be useful in providing us with high event statistics and permitting investigation of the WIMP mass [156]. The ever-increasing detector masses also lead to ever-increasing performance in background rejection by taking advantage of the strong self-shielding properties of the liquid Xe (see Section 2.1.6). As such, several proposals are being advanced by diverse Dark Matter detection groups to build detectors in the 1 T and 10 T scale over the next 10 years.

Thus, there is a need to model the improvement of the detector background performance for increasing mass, how a large detector (in the 10 T scale) will fare in terms of Dark Matter sensitivity, and what parameters can be optimized to maximize the detector sensitivity. This chapter looks into these 3 points, first by exploring the background model for larger detector (with 3 T , 10 T and 20 T masses); then characterizing in detail the major backgrounds for the LZ20 detector, a proposed joint venture between the LUX and ZEPLIN collaborations and with 20 T mass, and how the background will affect sensitivity; finally, by studying how the shape of the detector will affect the background models.

8.1 Self-Shielding

Large-scale detectors take advantage of the self-shielding properties of the liquid Xe observed in the smaller detectors (i.e. XENON10) to produce increasingly large masses with significantly reduced backgrounds. The self-shielding effect takes 3 forms, apparent in the use of 3 cuts: the fiducial volume cut, which defines the sensitive volume of the detector; the energy cut; and the single scatter cut. The majority of the backgrounds is localized on the outer surfaces of the liquid Xe volume, as only a small fraction of gammas and neutrons penetrate far into the liquid, thus creating a very active outer layer. If the incident fluxes and the background requirements of a given experiment do not change, the thickness of the outer layer remains the same as the detectors grow in size, thus making a much larger fraction of the total volume available with low background rates. The rejection power of the energy cut and single scatter cut also improves with larger detector - the larger the active volume, the more likely that a gamma or neutron will interact more than once, thus depositing more energy (specially true of the gamma background), or being tagged as a multiple scatter (as in the case of the neutron backgrounds).

However, background requirements and incident fluxes change as the detector grows in size. The investment in increasing the detector size must be justified by the increase of the sensitive volume *and* in the decrease of the background rate in the sensitive volume considerably, improving the detector sensitivity. In order to understand the improvements in both sensitive volume and background rate, simulations of the larger detectors are performed in order to construct models of how the background changes as we increase in size.

The improvement in background rejection is gauged by considering the PMT-induced gamma and neutron backgrounds. The PMT background is the most difficult to control in the liquid Xe, because of the required proximity of the PMTs to the active Xe volume. Liquid Xe detectors have typically been designed to have shields that render the external background subdominant to the internal background (i.e. XENON10 and LUX). It is expected that larger detectors will continue this trend, so that we need to focus only on the internal backgrounds to understand the larger detector background model.

From the Monte Carlo simulation one obtains the background event rate as a function

of fiducial volume, which in turn can be used to calculate the maximum size of the fiducial volume for a given background requirement. As an example, the LUX background requirement of 1 gamma background event in the WIMP signal box, after 99.4% ER-rejection, for 300 live-days sets a maximum fiducial volume of 100 kg (see Chapter 7). This choice of fiducial results in a NR event rate of $500\,\mathrm{ndru_r}$, which in turns results in ~ 0.1 events in the WIMP search box. We can use the LUX sensitivity as a benchmark to measure the performance of the larger detectors against. In the following simulations, we assume a goal of constant background Differential Event Rate $\times$ Detector Volume - that is, the event rate in the fiducial volume has to fall proportionally to the increase in the total mass of the detector.

8.1.1   Larger Detectors

A series of simulations of both the gamma and neutron backgrounds emitted by the PMTs were performed in order to assess the background rate for liquid Xenon detectors of several sizes. The detectors have the same cylindrical shape and aspect ratio as the proposed LUX design, and have their dimension scaled up proportionally to match the masses under consideration: 300 kg (LUX), 3 T , 10 T and 20 T. All large detectors are named LZ, as they are being developed by a partnership between the LUX and the ZEPLIN collaborations. All simulations include a water shield 2.5 m thick around the detector. All simulations use top and bottom arrays of R8778 PMTs, of the same size and shape, distributed evenly on the top and bottom surface of the detectors, in a similar fashion to the LUX detector. The number of PMTs scales with the surface area of the detector. The detector dimensions, along with the numbers of PMTs, are listed in Table 8.1.

The background simulations use the same initial spectrum and emission rate per PMT as the LUX simulations described in Chapter 7, for both gammas and neutrons. The gamma simulations assume the PMTs have the same contamination level measured at SOLO, as listed on Table 7.3. The neutron simulations assume a benchmark neutron production rate of 5 neutrons/PMT/year, $5\times$ greater than expected for the R8778 PMTs (see Section 7.1.2).

The simulations use the same techniques and cuts already detailed for the LUX back-

	Mass	Diameter	Height	Fiducial Mass	Fiducial Diameter	Fiducial Height	Number of PMTs
LUX	300 kg	49 cm	59 cm	100 kg	36 cm	33 cm	122
LZ 3 T	3 T	104 cm	119 cm	1.4 T	87 cm	78 cm	550
LZ 10 T	10 T	156 cm	177 cm	6 T	142 cm	128 cm	1240
LZ 20 T	20 T	196 cm	223 cm	13.5 T	186 cm	168 cm	1950

Table 8.1: Detector dimensions for LUX, and 3 possible versions of the LZ detector considered for background Monte Carlo simulations: 3 T, 10 T and 20 T. The LZ detector dimensions are proportional to the LUX dimensions, keeping an aspect ratio of H/D = 1.1 − 1.2. The fiducial dimensions are determined from the Monte Carlo simulations (shown in Fig. Figure 8.2 on page 318), and is defined as the maximum fiducial volume for a constant Event Rate × Total Mass ratio. The total number of PMTs (top and bottom) in the LZ detector is proportional to the number of PMTs in LUX and the detector surface area.

ground simulations. All event rates are quoted for the energy range of interest of $5 − 25 \, \mathrm{keV_r}$ for the neutron simulations, and $5 − 25 \, \mathrm{keV_{ee}}$ for the gamma simulations. Note that these 2 energy ranges are not equivalent. The actual energy range of interest for neutrons is $5 − 25 \, \mathrm{keV_r}$, as it is the energy range used for the XENON10 results (see Chapter 4), and it corresponds to $1.3 − 8 \, \mathrm{keV_{ee}}$ for gammas. However, such small energy range would reduce the statistics of the Monte Carlo results. The Monte Carlo simulations indicate that the gamma background energy deposition spectrum is fairly flat for energies $< 100 \, \mathrm{keV_{ee}}$ in the fiducial volumes, and thus looking at the $5 − 25 \, \mathrm{keV_{ee}}$ range is still indicative of the background level at $1.3 − 8 \, \mathrm{keV_{ee}}$.

A single scatter cut is applied to both gamma and neutron backgrounds to remove multiple scatter events based on the spread of the energy-weighted spatial distribution of scatters for each event, with thresholds of $\sigma_z \leq 10 \, \mathrm{mm}$ and $\sigma_r \leq 10 \, \mathrm{mm}$ (compared to XENON10's thresholds of $\sigma_z \leq 2 \, \mathrm{mm}$ and $\sigma_r \leq 5 \, \mathrm{mm}$) since the larger PMTs will have worse spatial resolution than the PMTs used in XENON10. Finally, we apply to the neutron background the "EM-veto" cut, first discussed in Section 7.1.2. This cut removes events that have a electromagnetic component with energy $E_{\mathrm{er}} > 20 \, \mathrm{keV_{ee}}$, and is designed to remove events with associated inelastic collisions and neutron capture. The effect of the cuts on the neutron background can be seen in Table 8.3, which lists the cut efficiencies for (α, n) neutron events in all simulated detectors.

8.1.2   PMT Neutrons Background

The simulation of neutrons emitted by the PMTs use the same initial energy spectrum as the XENON10 simulations described shown in Fig. 6.6. The simulations assume equal neutron production from ^{238}U fission and from (α,n) processes, and the neutron emission rate is normalized to the benchmark production rate of $5\,\text{n/PMT/year}$, the same used for the LUX PMTs (see Section 7.1.2).

The resulting nuclear recoil rate in the detector is shown in Fig 8.1, plotted against fiducial volume mass for each of the simulated detector masses: 300 kg (LUX), 3 T , 10 T and 20 T. The fiducial volume for larger detectors has the same shape as the LUX fiducial volume - no optimization procedure is undertaken in the analysis presented in this section, so that comparison between the detectors is easier. For a procedure to optimize the fiducial volume, please refer to Section 8.2.

The first result to catch one's eye is the change in slope in the event rate vs. fiducial mass lines for the different detector sizes. This means that for larger detectors, a larger fraction of the detector mass becomes available as fiducial volume. The self-shielding properties of liquid Xe becomes a more prominent feature for large detectors. For comparison, we can consider the fiducial mass fraction so that the event rate is reduced proportionally to the detector mass, relative to the LUX fiducial mass. For example, the mass of the 20 T detector is $66\times$ larger than the LUX mass (300 kg) in this simulation, and thus we want to find the mass fraction in which the event rate is $\times 1/66$ smaller than the rate in LUX, i.e. $500\,\text{ndru}_\text{r}/66 = 7\,\text{ndru}_\text{r}$; the fiducial mass fraction for the 20 T detector is 67%, $2\times$greater than the fraction for the 300 kg detector, 33% (see Fig. 8.2).
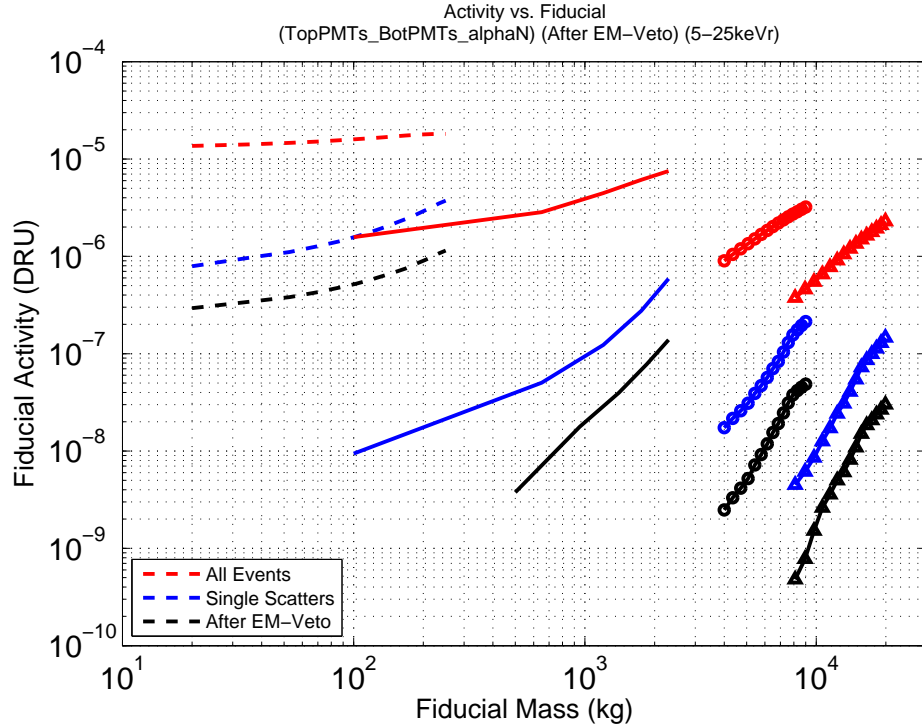
Figure 8.1: Nuclear recoil rate vs. fiducial volume, obtained from Monte Carlo simulation of neutrons generated by the PMTs for liquid Xe detectors of different sizes. Each set of lines corresponds to a detector size: LUX-300 kg (dashed), LZ 3 T (solid), 10 T (circles), 20 T (triangles). All event rates quoted are in the range $5 - 25\,\mathrm{keV_r}$. It is assumed that the neutrons are produced with the energy spectrum shown in Fig. 6.6, and with a benchmark neutron production rate of $5\,\mathrm{n/PMT/year}$. The "EM-Veto" cut removes events with a electromagnetic component, due to inelastic collisions and neutron captures.

The event rate due to PMT neutrons in each detector is listed in Table 8.2, for several cuts, normalized to events/kg/keV$_\mathrm{r}$/day. The effect of each cut is listed separately in Table 8.3. It can be readily seen that all cuts improve performance as the detector grows in size.

8.1.3 PMT Gamma Background

A series of simulations was also performed to assess the gamma event rate due to PMT radioactive contamination. The simulations are similar to the ones done for LUX and described in Section 7.1.1. The simulations assume the same PMT geometry as the R8778 PMTs and the same contamination levels as measured at SOLO, and listed on Table 7.3: $8.9/2.8/2.6/92\,\mathrm{mBq/PMT}$ for $^{238}\mathrm{U}/^{232}\mathrm{Th}/^{60}\mathrm{Co}/^{40}\mathrm{K}$. The event rate vs. fiducial volume mass is shown in Fig. 8.3; only events that deposit $5 - 25\,\mathrm{keV_{ee}}$ are shown. The drop
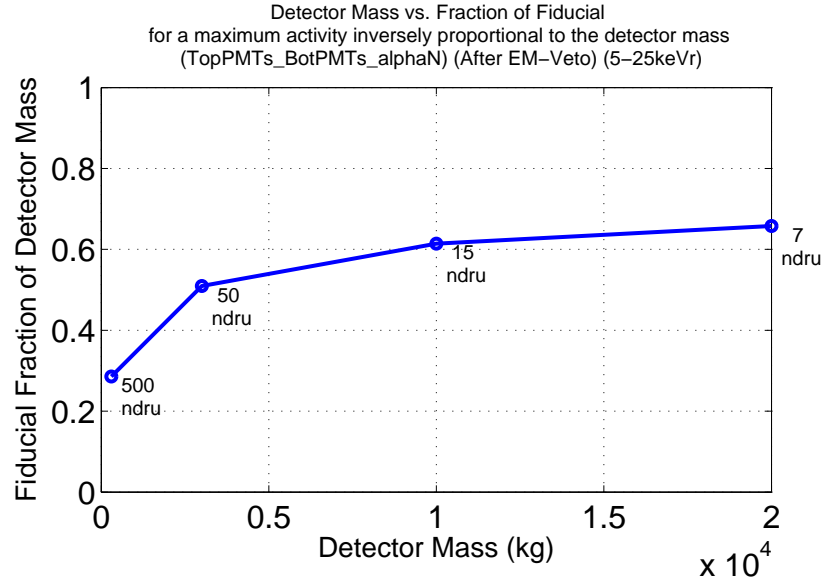
Figure 8.2: Fiducial fraction limit of constant Event Rate × Total Mass ratio, set by the neutron background for LUX, obtained from Monte Carlo simulation of neutrons generated by the PMTs for liquid Xe detectors of different sizes. The fiducial fraction is obtained from the curves shown in Fig. 8.1, after the application of the EM-Veto cut (which removes events with a electromagnetic component, due to inelastic collisions and neutron captures).

	300 kg	3 T	10 T	20 T
Total Event Rate	$28.2\,\mu\mathrm{dru_r}$	$20\,\mu\mathrm{dru_r}$	$14.9\,\mu\mathrm{dru_r}$	$11.5\,\mu\mathrm{dru_r}$
Fiducial Volume	$15.7\,\mu\mathrm{dru_r}$	$5.3\,\mu\mathrm{dru_r}$	$2.1\,\mu\mathrm{dru_r}$	$1.1\,\mu\mathrm{dru_r}$
Fiducial Single Scatter	$1.4\,\mu\mathrm{dru_r}$	$180\,\mathrm{ndru_r}$	$55\,\mathrm{ndru_r}$	$32\,\mathrm{ndru_r}$
Fiducial SS, EM-Veto	$0.44\,\mu\mathrm{dru_r}$	$40\,\mathrm{ndru_r}$	$10\,\mathrm{ndru_r}$	$6\,\mathrm{ndru_r}$

Table 8.2: Nuclear recoil rate for liquid Xe detectors of several sizes, obtained from Monte Carlo simulation of neutrons generated by the PMTs. Event rates are calculated after the application of different cuts - Fiducial Volume cut, Single Scatters cut, and the "EM-Veto" cut, which removes events with a electromagnetic component, due to inelastic collisions and neutron captures. The fiducial volume cut used is the detector volume in which the event rate is reduced inversely proportional to the total detector mass, so that we have a constant Differential Event Rate × Total Mass ratio, set by the neutron background for LUX. The used fiducial cuts are listed in Table 8.1, and are illustrated in Fig. 8.2. All event rates quoted are in the range $5 - 25\,\mathrm{keV_r}$. It is assumed that the neutrons are produced with the energy spectrum shown in Fig. 6.6, and with a benchmark neutron production rate of $5\,\mathrm{n/PMT/year}$.

	300 kg	3 T	10 T	20 T
Fiducial Cut	1/2	1/4	1/7	1/10
Single Scatter	1/11	1/30	1/38	1/34
EM Veto	1/3	1/4.5	1/5.5	1/5.5

Table 8.3: Reduction factor for each cut, obtained from Monte Carlo simulation of neutrons generated by the PMTs for liquid Xe detectors of different sizes. The reduction factors are calculated from the event rates in the range $5 - 25 \, \mathrm{keV_r}$, listed in Table 8.2. The reduction factor is sequential, but not cumulative (multiply them all to get the total reduction factor).

	300 kg	3 T	10 T	20 T
Total Rate	105.5 ± 0.3 $\mathrm{mdru_{ee}}$	160.3 ± 0.4 $\mathrm{mdru_{ee}}$	107.6 ± 0.2 $\mathrm{mdru_{ee}}$	84.1 ± 0.4 $\mathrm{mdru_{ee}}$
Fiducial Volume	379 ± 58 $\mathrm{\mu dru_{ee}}$	9.5 ± 4 $\mathrm{\mu dru_{ee}}$	2.6 ± 1.1 $\mathrm{\mu dru_{ee}}$	2.0 ± 1.3 $\mathrm{\mu dru_{ee}}$
Fiducial Single Scatter	374 ± 58 $\mathrm{\mu dru_{ee}}$	9.3 ± 4 $\mathrm{\mu dru_{ee}}$	2.4 ± 1.1 $\mathrm{\mu dru_{ee}}$	2.0 ± 1.3 $\mathrm{\mu dru_{ee}}$

Table 8.4: Electron recoil rate for liquid Xe detectors of several sizes, obtained from Monte Carlo simulation of the PMTs gamma background. The simulations use the fiducial volume cuts defined by the neutron background, and listed in Table 8.1; note that this is not the "gamma fiducial fraction" shown in Fig. 8.3. The gamma emission rate is normalized to the R8778 PMT contamination levels measured at SOLO, and listed on Table 7.3. All event rates quoted are in the range $5 - 25 \, \mathrm{keV_{ee}}$. The single scatters cut is very inefficient for gamma backgrounds, as events with more than one ER scatter tend to deposit more energy and fall outside of the energy range of interest.

in gamma event rate as we decrease the fiducial volume is very sharp for the tonne-scale detectors - a very large fraction of the detector volume should be available for use as low-background fiducial volume, demonstrating the self-shielding power of liquid Xe detectors.

The single scatters cut for gammas events is very ineffective, as the majority of multiple scatters has already been eliminated by the $5 - 25 \, \mathrm{keV_{ee}}$ energy cut. As it has been discussed before, events with more than one ER scatter tend to deposit more energy and fall outside of the energy range of interest. The gamma event rate before and after the cuts are listed in Table 8.4. Again, the efficiency of the fiducial cut in reducing the background is improved as the detector increases in size. Note that the fiducial cut listed is the same that has been defined by the neutron background, discussed in the previous section, and listed in Table 8.1.

The gamma background sets its own limit on the size of the fiducial volume that can
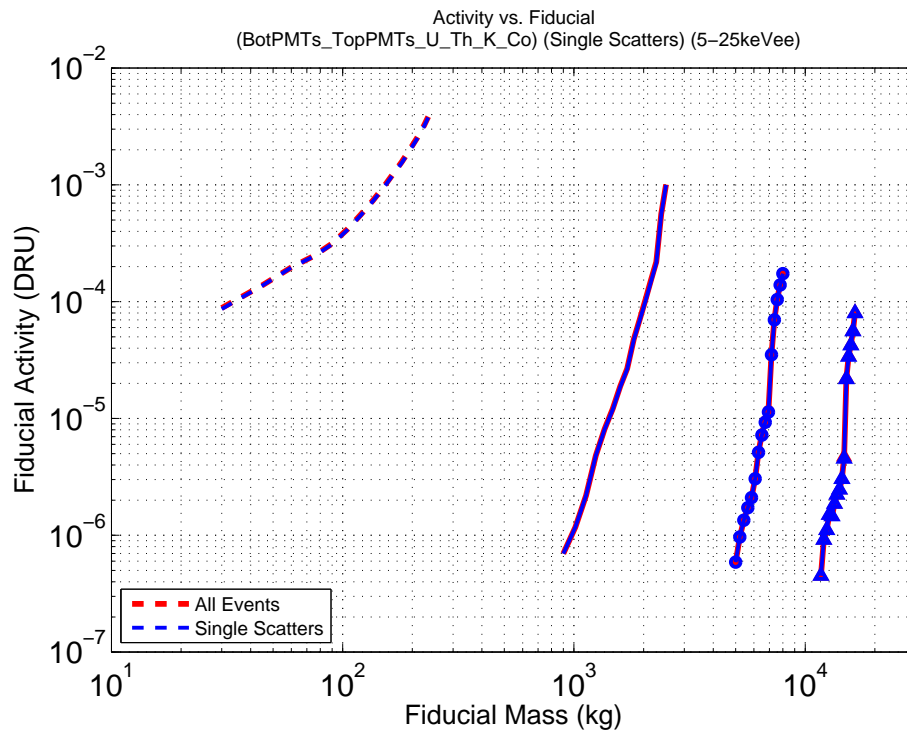
Figure 8.3: Electron recoil rate vs. fiducial volume, obtained from Monte Carlo simulation of the PMTs gamma background for liquid Xe detectors of different sizes. Each set of lines corresponds to a detector size: LUX-300 kg (dashed), LZ 3 T (solid), 10 T (circles), 20 T (triangles). All event rates quoted are in the range $5 - 25 \, \mathrm{keV_{ee}}$. The gamma emission rate is normalized to the R8778 PMT contamination levels measured at SOLO, and listed on Table 7.3: $8.9/2.8/2.6/92 \, \mathrm{mBq/PMT}$ for $^{238}\mathrm{U}/^{232}\mathrm{Th}/^{60}\mathrm{Co}/^{40}\mathrm{K}$.

Figure 8.4: "Gamma fiducial fraction" limit for a constant Differential Event Rate ×
Total Mass ratio, set by the gamma background for LUX, obtained from Monte Carlo
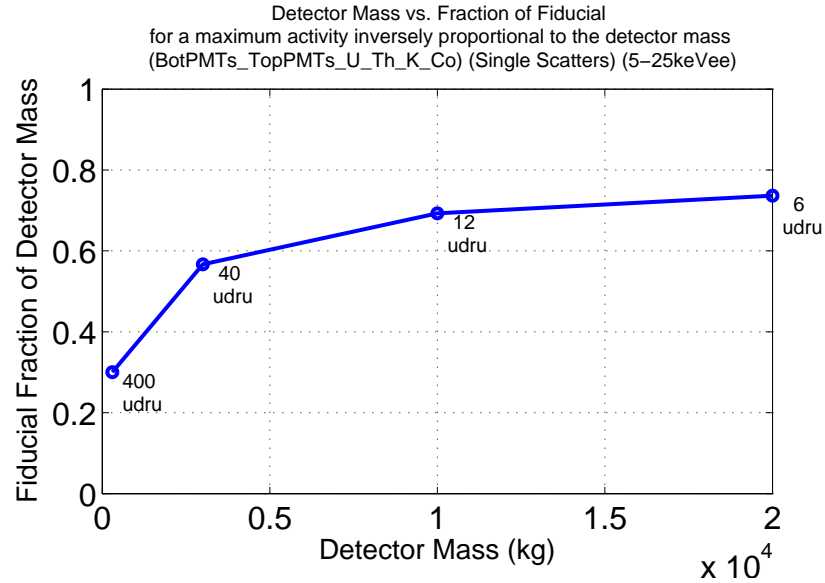simulation of gammas generated by the PMTs for liquid Xe detectors of different sizes. The
fiducial fraction is obtained from the curves shown in Fig. 8.3. This is done in a similar
fashion to the fiducial fraction obtained from the neutron background, shown in Fig. 8.2.
Note that the fiducial fraction used in the Monte Carlo simulations in this chapter (and
listed in Table 8.4) are defined by the neutron background, not by the gamma background.

be used. However, keep in mind that we are requiring the event rate in the LZ detectors
to match the rate in the LUX detector, that is, $\sim 0.1\,\mathrm{events/kg/keV_r/day}$ for neutrons and
$\sim 1\,\mathrm{events/kg/keV_r/day}$ for gammas. Therefore, the limits set by the gamma backgrounds
are less strict than the limits set by the neutron background.

As an example, if we use the LUX event rate as the benchmark value, and we stipulate
that we want to find the fiducial fraction for each detector mass so that the rate is reduced
proportionally to the detector mass (again, relative to LUX), then the maximum fiducial
fraction for the 20 T detector is 73%, compared to the 67% set by the neutron background.
The limits on the fiducial mass set by the gamma background in each of the detector
simulated is shown in Fig. 8.4.

8.1.4 Reducing the PMT radioactivity

Because of the self-shielding properties of liquid Xe, the PMT radioactive contamination
levels becomes less of a limiting factor as we increase the detector mass. Any gains in
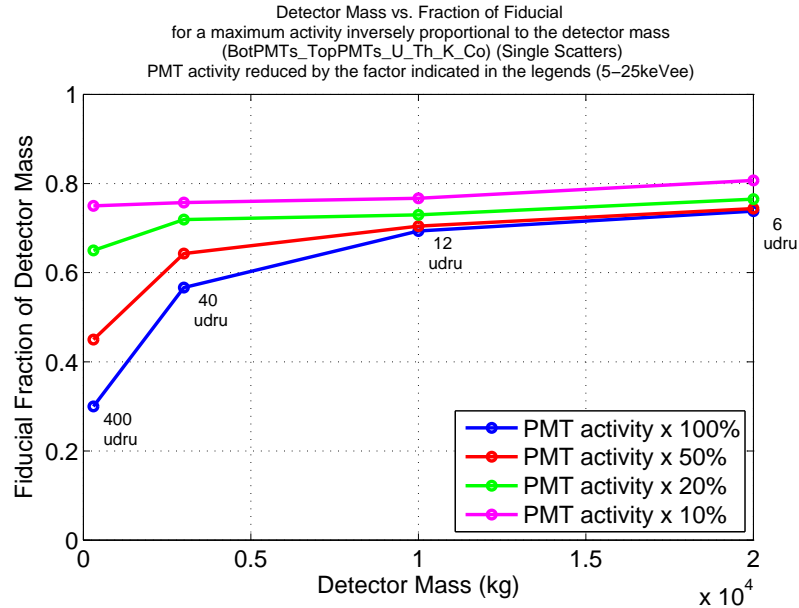
Figure 8.5: Reducing the PMT radioactivity greatly increases the fiducial region for a 100kg-scale detector (i.e. LUX). For large detectors ($\geq 10\,\mathrm{T}$ scale), the gain in fiducial mass for smaller PMT activity is constrained by the gamma event rate – the amount of available fiducial mass for PMTs of different activities converges, since the gammas do not penetrate deep into the detector.

background reduction derived from the decrease in PMT radioactivity can be easily matched by a modest decrease in fiducial volume. An example of this effect is shown in Fig. 8.5. For a detector the size of LUX (300 kg), a reduction of the PMT radioactivity by a factor of $\times 1/10$ leads to an increase in the fiducial volume of $\times 2.5$, which might be just enough to justify the investment in the reduction of PMT activity. However, for a $10\,\mathrm{T}$ liquid Xe detector, a reduction in the PMT radioactivity by a factor of $\times 1/10$ leads to an increase in the fiducial volume of only 10%. Therefore, the best strategy in improving an experiment exposure, and subsequently its sensitivity, is to increase its total size rather than to decrease the radioactivity of components.

8.1.5 Trigger rates

The LUX background model predicts that the event rate is dominated by the PMT gamma background. The LZ detectors are likely to be designed so that the PMT radioactivity is also the main contributor to the detector event rate, and is thus dominated by the PMT gamma background. One can estimate the trigger rate for a given detector by considering

the event rate due to gammas emitted by the PMTs.

For the purposes of this estimate, we will assume that all simulated detectors have a $5\,\mathrm{keV_{ee}}$ energy threshold (note that XENON10 demonstrated a $2\,\mathrm{keV_{ee}}$ threshold). Since the energy distribution of the background is flat below $200\,\mathrm{keV_{ee}}$, the use of one threshold or another will not change the event rate significantly *in the Monte Carlo* (noise at the lowest energy bins might actually increase event rate in a real experiment). The event rates are estimated for all events, and also for data taken either with a $100\,\mathrm{keV_{ee}}$ or $300\,\mathrm{keV_{ee}}$ high-energy veto. The 2 possible high-energy veto values reflect possible strategies for data taking in the large detector, designed specifically to reduce the trigger rate and thus the event pile-up (overlapping).

When calculating the event rate for the high-energy veto at $100\,\mathrm{keV_{ee}}$, we can assume that the activity for $E < 100\,\mathrm{keV_{ee}}$ is the same as for $5 < E < 25\,\mathrm{keV_{ee}}$, since the gamma energy spectrum is very flat below $200\,\mathrm{keV_{ee}}$. Thus, the event rate is simply:

$$\mathrm{Rate}_{100\,\mathrm{keV_{ee}}} = \mathrm{activity}_{5-25\,\mathrm{keV_{ee}}}\,(\mathrm{dru_{ee}}) \times \mathrm{mass} \times \Delta E /(\mathrm{s/day}), \qquad (8.1)$$

where $\Delta E = 100 - 5\,\mathrm{keV_{ee}} = 95\,\mathrm{keV_{ee}}$.

For the activities at higher energy, we need to extrapolate from the spectrum behavior observed in the XENON10 gamma background simulations (see Fig. 6.20). In the XENON10 spectrum, we observe that the activity in the bin $200 - 300\,\mathrm{keV_{ee}}$ is $\times 4$ larger than in the $0 - 100\,\mathrm{keV_{ee}}$ bin. The rate then becomes:

$$
\begin{aligned}
\mathrm{Rate}_{300\,\mathrm{keV_{ee}}} &= \mathrm{Rate}_{100\,\mathrm{keV_{ee}}} \times ratio_{activity} \times ratio_{energy} \\
&= \mathrm{Rate}_{100\,\mathrm{keV_{ee}}} \times \frac{(200-0)\times 1 + (300-200)\times 4}{300} \times \frac{300-5}{100-5} \\
&= 6.2 \times \mathrm{Rate}_{100\,\mathrm{keV_{ee}}}.
\end{aligned}
$$

For the rate without veto, we integrate the total event rate in XENON10, and find:

$$\text{Rate}_{2-12\,\text{keV}_{\text{ee}}} = 454\,\text{mdru}_{\text{ee}} \times 10\,\text{keV}_{\text{ee}} = 4.54\,\text{events/kg/day (XENON10)} \qquad (8.2)$$

and

$$\text{Rate}_{total} = 147\,\text{events/kg/day (XENON10)}. \qquad (8.3)$$

The ratio of the total event rate to the low energy event rate is $\times 33$, so that the total event rates can be scaled from the low energy event rate:

$$\text{Rate}_{total} = 33 \times \text{Rate}_{100\,\text{keV}_{\text{ee}}}. \qquad (8.4)$$

Table 8.5 lists the trigger rates for $100\,\text{keV}_{\text{ee}}$ high energy veto, for $300\,\text{keV}_{\text{ee}}$ veto, and for no veto at all. Using the electron drift velocity of $2\,\text{mm}/\mu\text{s}$, and the detector height given in Table 8.1, we calculate the maximum electron drift times to be $\Delta t = 295$, 595, 885 and 1100 μs, and the event window is $2\times$ the drift time, since peak identification algorithms typically search for peaks Δt before and after the trigger. The probability of event overlap occurring is the probability that 1 or more events will fall within the window of another event, and is thus determined by Poisson statistics:

$$f(k, \lambda) = \frac{\lambda^k \cdot e^{-\lambda}}{k!}, \qquad (8.5)$$

where k is the number of overlapping events, and $\lambda = \text{Rate} \times \text{Event Window}$. The probability that 1 or more events will fall within the given event window is:

$$
\begin{aligned}
\text{Prob} \;&=\; \sum_{k=1:\infty} f(k, \lambda) \\
&=\; 1 - f(k = 0, \lambda) \\
&=\; 1 - e^{-\text{Rate} \times \text{Event Window}} \qquad (8.6)
\end{aligned}
$$

	$100\,\mathrm{keV_{ee}}$ veto	$300\,\mathrm{keV_{ee}}$ veto	No veto
LUX 300 kg	0.04 Hz	0.2 Hz	1.2 Hz
LZ 3 T	0.6 Hz	3.4 Hz	18 Hz
LZ 10 T	1.3 Hz	7.8 Hz	41 Hz
LZ 20 T	2 Hz	12 Hz	64 Hz

Table 8.5: Total event rates for detector of several sizes, estimated from the PMT gamma background, using the number of PMTs listed in Table 8.1 and the PMT radioactive contamination levels for the Hamamatsu R8778 PMTs measured at SOLO and listed in Table 7.3. The event rates are calculated for a $5\,\mathrm{keV_{ee}}$ energy threshold. The table lists the total trigger rates, and the trigger rate after the application of a sharp high-energy veto at $100\,\mathrm{keV_{ee}}$ and $300\,\mathrm{keV_{ee}}$. No other cuts are applied.

Table 8.6 lists the probability of event overlap for each of the simulated detectors. We see that the overlap probability in the 20 T detector is $> 10\%$, which means that pile-up starts to become a concern. However, event overlap at this level should not present a problem. Overlapping events are easily rejected because there are 2 S1's, or because it looks like a multiple scatter event in the case in which one of the S1's is too small to see. Only 2 classes of events would present a problem: (1) Coincident S1's, which have a probability of at most 10^{-5}; and (2) S2 from a gamma coincident with S2 from a WIMP (that is, the 2 pulses are right on top of each other). Such cases are extremely rare and should not present a problem.

The problem with high event rate is that we might have to reject a lot of events due to event overlapping (identified by more than one S1 or because it looks like a multiple scatter). Thus, for a 20 T detector, we might have to reject as much as 13% of the data due to event pile-up. If we want to reduce this rejection to say 5%, then we need to reduce the trigger rate to 23 Hz, which means reducing the background by a factor of $\times 3$. If we want to bring the overlap rejection down to the same level as the ER rejection (99.4%), then we have a maximum rate of 2.7 Hz, which means that we have to reduce the background by $\times 24$. For a further discussion of the event rate and pile-up for a large liquid Xe detector, please refer to Section 8.3.3.

	Event length	Overlap probability		
		$100\,\mathrm{keV_{ee}}$ veto	$300\,\mathrm{keV_{ee}}$ veto	No veto
LUX 300 kg	$295\,\mu\mathrm{s}$	2×10^{-5}	1×10^{-4}	7×10^{-4}
LZ 3 T	$595\,\mu\mathrm{s}$	7×10^{-4}	4×10^{-3}	2%
LZ 10 T	$885\,\mu\mathrm{s}$	0.2%	1.4%	7%
LZ 20 T	$1100\,\mu\mathrm{s}$	0.4%	2.6%	13%

Table 8.6: Event overlap probability in LUX and LZ detectors for mass 3 T, 10 T and 20 T, estimated using the event rates listed in Table 8.5 and Eq. 8.6. The event probabilities are calculated for event rates with a $5\,\mathrm{keV_{ee}}$ energy threshold; no other cuts are applied. The overlap probabilities calculated using a high-energy veto (first 2 columns) consists of the the probability of overlap in which all events have energy $E < E_{high-E\,thresh}$.

8.2 The LZ20 detector

The LUX background goals shown in Table 7.1 list a benchmark NR neutron background of 2.2 neutrons for a fiducial volume exposure of 30,000 live-days (before the NR acceptance of 45%), which translates to 1 neutron for 30,000 kg-days exposure *after* the NR acceptance cut of 45%. The fiducial volume is 100 kg, and the live-time is 300 days. The LUX active mass is 300 kg. For the LZ20, the mass is increased by $\times 67$, and thus we require the WIMP signal sensitivity, and consequently the neutron background, to be reduced by at least $\times 1/67$. That is, the maximum acceptable neutron event rate in LZ20 would be 1 neutron events (after 45% NR acceptance) in 2,000,000 kg-days. However, for a program the size of LZ20, it is more appropriate to propose a science run of 1,000 live-days, using a fiducial of at least 2/3 of the total detector volume, or 13,500 kg. This sets a goal of 1 background event (after 45% NR acceptance) in 13,500,000 kg-days, or 4 ndru$_\mathrm{r}$ in the energy range of 5 - 25 keV$_\mathrm{r}$.

In this Section, we take a more detailed look at the background model for the LZ20 detector, with 20 tonnes of liquid Xe mass, with a baseline design shown in Fig. 8. We present an optimal method for calculating the fiducial volume shape, and we also look into a more accurate criterion for selecting the size of the fiducial volume: instead of looking for the fiducial volume such that the event rate is decreased inversely proportional to the total detector size, we look for the fiducial volume that will give us 1 event in the desired exposure, after all ER rejection and NR acceptance efficiencies have been taken into account.

Figure 8.6: Baseline design of the LZ20 detector, with a 20 T active liquid Xe mass.

8.2.1 Neutron Backgrounds and the Fiducial Volume

In the analysis presented in this section, the fiducial volume shape is calculated through an iterative process. We remove layers of a predefined thickness (1 cm) from the top/bottom and from the sides, and calculate the event rate in the remaining volume. We start with the total event rate for the total volume. Then we calculate the event rate for reducing the height, and for reducing the sides; the process that gives a lower rate gets chosen, and we calculate the new fiducial volume. We continue doing this until we have no more events.

The fiducial volume of the detector is defined by the desired NR rate goal. Due to the liquid Xe self-shielding, the center of the detector is fairly quiet, and we can greatly reduce the event rate by simply decreasing the fiducial volume. Figure 8.7 shows the differential event rate vs. fiducial volume mass for the LZ20 detector with "standard" shape (that is, similar shape to LUX, with aspect ratio of $H/D = 1.1$). The simulations described in this section use the same geometry and cuts used in the 20 T detector simulations in Section 8.1.

But what is the desired fiducial mass? The criteria for selecting a fiducial mass has already been mentioned above - a science run of 1,000 live days with only a single 1 neutron background event (after 45% NR acceptance cuts). Figure 8.8 shows the number of neutron events in 1,000 live-days vs. fiducial volume, and indicates that the optimal fiducial volume is 14,330 kg (approximately 2/3 of the total detector mass).

8.2.2 Gamma Background and the Fiducial Volume

A set of simulations using the same detector geometry show that the gamma background puts a larger constraint on the maximum fiducial volume. The LUX experiment sets a requirement of 99.4% electron recoil rejection for the energy range $5 - 25\,\mathrm{keV_r}$ ($\sim 1.3 - 8\,\mathrm{keV_{ee}}$) in its benchmark background model. The background goal is defined as 1 event in 1,000 live-days exposure. Figure 8.9 shows the differential event rate vs. fiducial volume, and the rate corresponding to the goal of 1 event in 1,000 live-days (black dashed line) after the 99.4% discrimination. We see that for the fiducial volume of $13,250\,\mathrm{kg}$, the event rate of 1.8 $\mu\mathrm{dru_{ee}}$ matches the goal of 1 background event in 1,000 days. After ER rejection of
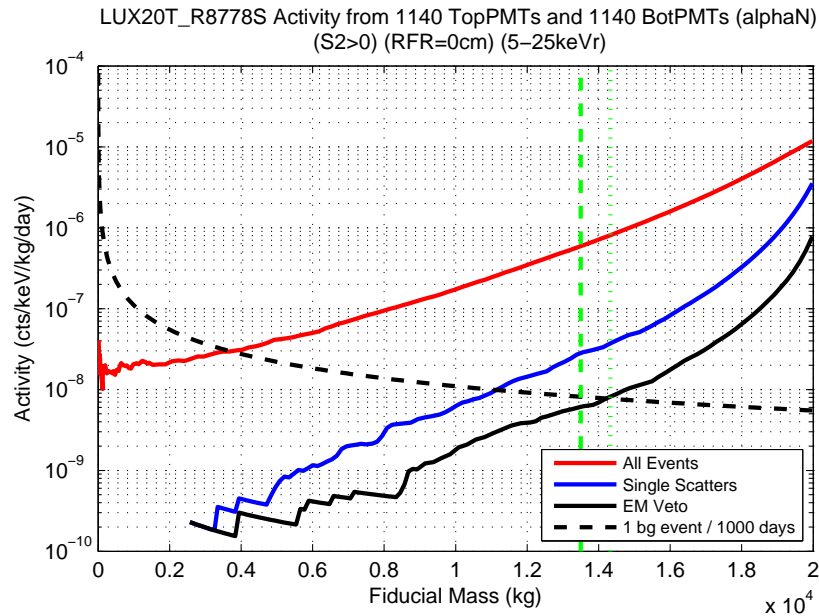
Figure 8.7: Nuclear recoil differential event rate vs. fiducial volume in the LZ20 detector (with aspect ratio H/D = 1.1, and dimensions listed in Table 8.9), due to PMT neutron background. The PMTs are assumed to have the same shape and size as the R8778 PMTs (5 cm diameter) and a benchmark neutron production rate of 5 n/PMT/year (see Section 7.1.2). The number of PMTs is listed in Table 8.9. The solid lines show the event rate in the energy deposition range $5 - 25 \, \text{keV}_\text{r}$ for all events (red), single scatter events (blue), and single scatter events after the "EM-veto" cut (black), which removes events with a electromagnetic component due to inelastic collisions and neutron captures. The black dashed line indicates the target event rate corresponding to 1 background event in 1,000 live-days for the given fiducial volume. The thick green dashed line indicates the fiducial volume of 13,500 kg. The green dotted line indicates the mass (14,330 kg) at which the neutron rate after the "EM-veto" cut matches the target rate after 45% NR acceptance.
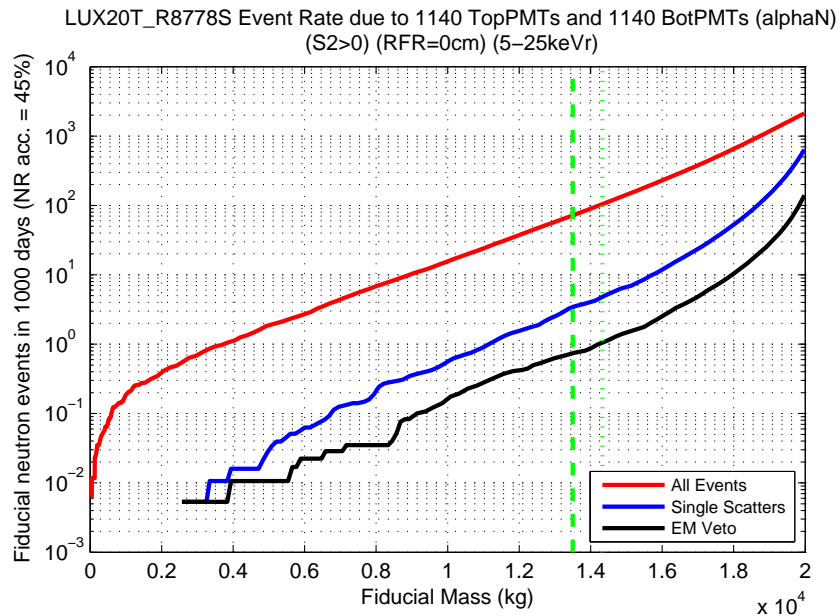
Figure 8.8: Nuclear recoil neutron events (after 45% NR acceptance) per 1,000 live-days vs. fiducial volume in the LZ20 detector (with aspect ratio H/D = 1.1 and dimensions listed in Table 8.9), due to PMT neutron background - the same data as Fig. 8.7. The PMTs are assumed to have the same shape and size as the R8778 PMTs (5 cm diameter) and a benchmark neutron production rate of $5\,\mathrm{n/PMT/year}$ (see Section 7.1.2). The number of PMTs is listed in Table 8.9. The solid lines show the event rate in the energy deposition range $5 - 25\,\mathrm{keV_r}$ for all events (red), single scatter events (blue), and single scatter events after the "EM-veto" cut (black), which removes events with a electromagnetic component due to inelastic collisions and neutron captures. The thick green dashed line indicates the fiducial volume of 13,500 kg. The green dotted line indicates the mass (14,330 kg) at which the neutron rate after the "EM-veto" cut, which removes events with a electromagnetic component due to inelastic collisions and neutron captures, matches the target rate of 1 event after 45% NR acceptance.
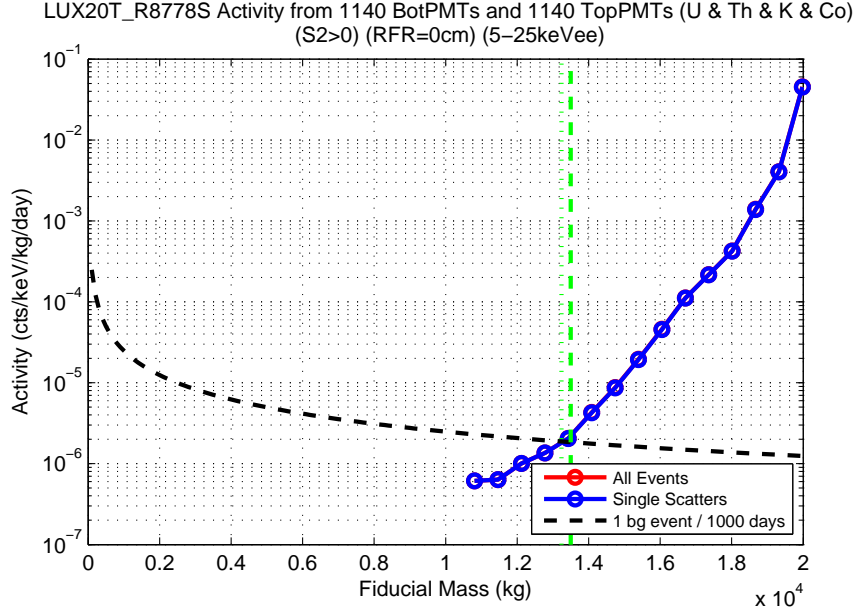
Figure 8.9: Electron recoil differential event rate vs. fiducial volume in the LZ20 detector (with aspect ratio H/D = 1.1 and dimensions listed in Table 8.9), due to PMT gamma background, in the LZ20 detector (with aspect ratio H/D = 1.1). The solid lines show the event rate in the energy deposition range $5-25\,\mathrm{keV_{ee}}$ for All Events (red) and Single Scatter events (blue). The event rate for All Events and Single Scatter events is indistinguishable in the plot. The event rate is normalized to the R8778 PMT contamination levels measured at SOLO and listed on Table 7.3: $8.9/2.8/2.6/92\,\mathrm{mBq/PMT}$ for $^{238}\mathrm{U}/^{232}\mathrm{Th}/^{60}\mathrm{Co}/^{40}\mathrm{K}$. The black dashed line indicates the target event rate corresponding to 1 background event in 1,000 live-days for the given fiducial volume, after 99.4% discrimination. The green dashed line indicates the fiducial volume of 13,500 kg.

99.4%, the gamma rate is reduced to 10 n**dru$_{\mathbf{ee}}$**. For this fiducial volume of $13,250\,\mathrm{kg}$, the neutron background produces a differential event rate of 6 ndru$_\mathrm{r}$, and the background is therefore dominated by the ER events. The predicted background event rate from both the neutron and electron recoil components (after ER-rejection) make clear that for a 20 tonnes detector, a fiducial volume of approximately 2/3 of the total mass is easily achievable. For the remainder of this chapter, we will consider a fiducial volume of $m_{fiducial} = 13,500\,\mathrm{kg}$ as the standard fiducial volume mass for the LZ20 detector.

8.2.3 Discrimination

The fiducial volume can be increased by either reducing the contamination levels of the PMTs, or by improving the discrimination. Figure 8.10 shows the discrimination needed
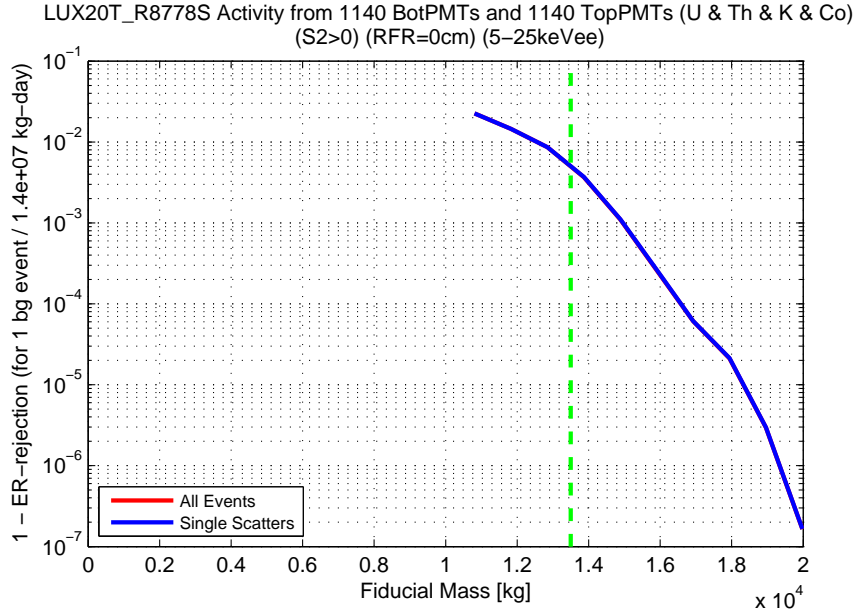
Figure 8.10: Discrimination necessary to achieve the target event rate of 1 gamma background event in 1,000 live-days exposure, plotted versus fiducial volume for LZ20 (with aspect ratio H / D = 1.1 and dimensions listed in Table 8.9). The y-axis shows the discrimination as $1-$ER rejection. The green dashed line indicates the fiducial volume of 13,500 kg. The solid lines show the event rate in the energy deposition range $5-25\,\text{keV}_{\text{ee}}$ for All Events (red) and Single Scatter events (blue). The event rate for All Events and Single Scatter events is indistinguishable in the plot. The event rate is normalized to the R8778 PMT contamination levels measured at SOLO and listed on Table 7.3: $8.9/2.8/2.6/92\,\text{mBq/PMT}$ for $^{238}\text{U}/^{232}\text{Th}/^{60}\text{Co}/^{40}\text{K}$.

to achieve 1 gamma background event in 1,000 live-days exposure (after the ER rejection) vs. fiducial volume. It can be seen that a large gain in discrimination power leads only to a modest increase in the fiducial volume. For example, pushing the discrimination from 99.4% to 99.9% results in a increase in fiducial volume of only 10%; going from 99.4% to 99.99% would result in an increase in fiducial volume of only 20%. Clearly, increasing the discrimination power of the detector is a poor strategy to increase the fiducial volume.

8.2.4 μ-induced neutrons

Although no simulation was performed for μ-induced neutrons in a 20 T scale detector, the μ-induced neutron background can be estimated by starting with the existing LUX simulations for μ-induced neutrons as a baseline, and estimating how the event rates scale as we increase detector size by using the results from the PMT neutron background simulations.

	NR Event Rate after 90% muon veto	Cut reduction factor
All Events	$38\,\mathrm{ndru_r}$	
Fiducial Events (100kg)	$29\,\mathrm{ndru_r}$	$\times 1/1.3$
Fiducial Single Scatters	$12\,\mathrm{ndru_r}$	$\times 1/2.4$

Table 8.7: Nuclear recoil event rate due to μ-induced neutrons produced in the LUX water shield, at the Homestake mine 4850 level (4.3 km.w.e.), and effect of the applied cuts on the event rate. NR event rate values obtained from Table 7.20. The NR event rate quoted take into consideration the effect of a 90% muon veto.

We will consider the μ-induced neutron background for a detector deployed in the Homestake mine, at 4.3 km.w.e. depth and a muon flux of $4.4\,\mu \cdot \mathrm{cm}^{-2}\mathrm{s}^{-1}$, inside a cylindrical water shield with 2.5 m water thickness.

The simulation of the μ-induced high energy neutron background generated in the rock and in the water tank for LUX is described in Section 7.2.2.2. The event rate in LUX due to μ-induced neutrons produced in the rock is 54 $\mathrm{ndru_r}$ after the standard fiducial volume (100 kg) and single scatter cuts were applied. After the same cuts, μ-induced neutrons from the water shield produced $120\,\mathrm{ndru_r}$ in the LUX detector, without any muon vetoing system. PMTs can be installed on the water tank to veto μ-associated events in the detector; this veto can easily reduce the background with a 90% efficiency, thus giving us an upper limit of $12\,\mathrm{ndru_r}$. The total μ-induced neutron background from rock and water shield in LUX is then $66\,\mathrm{ndru_r}$. The effect of the fiducial volume and single scatter cuts on high energy neutron events can be determined from the event rate due to μ-induced neutrons produced in the water tank, listed in Table 8.7.

Now let's consider the PMT fast neutron background for both LUX and LZ20 detector. We expect the fiducial and single scatter cuts to behave differently for the fast neutrons and the μ-induced neutrons, but the total rate (that is, before fiducial and single scatter cuts) should scale similarly in both cases. The LZ20 detector is large enough that it can be approximated as an infinite wall for incoming neutrons, and thus the difference in the neutron spectrum (and in their mean free path) should not play a significant role *in the total rate*. Therefore, the total rate for PMT neutrons and for μ-induced neutrons should scale in a similar way when going from LUX to LZ20:

- PMT neutrons: $28.2\,\mu\mathrm{dru_r} \rightarrow 11.5\,\mu\mathrm{dru_r}$ (LUX$\rightarrow$LZ20) (see Table 8.2)

- $\Rightarrow \mu$-induced neutrons (in water shield): $38\,\mathrm{ndru_r} \rightarrow 15.5\,\mathrm{ndru_r}$(LUX$\rightarrow$20T)

The cuts efficiencies for the large detector can be estimated by scaled the efficiencies of the cuts in LUX by using the mean free path of the neutrons. The fast neutrons generated in the PMTs have a peak energy at $4\,\mathrm{MeV}$, and a mean free path of $\sim 16\,\mathrm{cm}$. The μ-induced neutrons can have energies greater than $10\,\mathrm{MeV}$. However, the neutron rate falls very fast with energy, so we expect to be dominated by neutrons in the $10\,\mathrm{MeV}$ energy range, and the most penetrating neutrons in this range have a mean free path of $\sim 19\,\mathrm{cm}$. The efficiency of a cut (that is, the number of events not eliminated by the cut) is dependent on the probability that a neutron will transverse the characteristic length associated with the cut without scattering:

$$eff_{cut} = e^{-r/l}\,, \tag{8.7}$$

where $l =$mean free path and r is the characteristic length specific to the cut, to be determined below. The relative efficiency of the cut for fast neutrons and μ-induced neutrons is:

$$
\begin{aligned}
rel.\,eff_{cut} &= \frac{eff_{cut}(\mu\text{-induced})}{eff_{cut}(\text{fast})} = \frac{e^{-r/l}{}_{(\mu\text{-induced})}}{e^{-r/l}{}_{(\text{fast})}} \\
&= e^{-r\times(\frac{1}{l_{(10\,\mathrm{MeV})}} - \frac{1}{l_{(4\,\mathrm{MeV})}})} = e^{-r\times(\frac{1}{19}-\frac{1}{16})} \\
&= e^{r\times 0.0099}\,,
\end{aligned}
$$

The characteristic length r for the fiducial and single scatter cuts are:

- Fiducial cut: $r = 5\,\mathrm{cm}$ (the length of Xe the neutron must travel to enter the fiducial region).

$$r = 5\,\mathrm{cm} \Rightarrow rel.\,eff_{fid} = 1.05 \tag{8.8}$$

	Cut reduction factor	NR Activity
All Events		$15.5\,\mathrm{ndru_r}$
Fiducial Events (100kg)	$\times 1.05 \times (1/10) = \times 1/9.5$	$1.6\,\mathrm{ndru_r}$
Fiducial Single Scatters	$\times 2.64 \times (1/34) = \times 1/13$	$0.13\,\mathrm{ndru_r}$

Table 8.8: Nuclear recoil event rate due to μ-induced neutrons produced in the water shield for LZ20, deployed at the Homestake mine 4850 level (4.3 km.w.e.). The calculation assume a tank of 2 m water shield thickness in all directions, and the use of a 90% muon veto.

- Single Scatter cut: $r = 98\,\mathrm{cm}$ (a neutron that has scattered in the center of the detector has to travel through the radius of the detector without scattering again).

$$r = 98\,\mathrm{cm} \Rightarrow rel.\,eff_{ss} = 2.64 \tag{8.9}$$

The cuts efficiencies for the fast neutrons generated in the PMTs is given in Table 8.3. We can now scale them using the factors $rel.\,eff_{fid}$ and $rel.\,eff_{ss}$ factors listed above. The resulting event rate due to μ-induced neutron in the water shield (and assuming 90% muon veto efficiency) on the LZ20 detector is listed in Table 8.8.

In LUX, the μ-induced neutron activity from the rock was $2\times$ larger than the activity due to μ's in the water. If we scale accordingly, the total μ-induced neutron event rate for LZ20 is $0.13\,ndru_r\,(water) + 0.26\,ndru_r\,(rock) \approx 0.4\,ndru_r$, assuming 90% muon veto efficiency in the water shield (2.5 m thick). The goal of 1 nuclear recoil event in 1000 days for the fiducial mass of 13.5 T (67% of detector mass) corresponds to $4\,\mathrm{ndru_r}$, defined by the PMT fast neutron event rate (see Section 8.1.2). The estimated μ-induced neutron background of $\sim 0.4\,\mathrm{ndru_r}$ is a factor of 1/10 below the goal.

In order to further reduce the μ-induced neutron background, we can either (1) improve the muon veto, (2) put the detector inside a bigger water shield, or (3) reduce the muon flux by going deeper. The problem with the first approach is that it only reduces the event rate due to neutrons generated in the water tank, so that we can only go as low as $0.26\,\mathrm{ndru_r}$ if no other method is used. Likewise, the second approach only reduces the event rate due to neutrons generated in the rock. Furthermore, the attenuation of μ-induced neutrons in water is reduced with increasing thickness, because the least penetrating neutrons have already been screened out by the first 1 m of water, after which the attenuation becomes less efficient (see Figure 7.16 on page 275). In order to reduce the rock neutron background

by a further factor of $\times 10$, it is necessary to add 2.5 m to the total shield thickness, so that the water tank must have a size of at least 12 m height $\times$ 12 m diameter.

The neutron event rate calculated above is specific for a 20 T detector deployed at the 4850 ft level in the Homestake mine, which has an effective depth of 4.3 km.w.e. . Another site at the 7400 ft level of the Homestake mine might be available for deployment in the near future, increasing the effective depth to 6 km.w.e., comparable to the Sudbury mine depth (see Table 6.7). At this depth, the neutron flux due to muons is reduced by a factor of $\times 1/10$ (see Fig. 6.13). This reduces the estimated μ-induced neutron background of rock and water to ~ 0.04 ndru$_\mathrm{r}$, well below the neutron event rate goal.

8.3 Aspect Ratio

Another important question to explore relates to the shape of the detector - what happens if we make the detector flatter? As we decrease the height/diameter (H / D) ratio, we expect the event rate in the fiducial volume to increase. However, as we make the detector flatter, we are able to apply larger E-fields, and thus increase our ER-rejection efficiency. The question then becomes: what ER-rejection efficiency do we need to run a flatter detector?

8.3.1 Event rate vs. aspect ratio

A series of Monte Carlo simulations were performed to calculate the neutron and gamma event rate for a 20 T detector with different height/diameter aspect ratios. The dimensions used in the simulations are listed in Table 8.9. The simulations use the same techniques and cuts used above for the LZ20 detector background model, described in Section 8.2. The PMT neutron emission rate is normalized to the benchmark production rate of 5 neutrons/year/PMT, and the gamma emission rate is normalized to the radioactivity contamination levels measured at SOLO and listed on Table 7.3: 8.9/2.8/2.6/92 mBq/PMT for ^{238}U/^{232}Th/^{60}Co/^{40}K. The fiducial cut for the several detector shapes are found by using the method for optimization of fiducial volume also described above, in Section 8.2.1.

Fig. 8.11a-d show the spatial distribution of neutron events in the energy range 5-25 keV$_\mathrm{r}$ for detector shapes with the aspect ratios of H / D = 1.1, 0.8, 0.5 and 0.2, before

H / D ratio ratio	Height (H)	Diameter (D)	# of PMTs	Fiducial Height	Fiducial Diameter
1.1	223 cm	196 cm	2280	161 cm	190 cm
0.8	177 cm	221 cm	2880	132 cm	209 cm
0.5	129 cm	258 cm	3940	99 cm	242 cm
0.2	70 cm	351 cm	7260	47 cm	351 cm

Table 8.9: LZ20 detector dimensions, for several detector shapes (aspect ratios). All configurations have the same total mass of 20 tonnes, and a fiducial volume of 13,500 kg. The proposed LUX design has H/D = 1.1.

any cuts are applied. These plots illustrate how the flattening of the detector affects the fiducial volume. For a "flattened" detector, i.e. H/D = 0.2, it is impossible to discern a fiducial volume with low background. Figs. 8.12 and 8.13 show the neutron and gamma differential event rate due to PMTs vs. the fiducial volume, after all cuts applied. These plots show exactly how high the background event rate becomes as we flatten the detector. For H/D = 0.2, simply decreasing the fiducial volume is a inefficient strategy to achieve the background event rate goal of 1 event/1,000 days.

If we decide to change the H/D ratio from 1.1, it becomes necessary to reduce the neutron emission rate per PMT in order to achieve the background rate goal of 1 event in 13,500,000 kg-days (after 45% NR acceptance). Likewise, if we change the H/D ratio to either 0.5 or 0.2, and do not change the discrimination efficiency, we will need to reduce the PMT gamma activity to match the background rate goal with a reasonably large fiducial volume. Figure 8.14a-b shows the PMT activity reduction factor necessary to achieve the background rate goal for both neutron and gamma backgrounds (assuming current discrimination efficiency of 99.4%). Note that we can actually slightly *increase* the neutron activity for the least flat detector shape (H/D = 1.1).

8.3.2 Discrimination vs. aspect ratio

What ER-rejection efficiency do we need for each detector shape? Figure 8.15 shows the discrimination needed in order to achieve 1 background event in 1,000 live-days for the vs. fiducial volume for detectors with the selected aspect ratios. The necessary ER-rejection converges for very large fiducial volumes (relative to the total detector size), but it diverges
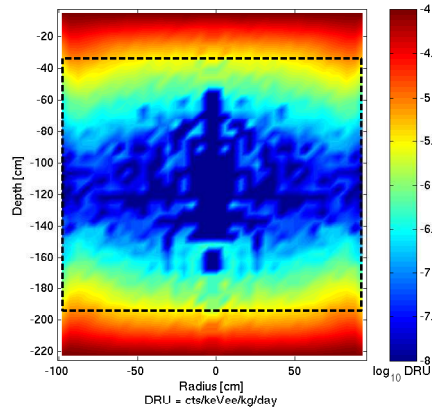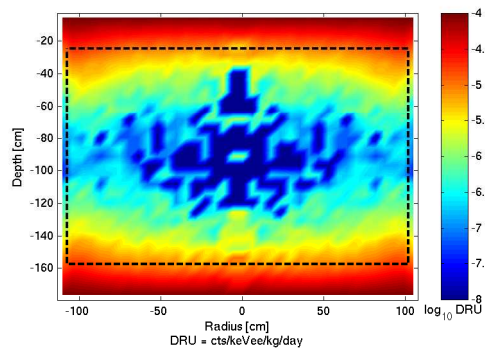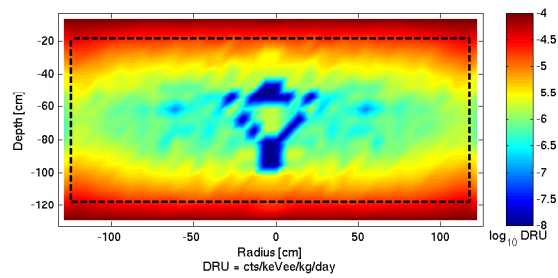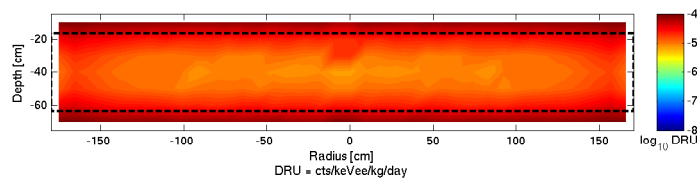
(a) H/D = 1.1

(b) H/D = 0.8

(c) H/D = 0.5

(d) H/D = 0.2

Figure 8.11: Spatial distribution of nuclear recoil events for several detector shapes, from the simulation of neutrons produced by the PMTs. Only events that deposit $5 - 25 \, \mathrm{keV_r}$ are shown; no other cuts are applied. The black dashed line indicates the optimal R and Z for fiducial volume cut of $m_{fiducial} = 13,500 \, \mathrm{kg}$. The event rates are normalized to the benchmark neutron emission rate of $5 \, \mathrm{n/PMT/year}$ assumed for R8778 PMTs (see Section 7.1.2). The detector dimensions and number of PMTs in each case are listed in Table 8.9.
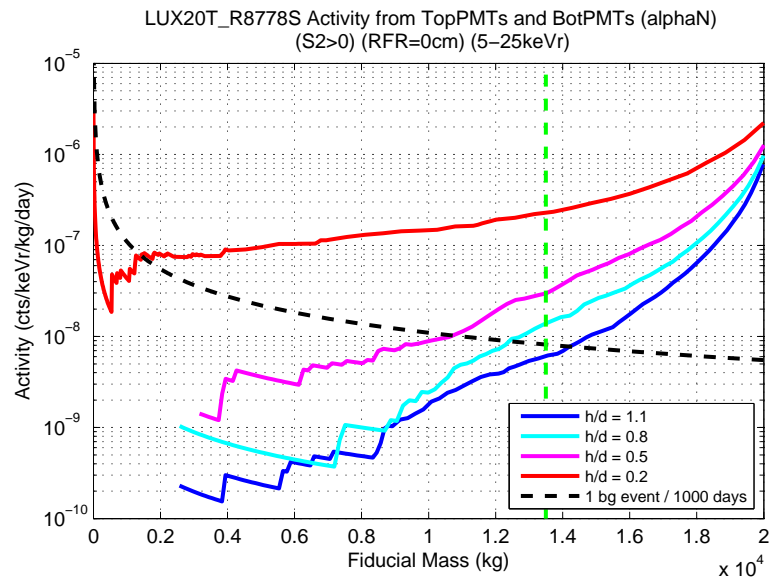
Figure 8.12: Nuclear recoil differential event rate vs. fiducial volume in the LZ20 detector due to PMT neutron background, normalized to the benchmark neutron emission rate of $5\,\mathrm{n/PMT/year}$ assumed for R8778 PMTs (see Section 7.1.2). The solid lines show the event rate for several aspect ratios (dimensions and number of PMTs in each case are listed in Table 8.9), for single scatter events in the energy range $5-25\,\mathrm{keV_r}$ after the "EM-veto" cut (black), which removes events with a electromagnetic component due to inelastic collisions and neutron captures. The black dashed line indicates the activity corresponding to 1 background event in 1,000 live-days for the given fiducial volume. The green dashed line indicates the fiducial volume of 13,500 kg.
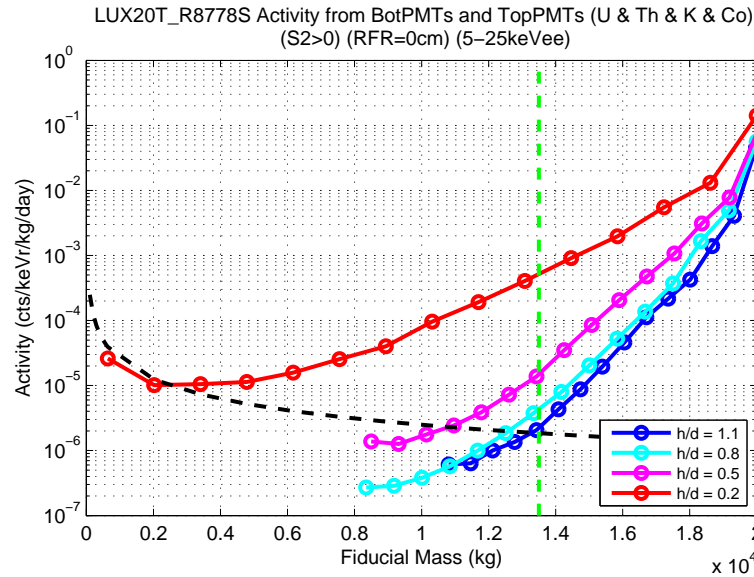
Figure 8.13: Electron recoil differential event rate vs. fiducial volume in the LZ20 detector due to PMT gamma background, normalized to the R8778 PMT contamination levels measured at SOLO and listed on Table 7.3: $8.9/2.8/2.6/92\,\mathrm{mBq/PMT}$ for $^{238}\mathrm{U}/^{232}\mathrm{Th}/^{60}\mathrm{Co}/^{40}\mathrm{K}$. The solid lines show the event rate for several aspect ratios (dimensions listed in Table 8.9), for single scatter events in the energy range $5-25\,\mathrm{keV_{ee}}$. The black dashed line indicates the activity corresponding to 1 background event in 1,000 live-days for the given fiducial volume, after 99.4% discrimination. The green dashed line indicates the fiducial volume of 13,500 kg.
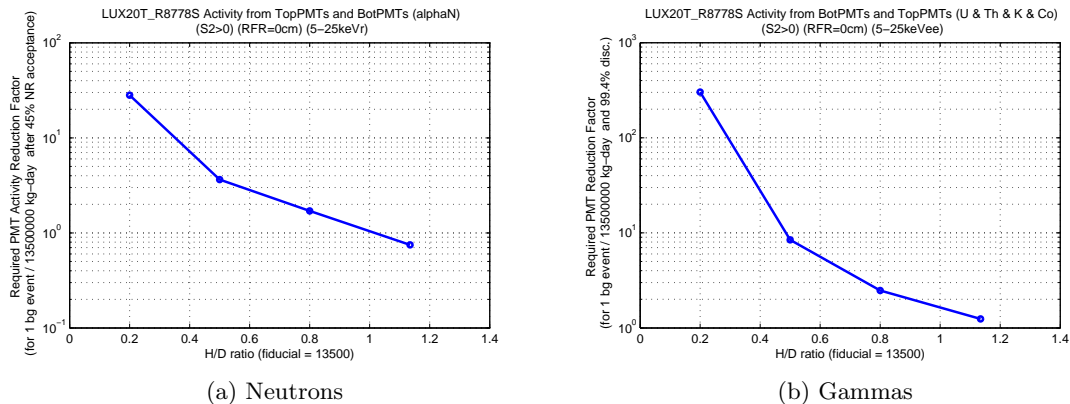

(a) Neutrons

(b) Gammas

Figure 8.14: PMT radioactivity reduction factor necessary to achieve 1 event in 1,000 live-days in 13,500 kg fiducial (after 45% NR acceptance for neutrons and 99.4% ER-rejection for gammas) in the LZ20 detector for several aspect ratios (dimensions listed in Table 8.9). The reduction factor is based on the event rate in the fiducial volume for each detector shape shown in Fig. 8.12 and Fig. 8.13.
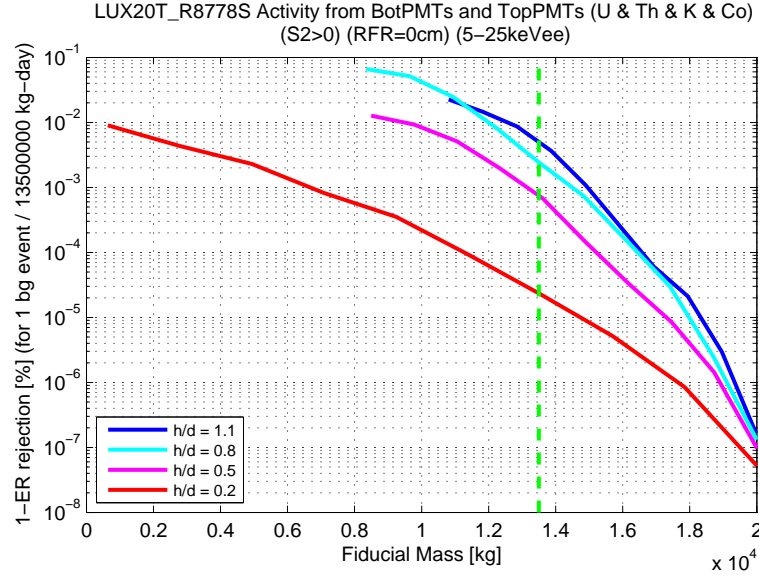
Figure 8.15: Discrimination necessary to achieve 1 event in 1,000 live-days vs. fiducial volume mass in the LZ20 detector for several aspect ratios (dimensions listed in Table 8.9). The required ER rejection efficiency increases exponentially as we increase the fiducial mass. The discrimination required is calculated from the event rates for each detector shape shown in Fig. 8.13. The green dashed line indicates the standard fiducial volume of 13,500 kg.

greatly for the desired fiducial volume mass of 13,500 kg. The necessary ER-rejection to achieve the background goal is listed in Table 8.10, and illustrated in Fig. 8.16. As an example, a detector with H/D = 0.2 aspect ratio needs a ER-rejection efficiency of 99.998% to achieve the background goal. Making "flattened" detectors is very challenging from the point of view of background reduction, because it fails to take advantage of the self-shielding properties of the liquid Xe. The flat detector has to rely on very good ER-rejection, and in the successful application of high E-fields to achieve such discrimination.

For comparison, the ZEPLIN-III detector, which operates with relatively high E-fields of $3.9\,\mathrm{kV/cm}$ and has an active Xe volume with aspect ratio of H/D = 0.1, has an average ER-rejection of 99.98% in the energy range of $2 - 16\,\mathrm{keV_{ee}}$ [72]. The discrimination power achieved is not enough to allow for the construction of a flat LZ20 detector, even if it was possible to apply such high E-fields in a detector of the size of the LZ20. Better background performance can be obtained by constructing a "tall" detector (H/D = 1.1), rather than by trying to push up the discrimination power of the detector.

Shape (height / diameter)	Neutron Rate	Gamma Rate	ER-rejection needed
1.1	6 ndru$_r$	2.3 μdru$_{ee}$	99.45%
0.8	14 ndru$_r$	4.6 μdru$_{ee}$	99.75%
0.5	30 ndru$_r$	15.6 μdru$_{ee}$	99.92%
0.2	230 ndru$_r$	558 μdru$_{ee}$	99.998%

Table 8.10: Nuclear and Electron recoil differential event rates in the LZ20 fiducial volume (13,500 kg) due to the neutron and gamma background generated by the PMTs, respectively. The table lists the event rate for single scatter events in the energy range $5 - 25$ keV$_{ee}$ for gammas, and $5 - 25$ keV$_r$ for neutrons. The neutron event rate is calculated after the "EM-veto" cut, which removes events with a electromagnetic component due to inelastic collisions and neutron captures. We also tabulate the ER-rejection efficiency needed to achieve 1 gamma background event in 13,500,000 kg-days.
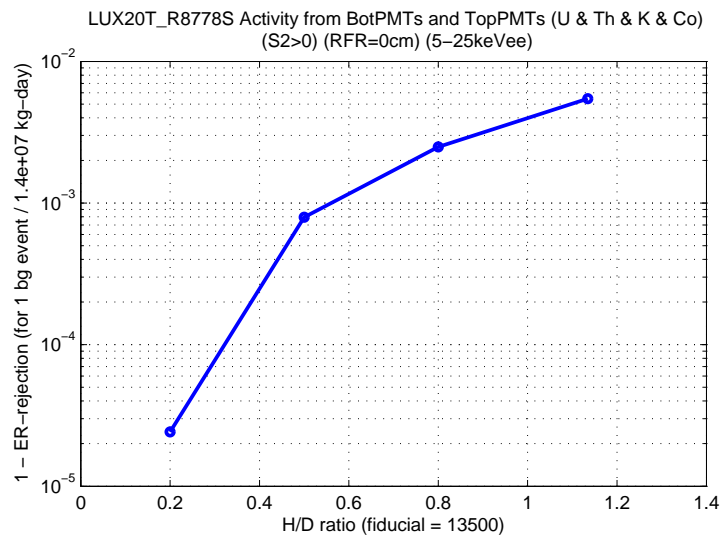

Figure 8.16: Discrimination necessary to achieve 1 event in 13,500,000 kg-days vs. vs. detector aspect ratio (H / D = 1.1, 0.8, 0.5 and 0.2) in the LZ20 detector. The discrimination is calculated using the gamma single scatter event rate in the energy deposition range of $5 - 25$ keV$_{ee}$, for 1,000 live days and fiducial volume of 13,500 kg.

H/D ratio	Total Event Rate			
	5 - 25 keV$_{ee}$	5 - 100 keV$_{ee}$	5 - 300 keV$_{ee}$	5 - 2600 keV$_{ee}$
1.1	0.2 Hz	6 Hz	18 Hz	56 Hz
0.8	0.3 Hz	8 Hz	23 Hz	72 Hz
0.5	0.4 Hz	11 Hz	32 Hz	101 Hz
0.2	0.7 Hz	20 Hz	60 Hz	192 Hz

Table 8.11: Total event rates for the LZ20 detector for several aspect ratios (dimensions listed in Table 8.9), estimated from the PMT gamma background. The event rates are calculated in the indicated energy ranges, using a 5 keV$_{ee}$ energy threshold and with no cuts applied.

8.3.3 Event Rate and Data Analysis

The background is also constrained by the effect the raw event rate has on analysis - if it's too high, there will be a lot of event overlap, making analysis very difficult and forcing us to throw away a large fraction of the acquired events. The event rate in the detector is dominated by the gamma background generated by the PMTs. Using the method to calculate the optimal fiducial shape described in Section 8.2.1, the total gamma event rate in the entire detector with no cuts applied is 56 Hz for H/D =1.1. Table 8.11 lists the event rate in the entire detector, before any cuts, for several energy ranges. Fig. 8.17 shows the total event rate for a given maximum energy.

How much overlap is there for such event rate? For the "standard" detector shape (H/D = 1.1), of height 223 cm and drift length 1.2 ms, there is a 12% probability of event overlap for 56 Hz rate. For all detector shapes, the event overlap probability is just above 10%. The overlap probability is shown in Fig. 8.18. The problem of overlap is solved by throwing away all event in which overlap seems to have occurred, i.e. events in which more than 1 S1 can be identified. The downside of such strategy is that the livetime is decreased proportionally. For the H/D = 1.1 case, the analysis will throw away roughly 12%, thus also decreasing the livetime by 12%.

This strategy assumes that all event overlap is equal. To 0$^{\text{th}}$ order, this is true. For example, an event overlap might contain 2 S1's and 3 S2's. Since we do not know which scatters are part of a multiple event scatter, we can't make any judgment on which S2 belongs to which S1 *a priori*. There are a few special cases that are exceptions to this
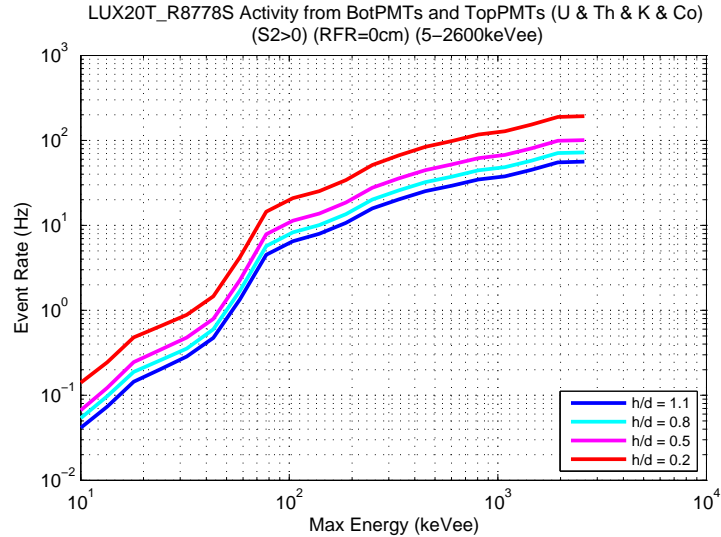
Figure 8.17: Total event rates versus maximum event energy for the LZ20 detector for several aspect ratios (dimensions listed in Table 8.9), estimated from the PMT gamma background. The event rates are calculated for a energy threshold of $E_{thresh} = 5\,\mathrm{keV_{ee}}$, and integrated up to the energy indicated in the x-axis. No cuts were applied.

problem. For example, all events in which the individual scatter S2's are consistent with a ER event with the given S1 can be immediately be identified as a gamma, and can be cut without reducing our WIMP sensitivity. Also, for events with one large S1 and one small S1, all S2's consistent with a ER-event of energy equal to the larger S1 can be ruled to be part of the larger event. However, large energy events also have more scatters, and it becomes difficult to determine which scatters belong to which S1 *a priori*. It is a very complex procedure to determine how much of a problem event overlap becomes.
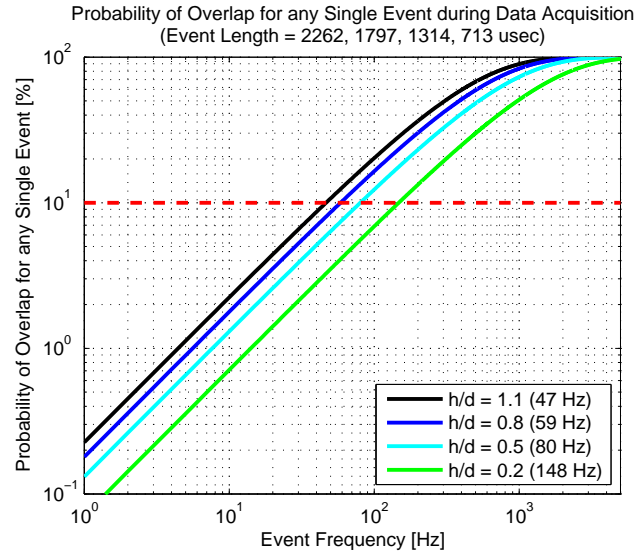
Figure 8.18: Event overlap probability in the LZ20 detector for several aspect ratios (dimensions listed in Table 8.9), estimated from the total event rates using Eq. 8.6. The event probabilities are calculated for event rates with in the $5\,\mathrm{keV_{ee}} - 2600\,\mathrm{keV_{ee}}$ energy range; no other cuts are applied. The red dashed line indicates a event overlap probability of 10%.

8.4   Closing Remarks

XENON10 was initially proposed as a prototype for larger dark matter detectors using liquid Xe, and its success demonstrates the power of this emerging technology in the field. At the end of its run, XENON10 had surpassed all existing WIMP-nucleon limits, and established liquid Xe detectors as key players in field. Presently, the direct detection of dark matter has become a highly competitive field, with several experiments in the process of being deployed and brought online, and several more being planned for the next generation. Higher and higher sensitivity is pursued by each generation of detector, and Fig. 8.19 shows the projected sensitivities for the detectors discussed in this work.

As detectors become larger, the understanding of their backgrounds becomes ever more critical. Several strategies are pursued in the search for more sensitive detectors, such as the improvement of PMT sensitivity, increasing in light collection, and better discrimination through higher electric fields. However, the single factor that contributes most to limiting sensitivity is the background event rate. This lesson was learned the hard way in XENON10, in which the presence of background events in the WIMP signal window and the failure of

the algorithms and cuts to identify all backgrounds in the primary blind analysis greatly increased the WIMP exclusion limits set by the detector. With this lesson in mind, the next generation of detectors (LUX and LZ) are designed with the goal of having no background events in the WIMP signal window for the entire exposure run. This will allow them not only to push the limits down by orders of magnitude, but also to demonstrate unambiguous discovery, in the case of positive signal detection.

The use of techniques such as fiducial volume, narrow energy windows and multiple scatter cuts make use of the self-shielding properties of liquid Xe to cope with the existing backgrounds. One of the most attractive features of liquid Xe detectors is relative ease with which they can be scaled up, since larger detectors are better able to take advantage of the self-shielding properties of liquid Xe. Self-shielding is the best background reduction tool available, to the extent that optimizing the detector to increase fiducial volume trumps even the background reduction gained from improved discrimination. Larger detector sizes, with design optimized to take advantage of self-shielding and reduce backgrounds, becomes the top priority in the quest for better sensitivity as we move into the next-generation of dark matter detectors.
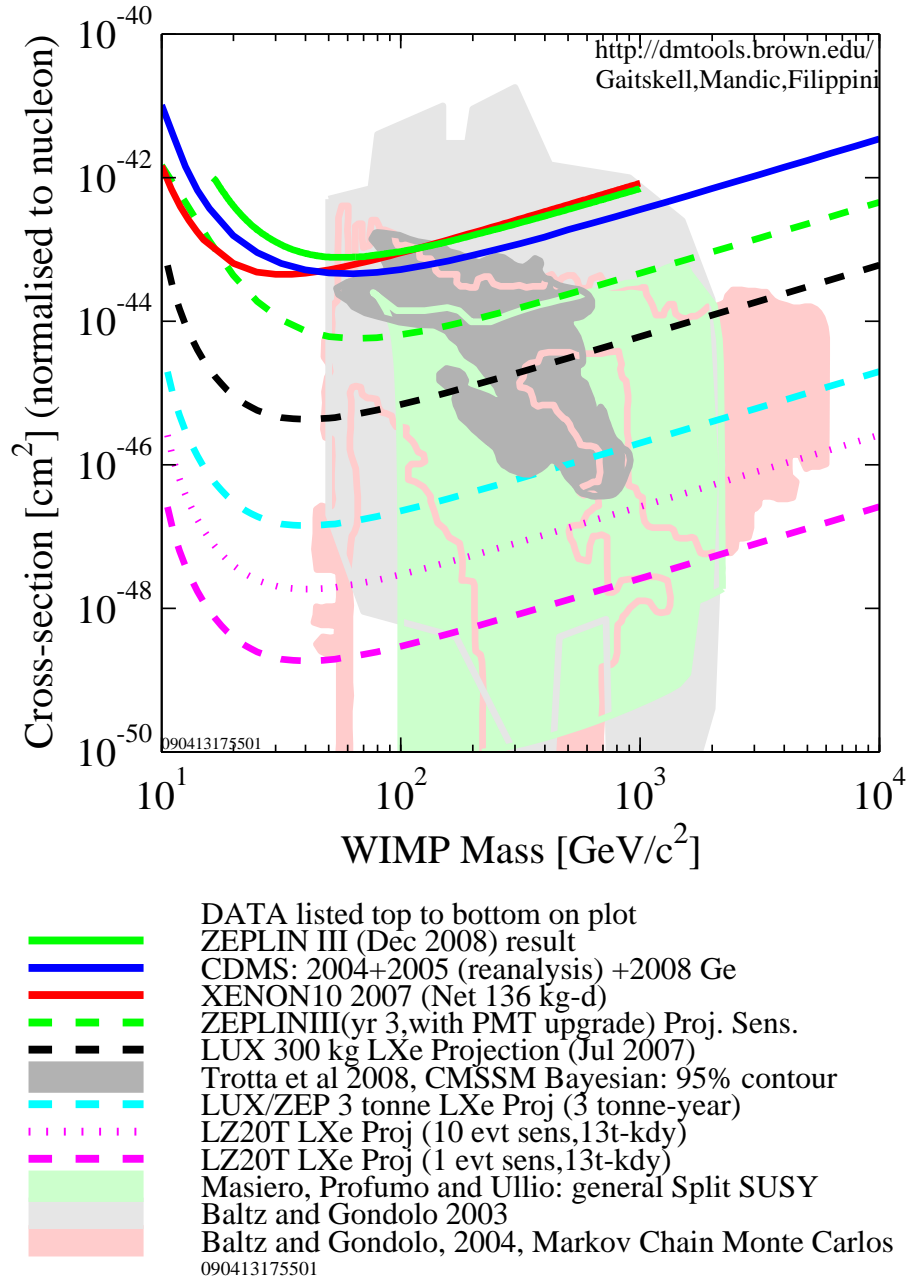
Figure 8.19: Projected sensitivity for the next generation liquid Xe detectors. The figure shows the projected upper limits (90% C.L.) on the Spin-Independent WIMP-nucleon cross-section versus WIMP mass for LUX (black dashed line), LZ3 (cyan dashed line) and LZ20 (purple dashed line). Plot generated using DMTools [100].

Bibliography

[1] D. Clowe, *et al.*, "A Direct Empirical Proof of the Existence of Dark Matter,"*Astrophys. J.* **648** (Sept., 2006) L109–L113. `astro-ph/0608407`.

[2] F. Zwicky, "Die Rotreshiebung von extragalaktishen Nebeln," *Helv. Phys. Acta* **6** (1933) 110–127.

[3] F. Zwicky, "On the Masses of Nebulae and of Clusters of Nebulae,"*ApJ* **86** (Oct., 1937) 217. `[link]`.

[4] S. M. Kent and J. E. Gunn, "The dynamics of rich clusters of galaxies. I - The Coma cluster,"*AJ* **87** (July, 1982) 945–971. `[link]`.

[5] V. C. Rubin and W. K. J. Ford, "Rotation of the Andromeda Nebula from a Spectroscopic Survey of Emission Regions,"*ApJ* **159** (Feb., 1970) 379. `[link]`.

[6] B. Ryden, *Introduction to Cosmology*. Benjamin Cummings, October, 2002. `[link]`.

[7] M. Persic, P. Salucci, and F. Stel, "The Universal rotation curve of spiral galaxies: 1. The Dark matter connection," *Mon. Not. Roy. Astron. Soc.* **281** (1996) 27. `arXiv:astro-ph/9506004`.

[8] M. S. Roberts and R. N. Whitehurst, "The rotation curve and geometry of M31 at large galactocentric distances.,"*ApJ* **201** (Oct., 1975) 327–346. `[link]`.

[9] **WMAP** Collaboration, G. Hinshaw *et al.*, "Five-Year Wilkinson Microwave Anisotropy Probe (WMAP) Observations: Data Processing, Sky Maps, & Basic Results," *Astrophys. J. Suppl.* **180** (2009) 225–245. `arXiv:0803.0732 [astro-ph]`.

[10] S. W. Barwick, *et al.*, "APS Neutrino Study: Report of the Neutrino Astrophysics and Cosmology Working Group,". `arXiv:astro-ph/0412544`.

[11] B. Leibundgut, "Cosmological Implications from Observations of Type Ia Supernovae," *ARAA* **39** (2001) 67–98. `[link]`.

[12] W. Hillebrandt and J. C. Niemeyer, "Type Ia Supernova Explosion Models," *Annual Review of Astronomy and Astrophysics* **38** (2000) no. 1, 191–230. `[link]`.

[13] S. Perlmutter and B. P. Schmidt, "Measuring Cosmology with Supernovae,". `arXiv:astro-ph/0303428`.

[14] **Supernova Cosmology Project** Collaboration, R. A. Knop, *et al.*, "New Constraints on ΩM, ΩΛ, and w from an Independent Set of 11 High-Redshift Supernovae Observed with the Hubble Space Telescope," *The Astrophysical Journal* **598** (2003) no. 1, 102–137. `[link]`.

[15] **Supernova Cosmology Project** Collaboration, M. Kowalski, *et al.*, "Improved Cosmological Constraints from New, Old, and Combined Supernova Data Sets,"*Astrophys. J.* **686** (Oct., 2008) 749–778. `arXiv:0804.4142`.

[16] C. L. Bennett, *et al.*, "Scientific Results from the Cosmic Background Explorer (COBE),"*Proceedings of the National Academy of Science* **90** (June, 1993) 4766–4773. `[link]`.

[17] P. D. Jackson, *et al.*, "COBE Differential Microwave Radiometer (DMR) data processing techniques," tech. rep., Dec., 1992.

[18] "WMAP Mission Homepage." http://map.gsfc.nasa.gov/. `[link]`.

[19] M. R. Nolta, *et al.*, "Five-Year Wilkinson Microwave Anisotropy Probe (WMAP) Observations: Angular Power Spectra," *The Astrophysical Journal Supplement Series* **180** (2009) no. 2, 296–305. `[link]`.

[20] W. Hu, N. Sugiyama, and J. Silk, "The Physics of microwave background anisotropies," *Nature* **386** (1997) 37–43. `arXiv:astro-ph/9604166`.

[21] D. J. Eisenstein, *et al.*, "Detection of the Baryon Acoustic Peak in the Large-Scale Correlation Function of SDSS Luminous Red Galaxies," *The Astrophysical Journal* **633** (2005) no. 2, 560–574. `[link]`.

[22] J. R. I. Gott, *et al.*, "A Map of the Universe," *The Astrophysical Journal* **624** (2005) no. 2, 463–484. `[link]`.

[23] M. Tegmark, *et al.*, "Cosmological constraints from the SDSS luminous red galaxies," *Physical Review D (Particles, Fields, Gravitation, and Cosmology)* **74** (2006) no. 12, 123507. `[link]`.

[24] G. Steigman, "Big bang nucleosynthesis: Probing the first 20 minutes,". `arXiv:astro-ph/0307244`.

[25] R. H. Cyburt, B. D. Fields, and K. A. Olive, "Primordial nucleosynthesis in light of WMAP," *Physics Letters B* **567** (2003) no. 3-4, 227 – 234. `[link]`.

[26] **Particle Data Group** Collaboration, C. Amsler *et al.*, "Review of particle physics," *Phys. Lett.* **B667** (2008) 1. `[link]`.

[27] R. H. Cyburt, *et al.*, "New BBN limits on physics beyond the standard model from 4He," *Astroparticle Physics* **23** (2005) no. 3, 313 – 323. `[link]`.

[28] R. H. Cyburt, B. D. Fields, and K. A. Olive, "A Bitter Pill: The Primordial Lithium Problem Worsens,". `arXiv:0808.2818 [astro-ph]`.

[29] R. Narayan and M. Bartelmann, "Lectures on gravitational lensing,"*ArXiv Astrophysics e-prints* (June, 1996) . `arXiv:astro-ph/9606001`.

[30] H. Hoekstra and B. Jain, "Weak Gravitational Lensing and Its Cosmological Applications,"*Annual Review of Nuclear and Particle Science* **58** (Nov., 2008) 99–123. `arXiv:0805.0139`.

[31] M. Bartelmann and P. Schneider, "Weak Gravitational Lensing," *Phys. Rept.* **340** (2001) 291–472. `[link]`.

[32] R. J. Gaitskell, "Direct Detection of Dark Matter," *Ann. Rev. Nucl. Part. Sci.* **54** (2004) 315–359. `[link]`.

[33] S. Weinberg, "A New Light Boson?,"*Phys. Rev. Lett.* **40** (Jan, 1978) 223–226. `[link]`.

[34] S. J. Asztalos, *et al.*, "Searches for Astrophysical and Cosmological Axions*," *Annual Review of Nuclear and Particle Science* **56** (2006) no. 1, 293–326. `[link]`.

[35] G. Jungman, M. Kamionkowski, and K. Griest, "Supersymmetric dark matter," *Phys. Rept.* **267** (1996) 195–373. `arXiv:hep-ph/9506380`.

[36] L. Bergström, P. Ullio, and J. H. Buckley, "Observability of [gamma] rays from dark matter neutralino annihilations in the Milky Way halo," *Astroparticle Physics* **9** (1998) no. 2, 137 – 162. `[link]`.

[37] G. Zaharijas and D. Hooper, "Challenges in detecting gamma-rays from dark matter annihilations in the galactic center," *Physical Review D (Particles, Fields, Gravitation, and Cosmology)* **73** (2006) no. 10, 103501. `[link]`.

[38] **IceCube** Collaboration, C. d. l. Heros, "Particle astrophysics from the cold: Results and perspectives of IceCube,". `arXiv:astro-ph/0802.0147`.

[39] E. A. Baltz and P. Gondolo, "Improved constraints on supersymmetric dark matter from muon g-2,"*Phys. Rev. D* **67** (Mar, 2003) 063503. `[link]`.

[40] J. D. Lewin and P. F. Smith, "Review of mathematics, numerical factors, and corrections for dark matter experiments based on elastic nuclear recoil," *Astroparticle Physics* **6** (1996) no. 1, 87 – 112. `[link]`.

[41] A. K. Drukier, K. Freese, and D. N. Spergel, "Detecting cold dark-matter candidates,"*Phys. Rev. D* **33** (Jun, 1986) 3495–3508. [link].

[42] C. Savage, *et al.*, "Compatibility of DAMA/LIBRA dark matter detection with other searches," *Journal of Cosmology and Astroparticle Physics* **2009** (2009) no. 04, 010. [link].

[43] E. I. Gates, G. Gyuk, and M. S. Turner, "The Local Halo Density,"*ApJL* **449** (Aug., 1995) L123+. astro-ph/9505039.

[44] R. R. Roy, B. P. Nigam, and F. Titus, *Nuclear Physics.* AAPT, 1968. [link].

[45] J. Engel, S. Pittel, and P. Vogel, "Nuclear Physics of Dark Matter Detection," *International Journal of Modern Physics E* **1** (1992) 1–37. [link].

[46] R. H. Helm, "Inelastic and Elastic Scattering of 187-Mev Electrons from Selected Even-Even Nuclei,"*Phys. Rev.* **104** (Dec, 1956) 1466–1475. [link].

[47] "WebElements." http://www.webelements.com/. [link].

[48] "NIST Thermophysical Properties of Fluid Systems." http://webbook.nist.gov/chemistry/fluid/. [link].

[49] L. M. Barkov, *et al.*, "Measurement of the refractive index of liquid xenon for intrinsic scintillation light," *Nuclear Instruments and Methods in Physics Research Section A: Accelerators, Spectrometers, Detectors and Associated Equipment* **379** (1996) no. 3, 482 – 483, Proceedings of the Sixth International Conference on Instrumentation for Experiments at e+ e- Colliders. [link].

[50] V. N. Solovov, *et al.*, "Measurement of the refractive index and attenuation length of liquid xenon for its scintillation light," *Nuclear Instruments and Methods in Physics Research Section A: Accelerators, Spectrometers, Detectors and Associated Equipment* **516** (2004) no. 2-3, 462 – 474. [link].

[51] G. M. Seidel, R. E. Lanou, and W. Yao, "Rayleigh scattering in rare-gas liquids," *Nuclear Instruments and Methods in Physics Research Section A: Accelerators,*

Spectrometers, Detectors and Associated Equipment **489** (2002) no. 1-3, 189 – 194. [link].

[52] *CRC Handbook of Chemistry and Physics, 87th Edition.* CRC Press, Boca Raton, 2006. [link].

[53] R. Sawada, *et al.*, "Capacitive level meter for liquid rare gases," *Cryogenics* **43** (2003) no. 8, 449 – 450. [link].

[54] H. M. Jones and E. E. Kunhardt, "Development of pulsed dielectric breakdown in liquids," *Journal of Physics D: Applied Physics* **28** (1995) no. 1, 178. [link].

[55] J. Jortner, *et al.*, "Localized Excitations in Condensed Ne, Ar, Kr, and Xe," *The Journal of Chemical Physics* **42** (1965) no. 12, 4250–4253. [link].

[56] T. Doke, *et al.*, "Absolute Scintillation Yields in Liquid Argon and Xenon for Various Particles," *Japanese Journal of Applied Physics* **41** (2002) no. Part 1, No. 3A, 1538–1545. [link].

[57] T. Doke and K. Masuda, "Present status of liquid rare gas scintillation detectors and their new application to gamma-ray calorimeters," *Nuclear Instruments and Methods in Physics Research Section A: Accelerators, Spectrometers, Detectors and Associated Equipment* **420** (1999) no. 1-2, 62 – 80. [link].

[58] A. Baldini, *et al.*, "Absorption of scintillation light in a 100 l liquid xenon [gamma]-ray detector and expected detector performance," *Nuclear Instruments and Methods in Physics Research Section A: Accelerators, Spectrometers, Detectors and Associated Equipment* **545** (2005) no. 3, 753 – 764. [link].

[59] N. Ishida, *et al.*, "Attenuation length measurements of scintillation light in liquid rare gases and their mixtures using an improved reflection suppresser," *Nuclear Instruments and Methods in Physics Research Section A: Accelerators, Spectrometers, Detectors and Associated Equipment* **384** (1997) no. 2-3, 380 – 386. [link].

[60] E. Aprile, *et al.*, *Noble Gas Detectors*, vol. 362. Wiley-VCH, December, 2006. ISBN-10: 3527405976 ISBN-13: 978-3527405978.

[61] S. Kubota, *et al.*, "Dynamical behavior of free electrons in the recombination process in liquid argon, krypton, and xenon,"*Phys. Rev. B* **20** (Oct, 1979) 3486–3496. [link].

[62] T. Doke, *et al. Jpn. J. Appl. Phys.* **42** (2002) 1528.

[63] E. Aprile *et al.*, "Simultaneous Measurement of Ionization and Scintillation from Nuclear Recoils in Liquid Xenon as Target for a Dark Matter Experiment," *Phys. Rev. Lett.* **97** (2006) 081302. arXiv:astro-ph/0601552.

[64] P. Sorensen, *A Position-Sensitive Liquid Xenon Time-Projection Chamber for Direct Detection of Dark Matter: The XENON10 Experiment.* PhD thesis, Brown University, July, 2008.

[65] L. S. Miller, S. Howe, and W. E. Spear, "Charge Transport in Solid and Liquid Ar, Kr, and Xe,"*Phys. Rev.* **166** (Feb, 1968) 871–878. [link].

[66] A. I. Bolozdynya, "Two-phase emission detectors and their applications," *Nuclear Instruments and Methods in Physics Research Section A: Accelerators, Spectrometers, Detectors and Associated Equipment* **422** (1999) no. 1-3, 314 – 320. [link].

[67] C. E. Dahl, *The physics of background discrimination in liquid xenon, and first results from Xenon10 in the hunt for WIMP dark matter.* PhD thesis, Princeton University, September, 2009.

[68] **XENON** Collaboration, J. Angle *et al.*, "First Results from the XENON10 Dark Matter Experiment at the Gran Sasso National Laboratory," *Phys. Rev. Lett.* **100** (2008) 021303. arXiv:0706.0039 [astro-ph].

[69] A. Hitachi, *et al.*, "Effect of ionization density on the time dependence of luminescence from liquid argon and xenon,"*Phys. Rev. B* **27** (May, 1983) 5279–5285. `[link]`.

[70] J. Kwong, *The development of two-phase xenon dark matter detectors.* PhD thesis, Princeton University, 2009.

[71] P. Sorensen *et al.*, "The scintillation and ionization yield of liquid xenon for nuclear recoils," *Nucl. Instrum. Meth.* **A601** (2009) 339–346. `arXiv:0807.0459 [astro-ph]`.

[72] V. N. Lebedenko, *et al.*, "Results from the first science run of the ZEPLIN-III dark matter search experiment," *Physical Review D (Particles and Fields)* **80** (2009) no. 5, 052010. `arXiv:0812.1150 [astro-ph]`.

[73] A. Manzur, *et al.*, "Scintillation efficiency and ionization yield of liquid xenon for mono-energetic nuclear recoils down to 4 keV,". `arXiv:0909.1063`.

[74] V. Chepel, *et al.*, "Scintillation efficiency of liquid xenon for nuclear recoils with the energy down to 5 keV," *Astroparticle Physics* **26** (2006) no. 1, 58 – 63. `arXiv:physics/0512136`.

[75] D. Akimov, *et al.*, "Measurements of scintillation efficiency and pulse shape for low energy recoils in liquid xenon," *Physics Letters B* **524** (2002) no. 3-4, 245 – 251. `[link]`.

[76] F. Arneodo, *et al.*, "Scintillation efficiency of nuclear recoil in liquid xenon," *Nuclear Instruments and Methods in Physics Research Section A: Accelerators, Spectrometers, Detectors and Associated Equipment* **449** (2000) no. 1-2, 147 – 157. `[link]`.

[77] E. Aprile *et al.*, "Scintillation response of liquid xenon to low energy nuclear recoils," *Phys. Rev.* **D72** (2005) 072006. `arXiv:astro-ph/0503621`.

[78] E. Aprile, *et al.*, "New measurement of the relative scintillation efficiency of xenon nuclear recoils below 10 keV," *Physical Review C (Nuclear Physics)* **79** (2009) no. 4, . `arXiv:0810.0274 [astro-ph]`.

[79] R. Bernabei, *et al.*, "Light response of a pure liquid Xenon scintillator irradiated with 2.5 MeV neutrons,"*EPJ direct* **3** (Mar., 2001) 1–8. `[link]`.

[80] A. Hitachi, "Properties of liquid xenon scintillation for dark matter searches," *Astroparticle Physics* **24** (2005) no. 3, 247 – 256. `[link]`.

[81] T. Shutt, *et al.*, "Performance and fundamental processes at low energy in a two-phase liquid xenon dark matter detector," *Nucl. Instrum. Meth.* **A579** (2007) 451–453. `arXiv:astro-ph/0608137`.

[82] A. Manzur, *Relative scintillation efficiency of liquid xenon in the XENON10 direct dark matter search.* PhD thesis, Yale University, 2009.

[83] R. Gomez, "Characterization of the Xenon-10 Dark Matter Detector with Regard to Electric Field and Light Response," Master's thesis, Rice University, 2007.

[84] M. Miyajima, S. Sasaki, and E. Shibamura, "Absolute number of photons produced by alpha-particles in liquid and gaseous xenon," *Nuclear Instruments and Methods in Physics Research Section B: Beam Interactions with Materials and Atoms* **63** (1992) no. 3, 297 – 308. `[link]`.

[85] M. Yamashita, *et al.*, "Scintillation response of liquid Xe surrounded by PTFE reflector for gamma rays," *Nuclear Instruments and Methods in Physics Research Section A: Accelerators, Spectrometers, Detectors and Associated Equipment* **535** (2004) no. 3, 692 – 698. `[link]`.

[86] CAEN SpA. http://www.caen.it/. `[link]`.

[87] Kyocera. http://global.kyocera.com/. `[link]`.

[88] A. Bolozdynya, *et al.*, "Cryogenics for the LUX detector," *IEEE Transactions on Nuclear Science* **Draft** (2008) , Draft, SORMA2008.

[89] H. M. Araújo, *et al.*, "Low-temperature study of 35 photomultiplier tubes for the ZEPLIN III experiment," *Nuclear Instruments and Methods in Physics Research Section A: Accelerators, Spectrometers, Detectors and Associated Equipment* **521** (2004) no. 2-3, 407 – 415. [link].

[90] Y. Ashie, "(in Japanese)," Master's thesis, University of Tokyo, 2004.

[91] Hamamatsu Photonics Co., "R8520 PMT data sheet," 2006.

[92] Struck Innovative Systems. http://www.struck.de/. [link].

[93] R. Dossi, *et al.*, "Methods for precise photoelectron counting with photomultipliers," *Nuclear Instruments and Methods in Physics Research Section A: Accelerators, Spectrometers, Detectors and Associated Equipment* **451** (2000) no. 3, 623 – 637. [link].

[94] J. Chapman. PhD thesis, Brown University, 2012.

[95] J. W. Marxh, D. J. Thomas, and M. Burke, "High resolution measurements of neutron energy spectra from Am-Be and Am-B neutron sources," *Nuclear Instruments and Methods in Physics Research Section A: Accelerators, Spectrometers, Detectors and Associated Equipment* **366** (1995) no. 2-3, 340–348. [link].

[96] J. Angle *et al.*, "Limits on spin-dependent WIMP-nucleon cross-sections from the XENON10 experiment," *Phys. Rev. Lett.* **101** (2008) 091301. arXiv:0805.2939 [astro-ph].

[97] G. Plante, *PhD Thesis*. PhD thesis, Columbia University, 2010.

[98] S. Yellin, "Finding an upper limit in the presence of an unknown background,"*Phys. Rev. D* **66** (Aug, 2002) 032005. [link].

[99] **CDMS** Collaboration, Z. Ahmed, *et al.*, "Search for Weakly Interacting Massive Particles with the First Five-Tower Data from the Cryogenic Dark Matter Search at

the Soudan Underground Laboratory," *Phys. Rev. Lett.* **102** (2009) no. 1, 011301. `arXiv:0802.3530`.

[100] R. Gaitskell, V. Mandic, and J. Filippini, "DMTools Dark Matter Results Plotter." http://dmtools.brown.edu. `[link]`.

[101] M. Herman, *et al.* http://www-nds.iaea.org/empire/. `[link]`.

[102] P. E. Hodgson, "The Optical Model of the Nucleon-Nucleus Interaction," *Annual Review of Nuclear Science* **17** (1967) no. 1, 1–32. `[link]`.

[103] S. Qingbiao and Z. Zhengjun, "to be published," *China Nuclear Data Center* .

[104] T. Belgya, *et al.*, "Handbook for calculations of nuclear reaction data,(RIPL-2)," Tech. Rep. IAEA-TECDOC-1506, International Atomic Energy Agency (IAEA), 2006. http://www-nds.iaea.org/RIPL-2/. `[link]`.

[105] M. Pigni, M. Herman, and P. Oblozinsky, "Low-fidelity covariances for neutron cross sections on 57 structural and 31 heavy nuclei in the fast region," Tech. Rep. BNL-79985-2008-IR, National Nuclear Data Center, Brookhaven National Laboratory, March, 2008. `[link]`.

[106] A. J. Koning and J. P. Delaroche, "Local and global nucleon optical models from 1 keV to 200 MeV," *Nuclear Physics A* **713** (2003) no. 3-4, 231 – 310. `[link]`.

[107] M. Attisha, *et al.*, "Soudan Low Background Counting Facility (SOLO)," vol. 785, pp. 75–78. AIP, 2005. `[link]`.

[108] C. Arpesella, "A low background counting facility at laboratori nazionali del Gran Sasso," *Applied Radiation and Isotopes* **47** (1996) no. 9-10, 991 – 996, Proceedings of the International Committee for Radionuclide Metrology Conference on Low-level Measurement Techniques. `[link]`.

[109] H. Neder, G. Heusser, and M. Laubenstein, "Low level [gamma]-ray germanium-spectrometer to measure very low primordial radionuclide

concentrations," *Applied Radiation and Isotopes* **53** (2000) no. 1-2, 191 – 195. [link].

[110] Fonderie de Gentilly, "http://www.fonderie-de-gentilly.com/.". [link].

[111] R. . H. D. . N. E. Smith, A.R. ; McDonald, "Capabilities and usage of the LBL low background counting facilities,"*Bulletin of the American Physical Society* **38** (Oct, 1993) , Fall meeting of the Division of Nuclear Physics of the American Physical Society, Pacific Grove, CA (United States), 20-23 Oct 1993.

[112] G. F. Knoll, *Radiation Detection and Measurement; 3rd ed.* John Wiley & Sons, New York, NY, 2000. 816 p.

[113] S. Chu, L. Ekström, and R. Firestone, "Table of Radioactive Isotope," 1, 2004. http://ie.lbl.gov/toi/. [link].

[114] J. K. Shultis and R. E. Faw, *Fundamentals of nuclear science and engineering.* CRC Press, 2002. [link]. pp. 137.

[115] D. Madland and J. Nix, "Prompt fission neutron spectra and average prompt neutron multiplicities," Conference LA-UR-83-3074; CONF-8310104-2, Los Alamos National Lab, Jan, 1983. Conference: Specialists meeting on yields and decay data of fission product nuclides, Upton, NY, USA, 24 Oct 1983.

[116] R. J. Howerton *et al.*, "Evaluated Nuclear Data Library (ENDL): Evaluation Techniques, Reaction Index, and Description of Individual Evaluations," Sept., 1975.

[117] H. Wulandari, *et al.*, "Neutron flux at the Gran Sasso underground laboratory revisited,"*Astroparticle Physics* **22** (Nov., 2004) 313–322. [link].

[118] H. R. Wulandari, *Study On Neutron-Induced Background in the Dark Matter Experiment CRESST.* PhD thesis, Institut fur Astro-Teilchenphysik der Technischen Universitat Munchen, June, 2003.

[119] R. Heaton, *et al.*, "Alpha-induced neutron activity in material," *Nucl. Geophys.* (1990) .

[120] ASTAR, "Stopping-power and Range Tables for Helium Ions." http://physics.nist.gov/PhysRefData/Star/Text/ASTAR.html. `[link]`.

[121] P. Belli, *et al.*, "Deep underground neutron flux measurement with large BF3 counters,"*Nuovo Cimento A Serie* **101** (June, 1989) 959–966. `[link]`.

[122] F. Arneodo *et al.*, "Neutron background measurements in the Hall C of the Gran Sasso Laboratory," *Nuovo Cim.* **A112** (1999) 819–831.

[123] R. Aleksan, *et al.*, "Measurement of fast neutrons in the Gran Sasso laboratory using a 6Li doped liquid scintillator," *Nuclear Instruments and Methods in Physics Research Section A: Accelerators, Spectrometers, Detectors and Associated Equipment* **274** (1989) no. 1-2, 203 – 206. `[link]`.

[124] E. Bellotti, *et al.*, "New Measurements of Rock Contaminations and Neutron Activity in the Gran Sasso Tunnel,", INFN/TC-85/19.

[125] A. Rindi, *et al.*, "Underground neutron flux measurement," *Nuclear Instruments and Methods in Physics Research Section A: Accelerators, Spectrometers, Detectors and Associated Equipment* **272** (1988) no. 3, 871 – 874. `[link]`.

[126] M. Cribler, *et al.*, "The neutron induced background in GALLEX," *Astroparticle Physics* **4** (1995) no. 1, 23 – 32. `[link]`.

[127] G. Luzón, "Neutron studies at The Canfranc Underground Laboratory," in *IDM2004, Edinburgh, September 2004.* 2004.

[128] T. K. Gaisser, *Cosmic rays and particle physics.* Cambridge Univ. Press, Cambridge, 1990. `[link]`.

[129] E. V. Bugaev, *et al.*, "Atmospheric muon flux at sea level, underground, and underwater,"*Phys. Rev. D* **58** (Jul, 1998) 054001. `[link]`.

[130] B. S. Meyer, *et al.*, "Cosmic-Ray Muon Intensity Deep Underground versus Depth,"*Phys. Rev. D* **1** (Apr, 1970) 2229–2244. `[link]`.

[131] D. Mei and A. Hime, "Muon-induced background study for underground laboratories," *Phys. Rev. D* **73** (2006) 053004. `arXiv:astro-ph/0512125`.

[132] D. E. Groom, N. V. Mokhov, and S. I. Striganov, "Muon Stopping Power and Range Tables 10 MeV-100 TeV,"*Atomic Data and Nuclear Data Tables* **78** (July, 2001) 183–356. `[link]`.

[133] P. H. Barrett, *et al.*, "Interpretation of Cosmic-Ray Measurements Far Underground,"*Rev. Mod. Phys.* **24** (Jul, 1952) 133–178. `[link]`.

[134] I. Rosenthal, "Interaction of cosmic muons of high energy,"*Soviet Physics - Uspekhi* **94** (January, 1968) 91–126.

[135] **MACRO** Collaboration, M. Ambrosio *et al.*, "Measurement of the residual energy of muons in the Gran Sasso underground laboratories," *Astropart. Phys.* **19** (2003) 313–328. `arXiv:hep-ex/0207043`.

[136] E.-I. Esch, *et al.*, "The cosmic ray muon flux at WIPP," *Nuclear Instruments and Methods in Physics Research Section A: Accelerators, Spectrometers, Detectors and Associated Equipment* **538** (2005) no. 1-3, 516 – 525. `[link]`.

[137] S. Kamat, *Extending the sensitivity to the detection of WIMP dark matter with an improved understanding of the limiting neutron backgrounds*. PhD thesis, Case Western Reserve University, 2005. FERMILAB-THESIS-2005-10.

[138] K. Eguchi, *et al.*, "First Results from KamLAND: Evidence for Reactor Antineutrino Disappearance,"*Phys. Rev. Lett.* **90** (Jan, 2003) 021802. `arXiv:hep-ex/0212021`.

[139] M. Robinson, *et al.*, "Measurements of muon flux at 1070 m vertical depth in the Boulby underground laboratory," *Nuclear Instruments and Methods in Physics Research Section A: Accelerators, Spectrometers, Detectors and Associated Equipment* **511** (2003) no. 3, 347 – 353. `[link]`.

[140] H. Wulandari, *et al.*, "Neutron background studies for the CRESST dark matter experiment,". `arXiv:hep-ex/0401032`.

[141] M. Cribier, *et al.*, "The muon induced background in the GALLEX experiment," *Astroparticle Physics* **6** (1997) no. 2, 129 – 141. [link].

[142] **SNO** Collaboration, C. Waltham, "Downward Muon Flux at the Sudbury Neutrino Observatory," in *XIX International Conference on Neutrino Physics & Astrophysics*. 2000. Sudbury, Canada, June 16 - 21.

[143] F. F. Khalchukov *et al.*, "Hadrons and other secondaries generated by cosmic ray muons underground," *Nuovo Cim.* **C18** (1995) 517–529. [link].

[144] V. A. Kudryavtsev, N. J. C. Spooner, and J. E. McMillan, "Simulations of muon-induced neutron flux at large depths underground," *Nuclear Instruments and Methods in Physics Research Section A: Accelerators, Spectrometers, Detectors and Associated Equipment* **505** (2003) no. 3, 688 – 698. [link].

[145] Y.-F. Wang, *et al.*, "Predicting neutron production from cosmic-ray muons," *Phys. Rev. D* **64** (Jun, 2001) 013012. [link].

[146] US Department of Energy, "US Department of Energy Report, 10 CFR Part 385," tech. rep., 1999. [link].

[147] N. Aoki and Y. Makide, "The Concentration of Krypton in the Atmosphere - Its Revision after Half a Century," *Chemistry Letters* **34** (2005) no. 10, 1396–1397.

[148] B. T. Cleveland, *et al.*, "Measurement of the Solar Electron Neutrino Flux with the Homestake Chlorine Detector," *The Astrophysical Journal* **496** (1998) no. 1, 505–526. [link].

[149] Hamamatsu Photonics Co. http://www.hamamatsu.com. [link].

[150] D. Mei and C. Zhang, "Neutron Yield in Materials," 2008. http://neutronyield.usd.edu/. [link].

[151] D. M. Mei, C. Zhang, and A. Hime, "Evaluation of (alpha,n) Induced Neutrons as a Background for Dark Matter Experiments," *Nucl. Instrum. Meth.* **A606** (2009) 651–660. arXiv:0812.4307 [nucl-ex].

[152] M. Carson, *et al.*, "Veto performance for large-scale xenon dark matter detectors," *Nuclear Instruments and Methods in Physics Research Section A: Accelerators, Spectrometers, Detectors and Associated Equipment* **548** (2005) no. 3, 418 – 426. [link].

[153] A. Smith, "Homestake (DUSEL) Samples - results of Radiometric Analyses at LBNL," tech. rep., LBNL, 2007.

[154] J. A. Formaggio and C. Martoff, "Backgrounds to sensitive experiments underground," *Annual Review of Nuclear and Particle Science* **54** (2004) no. 1, 361–412. [link].

[155] T. Trancynger, "Private Communication," 2008.

[156] A. M. Green, "Determining the WIMP mass from a single direct detection experiment; a more detailed study," *Journal of Cosmology and Astroparticle Physics* **2008** (2008) no. 07, 005 (18pp). [link].